

Uncertainties in the Estimation of the Shear-Wave Velocity and the Small-Strain Damping Ratio from Surface Wave Analysis

*Original*

Uncertainties in the Estimation of the Shear-Wave Velocity and the Small-Strain Damping Ratio from Surface Wave Analysis / Aimar, Mauro. - (2022 Oct 04), pp. 1-398.

*Availability:*

This version is available at: 11583/2972200 since: 2022-10-11T07:32:18Z

*Publisher:*

Politecnico di Torino

*Published*

DOI:

*Terms of use:*

openAccess

This article is made available under terms and conditions as specified in the corresponding bibliographic description in the repository

*Publisher copyright*

(Article begins on next page)



**Politecnico  
di Torino**

**ScuDo**

Scuola di Dottorato ~ Doctoral School

WHAT YOU ARE, TAKES YOU FAR

Doctoral Dissertation  
Doctoral Program in Civil and Environmental Engineering (34<sup>th</sup> Cycle)

# **Uncertainties in the estimation of the shear-wave velocity and the small-strain damping ratio from surface wave analysis**

**Mauro Aimar**

\*\*\*\*\*

**Supervisors:**

Prof. Sebastiano Foti

Prof. Brady R. Cox

**Doctoral Examination Committee:**

Prof. Clinton M. Wood, Referee, University of Arkansas (USA)

Dr. Paolo Bergamo, Referee, Swiss Seismological Service (Switzerland)

Prof. Renato M. Cosentini, Referee, Politecnico di Torino (Italy)

Prof. Geert Degrande, Referee, Katholieke Universiteit Leuven (Belgium)

Prof. Carlo G. Lai, Referee, University of Pavia (Italy)

Politecnico di Torino

2022

This dissertation is presented in partial fulfillment of the requirements for Ph.D. degree in the Graduate School of Politecnico di Torino (ScuDo).

This thesis is licensed under a Creative Commons License, Attribution - Noncommercial - NoDerivative Works 4.0 International: see [www.creativecommons.org](http://www.creativecommons.org). The text may be reproduced for non-commercial purposes, provided that credit is given to the original author.

I hereby declare that, the contents and organization of this dissertation constitute my own original work and does not compromise in any way the rights of third parties, including those relating to the security of personal data.

.....  
Mauro Aimar  
Torino, 2022

# Abstract

This dissertation deals with the in situ characterization of the small-strain shear-wave velocity and damping ratio from the interpretation of Multi-channel Analysis of Surface Waves (MASW) surveys. Indeed, low-strain parameters dramatically affect the ground response under dynamic loading. Due to their remarkable role, an in-situ estimate of these quantities is highly recommended. A promising way to obtain soil stiffness and dissipative parameters relies on the MASW scheme. This approach is based on the interpretation of the propagation characteristics of Rayleigh waves, namely the phase velocity and the phase attenuation.

The first goal of this research was to identify and quantify uncertainties affecting the estimated Rayleigh wave parameters, with a focus on phase attenuation. For this purpose, a suite of synthetic wavefields and in situ measurements were considered, thus obtaining a benchmark for understanding the issues in the estimate.

The study focused on modeling epistemic uncertainties affecting the Rayleigh phase attenuation. On the one side, the influence of the processing technique was addressed. In this context, a novel technique (named Frequency-Domain BeamForming-attenuation, FDBFa) is proposed. This technique incorporates an explicit modeling of the geometry of the wavefield, and it allows to isolate different Rayleigh propagation modes, through a filtering scheme. Therefore, it returns reliable attenuation estimates even in the presence of multi-mode wavefield, which is typical of complex stratigraphy conditions. Then, the study focused on the sensitivity of the Rayleigh wave parameters to the acquisition setup, in terms of the type of the active source and the recording device. As for source characteristics, results show that low-energy sources (e.g., a sledgehammer) return reliable estimates of the phase velocity and attenuation, albeit with larger variability. This result demonstrates the possibility of retrieving reliable attenuation data also in ordinary MASW surveys, in which the sledgehammer is commonly used. As for the sensing device, estimated phase velocity and phase attenuation data obtained from geophone and fiber-optic DAS data were compared. The latter represents an innovative technology in seismic measurements and monitoring, of which use in geophysics is still limited but promising. Indeed, also existing fiber-optic networks for telecommunication can be used for the acquisition of seismic data. The high degree of matching between observed data demonstrated that the DAS technology can be successfully used to jointly estimate the phase dispersion and attenuation data, obtaining the same level of reliability as an “ordinary” geophone array.

Furthermore, this dissertation proposed a statistical scheme to model aleatory variabilities in the estimated phase velocity and attenuation data. Indeed, various models have been proposed to quantify the dispersion variability, whereas no scheme was explicitly demonstrated for attenuation data. The model describes the variability in experimental data according to a bivariate lognormal distribution, although the observed low correlation allows using lognormal marginals for the statistical characterization. The lognormal scheme is preferred to the Gaussian model to describe highly variable data (as the phase attenuation) without including negative values. This assumption ensures greater consistency, from the physical point of view.

Then, the research focused on mapping the experimental Rayleigh wave parameters into soil models describing the profiles of shear-wave velocity and damping ratio with depth. A robust inversion algorithm was developed for this purpose. This technique is a Monte Carlo, global search algorithm, which implements a smart sampling procedure. This scheme exploits the scaling properties of the solution of the Rayleigh eigenvalue problem to modify the trial earth models and improve the matching with the experimental model. Thus, a reliable result can be achieved with a moderately small number of trial ground models. In general, estimated soil models exhibit well-defined shear-wave velocity profiles, whereas the damping ratio profile is affected by remarkably large scatter, although a trend can still be identified. This difference is the effect of the high variability characterizing experimental attenuation data, the limited wavelength range at which reliable values of these parameters can be retrieved, and the sensitivity of attenuation data to both damping ratio and the S-wave velocity. However, the resulting response to the ground motion is affected by moderately small variability, and it consistently matches in situ observed data. The result stresses the effectiveness of using damping ratio estimates from in situ surface wave data, as an alternative to other characterization techniques.

Overall, this research shows the feasibility of retrieving both stiffness and attenuation parameters from surface wave testing, highlighting also the issues related to the uncertainties and the different level of reliability affecting these two quantities. In general, great care is required when modeling the geometric features and the multi-mode nature of the wavefield, as well as model incompatibility effects. Indeed, these features dramatically affect the estimated attenuation. On the other side, under proper modeling of wavefield conditions and adopting robust inversion procedures, a reliable and accurate prediction of the actual behavior can be achieved.

# Acknowledgement



# Contents

Chapter 1 Introduction .....	1
1.1 Motivation .....	1
1.2 Research objectives and achievements .....	2
1.3 Dissertation outline .....	3
Chapter 2 Small-strain damping ratio .....	7
2.1 Response of soils to cyclic actions .....	7
2.1.1 Experimental evidence .....	7
2.1.2 Models .....	9
2.2 Parameters affecting the small-strain damping ratio .....	14
2.2.1 Loading frequency .....	15
2.2.2 Material parameters .....	18
2.2.3 Typical values of the small-strain damping ratio .....	20
2.3 Role of the small-strain damping ratio .....	24
2.3.1 Seismic site response .....	24
2.3.2 Ground vibrations .....	31
2.3.3 Dynamic soil-structure interaction .....	36
Chapter 3 Wave propagation .....	39
3.1 Body waves .....	41
3.1.1 Body waves in linear elastic media .....	41
3.1.2 Body waves in linear viscoelastic media .....	46
3.2 Surface waves .....	49
3.2.1 Rayleigh waves in isotropic, linear elastic media .....	50
3.2.2 Rayleigh waves in linear viscoelastic media .....	55
3.3 The source problem .....	59
3.4 Mechanisms of wave attenuation .....	65
Chapter 4 Experimental methods .....	69
4.1 Laboratory tests .....	70
4.1.1 Resonant column test .....	70



4.1.2 Cyclic tests.....	73
4.2 In situ geophysical tests: invasive methods .....	75
4.2.1 Cross-hole testing .....	76
4.2.2 Down-hole testing.....	78
4.3 In situ geophysical tests: non-invasive methods.....	81
4.3.1 Multichannel Analysis of Surface Waves (MASW) .....	84
4.3.1.1 Regression techniques .....	85
4.3.1.2 Maximum likelihood parameter estimation procedures.....	88
4.3.1.3 Transform-based techniques .....	90
4.3.2 Ambient vibration analysis .....	94
4.4 Back-analysis of downhole arrays .....	98
4.4.1 Seismogram inversion methods.....	99
4.4.2 $\kappa$ -informed damping estimation.....	101
4.4.3 Amplification analysis.....	103
4.4.4 Issues in the interpretation of downhole arrays .....	105
4.5 Laboratory vs. in situ estimates.....	108
Chapter 5 Novel processing approaches .....	111
5.1 Synthetic wavefields .....	111
5.2 Processing methods.....	117
5.2.1 The frequency-domain beamforming technique.....	117
5.2.2 Frequency-Domain BeamForming – Attenuation (FDBFa).....	120
5.2.3 Cylindrical Frequency-Domain BeamForming –Attenuation (CFDBFa).....	123
5.2.4 Applications.....	127
5.3 Dealing with multiple modes .....	131
5.3.1 Application to synthetic models .....	131
5.3.2 Proposed filtering technique .....	137
5.3.3 Applications.....	143
5.4 Influence of near- and far-field effects .....	150
5.4.1 Influence of the cylindrical shape of the wavefront .....	151
5.4.2 Influence of body waves: results for SW3 and SW4.....	154
5.4.3 Influence of body waves: parametric analysis.....	156

5.4.4 Influence of incoherent noise .....	163
5.5 Summary .....	169
Chapter 6 Surface wave datasets .....	171
6.1 Garner Valley Downhole Array .....	172
6.1.1 Site description .....	172
6.1.2 Previous geophysical studies .....	175
6.1.3 MASW survey .....	178
6.2 Hornsby Bend .....	180
6.2.1 Site description and previous geophysical studies .....	180
6.2.2 MASW survey .....	184
6.2.2.1 <i>First round of testing</i> .....	184
6.2.2.2 <i>Second round of testing</i> .....	186
Chapter 7 Uncertainties in dispersion and attenuation estimates .....	189
7.1 Inter-method differences .....	191
7.1.1 Synthetic data .....	192
7.1.1.1 <i>Results for SW3</i> .....	193
7.1.1.2 <i>Results for SW4</i> .....	197
7.1.2 Field data: Garner Valley Downhole Array .....	200
7.1.3 Field data: Hornsby Bend .....	205
7.2 Influence of source characteristics .....	212
7.2.1 Source characteristics .....	213
7.2.2 Source comparison .....	216
7.3 Influence of receiver characteristics: geophones vs. distributed acoustic sensing .....	220
7.3.1 The DAS technique .....	220
7.3.2 Principles of processing DAS data .....	221
7.3.3 Data processing at Hornsby Bend .....	228
7.4 Variability in dispersion and attenuation data .....	231
7.5 Summary .....	240
Chapter 8 Joint inversion of dispersion and attenuation data .....	243

8.1 The inversion problem .....	243
8.2 Target function .....	247
8.3 Model parameter space .....	249
8.4 A Monte Carlo algorithm for the joint inversion .....	253
8.4.1 Monte Carlo sampling .....	253
8.4.2 Misfit function .....	254
8.4.3 Scaling properties of the forward problem .....	256
8.4.3.1 Description of the scaling properties .....	257
8.4.3.2 Implementation of the scaling properties in the inversion algorithm .....	260
8.4.4 Inversion results .....	262
8.5 Summary .....	264
Chapter 9 Influence of the small-strain damping ratio on ground site analyses ..	267
9.1 Application of surface wave methods for ground response analyses	267
9.2 Case Study: Garner Valley Downhole Array .....	268
9.2.1 Derivation of S-wave velocity and damping ratio profiles .....	268
9.2.2 Variability of the derived ground models .....	272
9.2.3 Comparison with alternative models .....	273
9.2.4 Modeling of the ground response .....	275
Chapter 10 Conclusions and Recommendations .....	279
10.1 Conclusions .....	280
10.2 Recommendations for future research .....	286
Appendix A Frequency-domain beamforming attenuation: some technical aspects .....	289
A.1 Side lobes in FDBFa pseudospectrum .....	289
A.2 Basic concepts of digital filtering .....	291
A.3 Symmetry of complex filters .....	297
A.4 Calibration study of the FDBFaMF and the CFDBFaMF .....	298
A.4.1 Results for SW3 - FDBFaMF .....	300
A.4.2 Results for SW3 - CFDBFaMF .....	303
A.4.3 Results for SW4 - FDBFaMF .....	306
A.4.4 Results for SW4 - CFDBFaMF .....	309
Appendix B Implementation details of other SWM processing methods .....	313

B.1 Transfer function method .....	313
B.2 Wavefield decomposition approach .....	315
B.3 Generalized Half-Power Bandwidth and Circle Fit Methods .....	317
Appendix C Scaling properties of the solution of the forward Rayleigh problem .....	325
C.1 Layer velocities .....	328
C.2 Layer thicknesses .....	329
C.3 Layer damping ratios.....	330
References.....	333

# Index of figures

- Figure 2-1. a) Example of stress-strain loops of a geomaterial under cyclic loading, represented in the  $\tau$ - $\gamma$  domain, where  $\tau$  and  $\gamma$  are the shear stress and the shear strain, respectively. b-d) Variations in the loop geometry at increasing level of cyclic strain amplitude  $\gamma_c$  and the number of cycles  $N$  (modified from Lanzo and Silvestri, 1999). In the plots,  $\gamma_l$  is the linear cyclic threshold shear strain,  $\gamma_v$  is the volumetric cyclic threshold shear strain and  $N_1$  and  $N_2$  are two values for  $N$ . ..... 9
- Figure 2-2. Mechanical model of the Kelvin-Voigt (b) and Maxwell (c) solid, to represent the behavior of a soil element under uniaxial shear loading, represented by the shear stress  $\tau$  (a). The elastic component of the response is synthesized by a linear spring with stiffness  $G$ , whereas a viscous dashpot with viscosity  $\eta$  models the viscous component. .... 11
- Figure 2-3. Mechanical response under shearing of the isotropic, linear viscoelastic medium, represented in the  $\tau$ - $\gamma$  domain, where  $\tau$  and  $\gamma$  are the shear stress and the shear strain, respectively. At a fixed level of cyclic shear stress amplitude  $\tau_c$ , the response can be modelled as an elliptical loop with maximum absolute ordinate equal to the cyclic shear stress amplitude  $\tau_c$ . The average slope is the secant shear stiffness  $G$ . Instead, the area  $W_D$  enclosed within the loop describes the dissipated energy and  $W_E$  corresponds to the maximum elastic stored energy. .... 12
- Figure 2-4. Normalized modulus reduction and damping curves, describing variations of the normalized shear modulus  $G/G_{max}$  and damping ratio  $D_S$  as a function of the shear strain  $\gamma$ . The influence of the number of cycles  $N$  is included. The plot also highlights the location of the linear cyclic threshold shear strain  $\gamma_l$ , the volumetric cyclic threshold shear strain  $\gamma_v$  and the small-strain shear damping ratio  $D_{S,0}$  (modified from Lanzo and Vucetic, 1999) ..... 14
- Figure 2-5. a) Effect of loading frequency  $f$  on the small-strain damping ratio  $D_{S,0}$  of cohesive soils (modified from Shibuya et al., 1995); b) Effect of the loading frequency on the small-strain shear modulus  $G_{max}$  and damping ratio  $D_{S,0}$  for cohesive soils, as a function of the plasticity index  $PI$ . To highlight the influence of  $f$ , these parameters are normalized by the corresponding values measured at  $f = 1$  Hz, namely  $G_{max}^{1\text{ Hz}}$  and  $D_{S,0}^{1\text{ Hz}}$  (modified from Stokoe and Santamarina, 2000). ..... 16

Figure 2-6. Effect of the loading frequency $f$ on the small-strain shear modulus $G_{max}$ and damping ratio $D_{S,0}$ for saturated, gravelly soils, as a function of the plasticity index $PI$ . To highlight the influence of $f$ , these parameters are normalized by the corresponding values measured at $f = 1$ Hz, namely $G_{max}^{1\text{ Hz}}$ and $D_{S,0}^{1\text{ Hz}}$ (after Menq, 2003).	17
Figure 2-7. Relationship between plasticity index $PI$ and small-strain shear damping ratio $D_{S,0}^{1\text{ atm}}$ (normalized to the atmospheric pressure; after Zhang et al., 2005).	19
Figure 2-8. a) Effect of the confining pressure $\sigma'_m$ on the small-strain damping ratio $D_{S,0}$ in dry granular materials (after Laird, 1994); b) Effect of the moisture content on $D_{S,0}$ in granular materials. The saturated stage corresponds to a water content equal to 14.4% (after Menq, 2003).	20
Figure 2-9. a-c) Empirical estimates of the mean value of the small-strain damping ratio $D_{S,0}$ as a function of the plasticity index $PI$ , for confining pressures equal to 50 kPa (a), 300 kPa (b) and 1,000 kPa (c); a-c) Empirical estimates of the coefficient of variation (CoV) of $D_{S,0}$ as a function of $PI$ , for confining pressures equal to 50 kPa (a), 300 kPa (b) and 1,000 kPa (c).	22
Figure 2-10. Empirical estimates of the mean (a) and the coefficient of variation (CoV - b) of the small-strain damping ratio $D_{S,0}$ as a function of the mean confining stress $\sigma'_m$ for gravels and sands.	23
Figure 2-11. Distinction between source, path and site effects in propagating seismic waves (modified from Passeri, 2019). The plot highlights the motion recorded in the reference geological condition, represented in terms of the Fourier spectrum of the ground acceleration $\ddot{u}_{g,o}(f)$ and the elastic response spectrum $S_{e,o}(T)$ , and the motion inside the soil deposit, represented in terms of $\ddot{u}_g(f,\mathbf{x})$ and $S_e(T,\mathbf{x})$ .	25
Figure 2-12. a-b) Mean amplification factor AF vs. period $T$ for moderately stiff (a) and deformable (b) soil deposits, as a function of the additional damping contribution $\Delta D$ and seismicity level; c-d) Standard deviation (in logarithmic scale) of the AF $\sigma_{\ln(AF)}$ vs. $T$ for moderately stiff (a) and deformable (b) soil deposits, as a function of $\Delta D$ and the seismicity level (after Foti et al., 2021).	29
Figure 2-13. Comparison between the distribution of the amplification factor AF, obtained by varying the S-wave velocity $V_S$ and the MRD curves (represented in terms of $\mu \pm \sigma$ interval), and the AF curves as function of the additional damping contribution $\Delta D$ for (a) low-intensity motions and (b) high-intensity motions (after Foti et al., 2021).	30

Figure 2-14. Logic tree used for the analysis of the effect of epistemic uncertainties in GRAs (after Rodriguez-Marek et al., 2021).....	31
Figure 2-15. Sensitivity of the mean amplification factor AF to the various parameters involved in the logic tree (Figure 2-14), as a function of the investigated vibration period $T$ : 0.1 s (a) and 1.0 s (b). The size of each symbol is proportional to the weight assigned to the corresponding branch (after Rodriguez-Marek et al., 2021).....	31
Figure 2-16. Schematic representation of the propagation of ground-borne vibrations (after Lai and Özcebe, 2015).....	33
Figure 2-17. a-c) Parametric study with reference to the shear modulus: a) Probability density distribution; Ten realizations (grey lines) and 95% confidence regions (shaded area) of the transfer function amplitude for a receiver located at 4 m (b) and 32 m (c) from the source; d-f) Parametric study with reference to the shear damping ratio: d) Probability density distribution; Ten realizations (grey lines) and 95% confidence regions (shaded area) of the transfer function amplitude for a receiver located at 4 m (e) and 32 m (f) from the source. Darker lines correspond to higher values of the investigated parameter (after Schevenels, 2007). .....	35
Figure 2-18. a-b) Representative S-wave velocity $V_S$ and small-strain damping ratio $D_{S,0}$ profiles; c) Measured (solid line) vs. predicted (dashed line) vertical displacement transfer function $u$ at the ground floor of the target building. The grey solid lines denoted realizations for different soil profiles (after Papadopoulos et al., 2019). .....	36
Figure 3-1. a-b) Propagation of a nondispersive wave (a) and of a dispersive wave (b). c) Distinction between phase velocity $V$ and group velocity $V_g$ (modified from Foti et al., 2014).....	40
Figure 3-2. a) Variation of the ratio between P- and S-wave velocities $V_P/V_S$ as a function of the Poisson's ratio $\nu$ ; b) Variation of the P- and S-wave velocities in sandy specimens as a function of the saturation degree, quantified through the Skempton's $B$ -value (after Valle-Molina, 2006). .....	43
Figure 3-3. Space-time variation of the displacement field $u_\chi(x,t)$ induced by a body wave with amplitude $A$ propagating in an elastic body, in 1D conditions. The top portion shows the spatial variation of body waves, at a fixed time instant $t_0$ , characterized by the wavelength $\lambda_\chi$ . Instead, the left part represents the time variation, at a fixed location $x_0$ , characterized by the vibration period $T$ . .....	44

Figure 3-4. a) Wave components involved in the interaction of a body wave with a material interface between two media characterized by mass density and S-wave velocity equal to $\rho_1$ and $V_{\chi,1}$ , and $\rho_2$ and $V_{\chi,2}$ . These components are represented in terms of their amplitudes: $A_i$ (for the incident wave), $A_t$ (for the transmitted wave), and $A_r$ (for the reflected wave); b) Variations of $A_r$ and $A_t$ (normalized with respect to $A_i$ ) as a function of the impedance ratio $\alpha_{z,\chi}$ . .....	45
Figure 3-5. a) Ratio between viscoelastic and elastic velocities $ \mathcal{V}_\chi/V_\chi $ computed according to the exact and approximate damping relationships, as a function of the damping ratio $D_\chi$ (modified from Foti et al., 2014); b) Dispersion relationship for the body wave velocity ratio $V_\chi(\omega)/V_\chi(\omega_{ref})$ in hysteretic media (i.e., frequency-independent damping ratio), as a function of $D_\chi$ and the frequency $f$ . .....	48
Figure 3-6. Space-time variation of the displacement field $u_\chi(x,t)$ induced by a body wave with initial amplitude $A$ propagating in linear, viscoelastic medium, in 1D conditions. The top portion shows the spatial variation of body waves, at a fixed time instant $t_0$ , characterized by the wavelength $\lambda_\chi$ and amplitude decay $Ae^{-\alpha_\chi x}$ . Instead, the left part represents the time variation, at a fixed location $x_0$ , characterized by the vibration period $T$ and amplitude $Ae^{-\alpha_\chi x_0}$ . .....	49
Figure 3-7. Rayleigh waves and Love waves. ....	50
Figure 3-8. Variation of the horizontal and vertical displacement amplitude $ u(z) $ , normalized with respect to the motion amplitude at the surface $ u(0) $ , as a function of the depth $z$ (normalized with respect to the wavelength $\lambda$ ) and the Poisson's ratio $\nu$ (modified from Richart et al., 1970). ....	52
Figure 3-9. Scheme of layered linear elastic halfspace. ....	53
Figure 3-10. Physical interpretation of the geometrical dispersion of Rayleigh waves in layered linear elastic media: a) Qualitative sketch of the vertical displacement amplitude versus depth for three wavelengths $\lambda_1$ , $\lambda_2$ and $\lambda_3$ in a two-layer medium, with S-wave velocities $V_{S,A}$ and $V_{S,B}$ ; b) Dispersion curve in the phase velocity-wavelength $V_R - \lambda_R$ domain; c) Dispersion curve in the phase velocity-frequency $V_R - f$ domain (after Foti et al., 2018). ....	54
Figure 3-11. Example of Rayleigh dispersion curves for a layered linear elastic medium: a) Layered model, represented as S-wave velocity profile $V_S$ with depth $z$ ; b) Dispersion curves for the model in a), represented as R-wave phase velocity $V_R$ vs. frequency $f$ ; c) Horizontal and vertical	



	Rayleigh displacement eigenfunctions, at $f = 20$ Hz. Data reported in b) and c) refer to the first 4 modes, labeled as R0, R1, R2, and R3, respectively. ....	55
Figure 3-12.	Solutions of the characteristic equation in a layered linear viscoelastic medium: a-b) Profiles of S-wave velocity $V_S$ and damping ratio $D_S$ with depth of $z$ ; c-d) Modal dispersion and attenuation curves in terms of real wavenumber $k_R$ and attenuation $\alpha_R$ versus frequency $f$ ; e-f) Modal dispersion and attenuation curves in terms of phase velocity $V_{R,j}$ and phase damping ratio $D_{R,j}$ versus $f$ . ..	57
Figure 3-13.	Rayleigh particle displacement orbits at the free surface of a layered, linear viscoelastic half-space, at given frequencies $f$ and distances $r$ (after Foti et al., 2014). ....	59
Figure 3-14.	a) Scheme of the Lamb's problem, specifying the input force $F e^{i\omega t}$ and the distance from the source $r$ ; b) Geometry of wavefronts of body and surface waves generated from a source on the free surface (modified from Miller and Pursey, 1955). ....	59
Figure 3-15.	Amplitude $ u_z $ and phase $\arg u_z$ of the vertical displacement field of Rayleigh waves in a homogeneous elastic medium, as a function of the distance $r$ . ....	61
Figure 3-16.	Geometrical spreading function $\mathcal{Y}_z$ for the vertical displacement versus distance $r$ , computed for different types of half-space at a frequency $f$ equal to 7 Hz (a) and 90 Hz (b – after Foti et al., 2014). 63	
Figure 3-17.	Geometrical interpretation of the effective phase velocity $V_R^{app}$ (a) and of the effective phase attenuation $\alpha_R^{app}$ (b) at the distance $r_1$ . The graphs represent a) the spatial variation of the phase of the displacement field $\arg u(r, \omega)$ and b) the spatial variation of the logarithm of the amplitude $ u(r, \omega) $ corrected by the geometric spreading $\mathcal{Y}_z(r, \omega)$ . From these two quantities, both the effective wavenumber $k_R^{app}$ (hence, $V_R^{app}$ ) and $\alpha_R^{app}$ can be derived (after Lai and Rix, 1998b). ....	65
Figure 3-18.	a) Comparison between the geometrical attenuation (black line) and the intrinsic attenuation for a homogeneous halfspace (grey lines), computed from the geometric spreading function and Eq. 3.53, respectively. Data refer to frequencies equal to 10 Hz, 30 Hz, 50 Hz, and 70 Hz (from thick to thin grey line). b) Comparison between the geometrical attenuation (black lines) and the intrinsic attenuation for a normally dispersive medium, computed from the geometric spreading function and Eq. 3.53, respectively. Data refer to	

	frequencies equal to 10 Hz, 30 Hz, 50 Hz, and 70 Hz (from thick to thin grey line). Information about the soil model is available in Badsar (2012). .....	67
Figure 4-1.	a) Basic scheme of a RC test device, modified from Woods (1978); b-c) Typical results of a RC test: (b) output rotation amplitude $ \theta $ vs frequency $f$ curve; (c) free-vibration decay plot (modified from Foti et al., 2021). .....	71
Figure 4-2.	Results of a N-RC test: a) Estimated shear modulus $G$ and b) small-strain shear damping ratio $D_{s,0}$ , as a function of the loading frequency $f$ for a remolded kaolinite sample (after Rix and Meng, 2005). .....	73
Figure 4-3.	a-b) Idealized stress-strain loops measured in the deviatoric stress-axial strain $\sigma_d - \varepsilon_a$ plane in a CTx test (a) and in the shear stress-shear strain $\tau - \gamma$ plane in a CTS test (b); c) real loop measured in a CTS test at small strains (after Foti et al., 2021). .....	75
Figure 4-4.	a) Scheme of the CHT layout; b) resulting S-wave velocity $V_S$ and damping ratio $D_S$ curves versus frequency $f$ from the interpretation of CHT data (modified from Lai and Özcebe, 2015). .....	78
Figure 4-5.	a) Scheme of the DHT layout; b) Scheme of the SCPT layout, using a dual cone. ....	79
Figure 4-6.	Results from a SCPT survey: a) estimated S-wave velocity profile $V_S$ ; b) estimated S-wave small-strain damping ratio profile $D_{s,0}$ , according to the SRS method (after Karl et al., 2006). .....	80
Figure 4-7.	Application of the fitting of the Arias intensity on a synthetic case to derive the damping ratio profile: a) S-wave velocity profile; b) Original (thick grey curve) versus calibrated (thin black curve) damping ratio profile; c) Comparison between the experimental (thick grey curve) and the theoretical (thin black curve) normalized Arias intensity, i.e. ratio Arias intensity-experimental Arias intensity (modified from Badsar, 2012). .....	81
Figure 4-8.	Main steps of a SWM survey (after Foti et al., 2014; Passeri, 2019) .	83
Figure 4-9.	Investigated volumes in invasive tests and SWM (after Passeri, 2019) .....	84
Figure 4-10.	Scheme of the MASW setup, where the vertical displacement $u_z$ induced by an input force (e.g., a harmonic force $Fe^{i\omega t}$ ) is recorded by various sensors with varying distance $r$ . .....	85
Figure 4-11.	Regression of the experimental transfer function $T(r,\omega)$ with the distance $r$ for the coupled computation of dispersion and attenuation curves: (a) phase; (b) amplitude; (c) real part; (d) imaginary part. Data	

	refer to the Pisa Leaning Tower site, at the frequency of 11.5 Hz (modified from Foti, 2003). .....	88
Figure 4-12.	Application of the WaveDec approach for a synthetic case: a-b) S-wave velocity $V_S$ and small-strain damping ratio $D_{S,0}$ profiles; c) Acquisition layout; d) Estimated dispersion curve; e) Estimated attenuation curves; f) Estimated Rayleigh wave ellipticity (after Bergamo et al., 2019). .....	90
Figure 4-13.	Generalized half-power bandwidth method: a) Definition of the reference bandwidth $\Delta k_{R,j}$ from the spectrum of the experimental displacement transfer function $T(r,\omega)$ ; b) Performance of the classical half-power bandwidth vs. GHPB in the presence of multiple propagation modes. ....	92
Figure 4-14.	Application of the CFM scheme to identify the modal wavenumber $k_{Re,j}$ (hence, $V_R$ ) and $\alpha_R$ for a synthetic case, with a focus on the dominant mode: a) $f$ - $k$ spectrum of the particle displacement function, for a given frequency; b) Nyquist plot of the $f$ - $k$ spectrum of the particle displacement function. The dominant mode corresponds to the greatest circle and $k_{Re,j}$ is identified as the $k_t$ value at which the relative distance between subsequent points in the Nyquist plot is maximum. The plot highlights values corresponding to two wavenumber sample points $k_{t,a}$ and $k_{t,b}$ , that are used to compute $\alpha_R$ . The corresponding angles $\vartheta(k_{t,a})$ and $\vartheta(k_{t,b})$ are computed from the line connecting $k_{Re,j}$ and the circle center, and they increase according to the direction of growing $k_t$ . ....	93
Figure 4-15.	Acquisition layout for the SPAC method. ....	95
Figure 4-16.	a-c) Results of the grid search procedure in the velocity-attenuation domain, represented as pseudocolor plot mapping the normalized fit value, measured as $RMSE_{min}/RMSE$ , where RMSE is the root mean square error. White triangles identify the best fit values. Data refer to frequencies of a) 3.25 Hz, b) 5.61 Hz, and c) 10.16 Hz. d-f) Measured SPAC values (black dots) versus best-fitting functions considering attenuation (solid line) and ignoring attenuation (dashed line). Grey dots denote the SPAC values discarded in the fitting procedure. Data refer to frequencies of d) 3.25 Hz, e) 5.61 Hz, and f) 10.16 Hz. g) Obtained Rayleigh wave dispersion curve $V_R(\omega)$ . h) Obtained Rayleigh wave attenuation curve. Grey dots denote the theoretical $\alpha_R(\omega)$ resulting from an inversion procedure, which has not been reported for simplicity (after Parolai, 2014). ....	97

Figure 4-17. a-c) Obtained soil profiles in terms of S-wave velocity $V_S$ (a), small strain damping ratio $D_S$ (expressed as the reciprocal of the quality factor $Q$ , namely $1/Q = 2D_S$ ), (b) and mass density $\rho$ (c) in Asimaki et al. (2008). The dotted lines are the profiles obtained from geotechnical data, whereas the solid lines represent the results of the inversion procedure. d-g) Matching between observed and simulated time histories. ....	100
Figure 4-18. a) Definition of the spectral decay parameter (after Askan et al., 2014); b) Variation of the spectral decay between surface and borehole measurements (after Cabas et al., 2017). ....	101
Figure 4-19. Example of S-wave velocity $V_S$ profile and $\kappa$ -informed damping ratio $D_S$ profile (after Afshari and Stewart, 2019). ....	103
Figure 4-20. Application of the amplification analysis at the Garner Valley site: a) S-wave velocity $V_S$ profile; b) Calibration of the small-strain damping ratio $D_{S,0}$ profile; c) Comparison between theoretical and observed transfer function TF (after Tao and Rathje, 2019). ....	105
Figure 4-21. Obtained damping multipliers in Tao and Rathje (2019), at four sites: Garner Valley (GV), EuroseisTest (EST), Treasure Island (TI) and Delaney Park (DP). Multipliers are estimated based on the transfer function TF, the amplification function AF, the peak ground acceleration PGA or velocity PGV, the Arias intensity $I_a$ , the high-frequency attenuation $\kappa$ . ....	107
Figure 4-22. a) Comparison between the SWM-based and the laboratory-based small-strain damping ratio $D_{S,0}$ profile at the Pisa Leaning Tower site (modified from Foti, 2003); b) Comparison between the SCPT-based and the laboratory-based $D_{S,0}$ profile at a site in Belgium (after Karl et al., 2006). ....	109
Figure 5-1. Simulated planar and cylindrical waves (labeled as SW1 and SW2, respectively), described in terms of particle displacement: spatial variation of a) amplitude and b) phase. ....	113
Figure 5-2. Ricker pulse simulating the input force for SW3 and SW4: a) time history; b) Frequency content. ....	114
Figure 5-3. Main characteristics of the synthetic wavefield SW3: a-d) Reference ground model, described in terms of the S-wave velocity (a) and damping ratio (b); R-wave phase velocity curves (c) and phase attenuation curves (d); Time-domain traces (e) and $f$ - $k$ spectrum, where each mode is identified by the white patterns (f). To better	

	visualize spectral peaks corresponding to each propagation mode, the $f$ - $k$ spectrum is normalized frequency by frequency. ....	115
Figure 5-4.	Main characteristics of the synthetic wavefield SW4: a-d) Reference ground model, described in terms of the S-wave velocity (a) and damping ratio (b); R-wave phase velocity curves (c) and phase attenuation curves (d); Time-domain traces (e) and $f$ - $k$ spectrum, where each mode is identified by the white patterns (f). To better visualize spectral peaks corresponding to each propagation mode, the $f$ - $k$ spectrum is normalized frequency by frequency. ....	116
Figure 5-5.	Application of the FDBF for the dispersion analysis of SW3: a) pseudopower $P_{BF}(k_t, \omega)$ in the $f$ - $k$ spectrum domain; b) Cross-section of $P_{BF}(k_t, \omega)$ at the circular frequency $\omega_0$ . ....	118
Figure 5-6.	Application of the CFDBF for the dispersion analysis of SW3: a) pseudopower $P_{CBF}(k_t, \omega)$ in the $f$ - $k$ spectrum domain; b) Cross-section of $P_{CBF}(k_t, \omega)$ at the circular frequency $\omega_0$ . ....	119
Figure 5-7.	a-b) Original planar wave, in terms of a) log-amplitude and b) phase; c-d) Transformed wave, in terms of c) log-amplitude and d) phase; e) Pseudospectrum of the transformed wave, where the location of the spectral maximum $\alpha_e$ is compared with $\alpha$ . ....	121
Figure 5-8.	Effect of the tapering window on the pseudospectrum $P_{BFd}(\alpha_t)$ , computed for SW1. The tapering is carried out by means of a spatial Hanning window. The plot also includes a zoomed view to show the comparison between the peak location (the grey circle) and the theoretical attenuation $\alpha = 0.0015$ rad/m. ....	122
Figure 5-9.	Effect of phase wrapping on the pseudospectrum $P_{BFd}(\alpha_t)$ , computed for SW1: a-b) Original planar wave, in terms of a) log-amplitude and b) phase; c-d) Transformed wave, in terms of c) log-amplitude and d) phase; e) Pseudospectrum of the transformed wave. The plot also includes a zoomed view where the location of the spectral maximum $\alpha_e$ (the grey circle) is compared with the theoretical attenuation $\alpha = 0.0015$ rad/m. ....	123
Figure 5-10.	a-b) Original cylindrical wave, in terms of a) log-amplitude and b) phase; c-d) Transformed wave, in terms of c) log-amplitude and d) phase; e) Pseudospectrum of the transformed wave, where the location of the spectral maximum $\alpha_e$ is compared with $\alpha$ . ....	125
Figure 5-11.	a) Influence of the chosen wavenumber $k_{ref}$ on the estimated attenuation $\alpha_e$ in the CFDBFa; b-c) Amplitudes of the cylindrical waves corresponding to three different $k_{ref}$ values, represented in	

terms of b) amplitudes and c) logarithmic amplitudes normalized by the geometrical spreading factor. The parameter  $\Delta$  shifts the curves in c) and e) so that they share the same end point, thus facilitating the comparison of relative variations in the space. Data refer to SW2.. 127

- Figure 5-12. Typical ranges of the a) R-wave wavenumber  $k_R(\omega)$  and b) R-wave phase attenuation  $\alpha_R(\omega)$  as a function of the frequency..... 131
- Figure 5-13. Application of the FDBFa to the wavefield  $u_{pp}(r)$ : a-b) Wave components  $u_{p1}(r)$  and  $u_{p2}(r)$  and total wavefield  $u_{pp}(r)$ , in terms of a) amplitude and b) phase; c) Pseudopower spectrum of  $u_{pp}(r)$ , obtained by means of the FDBF; d) Pseudopower spectrum of  $u_{pp}(r)$ , obtained by means of the FDBFa. .... 133
- Figure 5-14. Application of the CFDBFa to the wavefield  $u_{cc}(r)$ : a-b) Wave components  $u_{c1}(r)$  and  $u_{c2}(r)$  and total wavefield  $u_{cc}(r)$ , in terms of a) amplitude and b) phase; c) Pseudopower spectrum of  $u_{cc}(r)$ , obtained by means of the CFDBF; d) Pseudopower spectrum of  $u_{cc}(r)$ , obtained by means of the CFDBFa. .... 134
- Figure 5-15. a-b) Application of the FDBFa algorithm to SW3: a) Estimated dispersion curve; b) Estimated attenuation curve; c-d) Application of the FDBFa algorithm to SW4: c) Estimated dispersion curve; d) Estimated attenuation curve. Estimated data points beyond the array resolution limits – i.e., the grey areas in a) and c) – are colored in grey. .... 135
- Figure 5-16. a-b) Application of the CFDBFa algorithm to SW3: a) Estimated dispersion curve; b) Estimated attenuation curve; c-d) Application of the CFDBFa algorithm to SW4: c) Estimated dispersion curve; d) Estimated attenuation curve. Estimated data points beyond the array resolution limits – i.e., the grey areas in a) in (a) and c) – are colored in grey. .... 136
- Figure 5-17. Steps of the modulation algorithm for constructing a  $N$ -order bandpass complex FIR filter: a-c) Real lowpass FIR filter in terms of a)  $k$ -response and c) impulse response; b-d) Complex bandpass FIR filter in terms of b)  $k$ -response and d) impulse response. .... 139
- Figure 5-18. Magnitude response specifications, with an explanation of parameters  $k_p$  and  $k_s$  and a visualization of the influence of the filter  $N$  on the fitting of the desired response. .... 140
- Figure 5-19. Influence of filter calibration parameters in extracting wave parameters for the two-component plane wave  $u_{pp}(r)$ : a-b) Wave  $u_{p1}(r)$ ; c-d) Wave  $u_{p2}(r)$ . The labels on the y axis identify different

	sets of $[k_p; k_s]$ , that control the passband and the stopband of the filter. The estimated attenuation through the FDBFa $\alpha_{e,FDBFa}$ is also reported, for comparison purposes.....	142
Figure 5-20.	Influence of filter calibration parameters in extracting wave parameters for the two-component cylindrical wave $u_{cc}(r)$ : a-b) Wave $u_{c1}(r)$ ; c-d) Wave $u_{c2}(r)$ . The labels on the y axis identify different sets of $[k_p; k_s]$ , that control the passband and the stopband of the filter. The estimated attenuation through the CFDBFa $\alpha_{e,CFDBFa}$ is also reported, for comparison purposes.....	143
Figure 5-21.	Application of the CFDBFaMF algorithm on SW3, with a focus on the first three modes: a-b) Estimated dispersion curves (a) and attenuation curves (b) for the fundamental mode, labeled as R0; c-d) Estimated dispersion curves (c) and attenuation curves (d) for the first higher mode, labeled as R1; e-f) Estimated dispersion curves (e) and attenuation curves (f) for the second higher mode, labeled as R2. Results correspond to the set of parameters $[k_p; k_s] = [1; 2]$ and $N = 20$ . Results of the CFDBFa are also reported, for comparison purposes. Estimated data points beyond the array resolution limits – i.e., the grey areas in (a), (c), and (e) – are colored in grey. ....	148
Figure 5-22.	Application of the CFDBFaMF algorithm on SW4, with a focus on the first three modes: a-b) Estimated dispersion curves (a) and attenuation curves (b) for the fundamental mode, labeled as R0; c-d) Estimated dispersion curves (c) and attenuation curves (d) for the first higher mode, labeled as R1; e-f) Estimated dispersion curves (e) and attenuation curves (f) for the second higher mode, labeled as R2. Results correspond to the set of parameters $[k_p; k_s] = [1; 2]$ and $N = 20$ . Results of the CFDBFa are also reported, for comparison purposes. Estimated data points beyond the array resolution limits – i.e., the grey areas in (a), (c), and (e) – are colored in grey. ....	149
Figure 5-23.	Planar wave vs. cylindrical wave, labeled as SW1 and SW2, respectively: amplitude and phase. ....	153
Figure 5-24.	Extracted fundamental-mode dispersion and attenuation curves for SW3 and SW4, for the FDBFaMF and the CFDBFaMF: a-b) Estimated dispersion curves (a) and attenuation curves (b) for SW3; c-d) Estimated dispersion curves (c) and attenuation curves (d) for SW4. Results refer to the fundamental mode only. Estimated data points beyond the array resolution limits – i.e., the grey areas in (a), (c), and (e) – are colored in grey. ....	156

Figure 5-25. Cylindrical wave and body wave: amplitude and phase .....	158
Figure 5-26. Results of the parametric analysis to assess the influence of body waves on the estimated R-wave parameters, represented in terms of normalized values vs. normalized array center distance NACD: a) Wavenumber; b) Attenuation. Results for the planar beamformer (i.e., FDBFa) and the cylindrical beamformer (i.e., CFDBFa) are reported. The annotations denote the points specifically analyzed in Figure 5.27.....	160
Figure 5-27. Spatial variation of the displacement measured in three virtual arrays (rows of the grid of plots), the location of which (in terms of NACD) is represented in Figure 5.26. The displacement is represented in terms of amplitude (left column) and phase (right column). .....	162
Figure 5-28. Results of the Monte Carlo procedure to simulate the presence of incoherent noise in the recorded signal: a-b) Randomized signals, represented in terms of amplitude (a) and phase (b); c) Variability in the amplitude; d) Variability in the phase. The sample signals in a-b) are overlapped by the noiseless signal (thick black line) and by the intervals defined by the mean and one standard deviation (thin red lines).....	165
Figure 5-29. Results of the parametric analysis to assess the influence of body waves and incoherent noise on the estimated R-wave parameters, represented in terms of normalized values vs. normalized array center distance NACD: a-b) Normalized wavenumber and attenuation estimates for the planar beamformer (i.e., FDBFa); c-d) Normalized wavenumber and attenuation estimates for the cylindrical beamformer (i.e., CFDBFa). The errorbars denote the interval defined by the mean and one standard deviation for each simulated acquisition layout. Results obtained from the parametric analysis on SW2-B are included, as a reference.....	166
Figure 5-30. Results of the parametric analysis to assess the influence of body waves and incoherent noise on the estimated R-wave parameters. a-b) Comparison between the theoretical distribution, according to the normal and the lognormal model, and the empirical one: a) Estimated wavenumber; b) Estimated attenuation. c-d) Variability in the estimates: c) Variability in the estimated wavenumber; d) Variability in the estimated attenuation. Results in a-b) refer to NACD = 2.....	168
Figure 6-1. a) Plane view of surface and borehole accelerometers locations at the Garner Valley site, California. The figure includes a zoomed view of	



	the sensors installed at the GVDA, as well as of the SFSI; b) Simplified geological cross section of the Garner Valley site, including a representation of the depth location of borehole sensors. Sensors GL-220 and GL-501 are not reported.....	174
Figure 6-2.	Three-dimensional velocity structure reconstruction by full waveform inversion: a) Acquisition setup; b) Estimated S-wave velocity model (after Fathi et al., 2016).....	<b>Errore. Il segnalibro non è definito.</b>
Figure 6-3.	a) Plane view of the GVDA, showing the location of some invasive and non-invasive surveys carried out at the site. As for the active-source (SASW and MASW) and passive measurements (MAM), the lines and the circles denote the shape underlying the sensors' setup; b) Estimated S-wave velocity profiles from various studies carried out at the GVDA; c) Estimated S-wave damping ratio profiles from various studies carried out at the GVDA. In the figure, DHT stands for results from the DHT by Gibbs (1989); Shallow PS and Deep PS report results from Steller (1996); SASW-1 labels results from the SASW survey by Brown et al. (2002); SASW-2 and SASW-3 label results from the SASW survey by Stokoe II et al. (2004); MASW+MAM labels results from the survey by Teague et al. (2018b); AA-1 denotes results from the fitting of DH-array data by Bonilla et al. (2002); IF labels results from the interferometry study by Chandra et al. (2015); AA-2 identifies results of the amplification analysis of DH-array data by Tao and Rathje (2019); and MASW+MAM+DH <sub>a</sub> denotes results from the combined inversion of SWM data and DH-array data by Seylabi et al. (2020). Only the first 150 m of depth are represented.....	177
Figure 6-4.	Acquisition setup of GV-H5 at the GVDA site: a) Location of sledgehammer shot points; b) Location of shaker shot points.....	181
Figure 6-5.	Acquisition setup of GV-HN at the GVDA site: a) Location of sledgehammer shot points; b) Location of shaker shot points.....	182
Figure 6-6.	a) Hornsby Bend site. The map also reports the location of the SASW surveys by Van Pelt (2010) (SASW-1) and Kallivokas et al. (2013) (SASW-2), together with the location of the MASW surveys herein discussed, namely HB-H5, HB-HN, HB-GP, and HB-DAS; b) Two-dimensional velocity model along the SASW-2 line, developed by Kallivokas et al. (2013); c) Simplified geological cross section along the SASW-2 line; d) S-wave velocity profiles, estimated by Van Pelt (2010) (SASW-1) and Kallivokas et al. (2013) (SASW-2).....	183

Figure 6-7. a) Acquisition setup of HB-H5 at the HB site; b) Acquisition setup of HB-HN at the HB site. ....	186
Figure 6-8. Acquisition setup of HB-DAS and HB-GP at the HB site.....	188
Figure 7-1. Assessment of the inter-method differences for the fundamental mode R-wave dispersion and attenuation curve, with reference to SW3: a) Theoretical vs. estimated dispersion curves; b) Theoretical vs. Estimated attenuation curves; c) Normalized phase velocity $V_{R,e}/V_R$ (i.e., the ratio between the estimated and the theoretical phase velocity), as a function of the frequency; d) Normalized phase attenuation $\alpha_{R,e}/\alpha_R$ (i.e., the ratio between the estimated and the theoretical phase attenuation), as a function of the frequency; and normalized phase attenuation $\alpha_{R,e}/\alpha_R$ . The vertical axis is represented in logarithmic scale as $\alpha_{R,e}/\alpha_R$ spans multiple orders of magnitude. Estimated data points beyond the array resolution limits – i.e., the grey areas in a) – are colored in grey. ....	194
Figure 7-2. Assessment of the inter-method differences for the R-wave dispersion and attenuation curves, with reference to SW3. Each plot contains bars spanning along the frequency range at which each method returned estimates of R-wave dispersion data (top row) and attenuation data (bottom row). The color scale is a function of the magnitude of the normalized phase velocity $V_{R,e}/V_R$ (i.e., the ratio between the estimated and the theoretical phase velocity), or the normalized phase attenuation $\alpha_{R,e}/\alpha_R$ (i.e., the ratio between the estimated and the theoretical phase attenuation): a-d) Fundamental mode; b-e) First higher mode; c-f) Second higher mode. The numeric values in brackets denote the maximum and the minimum detected wavelength. ....	196
Figure 7-3. Assessment of the inter-method differences for the fundamental mode R-wave dispersion and attenuation curve, with reference to SW4: a) Theoretical vs. estimated dispersion curves; b) Theoretical vs. Estimated attenuation curves; c) Normalized phase velocity $V_{R,e}/V_R$ (i.e., the ratio between the estimated and the theoretical phase velocity), as a function of the frequency; d) Normalized phase attenuation $\alpha_{R,e}/\alpha_R$ (i.e., the ratio between the estimated and the theoretical phase attenuation), as a function of the frequency; and normalized phase attenuation $\alpha_{R,e}/\alpha_R$ . The vertical axis is represented in logarithmic scale as $\alpha_{R,e}/\alpha_R$ spans multiple orders of magnitude.	

	Estimated data points beyond the array resolution limits – i.e., the grey areas in a) – are colored in grey. ....	198
Figure 7-4.	Assessment of the inter-method differences for the R-wave dispersion and attenuation curves, with reference to SW4. Each plot contains bars spanning along the frequency range at which each method returned estimates of R-wave dispersion data (top row) and attenuation data (bottom row). The color scale is a function of the magnitude of the normalized phase velocity $V_{R,e}/V_R$ (i.e., the ratio between the estimated and the theoretical phase velocity), or the normalized phase attenuation $\alpha_{R,e}/\alpha_R$ (i.e., the ratio between the estimated and the theoretical phase attenuation): a-d) Fundamental mode; b-e) First higher mode; c-f) Second higher mode. The numeric values in brackets denote the maximum and the minimum detected wavelength. ....	199
Figure 7-5.	MASW array setup. The larger circles represent the receivers belonging to the GV-H5 array, analyzed in this study. The blue area identifies the Garner Valley Downhole Array, where the instrumented boreholes are located.....	201
Figure 7-6.	Frequency-wavenumber representation of the wavefield recorded at GV-H5.....	202
Figure 7-7.	Assessment of the inter-method differences for the fundamental mode R-wave dispersion and attenuation curve, with reference to GV-H5: a) Median estimated dispersion curves; b) Median estimated attenuation curves; c) Logarithmic standard deviation of the estimated dispersion curves; d) Logarithmic standard deviation of the estimated attenuation curves. ....	203
Figure 7-8.	Assessment of the inter-method differences for the fundamental mode R-wave dispersion and attenuation curve, with reference to GV-H5. Each plot contains bars spanning along the frequency range at which each method returned estimates of R-wave dispersion data and attenuation data. The color scale is a function of the number of elementary data points returned at each frequency: a) Phase velocity; b-d) Phase attenuation. The numeric values in brackets denote the maximum and the minimum detected wavelength. ....	204
Figure 7-9.	Selected sub-arrays in HB-HN. The figure includes the original array, as a reference.....	206
Figure 7-10.	a) Frequency-wavenumber representation of the wavefield recorded at HB; b) Energy repartition between the fundamental and the first	

	higher mode. Data refer to sub-array HB-HN-4m, with the source-to-receiver distance equal to 7 m.....	207
Figure 7-11.	Assessment of the inter-method differences for the fundamental mode R-wave dispersion and attenuation curve, with reference to HB-HN: a) Median estimated dispersion curves; b) Median estimated attenuation curves; c) Logarithmic standard deviation of the estimated dispersion curves; d) Logarithmic standard deviation of the estimated attenuation curves. ....	208
Figure 7-12.	Assessment of the inter-method differences for the first higher mode R-wave dispersion and attenuation curve, with reference to HB-HN: a) Median estimated dispersion curves; b) Median estimated attenuation curves; c) Logarithmic standard deviation of the estimated dispersion curves; d) Logarithmic standard deviation of the estimated attenuation curves. ....	210
Figure 7-13.	Assessment of the inter-method differences for the R-wave dispersion and attenuation curves, with reference to HB-HN. Each plot contains bars spanning along the frequency range at which each method returned estimates of R-wave dispersion data (top row) and attenuation data (bottom row). The color scale is a function of the number of elementary data points returned at each frequency: a-c) Fundamental mode; b-d) First higher mode. The numeric values in brackets denote the maximum and the minimum detected wavelength. ....	211
Figure 7-14.	Recorded waveforms at HB-HN. The left column represents the input force, whereas the right column reports the recorded particle velocity data: b-c) Sledgehammer; d-e) Chirp; f-g) Stepped sine. ...	215
Figure 7-15.	Frequency-domain data. The top row represents the input force, with the interval defined by one standard deviation, whereas the bottom row includes pseudo-color maps of the signal-to-noise ratio: a-d) Sledgehammer; b-e) Chirp; c-f) Stepped sine.....	216
Figure 7-16.	Influence of the source type on the fundamental mode R-wave dispersion and attenuation curve, with reference to HB-HN: a) Median estimated dispersion curves; b) Median estimated attenuation curves; c) Logarithmic standard deviation of the estimated dispersion curves; d) Logarithmic standard deviation of the estimated attenuation curves. ....	217
Figure 7-17.	Influence of the source type on the first higher mode R-wave dispersion and attenuation curve, with reference to HB-HN: a)	

Median estimated dispersion curves; b) Median estimated attenuation curves; c) Logarithmic standard deviation of the estimated dispersion curves; d) Logarithmic standard deviation of the estimated attenuation curves. ....	218
Figure 7-18. Assessment of the inter-source differences for the R-wave dispersion and attenuation curves, with reference to HB-HN. Each plot contains bars spanning along the frequency range at which each method returned estimates of R-wave dispersion data (top row) and attenuation data (bottom row). The color scale is a function of the number of elementary data points returned at each frequency: a-c) Fundamental mode; b-d) First higher mode. The numeric values in brackets denote the maximum and the minimum detected wavelength. ....	219
Figure 7-19. a) Schematic model of the DAS system; b) Amplitude response...	222
Figure 7-20. Radial displacement $u_r(r, \omega)$ vs. radial strain $\epsilon_r(r, \omega)$ vs. average radial strain $e_r(r, \omega)$ induced by a cylindrical wave, characterized by $k_R = 0.1$ rad/m and $\alpha_R = 0.0015$ rad/m: a) Corrected amplitude; b) Phase; c) Relative difference in the corrected amplitude between the radial strain and the average radial strain; d) Relative difference in the phase between the radial strain and the average radial strain. ....	225
Figure 7-21. Recorded data at HB-GP (left column) and HB-DAS (right column). Data refer to the waveform generated from the active source located at an offset equal to 10 m: a-b) Time histories of particle velocity and average radial strain, respectively; c-d) Estimated signal-to-noise ratio, as a function of the frequency and the receiver location; e-f) $f$ - $k$ spectral images. ....	229
Figure 7-22. Comparison between the estimated dispersion and attenuation curves from the HB-DAS and the HB-GEO data: a-b) Resulting dispersion (a) and attenuation (b) curves for the fundamental mode; c-d) Resulting dispersion (c) and attenuation (d) curves for the first higher mode. Estimated data are represented in terms of intervals given by one logarithmic standard deviation around the median value.....	231
Figure 7-23. Elementary data points obtained from the combination of results of the HB-H5 and HB-HN arrays, for different locations and types of active source: a) Estimated dispersion curves; b) Estimated attenuation curves. ....	234
Figure 7-24. Comparison between the theoretical distribution, according to the normal and the lognormal model, and the empirical one, described in	

terms of a histogram, for R1 data: a) Experimental phase velocity at  $f = 13$  Hz; b) Experimental phase attenuation at  $f = 13$  Hz; c) Experimental phase velocity at  $f = 13$  Hz; d) Experimental phase attenuation at  $f = 35$  Hz. ....235

Figure 7-25. Lognormal quantile-quantile (Q-Q) plots for both the fundamental mode (R0) and the first higher mode (R1) data. The first row contains Q-Q plots for the phase velocity  $V_R$ , whereas the second row contains Q-Q plots for the phase attenuation  $a_R$ ; each column correspond to a specific frequency for a given propagation mode: a-e) Lognormal Q-Q plots of the experimental phase velocity (a) and phase attenuation (e) for R0 at  $f = 8.6$  Hz; b-f) Lognormal Q-Q plots of the experimental phase velocity (c) and phase attenuation (f) for R0 at  $f = 20$  Hz; c-g) Lognormal Q-Q plots of the experimental phase velocity (c) and phase attenuation (g) for R1 at  $f = 13$  Hz; d-h) Lognormal Q-Q plots of the experimental phase velocity (d) and phase attenuation (h) for R1 at  $f = 35$  Hz. ....236

Figure 7-26. Bivariate lognormal  $\chi^2$ -plot for R0 and R1 data: a) Bivariate lognormal  $\chi^2$ -plot for the R0 experimental phase velocity and attenuation at  $f = 8.6$  Hz; b) Bivariate lognormal  $\chi^2$ -plot for the R0 experimental phase velocity and attenuation at  $f = 20$  Hz; c) Bivariate lognormal  $\chi^2$ -plot for the R1 experimental phase velocity and attenuation at  $f = 13$  Hz; d) Bivariate lognormal  $\chi^2$ -plot for the R1 experimental phase velocity and attenuation at  $f = 35$  Hz. ....238

Figure 7-27. Inferred data statistics for the combined HB-HN and HB-H5 dataset, interpreted according to a bivariate lognormal distribution: a) Median phase velocity  $\mu_V$ ; b) Median phase attenuation  $\mu_a$ ; c) Logarithmic standard deviation of the phase velocity  $\sigma_{\ln V}$ ; d) Logarithmic standard deviation of the phase attenuation  $\sigma_{\ln a}$ ; e) Correlation coefficient  $\rho_{\ln V, \ln a}$  for R0 data, as a function of the frequency; f) Correlation coefficient  $\rho_{\ln V, \ln a}$  for R1 data, as a function of the frequency. Correlation data points are colored as a function of the  $p$ -value. ....240

Figure 8-1. Experimental phase velocity (a) and phase attenuation (b) data obtained from the HB-DAS array, that represent the target for the inversion procedure. The experimental dataset includes information on the variability of the derived R-wave parameters, represented as error bars the width of which is related with the logarithmic standard deviation. ....249

Figure 8-2. Range of $V_S$ and $D_S$ profiles corresponding to the investigated parameter domain, reported in Table 8.1. The search domain is overlapped by the “pseudo-depth” representation of the fundamental-mode experimental data, i.e. $1.1 \times V_R$ vs. $\lambda/2.5$ and $D_R$ vs. $\lambda/2.5$ .....	252
Figure 8-3. Quantities involved in the definition of the misfit function, namely theoretical estimates (subscript “ $t$ ”) and observed data (subscript “ $e$ ”). .....	256
Figure 8-4. Effect of S-wave velocity scaling on the dispersion and attenuation curves. ....	258
Figure 8-5. Effect of layer thickness scaling on the dispersion and attenuation curves. ....	259
Figure 8-6. Effect of S-wave damping ratio scaling on the dispersion and attenuation curves. ....	260
Figure 8-7. Best fitting ground models to HB-DAS experimental data: a-b) Theoretical vs. experimental data, for the phase velocity (a) and phase attenuation (b); c-d) Resulting S-wave velocity (c) and damping ratio (d) profiles. The boundary $z = \lambda_{\max}/2$ is an approximated value of the maximum investigable depth, that can be achieved from the available experimental data – layer interfaces beneath it are usually less reliable.....	264
Figure 9-1. Range of $V_S$ and $D_S$ profiles corresponding to the investigated parameter domain, reported in Table 9.1. The search domain is overlapped by the “pseudo-depth” representation of experimental data, i.e. $1.1 \times V_R$ vs. $\lambda/2.5$ and $D_R$ vs. $\lambda/2.5$ .....	270
Figure 9-2. Best fitting ground models to GV-H5 experimental data: a-b) Theoretical vs. experimental data, for the phase velocity (a) and phase attenuation (b); c-d) Resulting S-wave velocity (c) and damping ratio (d) profiles. The boundary $z = \lambda_{\max}/2$ is an approximated value of the maximum investigable depth, that can be achieved from the available experimental data – layer interfaces beneath it are usually less reliable. Besides, derived profiles in c-d) are overlapped with velocity and damping ratio models obtained in past studies (see Figure 6.2). .....	271
Figure 9-3. Variability of the best fitting ground models to GV-H5 experimental data: a) S-wave velocity profiles; b) Damping ratio profiles; c) Linear correlation coefficient between velocity and damping ratio profiles. The boundary $z = \lambda_{\max}/2$ is an approximated value of the maximum investigable depth, that can be achieved from the available	

experimental data – layer interfaces beneath it are usually less reliable.....	273
Figure 9-4. Comparison between the best fitting ground model to GV-H5 experimental data and velocity and damping ratio models obtained in past studies (see Figure 6.2 for further details): a) S-wave velocity profiles; b) S-wave damping ratio profiles. Results from past studies are represented in grey, with the exception of the models labeled as $D_{lab}$ , computed according to Darendeli (2001); $D_B$ , proposed by Bonilla et al. (2002); and $D_{T\&R}$ , proposed by Tao and Rathje (2019). .....	275
Figure 9-5. Comparison between experimental transfer function (ETF, extracted from Vantassel and Cox, 2019) and median theoretical transfer function for the best fitting 30 models in the inversion (SWM), for the reference depths of 6 m (a), 15 m (b), and 22 m (c). Experimental data are labelled as North-South (NS) and East-West (EW), corresponding to the components of seismometer records from which they were derived. Theoretical TFs obtained from results of the SWM survey by Teague et al. (2018b) are included. ....	277
Figure A-1. Schematic representation of a discrete-time system (modified from Mitra, 2006). .....	291
Figure A-2. Real vs. complex filter: a-b) Impulse response $h[n]$ for a) a real filter and b) a complex filter; c-d) Transfer function $H(e^{j\omega})$ for c) a real filter and d) a complex filter. ....	293
Figure A-3. a-d) Digital filter classification based on the magnitude vs. frequency response: a) Lowpass filter; b) Highpass filter; c) Bandpass filter; d) Bandstop filter; e) Ideal vs. physically realizable lowpass filter (only the positive frequency axis is represented). ....	294
Figure A-4. Example of lowpass, linear-phase filter: a) Magnitude response; b) Phase response. ....	295
Figure A-5. Effect of a $N$ -order FIR filter on a harmonic signal, highlighting the transient portion and the delay in the stationary response. ....	297
Figure A-6. Influence of filter calibration parameters in the application of the FDBFaMF algorithm on SW3, with a focus on the first three modes: a-b) Estimated dispersion curves (a) and attenuation curves (b) for the fundamental mode, labeled as R0; c-d) Estimated dispersion curves (c) and attenuation curves (d) for the first higher mode, labeled as R1; e-f) Estimated dispersion curves (e) and attenuation curves (f) for the second higher mode, labeled as R2. Results correspond to the set of	



parameters  $[k_p; k_s] = [1; 2]$ . Results of the FDBFa are also reported, for comparison purposes. Estimated data points beyond the array resolution limits – i.e., the grey areas in (a), (c), and (e) – are colored in grey. ....300

Figure A-7. Influence of filter calibration parameters in the application of the FDBFaMF algorithm on SW3, with a focus on the first three modes: a-b) Estimated dispersion curves (a) and attenuation curves (b) for the fundamental mode, labeled as R0; c-d) Estimated dispersion curves (c) and attenuation curves (d) for the first higher mode, labeled as R1; e-f) Estimated dispersion curves (e) and attenuation curves (f) for the second higher mode, labeled as R2. Results correspond to the set of parameters  $[k_p; k_s] = [2; 4]$ . Results of the FDBFa are also reported, for comparison purposes. Estimated data points beyond the array resolution limits – i.e., the grey areas in (a), (c), and (e) – are colored in grey. ....301

Figure A-8. Influence of filter calibration parameters in the application of the FDBFaMF algorithm on SW3, with a focus on the first three modes: a-b) Estimated dispersion curves (a) and attenuation curves (b) for the fundamental mode, labeled as R0; c-d) Estimated dispersion curves (c) and attenuation curves (d) for the first higher mode, labeled as R1; e-f) Estimated dispersion curves (e) and attenuation curves (f) for the second higher mode, labeled as R2. Results correspond to the set of parameters  $[k_p; k_s] = [3; 10]$ . Results of the FDBFa are also reported, for comparison purposes. Estimated data points beyond the array resolution limits – i.e., the grey areas in (a), (c), and (e) – are colored in grey. ....302

Figure A-9. Influence of filter calibration parameters in the application of the CFDBFaMF algorithm on SW3, with a focus on the first three modes: a-b) Estimated dispersion curves (a) and attenuation curves (b) for the fundamental mode, labeled as R0; c-d) Estimated dispersion curves (c) and attenuation curves (d) for the first higher mode, labeled as R1; e-f) Estimated dispersion curves (e) and attenuation curves (f) for the second higher mode, labeled as R2. Results correspond to the set of parameters  $[k_p; k_s] = [1; 2]$ . Results of the CFDBFa are also reported, for comparison purposes. Estimated data points beyond the array resolution limits – i.e., the grey areas in (a), (c), and (e) – are colored in grey. ....303

Figure A-10. Influence of filter calibration parameters in the application of the CFDBFaMF algorithm on SW3, with a focus on the first three modes: a-b) Estimated dispersion curves (a) and attenuation curves (b) for the fundamental mode, labeled as R0; c-d) Estimated dispersion curves (c) and attenuation curves (d) for the first higher mode, labeled as R1; e-f) Estimated dispersion curves (e) and attenuation curves (f) for the second higher mode, labeled as R2. Results correspond to the set of parameters  $[k_p; k_s] = [2; 4]$ . Results of the CFDBFa are also reported, for comparison purposes. Estimated data points beyond the array resolution limits – i.e., the grey areas in (a), (c), and (e) – are colored in grey. ....304

Figure A-11. Influence of filter calibration parameters in the application of the CFDBFaMF algorithm on SW3, with a focus on the first three modes: a-b) Estimated dispersion curves (a) and attenuation curves (b) for the fundamental mode, labeled as R0; c-d) Estimated dispersion curves (c) and attenuation curves (d) for the first higher mode, labeled as R1; e-f) Estimated dispersion curves (e) and attenuation curves (f) for the second higher mode, labeled as R2. Results correspond to the set of parameters  $[k_p; k_s] = [3; 10]$ . Results of the CFDBFa are also reported, for comparison purposes. Estimated data points beyond the array resolution limits – i.e., the grey areas in (a), (c), and (e) – are colored in grey. ....305

Figure A-12. Influence of filter calibration parameters in the application of the FDBFaMF algorithm on SW4, with a focus on the first three modes: a-b) Estimated dispersion curves (a) and attenuation curves (b) for the fundamental mode, labeled as R0; c-d) Estimated dispersion curves (c) and attenuation curves (d) for the first higher mode, labeled as R1; e-f) Estimated dispersion curves (e) and attenuation curves (f) for the second higher mode, labeled as R2. Results correspond to the set of parameters  $[k_p; k_s] = [1; 2]$ . Results of the FDBFa are also reported, for comparison purposes. Estimated data points beyond the array resolution limits – i.e., the grey areas in (a), (c), and (e) – are colored in grey. ....306

Figure A-13. Influence of filter calibration parameters in the application of the FDBFaMF algorithm on SW4, with a focus on the first three modes: a-b) Estimated dispersion curves (a) and attenuation curves (b) for the fundamental mode, labeled as R0; c-d) Estimated dispersion curves (c) and attenuation curves (d) for the first higher mode, labeled as R1;

e-f) Estimated dispersion curves (e) and attenuation curves (f) for the second higher mode, labeled as R2. Results correspond to the set of parameters  $[k_p; k_s] = [2; 4]$ . Results of the FDBFa are also reported, for comparison purposes. Estimated data points beyond the array resolution limits – i.e., the grey areas in (a), (c), and (e) – are colored in grey. ....307

Figure A-14. Influence of filter calibration parameters in the application of the FDBFaMF algorithm on SW4, with a focus on the first three modes: a-b) Estimated dispersion curves (a) and attenuation curves (b) for the fundamental mode, labeled as R0; c-d) Estimated dispersion curves (c) and attenuation curves (d) for the first higher mode, labeled as R1; e-f) Estimated dispersion curves (e) and attenuation curves (f) for the second higher mode, labeled as R2. Results correspond to the set of parameters  $[k_p; k_s] = [3; 10]$ . Results of the FDBFa are also reported, for comparison purposes. Estimated data points beyond the array resolution limits – i.e., the grey areas in (a), (c), and (e) – are colored in grey. ....308

Figure A-15. Influence of filter calibration parameters in the application of the CFDBFaMF algorithm on SW4, with a focus on the first three modes: a-b) Estimated dispersion curves (a) and attenuation curves (b) for the fundamental mode, labeled as R0; c-d) Estimated dispersion curves (c) and attenuation curves (d) for the first higher mode, labeled as R1; e-f) Estimated dispersion curves (e) and attenuation curves (f) for the second higher mode, labeled as R2. Results correspond to the set of parameters  $[k_p; k_s] = [1; 2]$ . Results of the CFDBFa are also reported, for comparison purposes. Estimated data points beyond the array resolution limits – i.e., the grey areas in (a), (c), and (e) – are colored in grey. ....309

Figure A-16. Influence of filter calibration parameters in the application of the CFDBFaMF algorithm on SW4, with a focus on the first three modes: a-b) Estimated dispersion curves (a) and attenuation curves (b) for the fundamental mode, labeled as R0; c-d) Estimated dispersion curves (c) and attenuation curves (d) for the first higher mode, labeled as R1; e-f) Estimated dispersion curves (e) and attenuation curves (f) for the second higher mode, labeled as R2. Results correspond to the set of parameters  $[k_p; k_s] = [2; 4]$ . Results of the CFDBFa are also reported, for comparison purposes. Estimated data points beyond the array

	resolution limits – i.e., the grey areas in (a), (c), and (e) – are colored in grey. ....	310
Figure A-17.	Influence of filter calibration parameters in the application of the CFDBFaMF algorithm on SW4, with a focus on the first three modes: a-b) Estimated dispersion curves (a) and attenuation curves (b) for the fundamental mode, labeled as R0; c-d) Estimated dispersion curves (c) and attenuation curves (d) for the first higher mode, labeled as R1; e-f) Estimated dispersion curves (e) and attenuation curves (f) for the second higher mode, labeled as R2. Results correspond to the set of parameters $[k_p; k_s] = [3; 10]$ . Results of the CFDBFa are also reported, for comparison purposes. Estimated data points beyond the array resolution limits – i.e., the grey areas in (a), (c), and (e) – are colored in grey. ....	311
Figure B-1.	Objective function of the nonlinear regression procedure adopted in the TFM, represent as pseudo-color plots mapping its magnitude as a function of trial values of the wavenumber and the attenuation: a) Waveform SW1, which represents the ideal case of a planar wave, where the estimated wave parameters $(k_e; \alpha_e)$ are compared with the theoretical values $(k; \alpha)$ ; b) Data from GV-H5 array (see Section 7.1), which represents a real case. ....	315
Figure B-2.	Application of the WD approach in the presence of three-component data or vertical displacement data only, for SW3 and SW4: a-b) Estimated dispersion and attenuation curves for SW3; c-d) Estimated dispersion and attenuation curves for SW4. ....	317
Figure B-3.	Influence of the model parameters $\gamma$ and $q$ onto the estimated R-wave data, according to the GHPB and the CFM: a-b) Influence of $q$ on the estimated wavenumber $k_e$ , for the GHPB (a) and the CFM (b); c-d) Influence of $q$ and $\gamma$ on the estimated attenuation $\alpha_e$ , for the GHPB (c) and the CFM (d). The estimation error in the attenuation is quantified by the relative error $\Delta\alpha$ , i.e., the error normalized with respect to the theoretical value. Data refer to SW2. ....	321
Figure B-4.	Influence of the model parameters $\gamma$ and $q$ onto the estimated R-wave data, according to the GHPB and the CFM: a-b) Influence of $q$ on the estimated wavenumber $k_e$ , for the GHPB (a) and the CFM (b); c-d) Influence of $q$ and $\gamma$ on the estimated attenuation $\alpha_e$ , for the GHPB (c) and the CFM (d). The estimation error in the attenuation is quantified by the relative error $\Delta\alpha$ , i.e., the error normalized with respect to the	

theoretical value. Data refer to a modified version of SW2, with  $k = 1.5$  rad/m and  $\alpha = 0.025$  rad/m.....323

Figure B-5. Influence of the model parameters  $\gamma$  and  $q$  onto the estimated R-wave data, according to the CFM: a-b) Influence of  $q$  on the estimated wavenumber  $k_e$ , for SW3 (a) and SW4 (b); c-d) Influence of  $q$  and  $\gamma$  on the estimated attenuation  $\alpha_e$ , for SW3 (c) and SW4 (d). The comparison is carried out for the fundamental mode. The dashed lines denote the array resolution limits.....324

Figure C-1. Numerical example showing the approximation error introduced by the assumption that the scaling of the damping ratio maps into an equivalent scaling of the attenuation curves: a-d) Original and scaled S-wave velocity (a) and damping ratio profiles (d); b-e) Original and scaled dispersion curves (b) and attenuation curves (e); c-f) Relative difference between the approximate and the true dispersion (c) and attenuation (f) data, computed for the scaled model.....332

# Index of tables

Table 2.1. Typical values of the small-strain damping ratio $D_{S,0}$ for some dry rock-like materials or cemented soils. ....	23
Table 3.1. Typical values of the S-wave velocity $V_S$ for different geomaterials (after Foti et al., 2018). ....	42
Table 5.1. Ground model parameters adopted to generate the synthetic wavefield SW3.....	113
Table 5.2. Ground model parameters adopted to generate the synthetic wavefield SW4.....	113
Table 5.3. Estimated wavenumber and phase attenuation from SW2 data, according to the FDBFa and the CFDBFa approaches. The values in brackets are the ratio between estimated and true values, that provide a measure of the entity of the error. ....	152
Table 5.4. Estimated wavenumber and phase attenuation from SW2-B data, according to the FDBFa and the CFDBFa approaches. The values in brackets are the ratio between estimated and true values, that provide a measure of the entity of the error. ....	157
Table 7.1. Estimated root mean square error for the phase velocity $\Delta V$ and for the phase attenuation $\Delta\alpha$ for the circle fit method (CFM), the wavefield decomposition approach (WD), and the cylindrical frequency-domain beamforming-attenuation with modal filtering (CFDBFaMF). The total error $\Delta V + \Delta\alpha$ is included in brackets. Residuals are computed with reference to the lowest-order three propagation modes (labeled as R0, R1 and R2, respectively) of the synthetic wavefield SW3. ....	<b>Errore. Il segnalibro non è definito.</b>
Table 7.2. Estimated root mean square error for the phase velocity $\Delta V$ and for the phase attenuation $\Delta\alpha$ for the circle fit method (CFM), the wavefield decomposition approach (WD), and the cylindrical frequency-domain beamforming-attenuation with modal filtering (CFDBFaMF). The total error $\Delta V + \Delta\alpha$ is included in brackets. Residuals are computed with reference to the lowest-order three propagation modes (labeled as R0, R1 and R2, respectively) of the synthetic wavefield SW4. ..	200
Table 7.3. Estimated wavenumber and phase attenuation from planar radial average strain data (representative of a Rayleigh wave with $k_R = 0.1$ rad/m and $\alpha_R = 0.0015$ rad/m), according to the displacement-based beamforming, strain-based beamforming, and average strain-based	

beamforming approaches. The values in brackets are the ratio between estimated and true values, that provide a measure of the entity of the error. ....	228
Table 8.1. Boundaries of the investigated parameter domain.....	252
Table 9.1. Boundaries of the investigated parameter domain.....	270

# Chapter 1

## Introduction

### 1.1 Motivation

The characterization of soil response to dynamic loading has great relevance in geotechnical earthquake engineering. In these conditions, the actual stress-strain response of soils depends on various quantities, which describe dynamic properties. Key parameters are the small-strain shear-wave velocity and the damping ratio, which quantify the stiffness and the internal energy dissipation by the soil at low strains, respectively. Although the uncertainties related to the small-strain damping ratio are usually referred as secondary (Idriss, 2004; Rathje et al., 2010; Cabas and Rodriguez-Marek, 2018), the choice of adequate values can strongly influence the soil response, especially in the small-strain field (e.g., Thompson et al., 2012; Tao and Rathje, 2019). Indeed, this quantity plays a key role in understanding low-intensity shaking (Schevenels, 2007; Tao and Rathje, 2019; Rodriguez-Marek et al., 2021) and anchoring soil nonlinear behavior when strong shaking is involved (e.g., Stewart et al., 2014b; Foti et al., 2021).

Many design applications rely on estimates of the small-strain damping ratio obtained through laboratory testing or empirical relationships, although some studies have inferred in-situ estimates of this quantity. The in-situ values are typically larger than the ones obtained through laboratory tests (e.g., Stewart et al., 2014b; Tao and Rathje, 2019). Indeed, at the site scale, complex wave propagation phenomena (e.g., wave scattering) induce additional energy dissipation besides material dissipation that cannot be captured by laboratory tests. Therefore, an in-situ estimate of this quantity should be adopted in ground response simulations. A promising technique for obtaining soil dissipative parameters relies on the Multichannel Analysis of Surface Waves (MASW; Foti, 2000). The MASW-based estimate of the small-strain damping ratio usually refers to the measurement of the spatial attenuation of Rayleigh waves along linear arrays with active sources (Foti et al., 2014). In this case, the S-wave velocity and damping ratio profiles are jointly estimated through an inversion scheme, where a theoretical soil model is calibrated to match the experimental dispersion and attenuation data.



However, the estimation of the dissipation parameters is a nontrivial task, especially in the presence of complex stratigraphy, and large uncertainties affect the estimated values. On the one side, various studies attempted to develop robust procedures for the estimate of the S-wave velocity and statistical models to quantify the related uncertainties (e.g., Foti et al., 2018; Passeri et al., 2020; Hallo et al., 2021). Instead, only a few methods for deriving the small strain damping ratio are available, and they often rely on limiting assumptions about the geometry and the composition of the recorded wavefield (e.g., Lai et al., 2002; Badsar et al., 2010). Furthermore, there is still a lack of knowledge on the uncertainties affecting the resulting damping ratio. A proper modeling is instead crucial when investigating the soil behavior in dynamic conditions, as the complex response does not allow the a priori choice of conservative values for the mechanical parameters. Instead, data uncertainties should be considered in an explicit way, within a probabilistic framework in order to Identify, Quantify, and Manage (i.e., IQM method; Passeri, 2019) all the uncertainties and variabilities involved in the analyses, to obtain reliable and accurate estimates of the actual response.

## **1.2 Research objectives and achievements**

The main purpose of this research is the assessment of the reliability and the uncertainties that characterize the estimated shear-wave velocity and small-strain damping ratio from the interpretation of MASW surveys. However, the main focus will be the derivation of the damping ratio, as only few studies addressed this parameter (e.g., Lai and Rix, 1998b; Foti, 2003; Misbah and Strobbia, 2014).

On the one side, the research addresses the estimation of the propagation characteristics of Rayleigh waves from measured waveform data, both in terms of velocity and attenuation. For this purpose, a vast dataset of synthetic seismograms and high-quality, in situ surface wave data were acquired in massive site characterization campaigns at two locations in the United States, where seismograms generated by artificial sources were recorded on arrays composed by receivers of different types. Besides, a novel technique (named Frequency-Domain BeamForming-attenuation, FDBFa) to estimate Rayleigh wave attenuation data is proposed. This technique relies on a wavefield transform, that allows to reduce the problem of the attenuation estimate into a dispersion analysis of the transformed data. Furthermore, it incorporates an explicit modeling of the geometry of the wavefield and it allows to isolate different Rayleigh propagation modes, through a filtering scheme. Furthermore, the research includes a thorough analysis of some sources of epistemic uncertainties affecting the estimated R-wave parameters, with a focus on the influence of modeling assumptions (that is,

near- and far-field effects; Foti et al., 2014), the adopted processing scheme, the type of active source, and the acquisition device (i.e., the sensors). Specifically, the study addresses the sensitivity of the derived velocity and attenuation data to perturbations in the recorded Rayleigh wavefield, due to body waves and incoherent noise. Furthermore, it assesses the quality of experimental data as a function of different interpretation techniques and various source types, quantifying the performance in terms of the reliability and the accuracy of the estimated propagation parameters. Finally, the analysis of the influence of the acquisition device compares geophone versus fiber-optic data, to investigate the sensitivity of estimated parameters to the receiver type. This study also aims at understanding the potential of the fiber-optic device in retrieving dissipation parameters. The research also addressed aleatory variability, by proposing a statistical model to jointly describe the variability in derived phase velocity and attenuation data.

On the other side, experimental Rayleigh-wave data need to be mapped into earth models that capture the stiffness and damping ratio variations with depth, by means of an inversion procedure. To address this topic, a robust inversion algorithm is proposed, which is based on a Monte Carlo procedure. The developed algorithm is based on a smart sampling technique of the model parameter space, by exploiting the scaling properties of the Rayleigh wave parameters in linear viscoelastic media. These properties are introduced in this study and they allow a significant saving in computation time, preserving the quality of the resulting ground models at the same time. Finally, the reliability of the derived earth models is assessed, by comparing them with the available information and by assessing the reliability in terms of the measured response to ground motion, compared with in situ observed data. The comparison highlighted an acceptable level of compatibility between estimated and empirical amplification, which stresses the effectiveness of using damping ratio estimates from in situ data.

### **1.3 Dissertation outline**

The dissertation starts with a literature review on the small-strain damping ratio, providing a definition of this parameter and an overview on the methods used for its derivation.

Specifically, Chapter 2 provides a quick overview of the soil behavior under cyclic loading at small strain levels, according to the theory of linear, viscoelastic media. Then, the focus shifts to the small-strain damping ratio, with a description of the influence of loading conditions and mechanical parameters and a list of empirical relationships for its prediction. The chapter ends with a description of

the role of the small-strain damping ratio in various engineering applications, to highlight its relevance.

Chapter 3 focuses on the propagation of body waves and Rayleigh waves in continuous media, both in linear elastic and in linear viscoelastic conditions. In particular, the governing equations and the relevant parameters are introduced. The chapter ends with a review of the main mechanisms of attenuation theory, to provide a list of the factors affecting the amplitude of perturbations propagating in a medium while moving away from the source.

Chapter 4 summarizes the most common estimation procedures for the S-wave small strain damping ratio. Specifically, the description focuses on laboratory tests and in situ characterization methods, based on invasive and noninvasive geophysical tests and down-hole arrays. Finally, a brief comparison of results from laboratory and in situ tests is reported.

The second part of the dissertation focuses on the processing stage of surface wave data, which infers the Rayleigh wave parameters from recorded waveform data.

Chapter 5 introduces the FDBFa algorithm, specifying the various modifications applied to accommodate for the geometrical shape of the Rayleigh wavefield and the presence of multiple propagation modes. The chapter ends with a parametric study on near-field effects and incoherent noise, to assess the performance of the proposed scheme in complex wave conditions and understand their effect on experimental data.

Chapter 6 presents the experimental dataset, consisting of a suite of MASW surveys devoted to the collection of high-quality surface wave data at the Garner Valley Downhole Array (GVDA) and the Hornsby Bend (HB) sites, in the United States.

Chapter 7 contains a thorough analysis of various sources of uncertainties affecting the estimated Rayleigh phase velocity and phase attenuation. On one side, epistemic uncertainties are addressed, by investigating the influence of the specific processing algorithm, the type of active source and the acquisition device on the estimated wave parameters. The investigation refers to both synthetic cases and to wavefield data extracted from in situ surveys. The overview of epistemic uncertainties ends with a comparison between the derived propagation parameters obtained from geophone and fiber-optic data at the HB site. The final part of this Chapter focuses on the aleatory variability, introducing a statistical model to jointly describe the variability of the experimental dispersion and attenuation data.

The final part of the dissertation addresses the derivation of the earth models from experimental data, with a focus on the stiffness and attenuation structure.

Chapter 8 describes a new algorithm for the joint inversion of velocity and attenuation data to retrieve both stiffness and dissipation parameters, that relies on an improved Monte Carlo scheme. It also includes the application of this algorithm at the HB site.

Chapter 9 contains a discussion of the retrieved earth models, obtained from the inversion procedure, with a focus on the related reliability and the implications of uncertainties in both the S-wave velocity and damping ratio on the predicted ground response. The discussion focuses on the experimental dataset collected at the GVDA.

Finally, Chapter 10 summarizes and discusses the main conclusions of the research, along with some indications on possible future studies on the topic.

Appendix A focuses on some technical aspects linked with the FDBFa procedure.

Appendix B collects implementation details of various literature approaches to derive experimental Rayleigh wave parameters.

Appendix C contains the mathematical demonstration of the scaling properties of the Rayleigh eigenvalue problem in linear viscoelastic media.



# Chapter 2

## Small-strain damping ratio

This Chapter addresses some key features of soil behavior, with a focus on the small-strain damping ratio. Specifically, a quick overview of the general behavior under cyclic loading is followed by a more detailed description of the response at small strain levels, according to the theory of linear, viscoelastic media. The main references for the description of this theory are the contributions by Kramer (1996), Ben-Menahem and Singh (2012), Foti et al. (2014), and Kokusho (2017). Then, the Chapter focuses on the influence of loading and mechanical parameters on the small-strain damping ratio, including a physical interpretation of such dependencies. This is followed by a literature review of some empirical relationships for its prediction, that allow to define an order of magnitude of this parameter. The Chapter ends with a description of the role of the small-strain damping ratio in various engineering applications, to highlight its relevance.

Part of this Chapter has been already published in Foti et al. (2021).

### 2.1 Response of soils to cyclic actions

#### 2.1.1 Experimental evidence

Many insights on the soil behavior under dynamic loads derive from experimental tests carried out in the laboratory, specifically from cyclic tests. Although the loading path does not perfectly simulate the actual action exerted by an earthquake (i.e., harmonic, cyclic loads instead of irregular, aperiodic load variations), the observed response allows to predict the soil response in seismic conditions.

In general, soil behavior is strongly dependent on the norm of the deviatoric strain tensor (e.g., Foti et al., 2014). In the simplified case of uniaxial, shear loading, this general statement maps into a dependence of the soil response on the magnitude of the shear strain.

Figure 2-1a shows a typical observed response of a soil sample to a given level of cyclic shear strain amplitude  $\gamma_c$ , corresponding to a specific cyclic shear stress amplitude  $\tau_c$ . The response is usually investigated in the  $\tau$ - $\gamma$  domain, where  $\tau$  and  $\gamma$  are the shear stress and the shear strain, respectively. This result could be

the output of a cyclic simple shear test (see Chapter 4 for further details). The response is characterized by strong nonlinearity and irreversibility in the loading-unloading cycles, as the initial strain state (i.e., null strain) is not restored after unloading. The irreversibility results in energy dissipation during cycles, whose main mechanism can be linked to hysteretic damping. In addition, soil response strongly depends on the cyclic strain amplitude and this relationship is also reflected in variations in the geometry of the stress-strain loops (Figure 2-1b-d). Finally, soil behavior depends on the number of cycles, as more cycles induce a degradation in mechanical properties, although this effect is remarkable only at great strains (Figure 2-1d).

Changes in soil behavior are not gradual and some threshold strain values can be identified (Vucetic, 1994). At very small strains, geomaterials exhibit a quasi-linear response, hence the hysteretic component in the energy dissipation is negligible (Figure 2-1b). However, the energy dissipation is not zero because other mechanisms contribute to this, as explained in Section 2.2. The upper bound of the corresponding strain range is termed as linear cyclic threshold shear strain  $\gamma_l$ . For increasing cyclic strains, stress-strain loops become gradually flatter and broader (Figure 2-1c), implying a reduction in stiffness and an increase of dissipated energy. On the other side, volumetric changes in drained conditions or residual pore-water pressure in undrained samples are not observed. At very large strains, the soil behavior is strongly nonlinear, with severe stiffness and strength degradation as the strain level increases. Besides, the effect of the number of cycles becomes relevant on the soil response (Figure 2-1d). In these conditions, there is a relevant modification in the microstructure, resulting macroscopically in a permanent volume change accumulation in drained conditions or a permanent pore-water pressure build-up in undrained conditions. The strain level at which these phenomena start to become relevant is called volumetric cyclic threshold shear strain  $\gamma_v$ .

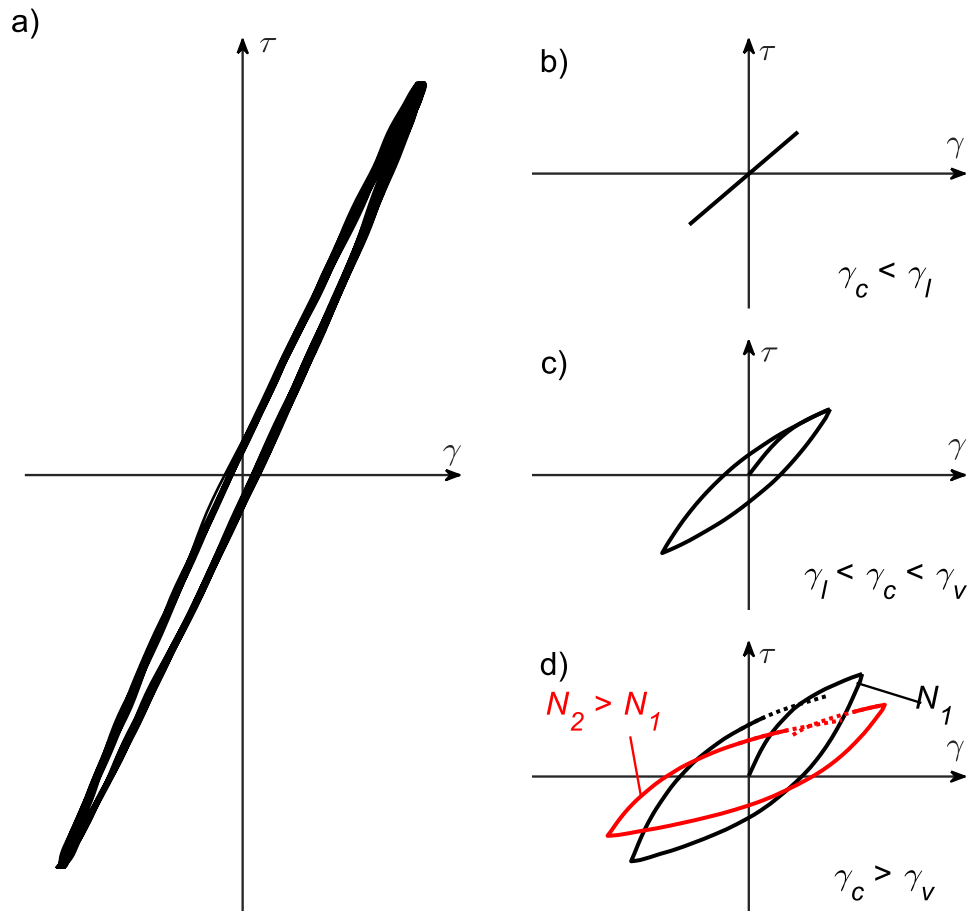


Figure 2-1. a) Example of stress-strain loops of a geomaterial under cyclic loading, represented in the  $\tau$ - $\gamma$  domain. b-d) Variations in the loop geometry at increasing level of cyclic strain amplitude  $\gamma_c$  and the number of cycles  $N$  (modified from Lanzo and Silvestri, 1999). In the plots,  $\gamma_l$  is the linear cyclic threshold shear strain,  $\gamma_v$  is the volumetric cyclic threshold shear strain and  $N_1$  and  $N_2$  are two values for  $N$ .

## 2.1.2 Models

Modeling the nonlinear, degrading soil behavior under cyclic loading is not straightforward, due to its intrinsic complexity. However, an effective model for describing the cyclic behavior of geomaterials at low strain levels is the equivalent linear model, which relies on the theory of linear, viscoelastic media (Ishihara, 1996). This model simplifies the various mechanisms responsible of the energy dissipation as a viscous damping. This assumption is necessary because the large number of mechanisms contributing to energy dissipation does not allow to represent them all with a single modification of the constitutive equations



(Ben-Menahem and Singh, 2012). However, the linear viscoelastic model is quite effective in describing the actual response of soils under dynamic loading. Furthermore, this model can be adapted to predict soil behavior at moderately large strains, by means of the equivalent linear procedure (Seed and Idriss, 1970).

A linear viscoelastic material satisfies two fundamental properties:

- The stress components are linearly related to strain components at a given time;
- The strain induced by two arbitrary, but different stress inputs applied at different times equals the sum of the strain states obtained from each of these stresses, acting separately. This property represents the principle of linear superposition (Ben-Menahem and Singh, 2012).

The models fulfilling the conditions of linear viscoelasticity rely on the superposition of two resisting mechanisms to deformation: linear elasticity and Stokes' viscosity. These two components can be synthetically described according to specific mechanical analogs, namely the Hooke's linear spring and the Newton's viscous dashpot. Different combinations of these elements in series or in parallel generate various models, with increasing level of complexity and capability of reproducing the actual behavior of geomaterials. However, the linear viscoelastic theory often relies on basic models, that allow to capture the main features in the response of anelastic materials. Their description and the formulation of the constitutive laws refers to the specific case of cyclic uniaxial shearing (Figure 2-2a), to make a parallelism with the loading conditions typically investigated in soil characterization.

On the one side, the Kelvin-Voigt model is rather popular in engineering mechanics. The mechanical analog is a system composed by a linear spring (with stiffness  $G$ ) and a viscous dashpot (with viscosity  $\eta$ ) connected in parallel (Figure 2-2b). Therefore, this rheological model decouples the overall action into an elastic component, following the Hooke's law, and a viscous component, following the Newton's law. Thus, in cyclic uniaxial shearing,  $\tau$  is balanced by the superposition of an elastic component, which is proportional to  $\gamma$ , and a viscous part, which is proportional to the strain rate. Therefore, the constitutive law for the Kelvin-Voigt solid under shearing is the following:

$$\tau = G\gamma + \eta \frac{\partial \gamma}{\partial t} \quad (2.1)$$

Alternatively, the Maxwell model can be described as a composition of a linear spring connected in series with a viscous dashpot (Figure 2-2c). In this case, the two elements share the same stress state and the strain is the summation of the

corresponding strains. From these considerations, the following constitutive law can be derived:

$$\frac{1}{\eta} \tau + \frac{1}{G} \frac{\partial \tau}{\partial t} = \frac{\partial \gamma}{\partial t} \quad (2.2)$$

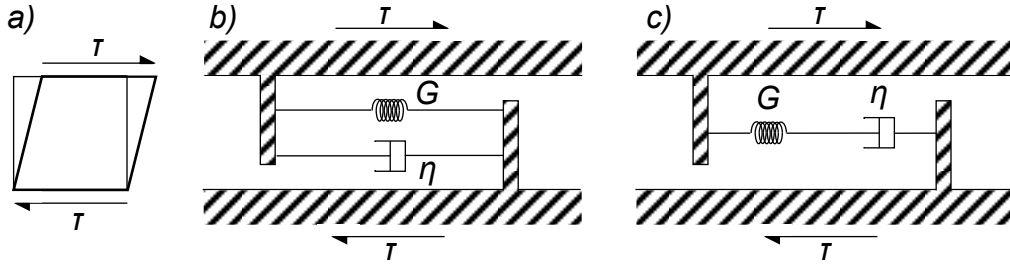


Figure 2-2. Mechanical model of the Kelvin-Voigt (b) and Maxwell (c) solid, to represent the behavior of a soil element under uniaxial shear loading, represented by the shear stress  $\tau$  (a). The elastic component of the response is synthesized by a linear spring with stiffness  $G$ , whereas a viscous dashpot with viscosity  $\eta$  models the viscous component.

However, the actual response of an isotropic, linear viscoelastic medium is provided by an integral relationship, linking the strain history to the stress history by means of a relaxation tensor function, which synthesizes the time-dependent behavior of the material (Christensen, 2012). In general, the derivation of the stress state is a nontrivial operation. On the other side, the constitutive relationship dramatically simplifies in the presence of uniaxial, harmonic loading. Specifically, the corresponding behavior is equivalent to the one provided by the Kelvin-Voigt model. For this reason, this section will continue referring to this simplified model for the description of the shear-stress response of isotropic, linear viscoelastic media.

In the presence of a harmonic shear strain with amplitude  $\gamma_c$ , the stress-strain response of a Kelvin-Voigt solid is a rotated ellipse (Figure 2-3). The ellipse is centered at the origin of the  $\tau$ - $\gamma$  domain, i.e. the null stress-strain state, and the slope of the major axis with respect to the  $\gamma$  axis is equal to the stiffness  $G$ . Interestingly, this shape matches well the hysteresis loops that geomaterials exhibit under shear at a fixed level of  $\gamma_c$  (Figure 2-1a). For this reason, the linear viscoelastic scheme is effective in describing soil behavior under dynamic conditions, at least at small strains.

Furthermore, the strong analogy between the response of the Kelvin-Voigt solid and geomaterials allows a synthetic description of the dynamic response at each strain level according to some parameters (termed as dynamic properties), extracted from the geometry of the loops and providing description of deformability and energy dissipation (Figure 2-3).

On the one side, the major axis of the ellipse has a slope equal to  $G$ , that is the stiffness of the spring in the Kelvin-Voigt solid. Therefore, the stiffness behavior (which continuously changes due to nonlinearity) can be synthesized through an “equivalent” parameter that describes the average stiffness of the soil across the loop. This is equal to the secant shear modulus (also denoted as  $G_S$ ), which is the slope of the secant line at the two extreme points of the loop.

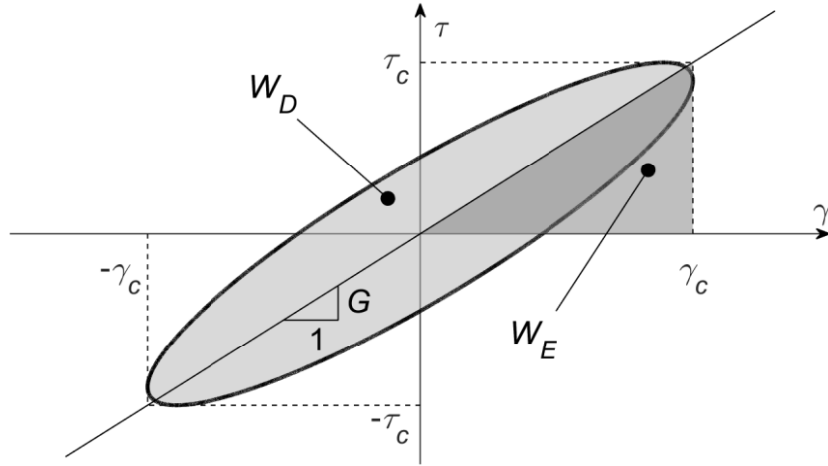


Figure 2-3. Mechanical response under shearing of the isotropic, linear viscoelastic medium, represented in the  $\tau$ - $\gamma$  domain. At a fixed level of cyclic shear stress amplitude  $\gamma_c$ , the response can be modelled as an elliptical loop with maximum absolute ordinate equal to the cyclic shear stress amplitude  $\tau_c$ . The average slope is the secant shear stiffness  $G$ . Instead, the area  $W_D$  enclosed within the loop describes the dissipated energy and  $W_E$  corresponds to the maximum elastic stored energy.

The description of energy dissipation relies on the analogy between the stress-strain response of the Kelvin-Voigt solid and the hysteresis loops that describe the behavior at resonance of an idealized Single-Degree of Freedom (SDOF) system composed by the linear spring and the viscous dashpot (Chopra, 2017). Therefore, a possible parameter to measure cyclic energy dissipation is the material shear damping ratio  $D_S$ , defined as the fractional part of the elastic stored energy which is dissipated during each cycle:

$$D_S = \frac{1}{4\pi} \frac{W_D}{W_E} \quad (2.3)$$

The dissipated energy  $W_D$  equals the work done by the stress (per unit volume of material) for an infinitesimal variation of strain and it is related to the size of the area enclosed within the loop (Figure 2-3):

$$W_D = \oint_{1 \text{ cycle}} \tau d\gamma = \pi\eta\omega\gamma_c^2 \quad (2.4)$$

The maximum elastic stored energy  $W_E$ , instead, corresponds to the area of the triangle defined by the secant line at the cyclic strain amplitude (Figure 2-3):

$$W_E = \frac{1}{2}G\gamma_c^2 \quad (2.5)$$

Being the dissipated energy proportional to the excitation frequency  $\omega$ , the damping ratio associated with the equivalent Kelvin-Voigt solid is frequency-dependent. However, experimental observations demonstrate that the intrinsic energy dissipation in geomaterials is independent from the loading rate, at least in the frequency range of engineering interest (see Section 2.2). For this reason, a modified version of the Kelvin-Voigt solid is usually adopted for modelling soil response, where the viscous dashpot is replaced by a nonviscous element (Theodorsen and Garrick, 1940; Kramer, 1996). In this model, an equivalent viscosity  $H$  is assumed, which is inversely proportional to the loading frequency.

$$H = \frac{\eta}{\omega} \quad (2.6)$$

Thus, the corresponding damping ratio is independent of frequency, consistently with the observed behavior of geomaterials.

The influence of  $\gamma_c$  on the soil mechanical behavior results in a strain-dependence of  $G$  and  $D_S$  (Figure 2-4). Indeed, for increasing  $\gamma_c$ ,  $G$  becomes smaller because the average slope of the cycles decreases. Conversely,  $D_S$  gets larger as the enclosed area becomes greater. Furthermore, the most relevant changes in these quantities are consistent with the cyclic strain thresholds (Vucetic, 1994). At very small strains, soil response is virtually linear, meaning that the cycles are regular and not sensitive to variations in the strain level. Therefore,  $G$  is constant and it assumes its maximum value, labeled as  $G_{max}$ . On the other side, the energy dissipation is almost constant and  $D_S$  equals the small-strain material damping ratio ( $D_{S,0}$ ). At larger shear strains, exceeding the linear threshold  $\gamma_l$ , nonlinearity in the stress-strain soil behavior leads to flatter and broader loops, with an increase of the energy dissipation. This entails a gradual decay of  $G$  and an increase in  $D_S$ . At high strain levels, the instability of stress-strain loops results in a dependence of  $G$  and  $D_S$  on the number of cycles. The variation of these quantities with  $\gamma_c$  is captured by the Modulus Reduction and Damping (MRD) curves, that provide  $G$  (or  $G$  normalized by  $G_{max}$ ) and  $D_S$  as a function of  $\gamma_c$ .

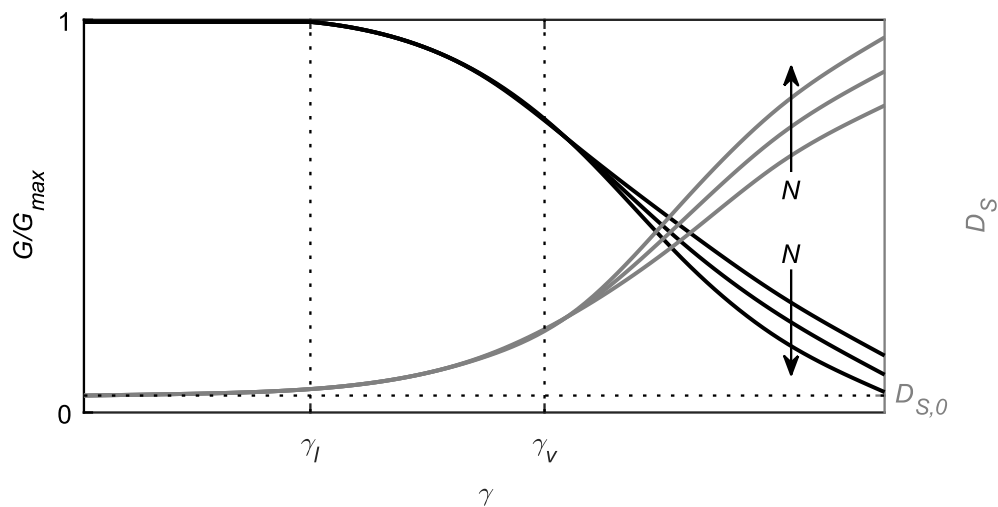


Figure 2-4. Normalized modulus reduction and damping curves, describing variations of the normalized shear modulus  $G/G_{max}$  and damping ratio  $D_s$  as a function of the shear strain  $\gamma$ . The influence of the number of cycles  $N$  is included. The plot also highlights the location of the linear cyclic threshold shear strain  $\gamma_l$ , the volumetric cyclic threshold shear strain  $\gamma_v$  and the small-strain shear damping ratio  $D_{s,0}$  (modified from Lanzo and Vucetic, 1999)

## 2.2 Parameters affecting the small-strain damping ratio

From this point onwards, the focus of the dissertation shifts to the small-strain range of the soil behavior and, specifically, on the small-strain shear damping ratio  $D_{s,0}$ . The focus on this specific aspect is corroborated by the common practice in soil dynamics to decompose the damping ratio into a small-strain component and a nonlinear, strain-dependent element (e.g., Darendeli, 2001). This separation allows to isolate the linear range from the nonlinear part, thus simplifying the modeling. Also, the partition has a specific physical meaning, linked to the mechanisms of energy dissipation intervening at different strain levels. Indeed, geomaterials under high-amplitude cyclic loading undergo a remarkable energy dissipation due to plastic deformations, that are visible as hysteretic loops. At small strains, instead, this component becomes negligible in favor of other mechanisms, of frictional and viscous nature.

The small-strain damping ratio depends both on material properties and on the loading conditions, e.g. the confinement level. Before addressing the role of soil mechanical parameters, the effect of the loading frequency on the small-strain damping ratio has to be investigated. The influence of these parameters is

assessed accounting for the physical phenomena occurring at the microstructural scale.

### 2.2.1 Loading frequency

The effect of the loading frequency – alternatively, the strain rate – on  $D_{s,0}$  strongly depends on the material type. Indeed, the energy dissipation is the combined effect of different mechanisms taking place in geomaterials during cyclic loadings (e.g., Stoll and Bryan, 1970; Shibuya et al., 1995; d'Onofrio et al., 1999). Part of the energy dissipation results from friction between soil particles, as they mutually slide to each other, and the anelastic behavior of the particles themselves. A relevant component of energy dissipation is linked to relative movement between the water and the soil skeleton, due to pore fluid viscosity – the corresponding viscous damping is frequency-dependent. The key role of pore fluid in the damping ratio at small strain levels is suggested by an observation that moonquakes, which occur in the vacuum environment presumably without any fluid, are known to keep vibrating for a much longer duration than earthquakes probably because of very low damping in small strain in the near-surface (Latham et al., 1970; Latham et al., 1971; Kokusho, 2017).

In fine-grained soils, Shibuya et al. (1995) performed a dynamic characterization of normally consolidated clays at low frequencies, less than 0.1 Hz. By merging results with those of other studies that investigated alternative frequency bands (Hara and Kiyota, 1977; Kim, 1991), they suggested the existence of three different branches (Figure 2-5a). At low frequencies ( $< 0.1\text{Hz}$ ),  $D_{s,0}$  tends to decrease with increasing frequencies. In the medium range (between 0.1 and 10 Hz, i.e., the typical seismic bandwidth) the damping is almost constant, irrespectively of the loading frequency. Finally, for higher frequencies  $D_{s,0}$  increases with  $f$  because of viscous effects. The “U”-shaped dependence of  $D_{s,0}$  with respect to the loading frequency has been also observed in other studies, although the trend displayed less sharp variations, entailing some influence of the loading frequency on  $D_{s,0}$  even in the seismic bandwidth (e.g., d'Onofrio et al., 1999; Stokoe and Santamarina, 2000; Darendeli, 2001; Matešić and Vucetic, 2003; Menq, 2003; Rix and Meng, 2005), as shown in Figure 2-5b. This effect is relevant especially in plastic soils (Stokoe and Santamarina, 2000; Darendeli, 2001). For this reason, the actual dependency on the loading frequency within the typical seismic bandwidth is still controversial. Some effect of the loading frequency is also visible on  $G$ , although the relative variations are negligible (Figure 2-5b). On the other side, the influence of the frequency is less remarkable

at high strain amplitudes. Indeed, the frequency-independent, hysteretic damping increase due to plastic deformation partially covers these aspects.

The motivation behind this behavior has to be found into the different mechanisms of energy dissipation taking place in cohesive soils during cyclic loadings (e.g., Shibuya et al., 1995; d'Onofrio et al., 1999). In fine-grained soils, indeed, dissipations are linked to complex phenomena occurring at the microstructure scale, controlled by electromagnetic interactions between water dipoles and microscopic solid particles (Foti et al., 2014). However, the degree of contribution of each component is not the same and it depends on the loading frequency, thus justifying the “U”-shaped trend of  $D_{S,0}$  with the frequency. A remarkable aspect is that dissipation due to frame inelasticity is dominant across a broad band of frequencies, whereas fluid losses are negligible due to limited fluid mobility, except at high frequencies (Stoll and Bryan, 1970; Stoll, 1977). In the very low-frequency range, the application of the load is quasi-static and creep phenomena occur. Due to creep, indeed, the elastic limit shear strain (i.e., the maximum strain level at which the tangent stiffness equals the maximum one) decreases at small strain rates, thus the stress-strain loops are enlarged proportionally as the loading frequency decreases (Dobry and Vucetic, 1987; d'Onofrio et al., 1999). Therefore, the slower is the application of the load, the higher is  $D_{S,0}$ . On the contrary, creep-induced energy dissipation becomes negligible at high frequencies. Instead, in the medium frequency range (i.e., the seismic band), energy dissipation is mainly the result of the anelastic soil behavior. At high frequencies, the  $D_{S,0}$  increase with growing  $f$  may be an effect of the relevant contribution of the pore fluid viscosity at high loading rates.

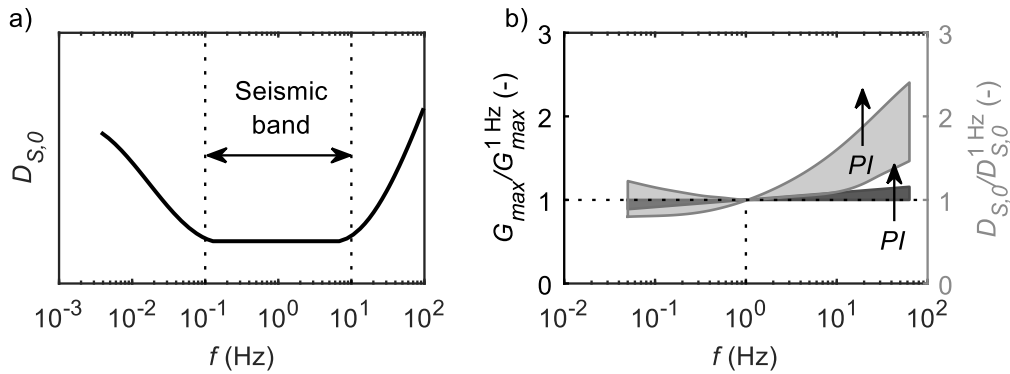


Figure 2-5. a) Effect of loading frequency  $f$  on the small-strain damping ratio  $D_{S,0}$  of cohesive soils (modified from Shibuya et al., 1995); b) Effect of the loading frequency on the small-strain shear modulus  $G_{max}$  and damping ratio  $D_{S,0}$  for cohesive soils, as a function of the plasticity index  $PI$ . To highlight the influence of  $f$ , these parameters are normalized by the corresponding values measured at  $f = 1$  Hz, namely  $G_{max}^{1\text{ Hz}}$  and  $D_{S,0}^{1\text{ Hz}}$  (modified from Stokoe and Santamarina, 2000).

In coarse-grained soils, where gravity forces are governing the overall behavior, the main dissipative mechanisms are losses at contacts between soil particles (mainly with frictional nature), matrix anelasticity and fluid flow losses due to the relative movement between the solid and the fluid phase (e.g., Stoll and Bryan, 1970; Stoll, 1977). Being the fluid mobility significant, the frequency-dependence of  $D_{S,0}$  strongly depends on the moisture content. In coarse-grained dry materials, the effect of loading frequency seems to be negligible in the frequency range of typical interest (Kim and Stokoe, 1994; Lo Presti et al., 1997; Menq, 2003). However, creep effects have been observed under quasi-static loading conditions (Di Benedetto, 1997). The moisture addition, instead, induces a remarkable dependence on the loading frequency, whereas  $G$  is almost constant in the seismic band (Figure 2-6). The variation is still described as a “U”-shaped trend, although the frequency boundaries differ from those identified in fine-grained soils. On the one side,  $D_{S,0}$  increases as frequency decreases below 1 Hz, as a result of creep at such slow loading rates. Then, it does not remain constant along a given bandwidth, but it immediately increases at higher frequencies – however, the relative variation is not strong (Menq, 2003). This is an effect of the viscous damping generated by relative movement between water and the soil skeleton, which is comparable with frame losses (or even dominant) even at low frequencies due to higher mobility of the pore fluid (Stoll, 1977).

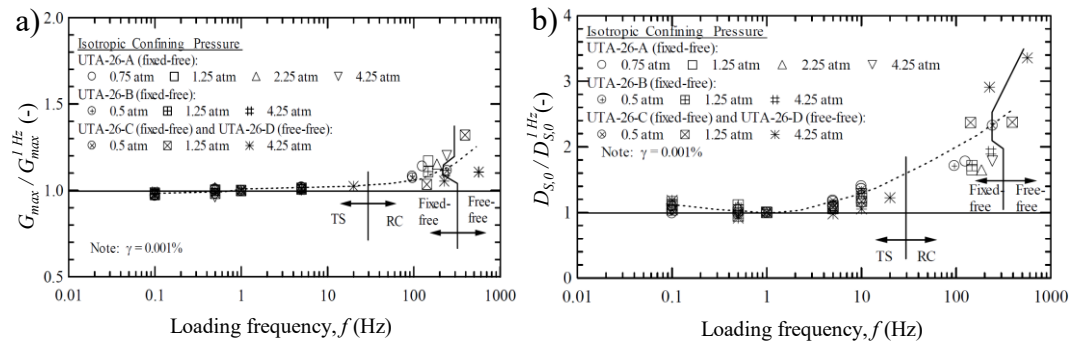


Figure 2-6. Effect of the loading frequency  $f$  on the small-strain shear modulus  $G_{max}$  and damping ratio  $D_{S,0}$  for saturated, gravelly soils, as a function of the plasticity index  $PI$ . To highlight the influence of  $f$ , these parameters are normalized by the corresponding values measured at  $f = 1$  Hz, namely  $G_{max}^{1\text{ Hz}}$  and  $D_{S,0}^{1\text{ Hz}}$  (after Menq, 2003).

A similar behavior is observed in rock-like materials, as results from laboratory data typically show that this parameter is independent of the loading frequency in dry rocks (Johnston et al., 1979). Indeed, the energy dissipation results from the combined effect of several mechanisms that are linked with the microstructure of rocks, which are a composition of intact rock matrix and discontinuities – macroscopic fractures or small cracks. Therefore, part of energy



losses are an effect of rock matrix anelasticity (Walsh, 1966) and friction-based dissipation in relative motion along cracks and grain boundaries, that induce a frequency-independent energy loss. As in soils, the presence of fluid may induce additional energy dissipation, mainly through water wetting – it enhances friction-like relative sliding – or complex phenomena linked to the interaction with small cracks, e.g. “squirting” type flow from small cracks to pores (Mavko and Nur, 1975; O’Connell and Budiansky, 1977) in fully saturated rocks. In most scenarios, however, fluid losses seem not to dominate the frequency-independent losses induced by the remaining mechanisms, especially in shear at seismic frequencies (e.g., Paffenholz and Burkhardt, 1989).

### **2.2.2 Material parameters**

As in the investigation of the frequency effect, the assessment of the role of material parameters on the small-strain damping ratio accounts for the soil type, due to the different mechanisms contributing into the energy dissipation.

In fine-grained soils,  $D_{S,0}$  is mainly affected by the plasticity index  $PI$ , as highly plastic soils tend to be more dissipative than low plastic ones (Stokoe et al., 1995; Stokoe et al., 1999; Darendeli, 2001; Roblee and Chiou, 2004; Zhang et al., 2005; Figure 2-7), whereas the influence of confining pressure is secondary. The plasticity index also affects the sensitivity of  $D_{S,0}$  to the loading frequency. In highly plastic soils, in fact, there is an increase by 100% over a log-cycle increase in the frequency (Figure 2-5b). Specifically, variations become relevant at frequencies higher than 10 Hz (Darendeli, 2001). The small-strain damping ratio also depends on the overconsolidation ratio and the confining pressure (Hardin and Drnevich, 1972b; Darendeli, 2001), as their increase leads to a reduction in  $D_{S,0}$ . However, the induced variation is a second order effect compared to changes in  $PI$ .

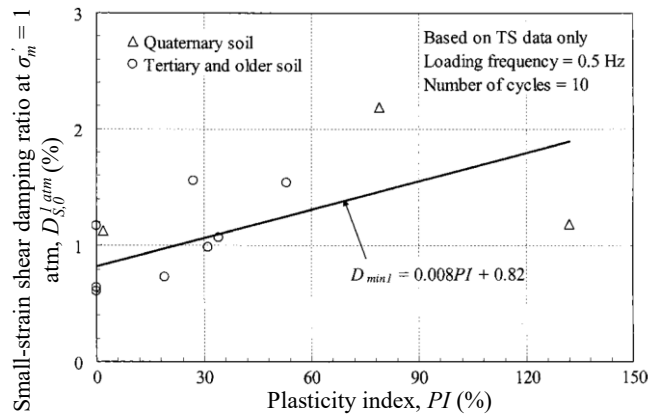


Figure 2-7. Relationship between plasticity index  $PI$  and small-strain shear damping ratio  $D_{S,0}^{I atm}$  (normalized to the atmospheric pressure; after Zhang et al., 2005).

In coarse-grained soils, instead, less case studies are available, due to issues in obtaining high quality measurements of the material damping ratio, especially for gravels. These difficulties stemmed from the rather low linear cyclic threshold (e.g.,  $10^{-4}\%$  in gravels), that force to investigate very low strain amplitudes, not easily achievable in laboratory testing (Menq, 2003). Nonetheless,  $D_{S,0}$  of coarse-grained soils is strongly dependent on the confining pressure  $\sigma'_m$  (Figure 2-8a; Laird, 1994; Menq, 2003). Menq (2003) also highlighted a remarkable effect of the grain size distribution, in terms of the uniformity coefficient  $C_u$  and the equivalent particle diameter  $D_{50}$ . Specifically,  $D_{S,0}$  decreases with increasing  $D_{50}$  and decreasing  $C_u$ . He also noticed a direct relationship with the void ratio (similar to Laird, 1994), albeit less well defined than in  $G_{max}$ .

Furthermore,  $D_{S,0}$  in coarse-grained materials is remarkably sensitive to the degree of saturation. Indeed, the moisture addition exerts a twofold effect on the damping ratio (Menq, 2003). On the one side,  $D_{S,0}$  becomes rather sensitive to the loading frequency, as reported in Section 2.2.1. Furthermore, it induces a strong increase with respect to the values measured on dry specimens, more than doubling itself (Figure 2-8b). The increase in magnitude and the frequency-dependence may be interpreted as the result of viscous damping caused by pore water movement in voids among soil particles.

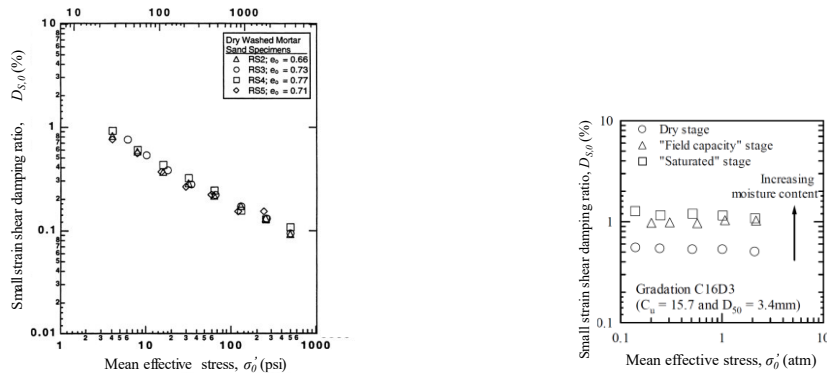


Figure 2-8. a) Effect of the confining pressure  $\sigma'_m$  on the small-strain damping ratio  $D_{S,0}$  in dry coarse-grained materials (after Laird, 1994); b) Effect of the moisture content on  $D_{S,0}$  in coarse-grained materials. The saturated stage corresponds to a water content equal to 14.4% (after Menq, 2003).

Finally, material damping in rock-like materials exhibits similar behavior to coarse-grained soils, as similar mechanisms of energy dissipation are involved. Specifically, this parameter depends on the confinement level and it is remarkably sensitive to the saturation degree, because the introduction of fluid in cracks introduces a slight frequency-dependence of  $D_{S,0}$  together with the increase in its value (e.g., Gardner et al., 1964).

### 2.2.3 Typical values of the small-strain damping ratio

This section provides an overview of typical values of  $D_{S,0}$ , to set an order of magnitude of this quantity as a function of the type of geomaterial. Furthermore, this section describes some of the most recent empirical relationships to estimate  $D_{S,0}$ , that also explicit the role of soil parameters. However, it should be remarked that the relationships presented below derive from laboratory tests, unless otherwise stated.

In fine-grained soils, the typical range of  $D_{S,0}$  is around 3÷5% (Kokusho, 2017). Darendeli (2001) calibrated an empirical equation for predicting  $D_{S,0}$  in fine-grained soils, that incorporates the dependency of  $D_{S,0}$  from  $f$  in the range between 0.2 and 100 Hz:

$$D_{S,0} = \left(0.8005 + 0.0129 \cdot PI \cdot OCR^{-0.1069}\right) \cdot \sigma'_m{}^{-0.2889} \cdot [1 + 0.2919 \cdot \ln(f)] \quad (2.7)$$

where  $PI$  is expressed in percentage,  $f$  in Hz, and  $\sigma'_m$  in atm. This relationship was developed from experimental tests carried out at  $\sigma'_m$  ranging from 30 to 2,500 kPa on soils characterized by  $PI$  ranging from 0 to 130% and  $OCR$  varying between 1 and 8. In addition, an estimation of the corresponding standard

deviation  $\sigma_D$  is provided, and the amount of variability depends on the mean estimate of  $D_{S,0}$  itself:

$$\sigma_D = 0.0067 + 0.78\sqrt{D_{S,0}} \quad (2.8)$$

Ciencimino et al. (2020) proposed a similar formulation for predicting  $D_{S,0}$  in fine-grained soils from Central Italy, in terms of the mean and  $\sigma_D$ :

$$\begin{aligned} D_{S,0} &= (1.281 + 0.036 \cdot PI) \cdot \sigma_m'^{-0.274} \cdot [1 + 0.134 \cdot \ln(f)] \\ \sigma_D &= e^{-0.6243} + e^{-1.5001} D_{S,0} \end{aligned} \quad (2.9)$$

This relationship was developed from experimental tests carried out at  $\sigma_m'$  ranging from 30 to 440 kPa on soils characterized by  $PI$  ranging from 0 to 42%.

However, both relationships for  $\sigma_D$  give only an estimation of the dispersion affecting the curves. Indeed, the adopted procedure does not propagate in a rigorous manner the uncertainties of the multiple variables related to the nonlinear relationships (Ciencimino et al., 2020). Furthermore, the dependence on the mean estimate of  $D_{S,0}$  was introduced mainly to account the increase in data uncertainty as the shear strain increases.

Figure 2-9 reports the mean  $D_{S,0}$  and the related variability (expressed through the coefficient of variation, CoV, defined as the ratio between standard deviation  $\sigma_D$  and mean) for fine-grained soils, as a function of  $PI$  in the range from 0 to 100%. Data were computed for three different confinement levels, i.e.,  $\sigma_m'$  equal to 50 kPa, 300 kPa and 1,000 kPa, to simulate conditions ranging from shallow to deep soil deposits. The computation accounted for the applicability constraints of the considered empirical relationships. Generally,  $D_{S,0}$  ranges around 1÷2%, up to 3% in plastic soils and the CoV varies between 0.5 and 1, meaning that the variability in the estimate is high.

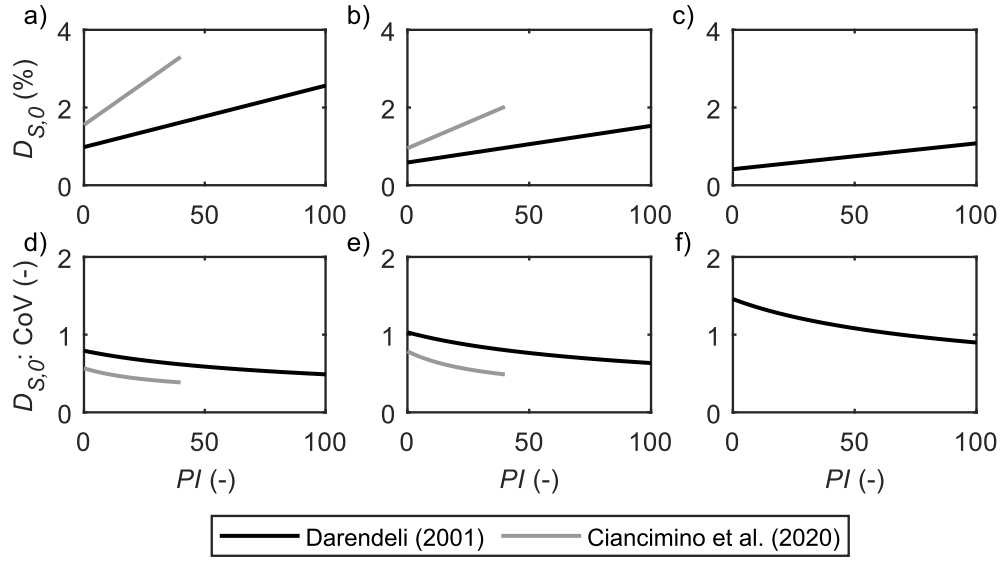


Figure 2-9. a-c) Empirical estimates of the mean value of the small-strain damping ratio  $D_{S,0}$  as a function of the plasticity index  $PI$ , for confining pressures equal to 50 kPa (a), 300 kPa (b) and 1,000 kPa (c); a-c) Empirical estimates of the coefficient of variation (CoV) of  $D_{S,0}$  as a function of  $PI$ , for confining pressures equal to 50 kPa (a), 300 kPa (b) and 1,000 kPa (c).

In coarse-grained soils, instead,  $D_{S,0}$  typically ranges around 1% (Kokusho, 2017). However, less case studies are available for gravels, due to difficulties in obtaining high quality measurements of material damping ratio at small strains (Menq, 2003). Menq (2003) proposed the following empirical relationship for dry coarse-grained materials, as a function of the uniformity coefficient  $C_u$ , the equivalent particle diameter  $D_{50}$  and the confining stress:

$$D_0 = 0.55 \cdot C_u^{0.1} \cdot D_{50}^{-0.3} \cdot \left( \frac{\sigma'_m}{p_{atm}} \right)^{-0.08} \quad (2.10)$$

He also provided a measure of variability, with a constant  $\sigma_D$  equal to 0.1%. Figure 2-10 compares the mean  $D_{S,0}$  and the related CoV for sands and gravels, as a function of  $\sigma'_m$ . Data were estimated from Menq (2003) relationships by setting  $C_u = 20$  and  $D_{50} = 8.0$  mm for gravels and  $C_u = 1.5$  and  $D_{50} = 0.5$  mm for sands. Compared to fine-grained soils, there is a reduction both in  $D_{S,0}$ , which is less than 1%, and in the CoV, which ranges around 0.2÷0.4.

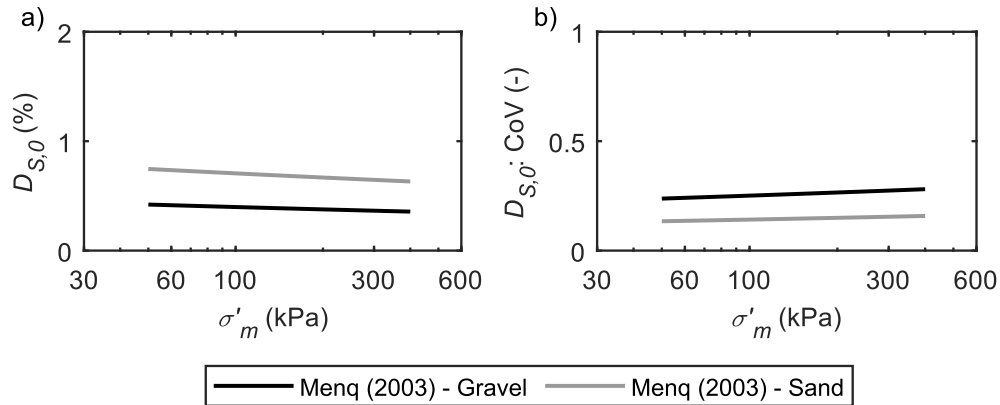


Figure 2-10. Empirical estimates of the mean (a) and the coefficient of variation (CoV - b) of the small-strain damping ratio  $D_{S,0}$  as a function of the mean confining stress  $\sigma'_m$  for gravels and sands.

Finally,  $D_{S,0}$  estimates for rock-like materials or cemented soils are mainly available through specific laboratory tests, whereas empirical relationships for its prediction are currently not available. Table 2.1 lists some typical values extracted from technical literature.

Table 2.1. Typical values of the small-strain damping ratio  $D_{S,0}$  for some dry rock-like materials or cemented soils.

Rock type	$D_{S,0}$
Tuffs (Choi, 2007)	0.4÷1%
Sandstone (Gardner et al., 1964; Paffenholz and Burkhardt, 1989)	0.2÷1.2%
Limestone (Paffenholz and Burkhardt, 1989)	0.1÷0.6%
Dolomite (Paffenholz and Burkhardt, 1989)	0.25÷0.6%

On the other hand, additional empirical relationships allow to infer  $D_{S,0}$  as a function of other mechanical parameters. A popular scheme relates the so-called “quality factor”  $Q_S$  (Carcione, 2007), which is an alternative dissipation parameter to  $D_{S,0}$  commonly used in seismology, with the S-wave velocity  $V_S$ . Many proposed formulations assume a proportionality between these parameters (e.g., Olsen et al., 2003; Campbell, 2009):

$$Q_S = \frac{1}{2D_{S,0}} = a + bV_S \quad (2.11)$$

Note that these relationships do not derive from laboratory-based damping estimates, but they are inferred from observations on ground motion data (see Chapter 4 for further details). Therefore, they are they are proxies of the in-situ

damping ratio and they might not necessarily provide a measure of intrinsic dissipation only.

## 2.3 Role of the small-strain damping ratio

### 2.3.1 Seismic site response

The proper prediction of the earthquake-induced ground motion is crucial for the seismic design of buildings and geotechnical systems. Typical design approaches do not model the complete propagation of seismic waves from the source (i.e., an active fault) to the target (e.g., a structure), as conventional ground motion prediction relies in a decomposition of the problem into three steps: source, path and site effects (Figure 2-11). Source effects analysis models the fault rupture and provides an estimation of the released energy, whereas path effects are linked with the propagation of seismic waves across the crust. Site effects, instead, represent alterations in amplitude and frequency content of seismic waves induced by local, near-surface geology. Modeling of source and path effects is typically carried out through Probabilistic Seismic Hazard Analyses (PSHA; Cornell, 1968). PSHA is performed for a reference geological condition, typically for rock-like outcropping formations. Therefore, site effects studies allow to map the ground motion from the reference conditions into a site-specific hazard estimate, that accounts for the site geomorphology. An effective indicator of variations in the ground motion characteristics due to local site conditions is the acceleration transfer function (TF), defined as follows:

$$TF = \frac{\ddot{u}_g(f, \mathbf{x})}{\ddot{u}_{g,o}(f)} \quad (2.12)$$

The TF measures relative variations between the Fourier spectrum of the ground acceleration  $\ddot{u}_g(f, \mathbf{x})$  at the generic location  $\mathbf{x}$  inside the soil deposit (typically, the free surface) and the Fourier spectrum of the ground acceleration  $\ddot{u}_{g,o}(f)$  recorded in rock-like outcropping formation, i.e. the reference geological condition (Figure 2-11). An alternative indicator commonly used in engineering seismology is the spectral amplification function AF, defined as the ratio between the 5%-damped elastic response spectrum  $S_e(T, \mathbf{x})$  in a location in the soil deposit and the reference one  $S_{e,o}(T)$ :

$$AF = \frac{S_e(T, \mathbf{x})}{S_{e,o}(T)} \quad (2.13)$$

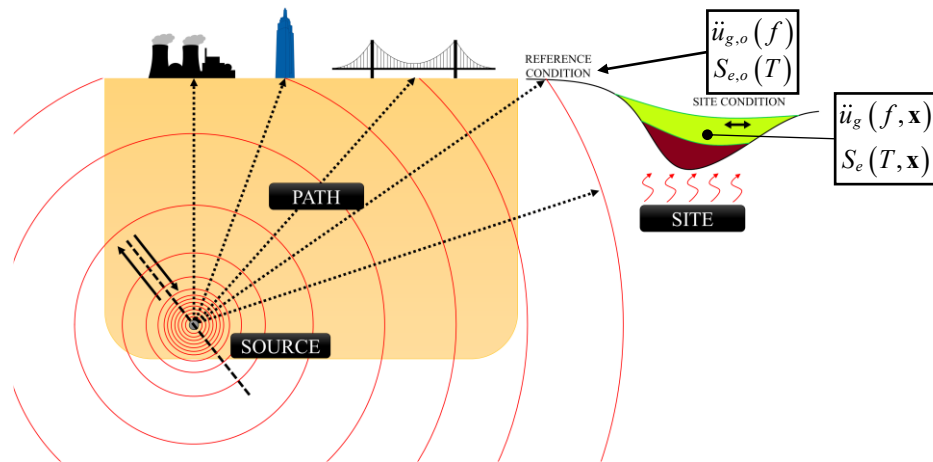


Figure 2-11. Distinction between source, path and site effects in propagating seismic waves (modified from Passeri, 2019). The plot highlights the motion recorded in the reference geological condition, represented in terms of the Fourier spectrum of the ground acceleration  $\ddot{u}_{g,o}(f)$  and the elastic response spectrum  $S_{e,o}(T)$ , and the motion inside the soil deposit, represented in terms of  $\ddot{u}_g(f, \mathbf{x})$  and  $S_e(T, \mathbf{x})$ .

The modifications in ground motion characteristics are the result of the mechanical properties of the soil deposit and the geometry of stratigraphic interfaces and they are usually termed as stratigraphic amplification and topographic amplification. A detailed assessment of the modification of the ground motion should take into account all these factors, by carrying 2D or even 3D analyses – typically termed as Site Response Analyses (SRAs). Yet, SRAs require a detailed geologic and geotechnical characterization of the location under examination for an adequate extent, able to cover the representative volume of interest. The large amount of investigations required and the necessity of sophisticated numerical codes make SRAs to be used only on specific project topics, e.g. for critical facilities. Ordinary design applications typically rely on 1D Ground Response Analyses (GRAs), that assume a 1D model for the site deposit and ignore the actual geometry (i.e., lateral variations, local heterogeneities, etc.) to focus on stratigraphic amplification. Even though this scheme is not applicable in every geological condition, GRAs have become very popular thanks to the limited amount of input parameters, the simplicity in the interpretation and the limited computational effort. In addition, GRAs have been proved to provide reliable estimates of site amplification in several cases.

Notwithstanding their simplicity, GRAs are affected by uncertainties due to several factors. Following the scheme devised by Idriss (2004) and Rathje et al. (2010) and extended by Passeri (2019), the main sources of uncertainties are the shear-wave velocity ( $V_s$ ) profile, the MRD curves, the shear strength, the small-



strain damping ratio, the input motions selection and the type of approach for modeling soil dynamic behavior. The choice of mechanical parameters is a nontrivial task, yet it is a critical step in conducting GRAs. Indeed, the key issue is the non-existence of a priori conservative values for the mechanical parameters. The reason of this difficulty is the coupled effect of the large amount of input information involved in GRAs, that may have mutual and/or opposite effects on the resulting amplification, and the remarkable nonlinearity that affects the problem. For this reason, GRAs should be carried out by considering the parameter uncertainties in an explicit way, within a probabilistic framework in order to Identify, Quantify, and Manage (i.e., IQM method; Passeri, 2019) all the uncertainties and variabilities involved in the analyses. A thorough discussion on the role of each parameter and the related uncertainties would be beyond the scope of this dissertation, which focuses on the effect of the small-strain damping ratio. A detailed overview of the remaining parameters is available in Foti et al. (2019a), Foti et al. (2019b), Passeri (2019), and Foti et al. (2021).

Although the uncertainties related to  $D_{S,0}$  are usually referred as secondary (Idriss, 2004; Rathje et al., 2010; Cabas and Rodriguez-Marek, 2018), the choice of adequate values can strongly affect the soil response, especially in the small-strain field (e.g., Thompson et al., 2012; Tao and Rathje, 2019). For instance, Field and Jacob (1993) observed that poorly constrained damping ratio values, together with uncertainties in the S-wave velocity of shallow layers, result in a large variability in simulated amplification data. Boaga et al. (2015) observed that  $D_{S,0}$  affects the 1-D amplification in presence of strong impedance contrasts and its effect is more relevant at high frequencies, whereas its impact is smaller in soil deposits with smooth variations of the mechanical properties. Indeed, in the presence of sharp variations in stiffness, the 1-D ground model exhibits a response closer to the theoretical case of a homogeneous medium over a rigid bedrock, where the entity of the ground motion amplification is inversely proportional to  $D_{S,0}$  (Kramer, 1996).

Ordinary applications estimate  $D_{S,0}$  by means of specific laboratory tests or from in-situ surveys, based on seismological methods or geophysical testing – the different estimation methods will be addressed in Chapter 4. Alternatively, empirical models (e.g., Hardin and Drnevich, 1972a; Kokusho et al., 1982; Seed et al., 1986; Vucetic and Dobry, 1991; Ishibashi and Zhang, 1993; Darendeli, 2001; Menq, 2003; Zhang et al., 2005; Senetakis et al., 2013; Vardanega and Bolton, 2013; Ciancimino et al., 2020) can be used to predict the soil behavior as a function of different variables (e.g., soil type,  $PI$ , mean confining pressure,  $OCR$ , loading frequency). The uncertainties on the empirical models related to the

experimental variability of MRD curves and possible experimental errors can be quantified through the standard deviation provided along with the mean values (e.g., Darendeli, 2001; Zhang et al., 2005; Akeju et al., 2017; Ciancimino et al., 2020). Conversely, when laboratory tests are carried out, the main uncertainties are related to the experimental limitations and the natural randomness of soil properties at the site scale, associated with geological spatial variations (Park and Hashash, 2005).

However, the applicability of  $D_{S,0}$  values obtained through laboratory tests for GRAs has been questioned by different Authors (e.g., Thompson et al., 2012; Stewart et al., 2014a; Zalachoris and Rathje, 2015; Xu et al., 2019). Indeed, experimental evidence from back-analysis of Down-Hole seismic arrays showed small-strain damping ratios in the field larger than the values obtained through laboratory tests (see Chapter 4). For clarity of interpretation, the small-strain damping ratio in field is hereafter referred as  $D_{S,0}^{site}$ , while  $D_{S,0}$  is adopted for the material small-strain damping ratio measured in the laboratory. These differences have to be interpreted taking into account the energy dissipation mechanisms acting at the site scale. Wave scattering effects can modify the propagating seismic waves due to heterogeneities in the soil profile (Field and Jacob, 1993; Thompson et al., 2009). This phenomenon, which is relevant especially in the presence of large contrasts of mechanical properties (Zalachoris and Rathje, 2015), causes additional energy dissipation to the material dissipation and cannot be captured by laboratory tests. As a consequence, the  $D_{S,0}^{site}$  should be adopted as small-strain damping when GRAs are performed. However, the proposed methods for estimating  $D_{S,0}^{site}$  rely on data and resources that are often not available in common engineering applications and there is no consensus about the best approach for its estimate. This difficulty has been highlighted by Stewart et al. (2014a), who suggested dealing the discrepancy between  $D_{S,0}^{site}$  and  $D_{S,0}$  as an epistemic uncertainty, when no measurements of  $D_{S,0}^{site}$  are available. Therefore, this uncertainty should be handled through a sensitivity study by assuming different  $D_{S,0}^{site}$  values, given as the sum of  $D_{S,0}$  and a depth-independent additional damping  $\Delta D$ , ranging between zero (i.e.,  $D_{S,0}^{site}$  coincides with  $D_{S,0}$ ) and 5%.

Foti et al. (2021) investigated the influence of the uncertainties in  $D_{S,0}$  in the seismic ground amplification, mapping the variations of  $D_{S,0}$  on the stratigraphic amplification of generic soil models, extracted from a stochastic database of GRAs (Aimar et al., 2020). In this dissertation, only results from two subsets are presented: a group of relatively stiff ground models, characterized by time-weighted average of the  $V_S$  profile ( $V_{S,H}$ ) of 400÷450 m/s and bedrock depth close

to 40 m; a group of soft soil deposits, with  $V_{S,H}$  close to 250 m/s and sediment thickness around 60 m. Following the recommendations prescribed in Stewart et al. (2014a), for each ground model multiple GRAs were performed, by computing for each layer  $D_{S,0}^{site}$  as the sum of  $D_{S,0}$ , derived through literature models, and an additional depth-independent damping  $\Delta D$  equal to 0%, 2.5% and 5%. Simulations were carried out with seismic input motions representative of small-to-moderate and high seismicity levels. Figure 2-12a-b shows the mean AF for each group of soil models, for low and high seismicity. The impact of  $D_{S,0}^{site}$  depends on the deformability of the ground model and on the level of seismicity. Variations in  $D_{S,0}^{site}$  have a strong influence on the seismic amplification in deformable soil deposits (Figure 2-12b), with a reduction of the AF up to 10% at resonance and 30% at high frequencies for  $\Delta D = 5\%$ . Similar features are observed under strong seismic input motions, even though the effect is less relevant. As for the variability in the stratigraphic amplification (Figure 2-12c-d), the increase of  $D_{S,0}^{site}$  induces a slight reduction in the variability of AF, especially at short vibration periods in soft soil deposits. This kind of ground models, indeed, usually exhibits local variations – i.e., thin layers, in 1-D conditions – that induce strong variability in the response. On the other side, increasing  $D_{S,0}^{site}$  leads to an overdamping of the high-frequency components of the wavefield, that are more sensitive to such variations. Furthermore, the effect of  $D_{S,0}^{site}$  on the response variability is observed on soft soil models under strong seismic inputs (Figure 2-12d). A possible reason might be the shifting of the  $D$  curve towards higher values at large strains due to the increase of  $D_{S,0}^{site}$ , resulting in an additional attenuation of the high-frequency components of the wave.

In the same study, Foti et al. (2021) addressed the influence of  $D_{S,0}$  on a site-specific amplification study, with reference to the site of Roccafluvione (Italy). The uncertainties of  $D_{S,0}^{site}$  were simulated through the approach suggested by Stewart et al. (2014a) also in this case, hence  $D_{S,0}^{site}$  was computed as the sum of  $D_{S,0}$  (derived from the model by Ciancimino et al., 2020) and an additional contribution  $\Delta D$ , equal to 0%, 2.5%, and 5%. GRAs were performed with reference to two suites of input motions, compatible with the site-specific Uniform Hazard Spectra for the return periods of 50 and 475 years.

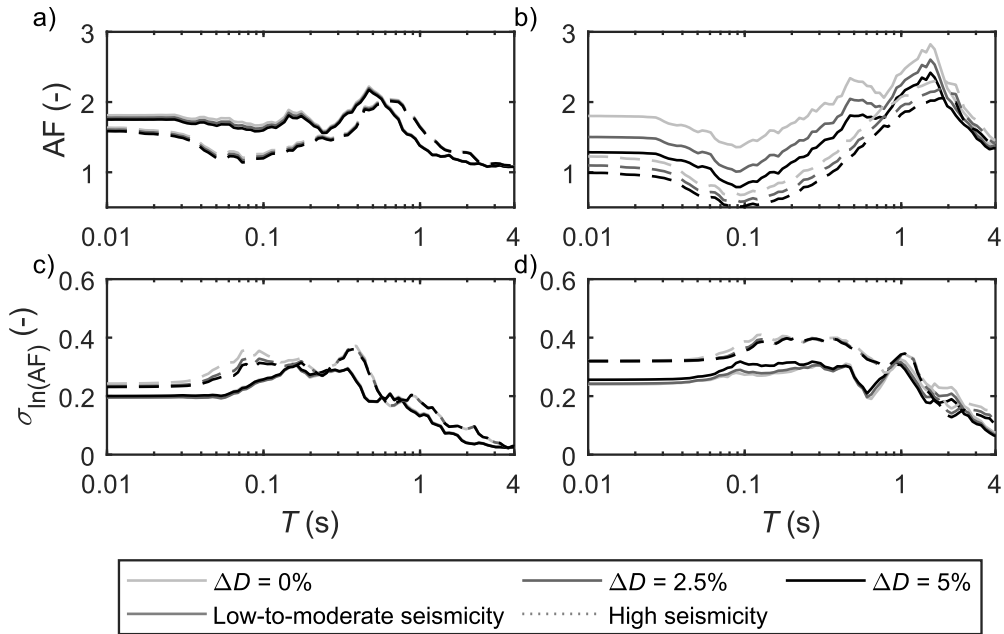


Figure 2-12. a-b) Mean amplification factor AF vs. period  $T$  for moderately stiff (a) and deformable (b) soil deposits, as a function of the additional damping contribution  $\Delta D$  and seismicity level; c-d) Standard deviation (in logarithmic scale) of the AF  $\sigma_{\ln(AF)}$  vs.  $T$  for moderately stiff (a) and deformable (b) soil deposits, as a function of  $\Delta D$  and the seismicity level (after Foti et al., 2021).

They compared variations in the AF due to the epistemic uncertainty in  $D_{S,0}$  with the variability due to  $V_S$  and the MRD curves. Such variability was computed over a statistical sample of ground models generated through a Monte-Carlo simulation from results of the geophysical investigations by keeping  $D_{S,0}^{site}$  as equal to  $D_{S,0}$  in Foti et al. (2019a). The corresponding AF distribution is represented in Figure 2-13 by the interval defined by the mean and one standard deviation (in logarithmic scale), together with the curves obtained as a function of  $\Delta D$ . A change in  $D_{S,0}^{site}$  leads to a variation in the amplification which is significant compared with the overall variability of the results. Indeed, for  $\Delta D = 2.5\%$ , the AF is close to the lower boundary of the distribution, whereas a value  $\Delta D = 5\%$  leads to a large reduction of the amplification, which lies completely below the bounds. This effect is relevant especially at high frequencies and close to the resonance peak, even when the soil profile is subjected to the higher seismicity level. This difference demonstrates that variations in  $D_{S,0}^{site}$  may have a considerable impact on stratigraphic amplification and its proper quantification is necessary for a good prediction of the ground response in seismic conditions.

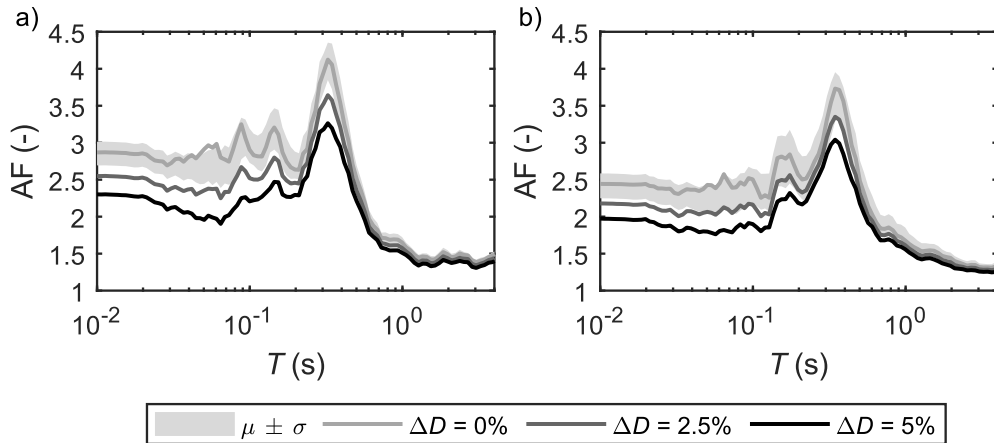


Figure 2-13. Comparison between the distribution of the amplification factor AF (represented in terms of  $\mu \pm \sigma$  interval), obtained by varying the S-wave velocity  $V_S$  and the MRD curves, and the AF curves as function of the additional damping contribution  $\Delta D$  for (a) low-intensity motions and (b) high-intensity motions (after Foti et al., 2021).

Finally, the recent study by Rodriguez-Marek et al. (2021) investigated the epistemic uncertainties affecting GRAs, with reference to a synthetic soil model. Differently from previous studies, they did not assess only the effect of variations in  $V_S$ , but they performed a thorough investigation of the role of various soil deposit mechanical parameters, including  $D_{S,0}^{site}$  as well. Their study, indeed, is an attempt to overcome issues in modeling epistemic uncertainties that, according to the Authors, are the result of an oversimplified and incomplete definition of such uncertainties. The mapping of epistemic uncertainties into the ground motion amplification was carried out through a logic tree approach, where multiple scenarios (called “branches”) – each corresponding to a possible outcome for any input variable – are modelled (Figure 2-14). In this study,  $D_{S,0}^{site}$  was assumed to be proportional to the laboratory-based estimate  $D_{S,0}$  and the related uncertainties were introduced by setting various values on the multiplier. Logic trees allow to infer both the statistical dispersion of the amplification and the relative contribution of the epistemic uncertainties of each parameter. The latter is provided by sensitivity analyses on results, that compute the mean amplification conditioned on a specific branch (i.e., a specific value) for each parameter being true. The conditioned means can then be compared to the overall mean, in terms of relative difference (in logarithmic scale), called “sensitivity” (Figure 2-15). Interestingly, the multiplier of  $D_{S,0}$  is the most influencing parameter at short vibration periods, with an impact even more relevant than  $V_S$ . This entails that the high-frequency amplification is strongly dependent on  $D_{S,0}$ . Conversely, the long-

period response is mainly affected by variations in the  $V_S$  of shallow layers, whereas  $D_{S,0}$  plays a secondary role.

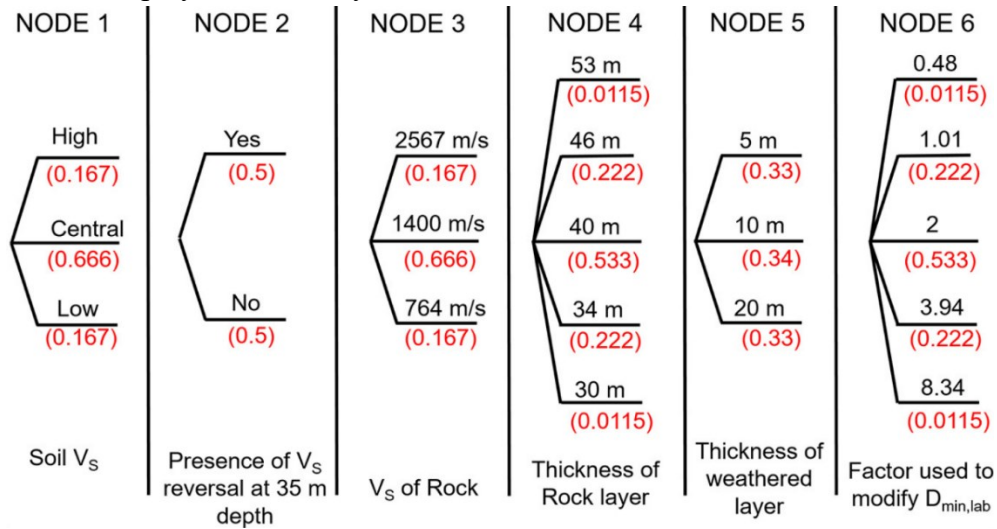


Figure 2-14. Logic tree used for the analysis of the effect of epistemic uncertainties in GRAs (after Rodriguez-Marek et al., 2021).

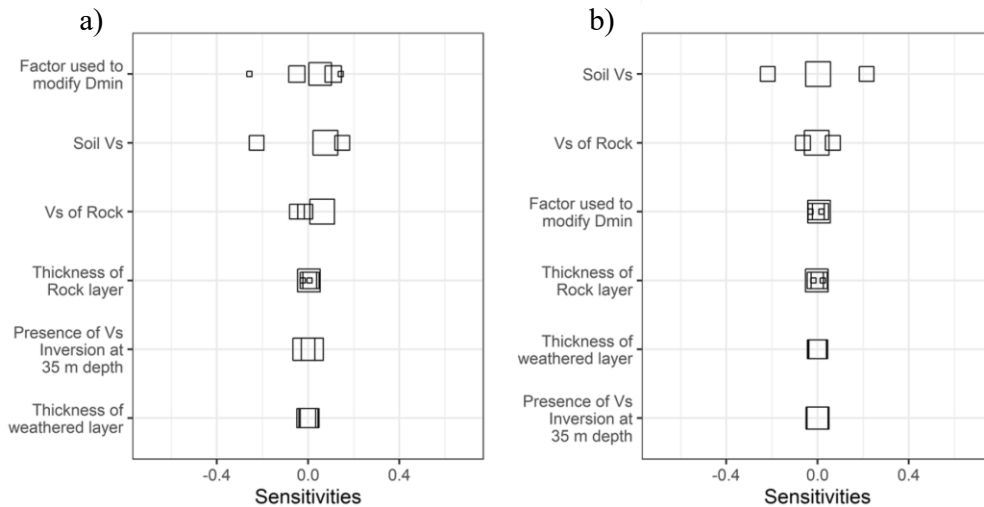


Figure 2-15. Sensitivity of the mean amplification factor AF to the various parameters involved in the logic tree (Figure 2-14), as a function of the investigated vibration period  $T$ : 0.1 s (a) and 1.0 s (b). The size of each symbol is proportional to the weight assigned to the corresponding branch (after Rodriguez-Marek et al., 2021).

### 2.3.2 Ground vibrations

The proper assessment and management of artificially induced vibrations has gained interest in the last decades, due to the growing environmental concern and

the impact on acoustic comfort of people. Besides, at very high levels, vibrations might induce structural damage. Sources of vibrations can be clustered into three main categories: traffic, industrial activity and construction activity. The distinction is just indicative and not exhaustive, although each category is characterized by different levels of amplitude and frequency content. National and international guidelines set proper constraints, based on various kinds of parameters, threshold levels and frequency ranges, as a function of potential consequences of vibrations in building. The considered scenarios are malfunctioning of sensitive equipment (e.g., Gordon, 1991), discomfort to people (e.g., British Standard Institution, 1992; International Organization for Standardization, 1999) and structural damage (e.g., Deutsches Institut für Normung, 1999). Generally, criteria rely on design parameters linked with the particle velocity field, hence this is the target quantity intervening in vibration-based problems.

The prediction of the entity of ground-borne vibration often relies on empirical approaches. However, the current trend is to perform a theoretical prediction to simulate the whole phenomenon of vibration propagation, based on physical modeling. From the physical viewpoint, vibrations are elastic waves that are generated by a source, which is simulated as a dynamic force applied onto the soil. These waves propagate inside the medium and they impinge on the receiver (e.g., the foundations of nearby buildings), thus generating structural vibrations and re-radiated noise (Figure 2-16). Typical modeling performs a decomposition of the problem into three subproblems, that are treated separately (e.g., Lai et al., 2005a): the characterization of the source, the transmission of elastic waves from the source to the receiver under free-field conditions, and the interaction of the receiver with the incident wave field. The decomposition does not account for the mutual dependence of the solutions of each subproblem, however the approximation introduced by such separation is acceptable when the characteristic wavelength of the generated wavefield is small compared to the source-receiver distance. In this case, indeed, the presence of the target element does not significantly affect the incident wavefield. Not surprisingly, this partition recalls the source-path-site separation used in engineering seismology. Indeed, seismic hazard analysis and vibration studies both address the propagation of mechanical waves in the soil, albeit with some key differences. On the one side, ground-borne vibrations induce low strain levels, lying below the linear cyclic threshold shear strain, whereas seismic waves usually have large amplitudes, hence the nonlinearity may be relevant. Therefore, the transmission of ground-borne vibrations may be modeled using a linear soil constitutive model. Furthermore,

vibrations involve waves with frequencies (up to 200 Hz) that are an order of magnitude higher than those induced by earthquakes (up to 30 Hz; Pyl, 2004).

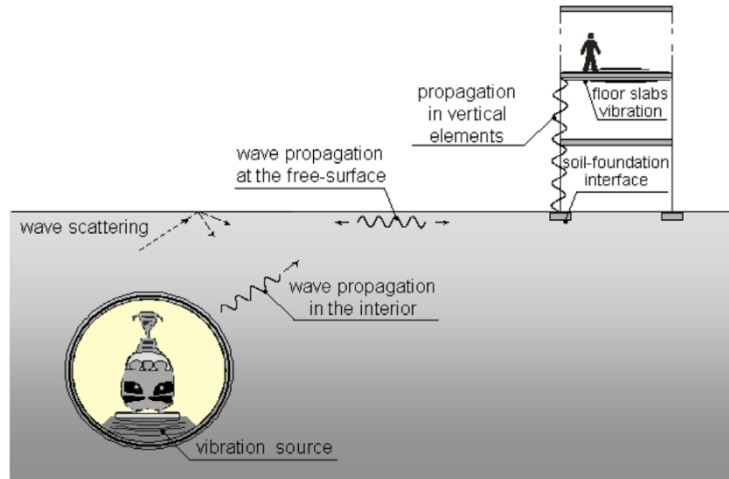


Figure 2-16. Schematic representation of the propagation of ground-borne vibrations (after Lai and Özcebe, 2015).

The soil model characteristics are relevant in the assessment of vibrational impact, as they affect both the source characterization, the propagation, and the interaction with the receiver. On the one side, the energy transmitted from the source into the ground is the result of an interaction among the source itself, the foundation and the soil, all of them affecting the entity of vibrations. Then, the energy spreads into the soil medium in free field conditions, undergoing changes in amplitude and frequency content as an effect of soil anelasticity. Finally, the ongoing wave impinges the receiver, and the induced motion is affected by the interaction between the foundation and the soil. This section focuses on key aspects about vibrations generation and propagation, whereas the interaction with the receiver is addressed in the next section, due to the remarkable analogies with the problem of seismic soil-structure interaction. Furthermore, several studies tend to couple the modeling of the source effects and the propagation of vibrations in the ground.

Modeling of the source effects often relies on physically-based analytical models or numerical schemes that account for the mutual interaction between the source and the underlying structure and soil (e.g., Lombaert et al., 2000; Clouteau et al., 2001; Hussein and Hunt, 2007). The relevant role of soil model characteristics is evident when focusing on prediction accuracy of such theoretical models. Comparing predicted vibrations to experimental data often reveals good qualitative agreement, whereas it is challenging to achieve a good quantitative accuracy, as the prediction in common models error usually ranges around 10 dB



(Hunt and Hussein, 2007). Furthermore, the degree of fit strongly depends on the excitation frequency. For instance, Lombaert and Degrande (2003) and Lombaert et al. (2006) noticed that simulated and experimental data compare well when dealing with noise generated by road traffic, whereas the matching quality is poor if effects of rail traffic are investigated. The different performance is the coupled effect of uncertainties in the soil model and the frequency content of the vibration generated by the source. On the one side, the complete spatial variation of dynamic soil characteristics is impossible to identify, hence soil models are subject to uncertainty (Lai and Özcebe, 2015). Furthermore, road vehicles mainly generate a low-frequency signal that, having large wavelengths, is poorly sensitive to small variations and local heterogeneities in the soil. Notwithstanding several studies explicitly recognize the paramount role of soil dynamic parameters in the ground-borne vibrations (e.g., Kouroussis et al., 2011), only few cases performed a thorough parametric analysis on this purpose or used in situ estimates of soil parameters, especially for the dissipative ones (e.g., Dos Santos et al., 2016).

Schevenels (2007) investigated in detail the influence of soil dynamic parameters on the free-field wave propagation. For this purpose, he carried out a parametric analysis on a homogeneous half space, by modifying each soil parameter separately and studying variations in the propagating wave. The variability in  $V_S$  and  $D_{S,0}$  was modeled assuming a lognormal distribution, where the mean value and standard deviation are consistent with typical studies of stochastic soil dynamics. The coefficient of variation of  $D_{S,0}$  is equal to 0.4, which is much higher than the dispersion in the soil stiffness (as the corresponding value is 0.2), to account for the high uncertainties affecting in situ estimates of  $D_{S,0}$  (Figure 2-17a-d; Karl, 2005). The vibration entity was measured through displacement transfer functions, that provide the displacement field due to a unit force applied on the surface of the medium. He noticed that variations in  $D_{S,0}$  impact in a similar way to those in  $V_S$  (Figure 2-17). Furthermore, the effect strongly depends on the investigated frequency, as the variability in the estimated transfer function exponentially increases with the frequency, especially at large distances from the source. For instance, the 95% confidence region of the transfer function estimated at high frequencies far from the source may span multiple orders of magnitude. This result demonstrates the strong impact of the uncertainties in  $D_{S,0}$  in the wave propagation at small strains.

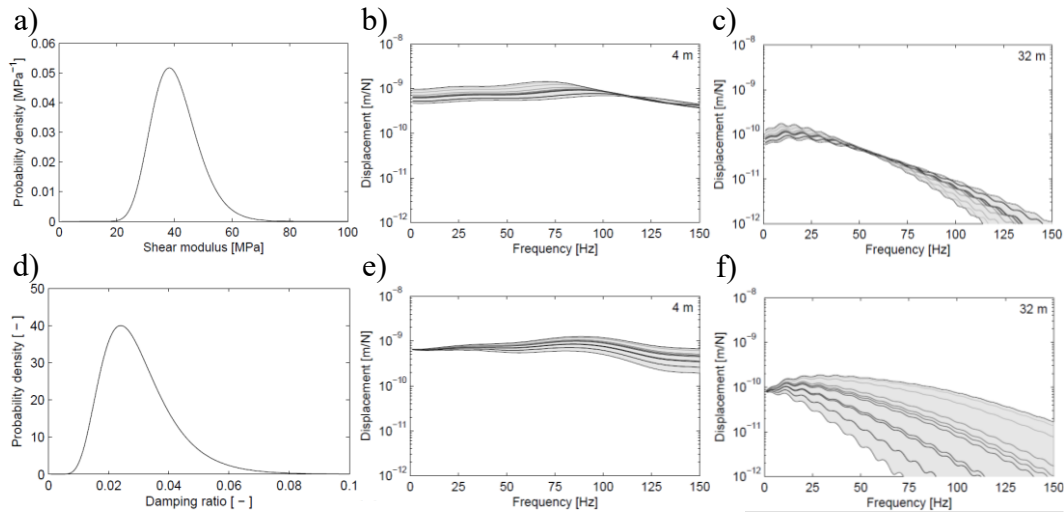


Figure 2-17. a-c) Parametric study with reference to the shear modulus: a) Probability density distribution; Ten realizations (grey lines) and 95% confidence regions (shaded area) of the transfer function amplitude for a receiver located at 4 m (b) and 32 m (c) from the source; d-f) Parametric study with reference to the shear damping ratio: d) Probability density distribution; Ten realizations (grey lines) and 95% confidence regions (shaded area) of the transfer function amplitude for a receiver located at 4 m (e) and 32 m (f) from the source. Darker lines correspond to higher values of the investigated parameter (after Schevenels, 2007).

Instead, Papadopoulos et al. (2019) investigated the effect of soil parameters uncertainties on the estimated transfer function for a real case. Specifically, they mapped soil uncertainties into the response of a real building, located in Belgium. Simulations considered a suite of representative soil profiles obtained from the interpretation of a MASW survey, with low-uncertainty  $V_S$  data, whereas  $D_{S,0}$  is well constrained in the shallow layers, but it is affected by high variability at greater depths (Figure 2-18a-b). The parameter uncertainty results in broad variability in the theoretical transfer function and in the estimated displacements in the structure that, however, allow to achieve a good prediction of the in situ observed data (Figure 2-18c).

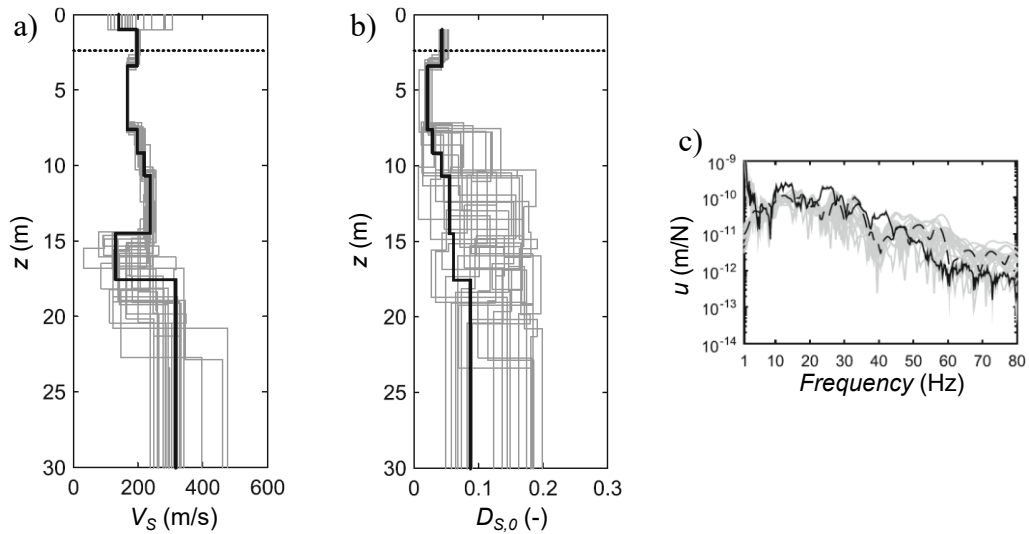


Figure 2-18. a-b) Representative S-wave velocity  $V_S$  and small-strain damping ratio  $D_{S,0}$  profiles; c) Measured (solid line) vs. predicted (dashed line) vertical displacement transfer function  $u$  at the ground floor of the target building. The grey solid lines denoted realizations for different soil profiles (after Papadopoulos et al., 2019).

### 2.3.3 Dynamic soil-structure interaction

The parameters describing the low-strain soil dynamic behavior are relevant also in problems of dynamic soil-structure interaction. Indeed, in the presence of dynamic loading, the deformability of the soil-foundation system affects the motion of the structure and, conversely, the motion of the structure itself affects the motion of the soil-foundation system. Therefore, there is a mutual effect of the components' deformability on the overall response of the system. Variations in the dynamic response in the structures due to the interaction between the superstructure, the foundation and the underlying soil are termed as Soil Foundation Structure Interaction (SFSI).

This kind of problem is relevant in all the geotechnical systems, and it is intrinsically complex. Indeed, the mechanisms involved in the dynamic interaction primarily depend on the foundation type because, for example, structures founded on footings or piles (e.g., Mucciacciaro and Sica, 2018) exhibit rather different responses. Furthermore, the characteristics of the superstructure itself affect the response of the system, as the interaction changes when dealing with isolated piers (e.g., Gaudio and Rampello, 2019), continuous-beam bridges or multi-storey buildings. Also, the boundary conditions of the system affect dynamic interaction. Typical examples are offshore systems, where water actively participates in the global response (e.g., Kementzetzidis et al., 2019), or earth-

retaining walls (e.g., Argyroudis et al., 2013). Even the degree of contact between the foundation and the underlying soils may affect the overall response, e.g. in the presence of local scour at bridge piers (e.g., Ciancimino et al., 2021).

Nonetheless, the global response of the soil-foundation-structure system involves some basic features, that are shared across different geotechnical systems. On the one side, the deformability of the supporting soil affects the dynamic response of the system, as the foundation is characterized by additional degrees of freedom in terms of translation and rotation. This interaction results in the lengthening of the fundamental period of the system and to an increase of energy dissipation, which is not only due to intrinsic structural damping, but it also occurs through wave radiation and hysteretic behavior of the soil (Veletsos and Meek, 1974). In most cases, the SFSI induces a reduction of the seismic demand in structures, hence a conservative design approach would disregard such effects. However, several Authors identified specific situations where SFSI could be detrimental to the dynamic response (e.g., Mylonakis and Gazetas, 2000). For instance, the period lengthening increases the seismic demand in stiff structures, whereas the SFSI might increase the displacement- and the ductility-demand in flexible structures. Furthermore, it could favor double resonance phenomena when the natural frequency of the whole system approaches the predominant frequency of the ground motion or the fundamental frequency of the soil deposit.

Proper modeling of SFSI is crucial for estimating the structural response to ground borne vibrations, especially when modeling three-dimensional effects of traffic induced vibrations. This interaction is relevant especially when the ground and structural stiffnesses are comparable or when a deformable structure lies on stiff soils (François et al., 2007). Furthermore, dynamic SFSI may be relevant in spatially variable soil deposits, even if they are moderately stiff, especially at high frequencies (Papadopoulos et al., 2018). Yet, this kind of modeling is more challenging than seismic SFSI due to the broader frequency range investigated. Indeed, the prediction of the high frequency response is more sensitive to modeling errors and local variations in the model.

Given the nature of the phenomenon, SFSI is strongly dependent on the geotechnical parameters of the soil deposit. The most relevant parameter is soil stiffness, as it governs soil deformability which, in turn, is responsible of the SFSI (Veletsos and Meek, 1974). Instead, the mapping of the soil dissipation characteristics into the SFSI is nontrivial. Indeed, energy dissipation in SFSI occurs as the composition of multifold phenomena, that combine geometrical and anelastic effects. Furthermore, different geotechnical systems involve different mechanisms of energy dissipation, where the role of soil damping can be variable.

For instance, in shallow foundations, energy dissipation is the result of three main mechanisms of energy dissipation. One component is dissipation due to inelastic phenomena occurring in the structure (termed as “structural damping”), which is usually modeled as equivalent viscous damping. Then, hysteretic dissipation in the soil deposit contributes to motion attenuation. Another component is radiation damping, which is the geometrical effect of radiation of waves emanated at the foundation-soil interface that, spreading outward, carry energy away from the foundation system. Radiation damping is highly dependent on the frequency, and it increases with the foundation width and embedment depth. However, it decreases when the soil deformability is lower, except in case of deep homogeneous soil deposits. In a completely different case, as in offshore structures and wind turbines, part of energy dissipation occurs geometrically through hydrodynamic damping, that mimics the energy carried away due to viscous drag exerted by water and wave radiation (e.g., Kementzetzidis et al., 2019).

Typical modeling assumes that the radiation damping represents the main mechanism of energy dissipation, especially at small strains. However, in stiff, slender structures with height-width ratios greater than one, large part of energy is dissipated by material damping (Ambrosini, 2006). Furthermore, Martakis et al. (2017) observed in centrifuge tests that the identified equivalent damping ratio in SSI is remarkably larger than the predicted one and it exhibits a strong dependence on the shaking intensity (hence, the strain level). The strain dependence supports the idea that the main dissipation mechanism is hysteretic and linked to soil intrinsic dissipation even at small strains, in contradiction with the common practice. However, most studies focused on the search for an appropriate modeling of soil nonlinearity and the choice of the constitutive model, whereas a specific study on the choice of soil parameters has not been carried out yet, especially in terms of dissipation at small-strains.

# Chapter 3

## Wave propagation

Mechanical waves represent the propagation in space of a perturbation of a physical attribute applied in a physical medium (Ben-Menahem and Singh, 2012). The propagation only involves a transfer of energy, whereas there is no transportation of material, as particle movement occurs through small distances about the equilibrium point in an oscillatory way, without permanent displacement.

In earthquake engineering, a basic classification of the mechanical waves of interest (also termed as seismic waves) distinguishes body waves and surface waves. Body waves are mechanical waves propagating within the body of the medium and many typical applications rely on two main classes: compression waves (or P-waves) and shear waves (S-waves). Surface waves, instead, exist when the medium includes a free surface. The attribute “surface” derives from the fact that the wave energy propagates only in the portion of the medium closest to the free surface. The most investigated surface waves are the Rayleigh waves, although some applications also involve Love and Scholte waves (e.g., Shinkarenko et al., 2021). Additional types of body and surface waves can carry energy inside a physical medium, depending on the specific boundary conditions or even the constitutive model (e.g., Biot, 1956). However, this dissertation will address only Rayleigh waves as they are widely used in site characterization studies.

The wave propagation theory involves alternative criteria for the classification of mechanical waves. A relevant distinction separates hyperbolic waves and dispersive waves. Hyperbolic waves propagate in the medium according to hyperbolic partial differential equations and they travel at a fixed velocity, depending on the medium mechanical properties. Body waves propagating in an isotropic, linear elastic medium are an example of hyperbolic waves. Dispersive waves, instead, assume a complex behavior, because the propagation speed is a function of the wave frequency. As each frequency component travels at a different speed, nonmonochromatic signals change shape as they propagate (Figure 3-1a-b). Due to this dependence, the description of the wave propagation velocity is nontrivial and it refers to two parameters: the phase velocity and the

group velocity. Their definition relies on the solution for dispersive waves, here referred to the simplified case of one-dimensional propagation along the spatial coordinate  $x$  (e.g., Foti et al., 2014):

$$u(x, t) = Ae^{i[kx - \omega(k)t]} \quad (3.1)$$

In the equation,  $u$  labels the displacement (but it can be any physical quantity),  $A$  is the wave amplitude and  $k$  is the wavenumber, which is a parameter characterizing the wave propagation, at the circular frequency  $\omega$ . The phase velocity is the propagation speed of the wavefront, which is the locus of points with equal phase, i.e.

$$kx - \omega(k)t = \text{const.} \quad (3.2)$$

Therefore, the phase velocity is defined as follows:

$$V = \frac{dx}{dt} = \frac{\omega(k)}{k} \quad (3.3)$$

The group velocity, instead, represents the propagation speed of the wave energy (Figure 3-1c) and it is defined as follows:

$$V_g = \frac{d\omega(k)}{dk} \quad (3.4)$$

Rayleigh waves propagating in a vertically heterogeneous, elastic medium are an example of dispersive waves.

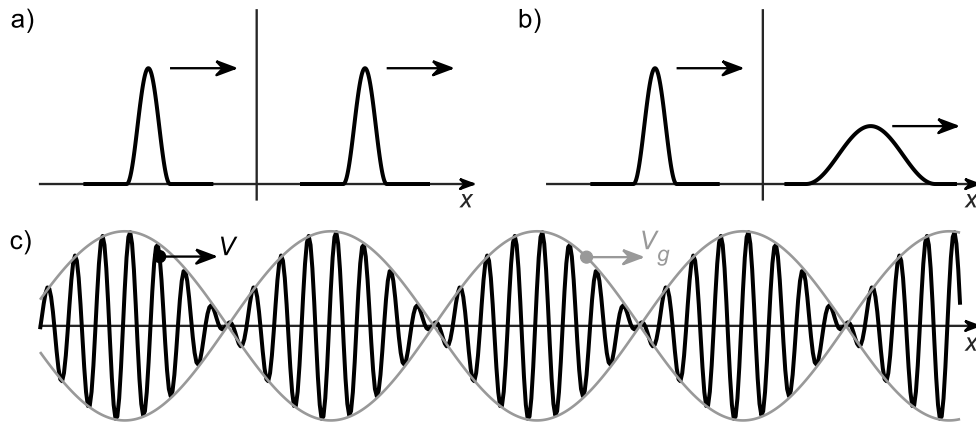


Figure 3-1. a-b) Propagation of a nondispersive wave (a) and of a dispersive wave (b). c) Distinction between phase velocity  $V$  and group velocity  $V_g$  (modified from Foti et al., 2014).

The next sections provide some details about the propagation of body waves and Rayleigh waves in continuous media, with a description of the governing equations and the main parameters. Firstly, wave propagation in linear elastic media is addressed, to introduce the main features and properties of body waves in

a simplified manner. Then, the propagation is generalized into the case of linear viscoelastic media, which is the focus of this dissertation. The following schemes will be generalized to Rayleigh waves. Part of this Chapter is based on the book by Foti et al. (2014).

## 3.1 Body waves

### 3.1.1 Body waves in linear elastic media

The wave propagation in a continuum body is described by the dynamic equilibrium equation, that prescribes the equilibrium conditions of an infinitesimal volume element in the presence of a dynamic excitation. The equation assumes a relatively simple form when introducing the hypothesis of small-strain levels and an isotropic, linear elastic and homogeneous behavior for the body. Under this assumption, the equilibrium equations degenerate in the Navier's displacement equations of motion:

$$(\lambda + \mu)\nabla\nabla\mathbf{u} + \mu\nabla^2\mathbf{u} = \rho\ddot{\mathbf{u}} \quad (3.5)$$

The equation provides the space-time variations of the displacement field  $\mathbf{u}$ , as a function of the relevant material parameters, that are the mass density  $\rho$  and the Lamé's elastic parameters  $\lambda$  and  $\mu$ . The Lamé parameters are an alternative description of the behavior of linear elastic and isotropic media, with respect to the engineering parameters – in soil dynamics, these are the shear modulus  $G$  and the Poisson's ratio  $\nu$ .

The Helmholtz's theorem allows to demonstrate that the wavefield is the combination of two uncoupled wave components. Specifically, a component gives rise to volumetric deformations only, hence the corresponding wave is termed as compression, longitudinal or primary (P) wave. The other component, instead, induces distortional deformations in the medium and the corresponding wave is labeled as shear, transversal or secondary (S) wave. Each wave propagates in the medium according to a propagation velocity  $V_P$  (i.e., the P-wave velocity) and  $V_S$  (i.e., the S-wave velocity), linked with the material mechanical properties as follows:

$$\begin{aligned} V_P &= \sqrt{\frac{\lambda + 2\mu}{\rho}} = \sqrt{\frac{2G(1-\nu)}{\rho(1-2\nu)}} \\ V_S &= \sqrt{\frac{\mu}{\rho}} = \sqrt{\frac{G}{\rho}} \end{aligned} \quad (3.6)$$



The propagation speeds are not identical, as P waves propagate faster than S waves. The ratio between these velocities is a function of  $\nu$ :

$$\frac{V_P^2}{V_S^2} = \frac{2(1-\nu)}{1-2\nu} \quad (3.7)$$

In typical geomaterials, where  $\nu$  is close to 0.3, the P-wave velocity is around twice the S-wave velocity. However, in saturated soils, body wave propagation occurs in undrained conditions, where  $\nu$  approaches 0.5 due to water (and soil) incompressibility (Figure 3-2a). In this condition,  $V_P$  tends to be infinite. Instead, laboratory and field tests showed much lower  $V_P$  values, around 1,500 m/s. In real geomaterials, indeed, water is compressible and intergranular voids always contain a small amount of air, that dramatically drops down the stiffness. For this reason,  $V_P$  is highly sensitive to the saturation degree (Figure 3-2b). Furthermore, propagation velocities do not depend on the frequency, hence P and S waves in linear elastic, isotropic media are nondispersive. Therefore,  $V_S$  can be viewed as a material parameter and as a proxy of the shear stiffness.

Table 3.1. Typical values of the S-wave velocity  $V_S$  for different geomaterials (after Foti et al., 2018).

<b>Geomaterial</b>	<b>S-wave velocity, <math>V_S</math> (m/s)</b>
Soft clay	80 ÷ 200
Stiff clay	200 ÷ 600
Loose sand	80 ÷ 250
Dense sand	200 ÷ 500
Gravel	300 ÷ 900
Weathered rock	600 ÷ 1,000
Competent rock	1,200 ÷ 2,500

As for the displacement field induced by body waves, P waves induce a local displacement parallel to the direction of propagation, whereas S waves induce a particle displacement acting along a plane perpendicular to the direction of propagation. For simplicity, the S-wave motion is typically decomposed into a vertically polarized SV-wave and a horizontally polarized SH-wave.

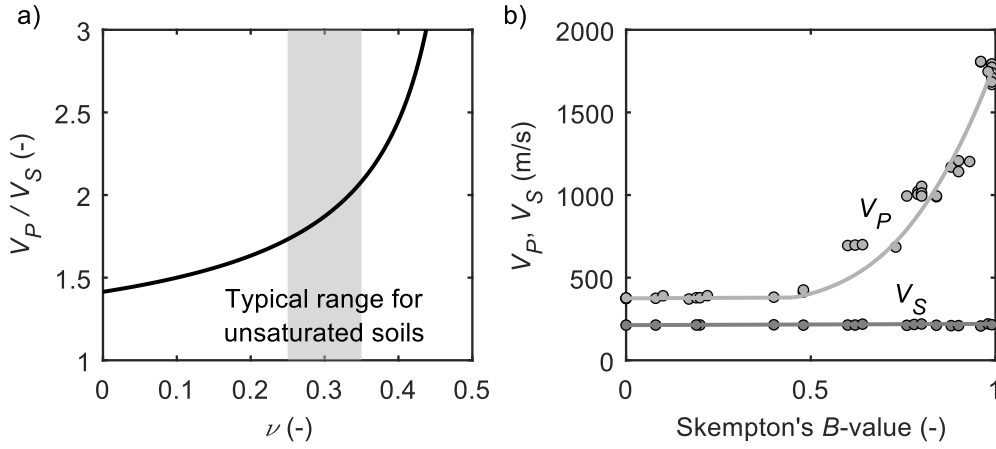


Figure 3-2. a) Variation of the ratio between P- and S-wave velocities  $V_P/V_S$  as a function of the Poisson's ratio  $\nu$ ; b) Variation of the P- and S-wave velocities in sandy specimens as a function of the saturation degree, quantified through the Skempton's  $B$ -value (after Valle-Molina, 2006).

Further insights on the propagation characteristics of body waves can be obtained by explicating the harmonic solution along the positive  $x$  direction for the specific case of 1D wave propagation:

$$u_\chi(x, t) = Ae^{i(\omega t - k_\chi x)} \quad (3.8)$$

The equation is valid both for P-wave or for S-wave propagation (i.e.,  $\chi = P, S$ ), and  $u_P$  denotes the axial displacement, whereas  $u_S$  labels the transverse displacement. The wavefield is a two-dimensional harmonic function in the space-time domain with amplitude  $A$  (Figure 3-3), where the wavenumber  $k_\chi$  describes the spatial variation and it is linked with the wave velocity as follows:

$$k_\chi = \frac{\omega}{V_\chi} \quad (3.9)$$

The time variation at a specific point is described by a sinusoidal variation with oscillation period  $T$ , linked with  $\omega$  as:

$$T = \frac{2\pi}{\omega} \quad (3.10)$$

Alternatively, time variations of the wavefield can be described in terms of frequency  $f$ , equal to the reciprocal of  $T$ . The spatial oscillation at a fixed time instant is also sinusoidal and the length of a single cycle is named wavelength  $\lambda$ , which is linked with the wavenumber  $k$  as:

$$\lambda_\chi = \frac{2\pi}{k_\chi} = \frac{V_\chi}{f} \quad (3.11)$$

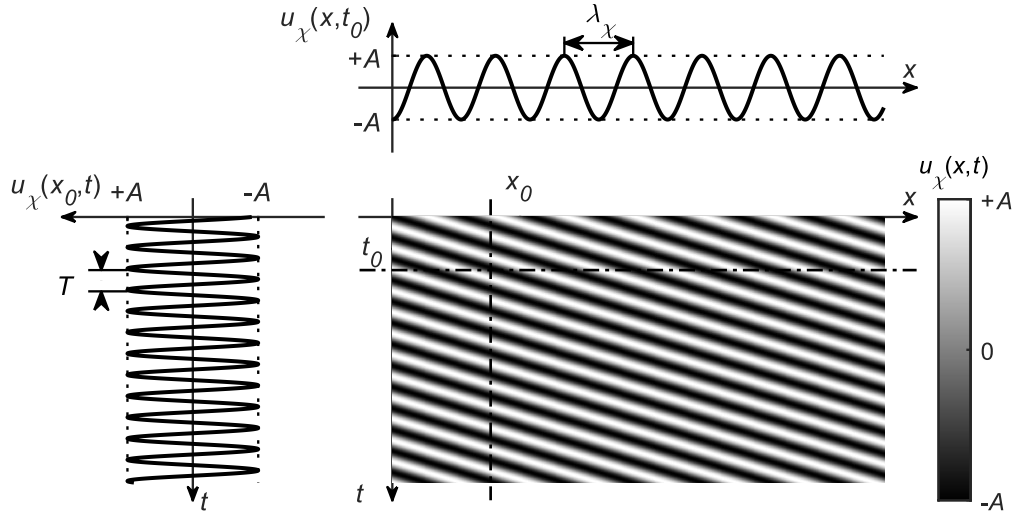


Figure 3-3. Space-time variation of the displacement field  $u_\chi(x,t)$  induced by a body wave with amplitude  $A$  propagating in an elastic body, in 1D conditions. The top portion shows the spatial variation of body waves, at a fixed time instant  $t_0$ , characterized by the wavelength  $\lambda_\chi$ . Instead, the left part represents the time variation, at a fixed location  $x_0$ , characterized by the vibration period  $T$ .

The wavefield solution in 1D conditions allows a simplified description of the behavior at the interface between materials with different mechanical properties. In this case, the interaction of an incident body wave with the interface generates one reflected wave and one transmitted wave (Figure 3-4a). The continuity of the displacement field and the equilibrium in the stress state set a constraint in the relationship between the amplitudes of the incident, reflected and transmitted wave, labeled as  $A_i$ ,  $A_r$  and  $A_t$  respectively:

$$A_r = \frac{1 - \alpha_{z,\chi}}{1 + \alpha_{z,\chi}} A_i, \quad A_t = \frac{2}{1 + \alpha_{z,\chi}} A_i \quad (3.12)$$

The parameter  $\alpha_{z,\chi}$  is the impedance ratio, which is the ratio between the mass-wave velocity product (i.e., the impedance) of the arrival medium and the one of the starting medium:

$$\alpha_{z,\chi} = \frac{\rho_2 V_{\chi,2}}{\rho_1 V_{\chi,1}} \quad (3.13)$$

The effect of  $\alpha_{z,\chi}$  on the amplitudes of the transmitted and reflected waves is shown in Figure 3-4b. When a body wave moves from a softer to a more rigid medium (i.e.,  $\rho_2 V_{\chi,2} > \rho_1 V_{\chi,1}$  and  $\alpha_{z,\chi} > 1$ ), the reflected wave has a smaller amplitude than the incident wave, with amplitude reversal; instead, the transmitted wave is concordant with the incident wave but with smaller amplitude. When a

body wave moves from a more rigid to a softer medium (i.e.,  $\rho_2 V_{\chi,2} < \rho_1 V_{\chi,1}$  and  $\alpha_{z,\chi} < 1$ ), the reflected wave has a smaller amplitude; instead, the transmitted wave is concordant with the incident wave but with greater amplitude. This aspect is relevant in the geotechnical earthquake engineering because seismic waves typically move from hard rock to soft soil deposits, thus undergoing a strong amplification. On the contrary, typical site characterization studies rely on waves generated on the free surface that propagate in materials with increasing impedance with depth, thus deamplifying. The deamplification limits the capability of investigating at large depths.

In 3D conditions, the interaction of body waves with interfaces between material with different mechanical properties is more complex as different types of waves might interact with each other (“mode conversion” of P and SV-waves; Foti et al., 2014). In this case, the prediction of the amplitude of reflected and refracted waves is less trivial (Richter, 1958; Aki, 2002).

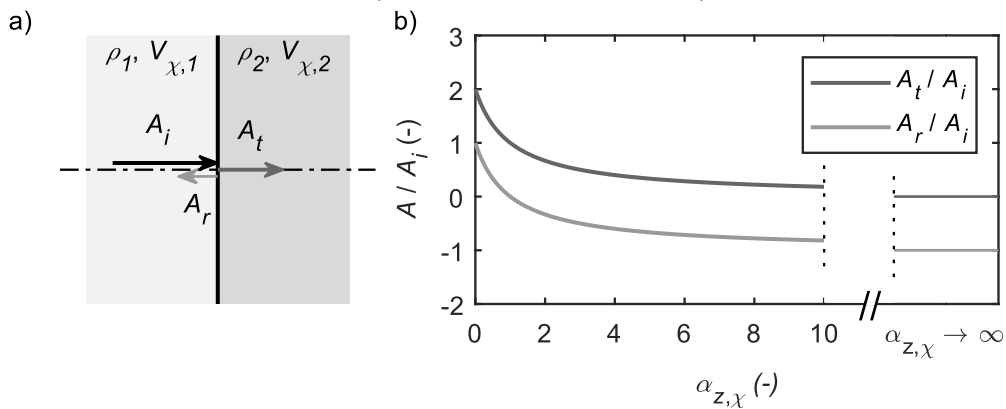


Figure 3-4. a) Wave components involved in the interaction of a body wave with a material interface between two media characterized by mass density and S-wave velocity equal to  $\rho_1$  and  $V_{\chi,1}$ , and  $\rho_2$  and  $V_{\chi,2}$ . These components are represented in terms of their amplitudes:  $A_i$  (for the incident wave),  $A_t$  (for the transmitted wave), and  $A_r$  (for the reflected wave); b) Variations of  $A_r$  and  $A_t$  (normalized with respect to  $A_i$ ) as a function of the impedance ratio  $\alpha_{z,\chi}$ .

The interaction of body waves with interfaces between material with different mechanical properties in 3D conditions follows similar rules as in the 1D case, although the phenomenon is more complex. In this case, the Snell’s refraction law and the Huygens’ principle state that an incident P-wave generates both two reflected and refracted P- and SV-waves and two refracted P- and SV-waves, as the incident wave generates both volume and distortion changes. Similarly, an incident SV-wave generates both two reflected and refracted P- and SV-waves and two refracted P- and SV-waves. This phenomenon of combination of P- and

SV-waves at media interfaces is called “mode conversion” (Foti et al., 2014). On the converse, incident SH-waves only generate one reflected SH-wave and one refracted SH-wave. In this case, the prediction of the amplitude of reflected and refracted waves is less trivial, as the equilibrium and compatibility conditions should account both for the ray path inclination and the mode conversion in P- and SV-waves. However, a prediction is possible when dealing with harmonic signals (Richter, 1958; Aki, 2002).

### 3.1.2 Body waves in linear viscoelastic media

A proper modeling of body wave propagation in a linear viscoelastic medium would require a workflow analogous to that illustrated for the linear elastic case. Specifically, new dynamic equilibrium equations should be built, in compliance with the new constitutive models, whence a solution is then derived. However, this operation is nontrivial as the dynamic equations in viscoelastic media assume a complex behavior and the identification of their solutions is not straightforward.

An alternative way relies on the elastic-viscoelastic correspondence principle (Ben-Menahem and Singh, 2012). This principle states that any solution of Navier’s equation in linear viscoelastic media is identical to the corresponding solution of Navier’s equation in linear elastic media, if the elastic parameters are replaced by complex-valued, frequency-dependent moduli. The correspondence principle allows an immediate derivation of the induced displacement field, as it is identical to the one in elastic conditions, but with mechanical parameters replaced by equivalent ones. Theoretically, the correspondence principle is valid only for time invariant boundary conditions and in the harmonic case. However, the Fourier synthesis allows the decomposition of any signal into its harmonic components, thus giving the possibility to extend the applicability of the principle also to arbitrary time functions (Foti, 2000).

The relevant parameter to be used in the correspondence principle is the wave propagation velocity, that directly depends on the mechanical properties. Specifically, the complex-valued equivalent quantity  $\mathcal{V}_x(\omega)$  is the following (Lai and Rix, 2002):

$$\mathcal{V}_x(\omega) = \frac{V_x(\omega)}{\sqrt{[1+4D_x^2(\omega)]}} \left[ \frac{1+\sqrt{[1+4D_x^2(\omega)]}}{2} + iD_x(\omega) \right] \quad (3.14)$$

However, the following relationship is typically used:

$$\mathcal{V}_x(\omega) = V_x(\omega) \cdot [1+iD_x(\omega)] \quad (3.15)$$

This formulation is an approximation that is valid in weakly dissipative media, where  $D_\chi(\omega) < 0.05$ , whereas it overestimates the magnitude of  $V_\chi(\omega)$  in strongly dissipative media (Figure 3-5a). Since the typical damping ratio value of geomaterials within the linear cyclic strain threshold range is smaller than 0.05, this approximation is acceptable (Foti et al., 2014).

On the other side, viscoelastic quantities exhibit a remarkable frequency-dependence. Indeed, mechanical parameters in viscoelastic media should fulfill the Kramers-Kronig relations, to comply with the causality principle (Christensen, 2012). This principle states that  $V_\chi(\omega)$  and  $D_\chi(\omega)$  are mutually linked and, as a corollary, they are frequency dependent, hence body waves are dispersive. In practical applications, however,  $D_\chi(\omega)$  is typically assumed as constant, because experimental evidence shows that dissipative properties are not strongly sensitive to the loading frequency, at least over the seismic bandwidth (i.e., between 0.1 Hz and 10 Hz – see Section 2.2). Under this hypothesis, the Kramers-Kronig relations provide an explicit solution for the phase velocity of body waves (Aki, 2002), that allows to predict the dispersion model of body wave velocities once the value at a reference frequency  $\omega_{ref}$  (typically equal to  $2\pi$ ) is known:

$$V_\chi(\omega) = \frac{V_\chi(\omega_{ref})}{\left[ 1 + \frac{2D_\chi}{\pi} \ln\left(\frac{\omega}{\omega_{ref}}\right) \right]} \quad (3.16)$$

This formulation provides an estimate of  $V_\chi(\omega)$ , which grows both for increasing loading frequency or for increasing damping ratio. However, in weakly dissipative media under seismic loading, the frequency dependence of the phase velocity is weak, as variations range within 5% (Figure 3-5b). For this reason, the phase velocity is typically assumed as constant with the frequency and equal to the elastic value (e.g., Badsar, 2012). The main drawback of this approach is that a linear viscoelastic model with frequency-independent stiffness and damping is not transformable precisely in the time domain due to non-causality, hence this dissertation will focus on the wave propagation in the frequency domain.

Furthermore, the application of the correspondence principle requires the definition of proper values of  $D_\chi(\omega)$ . In soil dynamics, various empirical relationships for predicting  $D_{S,\theta}(\omega)$  are available, as seen in Section 2.2.3. As for the P-wave damping ratio, instead, only few studies focus on its estimation. In general,  $D_{P,\theta}(\omega)$  is close to  $D_{S,\theta}(\omega)$  in unsaturated conditions (e.g., Mavko et al., 2005), whereas it might be greater in the presence of pore water (e.g., Winkler and Nur, 1982).

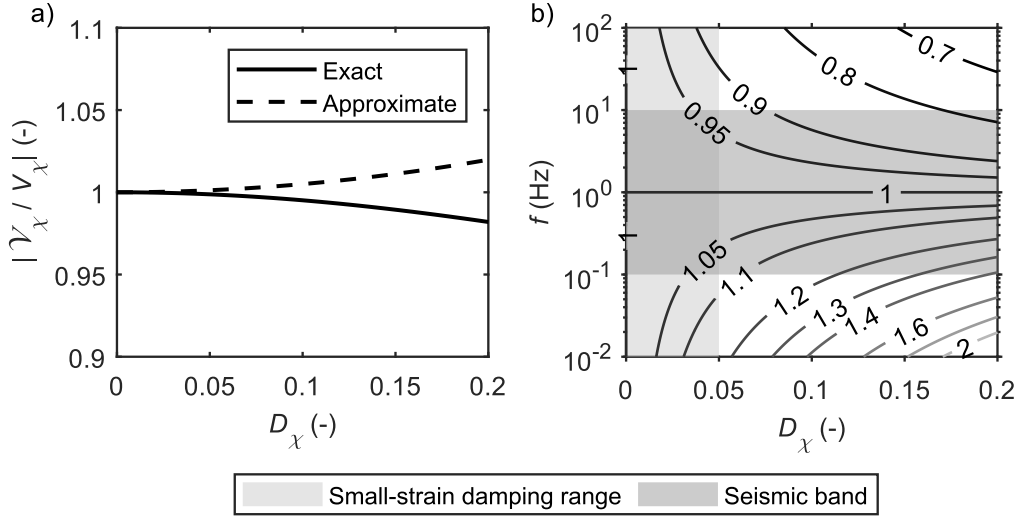


Figure 3-5. a) Ratio between viscoelastic and elastic velocities  $|V_z/V_x|$  computed according to the exact and approximate damping relationships, as a function of the damping ratio  $D_x$  (modified from Foti et al., 2014); b) Dispersion relationship for the body wave velocity ratio  $V_x(\omega)/V_x(\omega_{ref})$  in hysteretic media (i.e., frequency-independent damping ratio), as a function of  $D_x$  and the frequency  $f$ .

The description of the displacement field induced by the propagation of body waves in isotropic, linear viscoelastic and homogeneous media refers to the propagation in 1D conditions, for simplicity. In this case, the solution corresponds to the one for the elastic case, including a complex wavenumber  $\tilde{k}_x(\omega)$ , as it incorporates the constitutive parameters of the medium:

$$\tilde{k}_x(\omega) = \frac{\omega}{V_x(\omega)} \quad (3.17)$$

Therefore, the displacement field is the following:

$$u_x(x, t) = A e^{i(\omega t - \tilde{k}_x(\omega)x)} \quad (3.18)$$

An intuitive interpretation of the wave equation can be obtained by separating the real and the imaginary part of the complex wavenumber:

$$u_x(x, t) = A e^{-\text{Im}\tilde{k}_x(\omega)x} e^{i\omega\left(t - \frac{\text{Re}\tilde{k}_x(\omega)}{\omega}x\right)} \quad (3.19)$$

The resulting wavefield induces a particle displacement according to an exponentially decaying harmonic function. The cyclic variations are linked with the real part of  $\tilde{k}_x(\omega)$ , whereas the spatial decay depends on the imaginary part (Figure 3-6). Therefore, the real part  $k_x(\omega)$  is related to the phase velocity and the imaginary part  $\alpha_x(\omega)$  incorporates the material intrinsic dissipation:

$$\mathcal{K}_\chi(\omega) = k_\chi(\omega) - i\alpha_\chi(\omega) \quad (3.20)$$

The imaginary part  $\alpha_\chi(\omega)$  is called phase attenuation and it is related with  $V_\chi(\omega)$  and  $D_\chi(\omega)$  as follows (Lai and Rix, 2002):

$$\alpha_\chi(\omega) = \frac{\omega}{V_\chi(\omega)} \frac{\sqrt{1 + 4D_\chi^2(\omega)} - 1}{2D_\chi(\omega)} \xrightarrow{D_\chi(\omega) \rightarrow 0} \frac{\omega D_\chi(\omega)}{V_\chi(\omega)} \quad (3.21)$$

Thus, the solution can be rewritten by explicating the components of the complex wavenumber:

$$u_\chi(x, t) = A e^{-\alpha_\chi(\omega)x} e^{i[\omega t - k_\chi(\omega)x]} \quad (3.22)$$

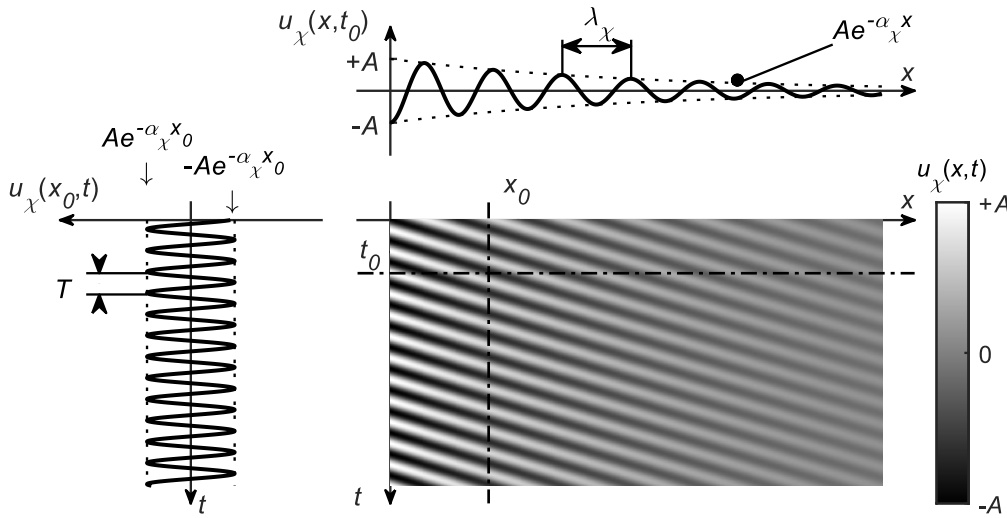


Figure 3-6. Space-time variation of the displacement field  $u_\chi(x, t)$  induced by a body wave with initial amplitude  $A$  propagating in linear, viscoelastic medium, in 1D conditions. The top portion shows the spatial variation of body waves, at a fixed time instant  $t_0$ , characterized by the wavelength  $\lambda_\chi$  and amplitude decay  $Ae^{-\alpha_\chi x}$ . Instead, the left part represents the time variation, at a fixed location  $x_0$ , characterized by the vibration period  $T$  and amplitude  $Ae^{-\alpha_\chi x_0}$ .

## 3.2 Surface waves

When the medium includes a free surface (or an interface with a change in the impedance), the dynamic equilibrium equation allows additional types of waves as a solution. In this kind of waves, the motion is mostly concentrated in the shallow portion of the medium, hence they are typically termed as “surface” waves.

Different types of surfaces waves can be identified. However, in soil dynamics, the most relevant categories are the Rayleigh waves and the Love



waves (Figure 3-7). In Rayleigh waves, the particle motion develops along a vertical plane parallel to the direction of propagation, according to elliptical trajectories. Love waves, instead, induce a particle motion only in the transverse, horizontal direction. A peculiar feature of Love waves is that they exist only in media where the shallow portion is softer than the underlying material. Therefore, they can only propagate in layered media, whereas Rayleigh waves exist also in a uniform half-space.

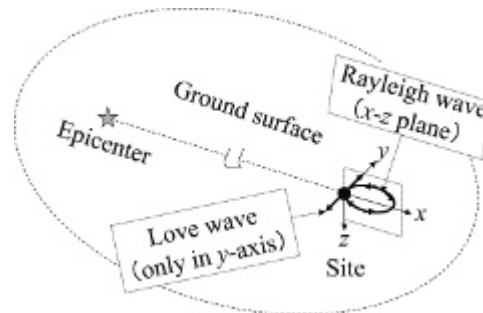


Figure 3-7. Rayleigh waves and Love waves.

The next section provides a detailed description of Rayleigh waves, as they are widely used in ordinary applications for near-surface site characterization. In analogy with the description of body waves, Rayleigh wave propagation in isotropic, linear, elastic media is firstly addressed. Thus, the main features are discussed in a simplified way, without loss of generality. Then, the propagation characteristics are generalized into the case of isotropic, linear viscoelastic medium. Finally, the Lamb's problem is described, as its solution represents the theoretical basis of several in situ characterizations techniques relying on the measurement of the Rayleigh waves propagation.

### 3.2.1 Rayleigh waves in isotropic, linear elastic media

Rayleigh or R-waves (Rayleigh, 1885) are surface waves generated from the interaction between P-waves and SV-waves at the free surface of a continuum body. These waves represent a solution of the Navier's equations for dynamic equilibrium, under the constraint of null stress state at the free surface. Specifically, the corresponding solution can be searched using Helmholtz's decomposition and assuming a decaying exponential form, to mimic the limited penetration depth of the surface wave motion amplitude.

The solution assumes an intuitive form when considering wave propagation over a homogenous half-space, in plane strain field conditions. In this case, the propagation characteristics respect the so-called "characteristic equation of

Rayleigh waves” (henceforth termed only as “characteristic equation”), which links the Rayleigh wave velocity  $V_R$  with body waves’ velocities:

$$B^6 - 8B^4 + (24 - 16R^2)B^2 + 16(R^2 - 1) = 0 \quad (3.23)$$

In the equation, parameters  $B$  and  $R$  are the ratios between Rayleigh and body wave velocities:

$$B = \frac{V_R}{V_S}, \quad R = \frac{V_S}{V_P} \quad (3.24)$$

As the frequency does not appear in the characteristic equation, Rayleigh waves in isotropic, linear elastic and homogeneous media are nondispersive and their propagation speed only depends on the P- and S-wave velocities. Viktorov (1967) provides an approximate solution of the characteristic equation, from which the R-wave velocity depends on  $\nu$ . However, the dependence is weak when considering the typical range of the Poisson’s ratio in geomaterials and  $V_R$  typically ranges around 0.9 times the S-wave velocity:

$$B = \frac{0.87 + 1.12\nu}{1 + \nu} \quad (3.25)$$

The induced displacement field lies in the plane of wave propagation and it involves a vertical and horizontal component that are out of phase of exactly  $90^\circ$ . Furthermore, the vertical component is generally larger in amplitude than the horizontal one. Therefore, the particle motion follows elliptical trajectories, whose geometry strongly depends on the depth and, secondarily, on  $\nu$  (Figure 3-8). Indeed, the amplitude of both components exhibits an exponential decay with depth and it tends to vanish quite immediately, being negligible at a depth approximately equal to one-two wavelengths. Besides, the horizontal component changes its sign with depth, implying a reversal in the direction of particle rotation. The remarkable decay in the motion amplitude with depth is consistent with the definition of surface waves, as they induce a perturbation lying only in the near-surface portion of the medium. Furthermore, this allows to state that the wave propagation is mainly influenced by the mechanical parameters of the material down to around one wavelength depth, as deeper portions of the half-space are not affected by the wave displacement field because it vanishes before.

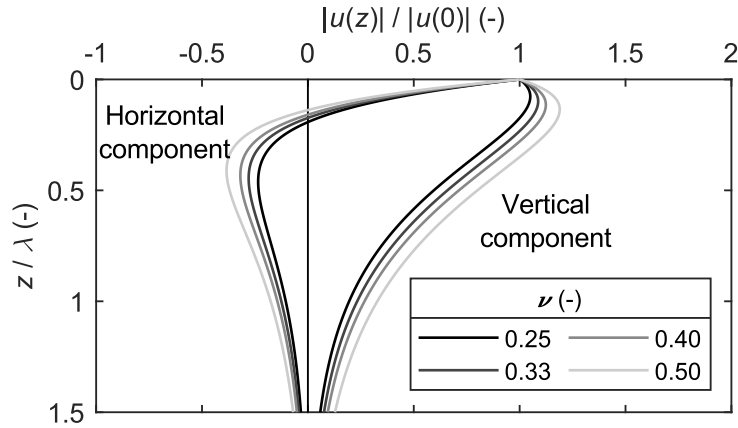


Figure 3-8. Variation of the horizontal and vertical displacement amplitude  $|u(z)|$ , normalized with respect to the motion amplitude at the surface  $|u(0)|$ , as a function of the depth  $z$  (normalized with respect to the wavelength  $\lambda$ ) and the Poisson's ratio  $\nu$  (modified from Richart et al., 1970).

Real media, however, are not homogeneous as the mechanical properties exhibit a spatial variation, which is remarkable with changing depth. A typical scheme is the vertically heterogeneous and transversely isotropic linear elastic half-space with interfaces parallel to the free surface, where mechanical properties only depend on the depth  $z$  (hereafter mentioned as “layered” linear elastic halfspace; Figure 3-9). This scheme is compatible with the stratigraphy of several soil deposits.

The solution linked with Rayleigh waves propagating in such media is now obtained from Navier's displacement equations of motion, supplemented by the same boundary conditions as in the homogeneous half-space (i.e., null stress field at the free surface and vanishing of stress and displacement fields at infinite depth) together with the constraint of continuity of the stress and displacement fields at each layer interface. For each frequency  $\omega$ , it can be demonstrated that the solutions linked with the Rayleigh wave are described by a differential eigenvalue problem, where the characteristic equation assumes an implicit form (Lai and Rix, 1998b):

$$\Phi_R [V_S(z), \nu(z), \rho(z), k_R, \omega] = 0 \quad (3.26)$$

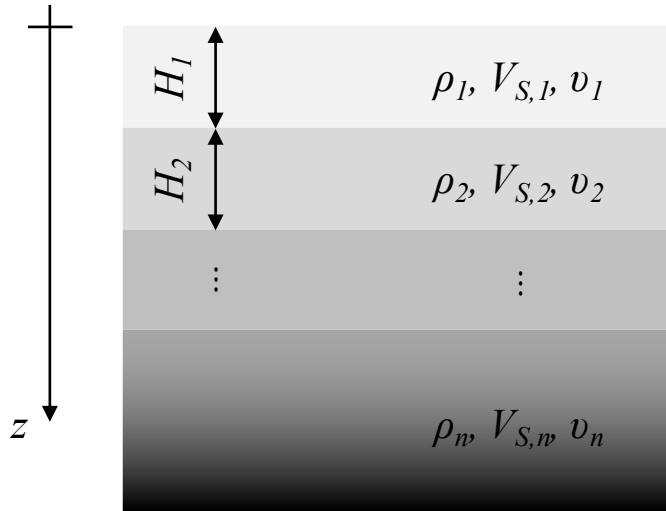


Figure 3-9. Scheme of layered linear elastic halfspace.

The functional form  $\Phi_R[\cdot]$  is named “secular function” and it is a highly nonlinear, transcendental function of the arguments. In the equation, the unknown is the wavenumber  $k_R$ , that synthesizes the Rayleigh wave propagation characteristics. Differently from the homogeneous halfspace, the characteristic equation has multiple solutions, each one being frequency dependent.

Each solution  $k_{R,j}$  of the characteristic equation depends on the frequency  $\omega$ . Therefore, the resulting wavefield is dispersive and the R-wave velocity  $V_R$  (computed as  $V_R(\omega) = \omega/k_{R,j}(\omega)$ ) has to be interpreted as a phase velocity. The dependence of  $V_R$  on the frequency in layered linear elastic media is termed “geometrical dispersion” because it is an effect of geometrical variations of mechanical parameters with depth (Foti, 2000). The variation of  $V_R$  over the frequency is described by the so-called “Rayleigh wave dispersion curve” (or simply “dispersion curve”, hereafter labeled with the symbol “ $V_R(\omega)$ ”). A physical interpretation of the dispersive nature of Rayleigh waves relies on the limited depth range at which the particle motion occurs, as its amplitude is negligible at depths larger than one wavelength (Figure 3-10). For this purpose, let us recall the link between propagation velocity and frequency, defined in Section 3.1.1:

$$V_R = f\lambda_R \quad (3.27)$$

Due to the inverse proportionality between frequency and wavelength, high-frequency waves typically correspond to short wavelengths and they only travel on the near-surface portion, hence their propagation mostly depends on the mechanical properties of the corresponding material. In the limit condition of  $f \rightarrow \infty$ ,  $V_R(\omega)$  tends to a velocity value equal to the R-wave velocity of a homogeneous

medium composed by the near-surface layer only. Instead, low-frequency waves induce a significant particle motion at greater depths, hence their propagation depends also on mechanical properties of deeper layers. At very low frequencies,  $V_R(\omega)$  tends to the R-wave velocity of the bottom layer, computed as if it was a half-space. Therefore, the shape of dispersion curves is intrinsically connected to stiffness variations with depth (Foti, 2000). This feature represents one of the principles of geophysical characterization methods based on the measurement of Rayleigh waves.

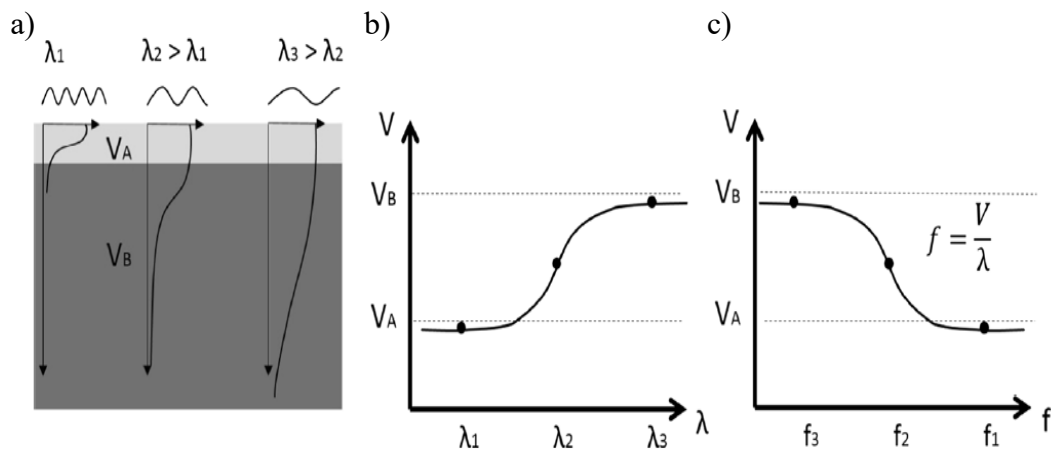


Figure 3-10. Physical interpretation of the geometrical dispersion of Rayleigh waves in layered linear elastic media: a) Qualitative sketch of the vertical displacement amplitude versus depth for three wavelengths  $\lambda_1$ ,  $\lambda_2$  and  $\lambda_3$  in a two-layer medium, with S-wave velocities  $V_{S,A}$  and  $V_{S,B}$ ; b) Dispersion curve in the phase velocity-wavelength  $V_R - \lambda_R$  domain; c) Dispersion curve in the phase velocity-frequency  $V_R - f$  domain (after Foti et al., 2018).

Furthermore, the characteristic equation has a finite set of possible solutions  $k_{R,j}(\omega)$ ,  $j = 1, \dots, M$  at each frequency – at least, beyond a well-defined cut-off frequency (Ewing, 1957). Instead, in a homogeneous half-space, a unique solution exists. Therefore, the Rayleigh wave propagation in layered media is characterized by a set of multiple and discrete dispersion curves and, correspondingly, by various displacement patterns, that are obtained by plugging each solution of the characteristic equation into the Rayleigh eigenvalue problem (Figure 3-11). Each solution is labeled as a mode of propagation of the R-wave, and they are characterized by different phase velocities. This difference can still be interpreted in the light of the penetration depth of the wave, as each mode assumes a specific displacement pattern whose amplitude decays quicker or slower with depth, thus sampling different portions of the medium, with different mechanical properties. Typically, the mode characterized by the lowest values of

phase velocity at every frequency is termed “fundamental mode”, whereas the remaining are called “higher modes”. From the physical viewpoint, the existence of multiple vibration modes at each frequency is the result of constructive interference phenomena occurring among waves undergoing multiple reflections at the layers interfaces (Foti et al., 2014).

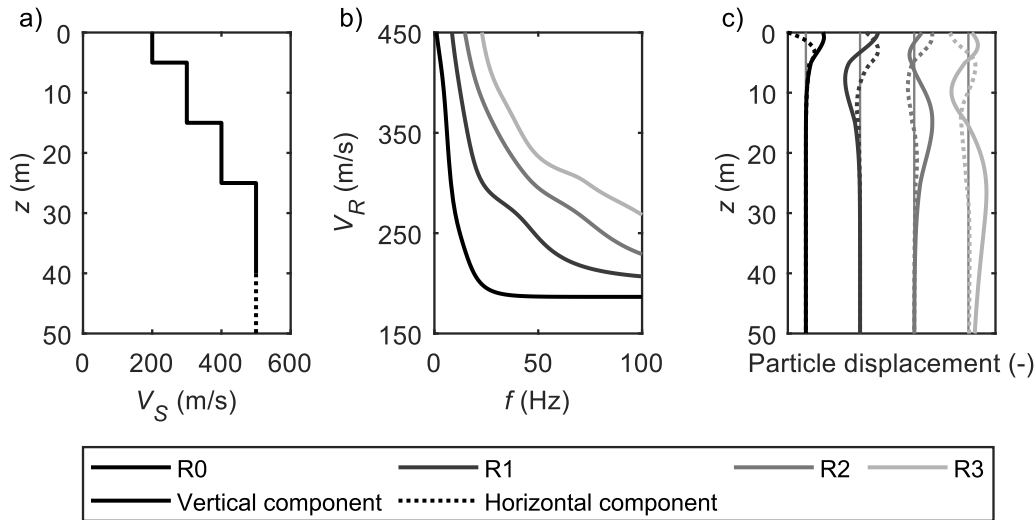


Figure 3-11. Example of Rayleigh dispersion curves for a layered linear elastic medium: a) Layered model, represented as S-wave velocity profile  $V_S$  with depth  $z$ ; b) Dispersion curves for the model in a), represented as R-wave phase velocity  $V_R$  vs. frequency  $f$ ; c) Horizontal and vertical Rayleigh displacement eigenfunctions, at  $f=20$  Hz. Data reported in b) and c) refer to the first 4 modes, labeled as R0, R1, R2, and R3, respectively.

The complexity in the investigation for solutions of the characteristic equation led to the development of several computational techniques to solve the Rayleigh eigenvalue problem. The most popular approaches are the transfer matrix method (Thomson, 1950; Haskell, 1953), the dynamic stiffness matrix method (Kausel and Roësset, 1981) and the method of reflection and transmission coefficients (Kennett, 1974).

### 3.2.2 Rayleigh waves in linear viscoelastic media

The modeling of Rayleigh wave propagation in a layered linear viscoelastic medium is straightforward when relying on the elastic-viscoelastic correspondence principle (Ben-Menahem and Singh, 2012). The correspondence principle modifies the secular function inside the characteristic equation as the mechanical parameters are replaced by complex-valued, equivalent quantities. Therefore, each modal solution is characterized by a complex wavenumber  $\hat{k}_{R,j}(\omega)$ . The real part describes the dispersion relationship and it is comparable to

the wavenumber of the Rayleigh wave in an elastic medium, hence it is typically labeled as  $k_{R,j}(\omega)$  (Figure 3-12c). Instead, the imaginary part  $\alpha_{R,j}(\omega)$  incorporates the material intrinsic dissipation and it is termed as “Rayleigh wave (modal) attenuation” because it controls the spatial decay in the displacement amplitude of the surface wave:

$$\tilde{k}_{R,j}(\omega) = \text{Re} \tilde{k}_{R,j}(\omega) + i \text{Im} \tilde{k}_{R,j}(\omega) = k_{R,j}(\omega) - i \alpha_{R,j}(\omega) \quad (3.28)$$

The R-wave attenuation variation with frequency is described by the modal attenuation curves (or simply “attenuation curves”, hereafter labeled by the symbol “ $\alpha_{R,j}(\omega)$ ”), that tend to increase with frequency (Figure 3-12d). The Rayleigh complex wavenumber can be related to material parameters, by referring to two quantities derived from the real part and the imaginary part of  $\tilde{k}_{R,j}(\omega)$ , respectively. On the one side, the modal phase velocity (or simply “phase velocity”)  $V_{R,j}(\omega)$  is computed from the real part of  $\tilde{k}_{R,j}(\omega)$ :

$$V_{R,j}(\omega) = \frac{\omega}{\text{Re} \tilde{k}_{R,j}(\omega)} \quad (3.29)$$

The phase velocity exhibits a direct link with layer velocities through the geometrical dispersion, as in the elastic case (Figure 3-12e). Indeed, the related dispersion curves are approximately identical to those of the corresponding elastic medium, especially in weakly dissipative media.

Then, the modal phase damping ratio (or simply “phase damping ratio”)  $D_{R,j}(\omega)$  is the ratio between the imaginary and the real part of the complex wavenumber (Misbah and Strobba, 2014):

$$D_{R,j}(\omega) = \frac{\text{Im}[\tilde{k}_{R,j}(\omega)]}{2 \text{Re}[\tilde{k}_{R,j}(\omega)]} \quad (3.30)$$

The phase damping ratio exhibits a variation with the frequency that is related to layers’ S-wave damping ratios through the geometrical dispersion (Figure 3-12f). The link is evident when considering the fundamental mode, as high-frequency values almost equal the top layer  $D_S$ , whereas the phase damping at low frequencies approach the  $D_S$  of the deepest layer. For this reason, the phase velocity and damping ratio are often used in place of the complex wavenumber for their immediate interpretation and link with the material properties.

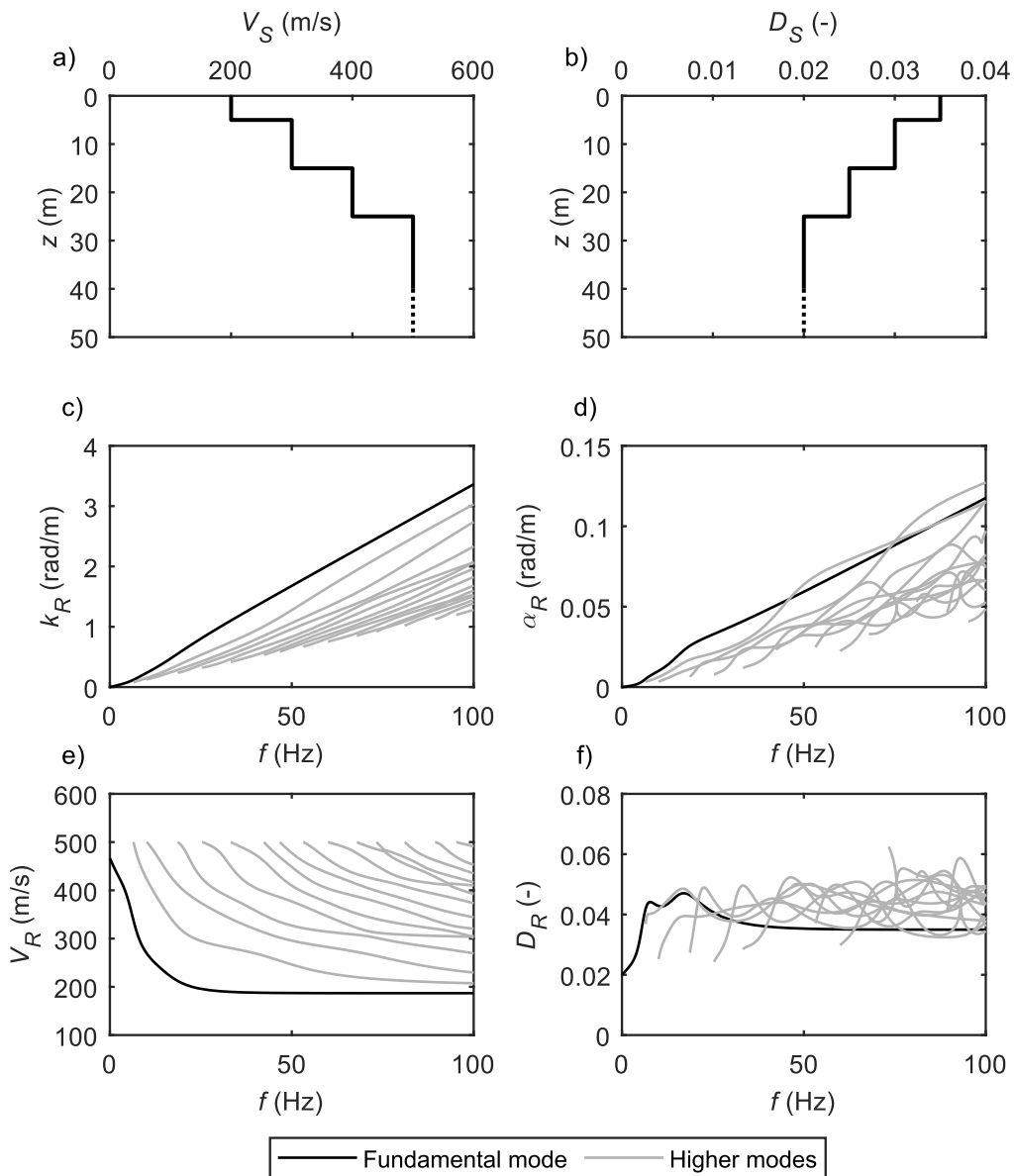


Figure 3-12. Solutions of the characteristic equation in a layered linear viscoelastic medium: a-b) Profiles of S-wave velocity  $V_S$  and damping ratio  $D_S$  with depth of  $z$ ; c-d) Modal dispersion and attenuation curves in terms of real wavenumber  $k_R$  and attenuation  $\alpha_R$  versus frequency  $f$ ; e-f) Modal dispersion and attenuation curves in terms of phase velocity  $V_{R,j}$  and phase damping ratio  $D_{R,j}$  versus  $f$ .

The solution of the characteristic equation in layered linear viscoelastic media is a nontrivial task, because the arguments of the secular function are complex-valued. Some numerical approaches rely on an extension of computational methods for the elastic eigenvalue problem into the viscoelastic case (e.g.,



Schevenels et al., 2009). Another strategy adopts the solution of the elastic eigenproblem as initial estimate of the viscoelastic Rayleigh eigenvalues (e.g., Schwab and Knopoff, 1971). This approach was questioned by Lai and Rix (2002), who proposed an elegant scheme, based on the Cauchy residue theorem of complex analysis, that works successfully both in weakly and strongly dissipative media. Under the assumption of weak dissipation, an alternative strategy relies on the Rayleigh variational principle to obtain a direct estimate of the dispersive and the dissipative properties, starting from the solution of the Rayleigh eigenproblem in elastic media (Aki, 2002).

In general, the R-wave attenuation is the combined effect of P-wave and S-wave dissipative characteristics. However, the two elements do not play the same role. For instance, Macdonald (1959) and Viktorov (1967) showed that the R-wave attenuation in a homogeneous, linear viscoelastic, low-loss medium is the linear combination of the P-wave and S-wave attenuation:

$$\alpha_r(\omega) = A\alpha_p(\omega) + (1 - A)\alpha_s(\omega) \quad (3.31)$$

The quantity  $A$  depends on the Poisson's ratio  $\nu$ . However,  $A$  is less than 0.2 in all geomaterials. Therefore,  $\alpha_{R,f}(\omega)$  strongly depends on S-wave attenuation, whereas P-wave dissipation characteristics are less relevant.

Finally, some remarks on the particle displacement are provided. In linear viscoelastic media, the phase difference between the vertical and the horizontal component is no longer equal to  $90^\circ$ , because the Rayleigh eigenfunctions are complex-valued. Therefore, the particle displacement occurs along ellipses whose principal axis is oblique with respect to the free surface (Figure 3-13; Borchardt, 1973). Furthermore, the degree of sloping and the semi-axes ratio varies independently with frequency, distance from the source and it depends on the mechanical properties of the medium (Foti et al., 2014). As for the motion amplitude, it decreases with the distance, with a stronger decay at high frequencies. Instead, the shape of the displacement profile with depth is compatible with the elastic case.

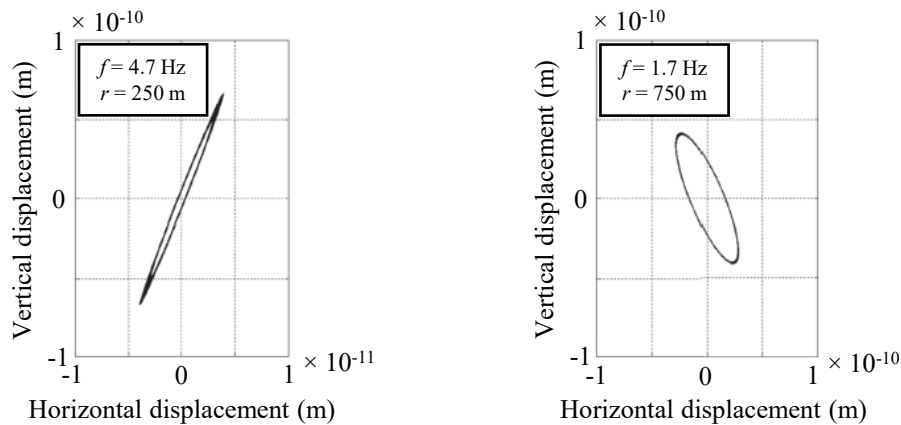


Figure 3-13. Rayleigh particle displacement orbits at the free surface of a layered, linear viscoelastic half-space, at given frequencies  $f$  and distances  $r$  (after Foti et al., 2014).

### 3.3 The source problem

The solutions described above deal only with one aspect of the dynamic problem, which is the propagation of Rayleigh waves under free vibration conditions, i.e., no external force is acting on the medium. However, near-surface characterization methods measure Rayleigh waves that are artificially generated from a source, hence the problem of forced vibrations has to be addressed.

Lamb (1904) provided an estimate of the displacement field induced by a point harmonic force applied on the free surface of a homogeneous, isotropic, linear elastic half-space (Figure 3-14a). He demonstrated that this kind of source generates a complex wavefield, including both body waves (P and S) and Rayleigh waves. The surface wave is the slowest wave, but it produces the largest amplitude in the motion, especially far from the source.

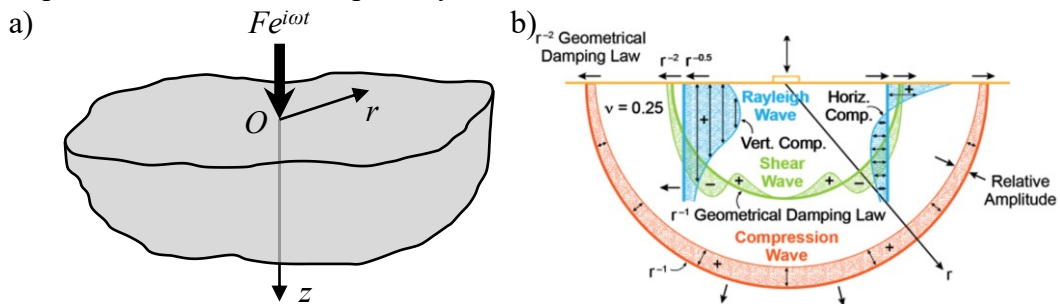


Figure 3-14. a) Scheme of the Lamb's problem, specifying the input force  $F e^{i\omega t}$  and the distance from the source  $r$ ; b) Geometry of wavefronts of body and surface waves generated from a source on the free surface (modified from Miller and Pursey, 1955).

Indeed, Lamb observed that the amplitude of motion induced by body waves attenuates proportional to the distance, whereas the displacement due to Rayleigh waves decays only with the square root of the distance. The reason is that body waves generated from a point source on the free surface propagate along hemispherical wavefronts and the associated energy distributes along this surface. Surface waves, instead, propagate along cylindrical wavefronts, as they involve a portion of the half-space with limited depth (Figure 3-14b). Furthermore, Miller and Pursey (1955) investigated a similar problem, i.e. the estimation of vibrations induced by a circular plate on a half-space, and they demonstrated that the largest portion of energy generated by the source is transmitted by surface waves. Therefore, the wavefield is mainly governed by Rayleigh waves, especially at moderate-to-large distances from the source.

The displacement field induced by the point source includes a vertical component  $u_z$  and a radial component  $u_r$ , being the problem axial symmetric. Many practical applications rely on the far-field approximation of the actual displacement field, comprising only the contribution of Rayleigh waves (Figure 3-15; Lamb, 1904):

$$\begin{aligned} u_z(r, \omega) &= F e^{i\omega t} \cdot M_z \cdot H_0^{(2)}(k_R r) \\ u_r(r, \omega) &= F e^{i\omega t} \cdot M_r \cdot H_1^{(2)}(k_R r) \end{aligned} \quad (3.32)$$

In the equations,  $F e^{i\omega t}$  is the time-harmonic point force and  $r$  is the distance from the source. The quantity  $M_\beta$  ( $\beta = z, r$ ) depends on  $k_R$ , derived from the frequency-independent  $V_R$  (in turn obtained as the solution of the characteristic equation), and on the mechanical properties of the half-space. The terms  $H_0^{(2)}[\bullet]$  and  $H_1^{(2)}[\bullet]$  denote the Hankel functions of the second kind of zero order and of first order, respectively. These functions are oscillatory functions that capture the cylindrical shape of the wavefront of the Rayleigh waves.

However, the Hankel functions can be approximated as complex exponentials when the argument  $k_R r$  is sufficiently large – typically, when  $r$  is on the order of one half of the R-wave wavelength (i.e., the far-field; Foti et al., 2014). Under this assumption, the displacement field assumes the following formulation:

$$u_\beta(r, \omega) = F e^{i\omega t} \cdot N_\beta \cdot \frac{1}{\sqrt{r}} \cdot e^{i(\varphi_\beta - k_R r)} \quad (3.33)$$

The quantity  $N_\beta$  depends on  $k_R$  and on the mechanical properties of the half-space, whereas  $\varphi_z$  equals  $\pi/4$  and  $\varphi_r$  equals  $-\pi/4$ . Interestingly, in the far-field, the Rayleigh wave is planar, i.e., it propagates with planar wavefront.

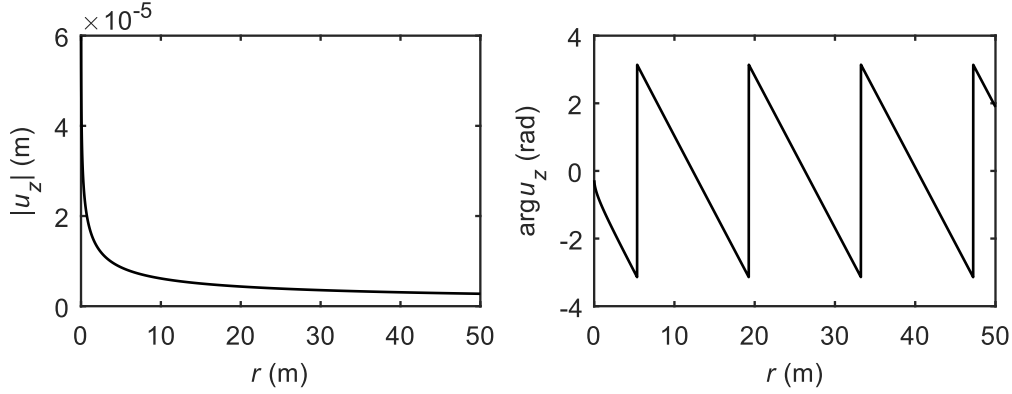


Figure 3-15. Amplitude  $|u_z|$  and phase  $\arg u_z$  of the vertical displacement field of Rayleigh waves in a homogeneous elastic medium, as a function of the distance  $r$ .

In a linear viscoelastic medium, the correspondence principle allows an immediate derivation of the induced displacement field, by replacing the elastic parameters with the complex-valued equivalent ones:

$$\begin{aligned} u_z(r, \omega) &= F e^{i\omega t} \cdot \mathcal{M}_z \cdot H_0^{(2)}(\tilde{\mathcal{K}}_R r) \\ u_r(r, \omega) &= F e^{i\omega t} \cdot \mathcal{M}_r \cdot H_1^{(2)}(\tilde{\mathcal{K}}_R r) \end{aligned} \quad (3.34)$$

and for the far-field approximation:

$$u_\beta(r, \omega) = F e^{i\omega t} \cdot \mathcal{N}_\beta \cdot \frac{1}{\sqrt{r}} e^{i(\varphi_\beta - \tilde{\mathcal{K}}_R r)} \quad (3.35)$$

The terms  $\mathcal{M}_\beta$  and  $\mathcal{N}_\beta$  depend on  $\tilde{\mathcal{K}}_R$  and on the mechanical properties of the medium.

By recalling the definition of  $\tilde{\mathcal{K}}_R$  (Eq. 3.28), a more intuitive expression is obtained, by separating the amplitude and the phase components:

$$u_\beta(r, \omega) = F e^{i\omega t} \cdot \mathcal{N}_\beta \cdot \frac{e^{-\alpha_R r}}{\sqrt{r}} \cdot e^{i(\varphi_\beta - k_R r)} \quad (3.36)$$

The amplitude component decays according to the square root and an exponent of the distance from the source. These components are the combined effect of the intrinsic attenuation and the geometric attenuation – linked with the spreading of energy across a cylindrical wavefront.

The solution can be generalized to the case of layered linear viscoelastic medium. Similarly to the homogeneous case, an analytical solution can be derived at moderately large distances from the source, where the effect of body waves is negligible. Under this assumption, the displacement field induced by Rayleigh waves is the summation of a number of distinct Rayleigh modal displacements, each described by a Hankel function (Ben-Menahem and Singh, 2012):

$$\begin{aligned}
u_z(r, \omega) &= Fe^{i\omega t} \sum_{j=1}^M [\mathbf{m}_z(\omega)]_j \cdot H_0^{(2)}[\mathcal{K}_{R,j}(\omega)r] \\
u_r(r, \omega) &= Fe^{i\omega t} \sum_{j=1}^M [\mathbf{m}_r(\omega)]_j \cdot H_1^{(2)}[\mathcal{K}_{R,j}(\omega)r]
\end{aligned} \tag{3.37}$$

A more intuitive interpretation of the displacement field can be obtained for sufficiently large distances, where the Hankel functions can be approximately replaced by the complex exponentials, thus the displacement field modifies as follows:

$$u_\beta(r, \omega) = Fe^{i\omega t} \sum_{j=1}^M [\mathbf{n}_\beta(r, \omega)]_j \cdot e^{-\alpha_{R,j}(\omega)r} e^{i[\varphi_\beta - k_{R,j}(\omega)r]} \tag{3.38}$$

These relationships account for the multimodal nature of the Rayleigh wave propagation in layered media, and the corresponding displacement field is computed through modal superposition. Indeed, each addendum represents the displacement field associated to a Rayleigh propagation mode, with wavenumber  $k_{R,j}(\omega)$  and attenuation  $\alpha_{R,j}(\omega)$ , which is weighted according to the corresponding amplitude function  $[\mathbf{n}_\beta(r, \omega)]_j$  in the vertical and radial direction for the  $j$ -th mode. The modal amplitudes depend on Rayleigh wave parameters, obtained through the solution of the Rayleigh eigenvalue problem, and on the distance from the source. Furthermore, the formulation for the layered medium assumes general validity and it incorporates the Lamb's solution as a special case. The corresponding expression can be obtained by setting the dispersion and attenuation characteristics derived for the homogeneous case and considering the contribution of a single mode.

It can be demonstrated that the displacement field  $u_\beta(r, \omega)$  can be rewritten as follows (Lai and Rix, 1998b):

$$u_\beta(r, \omega) = Fe^{i\omega t} \cdot \mathcal{Y}_\beta(r, \omega) \cdot e^{i\mathcal{F}_\beta(r, \omega)} \tag{3.39}$$

Interestingly, the mathematical formulation describing the displacement field in a layered medium resembles the one valid in a uniform half-space. However, the phase term assumes a complex dependence over the distance, whereas it was linear in a homogeneous medium. Therefore, the “equivalent” or “effective” wavenumber (i.e., the one of the waveform composed by multiple Rayleigh modes) is no longer constant. Similarly, the amplitude term  $\mathcal{Y}_\beta(r, \omega)$  exhibits a complex behavior, which is no longer decaying according to the square root of the distance. The difference is significant both in normally and inversely dispersive media, especially at high frequencies. In layered media, indeed, the Rayleigh wavefield is the result of the superposition of multiple modes, that are caused by

the constructive interference among waves undergoing multiple reflections and refractions at the layer interfaces. The function  $\mathcal{Y}_\beta(r, \omega)$  is named Rayleigh geometric attenuation function (Lai and Rix, 1998b), as it models the geometric attenuation of Rayleigh waves in layered media (Figure 3-16).

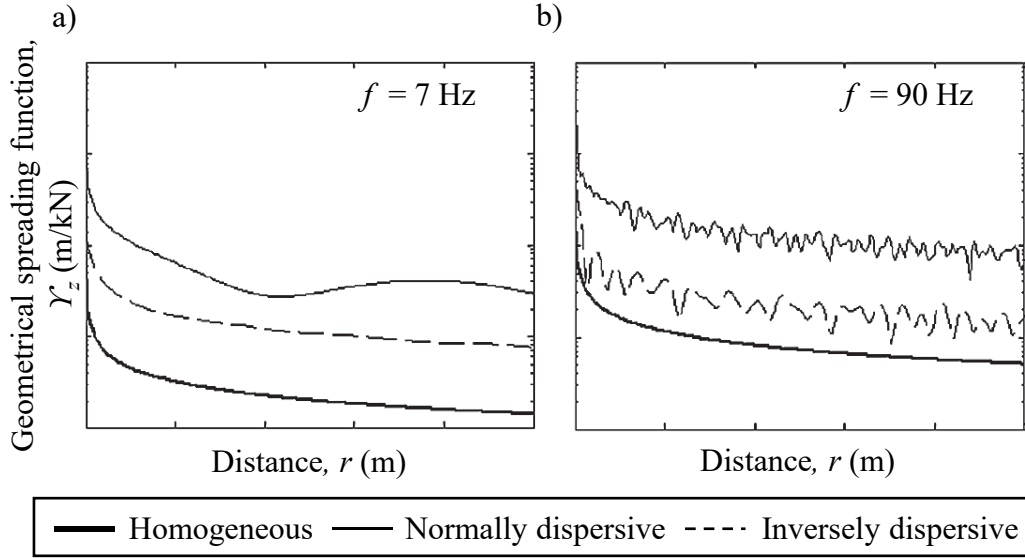


Figure 3-16. Geometrical spreading function  $\mathcal{Y}_z$  for the vertical displacement versus distance  $r$ , computed for different types of half-space at a frequency  $f$  equal to 7 Hz (a) and 90 Hz (b – after Foti et al., 2014).

When dealing with surface waves generated by point sources, a remarkable concept is the apparent phase velocity and apparent phase attenuation – or effective phase velocity and effective phase attenuation:

$$V_{R,\beta}^{app}(r, \omega) = \frac{\omega}{\frac{\partial \text{Re}[\mathcal{F}_\beta(r, \omega)]}{\partial r}}, \quad \alpha_{R,\beta}^{app}(r, \omega) = -\frac{\partial \text{Im}[\mathcal{F}_\beta(r, \omega)]}{\partial r} \quad (3.40)$$

These parameters describe the propagation of multi-mode Rayleigh waves in layered linear viscoelastic media, as they are linked with the slope of the phase and amplitude changes with the distance, at a fixed frequency (Figure 3-17a-b). Therefore, they represent the propagation velocity and spatial attenuation of a waveform composed by the superposition of multiple Rayleigh modes. The effective quantities can be estimated as a function of the solution of the Rayleigh eigenvalue problem. These parameters are dependent both on the frequency and the distance from the source, hence it is possible to describe the phase velocity and the phase attenuation variation with the frequency (i.e., the effective dispersion curve and the effective attenuation curve) only locally or globally

through a Rayleigh dispersion surface. Furthermore, they vary between the radial and the vertical component, meaning that they travel at different phase velocities.

The concepts of effective phase velocity and effective phase attenuation are of paramount importance in real testing. Indeed, site characterization methods measure the displacement field induced by a seismic source. Then, they infer the phase velocity from the phase lag and the phase attenuation from the spatial decay of the particle displacement, normalized to the geometrical damping. Therefore, these techniques measure the effective phase velocity and the effective phase attenuation. This aspect leads to two considerations. On the one side, field surveys might not estimate the modal dispersion curves, as the effective dispersion curve may not coincide with them. In normally dispersive media, where the impedance gradually increases with depth, the measured curve may be coincident with the fundamental mode dispersion curve in a broad frequency range, because the wave energy is mostly carried by the fundamental mode only. However, some deviation of the effective data might occur, especially in the low frequency range (Foti et al., 2014). The deviation becomes relevant in inversely dispersive media, i.e., half-spaces with impedance reversals, where higher modes highly contribute to the surface wave propagation. Therefore, the apparent dispersion curve does not follow a specific modal dispersion curve and it gradually shifts from one to another as a function of the frequency. Furthermore, the dominant mode cannot be predicted a priori. On the other side, the measured effective dispersion curve depends on the spatial configuration of the testing, due to the local nature of the effective quantities, i.e., their dependence from the distance. Therefore, its relationship with the modal curves may be variable as a function of the testing setup (Gucunski, 1992).

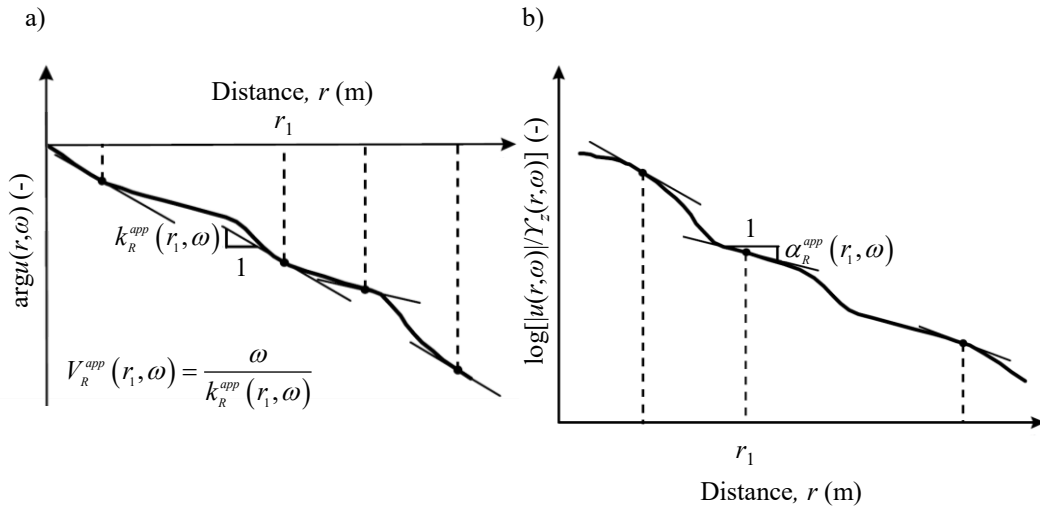


Figure 3-17. Geometrical interpretation of the effective phase velocity  $V_R^{app}$  (a) and of the effective phase attenuation  $\alpha_R^{app}$  (b) at the distance  $r_1$ . The graphs represent a) the spatial variation of the phase of the displacement field  $\arg u(r, \omega)$  and b) the spatial variation of the logarithm of the amplitude  $|u(r, \omega)|$  corrected by the geometric spreading  $Y_z(r, \omega)$ . From these two quantities, both the effective wavenumber  $k_R^{app}$  (hence,  $V_R^{app}$ ) and  $\alpha_R^{app}$  can be derived (after Lai and Rix, 1998b).

### 3.4 Mechanisms of wave attenuation

The attenuation theory seeks to identify the mechanisms responsible of changes in amplitude of perturbations propagating in a medium while moving away from the source. According to this theory, attenuation of seismic waves in real media may be interpreted as the superposition of three damping mechanisms: intrinsic damping, geometrical damping and extrinsic (or scattering) damping. These phenomena are associated with different levels of “complexity” in the medium, both in terms of constitutive behavior and of spatial variability of mechanical characteristics. However, the separation among the components is not trivial as they are often lumped into each other, because they all map into an amplitude decay with increasing distance from the source.

The partition of attenuation components is crucial in site characterization techniques. Indeed, their target is typically the intrinsic damping, however the measured displacement data reflect the combination of all three mechanisms. Therefore, a correct estimate of material attenuation geometric spreading and extrinsic damping must be accounted for obtaining reliable values of material attenuation (Jongmans, 1990; Yoon, 2005). On the other side, proper modeling and separation of these components is often not straightforward.



The main mechanism behind the spatial amplitude decay is intrinsic damping (or material damping), which is an effect of material anelastic behavior, that entails energy dissipation under dynamic excitation. When propagating, indeed, part of the elastic energy is converted into other forms – e.g., heat – due to internal friction. Modeling of this dissipation mechanism relies on proper rheological models, for instance the linear viscoelastic scheme mentioned above. In this case, the effect on the displacement field amplitude can be summarized through the following relationship:

$$A = A_0 e^{-\alpha r} \quad (3.41)$$

Geometrical damping, instead, represents a reduction in the motion amplitude due to the expansion of the wavefront. In this case, the wave energy is constant – if the wave is propagating in a linear elastic material – but the energy density decreases because the wavefront is spreading over a greater volume of material. Being the energy density proportional to the square root of the displacement amplitude, this reduces down as well (Kramer, 1996). Amplitude variations induced by geometrical damping depend on the type of wave and the mechanical and geometrical characteristics of the medium, and they assume a simple and intuitive trend in homogeneous bodies. In planar waves, the wavefront translates keeping its area unchanged, hence the energy density and the amplitude are constant while moving far from the source. Cylindrical waves (e.g., surface waves generated from a point source) are characterized by a wavefront expanding as a cylinder. Therefore, the displacement amplitude decays according to the square root of the distance. In spherical waves (e.g., body waves generated from a point source), the wavefront expands as a sphere, hence the displacement amplitude decays proportionally to the distance (Kokusho, 2017). In summary, geometrical damping in homogeneous media can be summarized through the following relationship:

$$A = A_0 r^{-n} \quad (3.42)$$

where  $n = 0$  for planar waves,  $n = 1/2$  for cylindrical waves, and  $n = 1$  for spherical waves.

In the case of Rayleigh wave propagation, geometrical damping is described through the geometrical spreading function  $\mathcal{Y}_\beta(r, \omega)$ . In a homogeneous halfspace,  $\mathcal{Y}_\beta(r, \omega)$  depends only on  $r$  (Eq. 3.36). Badsar (2012) compared the effect of intrinsic and the geometrical damping on the wave amplitude decay, as a function of the distance and the frequency (Figure 3-18a). The geometric damping is more relevant at short distances, whereas the material damping dominates into the displacement amplitude decay only far from the source. However, for increasing

frequencies, the role of material damping becomes more important, and it overcomes the geometrical one at progressively shorter distances from the source. This is an effect of the frequency-dependence of the phase attenuation of Rayleigh waves in homogeneous media, for which  $\alpha_R$  is greater at high frequencies. The inclusion of heterogeneities adds an extra level of complexity to the wave propagation, due to reflection phenomena and cumulative transmission loss at the layer interfaces. In layered media,  $Y_\beta(r,\omega)$  still decreases with the offset, albeit with remarkable oscillations (Figure 3-18b). The geometry of the oscillations depends on the medium characteristics and also on the frequency – at high frequencies, cycles elongate and assume a larger relative amplitude.

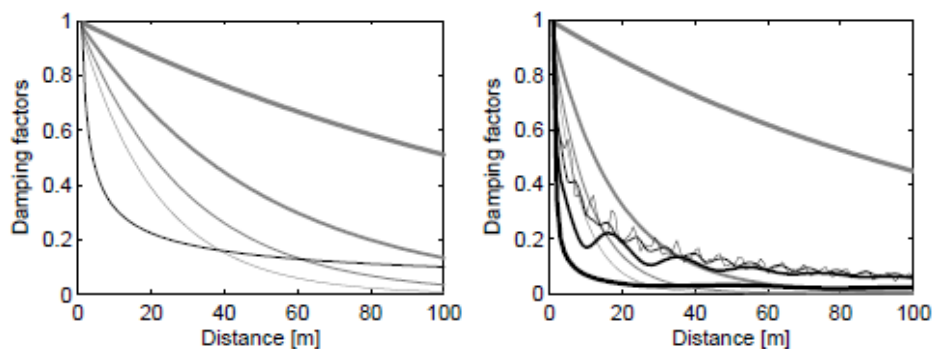


Figure 3-18. a) Comparison between the geometrical attenuation (black line) and the intrinsic attenuation for a homogeneous halfspace (grey lines), computed from the geometric spreading function and Eq. 3.53, respectively. Data refer to frequencies equal to 10 Hz, 30 Hz, 50 Hz, and 70 Hz (from thick to thin grey line). b) Comparison between the geometrical attenuation (black lines) and the intrinsic attenuation for a normally dispersive medium, computed from the geometric spreading function and Eq. 3.53, respectively. Data refer to frequencies equal to 10 Hz, 30 Hz, 50 Hz, and 70 Hz (from thick to thin grey line). Information about the soil model is available in Badsar (2012).

Finally, amplitude changes in real media are also an effect of scattering of energy at local heterogeneities (e.g., inclusions) or to lateral variability in the mechanical properties of the soil deposit. This mechanism is sometimes termed as extrinsic attenuation or apparent attenuation (O'Doherty and Anstey, 1971). As in the geometric attenuation, the overall energy of the wavefront is conserved – at least, in an elastic medium – but it diffuses inside the medium, which is perceived as an energy loss on the surface ground motion (Stein and Wysession, 2003; Zalachoris and Rathje, 2015). In this sense, geometric and apparent attenuation share common features because, at least theoretically, they represent the effect of identical physical phenomena. For instance, Rayleigh wave amplitude changes in layered media – described through the geometrical spreading function – can be interpreted as a form of apparent attenuation. However, apparent attenuation is

conventionally linked to local fluctuations and lateral variability in the soil deposit, especially in the near-surface characterization. The proposed approaches rely on an indirect modeling of the phenomenon, for instance introducing a frequency-dependent equivalent damping ratio (Wu, 1985).

# Chapter 4

## Experimental methods

Many approaches currently adopted for the estimation of the small-strain damping ratio are based on the interpretation of laboratory tests or in situ geophysical surveys.

On the one side, laboratory tests are carried out on small-size soil specimens by applying an imposed stress/strain history with known hydro-mechanical boundary conditions. In this way, there is full control on the response of the geomaterial and a rigorous estimate of the mechanical parameters is possible. However, the sample preparation may damage the soil microstructure, thus affecting the resulting estimates. Besides, obtained parameters may not be representative of the actual behavior of the soil deposit at the site scale.

Geophysical seismic tests are generally classified as invasive and non-invasive, and they are a common tool for site characterization, due to limited costs and the rapidity of execution. However, in situ tests require peculiar care in their interpretation and data quality is highly sensitive to the operator and to external perturbations (e.g., background incoherent noise). On the other side, all the geophysical methods investigate the medium in its undisturbed natural state, sampling a soil volume much larger than the size of a laboratory specimen. Specifically, they often return a layered earth model, wherein  $V_S$  and  $D_S$  are estimated for individual layers – instead, laboratory tests measure these quantities from a single sample, hence they provide a point measurement. Therefore, they can provide a reliable estimate of geotechnical parameters for design purposes, as they assess the soil behavior in undisturbed conditions at a spatial scale compatible with the geotechnical application of interest.

Geophysical seismic tests are widely adopted for the in situ determination of the shear modulus  $G$ . On the other hand, some methods have been proposed also for the estimation of the small-strain shear damping ratio  $D_{S,0}$ . The technical literature also includes some case studies of parameter estimation based on the interpretation of downhole arrays, hereafter labeled as “DH-arrays”. This approach is less common, as it requires instrumented boreholes with seismic records, but it provides useful data for the assessment of the soil behavior in seismic conditions. Although parameters obtained in this way may be interpreted

as in situ estimates, DH-arrays will be addressed in a devoted section, as they are not a common site characterization tool and have a role in the validation of theoretical models of ground motion amplification.

This Chapter starts with a description of typical laboratory tests, that currently represent the most common way for estimating dissipative parameters of geomaterials. The second part focuses on approaches returning damping ratio values from in situ observations, based on invasive and noninvasive geophysical tests and DH-arrays. Finally, a brief comparison of results from laboratory and in situ tests is reported.

## 4.1 Laboratory tests

Laboratory tests are often carried out to obtain dynamic properties of soils. The different tests can be grouped into two main categories: cyclic tests, performed at low frequencies, and dynamic tests, carried out at higher frequencies. The most common cyclic tests are the Cyclic Triaxial (CTx) test, the Cyclic Torsional Shear (CTS) test and the Cyclic Direct Simple Shear (CDSS) test, along with its Double-Specimens (CSDSS) variant. The stress-strain loops are directly used in cyclic tests to obtain the dynamic properties of the soil. On the other hand, a dynamic Resonant Column (RC) test can be performed to obtain stiffness and damping estimates analyzing the resonant conditions of the soil sample. Finally, some Authors investigated the possibility of measuring small-strain parameters through bender element tests (e.g., Karl, 2005; Karl et al., 2008; Cheng and Leong, 2018), although no further details on this will be provided in this dissertation.

In the following, the main features of the tests are firstly described, along with critical issues associated with the experimental measurement of  $D_{s,0}$ . Part of this Section has already been published in Foti et al. (2021).

### 4.1.1 Resonant column test

The Resonant Column (RC) test (ASTM D4015–15e1) is based on the theory of torsional waves propagation in the medium. The test is performed under loading control, applying torque loadings with increasing amplitudes at the free top of the sample, whereas the bottom is fixed (Figure 4-1a). For a given loading amplitude, several cycles are applied for variable frequencies over a wide range, to clearly identify the resonance condition of the first torsional mode of the specimen and the corresponding frequency  $f_0$ , associated to the cyclic shear strain reached. The soil response is tracked by measuring its rotation  $\vartheta$ . The test is able to investigate cyclic shear strain amplitudes ranging from  $10^{-5}$  to 0.5%.

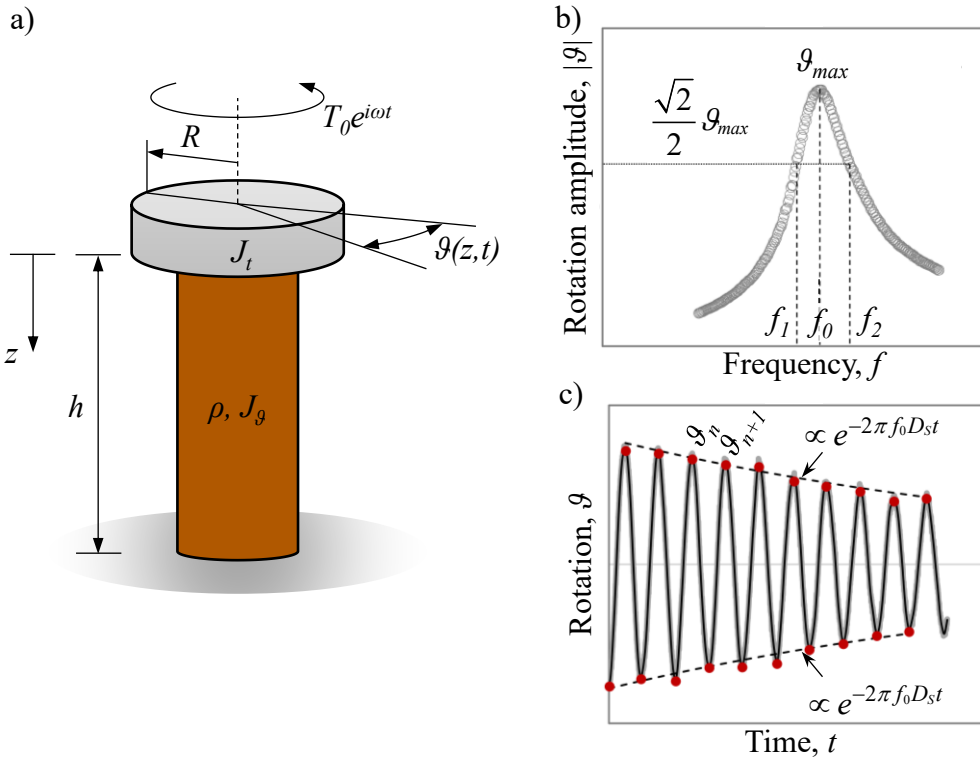


Figure 4-1. a) Basic scheme of a RC test device, modified from Woods (1978); b-c) Typical results of a RC test: (b) output rotation amplitude  $|\vartheta|$  vs frequency  $f$  curve; (c) free-vibration decay plot (modified from Foti et al., 2021).

The response of the soil to the dynamic excitation can be represented in terms of  $\vartheta$  vs. frequency curve, where the frequency associated with the maximum amplitude  $\vartheta_{max}$  is the  $f_0$  of the sample. The S-wave velocity  $V_S$  of the soil is then obtained via the equation of motion for torsional vibrations (Richart et al., 1970):

$$\frac{J_g}{J_t} = \frac{2\pi f_0 h}{V_S} \cdot \tan\left(\frac{2\pi f_0 h}{V_S}\right) \quad (4.1)$$

where  $J_g$  is the mass polar moment of inertia of the specimen,  $J_t$  is the driving system polar moment of inertia and  $h$  is the height of the specimen (Figure 4-1a). The  $G_S$  can then be obtained from the mass density of the soil, through Eq. 3.6.

Three different methods can be applied to define the S-wave damping ratio  $D_S$ , namely the half-power bandwidth, the free-vibration decay method, and the resonance factor method (Drnevich et al., 1978), although the latter is rarely used. In the half-power bandwidth method, the connection between the shape of the frequency response curve and the dissipated energy is exploited (Figure 4-1b). It can be shown that, for small values of  $D_S$ , the latter can be evaluated as:

$$D_S = \frac{f_2 - f_1}{2f_0} \quad (4.2)$$

where  $f_1$  and  $f_2$  are the frequencies associated with a  $\mathcal{G}$  amplitude equal to  $\sqrt{2}/2 \mathcal{G}_{max}$  (Figure 4-1b).

Alternatively, the free-vibration decay method can be used to obtain the damping ratio from the amplitude decay of the torsional free oscillations, after the application of the forced vibrations. By knowing two successive peak amplitudes ( $\mathcal{G}_n$  and  $\mathcal{G}_{n+1}$  corresponding, respectively, to the  $n$ -th and  $n+1$ -th cycle; Figure 4-1c), the logarithmic decrement  $\delta_{n+1}$  can be computed as:

$$\delta_{n+1} = \ln \frac{\mathcal{G}_n}{\mathcal{G}_{n+1}} \quad (4.3)$$

The logarithmic decrement is computed for different successive cycles, then an average value  $\delta$  is used to obtain the damping ratio as:

$$D_S = \frac{\delta}{2\pi} \quad (4.4)$$

The two methods are characterized by different advantages and disadvantages. When the free-vibrations method is used in the small-strain range, the background noise recorded by the accelerometer is not negligible and a filtering procedure has to be applied to the output signals prior to amplitude interpolation (Figure 4-1c). Moreover, given the small values of  $D_{S,0}$ , the difference between two consecutive peaks can be rather small, hence the variability in estimated values may be large. On the other side, RC measurements of  $D_S$  from forced vibrations are affected equipment-generated damping (e.g., Kim, 1991; Hwang, 1997; Cascante et al., 2003; Meng and Rix, 2003; Wang et al., 2003). The bias can be substantial, especially in the small-strain range where small values of  $D_S$  are expected. Different studies suggested correcting the results of the RC test by subtracting the equipment generated damping, obtained through a calibration procedure of the apparatus (e.g., Kim, 1991; Hwang, 1997; Wang et al., 2003). However, the extent of the bias is not yet totally understood.

Besides, the influence of the loading frequency on  $D_{S,0}$  (see Chapter 2) might be critical for RC tests. Indeed, these tests are usually carried out at variable frequencies, according to the resonance conditions at different strain amplitudes, beyond the typical seismic bandwidth. Ciancimino et al. (2020) proposed a procedure to correct results of a laboratory test by taking into account the loading frequency. Alternatively, an elegant strategy to deal with the frequency-dependence of cyclic parameters is given by the so-called Non-Resonance Column (N-RC) method (Lai and Rix, 1998a; Lai et al., 2001; Rix and Meng,

2005; Lai and Özcebe, 2015). The method directly measures the complex-valued S-wave velocity  $\hat{V}_S(\omega)$  of a soil specimen, idealized as a linear viscoelastic medium, by solving the following equation:

$$\frac{T_0 e^{i\omega t}}{\vartheta(0,t)} = \frac{\pi R^4}{2} \cdot \frac{\rho \omega}{\hat{V}_S(\omega)} \cdot \cot\left(\frac{\omega h}{\hat{V}_S(\omega)}\right) - J_t \omega^2 \quad (4.5)$$

where  $T_0 e^{i\omega t}$  is the driving harmonic torque,  $\vartheta(0,t)$  is the measured angle of twist at the top of the specimen,  $R$  is the radius of the specimen, and  $\rho$  is the mass density of the specimen (Figure 4-1a).  $\hat{V}_S(\omega)$  is then used to compute consistently  $V_S$  (hence,  $G$ ) and  $D_S$  (Figure 4-2), based on Eq. 3.14. Thus, the soil is assumed to be a dispersive medium and the frequency-dependence is inherently taken into account by the method, without prior assumptions on such dependence and in a fully coupled way. The application of the method in the current practice is anyway still limited by the complexity of the approach.

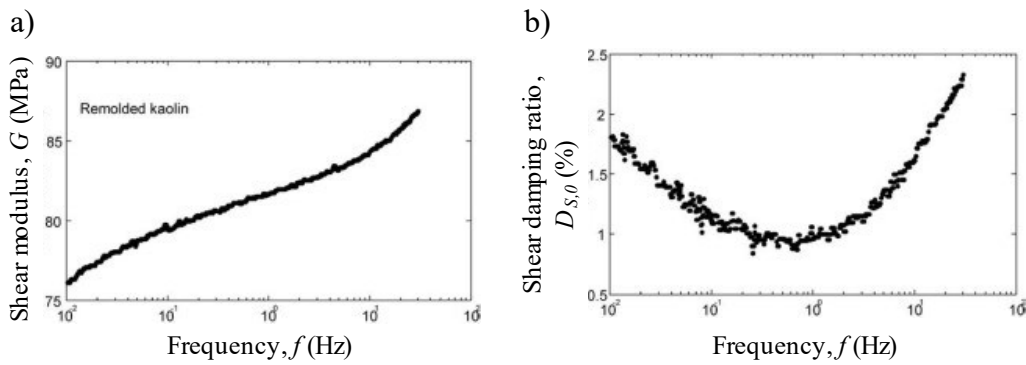


Figure 4-2. Results of a N-RC test: a) Estimated shear modulus  $G$  and b) small-strain shear damping ratio  $D_{S,0}$ , as a function of the loading frequency  $f$  for a remolded kaolinite sample (after Rix and Meng, 2005).

### 4.1.2 Cyclic tests

Despite the different configurations, cyclic tests are all based on the same concept, i.e., to measure soil parameters directly from the stress-strain response of the soil. The  $G$  is obtained as the average slope of the loop, while  $D$  can be computed from the energy dissipated  $W_D$  and the maximum elastic strain energy  $W_E$  for a given loading-unloading cycle, according to Eq. 2.6.

In Cyclic Triaxial (CTx) tests (ASTM D3999/D3999M-11e1 and ASTM D5311/D5311M-13), a cyclic deviator stress is applied to a cylindrical specimen by keeping constant the cell pressure and changing the axial stress cyclically with a low loading frequency (about 1 Hz). The stresses and the strains are used to



compute  $G$  and  $D_S$  (Figure 4-3a). The applicability of the CTx test is generally restricted to relatively high shear strains (greater than  $10^{-2}\%$ ) because of bedding errors and system compliance effects (Kramer, 1996). However, local strain measurements can produce an increase of the accuracy of the device (e.g., Burland and Symes, 1982; Ladd and Dutko, 1985; Goto et al., 1991).

Cyclic Torsional Shear (CTS) tests can be performed in the same device used for RC tests (Figure 4-1a). The driving system applies a fixed number of cycles for a given amplitude with a fixed loading frequency (usually between 0.1 Hz and 0.5 Hz). The rotation of the specimen is measured through a couple of displacement transducers connected to the top cap. The shear strain is then obtained from the rotation and, by knowing the input applied, it is possible to draw the loading-unloading loops, from which  $G$  and  $D_S$  are then estimated (Figure 4-3b).

Finally, in a Cyclic Direct Simple Shear (CDSS) test, a cylindrical specimen is cyclically loaded under displacement control by a horizontal piston. The stresses and the strains are then used to compute  $G$  and  $D_S$ . The applicability of the test in the small-strain range is limited mainly because of frictional problems. The range can be increased using the Cyclic Double-Specimen Direct Simple Shear (CDSOSS) device. The CDSOSS adopts a double specimen configuration, able to capture the soil behavior also at very small strains (Doroudian and Vucetic, 1998).

The main issue regarding cyclic tests is related to the measurement of the loops in the small-strain range. For example, Figure 4-3c shows a loop measured during a CTS test, for a  $\gamma_c$  below the linearity threshold (i.e., in the almost linear branch of the stress-strain response). Although the definition of  $G$  from the slope of the loop is quite straightforward, the small area inside the loop can be affected by the accuracy of the measurement. Consequently, the experimental relative error on  $D_{S,0}$  can be, again, substantial.

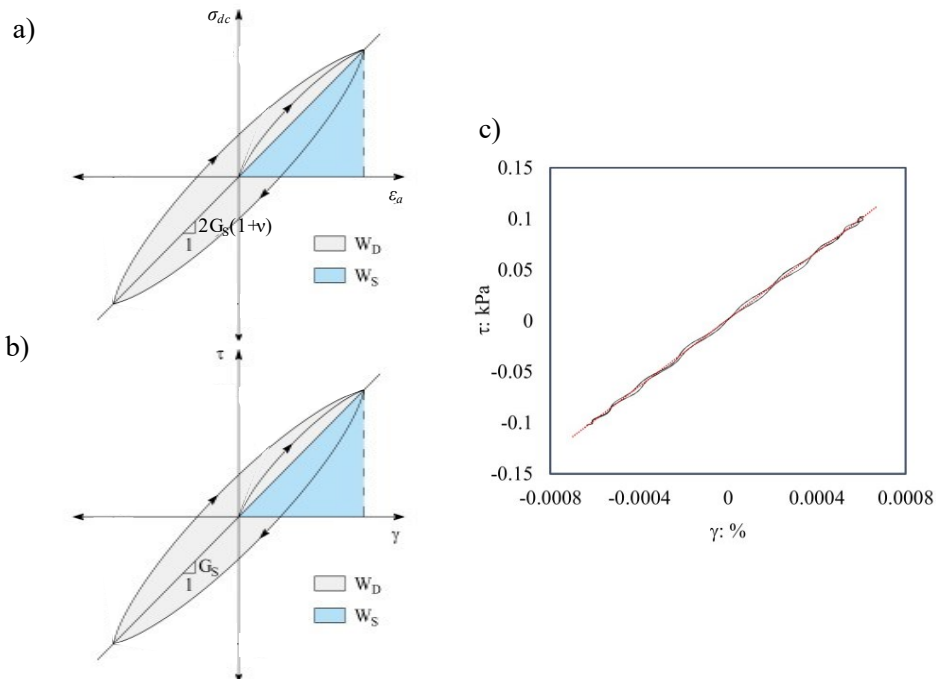


Figure 4-3. a-b) Idealized stress-strain loops measured in the deviatoric stress-axial strain  $\sigma_d - \epsilon_a$  plane in a CTx test (a) and in the shear stress-shear strain  $\tau - \gamma$  plane in a CTS test (b); c) real loop measured in a CTS test at small strains (after Foti et al., 2021).

## 4.2 In situ geophysical tests: invasive methods

Invasive tests are a family of geophysical seismic tests for which part of the instrumentation is installed in the ground. Typical methods are the Cross-Hole test (CHT; ASTM D4428/D4428M-14), Down-Hole test (DHT; ASTM D7400-17), and the P-S suspension logging test (Nigbor and Imai, 1994). Other techniques are the Seismic Cone Penetration Test (SCPT; Campanella, 1994), the Seismic Dilatometer Test (SDMT; Marchetti et al., 2008), the vertical seismic profiling (Balch and Lee, 1984), that are variants of the DHT, and the direct-push cross-hole test (Cox et al., 2018), that follows a scheme similar to the CHT.

The data acquisition in invasive tests requires great care, especially when attenuation measurements are carried out. The main issue related to invasive tests is linked to the sensor-ground coupling, which is crucial for an accurate tracking of the particle motion. Indeed, when using a borehole, there is no direct contact between receivers and the ground as the borehole is supported by a lining covered by a grouting layer. As the grouting may not be perfectly homogeneous, the soil-receiver interaction may be variable with depth (e.g., Lo Presti et al., 1997). SCPT and SDMT are effective in overcoming this limitation because the instrumentation

is pushed in the ground without any casing, hence good coupling between soil and sensors is achieved. Furthermore, recorded data should have reasonably high signal-to-noise ratio in the frequency band of interest (e.g., Sun, 2000) and the quality of the seismogram should be good enough. This allows an accurate identification and isolation of the body wave of interest (either the P- or the S-wave), otherwise the estimated attenuation data would be corrupted.

The technical literature proposes many robust approaches for the determination of  $V_S$  from the interpretation of the measured data. Conversely, the techniques aimed at estimating the in situ small-strain damping ratio  $D_{S,0}^{site}$  are limited to few attempts for CHT and DHT (and SCPT), that will be addressed in the following sections. Note that these techniques return an estimate of  $D_{S,0}^{site}$ ; however, the following Sections will denote the identified value as  $D_S$ , for simplicity. Part of this Section has already been published in Foti et al. (2021).

#### 4.2.1 Cross-hole testing

In CHT, the source and the receivers are installed in boreholes and measurements are performed at different depths (Figure 4-4a). The test measures the travel time of body waves generated by the source and propagating along the direct path to the receivers. Thus, knowing the source-receiver distance, the body-wave velocity  $V_\chi$  (where  $\chi = P$  or  $S$ ) can be estimated. Prescriptions about data acquisition and procedures for an accurate estimation of  $V_\chi$  are described in ASTM D4428/D4428M-14. Techniques for the estimate of  $D_S$  from CHT data are the random decrement approach (Aggour et al., 1982), the attenuation coefficient method (Hoar and Stokoe, 1984; Mok et al., 1988; Michaels, 1998; Hall and Bodare, 2000) and the causal dispersion approach (Crow et al., 2011; Lai and Özcebe, 2015; Lai and Özcebe, 2016).

A popular approach is the attenuation coefficient method, proposed by Hoar and Stokoe (1984) and Mok et al. (1988). Its framework is based on the spatial decay of the wave amplitude (Eq. 3.22), and it compares the measured spectral amplitudes of the signal  $S_1$  and  $S_2$  at two receivers at distances  $R_1$  and  $R_2$  from the source (Figure 4-4a):

$$D_\chi = \frac{\ln\left(\frac{R_1 |S_1(f)|}{R_2 |S_2(f)|}\right)}{2\pi f} \cdot V_\chi \quad (4.6)$$

This approach provides a frequency-independent estimate of  $D_\chi$ , which is reliable in the absence of receiver-coupling or casing effects and there are not

reflected or refracted waves induced by nearby layers of high velocity, that may affect measured amplitudes (Hall and Bodare, 2000).

However, many existing methodologies rely on the hypothesis of frequency-independent (i.e., hysteretic) damping or on enforcing a specific constitutive model in the interpretation of attenuation measurements. Moreover, they usually perform an uncoupled estimate of the low-strain parameters by using incompatible constitutive schemes:  $V_\chi$  is obtained according to a linear elastic model, whereas  $D_\chi$  estimates are based on inelastic models. Therefore, these approaches may return inconsistent and biased estimates. Instead, an effective strategy to overcome those limitations should accommodate rate-dependent behavior. For this reason, some Authors measured the body wave dispersive behavior from the unwrapped phase of the cross-power spectrum  $G_{R_1, R_2}^\chi$  of the corresponding signal, detected at the two receivers (Hall and Bodare, 2000; Lai and Özcebe, 2015; Lai and Özcebe, 2016):

$$V_\chi(\omega) = \frac{\omega(R_2 - R_1)}{\arg G_{R_1, R_2}^\chi} \quad (4.7)$$

Then, Lai and Özcebe (2015) and Lai and Özcebe (2016) proposed a smart technique for estimating  $D_\chi$  from the computed dispersion curves, by applying the solution of the Kramers-Kronig relation, that relates stiffness and attenuation characteristics in a linear viscoelastic medium (Christensen, 2012):

$$D_\chi(\omega) = \frac{\frac{2\omega V_\chi(\omega)}{\pi V_\chi(0)} \cdot \int_0^\infty \left( \frac{V_\chi(0)}{V_\chi(\tau)} \cdot \frac{d\tau}{\tau^2 - \omega^2} \right)}{\left[ \frac{2\omega V_\chi(\omega)}{\pi V_\chi(0)} \cdot \int_0^\infty \left( \frac{V_\chi(0)}{V_\chi(\tau)} \cdot \frac{d\tau}{\tau^2 - \omega^2} \right) \right]^2} - 1 \quad (4.8)$$

where  $V_\chi(0) = \lim_{\omega \rightarrow 0} V_\chi(\omega)$ .

This interpretation method only requires measurements of velocity for determining both the stiffness and the damping parameters of the material, hence an accurate tracking of particle motions is unnecessary. Moreover, the processing does not require a priori assumptions about the specific rheological behavior or the frequency-dependent nature of  $D_\chi$ . On the other side, broadband seismic sources are required to generate a wave signal with a wide frequency range, otherwise waveforms generated by usual sources restrict the ability to resolve the damping ratio at low frequencies, including the seismic band. If not possible, some assumptions about the dispersive behavior of the soil parameters are necessary to extrapolate the available data, introducing uncertainties in the

estimate linked to the way with which the extrapolation is performed (Figure 4-4b). Furthermore, an accurate estimation of both phase velocity and damping requires a preliminary step of windowing of the seismogram in the time-domain, to isolate the portion of interest (i.e., the signal corresponding to the arrival of the P- or the S-wave) and limit the influence of reflected waves (Hall and Bodare, 2000).

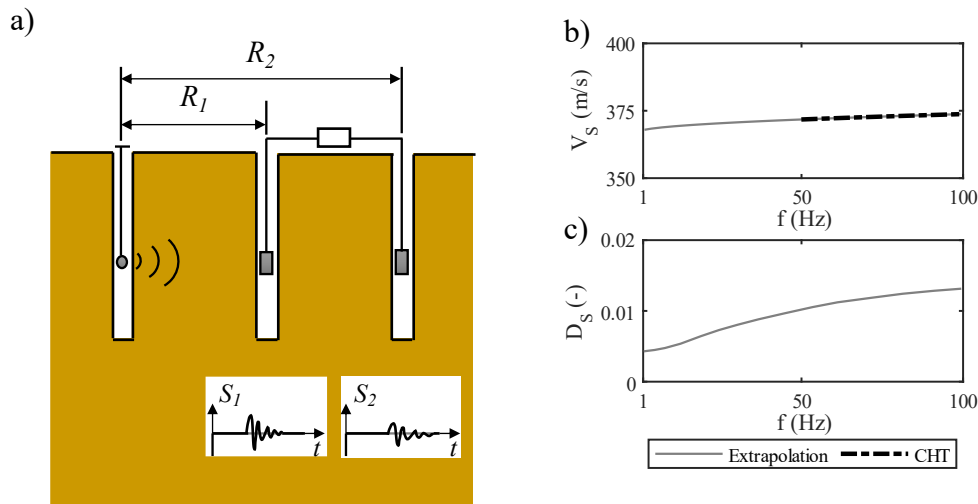


Figure 4-4. a) Scheme of the CHT layout; b) resulting S-wave velocity  $V_S$  and damping ratio  $D_S$  curves versus frequency  $f$  from the interpretation of CHT data (modified from Lai and Özcebe, 2015).

## 4.2.2 Down-hole testing

In DHT and SCPT, the source is located at the ground surface, whereas the receiver/s is/are installed in boreholes or pushed together with the cone probe (Figure 4-5). The test measures the travel time of body waves generated by the source and propagating to the receivers. The propagation occurs along slanted paths, that may be affected by refraction occurring at the layers' interfaces. The travel time (hence,  $V_\chi$ ) can be estimated by means of various techniques, such as interval methods, direct methods and raytracing algorithms. A detailed description about these procedures for an accurate estimation of  $V_\chi$  is available in ASTM D7400-17. Instead, the estimate of  $D_\chi$  in DHT and SCPT is theoretically more complex since it should account for the reflection and refraction phenomena at the layer interfaces in the computation of the attenuation. Some pioneering interpretation schemes rely on data processing in the time domain, such as the rise-time method (Gladwin and Stacey, 1974; Kjartansson, 1979) and the pulse-broadening method (Kjartansson, 1979; Liu et al., 1994). Alternative schemes are

based on the attenuation coefficient method (Hoar and Stokoe, 1984; Mok et al., 1988) or on a simulation of the downwards wave propagation in the DH testing (modified SHAKE method; Stewart and Campanella, 1991). Campanella and Stewart (1991) reported several issues in the application of such approaches, due to large variability in results and the need of correcting factors to model the effect of layer interfaces.

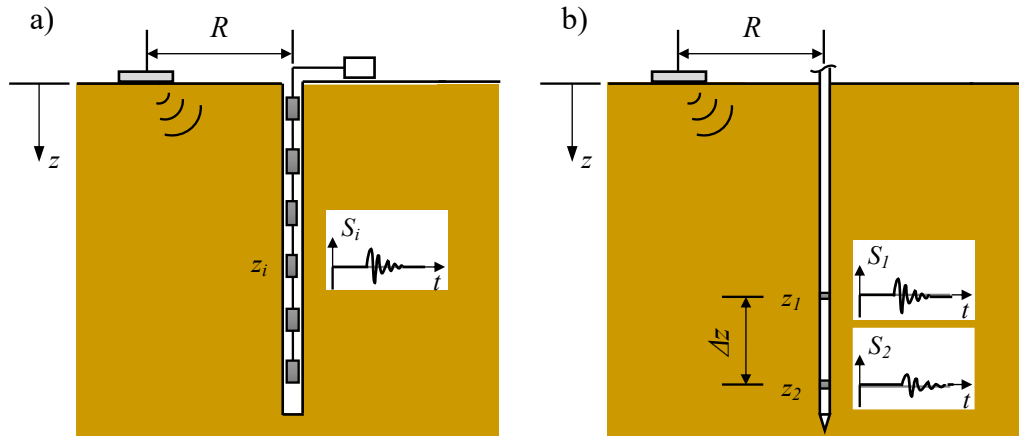


Figure 4-5. a) Scheme of the DHT layout; b) Scheme of the SCPT layout, using a dual cone.

A popular approach is the spectral ratio slope (SRS) method (Redpath et al., 1982; Mok et al., 1988; Lo Presti et al., 1997; Crow et al., 2011). The approach provides a frequency-independent estimate of  $D_\chi$  at depth  $z_i$  by computing the 2<sup>nd</sup> order derivative of the wave amplitude spectral ratio (i.e., the ratio of the spectra of the signals  $S_1$  and  $S_i$  recorded at the 1<sup>st</sup> and the  $i$ -th receiver) with respect to the depth and the frequency:

$$D_\chi = \frac{V_\chi}{2\pi} \cdot \frac{\partial^2}{\partial f \partial z} \ln \left( \frac{|S_1|}{|S_i|} \right) \Bigg|_{z=z_i} \quad (4.9)$$

This formula is valid for multichannel acquisition setups, whereas it simplifies for two-sensor schemes (e.g., SCPT; Toksöz et al., 1979; Liu et al., 1994; Karl et al., 2006). However, Badsar (2012) questioned the reliability of the SRS method in the determination of the  $D_\chi$  profile, especially in the presence of complex stratigraphy. Indeed, this technique models the vertical propagation of shear waves by assuming the geometrical damping as in a homogeneous medium. Therefore, the effect of reflected and refracted waves on measured wave amplitude is not properly accounted for. Thus, although the average of results is close to the theoretical value, the estimated  $D_\chi$  is affected by strong variability,

especially close to layer interfaces (Figure 4-6; Karl, 2005). The large scatter together with erratic values prevent a clear and accurate estimation of the  $D_{S,0}^{site}$  profile.

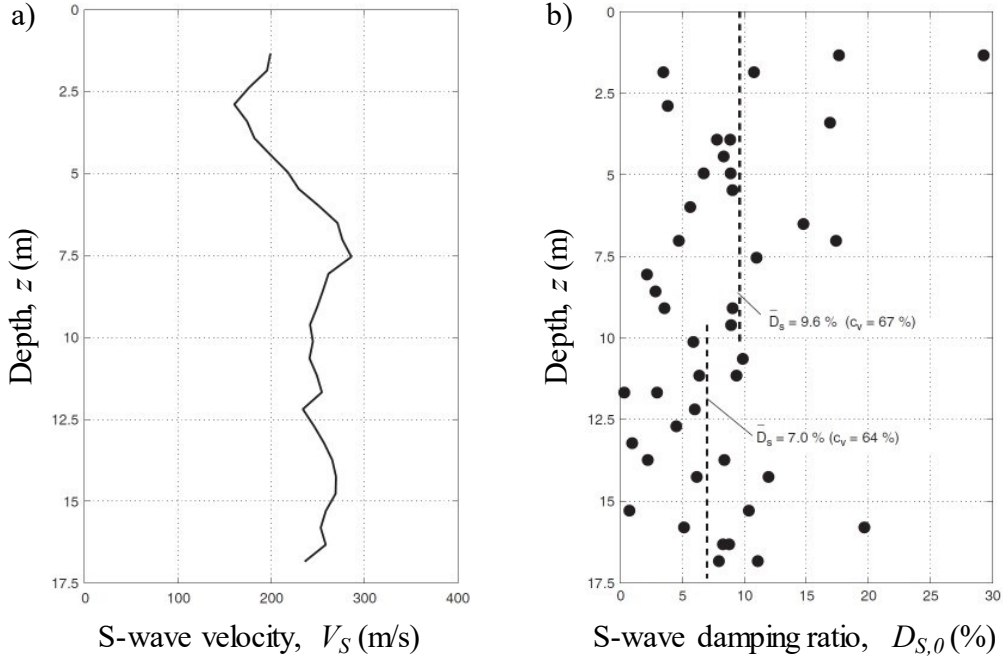


Figure 4-6. Results from a SCPT survey: a) estimated S-wave velocity profile  $V_S$ ; b) estimated S-wave small-strain damping ratio profile  $D_{S,0}$ , according to the SRS method (after Karl et al., 2006).

A more robust approach is based on the spatial decay of the Arias intensity, developed by Badsar (2012). The Arias intensity  $I_{A,\beta}$  (Arias, 1970) is a ground motion parameter defined from the acceleration time history  $a_\beta(z_i, t)$  at the  $i$ -th receiver (where  $\beta$  labels the motion component) or the corresponding spectrum:

$$I_{A,\beta}(z_i) = \frac{\pi}{2g} \int_{-\infty}^{+\infty} a_\beta^2(z_i, t) dt = \frac{1}{4g} \int_{-\infty}^{+\infty} a_\beta(z_i, \omega) \cdot a_\beta^*(z_i, \omega) d\omega \quad (4.10)$$

The method calibrates the  $D_\chi$  profile through an optimization algorithm minimizing the difference between the experimental evolution of  $I_{A,\beta}(z)$ , computed from the horizontal component of the acceleration, among the receivers and the theoretical one, computed for a vertical point force (Figure 4-7). The estimation of  $D_S$  is based on the horizontal component of the acceleration (i.e.,  $\beta = x$ ), whereas  $D_P$  is obtained from the vertical one (i.e.,  $\beta = z$ ). The forward modeling relies on appropriate numerical schemes to model the wave propagation in layered media (e.g., the stiffness matrix approach; Thomson, 1950), hence this method properly considers all the phenomena of reflection and refraction at the layers' interfaces.

On the other side, its application requires an accurate modelling of the  $V_S$  profile, due to the remarkable sensitivity of the Arias intensity to this parameter, and long computational time due to the multiple forward analyses.

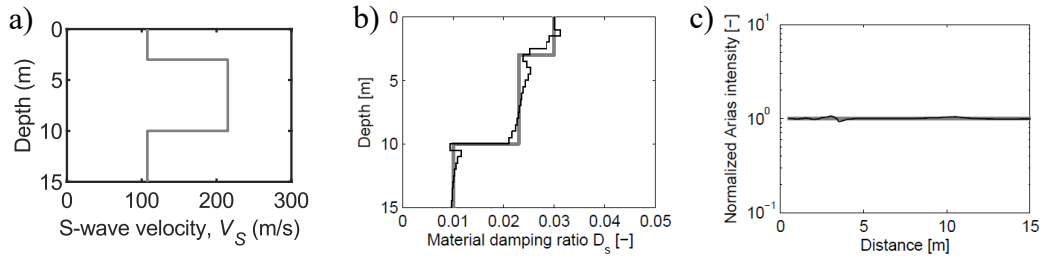


Figure 4-7. Application of the fitting of the Arias intensity on a synthetic case to derive the damping ratio profile: a) S-wave velocity profile  $V_S$ ; b) Original (thick grey curve) versus calibrated (thin black curve) damping ratio profile  $D_s$ ; c) Comparison between the experimental (thick grey curve) and the theoretical (thin black curve) normalized Arias intensity, i.e. ratio Arias intensity-experimental Arias intensity (modified from Badsar, 2012).

### 4.3 In situ geophysical tests: non-invasive methods

Non-invasive tests are geophysical seismic tests employing a set of receivers and a source (when required) on the ground surface. They include the seismic reflection survey (ASTM D7128), the seismic refraction survey (ASTM D5777), surface wave testing (Foti et al., 2014) and the horizontal-to-vertical spectral ratio (SESAME, 2004). This section will focus on techniques based on the measurement of surface waves. Furthermore, although surface wave testing can interpret various types of surface waves (e.g., Rayleigh waves, Love waves, Scholte waves), this section will address only methods based on the measurement of propagation characteristics of Rayleigh waves. Indeed, these techniques are the most used in ordinary engineering applications.

Surface Wave Methods (SWM) rely on the dispersive behavior of Rayleigh waves in layered media, for which the phase velocity  $V_R$  and the phase attenuation  $\alpha_R$  exhibit a dependence on frequency. The frequency-dependence of propagation parameters is a combined effect of geometric dispersion, which results from the variation of mechanical properties with depth, and intrinsic dispersion, due to the constitutive behavior of linear viscoelastic media. The standard testing procedure can be divided into three main steps (Figure 4-8):

- Acquisition of the particle motion;
- Processing of measured data to derive the experimental Rayleigh-wave dispersion curves  $V_R(\omega)$  and attenuation curves  $\alpha_R(\omega)$ ;



- Inversion: estimation of the  $V_S$  and the  $D_{S,0}^{site}$  profile with depth through an inversion scheme, where a theoretical soil model is calibrated to match the experimental  $V_R(\omega)$  and  $\alpha_R(\omega)$ .

Data acquisition consists in recording the particle motion induced by a propagating waveform on a single or multiple sensors (typically, geophones). The impinging wave is generated by an artificial source (e.g., a sledgehammer) or induced by ambient vibrations. The origin of the recorded wavefield is the basis of a key classification of SWM techniques: active methods, that use a source to generate the wavefield; and passive methods, that record ambient noise. Remarkable differences characterize the acquisition scheme and the techniques for data processing in these two families. On the one side, active methods often measure the wavefield by using a couple or a linear array of geophones and estimate the Rayleigh wave propagation parameters by means of a modeling or transformation of the recorded signal. Instead, passive methods record ambient vibrations on single receivers or 2D arrays of sensors and they adopt statistical tools to process the acquired data. In addition, these two categories of testing procedures are complementary in terms of resolution. Indeed, passive methods allow to resolve long wavelengths, whereas active data provide useful information in the high-frequency range, where ambient vibrations are typically corrupted by incoherent noise. For this reason, the current trend in site characterization consists in combining both approaches, to obtain high-quality profiles down to great depths (Tokimatsu, 1995; Rix et al., 2002; Foti et al., 2018). This task is possible because, although the two procedures rely on different acquisition and processing schemes, results can be combined in a single inversion scheme.

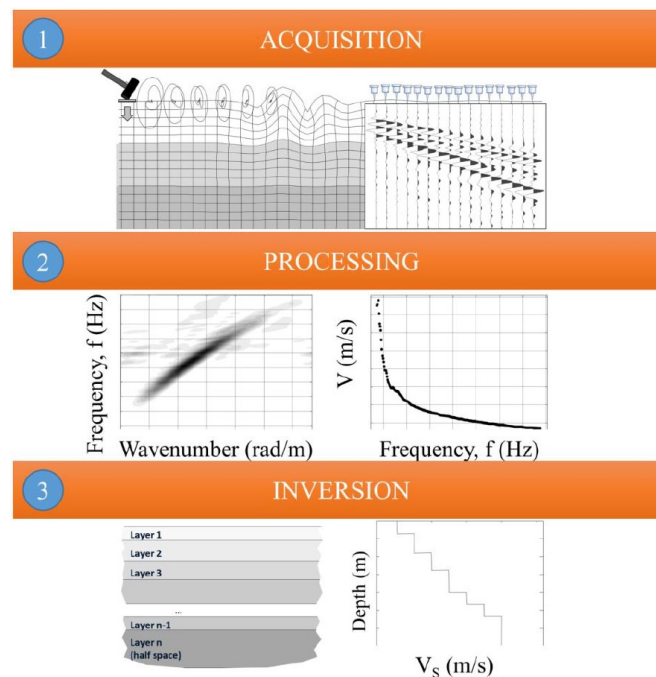


Figure 4-8. Main steps of a SWM survey (after Foti et al., 2014; Passeri, 2019)

SWM have always been considered an appealing site characterization tool, especially for ordinary design applications, thanks to their cost-effectiveness and limited time consumption. However, the interpretation of experimental data is a challenging task because the inference of material parameters requires the use of advanced processing techniques. For this reason, some expertise from the operator is requested in order to achieve reliable results. On the other side, the gradual introduction of accredited guidelines for the execution of this kind of surveys (e.g., SESAME, 2004; Socco and Strobbia, 2004; Socco et al., 2010; Foti et al., 2018) allowed a remarkable reduction of interpretation ambiguities, with a significant gain in confidence in SWM in the earthquake engineering community. Furthermore, it has been demonstrated that SWM provide results that are as reliable as those of invasive techniques, both in terms of accuracy and precision (e.g., Garofalo et al., 2016a). However, a key difference is that invasive techniques provide a local estimate of material parameters, which is representative of a small portion of soil around the borehole(s) (Figure 4-9). Instead, SWM investigate a large volume of the medium, whose size depends on the array geometry, and it returns an average measure of material properties in the reference volume of the soil deposit (Comina et al., 2011; Passeri, 2019). Therefore, SWM tend to provide data estimates at a scale compatible with those of the geotechnical system.

The next sections describe in more detail some applications of the active and the passive methods for the in situ estimate of  $V_S$  and  $D_S$ . The most relevant features in the data acquisition are addressed and some common algorithms for retrieving  $V_R(\omega)$  and  $\alpha_R(\omega)$  are introduced. However, additional information about the acquisition and the processing stage can be retrieved in the devoted textbooks and guidelines (e.g., Foti et al., 2014; Foti et al., 2018). A thorough description of the inversion stage is provided in Chapter 8.

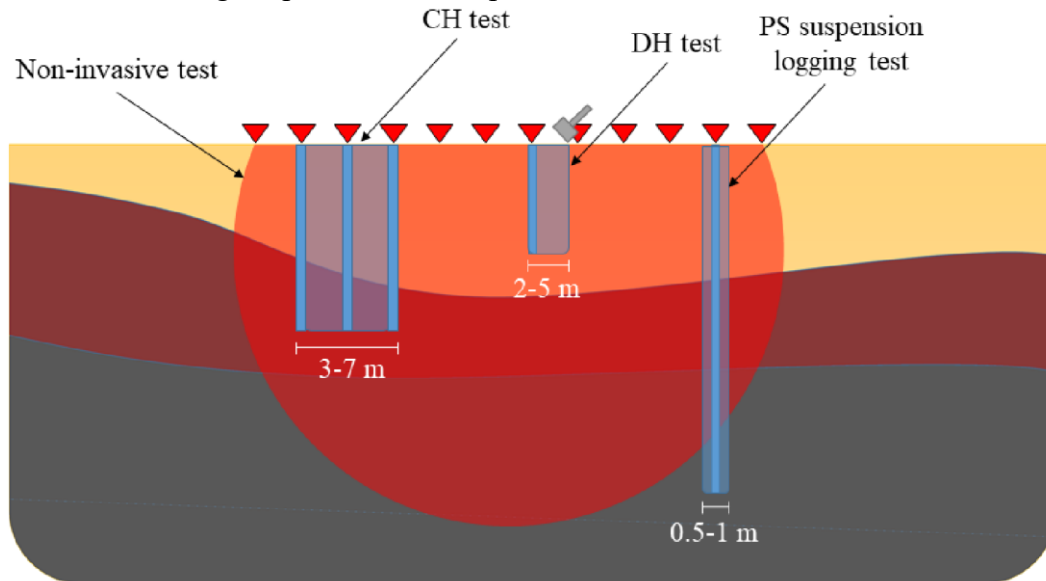


Figure 4-9. Investigated volumes in invasive tests and SWM (after Passeri, 2019)

### 4.3.1 Multichannel Analysis of Surface Waves (MASW)

The acquisition and processing of active-source data relies on various techniques. One of the pioneering applications of this approach is the Steady-State Rayleigh-wave Method by Jones (1958), which employs a single sensor to measure the wavefield generated by a monochromatic source. Then, Nazarian and Stokoe II (1984) exploited advanced digital signal processing schemes to derive Rayleigh wave parameters, developing the Spectral Analysis of Surface Waves. This technique uses an impulsive source to generate the wavefield, which is recorded by a pair of receivers, whose relative distance is gradually changed to investigate a broad range of wavelengths. Nowadays, the most popular testing configuration is the Multichannel Analysis of Surface Waves (MASW), which measures the wavefield on a linear array of receivers aligned with the source (Nolet and Panza, 1976; McMechan and Yedlin, 1981; Gabriels et al., 1987; Park et al., 1999; Foti, 2000). Typically, the recorded output is the vertical displacement at each sensor

$u_z(r,t)$  (or its spectrum  $u_z(r,\omega)$ ) with offset  $r$ , whereas the source can be described as a harmonic vertical force source  $Fe^{i\omega t}$  in the frequency domain (Figure 4-10). This setup allows a fast and robust estimate of Rayleigh wave propagation characteristics, even in sites with complex stratigraphy. For these reasons, the next Section will address processing techniques relying on MASW data.

The data acquisition in MASW testing requires great care, especially when attenuation measurements are carried out. The main issue is linked with the sensor-ground coupling, which is crucial for an accurate tracking of the particle motion. Furthermore, recorded data should have reasonably high signal-to-noise ratio in the frequency band of interest (e.g., Sun, 2000) and the quality of the seismogram should be good enough.

Processing schemes aimed at estimating Rayleigh wave dispersion and attenuation curves from MASW data can be clustered as regression techniques, maximum likelihood parameter estimation procedures, and transform-based techniques. On the one side, regression approaches infer the R-wave propagation parameters by fitting a theoretical model describing the particle motion with the experimental data. On the other side, transform-based techniques interpret the recorded wavefield in a transformed domain, where the desired parameters can be identified from the spectral maxima.

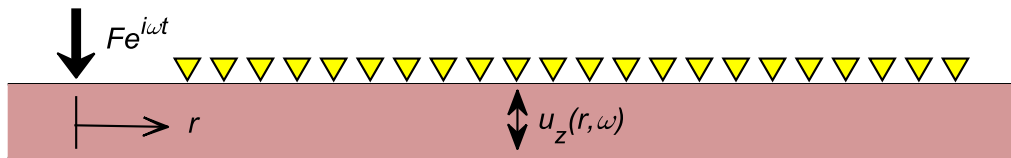


Figure 4-10. Scheme of the MASW setup, where the vertical displacement  $u_z$  induced by an input force (e.g., a harmonic force  $Fe^{i\omega t}$ ) is recorded by various sensors with varying distance  $r$ .

#### 4.3.1.1 Regression techniques

Regression techniques are the most commonly used category of processing techniques for the derivation of the attenuation parameters of the Rayleigh wave. Their principle consists in solving a problem of model identification, by fitting experimental data with a theoretical model, typically given by the equation describing the spatial attenuation of the displacement field due to a harmonic point force (Eq. 3.35; Lai and Rix, 1998a).

First applications of regression techniques estimated R-wave attenuation by comparing wave spectra recorded at different locations (e.g., Barker and Stevens, 1983), although they did not properly model the geometrical spreading. However, this scheme has been later adopted in more advanced techniques (e.g., Xia et al.,

2002; Gao et al., 2018; Mun and Zeng, 2018). Instead, Rix et al. (2000) estimated  $\alpha_R(\omega)$  based on the regression of the displacement amplitude versus offset data, accounting for uncertainties in the geometrical spreading function. For this purpose, they performed a preliminary characterization of the  $V_S$  profile, to obtain an approximate estimation of this function, which was then included in the regression to obtain the attenuation curve. However, the amplitude-offset regression provides an uncoupled estimate of the dispersion and attenuation data, which is not mathematically robust and ignores the intrinsic relationship between velocity and attenuation in a linear viscoelastic material (Lai and Rix, 1998a).

An upgrade of the approach is the transfer function method (TFM; Rix et al., 2001a; Lai et al., 2002). The technique is a multistation approach based on the estimate of the experimental displacement transfer function  $T(r, \omega)$ , i.e. the ratio between the measured vertical displacement at each sensor  $u_z(r, \omega)$  and the input harmonic source  $F e^{i\omega t}$  in the frequency domain:

$$T(r, \omega) = \frac{u_z(r, \omega)}{F \cdot e^{i\omega t}} \quad (4.11)$$

The TFM is based on the theoretical formulation of the particle vertical displacement induced by a propagating Rayleigh wave (Eq. 3.40), under the simplifying assumption the wavefield is dominated by a single Rayleigh mode of propagation, for which the complex-valued phase angle  $\mathcal{F}_v(r, \omega)$  becomes linearly dependent on the offset  $r$  through the complex wavenumber  $\hat{k}_R(\omega)$  (Lai and Rix, 1998a):

$$T(r, \omega) = \mathcal{Y}_z(r, \omega) \cdot e^{i\mathcal{F}_v(r, \omega)} \xrightarrow{\text{single mode}} T(r, \omega) = \mathcal{Y}_z(r, \omega) \cdot e^{-i\hat{k}_R(\omega)r} \quad (4.12)$$

Based on Eq. 4.12, the TFM estimates  $\hat{k}_R(\omega)$  through a nonlinear fitting of the experimental data, from which  $V_R(\omega)$  and  $\alpha_R(\omega)$  are then derived (Eq. 3.28-29). However, the geometrical spreading function  $\mathcal{Y}_z(r, \omega)$  is not known a priori, as it depends on the mechanical characteristics of the soil deposit. Therefore, it is usually assumed as equal to  $r^{-1/2}$  (e.g., Lai et al., 2002; Foti, 2003). The fitting of  $T(r, \omega)$  can be performed in an uncoupled way, based on the separate fitting of its amplitude and phase (Lai et al., 2002). However, a coupled fitting of the transfer function in the complex domain is mathematically more robust (Foti, 2003; Figure 4-11).

Foti (2003, 2004) proposed a generalized version of the TFM by removing the effect of the input force, as its measurement is nontrivial and requires controlled sources, that are often unavailable in ordinary applications. For this purpose, the Author reformulated the displacement transfer function in terms of deconvolution of the seismic traces. The principle of this method consists in computing the

experimental transfer function adopting the response of the closest receiver as the reference trace. Under this assumption, the theoretical transfer function modifies as follows:

$$\tilde{T}(r, \omega) = \frac{u_z(r, \omega)}{u_z(r_{ref}, \omega)} = \frac{y_z(r, \omega)}{y_z(r_{ref}, \omega)} \cdot e^{-i\mathcal{K}_R(\omega)(r-r_{ref})} \quad (4.13)$$

As in the TFM, Eq. 4.14 is the basis of a nonlinear regression procedure to compute  $\hat{k}_R(\omega)$  and derive the phase velocity curve and the phase attenuation curve.

The main limitation of the TFM is the assumption that the wavefield is dominated by a single Rayleigh mode of propagation. This approach may lead to wrong results when the effect of modal superposition is relevant. Indeed, the result is an estimate of apparent Rayleigh phase dispersion and attenuation curves, that can be affected by modal superposition when multiple propagation modes are relevant (Foti et al., 2014). Furthermore, the theoretical model relies on the far-field approximation of the displacement field induced by Rayleigh waves. Therefore, estimated value may be less reliable at low frequencies, where the corresponding wavelength becomes comparable with the offset of the closest receiver. Finally, an additional source of uncertainties derives from the simplification of the geometrical spreading function. A possible solution may consist in determining approximate profiles of  $V_S$  and  $D_S$  through coupled inversion of the experimental curves and setting an iterative procedure where the geometrical spreading function is updated according to the resulting profiles and new models are extracted until convergence. In this case, the processing and the inversion stages would be performed simultaneously and results would be more accurate. However, this procedure is time-consuming.

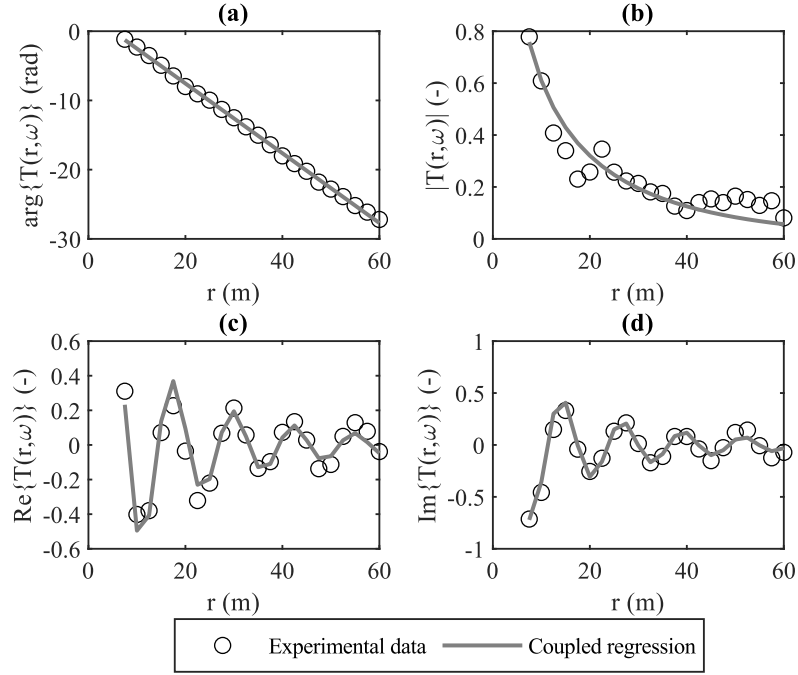


Figure 4-11. Regression of the experimental transfer function  $T(r, \omega)$  with the distance  $r$  for the coupled computation of dispersion and attenuation curves: (a) phase; (b) amplitude; (c) real part; (d) imaginary part. Data refer to the Pisa Leaning Tower site, at the frequency of 11.5 Hz (modified from Foti, 2003).

#### 4.3.1.2 Maximum likelihood parameter estimation procedures

A promising approach able to overcome limitations in the modeling of multimode Rayleigh waves is the Wavefront Decomposition (WaveDec, hereafter labeled as “WD”) technique. The method was originally designed for passive measurements (Maranò et al., 2012) and then extended for active measurements, by modeling the propagation of a cylindrical wavefield including spatial decay (Maranò et al., 2017; Bergamo et al., 2018; Bergamo et al., 2019). The WD relies on quite a general framework, which makes it usable even in the presence of 2D arrays. The approach interprets measured three-component displacement data to jointly estimate the Rayleigh wave parameters, i.e., the complex wavenumber  $\hat{\kappa}_R(\omega)$  and the ellipticity angle  $\zeta(\omega)$ , which is the arctangent of the ratio between the horizontal and the vertical component of the displacement field. These parameters are clustered in an unknown parameter vector  $\boldsymbol{\theta} = (\hat{\kappa}_R(\omega); \zeta(\omega))$ . The WD approach returns a maximum likelihood estimation of  $\boldsymbol{\theta}$ , labeled as  $\hat{\boldsymbol{\theta}}$ , where the likelihood function is defined as follows:

$$\hat{\boldsymbol{\theta}} = \arg \max_{\boldsymbol{\theta}} f(\boldsymbol{\theta}), \quad f(\boldsymbol{\theta}) = \prod_{\beta=1}^3 \prod_{n=1}^N \prod_{m=1}^M \frac{1}{\sqrt{2\pi\sigma_{\beta,n}^2}} \exp \left[ -\frac{(y_{\beta,n,m} - u_{\beta,n,m})^2}{2\sigma_{\beta,n}^2} \right] \quad (4.14)$$

where  $y_{\beta,n,m}$  is the measured displacement, whereas  $u_{\beta,n,m}$  is the predicted displacement according to Eq. 3.34 ( $\beta$  is the component index,  $n$  is the receiver index, and  $m$  is the sample index). Instead,  $N$  is the number of receivers,  $M$  is the number of samples and  $\sigma_{\beta,n}$  represents the standard deviation of the signal noise of the displacement component at the sensor. This approach accommodates for the presence of multiple modes of propagation in the recorded wavefield by performing multiple fittings of the experimental wavefield, assuming different number of modes in the predicted displacement. The selection of the most suitable number of modes to describe the recorded wavefield represents a problem of model selection, for which an effective indicator is the Bayesian Information Criterion (BIC; Schwartz, 1978). The Authors adopted a penalized version of BIC, defined as follows:

$$BIC_{\gamma} = -2f(\hat{\boldsymbol{\theta}}) + \gamma N_p \ln(3N \cdot M) \quad (4.15)$$

where  $N_p$  denotes the number of parameters calibrated in the fitting model (hence, it is linked to the assumed number of modes) and  $\gamma$  is a control parameter ranging between 0 and 1, that allows to control the complexity of the model and the fitting quality – specifically, at smaller  $\gamma$ , the algorithm returns a larger number identified propagation modes and it tends to overfit experimental data. Given the large number of evaluations of the likelihood function, the approach does not carry out a direct computation but it models it by means of a factor graph (Loeliger et al., 2007), achieving more efficient computation.

Figure 4-12 shows the application of WD on a synthetic case, where a linear and a 2D survey were simulated. For both arrays, this approach returns reliable estimates of  $V_R(\omega)$  and  $\alpha_R(\omega)$  and the ellipticity angle, for both the fundamental mode and the first higher mode. Furthermore, the fitting quality is good also at low frequencies, because the method models the cylindrical shape of the Rayleigh wavefront, thus mitigating near-field effects.



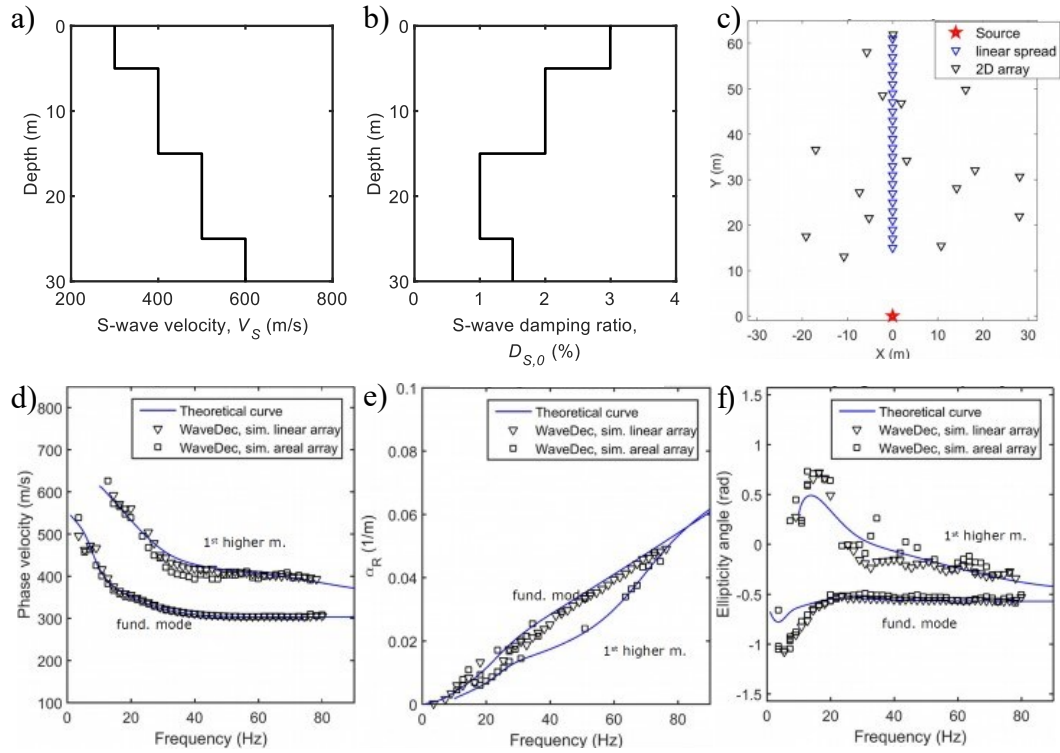


Figure 4-12. Application of the WaveDec approach for a synthetic case: a-b) S-wave velocity  $V_S$  and small-strain damping ratio  $D_{S,0}$  profiles; c) Acquisition layout; d) Estimated dispersion curves; e) Estimated attenuation curves; f) Estimated Rayleigh wave ellipticity (after Bergamo et al., 2019).

#### 4.3.1.3 Transform-based techniques

Transform-based techniques rely on the application of appropriate transformations to the recorded wavefield to retrieve the R-wave propagation parameters. These techniques map the time-space seismograms into spectra defined in alternative domains, for instance the frequency-wavenumber ( $f-k$ ) domain. A significant advantage is the capability of these approaches to separate the different components of the wavefield (i.e., different modes), although the possibility of isolating modes also depends on the spatial resolution of the array. For this reason, dispersion analysis is often carried out by interpreting the transformed wavefield, e.g. by means of a double Fourier transform, the frequency-domain beamformer (Lacoss et al., 1969), the high-resolution frequency-wavenumber approach (Capon, 1969), the linear Radon transform (McMechan and Yedlin, 1981; Luo et al., 2008), the phase-shift (Park et al., 1999), the multiple signal classification (Iranpour et al., 2002), and the frequency decomposition and slant stack (Xia et al., 2007).

Only few applications of transform-based techniques to retrieve attenuation data can be identified. One of the first attempts is attributed to Yoon (2005), who proposed a hybrid scheme for the attenuation estimate, combining a regression method and the double Fourier transform. Indeed, the algorithm derives  $V_R(\omega)$  from the location of peaks of the  $f$ - $k$  spectrum, whereas  $\alpha_R(\omega)$  is obtained through nonlinear regression of an equivalent displacement field, derived from the amplitude of the spectral peaks. More recent approaches relying on the interpretation of  $f$ - $k$  spectra have been proposed by Badsar et al. (2010) and Verachtert et al. (2017). In both cases, the Authors generalized modal identification techniques commonly used in structural engineering to the characterization of R-waves. Further details on these techniques will be provided in the following. Instead, other Authors tried to extend dispersion analysis schemes into dissipative media (e.g., Misbah and Strobba, 2014).

Badsar et al. (2010) proposed a simplified method for the estimate of the  $\alpha_R(\omega)$ , based on a generalization of the half-power bandwidth method (Chopra, 2017). This method is hereafter referred as Generalized Half-Power Bandwidth (GHPB). The GHPB is able to reduce the interpretation complexity and capture the propagation characteristics of multiple Rayleigh modes. The GHPB provides an uncoupled estimate of  $V_R(\omega)$  and  $\alpha_R(\omega)$ , from the interpretation of the  $f$ - $k$  spectrum of the experimental displacement transfer function  $T(r, \omega)$ . The transform is calculated through a Hankel transformation, to account for the cylindrical shape of the wavefront (Forbriger, 2003):

$$T(k_r, \omega) = \frac{1}{2} \int_0^{r_N} T(r, \omega) J_0(k_{R,t} r) r dr \quad (4.16)$$

where  $J_0(k_{R,t} r)$  is the zeroth-order Bessel function of the first kind and  $k_{R,t}$  is the (trial) wavenumber at which the transform is computed. The dispersion curves of each mode of propagation are first identified as spectral peaks of the  $f$ - $k$  spectrum. Then, for each propagation mode, the GHPB derives  $\alpha_R$  at every frequency from the width of the corresponding peak. At each frequency, the bandwidth  $\Delta k_{R,j}(\omega)$  is the width of the  $f$ - $k$  spectral peak of the  $j$ -th mode, measured at an amplitude level equal to a fraction  $\gamma$  of the peak value (Figure 4-13a). Then,  $\alpha_R(\omega)$  is derived as follows:

$$\alpha_{R,j}(\omega) = \frac{\Delta k_{R,j}(\omega)}{2\sqrt{\gamma^2 - 1}} \quad (4.17)$$

The amplitude decay parameter  $\gamma$  equals  $\sqrt{2}/2$  in the half-power bandwidth, whereas a much larger value is recommended in the GHPB, to avoid mixing of adjacent peaks and modal interference in the estimated phase attenuation (Figure 4-13b). In this way, the approach is not sensitive to multiple Rayleigh modes. The

parameter  $\gamma$  should be tuned up as a function of the soil deposit characteristics and the testing setup, although a value equal to 0.99 is suitable in various conditions.

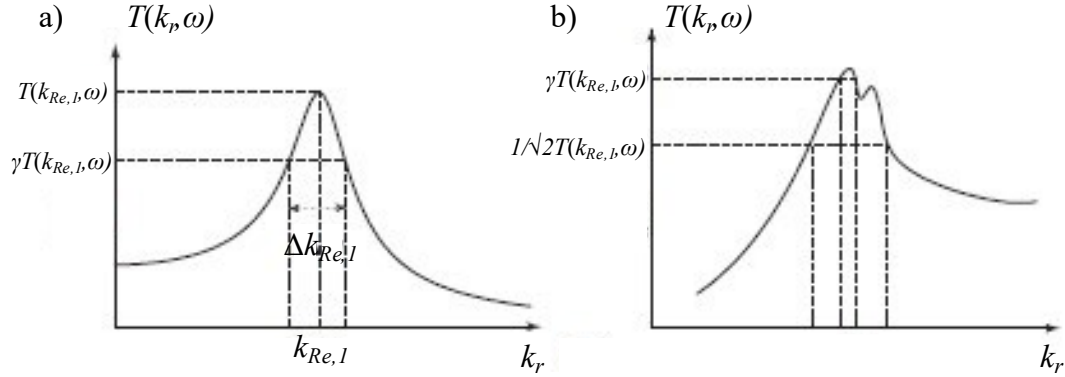


Figure 4-13. Generalized half-power bandwidth method: a) Definition of the reference bandwidth  $\Delta k_{R,j}$  from the spectrum of the experimental displacement transfer function  $T(r, \omega)$ ; b) Performance of the classical half-power bandwidth vs. GHPB in the presence of multiple propagation modes.

However, the estimated  $V_R(\omega)$  and  $\alpha_R(\omega)$  depend on two control parameters, that are the amplitude decay parameter  $\gamma$  and the quantity  $q$ . The latter controls the spatial window applied to the recorded wavefield, to minimize truncation effects in the computation of the  $f$ - $k$  spectrum according to Eq. 4.17, that might induce an overestimation of  $\alpha_R(\omega)$ . In general  $q$  is typically equal to  $10^{-4}$ , although it should be calibrated based on in situ conditions.

Instead, Verachtert et al. (2017) proposed an alternative methodology for the determination of multimodal R-wave dispersion curves and attenuation curves, namely the Circle Fit Method (CFM). The CFM is intimately connected with the GHPB as it uses the corresponding  $V_R(\omega)$  and  $\alpha_R(\omega)$  estimates as starting point. The principle of the CFM relies on an alternative representation of the  $f$ - $k$  spectrum of the displacement transfer function, based on the Nyquist plot, which compares the real and the imaginary part of a complex number. From the analogy between the spectral shape of the R-wave spectrum at each frequency and the frequency response function of a Multiple-Degree-Of-Freedom (MDOF) system, it can be demonstrated that the Nyquist plot of the  $f$ - $k$  spectrum is a combination of circles, each one corresponding to a single Rayleigh mode (Ewins, 1984; Figure 4-14b). The CFM estimates  $V_R(\omega)$  and  $\alpha_R(\omega)$  based on the geometry of the circles. Specifically, the modal wavenumber  $k_{R,j}(\omega)$  corresponds to the value where the angular sweep at the center  $\mathcal{G}_f(k_r, \omega)$  is maximum and it is obtained through a search method. The phase attenuation, instead, is computed by

combining the wavenumber sample points  $k_{t,a}$  and  $k_{t,b}$  and the corresponding angles close to the modal wavenumber (Figure 4-14b):

$$\alpha_{Re,j}(\omega) = \frac{k_{R,b}^2 - k_{R,a}^2}{2k_{Re,j}(\omega) \left[ \tan\left(\frac{|\mathcal{G}_j(k_{t,b}, \omega)|}{2}\right) + \tan\left(\frac{|\mathcal{G}_j(k_{t,a}, \omega)|}{2}\right) \right]} \quad (4.18)$$

Verachtert et al. (2017) demonstrated that the CFM provides more accurate estimates of  $V_R(\omega)$  than the peak picking of the  $f$ - $k$  spectrum (Figure 4-14a) and it is more reliable at deriving  $\alpha_R(\omega)$  than the GHPB, for both the fundamental mode and higher modes. Furthermore, estimated data span a broader frequency range. Indeed, the CFM exploits all the information provided by the  $f$ - $k$  spectrum, whereas the GHPB focuses only on its amplitude. However, both GHPB and CFM depend on two parameters (i.e.,  $\gamma$  and  $q$ ) that depend on the soil deposit characteristics and on the layout of the survey. Although some indicative values are prescribed, a proper application of these methods would require a site-specific calibration of these quantities, to avoid biased estimates. Furthermore, both methods tend to overestimate  $\alpha_R(\omega)$  at low frequencies (less than about 15 Hz), due to leakage. Therefore, they are less reliable at long wavelengths.

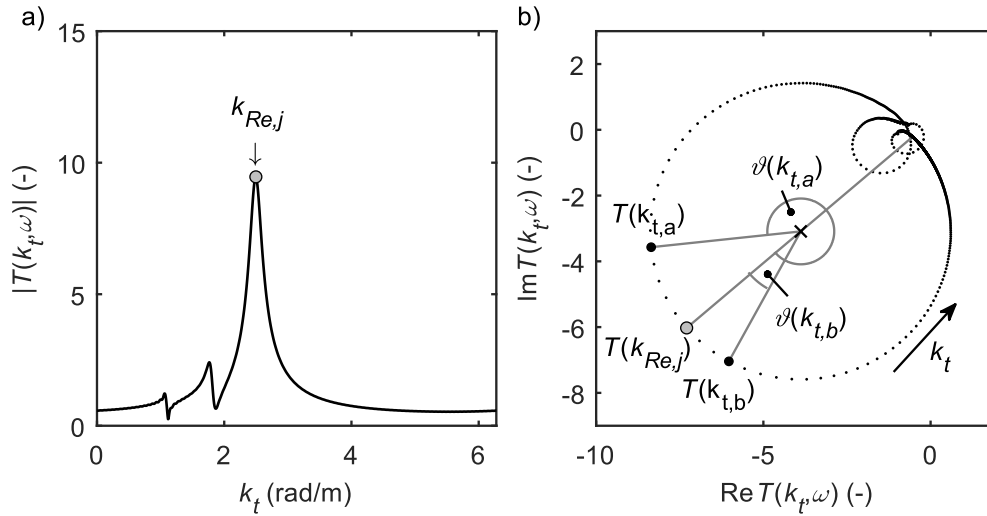


Figure 4-14. Application of the CFM scheme to identify the modal wavenumber  $k_{Re,j}$  (hence,  $V_R$ ) and  $\alpha_R$  for a synthetic case, with a focus on the dominant mode: a)  $f$ - $k$  spectrum of the particle displacement function, for a given frequency; b) Nyquist plot of the  $f$ - $k$  spectrum of the particle displacement function. The dominant mode corresponds to the greatest circle and  $k_{Re,j}$  is identified as the  $k_t$  value at which the relative distance between subsequent points in the Nyquist plot is maximum. The plot highlights values corresponding to two wavenumber sample points  $k_{t,a}$  and  $k_{t,b}$ , that are used to compute  $\alpha_R$ .

The corresponding angles  $\vartheta(k_{t,a})$  and  $\vartheta(k_{t,b})$  are computed from the line connecting  $k_{Re,j}$  and the circle center, and they increase according to the direction of growing  $k_t$ .

### 4.3.2 Ambient vibration analysis

Passive methods derive propagation characteristics of the seismic ambient noise, which is mainly composed by surface waves generated by anthropic activities or natural events. The measurement of ambient vibrations is possible through single-station measurements or multiple-station measurements. Multichannel measurements might employ linear acquisition arrays of receivers, which forms the basis of the ReMi<sup>TM</sup> technique (Refraction Microtremors; Louie, 2001; Zywicki, 2007; Strobbia and Cassiani, 2011). However, the current trend relies on 2D acquisition arrays, termed as Ambient Vibration Arrays (AVA; Tokimatsu et al., 1992; Okada and Suto, 2003). Indeed, the related measurements provide more reliable and robust measurements of dispersion characteristics of surface waves (Cox and Beekman, 2010; Foti et al., 2018). The optimal scheme is based on circular arrays, although other geometries (e.g., L-shaped, triangles) are often adopted, especially in the presence of external constraints (e.g., in the urban environment). During the acquisition stage, a proper ground-sensor coupling should be guaranteed, due to the sensitivity to wind conditions (e.g., Foti et al., 2018). Furthermore, recorded ambient vibrations may be corrupted by the presence of nearby structures (e.g., forests and infrastructures). Finally, measurements should be carried out according to adequately long time windows, to acquire a statistically significant number of propagating waves (SESAME, 2004).

The processing of acquired data is based on statistics computed on multiple time windows extracted from the recorded signals. However, the technique used to interpret data of each window depends on the acquisition scheme.

For single-station methods, the Horizontal to Vertical Spectral Ratio (HVSr; Nogoshi and Igarashi, 1970; Nakamura, 1989) is used, which provides an estimate of the fundamental resonance frequency of the soil deposit (SESAME, 2004; Bonnefoy-Claudet et al., 2008). Furthermore, HVSr data provide useful indications about the location of strong impedance contrasts, they may provide an additional constraint in the inversion of surface wave data, allowing for better defined soil models or even extending the investigated depth range (e.g., Arai and Tokimatsu, 2005; Parolai et al., 2005; Passeri, 2019). Also, HVSr data allow to assess for the spatial variability of the investigated site (e.g., Vantassel et al., 2018; Cheng et al., 2021). In some cases, single station measurements have also been used for soil damping characterization. However, the proposed techniques

identify a characteristic damping value, representing a global, equivalent value that reflects the overall response of the soil deposit (e.g., Yang et al., 1989; Huerta et al., 1994; Huerta et al., 1998; Mucciarelli and Gallipoli, 2006; Fernández-Heredia et al., 2012; Castellaro, 2016).

Array-based methods rely on multistation measurements of the ambient noise. The processing techniques may be clustered into two major families: transform-based approaches and spatial correlation methods.

On the one side, transform-based approaches (or  $f$ - $k$  methods) interpret recorded data after applying a proper transformation, in which wave parameters are identified as spectral maxima. Several techniques have been developed for the dispersion estimate, as the conventional frequency wavenumber (Burg, 1964; Lacoss et al., 1969), high resolution frequency wavenumber (Capon, 1969), and the MUSIC approach (Iranpour et al., 2002). However, no attempt to estimate dissipation parameters is currently available.

On the other side, spatial autocorrelation (SPAC) methods rely on the link between the spatial correlation of the recorded wavefield with the Green's function of surface waves. These techniques include the traditional SPAC (Aki, 1957), the extended SPAC (Ling and Okada, 1993), the modified SPAC (Bettig et al., 2001), the two-site SPAC (Morikawa et al., 2004), and the multi-mode SPAC (Asten et al., 2004). The SPAC method is a regression-based approach that measures the ambient noise on a circular (or pseudo-circular) array with a central sensor. Sensors position is described by the distance  $r$  and the azimuth angle  $\varphi$  with respect to the central sensor (Figure 4-15). Then, it computes the azimuthal average of the spatial correlation of the noise across each couple of sensors, which is related to the Green's function of surface waves. By virtue of this relationship, the SPAC method is capable to provide a measure of the dispersion curve, frequency by frequency.

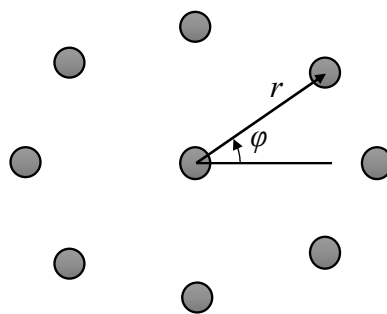


Figure 4-15. Acquisition layout for the SPAC method.

The SPAC technique has also been applied to retrieve the dissipative parameters of surface waves. For instance, Albarello and Baliva (2009) estimated attenuation data through a linear fit of the time derivative of the noise cross-correlation. However, several studies rely on the modification of the Aki's SPAC function proposed by Prieto et al. (2009), whose validity has been demonstrated theoretically by Nakahara (2012) and numerically by Lawrence et al. (2013):

$$\bar{\rho}(r, \omega) = J_0[k_R(\omega)r] e^{-\alpha_R(\omega)r} \quad (4.19)$$

Therefore, dispersion and attenuation data are estimated through an uncoupled fitting of the experimental correlation data with the theoretical model, described by the right term in Eq. 4.19. The fitting procedure is carried out within a proper wavelength range, so that the inter-receiver distance is bounded with one or two times the investigated wavelengths. Indeed, due to the attenuation, coherence is lost after short propagation distance and the fit beyond this limit would lead to unstable and unreliable estimates of wave parameters (Parolai, 2014). This scheme was also used for the derivation of dissipative characteristic in seismic interferometry (e.g., Weemstra et al., 2012; Weemstra et al., 2014; Magrini and Boschi, 2021). Figure 4-16 reports some results of the fitting procedure at a site in Italy (Parolai, 2014). Interestingly, the quality of the fit dramatically improves with respect to the elastic model, as a scheme closer to the actual behavior is used (Figure 4-16d-f; Prieto et al., 2009). However, although estimated  $V_R(\omega)$  are quite well constrained, the phase attenuation is affected by large uncertainties, with standard deviation increasing with the investigated frequency. This is also an indirect effect of the smaller accuracy in the estimated  $\alpha_R(\omega)$  attenuation with respect to  $V_R(\omega)$ , which is visible by the shape of the normalized misfit in Figure 4-16a-c (Boxberger et al., 2017).

Lawrence et al. (2013) observed that the SPAC method provides reliable attenuation estimates in the presence of far-field sources with reasonable azimuthal distribution and well-distributed receivers. Furthermore, the fitting model is valid for a single mode of propagation with small attenuation levels and large separation distance (i.e., the argument  $k_R r$  in Eq. 4.23 is much larger than the unit; Nakahara, 2012). Therefore, it returns only an apparent mode of R-wave propagation.

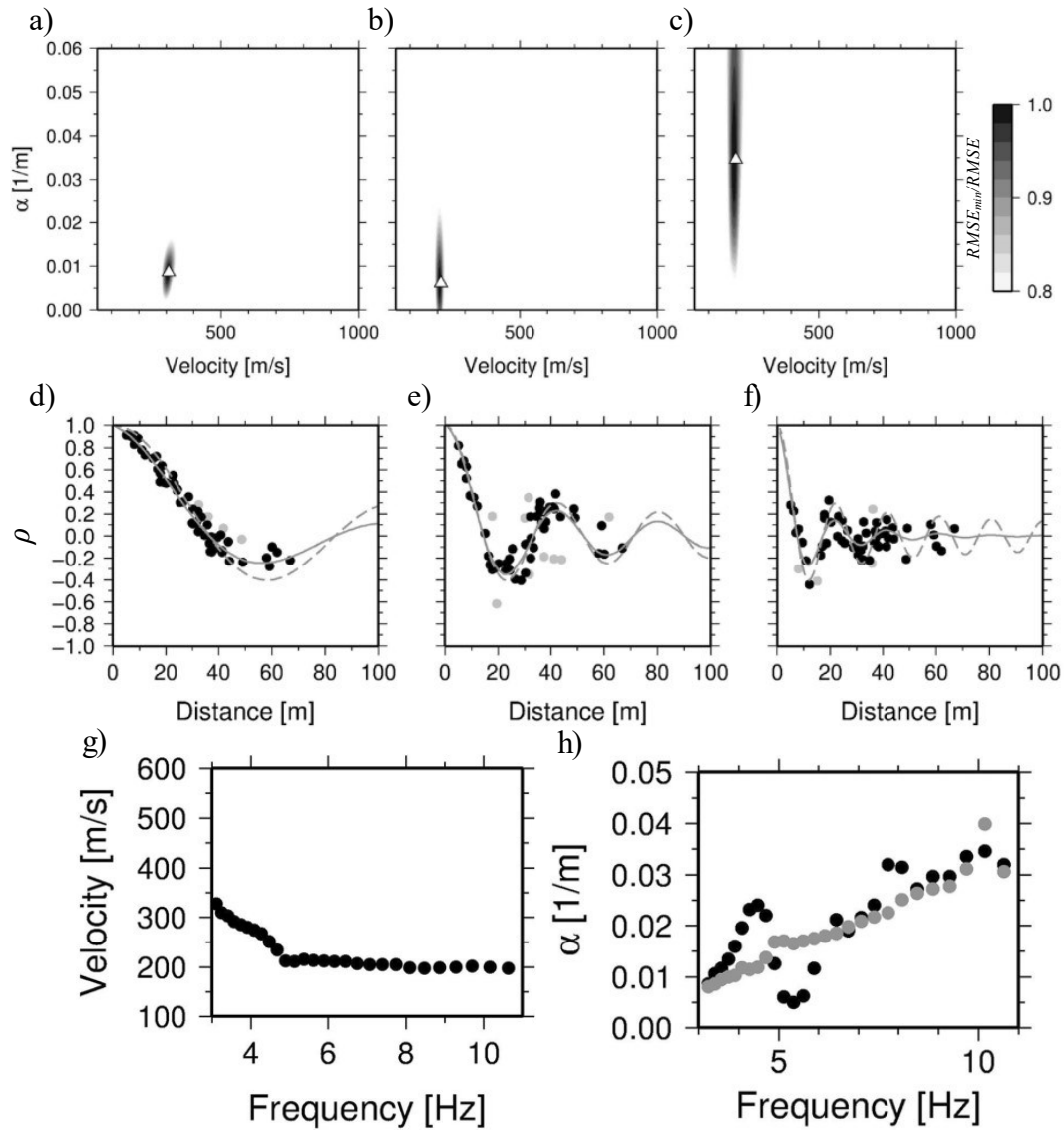


Figure 4-16. a-c) Results of the grid search procedure in the velocity-attenuation domain, represented as pseudocolor plot mapping the normalized fit value, measured as  $RMSE_{min}/RMSE$ , where RMSE is the root mean square error. White triangles identify the best fit values. Data refer to frequencies of a) 3.25 Hz, b) 5.61 Hz, and c) 10.16 Hz. d-f) Measured SPAC values (black dots) versus best-fitting functions considering attenuation (solid line) and ignoring attenuation (dashed line). Grey dots denote the SPAC values discarded in the fitting procedure. Data refer to frequencies of d) 3.25 Hz, e) 5.61 Hz, and f) 10.16 Hz. g) Obtained Rayleigh wave dispersion curve  $V_R(\omega)$ . h) Obtained Rayleigh wave attenuation curve. Grey dots denote the theoretical  $\alpha_R(\omega)$  resulting from an inversion procedure, which has not been reported for simplicity (after Parolai, 2014).



## 4.4 Back-analysis of downhole arrays

Downhole arrays, hereafter referred as DH-arrays, are boreholes equipped with an array of seismometers located at different depths, recording earthquake-induced ground motion. Their aim is to measure variations in the ground shaking as seismic waves propagate from depth up to the surface. DH-arrays represent a valuable tool for understanding the physics of seismic amplification. Therefore, they represent the basis for verification and for the development and calibration of predictive tools for the estimate of ground motion amplification (Elgamal et al., 2001).

On the one side, DH-array data highlighted issues due to the erroneous or coarse estimates of material parameters (e.g., Assimaki et al., 2008; Régnier et al., 2018) or induced by simplifying assumptions about the soil constitutive behavior (e.g., Kwok et al., 2008; Kaklamanos et al., 2013a), thus motivating the development of more advanced models for predicting site amplification (e.g., Shi and Assimaki, 2017). Besides, they demonstrated the limitations of classical propagation models (i.e., the 1D scheme) in some sites (e.g., Thompson et al., 2012).

Furthermore, DH-array data can be exploited for characterization purposes, as the back-calculation from observed weak motions can be an effective tool for the calibration of mechanical parameters of the soil deposit, with a particular focus on material dissipative characteristics, provided that 2D/3D resonance phenomena do not occur. However, it should be remarked that the high installation costs and the need of earthquake records do not allow their use for common applications.

The technical literature reports various attempts of in situ characterization of the soil deposit, based on DH-arrays. In general, DH-arrays can be interpreted by means of a large variety of techniques. In order to simplify the description, a basic and non-exhaustive classification is proposed: waveform inversion techniques, amplification analysis and  $\kappa$ -informed damping estimation. This partition refers to the quantity that is adopted as reference to constrain  $D_{S,0}^{site}$  data. Waveform inversion techniques deal with time histories recorded in the DH-array sensors, whereas amplification analysis calibrates  $D_{S,0}^{site}$  based on synthetic ground motion parameters. Similarly,  $\kappa$ -informed damping estimation exploits another parameter, i.e. the high-frequency spectral decay  $\kappa$  (e.g., Ktenidou et al., 2014). However, being this approach mostly used in seismological studies rather than for site characterization purposes, it will be addressed separately.

Part of this Section has already been published in Foti et al. (2021).

### 4.4.1 Seismogram inversion methods

Seismogram inversion methods provide a coupled estimate of stiffness and dissipation parameters based on low-amplitude motions recorded in DH-arrays. The principle of these techniques consists in calibrating ground models to achieve an acceptable degree of compatibility between predicted and measured ground motion, typically checked in the time domain. The calibration may also include results from other geophysical surveys, that provide additional data to better constrain the inferred model. In some cases, such integration is carried out in an uncoupled way, where geophysical data provide a starting model to be refined with ground motion records (e.g., Assimaki et al., 2006; Parolai et al., 2010). However, newly developed schemes implement a joint inversion scheme, where both data types simultaneously contribute to constrain the soil model (e.g., Seylabi et al., 2020).

Assimaki et al. (2006) implemented an elegant seismic waveform inversion algorithm for the estimate of the small-strain parameters from weak motion records in DH-arrays. The procedure estimates the mechanical parameters, i.e.  $V_S$ ,  $D_{S,0}^{site}$  (hereafter simply labeled as  $D_S$ ) and density through a two-step optimization algorithm, consisting of a genetic algorithm in the wavelet domain and a nonlinear least-squares scheme in the frequency domain. The stochastic optimization minimizes the misfit between theoretical and observed acceleration time histories, represented in the wavelet domain – rather than in the time domain – to ensure equal weighting of the information across all frequency bands. The corresponding objective function is the normalized correlation between observed and synthetic seismograms and synthetic ones, which should be maximized. On the other side, the local search process is a nonlinear least-squares optimization algorithm in the frequency domain, minimizing the energy error between the empirical and theoretical transfer function (TF; see Section 2.4.1 for the definition). The combination of a stochastic search algorithm with a local search one results in a fast and robust model identification scheme.

Assimaki et al. (2006) tested this approach with reference to a borehole station of the Kik-Net Strong Motion Network (Figure 4-17). The resulting soil models are quite comparable with the profiles inferred from the available geotechnical information, although discrepancies are observed at great depths. The matching with observed S-wave travel time data is sensibly improved, meaning that the estimated average  $V_S$  is now reliable. A possible reason behind such improvement could be the high resolution of the stratigraphy adopted in the inversion, that overcomes the limitations of the coarse description of the soil

profile in the available information. Furthermore, the  $D_{S,0}^{site}$  profile exhibits strong variability in the shallow layers. The Authors interpreted the large variability as a side effect of the modeling the 3D propagation of waves in a heterogeneous medium into a 1D layered medium, where they synthesized the intrinsic attenuation and scattering energy redistribution into a single, frequency-independent parameter.

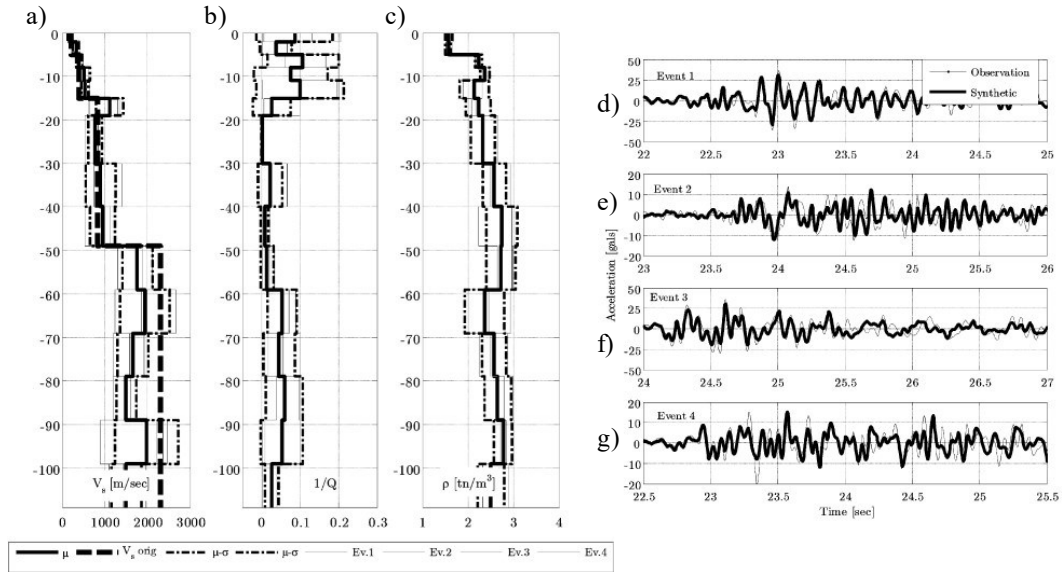


Figure 4-17. a-c) Obtained soil profiles in terms of S-wave velocity  $V_S$  (a), small strain damping ratio  $D_S$  (expressed as the reciprocal of the quality factor  $Q$ , namely  $1/Q = 2D_S$ ), (b) and mass density  $\rho$  (c) in Asimaki et al. (2008). The dotted lines are the profiles obtained from geotechnical data, whereas the solid lines represent the results of the inversion procedure. d-g) Matching between observed and simulated time histories.

Instead, Seylabi et al. (2020) combined information from DH arrays and geophysical surveys into an ensemble Kalman inversion scheme, to estimate the  $V_S$  and the  $D_S$  profile at the Garner Valley site, in California. This inversion scheme has been proposed as a possible strategy for mitigating the solution non-uniqueness that characterizes the inversion problem in SWM (more details on this will be addressed in Chapter 8). This issue is usually tackled by adding complementary information, e.g. HVSR data. Seylabi et al. (2020) demonstrated the effectiveness of integrating DH-array data in the inversion problem, as they allow a remarkable constraint of the inferred soil models. Specifically, synthetic tests demonstrated the effectiveness of the joint inversion with respect to using different data types separately. Besides, tests on real data resulted in ground models with amplification features perfectly compatible with observed data.

#### 4.4.2 $\kappa$ -informed damping estimation

The spectral decay parameter  $\kappa$  has been introduced by Anderson and Hough (1984), who observed that the high-frequency amplitude spectrum of acceleration data induced by S-waves exhibits an exponential decay, independently from the specific event considered or the location of the sensor (Figure 4-18a):

$$A(f) \propto e^{-\pi\kappa f}, \quad f_E < f < f_X \quad (4.20)$$

where  $f_E$  and  $f_X$  denote the boundaries of the frequency range in which this trend is observed.

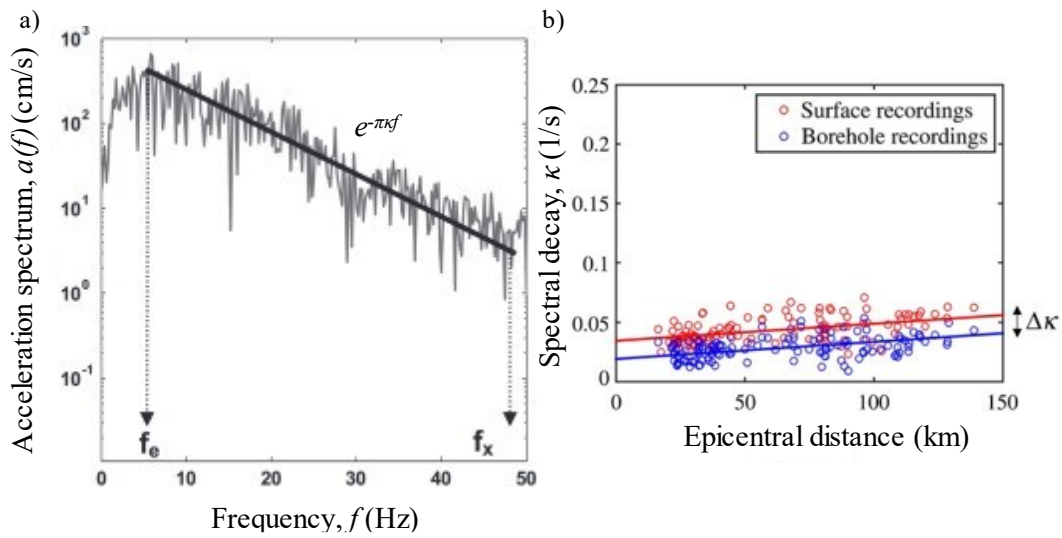


Figure 4-18. a) Definition of the spectral decay parameter, including the boundaries  $f_E$  and  $f_X$  of the reference frequency range (after Askan et al., 2014); b) Variation of the spectral decay between surface and borehole measurements (after Cabas et al., 2017).

The  $\kappa$  can be estimated by a robust linear fitting of the amplitude decay in the high frequency range in a log-linear space. Ktenidou et al. (2013) and Ktenidou et al. (2014) provide useful prescriptions for an accurate estimation of this parameter. The  $\kappa$  increase as the epicentral distance grows (Figure 4-18b; Anderson and Hough, 1984; Ktenidou et al., 2015). The increase with the distance represents a path effect of regional attenuation, whereas the intercept at zero distance, labeled as  $\kappa_0$ , is a function of geological conditions close to the site. Indeed,  $\kappa_0$  has been used in several seismological studies to infer the attenuation structure of the Earth (e.g., Cormier, 1982; Hough and Anderson, 1988; Campbell, 2009). Alternatively, in the presence of records on outcropping bedrock close to the investigated site, the damping structure of soil deposits can

be inferred, by assuming that the corresponding  $\kappa_0$  only incorporates the sedimentary component (e.g., Chapman et al., 2003; Campbell, 2009).

When interpreting DH-arrays,  $\kappa$  data from surface and borehole records at a specific site tend to align along two parallel lines, as the sensors share the same path terms (Figure 4-18b; Douglas et al., 2010; Ktenidou et al., 2013; Ktenidou et al., 2015). The constant difference  $\Delta\kappa$  provides a measure of the attenuation along the borehole and it is related to the small-strain parameters of the soil deposit, under the assumption of frequency-independent damping ratio (Hough and Anderson, 1988; Cabas et al., 2017; Xu et al., 2019):

$$\Delta\kappa = \int_0^z \frac{2D_S}{V_S} dz \quad (4.21)$$

Given the  $V_S$  profile, the  $\kappa$ -informed damping estimation consist in calibrating  $D_{S,0}$  so that the theoretical  $\Delta\kappa$  matches the corresponding observed value, thus suiting the observed high-frequency attenuation (e.g., Cabas et al., 2017; Afshari and Stewart, 2019; Xu et al., 2019). For instance, Figure 4-19 shows the resulting soil model at a site characterized by complex stratigraphy, where the  $D_S$  profile was calibrated starting from laboratory-based values (Afshari and Stewart, 2019).

Notwithstanding the apparent simplicity of these approach, the relation between  $\kappa_0$  and  $D_S$  is not always straightforward, due to wave scattering phenomena that may be relevant in presence of complex stratigraphy (Ktenidou et al., 2015).

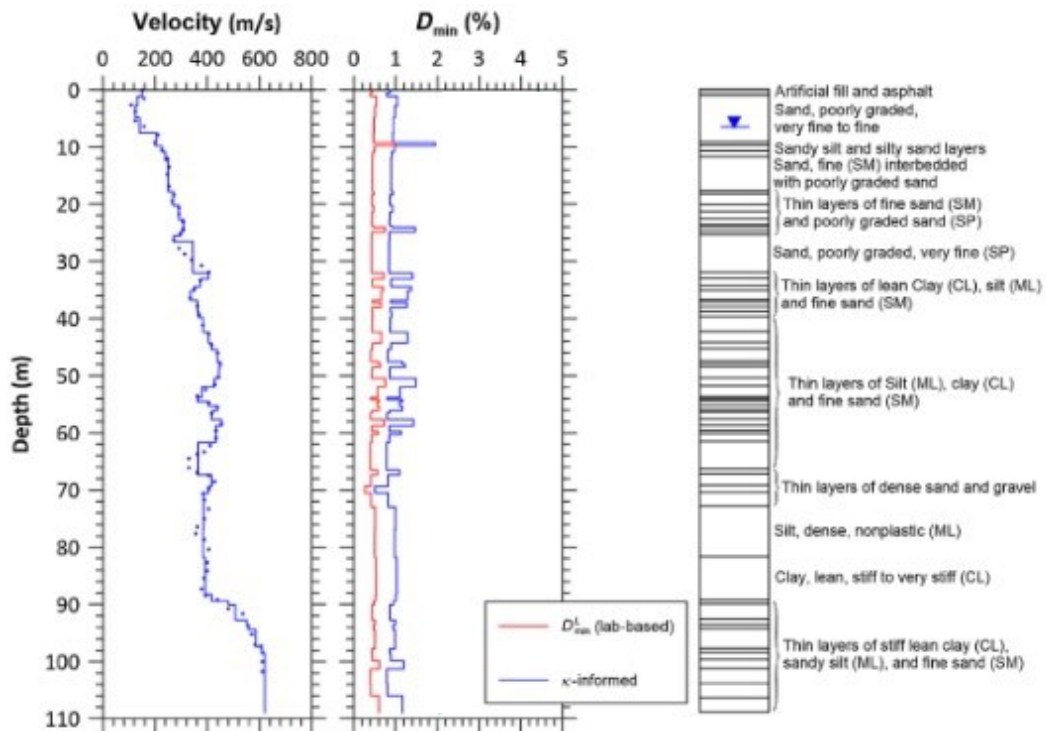


Figure 4-19. Example of S-wave velocity  $V_S$  profile and  $\kappa$ -informed damping ratio  $D_S$  profile (after Afshari and Stewart, 2019).

#### 4.4.3 Amplification analysis

A quite popular approach of  $D_S$  estimation is based on site-amplification synthetic parameters. Similar to the  $\kappa$ -informed damping estimation, the strategy calibrates  $D_S$  to obtain a good level of compatibility between the predicted and the observed amplification response, described by means of a synthetic parameter. Although this procedure is computationally intensive, as multiple GRAs are required, the resulting  $D_S$  is consistent with the ground response in seismic conditions, and it can be used for GRAs. Conventional approaches rely on frequency-domain parameters, that capture variations in both amplitude and frequency content of the waveform while propagating in the soil deposit. Typical proxies are the transfer function TF (Figure 4-20; Pecker, 1995; Tsai and Hashash, 2009; Thompson et al., 2012; Kaklamanos et al., 2013b; Yee et al., 2013; Zalachoris and Rathje, 2015; Tao and Rathje, 2019) or the amplification function AF (e.g., Thompson et al., 2012), the definition of which is available in Section 2.4.1. The description might refer also to time-domain parameters, as the peak values of acceleration and velocity and the Arias intensity (Tao and Rathje, 2019).

A critical issue in the amplification analysis is the choice of an appropriate goodness-of-fit metric. This applies especially when dealing with frequency-domain data. Indeed, TFs and AFs are oscillating functions usually spanning over a broad range of frequencies and the various peaks and troughs may be of different orders of magnitude. Most studies rely on misfit magnitude-based estimates, because a deviation between theoretical and experimental data may be interpreted as an effect of biased material parameters or modeling errors, e.g. linked with lateral variability of the soil deposit (Thompson et al., 2009). Valid indicators of closeness between target and predicted data are the mean-squared error (MSE), the corresponding root (RMSE; Zalachoris and Rathje, 2015), or the coefficient of efficiency (Legates and McCabe Jr, 1999). An alternative family of goodness-of-fit statistics focuses on the shape similarity between target and theoretical data. An example is the Pearson's sample correlation coefficient, that provides a direct measure of similarity, e.g. in terms of the peak alignment (Thompson et al., 2012). However, Legates and McCabe Jr (1999) questioned the high sensitivity of the correlation coefficient to extreme values in the target or in the experimental data. To overcome this limitation, a more robust metric is the index of agreement (Legates and McCabe Jr, 1999; Tao and Rathje, 2019). Furthermore, the assessment of the degree of fit is restricted within a moderately narrow frequency range, typically between the first and the fourth peak of the observed TF, to avoid biased estimates (Thompson et al., 2012).

On the other side, the choice of an adequate fitting metric is even more complex when focusing on time-domain data. For instance, Tao and Rathje (2019) adopted a simple strategy as they focused on peak values of time histories (e.g., peak ground acceleration PGA) or the Arias intensity, for which the misfit estimation is immediate. Other studies (e.g., Shi and Asimaki, 2017), instead, adopt more refined approaches already used in seismological simulations, e.g. the Anderson (2004) criteria and the GOF method (Kristeková et al., 2006; Olsen and Mayhew, 2010).

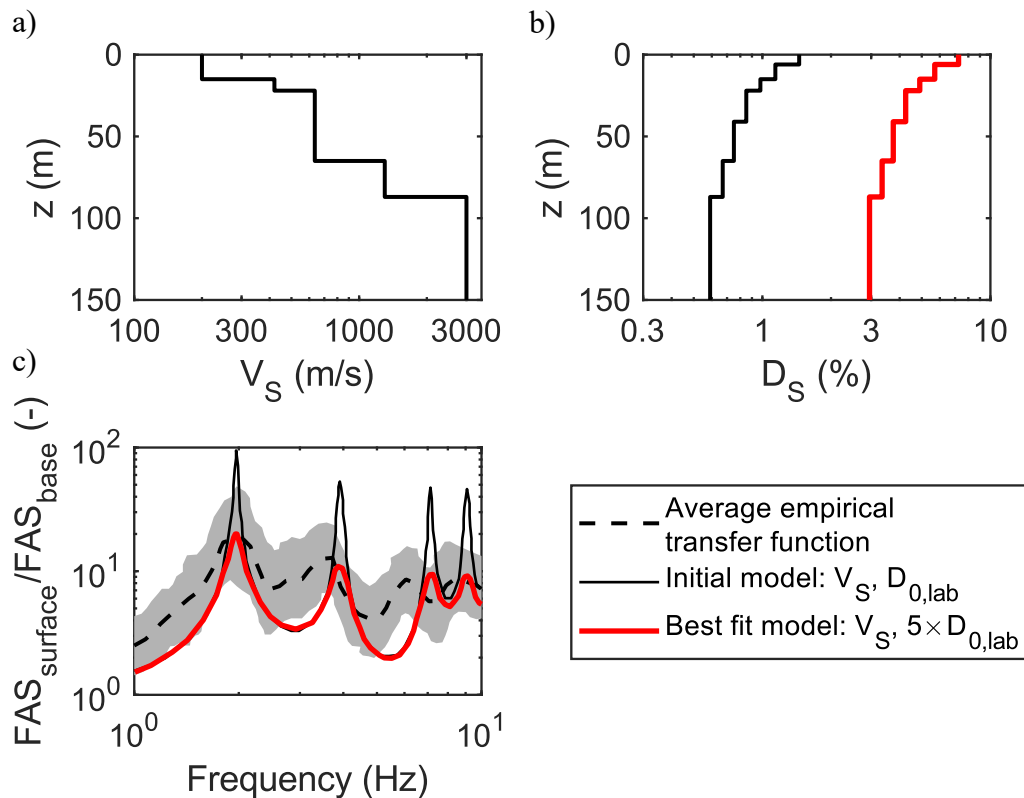


Figure 4-20. Application of the amplification analysis at the Garner Valley site: a) S-wave velocity  $V_S$  profile; b) Calibration of the small-strain damping ratio  $D_{S,0}$  profile; c) Comparison between theoretical and observed transfer function TF (after Tao and Rathje, 2019).

#### 4.4.4 Issues in the interpretation of downhole arrays

The DH-array data processing is not straightforward and it incorporates some drawbacks.

Firstly, DH-arrays are installed at a limited number of sites, hence these approaches cannot be easily applied in ordinary site characterization projects. Furthermore, the computation of the empirical site response requires the selection of an adequate number of ground motion records (Assimaki et al., 2008). Only weak motions should be included, to avoid the rise of nonlinear phenomena (Beresnev and Wen, 1996; Thompson et al., 2012; Zalachoris and Rathje, 2015; Cabas et al., 2017; Tao and Rathje, 2019; Xu et al., 2019). For this reason, processing should rely on seismic records with PGA smaller than  $0.05 \div 0.1g$  (e.g., Zalachoris and Rathje, 2015; Tao and Rathje, 2019) or with a shear strain index  $I_\gamma$ ,



i.e. the ratio between the peak ground velocity and the equivalent S-wave velocity  $V_{S,30}$  (Idriss, 2011; Kim et al., 2016), smaller than 0.1% (e.g., Cabas et al., 2017).

A critical issue is the ambiguity about wavefield conditions at the downhole sensors. Indeed, these sensors record both the upgoing incident wavefield and downgoing waves that are reflected off of the free surface. This condition is conventionally labeled as the “within” assumption (e.g., Zalachoris and Rathje, 2015), to make a distinction from sensors on the free surface, where the downgoing and upgoing waves are equal (“outcrop” assumption). Due to the impossibility of separating them, the modelling of such conditions is complex (e.g., Shearer and Orcutt, 1987; Steidl et al., 1996; Bonilla et al., 2002; Cadet et al., 2012). However, in deep borehole sensors, the contribution of the downgoing wave might be negligible as its energy rapidly decays with depth, due to intrinsic attenuation and wave scattering. In this case, the upgoing component should be only considered in the estimate of the experimental TF. Therefore, particular care should be devoted in the assignment of proper boundary conditions at the downhole sensors, as a function of the depth and the mechanical characteristics of the medium (e.g., Bonilla et al., 2002; Stewart and Kwok, 2008; Thompson et al., 2009).

Finally, the quality of the estimate strongly depends on the reliability of the available geotechnical information and the absence of lateral variabilities or 2D/3D resonance phenomena (Thompson et al., 2012). For instance, Assimaki et al. (2008) and Kaklamanos and Bradley (2018) pointed out that the coarseness in the provided information may result in apparent drifts between theoretical and effective data, that may be erroneously interpreted as other effects such as wave scattering.

A special remark about the role of the ground motion parameter adopted for measuring the site response should be pointed out. The approaches listed above rely on different descriptors of the ground motion amplification: frequency-domain parameters (e.g., TF, AF,  $\kappa$ ) and time-domain parameters (e.g., PGA,  $I_A$ ). There is no consensus about the best reference parameter, also because only a few studies carried out a comparative analysis to investigate the influence of the amplification descriptor. For instance, Tao and Rathje (2019) calibrated a multiplying factor of the laboratory-based  $D_{S,0}$  to derive the in situ  $D_{S,0}^{site}$  profile in 4 sites with different geology, each equipped with a DH-array. As reported in Figure 4-21, the calibrated factor is site-dependent and it is remarkably sensitive to the reference parameter. For instance, the multiplier derived from the TF oscillates between 3 and 6 and it is larger than the one obtained from the AF (its range is 1 to 5.5). Instead, constraining the ground model to time-domain data

leads to more scattered multiplier values, due to the request of matching a time instant parameter. Finally, the  $\kappa$ -informed estimate is close to 3.3, regardless the site conditions. The Authors suggest keeping the time domain parameters as reference, since they capture the overall response of the site. On the other side, the calibration in the frequency domain may lead to an overestimation of the damping due to the necessity of reducing the high-amplitude peaks of the theoretical estimate to match the empirical data, especially for the TF-based estimate.

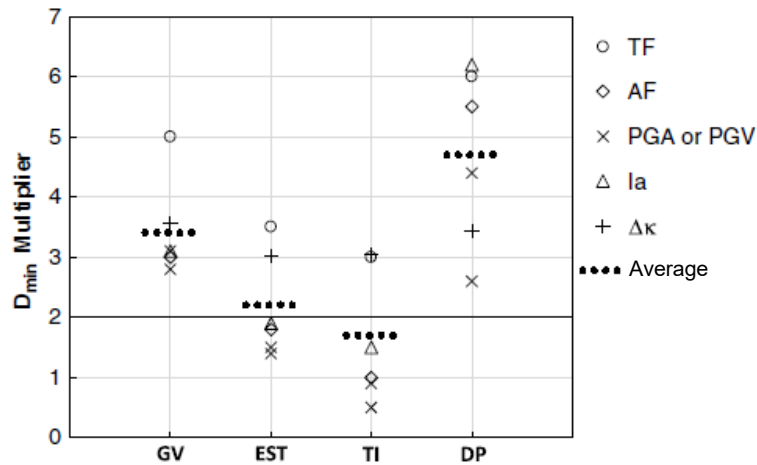


Figure 4-21. Obtained damping multipliers in Tao and Rathje (2019), at four sites: Garner Valley (GV), EuroseisTest (EST), Treasure Island (TI) and Delaney Park (DP). Multipliers are estimated based on the transfer function TF, the amplification function AF, the peak ground acceleration PGA or velocity PGV, the Arias intensity Ia, the high-frequency attenuation  $\Delta\kappa$ .

An additional source of uncertainties in the in situ  $D_{S,0}^{site}$  estimates from DH-arrays is the starting damping ratio profile, together with the correction applied in the calibration procedure. The trial values of  $D_{S,0}^{site}$  can be assumed a priori (Thompson et al., 2012), on the basis of seismological relationships (Cabas et al., 2017) or from laboratory results (e.g., Zalachoris and Rathje, 2015).  $D_{S,0}^{site}$  is often obtained from laboratory-based empirical relationships and updated through a multiplicative factor or an additive term, which is calibrated based on observed data. Cabas et al. (2017) highlighted the influence of the starting value of  $D_{S,0}^{site}$  and of the type of correction.

## 4.5 Laboratory vs. in situ estimates

The description of the current techniques deemed to estimate the small-strain damping ratio ends with an inter-method comparison, aimed at understanding the relative differences between  $D_{S,0}$  values obtained through laboratory testing and the  $D_{S,0}^{site}$  measured in situ (from geophysical tests or DH-arrays). Indeed, the different disturbance degree, boundary conditions and representative scale result into a discrepancy in measured parameters, especially for those linked to the cyclic behavior of geomaterials. For instance, several studies (e.g., Stokoe and Santamarina, 2000) demonstrated that laboratory tests tend to underestimate  $V_S$  of the geomaterial, probably because of perturbations in the soil microstructure during the sampling stage.

As for geophysical testing, for instance, Rix et al. (2000) compared  $D_{S,0}$  with  $D_{S,0}^{site}$  values obtained through CHT and SWM at the Treasure Island site, in California. While SWM data are quite similar to laboratory-based values, CHT tends to provide estimates of  $D_{S,0}^{site}$  larger than  $D_{S,0}$ . The Authors justify such difference in terms of investigated volumes, as CHT provide a local measure whereas SWM yield results that are averaged over a much large volume. Furthermore, CHT measures high-frequency waveforms, which are more sensitive to local variations in material properties and falling in a range where material damping tends to be significantly rate-dependent. Foti (2003) compared the SWM-based  $D_{S,0}^{site}$  and  $D_{S,0}$  at the well-known site of the Pisa Leaning Tower. He observed that the in situ value slightly overestimates the laboratory-based  $D_{S,0}$ , due to the presence of additional attenuation mechanisms other than geometric and intrinsic attenuation, especially at shallow layers (Figure 4-22). Finally, Karl et al. (2006) carried out a characterization study at a site in Belgium, through laboratory tests and a SCPT survey. In this case,  $D_{S,0}^{site}$  slightly overestimates  $D_{S,0}$ , although the remarkable variability in the in-situ estimated values does not allow drawing general conclusions (Figure 4-22).

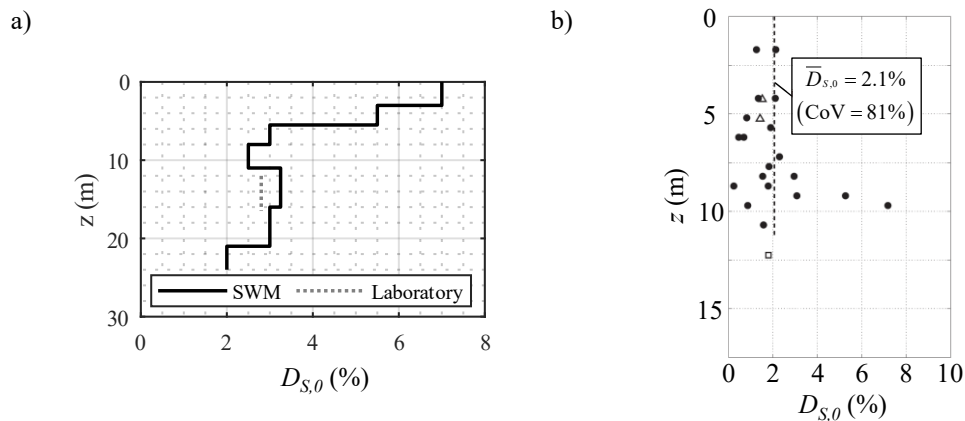


Figure 4-22. a) Comparison between the SWM-based and the laboratory-based small-strain damping ratio  $D_{S,0}$  profile at the Pisa Leaning Tower site (modified from Foti, 2003); b) Comparison between the SCPT-based (black circles) and the laboratory-based (hollow symbols)  $D_{S,0}$  profile at a site in Belgium (after Karl et al., 2006).

Numerous studies based on DH-arrays observed high  $D_{S,0}^{site}$  values compared with laboratory data (e.g., Tsai and Housner, 1970; Dobry et al., 1971; Tsai and Hashash, 2009; Yee et al., 2013). The difference is remarkable especially in soft shallow layers, that usually exhibit strong heterogeneities resulting in relevant scattering phenomena (Assimaki et al., 2006; Zalachoris and Rathje, 2015). For instance, Ktenidou et al. (2015) observed that the  $\kappa$ -informed  $D_{S,0}^{site}$  significantly overestimates both laboratory-based  $D_{S,0}$  and  $D_{S,0}$  data obtained from the interpretation of surface waves. The reason behind this discrepancy is the presence of additional wave attenuation due to scattering, which is not accounted for in laboratory data and has less impact on the horizontal propagation of Rayleigh waves compared with the vertical propagation of S-waves.

In summary, part of the differences in the various estimation techniques is linked to disturbance effects and the sampled soil volume, for which they might provide different results, as a function of the degree of heterogeneity of the soil deposit (Foti et al., 2014). However, one of the most important factors affecting  $D_{S,0}^{site}$  estimates is the presence of wave scattering phenomena, which is an additional dissipation mechanism not accounted in the laboratory measurements. Seismic wave scattering is a phenomenon characteristic of the wave propagation in heterogeneous media, where the multiple reflections and refractions lead to a non-planar propagation and to the diffusion of the seismic energy. This component typically affects in situ estimates, due to the difficulty in separating geometric and intrinsic attenuation, i.e. the energy loss due to wavefront

expansion and to wave scattering in heterogeneous media, on one side, and the one due to intrinsic material attenuation, on the other.

# Chapter 5

## Novel processing approaches

This Chapter describes a novel methodology, that aims at extending the framework of dispersion estimation techniques to obtain the R-wave phase attenuation. The principle of this approach consists in applying a transformation to the wavefield, whose resulting function may be interpreted as a pseudo-wave. It is demonstrated that the phase attenuation can be derived through the dispersion analysis of the obtained pseudo-wavefield. In addition, a new modal filtering scheme is proposed, with the aim to isolate the contribution of each Rayleigh propagation mode. In this way, the quality and robustness in the modal dispersion and attenuation estimates can be improved.

This Chapter starts by introducing a suite of synthetic waveforms, that represent the benchmark for the validation of the proposed techniques. The second part provides a detailed description of the proposed methods, that are firstly applied to simple wave models, to be then generalized to the analysis of surface wave data. Then, the inclusion of the modal filtering technique is reported. The Chapter ends with an assessment of the performance of the proposed technique on more complex wavefields, in which the Rayleigh wave is corrupted by the presence of body waves and incoherent noise.

### 5.1 Synthetic wavefields

The reliability of the proposed approach is tested with reference to a set of synthetic wavefields, each characterized by a different degree of complexity. On the one side, a collection of simplified waveforms, consisting of plane and cylindrical waves, is considered. The choice of focusing on idealized plane or cylindrical waves aims at providing an effective benchmark for testing the proposed algorithms, as the influence of model incompatibility effects (e.g., near field effects) is minimized. Then, realistic datasets of surface wave data are considered. These are obtained by simulating results of MASW surveys carried out on idealized soil models. Selected soil models are compatible with the stratigraphy of typical soil deposits in engineering practice and the generated wavefields are characterized by a different degree of complexity.

The first synthetic wavefield (SW1) is a planar wave:

$$u_p(r) = e^{-\alpha r} e^{-ikr} \quad (5.1)$$

The displacement field  $u_p(r)$  is computed at 100 equally spaced receiver locations, with spacing equal to 1 m, by setting  $k$  equal to 0.1 rad/m and  $\alpha$  equal to 0.0015 rad/m (Figure 5-1). The simulated wavefield may be representative of the vertical displacement field induced by Rayleigh waves due to a monochromatic vertical point force, according to the asymptotic expansion of the Lamb solution and normalized by  $r^{1/2}$  (other normalization constants are not reported, in this case). For instance, this may correspond to a R-wave with  $V_R$  approximately equal to 315 m/s and  $D_R$  equal to 0.015, at a frequency of 5 Hz.

Besides, this study focuses on another synthetic wavefield (SW2), that models the propagation of a cylindrical wave, which is computed from the Hankel function for fixed values of wavenumber  $k$  and attenuation  $\alpha$ :

$$u_c(r) = H_0^{(2)}(\tilde{k}r) = H_0^{(2)}[(k - i\alpha)r] \quad (5.2)$$

The displacement field  $u_c(r)$  is computed at the same locations of the planar wave, adopting the  $k$  and  $\alpha$  values defined above (Figure 5-1). The simulated wavefield may be representative of the vertical displacement field induced by Rayleigh waves due to a monochromatic vertical point force, according to the far-field solution of the Lamb problem for a homogeneous halfspace (other normalization constants are not reported, in this case).

Being  $k$  moderately small,  $u_p(r)$  and  $u_c(r)$  do not exhibit identical spatial variation in the amplitude and in the phase. On the one side, the amplitude decay of the two waves is not the same, because of the different geometrical attenuation mechanism affecting the displacement field. Furthermore, the error introduced by the asymptotic solution increases at small  $kr$  values. For this reason, the two modeled waves diverge close to the location of the ideal source, i.e., for  $r$  close to 0. The deviation can be immediately noticed by visual inspection the displacement phase (Figure 5-1b).

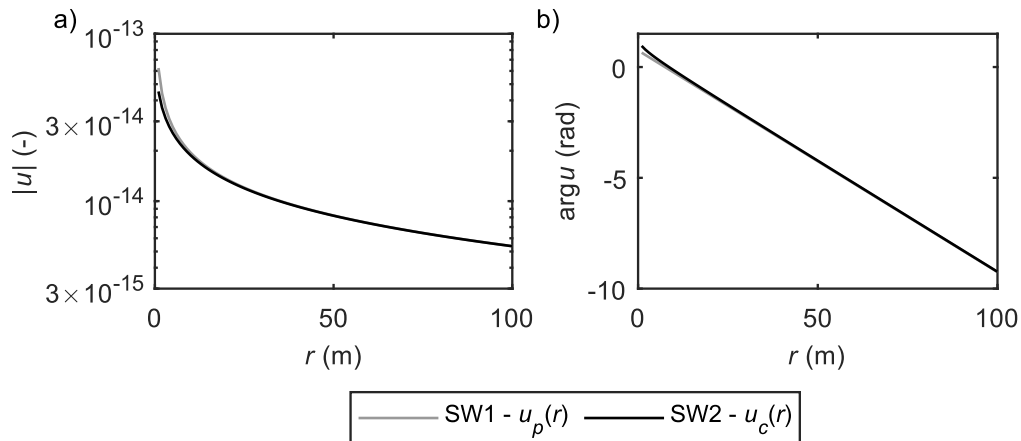


Figure 5-1. Simulated planar and cylindrical waves (labeled as SW1 and SW2, respectively), described in terms of particle displacement: spatial variation of a) amplitude  $|u|$  and b) phase  $\arg u$ .

The wavefield SW3 simulates results of a MASW survey carried out on a normally dispersive soil deposit (Table 5.1; Figure 5-3a-b). In this case, the Rayleigh wavefield is multimodal, although the fundamental mode of propagation is dominant for a broad range of frequencies. For this reason, SW3 allows to investigate the performance of the proposed methods in the presence of a wavefield mostly composed by a single mode. The final synthetic example (labeled as SW4) is obtained from the simulation of a MASW survey on an inversely dispersive profile (Table 5.2; Figure 5-4a-b). In this case, higher modes significantly contribute to the simulated wavefield SW4. Therefore, the performance of the novel approaches in the presence of a multimodal wavefield can be addressed. In both models, constant values of  $\nu = 0.33$  and  $\rho = 1800 \text{ kg/m}^3$  are kept throughout the layers, whereas  $D_P$  is assumed as equal to  $D_S$ .

Table 5.1. Ground model parameters adopted to generate the synthetic wavefield SW3.

Thickness (m)	S-wave velocity, $V_S$ (m/s)	S-wave damping ratio, $D_S$ (%)
5	200	3.5
10	300	3
10	400	2.5
-	500	2

Table 5.2. Ground model parameters adopted to generate the synthetic wavefield SW4.

Thickness (m)	S-wave velocity, $V_S$ (m/s)	S-wave damping ratio, $D_S$ (%)
5	250	2.5
3	150	4
-	350	1



SW3 and SW4 are computed by means of the ElastoDynamics Toolbox (EDT; Schevenels et al., 2009). EDT estimates the displacement transfer function, i.e. the displacement induced by a vertical point load at the surface, by means of the direct stiffness method (Kausel and Roësset, 1981). Actual displacement data are the result of the multiplication between the transfer function and a loading function  $F(t)$ , representing the force applied by the source onto the ground. The selected loading function is a Ricker wavelet, which reproduces the typical frequency content of an impulsive source, e.g., a sledgehammer (Figure 5-2):

$$F(t) = \left\{ 2 \left[ \frac{\pi(t-t_s)}{T_D} \right]^2 - 1 \right\} e^{-\left[ \frac{\pi(t-t_s)}{T_D} \right]^2} \quad (5.3)$$

The parameter  $t_s$  is a time shift, whereas  $T_D$  is the characteristic period of the wavelet. In this study,  $t_s$  is assumed equal to 0.05 s and  $T_D$  equal to 0.03 s, as proposed by Badsar (2012). SW3 and SW4 include vertical displacement data computed at 48 evenly spaced locations on the surface of the model, with spacing equal to 2 m. Thus, the offset from the source ranges between 2 m and 94 m. Both the number of receivers and the receiver spacing are consistent with the acquisition layout of MASW surveys for near-surface site characterization (Foti et al., 2018). The investigated frequency range spans between 1 Hz and 100 Hz.

The resulting waveforms are plotted in Figure 5-3 and in Figure 5-4, both in terms of seismic traces defined in the time domain and of the  $f$ - $k$  spectrum, computed by means of a 2D Fourier transform. As expected, the wave energy of SW3 is mostly carried out by a single mode (Figure 5-3f), whereas SW4 exhibits a remarkably strong multimodal propagation, with the dominant mode shifting to high-order propagation modes for increasing frequency (Figure 5-4f). Figure 5-3c-d and Figure 5-4c-d report the theoretical phase velocity curves  $V_R(\omega)$  and phase attenuation curves  $\alpha_R(\omega)$  corresponding to the models, as computed through EDT.

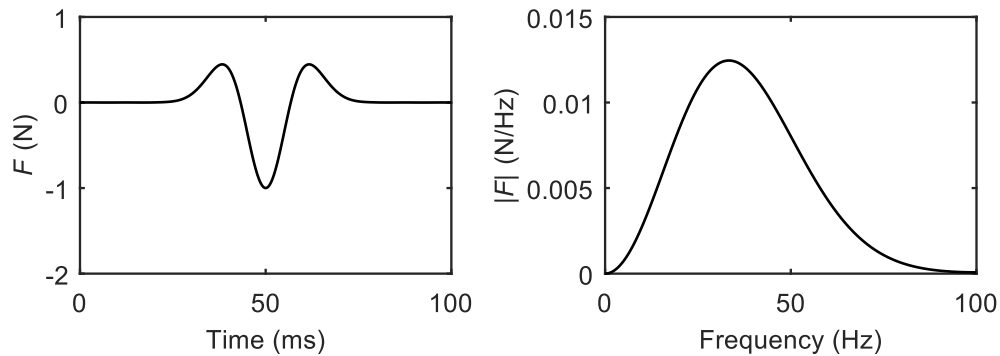


Figure 5-2. Ricker pulse simulating the input force for SW3 and SW4: a) time history; b) Frequency content.

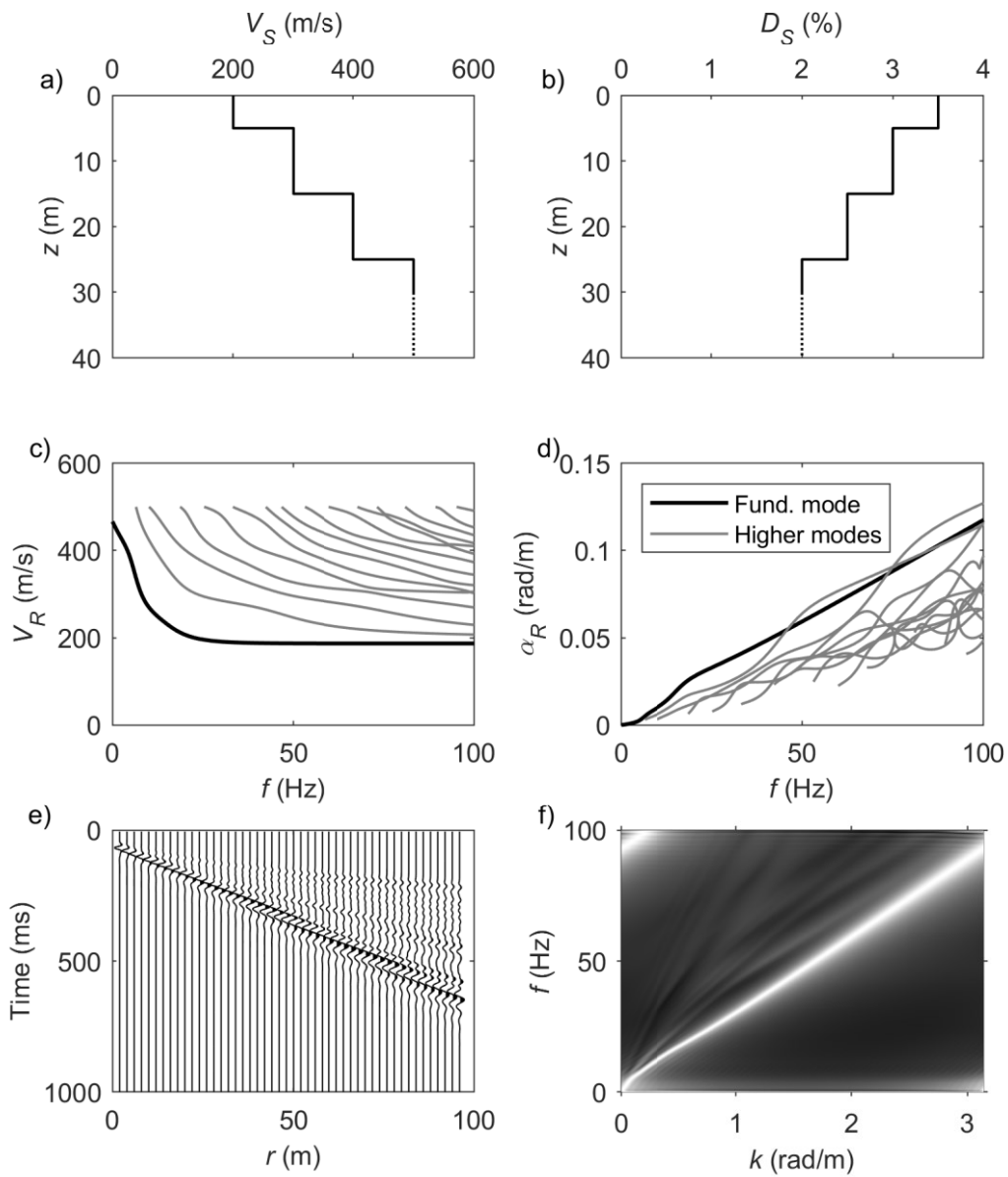


Figure 5-3. Main characteristics of the synthetic wavefield SW3: a-d) Reference ground model, described in terms of the S-wave velocity (a) and damping ratio (b); R-wave phase velocity curves (c) and phase attenuation curves (d); Time-domain traces (e) and  $f$ - $k$  spectrum, where each mode is identified by the white patterns (f). To better visualize spectral peaks corresponding to each propagation mode, the  $f$ - $k$  spectrum is normalized frequency by frequency.

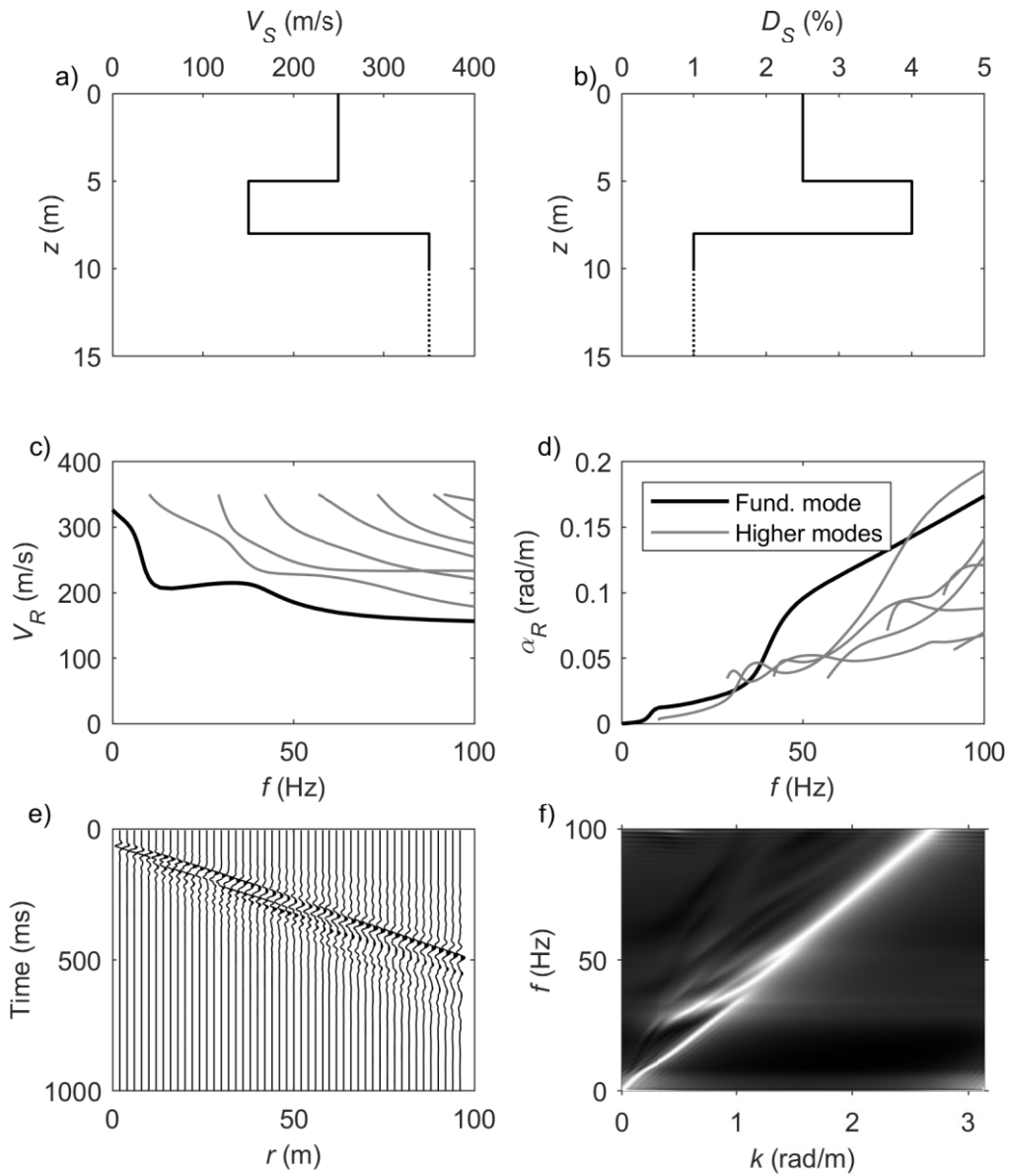


Figure 5-4. Main characteristics of the synthetic wavefield SW4: a-d) Reference ground model, described in terms of the S-wave velocity (a) and damping ratio (b); R-wave phase velocity curves (c) and phase attenuation curves (d); Time-domain traces (e) and  $f$ - $k$  spectrum, where each mode is identified by the white patterns (f). To better visualize spectral peaks corresponding to each propagation mode, the  $f$ - $k$  spectrum is normalized frequency by frequency.

## 5.2 Processing methods

This section starts with an overview of the frequency-domain beamforming approach, as it represents the basis of the approach proposed in this study. Then, the frequency-domain beamforming – attenuation is described, with reference to the synthetic wave models SW1 and SW2. This section ends with the definition of an algorithm that applies this method for the analysis of surface wave data.

### 5.2.1 The frequency-domain beamforming technique

The Frequency-Domain BeamForming (FDBF; Lacoss et al., 1969) technique is a transform-based method, that interprets measured waveform data in the frequency-wavenumber ( $f$ - $k$ ) domain (or alternatively the frequency-velocity domain), where R-wave propagation parameters can be identified as maxima of the amplitude spectrum. A significant advantage of this approach is the capability to identify the contribution of different modes of the Rayleigh wavefield as separate spectral peaks, although the actual possibility of isolating modes depends on the spatial resolution of the array.

The FDBF approach estimates  $k_R$  (hence,  $V_R$ ) under the assumption that the recorded wavefield is composed by Rayleigh waves, propagating according to planar wavefronts. The description of the method herein provided assumes that the measured wavefield consists of recorded particle displacement spectral data in the vertical direction  $u(r, \omega)$  along a linear array, where  $r$  is the sensor offset from the active source. However, the method can be easily generalized to 2D acquisition setups, with single- or three-component data (e.g., Zywicki and Rix, 2005; Wathelet et al., 2018).

The FDBF technique combines recorded spectra into the spatio-spectral correlation matrix  $\mathbf{R}(\omega)$ , which is a Hermitian-symmetric matrix where each element is the cross-power spectrum between the  $m$ -th and the  $n$ -th sensors, defined as follows:

$$R_{m,n}(\omega) = u(r_m, \omega)u^*(r_n, \omega) \quad (5.4)$$

The components of  $\mathbf{R}(\omega)$  carry information about spatial properties of the wavefield (Zywicki, 1999), as they contain the phase change between sensors.

To exploit the phase change information contained in  $\mathbf{R}(\omega)$ , the FDBF applies a linear phase shift to the recorded traces, as a function of a trial wavenumber  $k_t$ , and it stacks the slanted traces. When the total energy is maximum, the steered traces are in equal phase and the corresponding  $k_t$  equals the true wavenumber  $k_R$ .

From the mathematical viewpoint, this operation is equivalent to compute the so-called pseudopower  $P_{BF}(k_t, \omega)$ :

$$P_{BF}(k_t, \omega) = \mathbf{e}^H(k_t) \mathbf{R}(\omega) \mathbf{e}(k_t) \quad (5.5)$$

where H denotes the Hermitian transpose, and  $\mathbf{e}(k_t)$  is the planar steering vector, that is the mathematical representation of the linear phase shift:

$$\mathbf{e}(k_t) = [e^{-ik_t r_1}, \dots, e^{-ik_t r_N}]^T \quad (5.6)$$

The location of the peak of the  $P_{BF}(k_t, \omega)$  in the  $f$ - $k$  domain corresponds to the actual wavenumber  $k_R$ , from which  $V_R$  can be derived (Figure 5-5). If the recorded wavefield includes multiple plane waves (e.g., multimode Rayleigh waves),  $P_{BF}(k_t, \omega)$  exhibits several peaks, each corresponding to a single wave component.

The investigation of  $P_{BF}(k_t, \omega)$  is carried out on an adequate search domain, where the boundaries of  $k_t$  are compatible with spatial sampling capability of the array. The search domain should account for the effects of limited spatial sampling on the spectral estimates (Foti et al., 2002). On the one side, spatial aliasing limits the investigation range to a maximum  $k_t$  value equal to  $\pi/d$  in uniformly spaced arrays with spacing  $d$ , according to the Nyquist-Shannon theorem. In addition, a fine discretization of the search domain is helpful for a more precise estimation of  $k_R$ . Theoretically, a refined mesh would allow for easier identification of different wave components in measured data (e.g., different Rayleigh propagation modes). However, the actual wavenumber resolution depends only on the array length  $D$ , as it equals  $2\pi/D$ . Therefore, the increased accuracy obtained with a finer  $k_t$  grid is only apparent, as the actual resolution is unchanged.

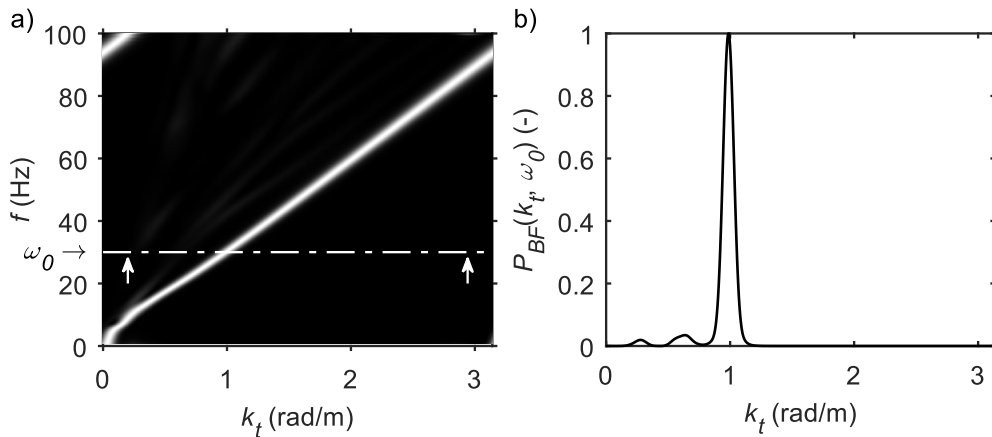


Figure 5-5. Application of the FDBF for the dispersion analysis of SW3: a) pseudopower  $P_{BF}(k_t, \omega)$  in the  $f$ - $k$  spectrum domain; b) Cross-section of  $P_{BF}(k_t, \omega)$  at the circular frequency  $\omega_0$ .

One of the basic assumptions of the FDBF is that the recorded wavefield is composed by plane waves. However, in MASW tests, Rayleigh waves spread from the source with cylindrical wavefronts and modeling their propagation as plane waves might result in biased estimates of the wavenumber, especially for the usually adopted offsets. For this reason, Zywicki and Rix (2005) introduced a modified version of the FDBF, that accounts for the cylindrical wavefield. The Cylindrical FDBF (CFDBF; Zywicki, 1999) shares a similar scheme to the conventional FDBF, as it computes the pseudospectrum  $P_{CBF}(k_t, \omega)$  from  $\mathbf{R}(\omega)$  as:

$$P_{CBF}(k_t, \omega) = \mathbf{h}^H(k_t) \mathbf{R}(\omega) \mathbf{h}(k_t) \quad (5.7)$$

However, the cylindrical steering vector  $\mathbf{h}(k_t)$  depends on the trial wavenumber  $k_t$  by means of the Hankel function, which is a descriptor of the propagation of cylindrical waves:

$$\mathbf{h}(k_t) = \left[ e^{-i \arg H_0^{(2)}(k_t r_1)}, \dots, e^{-i \arg H_0^{(2)}(k_t r_N)} \right]^T \quad (5.8)$$

Note that  $H_0^{(2)}(\bullet)$  should be replaced by  $H_1^{(2)}(\bullet)$  when processing radial displacement data.

The steering vector  $\mathbf{h}(k_t)$  ensures that the sensors are aligned with the Hankel function phase, so that the maxima of  $P_{CBF}(k_t, \omega)$  provide an estimate of the wave parameters of the cylindrically spreading wavefield (Figure 5-6). As it properly models the cylindrical wavefield, the CFDBF entails major computational complexity (Zywicki and Rix, 2005). On the other side, this method improves the quality and reliability in the estimated dispersion data, with respect to the planar wavefield.

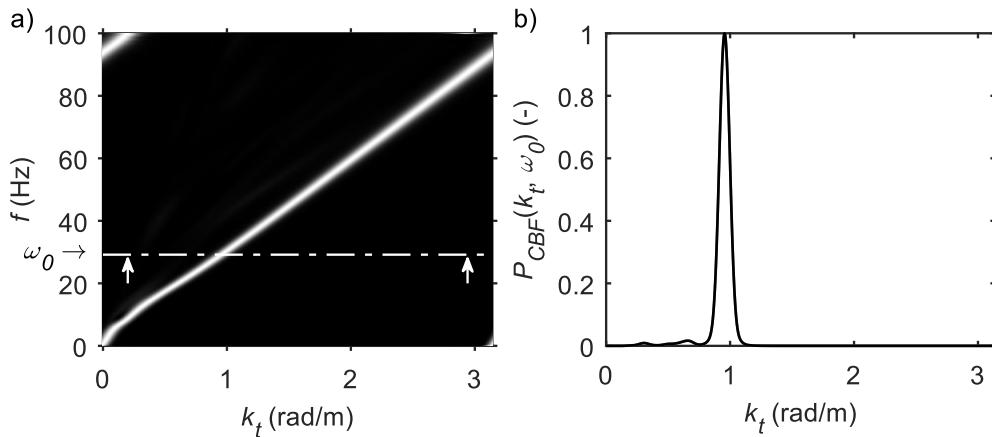


Figure 5-6. Application of the CFDBF for the dispersion analysis of SW3: a) pseudopower  $P_{CBF}(k_t, \omega)$  in the  $f$ - $k$  spectrum domain; b) Cross-section of  $P_{CBF}(k_t, \omega)$  at the circular frequency  $\omega_0$ .

## 5.2.2 Frequency-Domain BeamForming – Attenuation (FDBFa)

The Frequency-Domain BeamForming – Attenuation (FDBFa), proposed in this dissertation, is a transform-based approach that seeks to provide robust and reliable attenuation estimates. The FDBFa approach estimates  $\alpha$  under the assumption that the recorded wavefield is composed by a single planar wave (e.g., a Rayleigh wave with a dominant propagation mode, recorded in the far field). The principle of this approach consists in applying a transformation to the recorded wavefield, such that the resulting function may be interpreted as a pseudo-wave, with dispersion characteristics corresponding to the attenuation of the original one. Thus,  $\alpha$  can be derived by estimating the wavenumber of the pseudo-wavefield, for which a broad variety of tools is currently available. In this study, the wavenumber estimate is carried out by means of the FDBF method, hence the FDBFa may be interpreted as a generalization of the FDBF for the attenuation estimate. Indeed, the FDBF scheme is computationally fast and robust. Furthermore, the FDBF allows an immediate generalization to non-planar waves, as the inclusion of geometric effects due to the cylindric shape of the Rayleigh wavefront is straightforward.

The FDBFa method is based on the following wavefield transformation:

$$v(r) = [u_p(r)]^i \quad (5.9)$$

where “i” is the imaginary unit. If the recorded wavefield is a plane wave inducing the displacement field  $u_p(r)$ , it can be demonstrated that resulting function  $v(r)$  can be interpreted as a planar pseudo-wave, whose wavenumber corresponds to the attenuation of  $u_p(r)$ . Indeed, the application of the transformation (5.9) to  $u_p(r)$  returns the following function:

$$v(r) = [u_p(r)]^i = e^{kr} e^{-i\alpha r} \quad (5.10)$$

Comparing Eq. (5.10) with (5.2),  $v(r)$  can be interpreted as a plane wave, whose displacement amplitude varies across space as  $e^{kr}$ , with harmonic oscillations according to  $e^{-i\alpha r}$ . Therefore,  $\alpha$  is the wavenumber of the “pseudo”-wavefield  $v(r)$ , whereas  $k$  controls the spatial variation of the particle displacement amplitude (Figure 5-7a-d). Thus,  $\alpha$  of the original planar wave  $u_p(r)$  can be retrieved by searching for the wavenumber of  $v(r)$ .

In this study, the FDBF technique is adopted to carry out the wavenumber analysis of  $v(r)$ . Therefore,  $v(r)$  data across all the receivers are first combined into the spatio-spectral correlation matrix  $\mathbf{R}$ . Then, the pseudospectrum  $P_{BFa}(\alpha_t)$  is obtained by combining  $\mathbf{R}$  with a planar steering vector  $\mathbf{e}(\alpha_t)$  (defined as in Eq. 5.6), as a function of the trial attenuation value  $\alpha_t$ :

$$P_{BFa}(\alpha_t) = \mathbf{e}^H(\alpha_t) \mathbf{R}(\omega) \mathbf{e}(\alpha_t) \quad (5.11)$$

Ideally,  $P_{BFa}(\alpha_t)$  exhibits a single peak, with location  $\alpha_e$  (i.e., the estimated attenuation) corresponding to the actual attenuation  $\alpha$  of the recorded wave (Figure 5-7e).

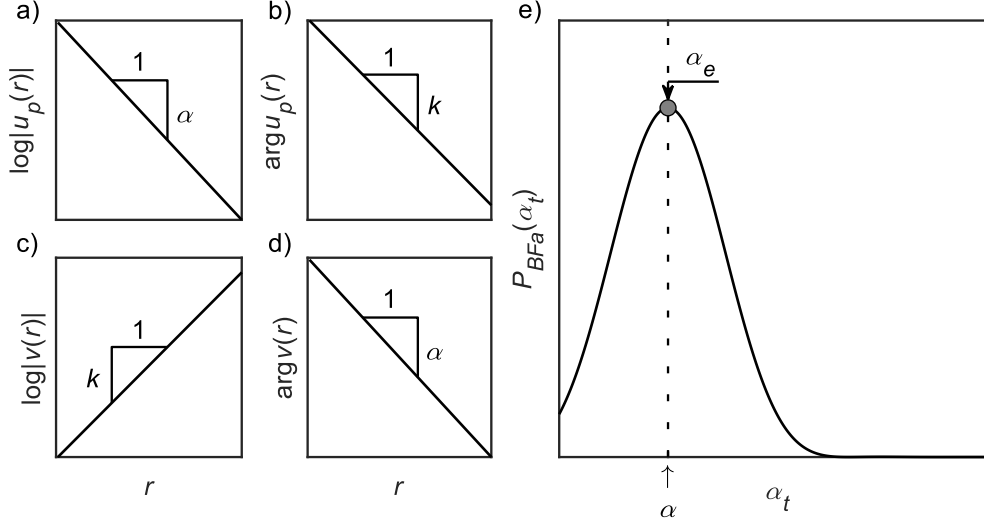


Figure 5-7. a-b) Original planar wave  $u_p(r)$ , in terms of a) log-amplitude and b) phase; c-d) Transformed wave, in terms of c) log-amplitude and d) phase; e) Pseudospectrum of the transformed wave  $v(r)$ , where the location of the spectral maximum  $\alpha_e$  is compared with  $\alpha$ .

However, the resulting pseudospectrum often exhibits side lobes together with the main peak. Differently from the FDBF, the presence of multiple waves in the recorded wavefield does not result in multiple local maxima in  $P_{BFa}(\alpha_t)$  because a single peak still appears, as it will be addressed in the Section 5.3.1. Instead, side lobes may partially be the effect of spectral leakage, induced by windowing of the pseudo-wave. This perturbation can be mitigated by applying an appropriate tapering to  $v(r)$  prior the computation of  $P_{BFa}(\alpha_t)$ , e.g. by means of a Hanning window (Figure 5-8).



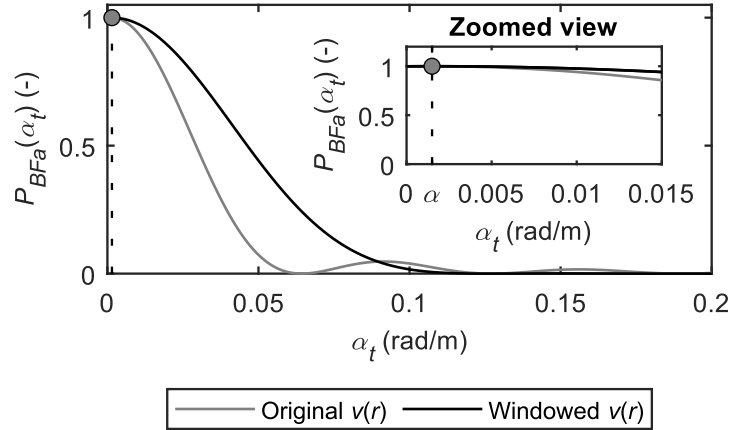


Figure 5-8. Effect of the tapering window on the pseudospectrum  $P_{BFa}(\alpha_t)$ , computed for SW1. The tapering is carried out by means of a spatial Hanning window. The plot also includes a zoomed view to show the comparison between the peak location (the grey circle) and the theoretical attenuation  $\alpha = 0.0015$  rad/m.

On the other hand, side peaks are artifacts induced by the spatial variation of the amplitude of  $v(r)$ . Indeed, the corresponding amplitude usually assumes a sawtooth-like shape, where each segment increases according to an exponential function. This peculiar trend is due to the strategy used for the numerical computation of wavefield data. Indeed, although the phase of  $u_p(r)$  is linear with the distance, numerically it is wrapped. Thus, it appears as a sawtooth signal bounded between  $-\pi$  and  $+\pi$  and varying as  $-kr$  in each segment. Due to the transformation (5.9), the phase of  $u_p(r)$  becomes the exponent governing the amplitude of  $v(r)$ , with opposite sign. Therefore, such amplitude assumes a piecewise exponential trend, with “jump” discontinuities. It can be demonstrated that the presence of these discontinuities in  $v(r)$  maps into a set of equally spaced side lobes inside  $P_{BFa}(\alpha_t)$ , with spacing equal to the wavenumber  $k$  (Figure 5-9). The demonstration is provided in the Appendix A. To avoid confusion in the identification of the peak of  $P_{BFa}(\alpha_t)$ , a possible strategy consists in normalizing  $v(r)$  by its amplitude, so that the discontinuities cancel out, prior to the tapering. Alternatively, the transformation (5.9) may be applied only to the  $|u(r)|$ , discarding the phase contribution. In both cases, the discontinuities in  $v(r)$  cancel out, and  $P_{BFa}(\alpha_t)$  exhibits a single peak.

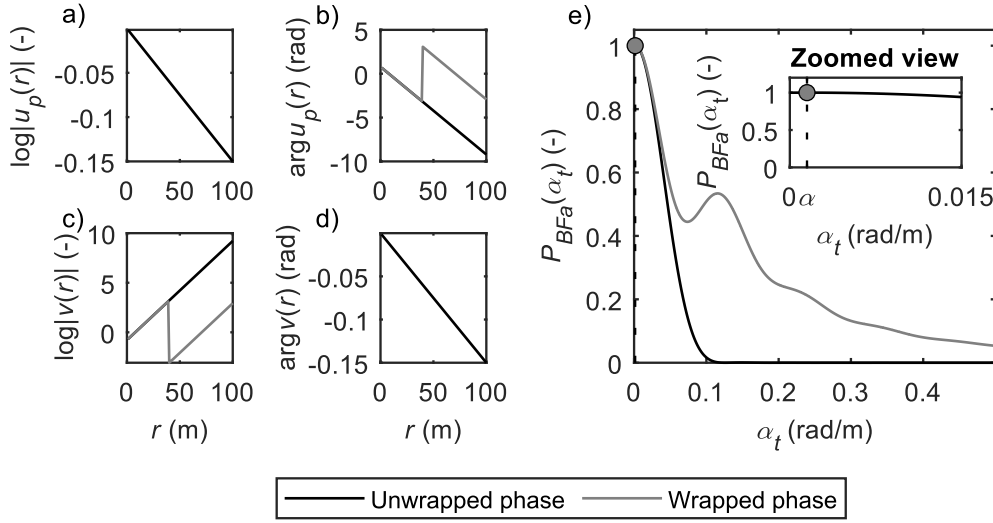


Figure 5-9. Effect of phase wrapping on the pseudospectrum  $P_{BFa}(\alpha_t)$ , computed for SW1: a-b) Original planar wave  $u_p(r)$ , in terms of a) log-amplitude and b) phase; c-d) Transformed wave  $v(r)$ , in terms of c) log-amplitude and d) phase; e) Pseudospectrum of the transformed wave. The plot also includes a zoomed view where the location of the spectral maximum  $\alpha_e$  (the grey circle) is compared with the theoretical attenuation  $\alpha = 0.0015$  rad/m.

### 5.2.3 Cylindrical Frequency-Domain BeamForming –Attenuation (CFDBFa)

The FDBFa method relies on a key assumption, namely the recorded wavefield is composed by a single, plane wave. For this reason, the application of the FDBFa method to retrieve the phase attenuation of Rayleigh waves might lead to biased estimates, as they propagate according to a cylindrical wavefront. A potential solution to mitigate this problem consists in processing recorded traces after having scaled them according to  $r^{1/2}$ . Indeed, cylindrical waves asymptotically tend to be described as a spatially harmonic function (i.e., plane waves), but with amplitude scaled down by  $r^{1/2}$ . However, this strategy does not model properly the geometrical characteristics of the wavefront, as it relies on an asymptotic approximation which, by definition, is valid only at great distances from the source. Therefore, the resulting attenuation estimates may still not be accurate enough.

For this reason, the FDBFa method is modified to introduce an explicit modeling of the cylindrical shape of the wavefront. The proposed scheme is hereafter termed as Cylindrical FDBFa (CFDBFa), which can be seen as a generalization of the CFDBF technique.

In this case, the application of the transformation (5.9) to the displacement field  $u_c(r)$  returns a function  $v(r)$ , for which the derivation of the expression is not straightforward, because a closed-form formulation for the Hankel function is not currently available. However, based on an analogy with the application of (5.9) to a plane wave, an intuitive description of  $v(r)$  assumes that it represents a pseudo-wavefield, whose phase variations reflect spatial changes of the amplitude of the Hankel function and amplitude is linked to the corresponding phase of the original wavefield (Figure 5-10a-d). Therefore, the attenuation  $\alpha$  can be retrieved by exploiting the phase information carried in  $v(r)$ . For this purpose, the CFDBFa follows a procedure similar to the CFDBF, where it computes the pseudospectrum  $P_{CBFa}(\hat{\mathbf{k}}_t)$  from the spatio-spectral correlation matrix  $\mathbf{R}$  of  $v(r)$  as:

$$P_{CBFa}(\hat{\mathbf{k}}_t) = \mathbf{a}^H(\hat{\mathbf{k}}_t) \mathbf{R} \mathbf{a}(\hat{\mathbf{k}}_t) \quad (5.12)$$

The steering vector  $\mathbf{a}(\hat{\mathbf{k}}_t)$  is defined as follows:

$$\mathbf{a}(\hat{\mathbf{k}}_t) = \left[ e^{-i \arg\{h_0(\hat{\mathbf{k}}_t, r_1)\}}, \dots, e^{-i \arg\{h_0(\hat{\mathbf{k}}_t, r_N)\}} \right]^T \quad (5.13)$$

where the function  $h_0$  is the power of the Hankel function to the imaginary unit:

$$h_0(\bullet) = \left[ H_0^{(2)}(\bullet) \right]^i \quad (5.14)$$

Note that  $H_0^{(2)}(\bullet)$  should be replaced by  $H_1^{(2)}(\bullet)$  when processing radial displacement data. In Eq. 5.13,  $\hat{\mathbf{k}}_t$  is a trial complex wavenumber. The reason behind the use of this quantity is discussed below.

The steering vector  $\mathbf{a}(\hat{\mathbf{k}}_t)$  stretches the pseudo-wavefield according to phase variations of the power of a Hankel function to the imaginary unit, thus accounting spatial changes in phase of  $v(r)$  in a proper way. In this way, the pseudo-cylindrical wavefield is converted into an equivalent plane wavefield, and attenuation of the cylindrical wave is properly estimated.  $P_{CBFa}(\hat{\mathbf{k}}_t)$  ideally exhibits a main peak with location  $\alpha_e$  coincident with  $\alpha$  (Figure 5-10e). However, actual data may provide side lobes in the pseudospectrum, that may corrupt the correct identification of the peak. Their presence can be mitigated by normalizing the pseudo-wavefield by its amplitude and applying a proper tapering, as in FDBFa.

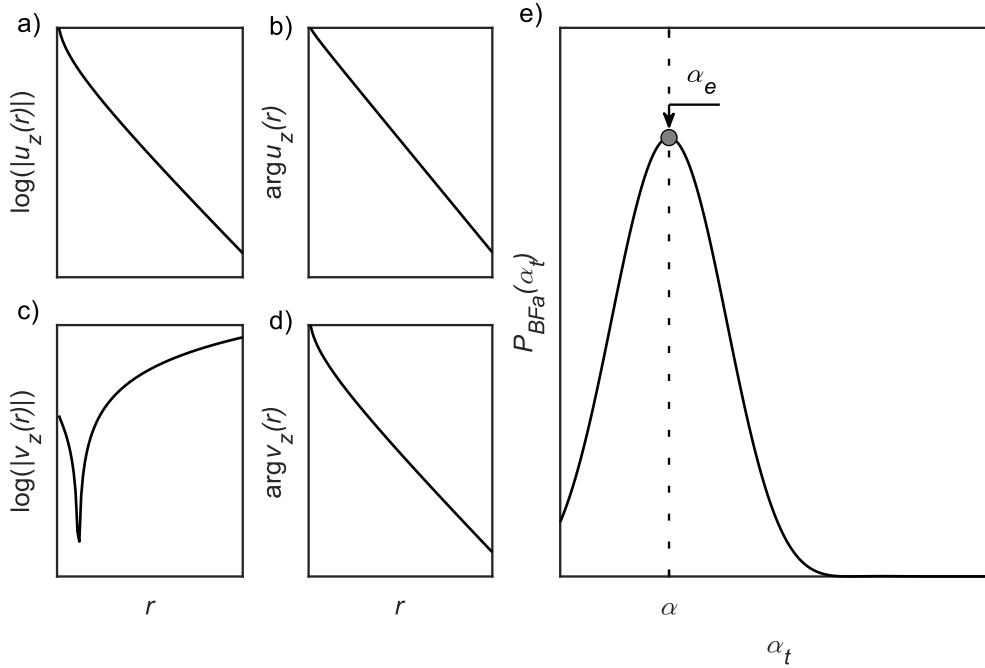


Figure 5-10. a-b) Original cylindrical wave  $u_c(r)$ , in terms of a) log-amplitude and b) phase; c-d) Transformed wave  $v(r)$ , in terms of c) log-amplitude and d) phase; e) Pseudospectrum of the transformed wave, where the location of the spectral maximum  $\alpha_e$  is compared with  $\alpha$ .

Differently from FDBFa, the argument of  $\mathbf{a}(\hat{k}_t)$  is a trial complex wavenumber  $\hat{k}_t$  which, by definition, includes both the real wavenumber and the phase attenuation term. Indeed, the estimate of the attenuation for a cylindrical wave should also account for the real wavenumber, as it affects spatial variations of the wave amplitude.

As the CFDBFa searches for  $\alpha$ , the real wavenumber has to be fixed to a value  $k_{ref}$ , whereas trial values  $\alpha_t$  for the attenuation are adopted. However, the choice of  $k_{ref}$  is not arbitrary, as it should be as close as possible to the actual wavenumber  $k$  characterizing the measured wavefield. Figure 5-11 describes the influence of  $k_{ref}$  on the estimated attenuation, with reference to SW2. If  $k_{ref} > k$ , the resulting attenuation  $\alpha_e$  would underestimate  $\alpha$ . Furthermore, for increasing  $k_{ref}$ ,  $\alpha_e$  tends to decrease down to a stable value. Instead, when  $k_{ref} < k$ ,  $\alpha_e$  overestimates  $\alpha$  (Figure 5-11 a). An interpretation of the discrepancy in the attenuation estimate is provided in Figure 5-11b-c, that compares the original wavefield SW2 with two cylindrical waves, with the same wavenumber  $k_{ref} > k$  and attenuation equal to  $\alpha$  and  $\alpha_e$ , respectively. These waves are hereafter labeled as  $u_c(k, \alpha)$ ,  $u_c(k_{ref}, \alpha)$  and  $u_c(k_{ref}, \alpha_e)$ , respectively. Figure 5-11b shows the corresponding the spatial variation of wave

amplitude, whereas Figure 5-11c reports the spatial variation of the cylindrical wave amplitude corrected by the geometrical spreading factor  $r^{1/2}$  and converted in logarithmic scale. According to this representation, each curve tends to become linear at great  $r$  values, with a slope equal to the corresponding attenuation, by virtue of the asymptotic approximation of the Hankel function. Thus, a visual inspection of the slope of the modified amplitude at far offsets allows an immediate visualization of the fitting of  $\alpha$ . Note that in Figure 5-11c, curves corresponding to  $u_c(k_{ref}, \alpha)$  and  $u_c(k_{ref}, \alpha_e)$  are shifted by a quantity  $\Delta$  so that they share the same end point, to facilitate the visual comparison of the slopes. When  $k_{ref} < k$ , the wave  $u_c(k_{ref}, \alpha)$  matches the slope of SW2 at great offsets but the predicted amplitude significantly overpredicts SW2 close to the source. In order to improve the fitting by keeping a similar shape (which is controlled by  $k_{ref}$ ), a reduction of  $\alpha_e$  is required. Figure 5-11d-e report an equivalent comparison for  $k_{ref} < k$ . In this case, although  $u_c(k_{ref}, \alpha)$  is compatible with SW2 at great  $r$ , it systematically underestimates SW2 amplitude at short distances. An improvement in the fitting quality is obtained by increasing  $\alpha_e$ . In summary, the sensitivity of  $\alpha_e$  to  $k_{ref}$  is the result of the nonlinearity of the shape of spatial variations of the Hankel function amplitude with the offset and its sensitivity to this parameter. Due to the nonlinear variation, it is also believed that the entity of divergence between  $\alpha_e$  and  $\alpha$  for  $k_{ref} \neq k$  depends on the array geometry, namely the range of investigated spatial coordinates. In plane waves, instead, there is no influence of the wavenumber characteristics on the attenuation estimate, as the amplitude variations only depend on the attenuation itself.

Therefore, the CFDBFa should be combined with a robust method for estimating  $k$  prior to the derivation of  $\alpha$ . For this purpose, the CFDBF represents an effective strategy because of its accuracy and robustness. Furthermore, combining the CFDBF and the CFDBFa provides a physically consistent approach for estimating wave parameters, as both of them model the propagation of the wavefield according to a cylindrical scheme.

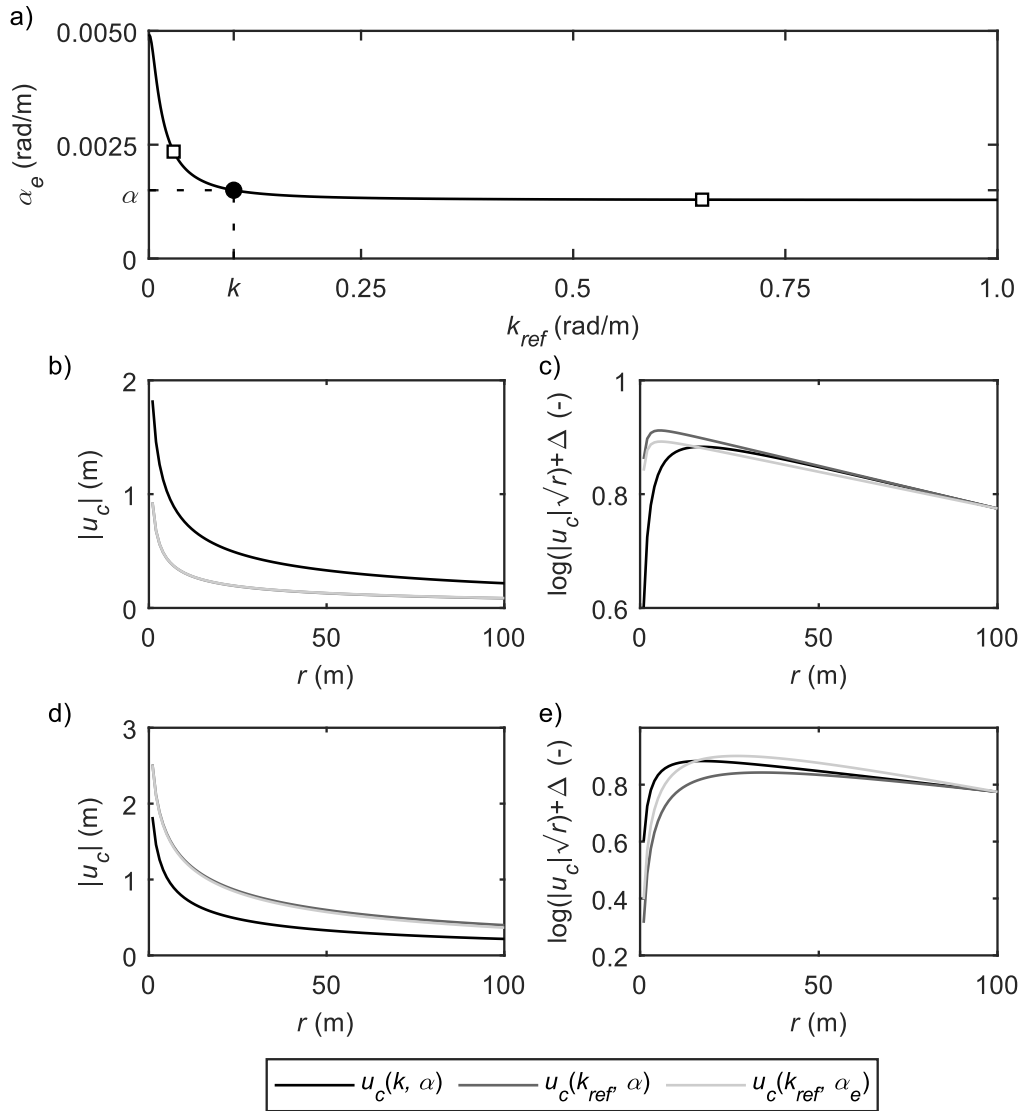


Figure 5-11. a) Influence of the chosen wavenumber  $k_{ref}$  on the estimated attenuation  $\alpha_e$  in the CFDBFa; b-c) Amplitudes of the cylindrical waves corresponding to three different  $k_{ref}$  values, represented in terms of b) amplitudes and c) logarithmic amplitudes normalized by the geometrical spreading factor. The parameter  $\Delta$  shifts the curves in c) and e) so that they share the same end point, thus facilitating the comparison of relative variations in the space. Data refer to SW2.

## 5.2.4 Applications

The application of the FDBFa and of the CFDBFa for retrieving Rayleigh wave parameters from the interpretation of surface wave data is quite straightforward. Indeed, although both methods have been introduced with reference to

monochromatic planar or cylindrical waves, the generalization to nonharmonic signals can be easily achieved by means of the Fourier decomposition of the wavefield. In this way, each frequency component of the recorded wavefield is separated and it may be processed according to these techniques. The resulting wave parameters are then combined frequency by frequency to obtain the experimental dispersion and attenuation curves.

Although Rayleigh waves propagate with cylindrical wavefronts, using a planar model for estimating propagation parameters is often a valid choice, because the influence of this approximation on the quality of results is moderately small. This is valid especially when waveform data are recorded moderately far from the active source. Furthermore, techniques based on this assumption are computationally fast. However, an accurate processing requires a preliminary scaling of recorded data by  $\sqrt{r}$ , to remove the influence of geometric damping effect that characterizes cylindrical waves. When using a planar model, the FDBFa method provides an attenuation estimate that is independent from the wavenumber, entailing that dispersion and attenuation analysis of the wavefield can be carried out separately. Therefore, the algorithm adopted in this study first estimates dispersion curves by means of the FDBF approach, which also relies on a planar scheme. Then, attenuation data are obtained through the FDBFa method. The main steps of this algorithm are listed in Algorithm 1.

Algorithm 1 Frequency-Domain BeamForming – Attenuation (FDBFa) algorithm for MASW processing	
<b>Input:</b>	$\{u_z(r_n, t_s)\}_{n=1, s=1}^{N, N_T}$ : particle displacement recorded at $N$ sensors with offset $r_n$ , at $N_T$ time samples $t_s$
1:	Compute frequency spectra $\{u_z(r_n, \omega_i)\}_{n=1, j=1}^{N, N_\omega}$ , for $N_\omega$ frequencies $\omega_i$
2:	Geometrical spreading removal: $\{u_z(r_n, \omega_i)\}_{n=1, j=1}^{N, N_\omega} \leftarrow \{u_z(r_n, \omega_i)\}_{n=1, j=1}^{N, N_\omega} \cdot \sqrt{r_n}$
3:	<b>for</b> $i = 1 : N_\omega$ <b>do</b>
4:	Compute pseudopower spectrum $P_{BF}(k_t, \omega_i)$ through FDBF
5:	Identify wavenumber $k_{Re}(\omega_i)$ (hence, the phase velocity $V_{Re}(\omega_i)$ ) of the dominant peak of $P_{BF}(k_t, \omega_i)$
6:	Calculate $v_z(r_n, \omega_i)$ from Eq. 5.9
7:	Remove the amplitude term $v_z(r_n, \omega_i) \leftarrow v_z(r_n, \omega_i) /  v_z(r_n, \omega_i) $
8:	Apply the window $v_z(r_n, \omega_i) \leftarrow w(r_n, \omega_i) v_z(r_n, \omega_i)$
9:	Compute spatio-spectral correlation matrix $R_{m,n}(\omega_i) = v_z(r_n, \omega_i) [v_z(r_n, \omega_i)]^*$
10:	Construct steering vector with trial attenuation $\alpha_i$ : $\mathbf{e}(\alpha_i) = [e^{-i\alpha_i r_1}, \dots, e^{-i\alpha_i r_N}]^T$
11:	Calculate pseudospectrum for varying $\alpha_i$ : $P_{BFa}(\alpha_i, \omega_i) = \mathbf{e}^H(\alpha_i) \mathbf{R}(\omega_i) \mathbf{e}(\alpha_i)$
12:	Peak picking of $P_{BFa}(\alpha_i, \omega_i)$ : $\alpha_{R,e}(\omega_i) \leftarrow \text{argmax} P_{BFa}(\alpha_i, \omega_i)$
13:	<b>end for</b>

Instead, when an explicit modeling of the cylindrical wavefield is considered, the coupling between dispersion and attenuation estimates becomes more relevant. For this reason, the adopted algorithm first estimates dispersion curves by means of the CFDBF approach. Then, the attenuation analysis is carried out by means of the CFDBFa method. In this step, wavenumber data returned by the CFDBF are plugged into the steering vectors used in the CFDBFa, frequency by frequency. The main steps of this algorithm are listed in Algorithm 2, which assumes that the recorded motion is the particle displacement in the vertical direction. Note that  $H_0^{(2)}(\cdot)$  should be replaced by  $H_1^{(2)}(\cdot)$  when processing radial displacement data.

Algorithm 2 Cylindrical Frequency-Domain BeamForming – Attenuation (CFDBFa) for MASW processing	
<b>Input:</b>	$\{u_z(r_n, t_s)\}_{n=1, s=1}^{N, N_T}$ : particle displacement recorded at $N$ sensors with offset $r_n$ , at $N_T$ time samples $t_s$
1:	Compute frequency spectra $\{u_z(r_n, \omega_i)\}_{n=1, j=1}^{N, N_\omega}$ , for $N_\omega$ frequencies $\omega_i$
2:	<b>for</b> $i = 1 : N_\omega$ <b>do</b>
3:	Compute pseudopower spectrum $P_{CBF}(k_i, \omega_i)$ through CFDBF
4:	Identify wavenumber $k_{Re}(\omega_i)$ (hence, the phase velocity $V_{Re}(\omega_i)$ ) of the dominant peak of $P_{CBF}(k_i, \omega_i)$
5:	Calculate $v_z(r_n, \omega_i)$ from Eq. 5.9
6:	Remove the amplitude term $v_z(r_n, \omega_i) \leftarrow v_z(r_n, \omega_i) /  v_z(r_n, \omega_i) $
7:	Apply the window $v_z(r_n, \omega_i) \leftarrow w(r_n, \omega_i) v_z(r_n, \omega_i)$
8:	Compute spatio-spectral correlation matrix $R_{m,n}(\omega_i) = v_z(r_m, \omega_i) [v_z(r_n, \omega_i)]^*$
9:	Construct steering vector with trial complex wavenumber $\hat{k}_i$ : $\mathbf{a}(\hat{k}_i) = \left[ e^{-i \arg\{h_0(\hat{k}_i)\}}, \dots, e^{-i \arg\{h_0(\hat{k}_i)\}} \right]^T$ , with $\hat{k}_i = k_{Re}(\omega_i) - i\alpha_i$
10:	Calculate pseudospectrum for varying $\alpha_i$ : $P_{CBFa}(\hat{k}_i, \omega_i) = \mathbf{a}^H(\hat{k}_i) \mathbf{R}(\omega_i) \mathbf{a}(\hat{k}_i)$
11:	Peak picking of $P_{CBFa}(\hat{k}_i, \omega_i)$ : $\alpha_{R,e}(\omega_i) \leftarrow \arg\max P_{CBFa}(\hat{k}_i, \omega_i)$
12:	<b>end for</b>

A potentially critical step is the definition of the grid of trial attenuation values  $\alpha_i$ . Indeed, the search domain should include a broad range of trial attenuation values, up to the limit value provided by the Nyquist-Shannon theorem. However, in usual acquisition setups for near-surface characterization (where the geophone spacing  $d$  is generally 1÷5 m), the maximum investigable  $\alpha_i$  is 0.6÷3 rad/m. On the other side, typical attenuation values in Rayleigh waves range between  $10^{-3}$  and  $3 \times 10^{-1}$  rad/m. Therefore, the grid of  $\alpha_i$  should be adequately refined, otherwise the attenuation estimate would be biased because of the coarseness of the grid. For instance, if the Nyquist limit is equal to 3.14 rad/m (i.e.,  $d = 1$  m) and the  $\alpha_i$  grid has spacing equal to  $7.7 \times 10^{-4}$  rad/m (i.e., it includes 8192 data points), the maximum error due to the grid discretization might be



quantified as  $\Delta\alpha = 3.8 \times 10^{-4}$  rad/m. Thus, the corresponding relative error  $\Delta\alpha/\alpha_R(\omega)$  may rise up to 4% when  $\alpha_R(\omega) = 10^{-2}$  rad/m and up to 40% when  $\alpha_R(\omega) = 10^{-3}$  rad/m. The grid coarseness may result in biased estimates of the attenuation curves especially at low frequencies, where  $\alpha_R(\omega)$  is small, thus reducing the quality in estimated dissipation parameters at greater depths. Note that the influence of the grid sampling is much less relevant on the estimate of  $k_R(\omega)$ , being this quantity usually one or two orders of magnitude greater than  $\alpha_R(\omega)$ . On the other side, a refined discretization of the search domain would require an overwhelmingly large number of grid points, entailing a remarkable increase in computation time. This aspect is relevant when processing surface wave data, as the computation of the pseudospectra has to be carried out at each investigated frequency. A reasonable tradeoff between refined discretization and computation speed can be achieved by investigating a narrower range of  $\alpha_i$ , which is limited to a maximum value which represents an upper bound in the usual range of  $\alpha_R(\omega)$  in near-surface applications, compatibly with the constraints by the Nyquist-Shannon theorem. For instance, a reasonable value for such upper bound may be an attenuation equal to 0.5 rad/m, which may be lowered when investigating low-frequency Rayleigh waves. However, a narrower range may be adopted as search domain, by combining typical values of  $k_R(\omega)$  and of  $\alpha_R(\omega)$  (or phase damping ratio). For instance, MASW surveys for ordinary applications usually investigate frequencies ranging between 1 Hz and 100 Hz and the retrieved  $V_R(\omega)$  ranges between 100 m/s and 1000 m/s. Therefore,  $k_R(\omega)$  typically lies between  $10^{-3}$  rad/m and  $10^1$  rad/m. Recalling that  $\alpha_R(\omega) = k_R(\omega)D_R(\omega)$  and that  $D_R(\omega)$  usually varies between  $10^{-3}$  and  $10^{-1}$ , then a suitable range of variation for  $\alpha_R(\omega)$  is  $10^{-6} \div 10^0$  rad/m. The range of  $\alpha_R(\omega)$  can be also reduced, by exploiting the variation of this parameter with the frequency (Figure 5-12). Specifically,  $\alpha_R(\omega)$  usually ranges between  $10^{-6}$  rad/m and  $10^{-2}$  rad/m at 1 Hz,  $10^{-5}$  rad/m and  $10^{-1}$  rad/m at 50 Hz, and  $10^{-4}$  rad/m and  $10^0$  rad/m at 100 Hz. This strategy allows a reduction in computation time and to obtain good quality estimates. However, these boundaries only represent suggested values valid for generic site conditions, that can be tightened in the presence of site-specific information. Furthermore, the maximum value is bounded to comply with the restrictions by the Nyquist-Shannon theorem.

The application of the proposed algorithms to SW3 and SW4 will be addressed in the next Section, as it will be useful to highlight some drawbacks of the FDBFa and the CFDBFa approaches in processing measurements of surface wave data.

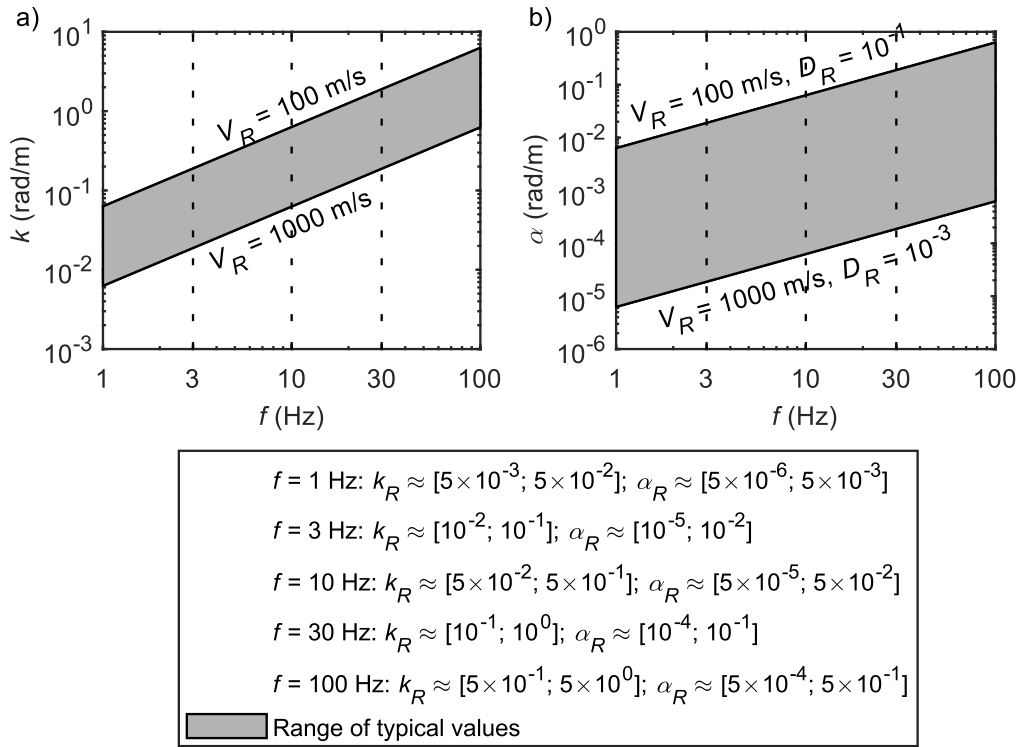


Figure 5-12. Typical ranges of the a) R-wave wavenumber  $k_R(\omega)$  and b) R-wave phase attenuation  $\alpha_R(\omega)$  as a function of the frequency.

## 5.3 Dealing with multiple modes

In this Section, an application of the FDBFa and the CFDBFa algorithms to synthetic MASW data (i.e., SW3 and SW4) highlights that they tend to provide estimates of the dispersion and attenuation, that may not be coincident with modal curves. To achieve reliable estimates of modal data, the contribution by each propagation mode needs to be separated. For this reason, this study proposes a filtering technique, that exploits basic principles of digital signal processing. This section describes the novel filtering scheme and how it is incorporated in the reference algorithms.

### 5.3.1 Application to synthetic models

A fundamental assumption of the FDBFa and of the CFDBFa methods is that the recorded wavefield should consist of a single wave or, in surface wave analysis, that a single Rayleigh mode is dominant (generally, the fundamental mode). When this hypothesis is violated, both methods tend to return biased estimates of the attenuation.

To understand the reasons behind the unreliability of such approaches in the presence of multiple waves, let us consider a simple case, where the wavefield  $u_{pp}(r)$  is the composition of two plane waves  $u_{p1}(r)$  and  $u_{p2}(r)$ :

$$u_{pp}(r) = u_{p1}(r) + u_{p2}(r) = A_1 e^{-\alpha_1 r} e^{-ik_1 r} + A_2 e^{-\alpha_2 r} e^{-ik_2 r} \quad (5.15)$$

In this specific case, the wavenumbers  $k_1$  and  $k_2$  are equal to 0.1 rad/m and 0.4 rad/m; the attenuations  $\alpha_1$  and  $\alpha_2$  are equal to 0.0015 rad/m and 0.0028 rad/m, respectively; the amplitudes  $A_1$  and  $A_2$  are both unitary. The resulting wavefield assumes an irregular variation of the amplitude with the offset, with complex patterns (Figure 5-13a). Indeed, the resulting amplitude is the weighted sum of the amplitudes of each wave component, plus an additional term depending on the phase lag between them, that incorporates the effect of constructive or destructive interferences occurring between  $u_{p1}(r)$  and  $u_{p2}(r)$  (Misbah and Strobba, 2014). Instead, the phase assumes some oscillations, but it tends to match that of  $u_{p1}(r)$  (Figure 5-13b). Indeed,  $u_{p1}(r)$  slightly dominates the simulated wavefield, especially at large offsets, because it undergoes less spatial attenuation. This behavior is also visible in the spectral domain, as  $P_{BF}(k)$  exhibits two peaks located at  $k_1$  and  $k_2$  (hence, it properly identifies the two waves), but the first one has greater amplitude (Figure 5-13c). However, the application of the FDBFa to  $u_{pp}(r)$  returns an estimate of attenuation which is not consistent with  $\alpha_1$  nor  $\alpha_2$ , and it falls between these values (Figure 5-13d). The resulting  $\alpha_e$  is an apparent attenuation, that depends both on the propagation parameters of the wave components and on the acquisition scheme, being a local quantity. In some cases, even zero or negative  $\alpha_e$  values might be identified, when constructive interference is dominant.

Similar considerations are valid when considering a wavefield  $u_{cc}(r)$  composed by a combination of two cylindrical waves  $u_{c1}(r)$  and  $u_{c2}(r)$ , with the same parameters of  $u_{p1}(r)$  and  $u_{p2}(r)$  (Figure 5-14a-b). However, the application of the CFDBFa is not straightforward as a reference wavenumber is required to obtain  $\alpha_e$ . A reasonable approach may refer to the wavenumber of the dominant wave, which is the one with larger spectral amplitude, i.e.  $k_1$ . (Figure 5-14c). In this specific case,  $\alpha_e$  is quite close to  $\alpha_1$ , but it is not coincident with it because it is an estimate of the apparent attenuation (Figure 5-14d).

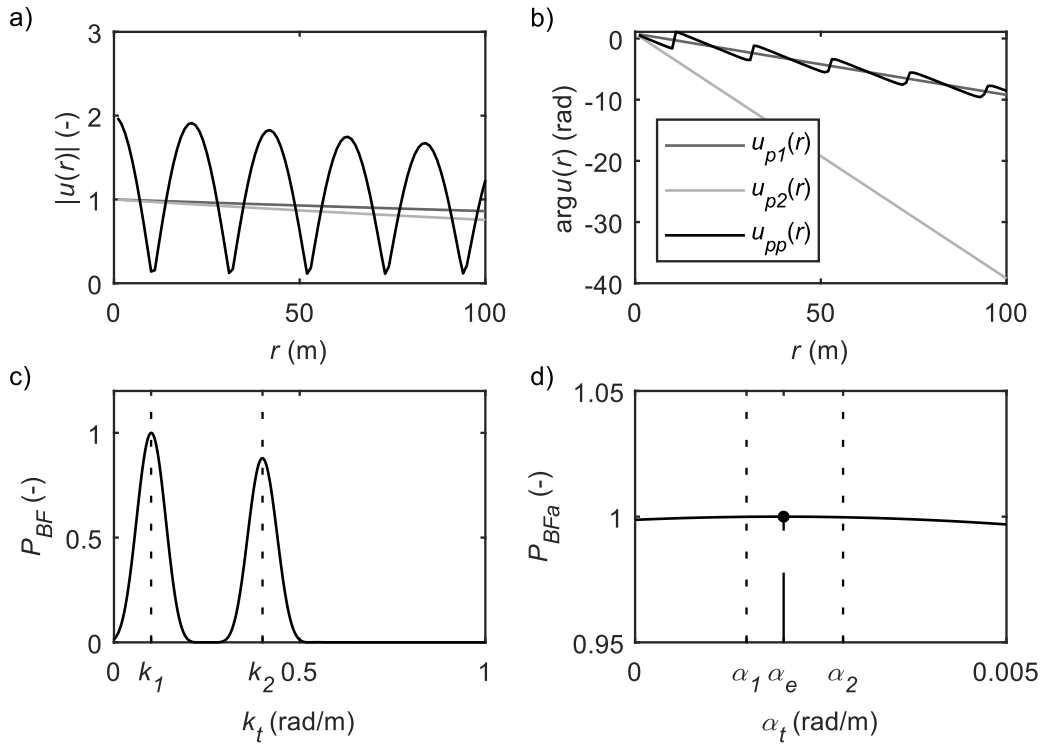


Figure 5-13. Application of the FDBFa to the wavefield  $u_{pp}(r)$ : a-b) Wave components  $u_{p1}(r)$  and  $u_{p2}(r)$  and total wavefield  $u_{pp}(r)$ , in terms of a) amplitude and b) phase; c) Pseudopower spectrum of  $u_{pp}(r)$ , obtained by means of the FDBF; d) Pseudopower spectrum of  $u_{pp}(r)$ , obtained by means of the FDBFa.

At this point, it is possible to describe the application of the FDBFa and of the CFDBFa to the synthetic wavefields SW3 and SW4, thus assessing their performance in the presence of a wavefield composed of Rayleigh waves. As they model the propagation of Rayleigh waves in layered media, the wavefield is the composition of several Rayleigh modes. In other words, recorded data are the superposition of multiple waves, interfering with each other. Instead, the FDBFa and of the CFDBFa model the wavefield as a single wave. Therefore, these approaches theoretically return a single dispersion curve and a single attenuation curve, that may not coincide with any modal curve. Specifically, estimated data correspond to the dominant component of the wavefield. This aspect is crucial especially for CFDBFa, as it requires the specification of a reference dispersion curve, in this case assumed to be coincident with the effective dispersion curve, i.e., the dominant one in the CFDBF spectrum. Thus, the proposed algorithms tend to return the dominant wave components, that are representative of the effective dispersion and attenuation curve.

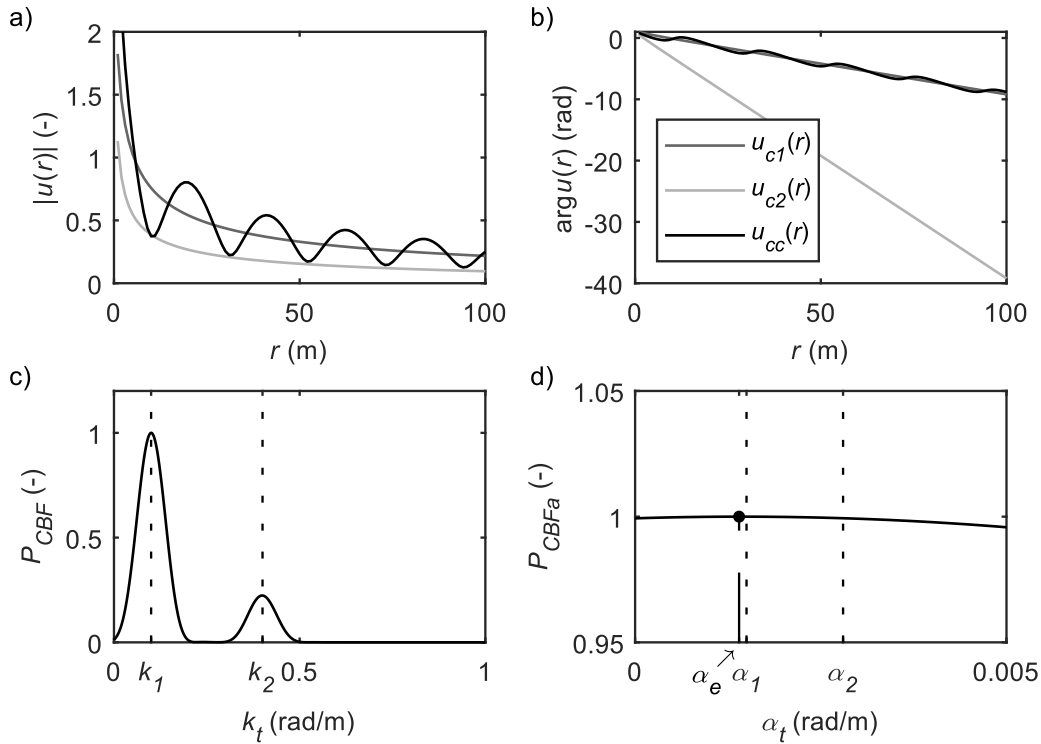


Figure 5-14. Application of the CFDBFa to the wavefield  $u_{cc}(r)$ : a-b) Wave components  $u_{c1}(r)$  and  $u_{c2}(r)$  and total wavefield  $u_{cc}(r)$ , in terms of a) amplitude and b) phase; c) Pseudopower spectrum of  $u_{cc}(r)$ , obtained by means of the CFDBF; d) Pseudopower spectrum of  $u_{cc}(r)$ , obtained by means of the CFDBFa.

Figure 5-15 and Figure 5-16 report the estimated  $V_R(\omega)$  and  $\alpha_R(\omega)$  for SW3 and SW4, according to the FDBFa and the CFDBFa schemes, respectively. Results were sampled with a sampling frequency of 1 Hz, across the frequency band ranging between 3 Hz and 100 Hz. For comparison purposes, the theoretical modal curves are included. Although synthetic data virtually enable the investigation of a broad frequency range, a proper investigation of the performance of each processing scheme should account for the restrictions due to the limited spatial sampling in the acquisition layout. Therefore, data above the maximum investigable wavelength  $\lambda_{max} = D$  (where  $D = 100$  m is the array length) and below the minimum one  $\lambda_{min} = d$  (where  $d = 2$  m is the receiver spacing) – if any – are included in the comparison, but a different coloring is adopted to highlight their peculiar condition.

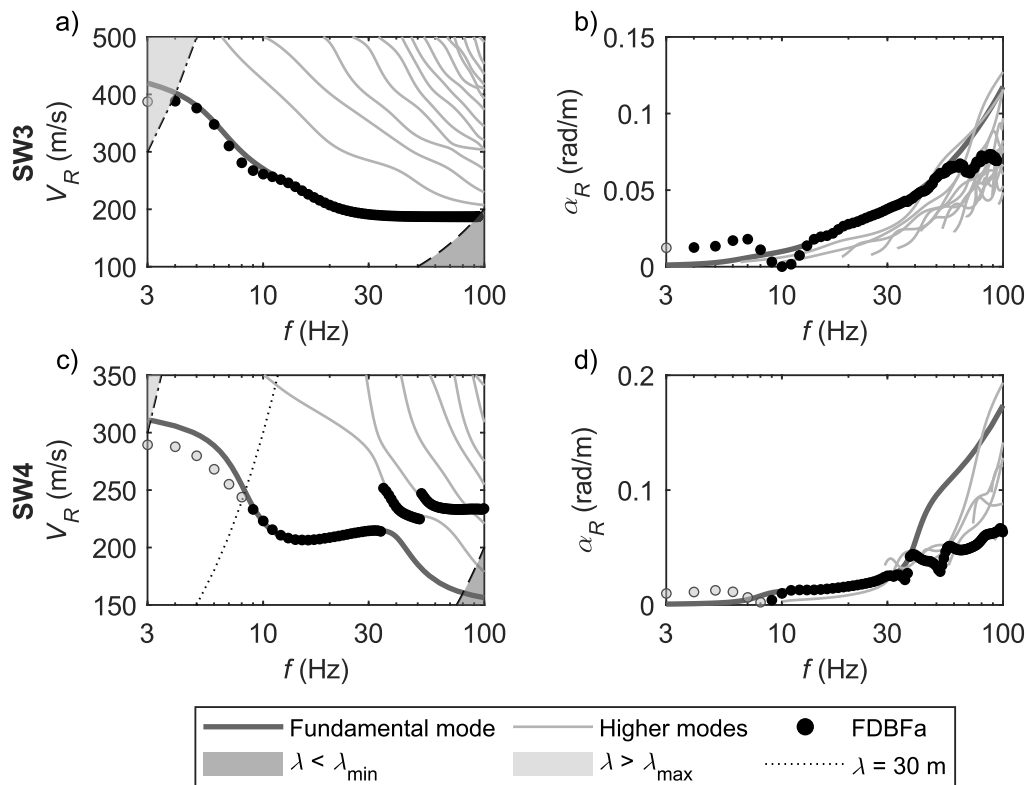


Figure 5-15. a-b) Application of the FDBFa algorithm to SW3: a) Estimated phase velocity curve; b) Estimated phase attenuation curve; c-d) Application of the FDBFa algorithm to SW4: c) Estimated phase velocity curve; d) Estimated phase attenuation curve. Estimated data points beyond the array resolution limits – i.e., the grey areas in a) and c) – are colored in grey.

The application of the FDBFa algorithm to SW3 provides an estimated dispersion curve that matches the one corresponding to the fundamental mode, except at low frequencies (Figure 5-15a). Indeed, the Rayleigh wavefield in normally dispersive media is typically governed by the fundamental mode, as highlighted in Figure 5-3e. However, the resulting attenuation curve equals the fundamental mode only at intermediate frequencies, whereas it tends to underestimate it at  $f > 30$  Hz (Figure 5-15b). At this frequency, higher modes start to contribute to the wavefield, thus the estimated attenuation is partially affected by them.

As for SW4, the wavefield is the combination of multiple Rayleigh modes, each one providing a different degree of contribution as a function of the frequency. This situation is quite usual in inversely dispersive media. Therefore, the estimated dispersion curve gradually shifts from the fundamental mode up to the second higher mode (Figure 5-15c). In a consistent way, the estimated

attenuation curve tends to follow the corresponding modal ones, and each transition occurs at the same frequency of the passages in the dispersion data (Figure 5-15d). However, estimated data do not exactly match modal curves, especially at moderately low frequencies (i.e.,  $f < 30$  Hz), where the estimated attenuation data lie between the fundamental mode and the first higher mode attenuation curves. This means that the wavefield amplitude is affected by both components, although its phase variations mainly depend on the fundamental mode. However, if the comparison is restricted to  $\lambda_{max} = 30$  m, then the deviations in the low-frequency range are negligible. This  $\lambda$  value represents the upper boundary of the range of wavelengths needed to fully resolve the layers' interfaces of the medium, as the deepest one is located at 10 m depth (Figure 5-4). Therefore, if SW4 represented the output of a survey deemed to characterize the corresponding soil profile, this would represent the range of interest. On the other side, the drift at higher frequencies is still relevant due to the influence of higher modes.

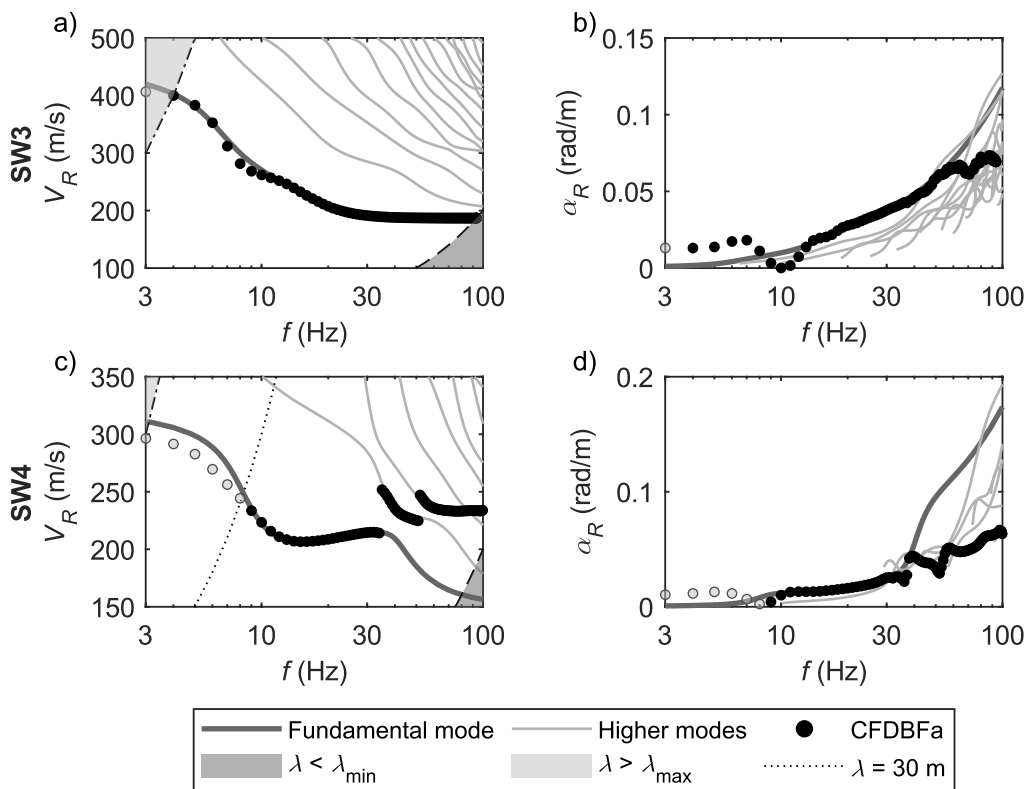


Figure 5-16. a-b) Application of the CFDBFa algorithm to SW3: a) Estimated phase velocity curve; b) Estimated phase attenuation curve; c-d) Application of the CFDBFa algorithm to SW4: c) Estimated phase velocity curve; d) Estimated phase attenuation curve. Estimated data points beyond the array resolution limits – i.e., the grey areas in a) in (a) and c) – are colored in grey.

Similar results are observed in the application of the CFDBFa on SW3 and SW4 (Figure 5-16), although a slight improvement in the quality of the estimated  $V_R(\omega)$  occurs at low frequencies. The reasons behind discrepancies in the very low-frequency range (i.e.,  $f < 10$  Hz) will be addressed in Section 5.4.

In summary, the algorithms based on the FDBFa and on the CFDBFa tend to return estimates of the effective dispersion and attenuation curves, that may not be coincident with modal curves. Even when a single dominant mode characterizes the wavefield, the estimated attenuation data may not match the corresponding modal values at all the frequencies. Indeed, the amplitude of the Rayleigh wavefield is dramatically sensitive to constructive and destructive interference among different propagation modes. Therefore, ignoring the influence of this mutual interaction may lead to attenuation estimates that, when misinterpreted as modal values, might return biased estimates of the  $D_S$  profile in the inversion stage. For this reason, both the FDBFa and the CFDBFa are modified to account for the presence of multiple propagation modes, by including an additional step. This further step aims at isolating each propagation mode by means of an appropriate filtering technique, that exploits basic principles of digital signal processing.

### 5.3.2 Proposed filtering technique

This study proposes a novel filtering technique, that seeks to isolate a single wave in multicomponent waveforms or a single R-wave propagation mode from waveforms recorded in multilayered media. In this way, the main hypothesis of the FDBFa and of the CFDBFa is satisfied, and these techniques can be effectively applied to obtain reliable estimates of the wave attenuation. Some algorithms have already been applied in seismological studies and in geophysical prospecting, based on the time-variable filter (Pilant and Knopoff, 1964; Karray and Lefebvre, 2009) or relying on the high-resolution linear radon transform (HRLRT; Luo et al., 2008; Gao et al., 2018). However, an effective modal separation in recorded waveform data is a nontrivial task (Ivanov et al., 2005).

The proposed technique is based on a complex, bandpass and linear-phase Finite Impulse Response (FIR) filter. A complete description of their features and the relevant parameters is provided in Appendix A. The filter operates along the spatial direction, and the input sequence is the vector of the traces in the frequency domain of the recorded wavefield, in which the sample points correspond to the receivers locations. Although usual filtering schemes apply for time-domain signals, they are also valid also for data defined in the space domain. In this case, the frequency variable  $\omega$  is replaced by the wavenumber  $k$ .



The adopted filter is a bandpass filter that isolates the wavenumber component corresponding to the target wave, thus limiting the contribution of additional components to the wavefield. The chosen filter is a FIR-type system, because they are stable and they represent the optimal choice when the linearity in the phase response is crucial (Mitra, 2006). In this case, the phase-linearity is strongly desired as any distortion in the target wave component may affect the estimated attenuation. Finally, the filter has complex-valued coefficients because it operates with complex-valued wavefield traces, for which the wavenumber spectrum is not an even function. In these conditions, the application of a real bandpass filter would enhance spectral components that are outside the desired target. Instead, a complex FIR filter with passband centered at the target wavenumber is guaranteed to select and favor only the investigated wave component.

Designing complex FIR filters is usually a nontrivial task, because the frequency response is a non-symmetric function and the number of design parameters (i.e., the filter coefficients) is twice the ones of a real filter of the same order, as both real and imaginary values need to be calibrated. However, being a bandpass filter, the wavenumber response (hereafter labeled as  $k$ -response) has to be symmetric around the target wavenumber  $k_{tg}$ . This constraint allows to exploit a simplified algorithm for designing the desired complex FIR filter  $h[n]$ , namely the modulation method, starting from a real filter  $g[n]$  as follows:

$$h[n] = e^{i\vartheta_{tg}n} g[n] \quad (5.16)$$

where  $n$  labels the spatial sample. The system  $g[n]$  is a lowpass real filter whose  $k$ -response is an even function, and it exhibits a passband centered at the zero wavenumber. The factor  $e^{i\vartheta_{tg}n}$  is a modulation term, that shifts the passband of the filter in correspondence of the target wavenumber  $k_{tg}$ . Indeed, the parameter  $\vartheta_{tg}$  is linked with  $k_{tg}$  as follows:

$$\vartheta_{tg} = \frac{2\pi}{2k_{Nyq}} (2k_{Nyq} - k_{tg}) \quad (5.17)$$

The subtraction accounts for the different spectral coordinates in the  $f$ - $k$  spectrum and in the Fourier transform, whereas the factor  $2\pi/2k_{Nyq}$  scales the range of wavenumbers from  $[-k_{Nyq}; k_{Nyq}]$  to  $[-2\pi; 2\pi]$ , i.e. the domain where the transfer function of the filter is defined (equal to the range of the DTFT). In this way, the lowpass real filter  $g[n]$  is converted into the bandpass complex filter  $h[n]$  (Figure 5-17).

This design approach has multifold advantages. Firstly, the modulation method allows to shift the design problem of a complex filter into the design of a

real filter, for which a broad variety of reliable and fast algorithms is available. Furthermore, the modulation of the symmetric filter  $g[n]$  returns a symmetric filter, hence  $h[n]$  is a linear-phase filter that, by consequence, does not introduce any phase distortion to the signal. A more detailed explanation on this is provided in Appendix A.

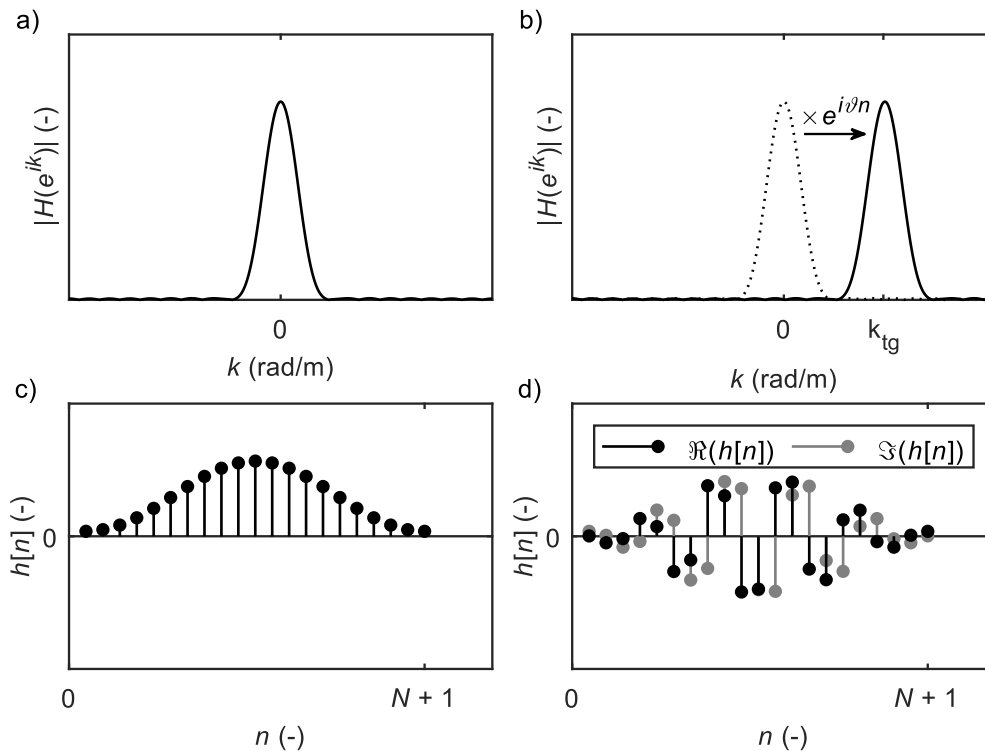


Figure 5-17. Steps of the modulation algorithm for constructing a  $N$ -order bandpass complex FIR filter: a-c) Real lowpass FIR filter in terms of a)  $k$ -response and c) impulse response; b-d) Complex bandpass FIR filter in terms of b)  $k$ -response and d) impulse response.

Thus, the design of  $h[n]$  can be achieved by designing the lowpass real filter  $g[n]$ . The key steps in the design of  $g[n]$  consist in specifying the desired  $k$ -response  $G_d(e^{jk})$  and in estimating an adequate filter order  $N$ , so that the effective  $k$ -response  $G(e^{jk})$  adequately matches the theoretical one. Then, the estimation of the filter coefficients is carried out by means of the frequency sampling approach (Gold and Jordan, 1969). This algorithm is implemented in the MATLAB function `fir2`.

The desired  $k$ -response of  $g[n]$  should be compatible with both the desired magnitude specifications and with the constraints of the physical realizability of the filter. Therefore, the definition of  $G_d(e^{jk})$  should involve the specification of an adequate passband together with an adequate transition band to control the decay

in the response magnitude (Figure 5-18). On the other side, the definition of the filter order is a critical task. High-order filters are desirable because they well reproduce  $G_d(e^{ik})$  and they manage to realize narrow transition bands. Instead, low-order filters only approximate  $G_d(e^{ik})$ , as the corresponding transition bands are broader, entailing a partial loss in the filtering capability (Figure 5-18). However, high-order filters require long computation time. Besides, the stationary response is shorter, as it includes only  $n-N$  samples. The stationary portion is crucial because it represents the “true” output of the filter, and it contains the desired signal. Therefore,  $N$  should be adequately less than  $n$  to allow processing of filtered values (see Appendix A). This issue may be critical when dealing with spatially sampled data, especially in geophysical applications. Indeed, each spatial sample corresponds to a physical sensor and usual acquisition setups employ a small number of sensors because of logistical issues, hence recorded signals only include a few tens of samples. Therefore,  $N$  has to be bounded within a proper maximum value, so that the number of samples in the stationary response is large enough to allow a robust estimate of wave parameters from the filtered signal.

Finally, the filter response specifications (i.e., the definition of  $G_d(e^{ik})$ ) and the assignment of the filter order are not two independent steps. Indeed, narrow bandpass filters are effective in isolating the desired component of the wavefield, although such behavior can be achieved only with high-order filters. Instead, if  $G_d(e^{ik})$  assumes smoother variations between the passband and the stopband, the separation capability of wave components is reduced but low-order filters can adequately reproduce the target response. Furthermore, low-order filters are preferred when dealing with spatially sampled data. Therefore, the definition of the design parameters is not straightforward, and it should achieve a trade-off between filter separation capability, feasibility and data availability.

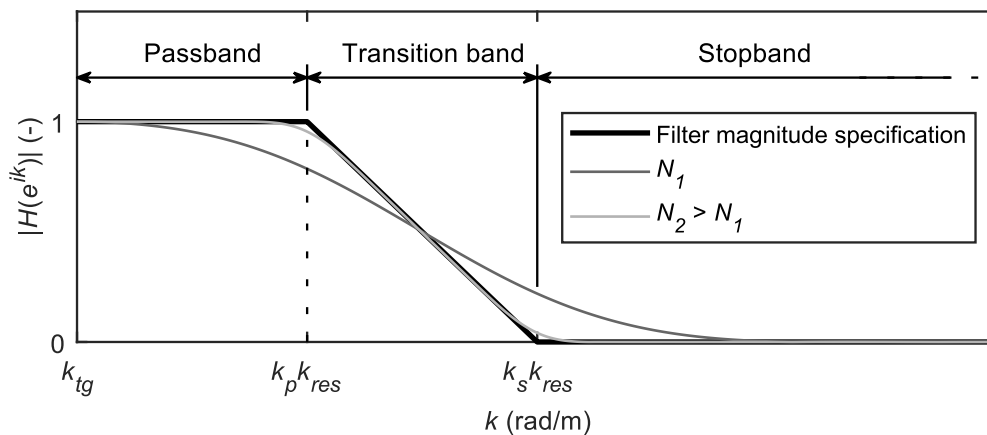


Figure 5-18. Magnitude response specifications, with an explanation of parameters  $k_p$  and  $k_s$  and a visualization of the influence of the filter  $N$  on the fitting of the desired response.

For this reason, a calibration study is carried out, to investigate the influence of both target response specifications, in terms of the passband and the stopband, and the order of the filter. In this study, the boundaries of the transition band are quantified as  $k_p k_{res}$  and  $k_s k_{res}$ , where  $k_{res} = 2\pi/D$  is the wavenumber resolution of the sensor array (Figure 5-18). Parameters  $k_p$  and  $k_s$  are constants that allow to select a range of wavenumbers around the target wavenumber  $k_{ig}$ , and they need to be calibrated. Specifically, the following sets of parameters  $[k_p; k_s]$  are investigated: [1; 2], [2; 4], [3; 10]. Each couple describes a different specification of  $G_d(e^{ik})$ , with different size of the passband and of the transition band. The choice of referring to  $k_{res}$  is not casual, as it describes the width of the spectral mainlobe of a wavefield composed by a single propagating wave (Zywicki, 1999). Thus, by setting the passband larger than  $k_{res}$  (as  $k_p \geq 1$ ), the filter tends not to alter spectral information related to the target wave. As for the filter order, the following  $N$  values are considered: 10, 20, 30, 40 and 80. Only even  $N$  values are considered, so that the filtered signal is exactly a shifted version of the desired wave component (see Appendix A). Alternative values of  $[k_p; k_s]$  and of  $N$  can be considered, however results undergo only small variations because the actual filter response is almost the same when design parameters are slightly modified.

Figure 5-19 shows results of this calibration study for the wavefield  $u_{pp}(r)$  (see Section 5.3.1), where the modal filtering technique aims at extracting the two plane waves  $u_{p1}(r)$  and  $u_{p2}(r)$ . Specifically, it reports the estimated wavenumber  $k_e$  and attenuation  $\alpha_e$  of each isolated wave, computed according to the FDBF and the FDBFa, respectively. For comparison purposes, the theoretical values  $k_i$  and  $\alpha_i$  ( $i = 1, 2$ ) are reported. Besides, Figure 5-19b-c include the estimated attenuation according to the FDBFa from the total wavefield, labeled as  $\alpha_{e,FDBFa}$ . In this way, the influence of the filter on the attenuation estimate is addressed. The calibration study highlights that the geometry of the transition band (i.e.,  $[k_p; k_s]$ ) does not have remarkable influence on the resulting wave parameters, when the band is quite narrow around  $k_{ig}$ . Instead, the quality of estimates drops for  $[k_p; k_s] = [3; 10]$ . Indeed, this range identifies a filter where the stopband is quite far from  $k_{ig}$ , hence the capability of removing the contribution of other wave components is reduced. Furthermore, the filter order dramatically affects  $\alpha_e$ . When  $N$  is low,  $\alpha_e$  is quite close to  $\alpha_{e,FDBFa}$ , hence the filter is not significantly changing the shape of the waveform, which is still close to  $u_{pp}(r)$ . Instead, high-order filters tend to provide more precise estimates, and the discrepancy from the theoretical value becomes almost negligible already for  $N = 30$ . On the converse,  $k_e$  is not sensitive to  $N$ , except for  $[k_p; k_s] = [3; 10]$ , for the reasons stated before.

Similar considerations are valid when cylindrical waves are investigated, i.e. with  $u_{cc}(r)$  (see Section 5.3.1; Figure 5-20). In this case, the influence of calibration parameters was analyzed considering  $k_e$  and  $\alpha_e$  for each wave component, by means of the CFDBF and CFDBFa, respectively. Differently from the plane wave case, it appears that the quality of the estimated parameters for  $u_{p2}(r)$  is worse than the one for  $u_{p1}(r)$ . Indeed,  $u_{p1}(r)$  is the dominant component inside  $u_{cc}(r)$ , hence the modal filter does not manage to completely remove it when isolating  $u_{c2}(r)$ . This issue is highlighted when inspecting  $k_e$  for the corresponding wave component (Figure 5-20c), as low-order filters or filters with broad transition range tend to return  $k_e = k_1$ . Besides, the resulting  $\alpha_e$  is quite sensitive to  $N$ , especially when focusing on  $u_{c2}(r)$ . In general, high-order filters tend to return an overestimation of the attenuation, and the best matching is achieved by using  $N = 20 \div 50$  with a moderately narrow transition band (i.e.,  $[k_p; k_s] = [2; 4]$ ).

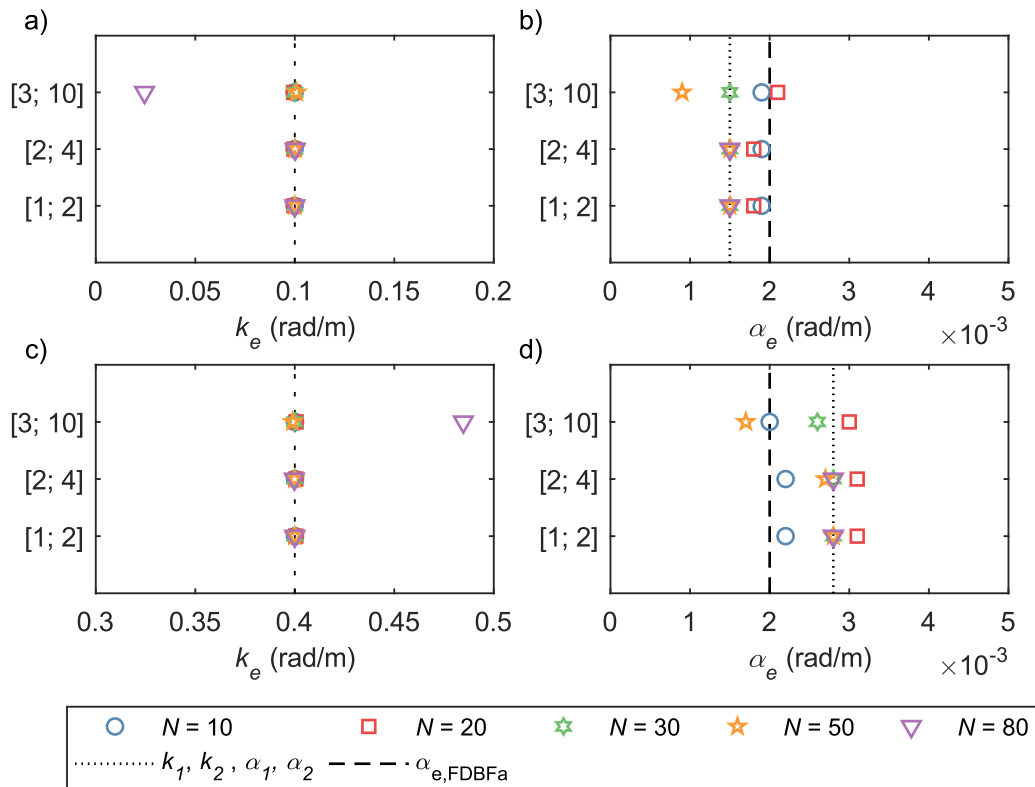


Figure 5-19. Influence of filter calibration parameters in extracting wave parameters for the two-component plane wave  $u_{pp}(r)$ : a-b) Wave  $u_{p1}(r)$ ; c-d) Wave  $u_{p2}(r)$ . The labels on the y axis identify different sets of  $[k_p; k_s]$ , that control the passband and the stopband of the filter. The estimated attenuation through the FDBFa  $\alpha_{e,FDBFa}$  is also reported, for comparison purposes.

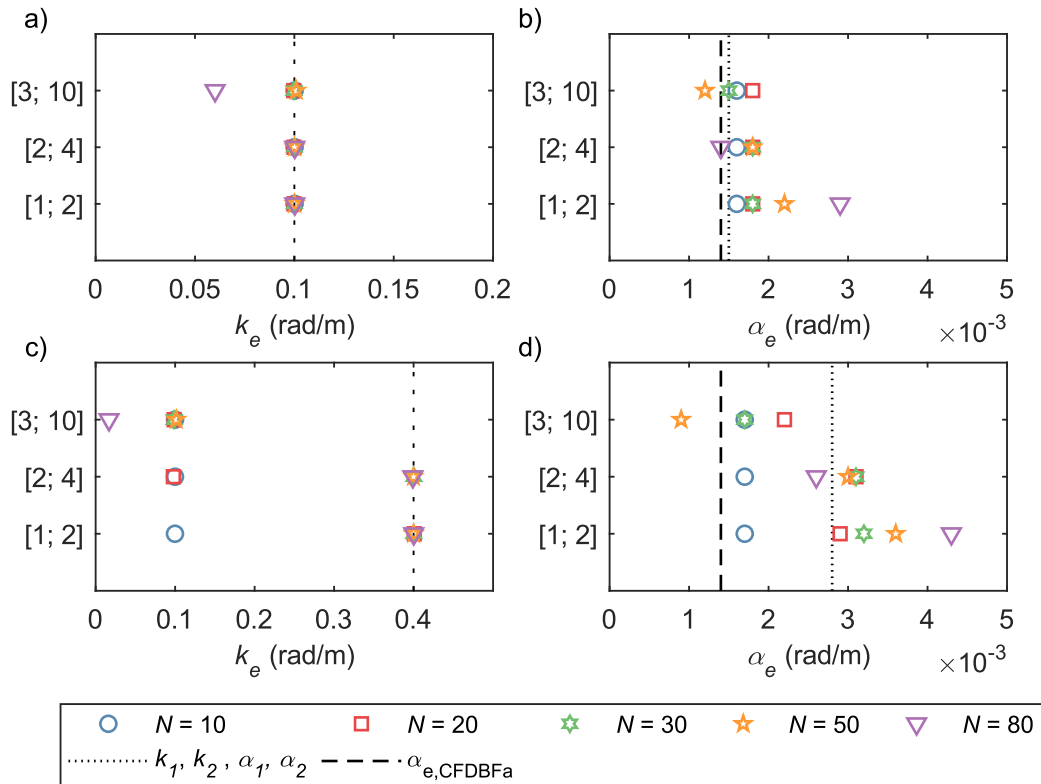


Figure 5-20. Influence of filter calibration parameters in extracting wave parameters for the two-component cylindrical wave  $u_{cc}(r)$ : a-b) Wave  $u_{c1}(r)$ ; c-d) Wave  $u_{c2}(r)$ . The labels on the y axis identify different sets of  $[k_p; k_s]$ , that control the passband and the stopband of the filter. The estimated attenuation through the CFDBFa  $\alpha_{e,CFDBFa}$  is also reported, for comparison purposes.

### 5.3.3 Applications

The inclusion of the modal filtering step inside the FDBFa and CFDBFa algorithms for processing results of MASW surveys is quite straightforward.

The principle of the updated workflows consists in performing a preliminary dispersion analysis, aimed at identifying different Rayleigh modes contributing to the recorded wavefield. This stage identifies the modes from the peaks of the  $f$ - $k$  spectrum, computed through the FDBF (or the CFDBF). Then, each mode is isolated and extracted from the wavefield, by applying the modal filter to the recorded displacement. The filter is defined by Eq. 5.16-17, by setting  $k_{tg}$  equal to the wavenumber of the investigated mode. In this way, the recorded wavefield is transformed into a set of displacement data, each representative of a single Rayleigh mode. Thus, the application of the FDBFa algorithm (or CFDBFa scheme) to filtered data will return the modal phase velocity and the modal phase

attenuation, for each considered propagation mode. Note that a preliminary estimate of the phase velocity is available from the initial stage of identification of Rayleigh modes, however this quantity is updated posterior to the filtering, also to assess the effectiveness of the modal extraction.

The FDBFa algorithm with Modal Filtering will be hereafter labeled as FDBFaMF, and a complete description is provided in Algorithm 3. Instead, the CFDBFa algorithm with Modal Filtering will be denoted as CFDBFaMF and a list of the main steps is provided in Algorithm 4. The latter assumes that the recorded motion is the particle displacement in the vertical direction. Note that  $H_0^{(2)}(\bullet)$  should be replaced by  $H_1^{(2)}(\bullet)$  when processing radial displacement data.

Algorithm 3 Frequency-Domain BeamForming – Attenuation with Modal Filtering (FDBFaMF)	
<b>Input:</b>	$\{u_z(r_n, t_s)\}_{n=1, s=1}^{N, N_T}$ : particle displacement recorded at $N$ sensors with offset $r_n$ , at $N_T$ time samples $t_s$
1:	Compute frequency spectra $\{u_z(r_n, \omega_i)\}_{n=1, j=1}^{N, N_\omega}$ , for $N_\omega$ frequencies $\omega_i$
2:	Geometrical spreading removal: $\{u_z(r_n, \omega_i)\}_{n=1, j=1}^{N, N_\omega} \leftarrow \{u_z(r_n, \omega_i)\}_{n=1, j=1}^{N, N_\omega} \cdot \sqrt{r_n}$
3:	<b>for</b> $i = 1 : N_\omega$ <b>do</b>
4:	Compute pseudopower spectrum $P_{BF}(k_i, \omega_i)$ through FDBF
5:	Identify peaks $\{k_{Re, j}(\omega_i)\}_{j=1}^{M(\omega_i)}$ of $P_{BF}(k_i, \omega_i)$ , for $M(\omega_i)$ modes
6:	<b>for</b> $j = 1 : M(\omega_i)$ <b>do</b>
7:	Define filter $h[n]$ from Eq. 5.16-17, based on $k_{Re, j}(\omega_i)$
8:	Mode extraction $\{u_{z, j}(r_n, \omega_i)\}_{n=1}^N \leftarrow \{u_z(r_n, \omega_i)\}_{n=1}^N \otimes h[n]$
9:	Compute pseudopower spectrum $P_{BF}(k_i, \omega_i)$ through FDBF
10:	Peak picking of $P_{BFa}(\alpha_{R, t}, \omega_i)$ : $\alpha_{R, e}(\omega_i) \leftarrow \text{argmax} P_{BFa}(\alpha_{R, t}, \omega_i)$
11:	Calculate $v_{z, j}(r_n, \omega_i)$ from Eq. 5.9
12:	$v_{z, j}(r_n, \omega_i) \leftarrow v_{z, j}(r_n, \omega_i) /  v_{z, j}(r_n, \omega_i) $
13:	Apply the window $v_{z, j}(r_n, \omega_i) \leftarrow w(r_n, \omega_i) v_{z, j}(r_n, \omega_i)$
14:	Compute spatio-spectral correlation matrix $R_{m, n}(\omega_i) = v_{z, j}(r_m, \omega_i) [v_{z, j}(r_n, \omega_i)]^*$
15:	Construct steering vector with trial attenuation $\alpha_{R, t}$ : $\mathbf{e}(\alpha_t) = [e^{-i\alpha_t r_1}, \dots, e^{-i\alpha_t r_N}]^T$
16:	Calculate pseudospectrum for varying $\alpha_{R, t}$ : $P_{BFa}(\alpha_{R, t}, \omega_i) = \mathbf{e}^H(\alpha_{R, t}) \mathbf{R}(\omega_i) \mathbf{e}(\alpha_{R, t})$
17:	Peak picking of $P_{BFa}(\alpha_{R, t}, \omega_i)$ : $\alpha_{R, j, e}(\omega_i) \leftarrow \text{argmax} P_{BFa}(\alpha_{R, t}, \omega_i)$
18:	<b>end for</b>
19:	<b>end for</b>

Algorithm 4 Cylindrical Frequency-Domain BeamForming – Attenuation with Modal Filtering (CFDBFaMF)

**Input:**  $\{u_z(r_n, t_s)\}_{n=1, s=1}^{N, N_T}$  : particle displacement recorded at  $N$  sensors with offset  $r_n$ , at  $N_T$  time samples  $t_s$

- 1: Compute frequency spectra  $\{u_z(r_n, \omega_i)\}_{n=1, j=1}^{N, N_\omega}$ , for  $N_\omega$  frequencies  $\omega_i$
- 3: **for**  $i = 1 : N_\omega$  **do**
- 4:     Compute pseudopower spectrum  $P_{BF}(k_t, \omega_i)$  through CFDBF
- 5:     Identify peaks  $\{k_{Re, j}(\omega_i)\}_{j=1}^{M(\omega_i)}$  of  $P_{CBF}(k_t, \omega_i)$ , for  $M(\omega_i)$  modes
- 6:     **for**  $j = 1 : M(\omega_i)$  **do**
- 7:         Define filter  $h[n]$  from Eq. 5.16-17, based on  $k_{Re, j}(\omega_i)$
- 8:         Mode extraction  $\{u_{z, j}(r_n, \omega_i)\}_{n=1}^N \leftarrow \{u_z(r_n, \omega_i)\}_{n=1}^N \otimes h[n]$
- 9:         Compute pseudopower spectrum  $P_{CBF}(k_t, \omega_i)$  through CFDBF
- 10:         Peak picking of  $P_{CBF}(k_t, \omega_i)$ :  $k_{R, e}(\omega_i) \leftarrow \text{argmax} P_{CBF}(k_t, \omega_i)$
- 11:         Calculate  $v_{z, j}(r_n, \omega_i)$  from Eq. 5.9
- 12:          $v_{z, j}(r_n, \omega_i) \leftarrow v_{z, j}(r_n, \omega_i) / |v_{z, j}(r_n, \omega_i)|$
- 13:         Apply the window  $v_{z, j}(r_n, \omega_i) \leftarrow w(r_n, \omega_i) v_{z, j}(r_n, \omega_i)$
- 14:         Compute spatospectral correlation matrix  $R_{m, n}(\omega_i) = v_{z, j}(r_m, \omega_i) [v_{z, j}(r_n, \omega_i)]^*$
- 15:         Construct steering vector with trial attenuation  $\alpha_{R, i}$ :  

$$\mathbf{a}(\hat{\mathbf{k}}_i) = \left[ e^{-i \arg\{h_0(\hat{\mathbf{k}}_i, r_1)\}}, \dots, e^{-i \arg\{h_0(\hat{\mathbf{k}}_i, r_N)\}} \right]^T$$
, with  $\hat{\mathbf{k}}_i = k_{Re}(\omega_i) - i\alpha_i$
- 16:         Calculate pseudospectrum for varying  $\alpha_{R, i}$ :  $P_{CBFa}(\alpha_{R, i}, \omega_i) = \mathbf{e}^H(\alpha_{R, i}) \mathbf{R}(\omega_i) \mathbf{e}(\alpha_{R, i})$
- 17:         Peak picking of  $P_{CBFa}(\alpha_{R, i}, \omega_i)$ :  $\alpha_{R, j, e}(\omega_i) \leftarrow \text{argmax} P_{CBFa}(\alpha_{R, i}, \omega_i)$
- 18:     **end for**
- 19: **end for**

As in the simplified examples SW1 and SW2, a calibration study is carried out also for SW3 and SW4, to identify optimal filter parameters that allow to properly capture modal parameters. Differently from the previous cases, the wavefield in SW3 and SW4 exhibits complex features. Indeed, the number of waves (i.e., R-wave modes) varies with the investigated frequency and their amplitude and relative distance in terms of  $k$  range are not a constant. Therefore, it is expected that the most appropriate filter parameters for SW3 and SW4 might not match those obtained in the analysis of SW1 and SW2.

The calibration study investigated the same sets of parameters  $[k_p; k_s]$  used for SW1 and SW2, whereas the following  $N$  values are considered: 10, 20, 30, and 40. Indeed, the number of available spatial samples, i.e. 48 data points, does not



allow to apply higher order filters. For the sake of brevity, only results for the parameter set  $[k_p; k_s] = [1; 2]$  and  $N = 20$  are herein reported, as they provided the best-quality estimates. Indeed, the calibration study demonstrated that filters with order  $N = 1/2 \div 2/3$  times the number of receivers may be considered as a valid reference for applying the FDBFaMF and CFDBFaMF in various site conditions. Furthermore, the following discussion focuses on results for the CFDBFaMF, as similar results are observed in the application of the FDBFaMF to SW3 and SW4. A complete overview of results is available in Appendix A.

Figure 5-21 compares resulting dispersion and attenuation estimates obtained through the CFDBFaMF algorithm for the first three modes for SW3, labeled as R0, R1 and R2, respectively. Reported data are sampled with a sampling frequency of 1 Hz, across the frequency band ranging between 3 Hz and 100 Hz. Furthermore, the regions associated with wavelengths beyond the resolution limits of the simulated array are highlighted, as the corresponding results should be interpreted with care. Interestingly, reliable estimates of  $\alpha_R(\omega)$  for R0 can be obtained regardless  $N$ , even at high frequencies, where the CFDBFa-based attenuation estimate diverges from modal values. In addition, the estimated  $V_R(\omega)$  well matches the R0 dispersion curve, as demonstrated by the low estimation error. This result is not surprising, being the fundamental mode the dominant component of SW3, whereas higher modes provide a small contribution. Therefore, isolating the fundamental mode by removing other components is an easy task, that can be achieved even with smooth filters. The converse occurs when dealing with higher modes, because of the higher difficulties in extracting the desired mode, especially with low-order filters. For instance, the application of a filter with  $N = 10$  to isolate R1 returns a wavefield where the fundamental mode is still dominant. Therefore, the estimated  $\alpha_R(\omega)$  does not tend to match the corresponding modal value, except at higher frequencies. A similar result is observed for R2, where the degree of fit is improved at high frequencies (Figure 5-21e-f). When using the parameter set  $[k_p; k_s] = [2; 4]$ , the quality of the estimated  $V_R(\omega)$  and  $\alpha_R(\omega)$  is still good and even less sensitive to  $N$ , although some oscillations in  $\alpha_R(\omega)$  are observed at the low-frequency range. These oscillations become more relevant when higher modes are investigated. Finally, results obtained by setting  $[k_p; k_s] = [3; 10]$  exhibit some instability both in  $V_R(\omega)$  and  $\alpha_R(\omega)$ , especially when  $N$  is large.

Instead, Figure 5-22 represents the calibration results of the CFDBFaMF algorithm for SW4. Similar to SW3, the estimated  $V_R(\omega)$  and  $\alpha_R(\omega)$  consistently match the corresponding modal values for all the considered propagation modes, regardless  $N$ . However, this result is valid mainly in the frequency ranges where

each mode dominates the wavefield. Instead, at other frequencies, the filter has to isolate a wave component which is not dominant and quite close to other modes, as the relative distance in the wavenumber domain is quite small. Therefore, the estimated  $V_R(\omega)$  and  $\alpha_R(\omega)$  are sensitive to filter characteristics and they do not tend to match the corresponding modal curves, entailing that the filter does not completely remove undesired wave components. This issue is even more evident when setting larger values of  $[k_p; k_s]$ .

Finally, estimated  $V_R(\omega)$  and  $\alpha_R(\omega)$  for SW3 and SW4 systematically differ from the corresponding modal values at low frequencies, for both FDBFaMF and CFDBFaMF. The factors behind such discrepancy will be addressed in Section 5.4.

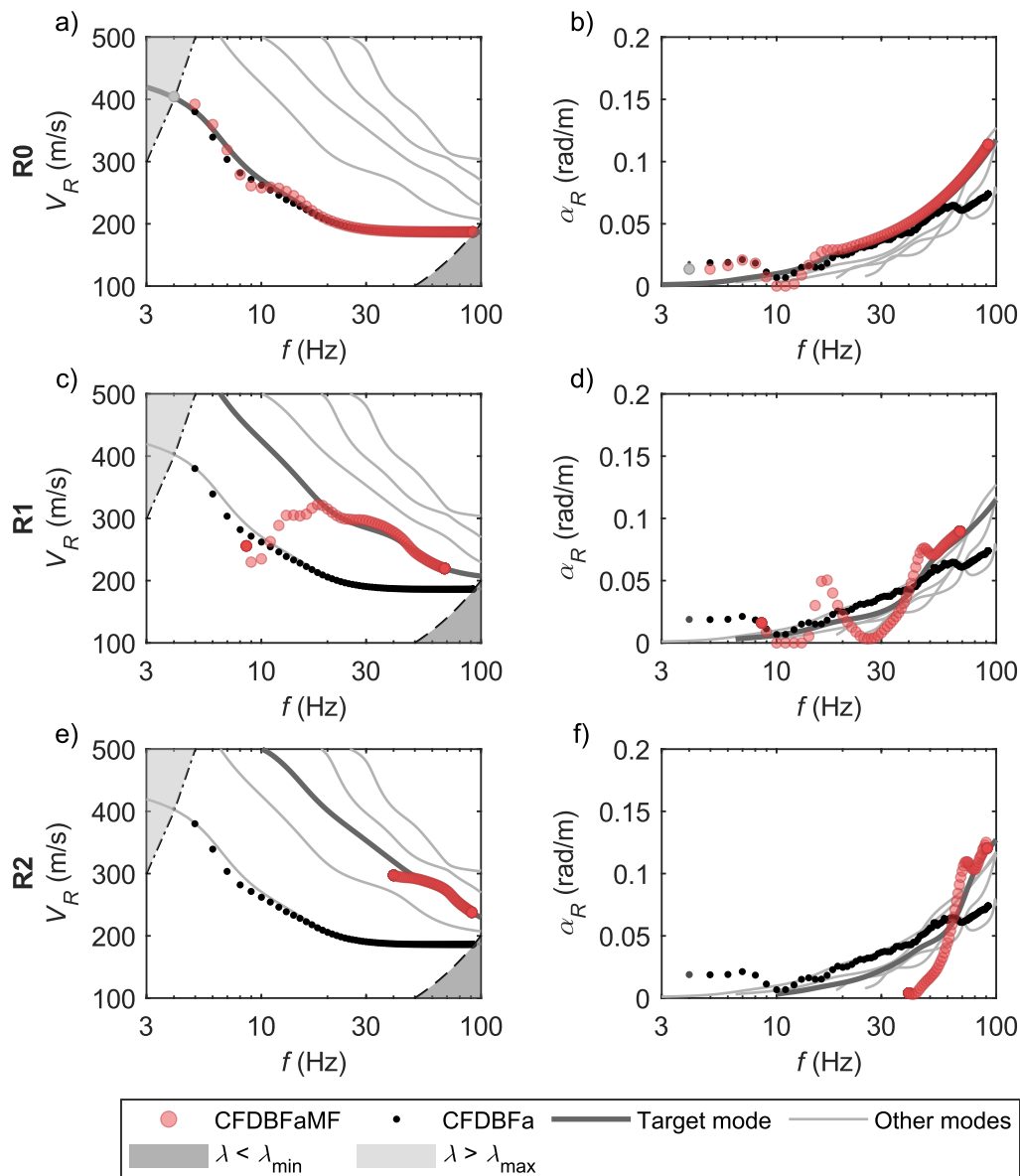


Figure 5-21. Application of the CFDBFaMF algorithm on SW3, with a focus on the first three modes: a-b) Estimated dispersion curves (a) and attenuation curves (b) for the fundamental mode, labeled as R0; c-d) Estimated dispersion curves (c) and attenuation curves (d) for the first higher mode, labeled as R1; e-f) Estimated dispersion curves (e) and attenuation curves (f) for the second higher mode, labeled as R2. Results correspond to the set of parameters  $[k_p; k_s] = [1; 2]$  and  $N = 20$ . Results of the CFDBFa are also reported, for comparison purposes. Estimated data points beyond the array resolution limits – i.e., the grey areas in (a), (c), and (e) – are colored in grey.

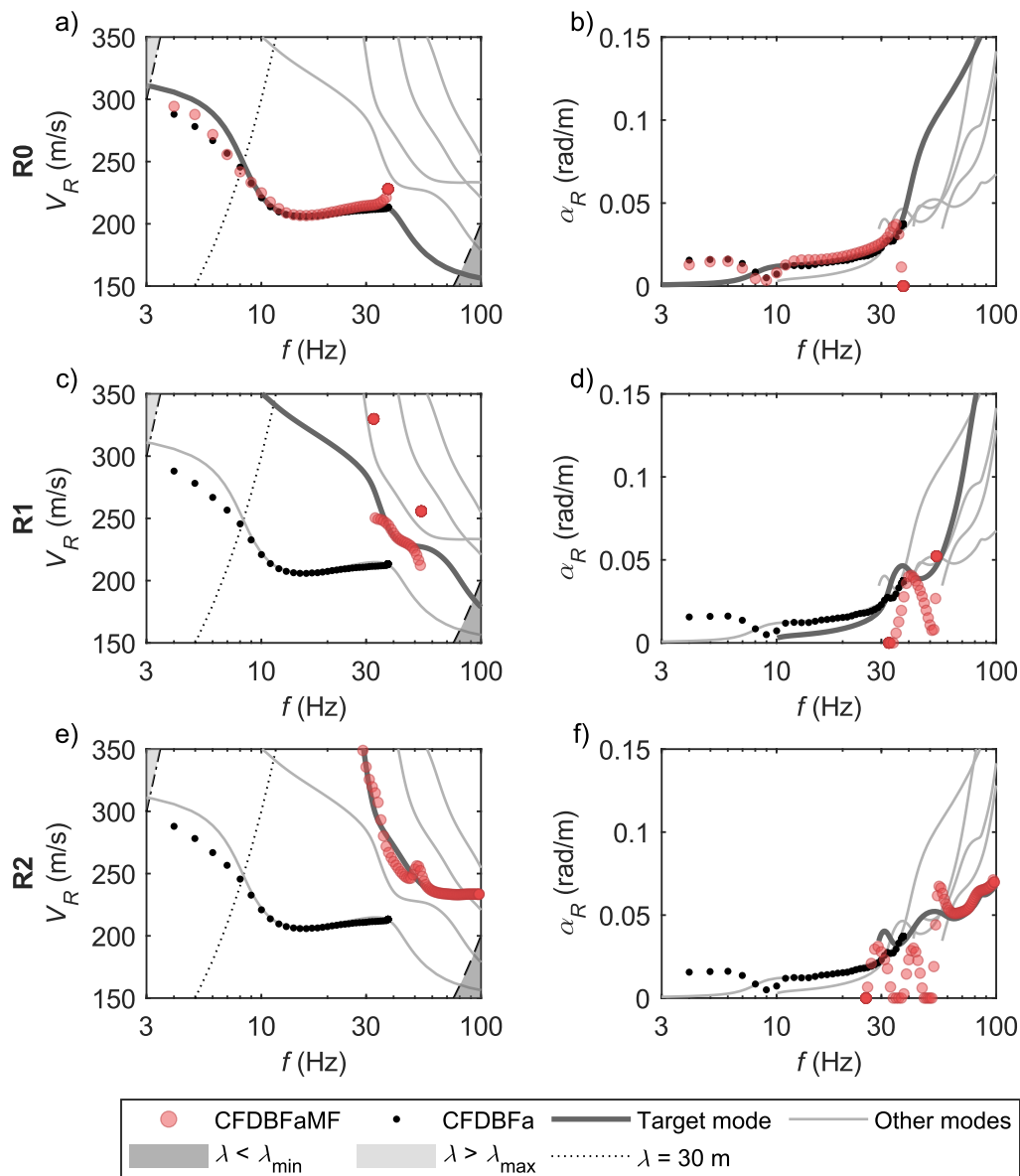


Figure 5-22. Application of the CFDBFaMF algorithm on SW4, with a focus on the first three modes: a-b) Estimated dispersion curves (a) and attenuation curves (b) for the fundamental mode, labeled as R0; c-d) Estimated dispersion curves (c) and attenuation curves (d) for the first higher mode, labeled as R1; e-f) Estimated dispersion curves (e) and attenuation curves (f) for the second higher mode, labeled as R2. Results correspond to the set of parameters  $[k_p; k_s] = [1; 2]$  and  $N = 20$ . Results of the CFDBFa are also reported, for comparison purposes. Estimated data points beyond the array resolution limits – i.e., the grey areas in (a), (c), and (e) – are colored in grey.

## 5.4 Influence of near- and far-field effects

The FDBFa and the CFDBFa techniques rely on the hypothesis that the recorded wavefield consists in an idealized planar or cylindrical Rayleigh wave, respectively. However, in situ recorded data are more complex and the simplifying assumptions about geometrical attenuation might introduce some bias in the estimated values. The collection of mechanisms that are responsible of discrepancies between estimated and expected R-wave parameters due to modeling issues is conventionally labeled as near-field effects. Furthermore, incoherent noise in recorded data may affect the quality of the estimated parameters, introducing a bias termed as far-field effects.

The main source of near-field effects is the model incompatibility. Indeed, usual processing schemes rely on the hypothesis that the recorded wavefield consists solely of Rayleigh waves. Furthermore, some techniques assume that Rayleigh waves propagate according to planar wavefronts. However, the application of a point force onto the surface generates both surface waves and body waves, and surface waves propagate according to cylindrical wavefronts. The discrepancy between the modeled behavior and the actual recorded wavefield leads to adverse effects in the quality and reliability of the estimate. On the one side, the schematization of Rayleigh waves as planar waves results in a drift in the estimated phase velocity, usually with an underprediction (Sanchez-Salinero et al., 1987; Zywicki and Rix, 2005) but sometimes with a positive error (Yoon and Rix, 2009). Furthermore, the lack of an explicit modeling of body waves introduces a perturbation in the recorded data, that maps into oscillations in the low-frequency phase velocity (Rahimi et al., 2021). Actually, such oscillations may also be the effect of Gibbs' phenomenon (Park and Carnevale, 2010). Hopefully, the assumed displacement field well compares with the effective one at moderately far distances from the sources, with respect to the investigated wavelength. Indeed, the cylindrical shape of the wavefront can be approximated by a plane wave model in these conditions, and the contribution of body waves is negligible as they undergo stronger spatial amplitude decay than surface waves. Therefore, the resulting wave parameters gradually acquire reliability as the array distance from the source increases. For this reason, the bias introduced by the plane wave estimator is negligible with increasing frequency (Zywicki, 1999). On the other side, recorded data at great distances from the source are affected by incoherent noise, whose contribution may dramatically alter the estimated wave parameters.

Several numerical and experimental studies addressed near-field effects on dispersion data, with the primary aim to quantify them, for both SASW and

MASW surveys. In general, MASW surveys tend to be less sensitive to near-field effects than the SASW processing (Tokimatsu, 1995; Foti, 2000; Rix et al., 2001b; Foti, 2004). Furthermore, Rahimi et al. (2022) observed a dependence on the acquisition setup and on the number of receivers, as well as the investigated wave, site conditions and the source type. As a result, they proposed criteria to identify a critical condition wherein the related error becomes relevant. These criteria rely on statistical tests (Strobbia and Foti, 2006) and on wavelength-based normalized distances, referred to the closest sensor to the source (Sanchez-Salinerio et al., 1987; Tokimatsu, 1995) or the average location of the array (Li and Rosenblad, 2009; Yoon and Rix, 2009; Rahimi et al., 2021; Rahimi et al., 2022). On the other side, only few studies investigated the influence of near-field effects on the R-wave phase attenuation. Yoon (2005) observed that they induce an overestimation in the low-frequency attenuation, mostly due to the inaccurate modeling of the geometry spreading. Besides, the magnitude of the estimation error is much greater than the bias in the phase velocity. Yoon (2005) also attempted to define a criterion to identify when the effect of the near-field on attenuation data becomes significant, based on the normalized average location of the array. However, the lack of a consistent and clear trend in the estimated attenuation did not allow to identify a threshold value, especially in inversely dispersive media.

This Section aims at understanding the influence of the modeling of the geometrical spreading on the estimated R-wave parameters, with a focus on the phase attenuation. For this purpose, the performance of both the planar-based scheme (i.e., the FDBFa technique) and the cylindrical-based approach (i.e., the CFDBFa technique) are tested in different conditions, with increasing complexity. Specifically, the two methods are applied to interpret an ideal cylindrical wave, also when corrupted by body waves and incoherent noise.

#### **5.4.1 Influence of the cylindrical shape of the wavefront**

A useful example to understand the influence of assumptions about the shape of the wavefront on the estimated R-wave parameters is represented by the synthetic dataset SW2 (see Section 5.1). Indeed, SW2 is an ideal cylindrical wave which may be interpreted as a “pure” Rayleigh wave (i.e., no body waves are included) generated on a homogeneous halfspace due to a monochromatic, unit-amplitude vertical force. The corresponding wave parameters are extracted by means of the FDBFa and the CFDBFa approaches, that model waveform data as a plane wave and as a cylindrical wave, respectively. Estimated wave parameters are listed in Table 5.3.

Table 5.3. Estimated wavenumber and phase attenuation from SW2 data, according to the FDBFa and the CFDBFa approaches. The values in brackets are the ratio between estimated and true values, that provide a measure of the entity of the error.

	FDBFa	CFDBFa	True value
<b>Estimated wavenumber <math>k_e</math> (rad/m)</b>	0.1009	0.1000	$k_R = 0.1$ rad/m
<b><math>[k_e / k_R]</math></b>	[1.0085]	[0.9999]	
<b>Estimated attenuation <math>\alpha_e</math> (rad/m)</b>	0.0013	0.0015	$\alpha_R = 0.0015$ rad/m
<b><math>[\alpha_e / \alpha_R]</math></b>	[0.8564]	[1.0000]	

An explicit modeling of the cylindrical wavefield leads to an almost exact estimate of the wave parameters, whereas the use of a planar scheme results in some discrepancies between theoretical and estimated values. On the one side, the FDBFa tends to slightly overestimate  $k_R$  – although the error is less than 1%. This bias is consistent with various studies on surface wave testing, that claimed that a planar propagation model often underestimates dispersion data (i.e., the resulting wavenumber is excessively large), especially at low frequencies (e.g., Zywicki and Rix, 2005). Instead,  $\alpha_R$  is significantly underestimated when using the FDBFa, with a relative difference around 15%.

The error in both  $k_R$  and  $\alpha_R$  estimates rises from the simplifying assumptions introduced by the planar model, that ignores the actual shape of the wavefront. Indeed, planar and cylindrical waves exhibit significant differences in the spatial variation of the amplitude and phase of the displacement field. Figure 5-23 provides an example on this, comparing SW1 (i.e., a planar wave) and SW2 (i.e., a cylindrical wave). On the one side, the displacement phase of planar wavefield undergoes a linear variation with the offset. Instead, the phase of the cylindrical wavefield does not linearly change with space. As for the displacement amplitude, an effective comparison refers to an alternative metric, equal to the logarithm of the magnitude scaled by the square root of the distance (i.e.,  $|u|_c = \log(r^{1/2}|u|)$ ). According to this specific representation, the  $|u|_c$  of a plane wave is linear with the distance. Conversely, in the presence of a cylindrical wavefield,  $|u|_c$  is strongly nonlinear with the distance. At short distances, this quantity is monotonically increasing from 0 up to a maximum. At large distances, the modified displacement amplitude is monotonically decreasing, and it gradually assumes a linear behavior as the distance is larger. The slope associated with the linear trend equals the exact attenuation, by the virtue of the asymptotic expansion. This result also applies for the displacement phase. Therefore, cylindrical waves are associated with a nonlinear change in both the displacement amplitude and phase with the distance, and this effect is more relevant at low  $k_R$  (hence, low-frequency R-waves).

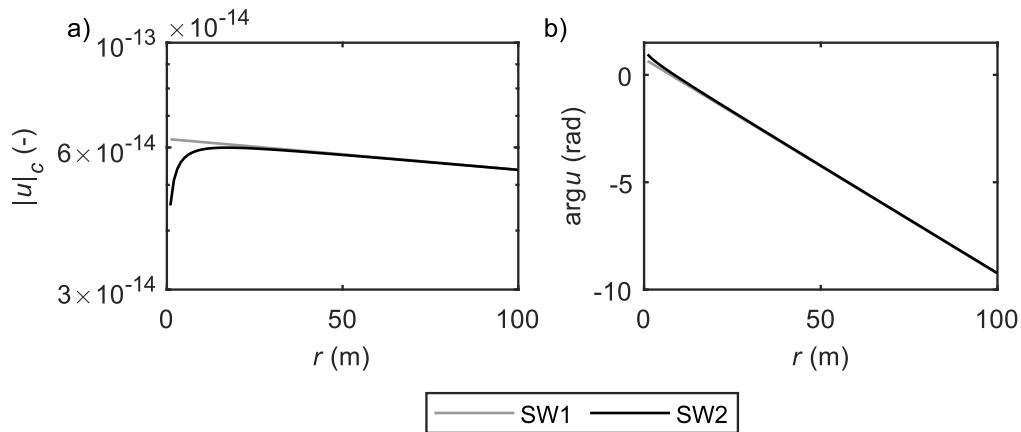


Figure 5-23. Planar wave vs. cylindrical wave, labeled as SW1 and SW2, respectively: amplitude and phase.

By definition, the cylindrical model inherently incorporates the spatial variations in the displacement amplitude and phase linked with cylindrical spreading (Zywicki and Rix, 2005), hence wave parameters are correctly estimated. Instead, interpreting cylindrical wave data according to a planar model returns a plane wave best matching actual displacement data. In other words, the resulting wave exhibits a slope in both the modified displacement amplitude and phase that averages the actual ones. As the actual phase variation with the distance is a convex function, the use of a linear model returns an average slope greater than the slope of the final portion, entailing an overestimation of  $k_R$ . Instead, spatial changes in the modified amplitude occur according to a concave shape, hence constraining observed data with a linear model induces an underestimation of  $\alpha_R$ . Furthermore, as the degree of nonlinearity in the displacement phase is not significant, the wavenumber estimation error introduced by the planar scheme is generally small. Instead, the discrepancy in the estimated attenuation values is much greater, due to the remarkable nonlinear variations in the modified displacement amplitude.

As an additional consequence of the nonlinear spatial changes in the amplitude and the phase of the displacement field with the offset, the estimated plane-wave parameters are dependent on the considered distance range. Indeed, acquisition setups located far from the source tend to return similar estimates of wave parameters both with the planar and the cylindrical estimators, as the displacement exhibits a quasi-linear variation with the offset. On the converse, at short offsets from the source, the strong nonlinearity results in large differences between the estimates.



Thus, modeling the propagation of R-waves as plane waves would disregard actual shape of the wavefront, entailing a bias in the estimated phase wavenumber and the attenuation, especially for the usual offsets adopted in active-source SWM. This may dramatically alter the resulting damping ratio profile at greater depths. For this reason, an accurate modeling of the geometric spreading is crucial to achieve robust and reliable estimates of dispersion and attenuation data. For this reason, an explicit modeling of the geometry of the cylindrical modeling has been strongly recommended by several Authors, as a tool to mitigate near-field effects, due to the proper modeling of geometric spreading (Rahimi et al., 2021). Thus, the CFDBFa is a superior technique with respect to the use of a planar model.

#### **5.4.2 Influence of body waves: results for SW3 and SW4**

A more thorough investigation of the differences induced by the planar model and the cylindrical model on the estimated wave parameters requires a comparison on a more realistic wavefield. For this purpose, the synthetic wavefields SW3 and SW4 are an additional benchmark to address the role of the geometric spreading assumptions on the derived R-wave parameters. Indeed, both wavefields mimic the output of a usual MASW survey, carried out on realistic soil profiles. Furthermore, the study of these wavefields includes additional elements of complexity with respect to SW2, as they combine multiple R-wave propagation modes, as well as body waves.

Figure 5-24 compares the estimated dispersion and attenuation curves for SW3 and SW4, computed through the FDBFaMF and the CFDBFaMF techniques. Reported data are sampled with a sampling frequency of 1 Hz, across the frequency band ranging between 3 Hz and 100 Hz. The graph includes estimated wave parameters for the fundamental mode only, for simplicity. However, the following considerations are also valid for higher modes. Furthermore, the regions associated with wavelengths beyond the resolution limits of the simulated array are highlighted, as the corresponding results should be interpreted with care. The discussion reported in this section does not focus on the compatibility between estimated and theoretical wave parameters, as a more detailed description on this is provided in Chapter 7. However, the target mode obtained from the solution of the Rayleigh eigenvalue problem is represented, as a reference. Instead, the differences between the FDBFaMF and the CFDBFaMF estimates are addressed, to focus on the influence on the effect of the geometric spreading assumption.

For both SW3 and SW4, the FDBFaMF and the CFDBFaMF return rather similar estimates of dispersion data and attenuation data. Furthermore, derived dispersion curves almost equal the corresponding theoretical ones especially at high frequencies. Instead, low-frequency data undergo some oscillations around the target value. This oscillation might be an artifact introduced by other wave components (e.g., body waves), whose contribution is usually significant in this range (Rahimi et al., 2021). As for  $\alpha_R(\omega)$ , the FDBFaMF and the CFDBFaMF underestimate the phase attenuation close to 10 Hz, perhaps due to some influence of the first higher mode, whose contribution to the wavefield might not have been completely removed by the modal filter. At lower frequencies, they tend to overestimate it, with a relative error which is on average much greater than the corresponding one on dispersion data. Specifically, at low frequencies, the estimation attenuation can be even tens or even hundreds of times greater than the theoretical value.

In summary, the performance of the two schemes on SW3 and SW4 is almost identical, hence the cylindrical and the planar model return similar results, regardless the investigated frequency (or wavelength) range. Furthermore, both approaches undergo similar errors in both dispersion and attenuation in the low-frequency range. This result contradicts the findings obtained from the analysis of SW2, that demonstrated the superiority of the explicit modeling of the cylindrical wavefield to reliably derive R-wave parameters. However, such conclusion is valid for a rather simplified case, where the recorded wavefield consists in a unique cylindrical wave, that may be interpreted as an ideal Rayleigh wave. Instead, SW3 and SW4 are a superposition of multiple Rayleigh propagation modes, where also body waves contribute to the simulated particle displacement. Actually, the influence of the multimodal nature of the wavefield should not be significant at low frequencies, as the displacement field mostly depends on the fundamental mode, especially for SW4. Therefore, the influence of body waves in the recorded wavefield may be the reason for which a more accurate modeling of the geometrical spreading of the wavefield is not sufficient to improve the quality of the estimated R-wave parameters, especially at low frequencies. Even, it appears that the improvement introduced by an explicit model of the cylindrical wavefront is canceled by the effect of body waves. A more detailed study on the influence of body waves in the estimated R-wave parameters is presented in the next Section.

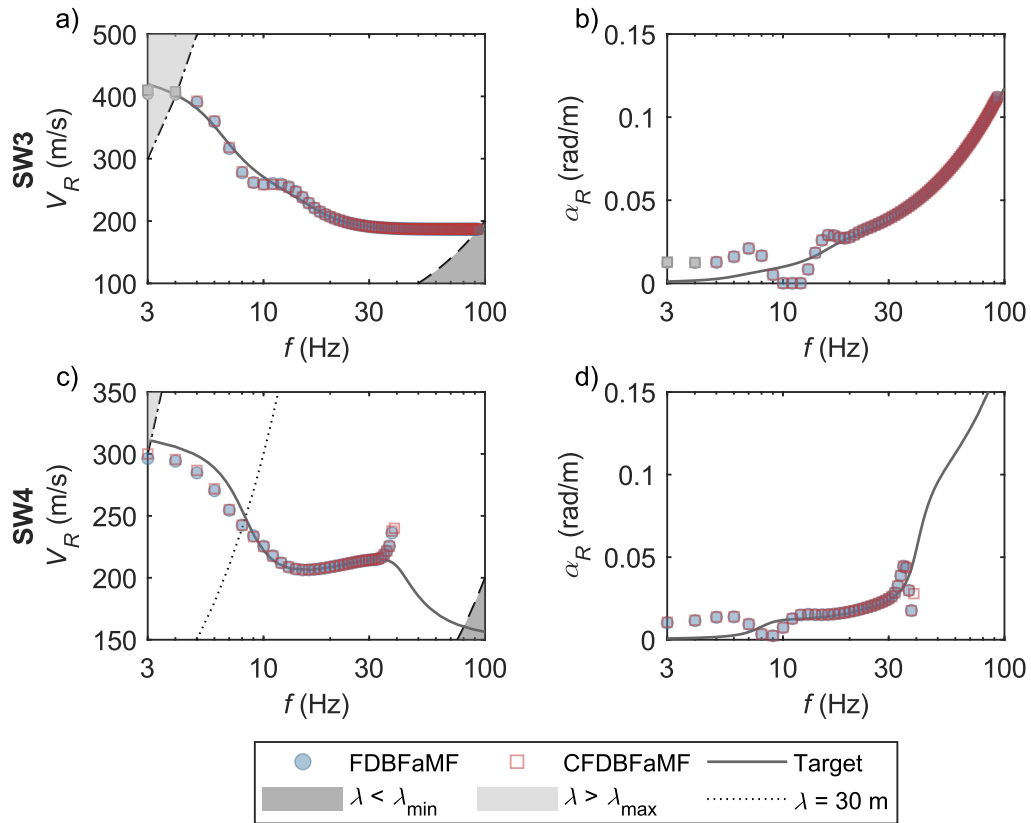


Figure 5-24. Extracted fundamental-mode dispersion and attenuation curves for SW3 and SW4, for the FDBFaMF and the CFDBFaMF: a-b) Estimated dispersion curves (a) and attenuation curves (b) for SW3; c-d) Estimated dispersion curves (c) and attenuation curves (d) for SW4. Results refer to the fundamental mode only. Estimated data points beyond the array resolution limits – i.e., the grey areas in (a), (c), and (e) – are colored in grey.

### 5.4.3 Influence of body waves: parametric analysis

To better understand the influence of body waves on estimated R-wave parameters, the wavefield SW2 is modified to include their contribution. The new synthetic wavefield (hereafter labeled as SW2-B) is the solution of a boundary value problem, which models the response (in terms of vertical displacement on the free surface) of a homogeneous half-space to a vertical, unit-amplitude, harmonic force applied onto the free surface. The direct stiffness approach was adopted to solve the problem, by means of the EDT software (Schevenels et al., 2009). In this way, the corresponding wavefield is the combination of both body and Rayleigh waves. The mechanical properties of the medium are the following:  $V_S$  is 336 m/s,  $V_P$  is 698 m/s,  $D_S$  and  $D_P$  both equal 0.015, and  $\rho$  is 2,000 kg/m<sup>3</sup>.

The adopted values are the result of a calibration study, so that the solution of the R-wave eigenvalue problem returns wave parameters identical to those of SW2. Thus, SW2-B is equivalent to SW2, but it includes the additional contribution of body waves.

Table 5.4 compares the estimated R-wave parameters for SW2-B, obtained by means of the FDBFa and the CFDBFa approaches. This result provides useful insights about the relative performance of the planar and the cylindrical beamformer in the combined presence of body waves and cylindrically-spreading surface waves. As in SW2 (Table 5.3), the FDBFa and the CFDBFa tend to return quite similar results. However, both the planar and the cylindrical model slightly overestimate  $k_R$ , with a relative error of about 4.5%. Besides, the CFDBFa returns a slightly more reliable estimate. Conversely, both approaches strongly overestimate  $\alpha_R$ , as they return a value which is some 5.5 times greater than the theoretical one. Even, the error associated with the cylindrical model is a bit larger than the one obtained according to the planar scheme.

Table 5.4. Estimated wavenumber and phase attenuation from SW2-B data, according to the FDBFa and the CFDBFa approaches. The values in brackets are the ratio between estimated and true values, that provide a measure of the entity of the error.

	FDBFa	CFDBFa	True value
Estimated wavenumber $k_e$ (rad/m)	0.1052	0.1041	$k_R = 0.1$ rad/m
$[k_e / k_R]$	[1.0520]	[1.0410]	
Estimated attenuation $\alpha_e$ (rad/m)	0.0085	0.0088	$\alpha_R = 0.0015$ rad/m
$[\alpha_e / \alpha_R]$	[5.6667]	[5.8667]	

The reason behind the biased velocity and attenuation estimates derives from the discrepancies between the planar or cylindrical model and the actual spatial changes variation of the amplitude and phase of the displacement field of SW2-B (Figure 5-25). On the one side, the displacement phase of SW2-B occurs with a steeper slope than SW2, thus resulting in a slight overestimation of  $k_R$ . Furthermore, the inclusion of body waves dramatically affects the spatial variation of the displacement amplitude. With a focus on the corrected amplitude  $|u|_c$ , this quantity is much greater than the one obtained for SW2 at short offsets, and it exhibits more complex changes. Besides, the amplitude undergoes large changes over a moderately narrow range of distances. This is a clear footprint of the presence of body waves, as they are affected by stronger geometric attenuation than surface waves. The combination between the different shape – the corrected amplitude tends to behave as a convex function – and the broader range of encompassed amplitudes result in a strong overestimation of  $\alpha_R$ , when SW2-B is

modeled according to a planar or a cylindrical scheme (i.e., according to the FDBFa and the CFDBFa, respectively).

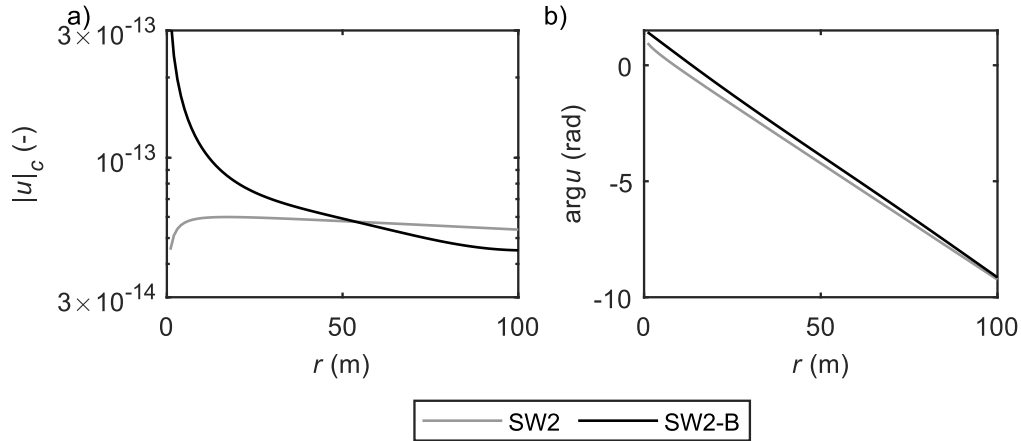


Figure 5-25. Cylindrical wave and body wave: amplitude and phase.

Results reported in Table 5.4 provide a first insight on the influence of near-field effects on the estimated R-wave parameters. However, this result does not have general validity. Indeed, due to the complexity and the remarkable nonlinearity in the amplitude and phase variation of the displacement field with the offset, the entity of the estimation error introduced by the planar and of the cylindrical estimators is sensitive to the investigated offset range. On the one side, the interpretation of waveform data recorded quite close to the source tends to return moderately biased estimates, because of the relevant contribution of body waves, that are not modeled. As body waves strongly attenuate with the distance, data acquired far from the source tend to return more accurate estimates of wave parameters, asymptotically matching the exact values at very large distances. Actually, this result is valid only on a theoretical basis, because real data are corrupted by incoherent noise, that mostly affects at great distances.

The influence of the average distance on the quality of the estimated R-wave parameters is addressed in a parametric study, where SW2-B is assumed to be recorded according to different acquisition layouts. The simulation considers different ideal uniformly-spaced sensor arrays, the geometry of which can be described by three parameters: the number of sensors  $n$ , the inter-receiver spacing  $\delta$ , and the offset between the source and the closest receiver  $r_l$ . The adopted  $n$  were equal to 12, 24, 48, and 100, as they are compatible with the number of geophones usually adopted in ordinary MASW surveys. As for  $\delta$ , several values were included, namely 0.3 m, 0.5 m, 1 m, 1.5 m, 2 m, 2.5 m, 3 m, 5 m, 10 m, 15 m, 20 m, and 30 m. The large number of values attempts to model different

acquisition geometries, and the maximum inter-receiver spacing complies with limitations by the Nyquist-Shannon theorem, to properly process SW2-B without undergoing aliasing. Finally,  $r_l$  is chosen as an integer multiple of the sensor spacing, where the multiplying factor equals 1, 3 and 5, respectively. Thus, a total of 144 ideal acquisition geometries is modeled.

For the sake of simplicity, each idealized testing setup is synthetically described in terms of the normalized array center distance (NACD; Yoon and Rix, 2009). This quantity is defined as the ratio between the gravity center of the array (i.e., the average between the sensors' locations) and the investigated R-wave wavelength:

$$NACD = \frac{1}{N} \frac{\sum_{i=1}^N r_i}{\lambda_R} \quad (5.18)$$

In this case,  $\lambda_R$  equals 62.8 m as  $k_R$  is 0.1 rad/m in SW2-B. The NACD combines both information about the MASW acquisition geometry and the target R-wave, the latter expressed in terms of the wavelength. Large NACD values are representative of array setups that, on average, are far from the source, with respect to the investigated wavelength. The usefulness of this parameter is twofold, as it condensates the whole array geometry into a single parameter and it is effective in describing discrepancies due to model incompatibility issues.

For each acquisition setup, SW2-B data are processed both with the FDBFa and the CFDBFa, thus obtaining estimates associated with the planar and the cylindrical estimator. To address the reliability of the estimators, a comparison between the resulting R-wave parameters and the corresponding theoretical values takes place by considering the normalized estimates (Yoon and Rix, 2009). Each of these quantities is defined as the ratio between the estimated R-wave wavenumber (or attenuation) and the corresponding ideal value. Figure 5-26 summarizes the results of the parametric analysis, reporting the normalized wave parameters as a function of the NACD. Note that results also include values obtained from rather short arrays compared to the investigated wavelength, with the aim to investigate this condition. Indeed, in this case the wavenumber resolution is not an issue being the wavefield composed by a single Rayleigh mode. However, as these data points are representative of conditions not usually investigated in MASW surveys, they are highlighted with a transparent layer.

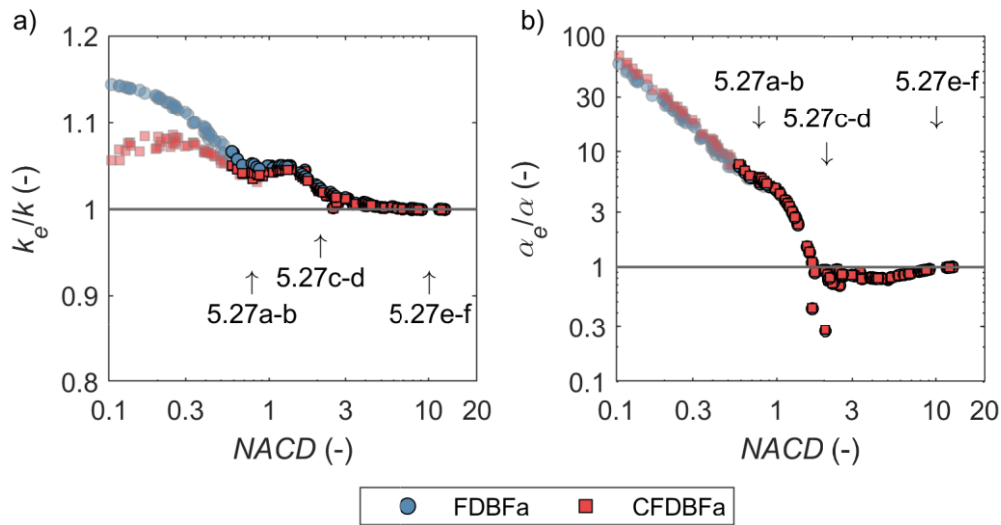


Figure 5-26. Results of the parametric analysis to assess the influence of body waves on the estimated R-wave parameters, represented in terms of normalized values vs. normalized array center distance NACD: a) Wavenumber; b) Attenuation. Results for the planar beamformer (i.e., FDBFa) and the cylindrical beamformer (i.e., CFDBFa) are reported. The annotations denote the points specifically analyzed in Figure 5.27.

Both the planar and the cylindrical model return identical and reliable estimates of the wavenumber and the attenuation when the NACD is large, i.e. when the acquisition is carried out at large distances from the source. As the NACD reduces down, both the wavenumber and the attenuation are overpredicted, with a gradually increasing estimation error. However, the entity in the discrepancy in the wavenumber estimate is sensibly different from the one for the attenuation. As for the wavenumber, the estimators tend to slowly diverge from the unit value at NACD less than 3. Specifically, the planar scheme returns monotonically increasing wavenumber estimates, and the normalized value grows up to 1.2. When referring to the cylindrical model, the normalized value is quite smaller and slightly oscillates around a center point close to 1.1. This oscillatory behavior in the estimated dispersion data is a direct effect of body waves, as confirmed by various in-situ observations (Rahimi et al., 2021). Notwithstanding these differences, the bias introduced in dispersion estimates by not properly incorporating body waves is less than 10%, and it becomes negligible at normalized distances greater than 1. When focusing on the attenuation, instead, the entity of the estimation error dramatically changes. Indeed, both schemes tend to significantly overpredict the attenuation at short NACD values, with a sudden deviation of the normalized value from the unit at NACD close to 2. Besides, at shorter distances, they return attenuation estimates even 10÷100 times greater than

the theoretical one. Furthermore, the difference in both models is qualitatively negligible. Although the drop in the bias magnitude as NACD increases is steeper than the one in the wavenumber, the error in the attenuation estimate is relevant even at moderately large distances. Indeed, the error starts to be negligible only at normalized distances greater than 2, and it still assumes some minor oscillation at even greater distances.

To identify the reasons behind such discrepancies, Figure 5-27 reports some results of the processing, with reference to three different arrays, representative of increasing NACD values and highlighted in Figure 5-26. For each acquisition setup, the graphs represent both the displacement field induced by SW2-B (i.e., the combination of body and Rayleigh waves) and the one associated with SW2 (i.e., R-waves only). The latter represents the theoretical Rayleigh wavefield. Furthermore, the actual wavefield is overlapped with the displacement field obtained according to the estimated parameters. Interestingly, the displacement phase of SW2-B is almost linear throughout the whole range of investigated distances. Therefore, both the planar and the cylindrical estimators return similar wavenumber data, that are rather close to the theoretical one for any considered array. Instead, the spatial variation of the modified amplitude  $|u|_c$  exhibits a strongly nonlinear trend, which is sensibly different from the one ideally assumed by a cylindrical wave or a planar wave, especially at short NACD (i.e., less than  $1 \div 2$ ). In this case, the contribution of body waves on the wave amplitude is overwhelming. As a consequence of the incompatibility between the modeled and the actual spatial variation of the amplitude, both the planar and the cylindrical beamforming strongly overpredict the attenuation. Indeed, these schemes interpret the combined amplitude decay of body waves and surface waves as only an amplitude decay of a cylindrical (or planar) wave, thus overestimating the wave attenuation. As the NACD increases, the spatial variation of the amplitude is still not fully compatible with the one of a pure cylindrical wave. Specifically, the amplitude undergoes some oscillations, perhaps induced by some destructive interference between the body and the surface waves. However, the average slope approaches the one of the corresponding R-wave (i.e., SW2). Therefore, the estimated wave attenuation gradually approaches the expected value. Similarly, at great distances some oscillations in the amplitude trend are still noticeable, but the strong linearity and the closeness to the ideal trend results in attenuation estimates rather close to the theoretical value.



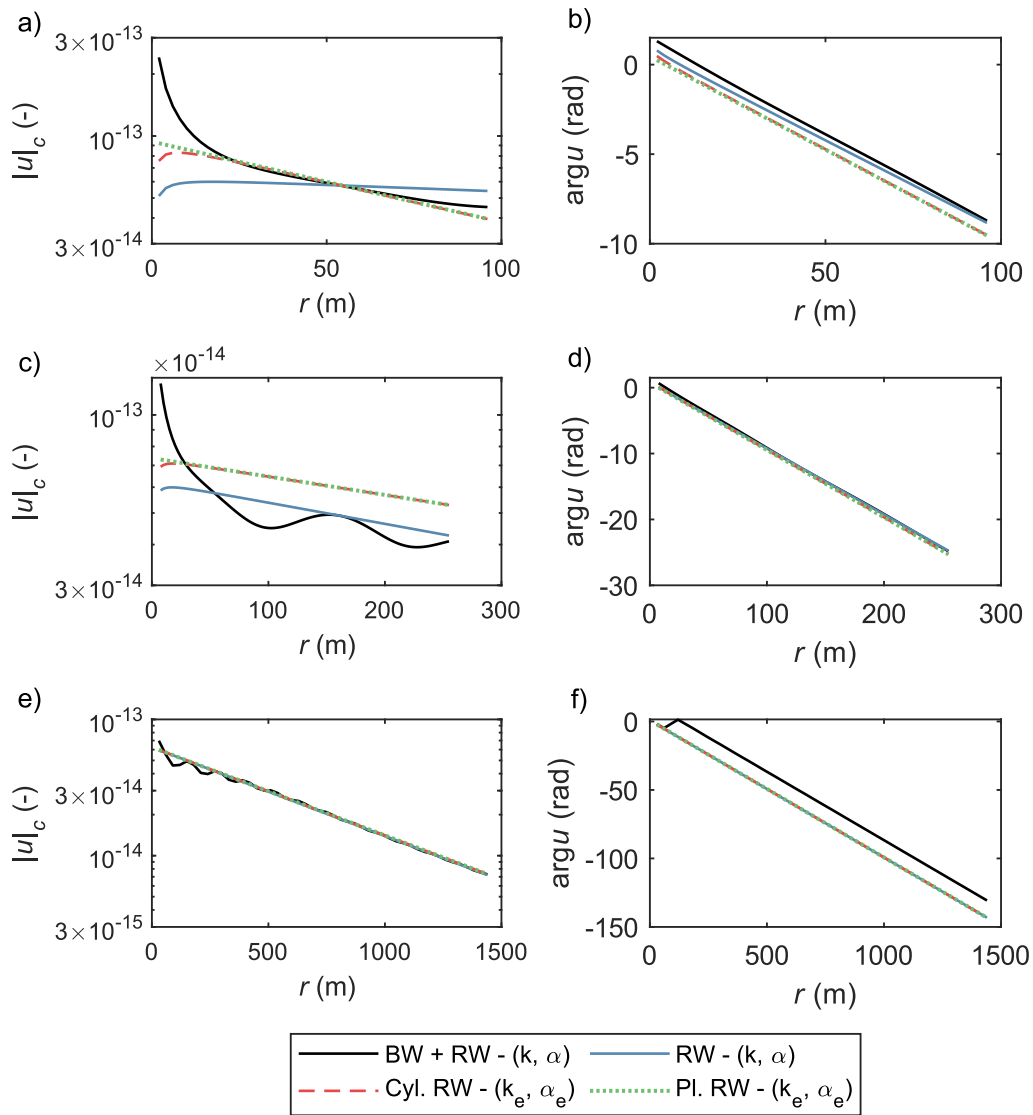


Figure 5-27. Spatial variation of the displacement measured in three virtual arrays (rows of the grid of plots), the location of which (in terms of NACD) is represented in Figure 5.26. The displacement is represented in terms of amplitude (left column) and phase (right column).

In summary, the improvement in the quality of the estimated parameters introduced by an explicit modeling of the geometric spreading is partially balanced by the presence of body waves. In this condition, both the planar and the cylindrical scheme return similar estimates of wave attenuation when the wavefield includes body waves. On the other side, the use of a cylindrical beamformer still improves the quality in the dispersion estimate, as the bias affecting the estimated wavenumber is smaller with respect to the planar model.

#### 5.4.4 Influence of incoherent noise

The investigation of the influence of near-field effects on the estimated phase velocity and phase attenuation highlighted that the lack of an explicit modeling of the contribution of body waves in the displacement field results in a slight deviation in the wavenumber and in a strong overestimation of the attenuation. The entity of the bias decreases as the average distance of the acquisition array is moderately large compared to the investigated wavelength, and it becomes negligible at NACD greater than 2. In ideal conditions, as body waves strongly attenuate with distance, data acquired far from the source tend to return more accurate estimates of wave parameters, asymptotically matching the exact values at very large distances. Actually, this result has only theoretical validity because the modeled displacement data include only the contribution of the true wavefield, not accounting for incoherent noise which affects field data. In fact, ambient random noise may dramatically affect estimated wave parameters. Furthermore, the influence of noise is most relevant at sensors far from the source, due to the amplitude decay of the signal. For this reason, any perturbation in the resulting wave parameters due to incoherent noise is usually labeled as “far-field effects”.

The influence of incoherent noise on the quality of the estimated R-wave parameters is investigated in a similar parametric analysis to the previous one, where a wavefield composed by the combination of SW2-B and white noise is assumed to be recorded according to different acquisition layouts. This study adopts the same suite of ideal acquisition geometries used to inspect near-field effects. Thus, the influence of body waves and of incoherent noise are jointly involved and investigated, as a function of the average array location – expressed in terms of NACD.

The noise modeling requires a Monte Carlo procedure to simulate its random nature. This study adopts a white gaussian noise model, where the noise assumes a normal distribution. The selection of an adequate power level of the noise is critical, in order to reproduce noise conditions usually affecting in situ recorded data. A valid reference might consist in comparing the noise level with the ground force applied by the active source. For instance, the noise amplitude measured at the Garner Valley Downhole Array and the Hornsby Bend sites equals  $10^{-8} \div 10^{-6}$  m/s (this value is compatible with the common noise range identified by Peterson, 1993), whereas the force magnitude ranges between  $10^3$  N (for light sources) and  $10^4$  N (for vibrators). Therefore, a realistic noise level can be obtained by scaling down the input force by a factor equal to  $10^{-12}$ . This assumption reproduces typical signal-to-noise conditions when a mechanically-controlled source is used.

In the Monte Carlo procedure, recorded data are simulated as the sum of the “true” signal (i.e., SW2-B) and the gaussian noise. The simulation involves 50 random samples, namely 50 noisy signals. The number of generated signals adequately reproduces the stochastic process, as it allows to achieve a stable estimate of the mean value and the standard deviation of both the displacement amplitude and phase, regardless the location of the virtual sensor. Figure 5-28 represents the simulated waveforms in the stochastic procedure, in terms of displacement amplitude and phase, compared with SW2-B. On average, the displacement phase well matches the theoretical one, whereas the amplitude exhibits a gradually increasing positive deviation at great distances from the source. At these locations, the noise becomes gradually relevant in the recorded data, due to the attenuation of SW2-B, and the average amplitude converges towards the noise level. As for the data variability, the coefficient of variation (CoV) of the amplitude exhibits a quasi-linear increase with the distance, that asymptotically converges at 0.7, which is associated with the predominant noise level. Instead, the phase CoV is almost null across a broad range of distances, and it starts increasing only at  $r > 500$  m, due to the strong influence of noise in this range.

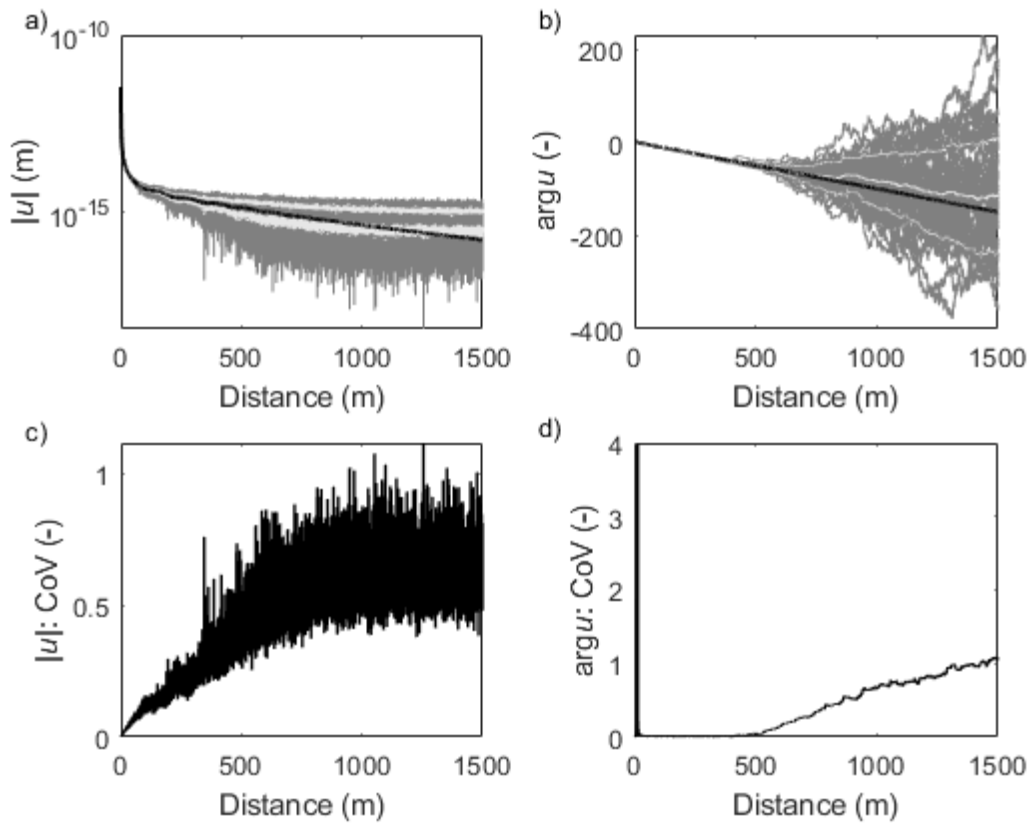


Figure 5-28. Results of the Monte Carlo procedure to simulate the presence of incoherent noise in the recorded signal: a-b) Randomized signals, represented in terms of amplitude (a) and phase (b); c) Variability in the amplitude; d) Variability in the phase. The sample signals in a-b) are overlapped by the noiseless signal (thick black line) and by the intervals defined by the mean and one standard deviation (thin red lines).

Waveform data for every stochastic signal are processed both with the FDBFa and the CFDBFa, thus obtaining estimates associated with the planar and the cylindrical estimator, for each acquisition setup. As in the previous Section, the geometry of each array layout is described in terms of NACD, whereas the normalized wavenumber and the normalized attenuation are used as metric to assess the reliability of the estimated R-wave parameters. Every virtual array is associated with a collection of normalized wave parameters, each obtained from a single randomized signal. As an effect of incoherent noise, these data are randomly distributed along a certain range. Figure 5-29 reports the resulting normalized wave parameters as a function of the NACD, in which the statistical distribution is synthetically described by errorbars, centered at the median value and with extent equal to the logarithmic standard deviation. Indeed, the variability in the estimated wave parameters due to incoherent noise can be modeled as a

lognormal distribution (Figure 5-30a-b). This kind of model well describes the statistical distribution of attenuation data, as it well captures the skewness and it ensures that negative values have no probability of occurrence. However, wavenumber data are also well matched by the gaussian model, consistently with other studies (e.g., Lai et al., 2005b).

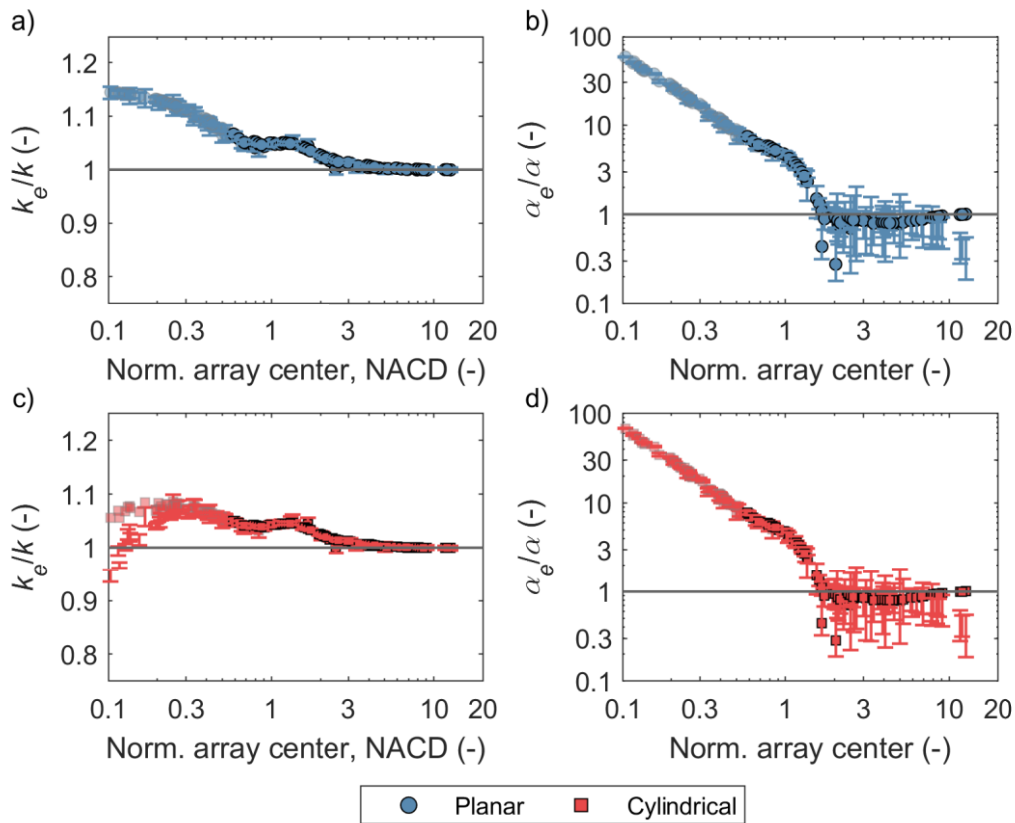


Figure 5-29. Results of the parametric analysis to assess the influence of body waves and incoherent noise on the estimated R-wave parameters, represented in terms of normalized values vs. normalized array center distance NACD: a-b) Normalized wavenumber and attenuation estimates for the planar beamformer (i.e., FDBFa); c-d) Normalized wavenumber and attenuation estimates for the cylindrical beamformer (i.e., CFDBFa). The errorbars denote the interval defined by the mean and one standard deviation for each simulated acquisition layout. Results obtained from the parametric analysis on SW2-B are included, as a reference.

When using the planar or the cylindrical scheme under the combined presence of body and cylindrical waves and incoherent noise, an excellent degree of matching occurs for the wavenumber along the whole investigated NACD range. Besides, the variability in the estimated data is generally small (i.e.,  $\sigma_{ln}$  less than 0.02) and it slowly decreases at greater NACD values (Figure 5-30c). However, at rather small NACD, the cylindrical scheme tends to systematically underestimate

the wavenumber. As this deviation does not occur when analyzing SW2-B data, the loss of reliability of this scheme is an effect of the incoherent noise. Therefore, the cylindrical beamformer appears to be not robust in the presence of incoherent noise. On the other side, this issue is observed only at rather small NACD values, that are not usually involved in usual MASW processing, as beyond the typical resolution limits. At  $\text{NACD} > 0.3$ , the drift is negligible and the average normalized wavenumber is smaller than the one obtained according to the planar beamformer. Therefore, the cylindrical model is still effective, when focusing on a range of investigated wavelengths, compatible with the array resolution limits. Furthermore, the variability in the estimated wave parameters is almost identical for the two schemes (Figure 5-30c).

When focusing on the attenuation, instead, the mean normalized attenuation starts to deviate from the deterministic trend at moderately large NACD values, i.e.  $\text{NACD} > 5$ , and the inclusion of noise generally induces a significant underestimation of the true attenuation. Indeed, in arrays quite far from the source, the noise level is a relevant component in the recorded signal and the ideal spatial decay is partially masked by the noise, whose spatial stationarity induces a reduction in the estimated attenuation. Furthermore, the variability in the normalized attenuation is much larger than the corresponding  $\sigma_{\text{ln}}$  for the wavenumber, and it exhibits a nonlinear increase with the NACD, up to 1 at NACD close to 3 (Figure 5-30d). The large variability in the estimated attenuation is a direct consequence of the broad range encompassed by the simulated displacement amplitude data, the variability of which gradually increases as the NACD grows (Figure 5-28). Finally, no significant influence of the geometrical spreading model on the estimated attenuation is observed, as the corresponding reliability and variability are identical.

In summary, the presence of incoherent noise in the recorded wavefield implies a significant drop in the accuracy of conventional schemes to infer R-wave parameters, relying on the planar and the cylindrical scheme. Besides, this affects also the reliability in the estimated attenuation. On the one side, the addition of incoherent noise does not significantly affect the quality of the estimated wavenumber, as the average does not drift from the value obtained in noiseless conditions. Furthermore, the accuracy in the estimate is rather high, due to the small  $\sigma_{\text{ln}}$ . Instead, the influence of incoherent noise on the inferred phase attenuation is highly dependent on the NACD. Indeed, at short distances, only a slight reduction in accuracy occurs. For increasing NACD, instead, the incoherent noise induces a significant loss in the accuracy, combined with a reduction in reliability, due to the drift of the mean value at great NACD values. Therefore, the

presence of incoherent noise in the recorded wavefield exerts a twofold negative effect on the quality of the estimated attenuation at great distances, with a loss of both reliability and accuracy. This result also highlights that good quality attenuation estimates can be achieved only at a limited range of distances from the sources, where both the influence of body waves and incoherent noise are minimized. In this specific case, the optimal range of NACD varies between 2 and 4. However, a proper analysis of the wave attenuation must not disregard the strong variability intrinsically affecting the estimate, which is a direct effect of noise. These issues are much less relevant in the dispersion analysis, as conventional estimators usually return reliable and accurate estimates of the R-wave wavenumber, at almost all the NACD values and noise levels.

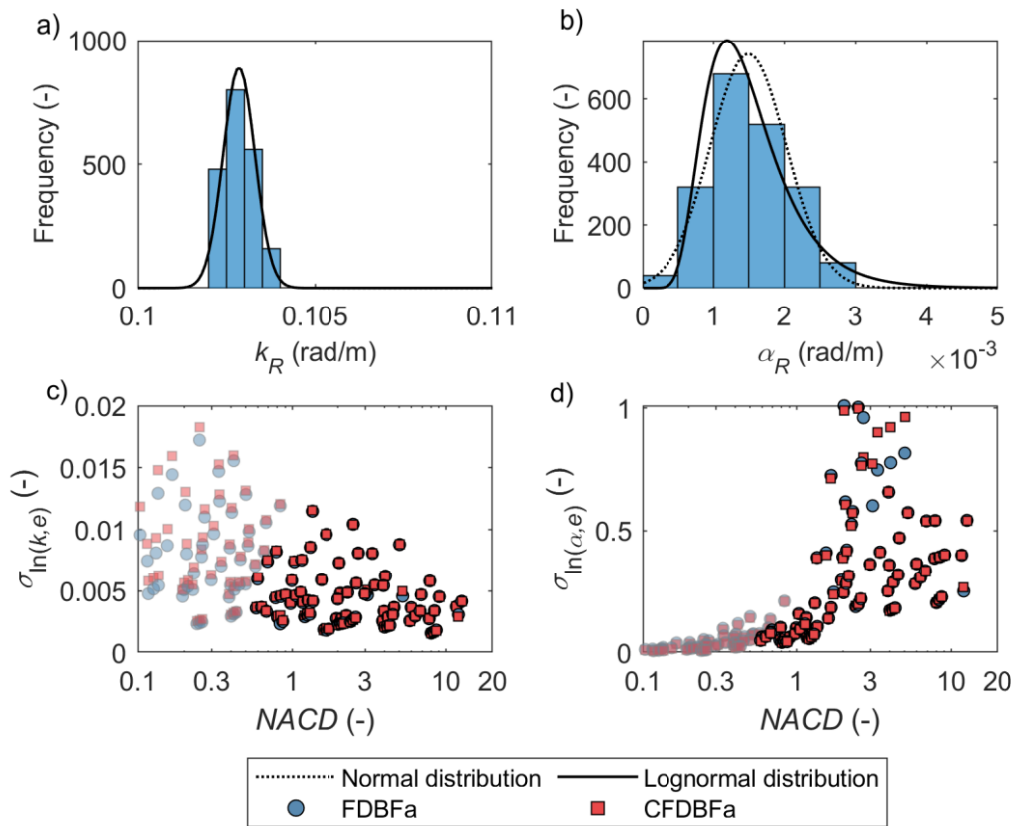


Figure 5-30. Results of the parametric analysis to assess the influence of body waves and incoherent noise on the estimated R-wave parameters. a-b) Comparison between the theoretical distribution, according to the normal and the lognormal model, and the empirical one: a) Estimated wavenumber; b) Estimated attenuation. c-d) Variability in the estimates: c) Variability in the estimated wavenumber; d) Variability in the estimated attenuation. Results in a-b) refer to NACD = 2.

## 5.5 Summary

This Chapter presented a novel family of techniques, named as FDBFa and CFDBFa, for the estimation of the Rayleigh wave dispersion and attenuation data. Both techniques rely on a transformation of the wavefield, that allows to obtain the phase attenuation by carrying out a dispersion analysis on transformed data. In this way, a robust estimate of the phase attenuation can be achieved, by using a computationally fast algorithm. As the FDBFa and CFDBFa assume that the recorded wavefield consists of a single mode, they theoretically return an estimate of the effective phase velocity and phase attenuation, that might not be coincident with modal values. Therefore, an additional step has been included in the proposed algorithms, in which each propagation mode is isolated to fulfil the main assumptions of the FDBFa and CFDBFa. The modified algorithms are named FDBFaMF and CFDBFaMF, respectively. The extraction of each wave component is carried out by applying a bandpass filter to the recorded wavefield, that preserves the mode of interest and removes additional waves. However, the design of an effective filter is nontrivial because the capability to separate the desired component depends on a suite of parameters, for which an a priori choice is often impossible. For this purpose, a calibration study has been carried out, to address the influence of filter parameters on the estimated wave parameters. In general, moderately narrow, intermediate-order filters allow to obtain reliable estimates of the modal dispersion and attenuation curves. For instance, filters with order  $N = 1/2 \div 2/3$  times the number of receivers, passband extended up to  $k_{res}$  (i.e., the resolution wavenumber of the array) and stopband starting from  $2k_{res}$  may be considered as a valid reference for applying the FDBFaMF and CFDBFaMF in various site conditions. Indeed, the corresponding estimates of Rayleigh wave parameters are almost identical to the theoretical values, especially when the target mode is dominant. Thus, the modal filtering technique can be an effective tool for a broad variety of surface wave applications. However, this technique can only be applied to uniformly sampled spatial data, whereas it is not compatible with waveforms measured in irregular arrays. Furthermore, it is less effective when data include a small number of spatial samples, as the usable filter order is so low that it cannot effectively isolate the desired wave component. Specifically, the filtering procedure is valid when at least 20÷24 receivers are available. These issues will be addressed in future studies, to generalize the modal filtering technique and improve its robustness also in these cases.

The last section of this Chapter addressed the influence of alternative models of the geometric spreading (i.e., the planar and the cylindrical beamformer) on



synthetic cases, each representative of a measure of a harmonic Rayleigh wave in different conditions. When the recorded wavefield consists of a pure, cylindrical R-wave, the cylindrical beamformer (hence the CFDBFa algorithm) perfectly matches the desired wave parameters. Instead, the use of a planar scheme would result in an overestimation of the wavenumber and an underestimation of the attenuation. On the other side, the inclusion of body waves and incoherent noise in the recorded wavefield implies a significant drop in the performance of both estimation procedures. Specifically, both the reliability (i.e., the capacity of returning estimates close to the true value) and the accuracy (i.e., the capacity of returning lowly variable estimates) are negatively affected by these two elements. As for the wavenumber, the presence of body waves induces a slight loss in the reliability of the estimated data at small NACD values, whereas the addition of incoherent noise mainly results in a slight loss in the accuracy, due to the small CoV. Focusing on the attenuation, the inclusion of body waves determines a dramatic drop in the reliability of the resulting values, due to the strong overestimation at small NACD values. Furthermore, for increasing NACD, the incoherent noise induces a significant loss in the accuracy, combined with a reduction in reliability, due to the drift of the mean value at great NACD values. Therefore, the presence of incoherent noise in the recorded wavefield exerts a twofold negative effect on the quality of estimated attenuation at great distances, with a loss of both reliability and accuracy. For this reason, a reliable and moderately accurate estimate of attenuation data can be achieved only at a limited range of distances from the sources, where both the near-field and the far-field effects are minimal. In this specific case, the optimal range of NACD varies between 2 and 4. Finally, the planar and the cylindrical beamformer have a rather similar performance, although the latter tends to return slightly more reliable wavenumber estimates at low NACD values. For this reason, the CFDBFa algorithm will be the preferred choice in the processing stages reported in the next Chapters.

# Chapter 6

## Surface wave datasets

This Chapter describes a series of experimental surveys devoted to the collection of high-quality surface wave data at two different sites in the United States. On the one hand, the Garner Valley Down-Hole Array is a site located in Southern California. The purpose of the field survey is the characterization of the velocity and damping structure of the site. The reliability of the estimated ground models is then tested, by comparing the expected ground motion amplification with observed data extracted from a seismic monitoring system herein installed. On the other hand, Hornsby Bend is a site close to Austin, Texas, in which waveforms generated by different sources were acquired in arrays with different layouts. Thus, the influence of the source characteristics and of the array geometry on the estimated R-wave parameters can be addressed. Besides, an innovative acquisition setup has been employed to carry out the MASW survey, based on utilizing a fiber-optic cable rather than geophones. Therefore, this field test allows to investigate the capability of this new system in retrieving attenuation data. In summary, the result of both experimental surveys is a valuable dataset that can represent an effective benchmark for investigating issues and uncertainties affecting the estimate of the R-wave parameters, with a focus on the derivation of the phase attenuation and the consequent profile of S-wave damping ratio. Besides, the resulting S-wave velocity and damping ratio profiles allow to address the impact of the uncertainties of in situ estimates in the ground motion amplification, and to assess the reliability of such estimates, in the case of the Garner Valley Down-Hole Array.

This Chapter first describes the survey carried out at the Garner Valley Down-Hole Array, then it focuses on Hornsby Bend. For each site, a brief overview of the geological layout and of the available geophysical information is provided. Then, it describes in detail the acquisition setup of each MASW survey.

## 6.1 Garner Valley Downhole Array

### 6.1.1 Site description

The Garner Valley Down-Hole Array (GVDA, 33°40.127'N, 116°40.427'W – in the WGS84 Datum) is located in a narrow valley in Southern California, USA. The site stratigraphy is characterized by three main geological units. The top unit is composed by soft silty and sandy alluvial soil, interbedded with some clay layers and lenses (Hill, 1981). The water table oscillates between the ground surface down to 1–3 m depth. At about 20 m depth, the alluvium transitions into a layer of gravelly sand resulting from weathered granite, which overlies a competent granite bedrock at around 90 m depth (Figure 6-1b). However, the depth of the interface between alluvium and weathered granite is variable in space.

The presence of stratigraphic units with sharp variations in dynamic impedance results in a complex site response to ground motions, with multifold amplification peaks. Indeed, the site exhibits a moderately low resonance frequency, equal to 1.7 Hz (e.g., Chandra et al., 2015), combined with higher amplification peaks at 3, 6, 8, and 12 Hz. Furthermore, the combination between this peculiar stratigraphy, the near-surface water table and the site vicinity to seismically active faults (e.g., the San Jacinto fault and the San Andreas fault) has generated great interest of the earthquake engineering community. For this reason, the GVDA has become a reference site for ground motion amplification, liquefaction and soil-foundation-structure interaction (Archuleta et al., 1992).

The GVDA site has been characterized by several geotechnical and geophysical tests, that will be described in the next Section. Furthermore, this site is instrumented with a seismic monitoring system, which has been installed in 1989 as a cooperation of the French Institute de Protection et de Sûreté Nucléaire and the U.S. Nuclear Regulatory Commission. The system is currently managed by the George E. Brown, Jr., Network for Earthquake Engineering Simulation at the University of California, Santa Barbara (NEES@UCSB; <http://nees.ucsb.edu/facilities/GVDA>). The site is instrumented with surface and borehole accelerometers, as well as with a ground water monitoring system. The equipment includes a one-story soil-foundation-structure-interaction (SFSI) structure for the study of dynamic response of this structure during earthquakes (Figure 6-1a). The surface equipment is a 244-m long array of five accelerometers, labeled as S-01, GL-0, S-02, S-03, and S-04. The array is aligned in the NW-SE direction, with the sensor spacing being equal to 61 m. The Down-

Hole array of accelerometers consists of a system of sensors, with one surface accelerometer and five downhole accelerometers, at depths of 6 m, 15 m, 22 m, 50 m, 150 m, and 220 m – however, the latter is no longer operational. The equipment was upgraded in 1995 by including a deep bedrock borehole, with accelerometers installed at 500 m and 501 m depth. The sensors of the vertical seismic array are labeled as GL-*i*, with *i* being equal to the corresponding installation depth (Figure 6-1b). The sensors are installed in a 3×3 m area, and GL-0 is aligned with the array of surface sensors (Figure 6-1a). Finally, the site includes a small group of borehole and surface sensors installed on the outcropping bedrock, 3 km far from GVDA (Steidl et al., 1998).

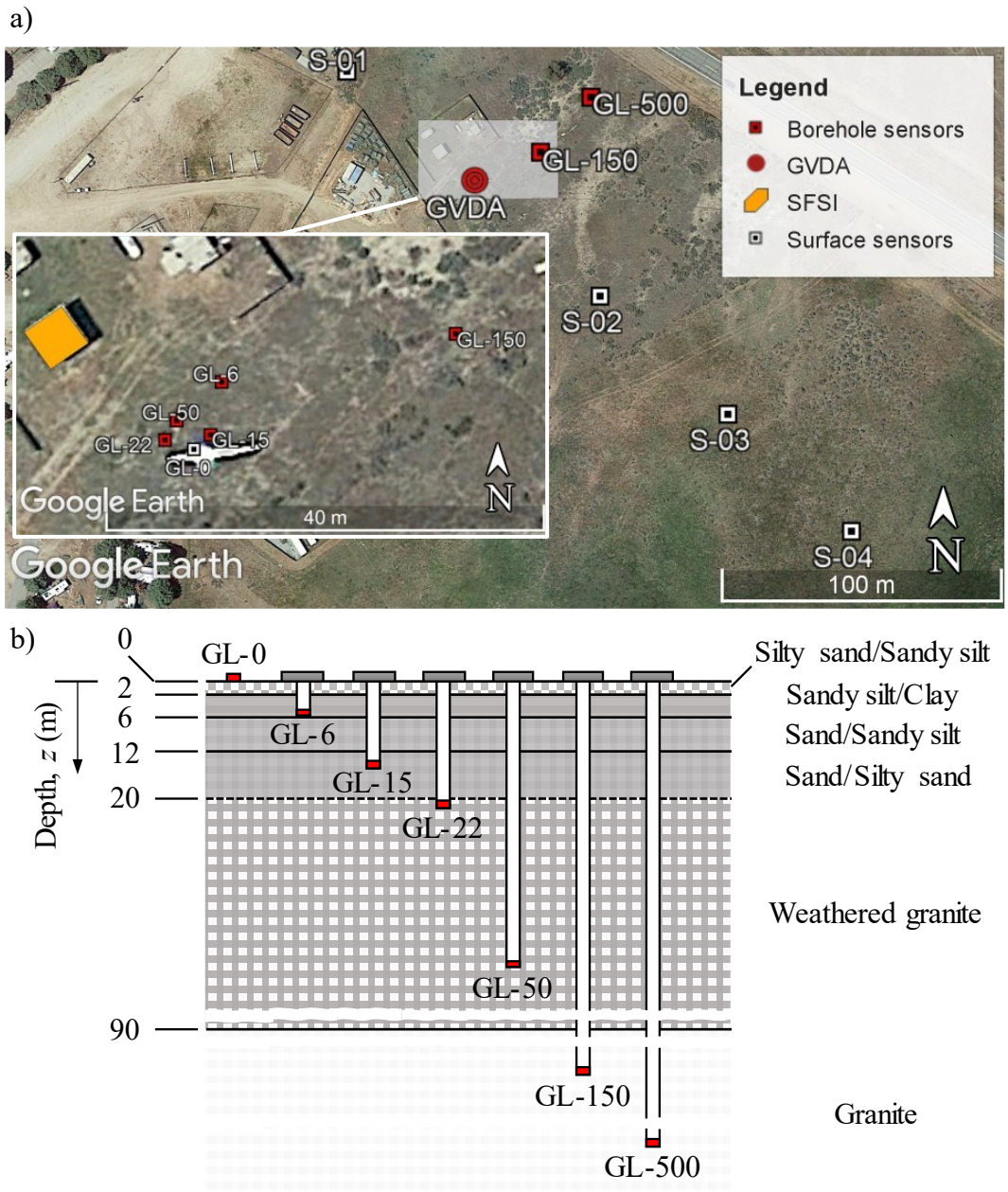


Figure 6-1. a) Plane view of surface and borehole accelerometers locations at the Garner Valley site, California. The figure includes a zoomed view of the sensors installed at the GVDA, as well as of the SFSI; b) Simplified geological cross section of the Garner Valley site, including a representation of the depth location of borehole sensors. Sensors GL-220 and GL-501 are not reported.

## 6.1.2 Previous geophysical studies

Due to the high interest of the earthquake engineering research community on measuring site effects at the GVDA, several geophysical and geotechnical studies have been carried out to define a complete and precise model of the ground conditions. Figure 6-2 reports some significant results in terms of velocity and damping ratio structure estimated in past studies, as well as the locations of past surveys.

The surveys include a seismic refraction survey (Pecker and Mohammadioun, 1991), a DH survey that explored down to 100 m of depth (Gibbs, 1989) and two PS suspension logging tests, that investigated a 50-m borehole in 1994 and a 100-m borehole in 1996 (Steller, 1996). In general, the estimated velocity structure is consistent with the local geology. Indeed, it involves a surface alluvium layer, with  $V_S$  around 220 m/s and  $V_P$  increasing from 400 m/s to 1200 m/s, although the latter estimate is less reliable due to the limited number of measured data. Furthermore, other studies showed  $V_S$  values close to 100 m/s in the uppermost layer (Chandra et al., 2015). Then, after a 4-m thick transition zone,  $V_S$  rises to 450 m/s and it increases up to 1200 m/s with depth, whereas  $V_P$  ranges from 1700 m/s to 2400 m/s. This portion corresponds to the layer of weathered granite. The velocity characteristics of the competent granite at 100 m depth have not been directly characterized yet. However, a  $V_S$  value equal to 2500 m/s is usually assumed, based on the extrapolation of the  $V_S$  structure of a close-by site sharing similar crystalline rocks with the bedrock itself (Coutant, 1996). However, ultrasonic measurements with a 15-kHz signal in a 500-m borehole returned much higher values of  $V_S$ , equal to 3150 m/s. In summary, the site profile includes two main impedance contrasts, namely the interface between soft alluvium and weathered rock and the transition to competent rock, and the latter is believed to mainly control the ground motion amplification at the site (Bonilla et al., 2002).

In addition, several noninvasive geophysical surveys have been carried out, based on the measurement of both ambient noise (Liu et al., 2000) and active-source data (Brown et al., 2002; Stokoe II et al., 2004). Moreover, Teague et al. (2018b) carried out an extensive survey involving both active-source MASW and passive ambient noise acquisition, considering linear and circular arrays located at three different locations, each on the vicinity of an accelerometer of the surface array. These studies observed that the Rayleigh wavefield at GVDA is mostly controlled by the fundamental mode of propagation of Rayleigh waves. Furthermore, they confirmed the velocity structure obtained from invasive

surveys. However, resulting profiles exhibit slightly different variations of  $V_S$  with depth, which can be an effect of lateral variability at the GVDA site.

This reference velocity structure has been gradually modified, based on observations of the ground motion at the GVDA alone or combined with other surveys (e.g., Seylabi et al., 2020). For instance, Bonilla et al. (2002) inferred a detailed velocity model down to 500 m depth, trying to match the arrival time and the amplitude of a target weak-motion. They also derived a preliminary damping structure, in terms of  $D_P$  and  $D_S$ . Instead, Chandra et al. (2015) carried out a seismic interferometry study, combining weak motion records to obtain the  $V_S$  profile. The resulting velocity structure is quite compatible with other studies in the uppermost 50 m of the soil deposit, whereas it tends to provide lower values of  $V_S$  at greater depths. This discrepancy could be a side effect of using the interferometry in the presence of strong impedance variations, as in this case. Finally, Tao and Rathje (2019) interpreted recorded seismic data in the DH-array, according to the amplification approach (see Section 4.4.3) and they provided an alternative estimate of the  $D_S$  structure, whereas they referred to DHT results for the  $V_S$  profile.

These studies also highlighted some pitfalls in adopting a 1D ground model to describe the seismic amplification at the GVDA. On the one side, Bonilla et al. (2002) noticed that the synthetic model does not capture late arrivals especially in the shallow sensors. Indeed, these events are likely the effect of surface waves and scattered waves generated by the three-dimensional geometry of the transition between weathered and competent material at around 90 m depth and by inhomogeneities in the alluvium (Coutant, 1996). In addition, anisotropy in the velocity structure has been identified, even in the shallow layers. The anisotropy in rock layers may be an effect of oriented cracks in the material (Nur, 1971; Kelner et al., 1999; Chandra et al., 2015), whereas in soil layers this could be the result of spatially variable mechanical properties (Coutant, 1996). The anisotropy may be a source of complexity in the ground motion amplification (e.g., Bonilla et al., 2002). Therefore, Fathi et al. (2016) attempted to obtain a 3D estimate of the velocity model of the GVDA down to 40 m depth, by interpreting active-source data measured on a spatial array by means of a full wave inversion algorithm. The identified  $V_S$  and  $V_P$  well compare with results from a SASW survey carried out inside the acquisition area, except at greater depths. However, some lateral variations in  $V_S$  are highlighted, especially in the shallow portion (Figure 6-3).

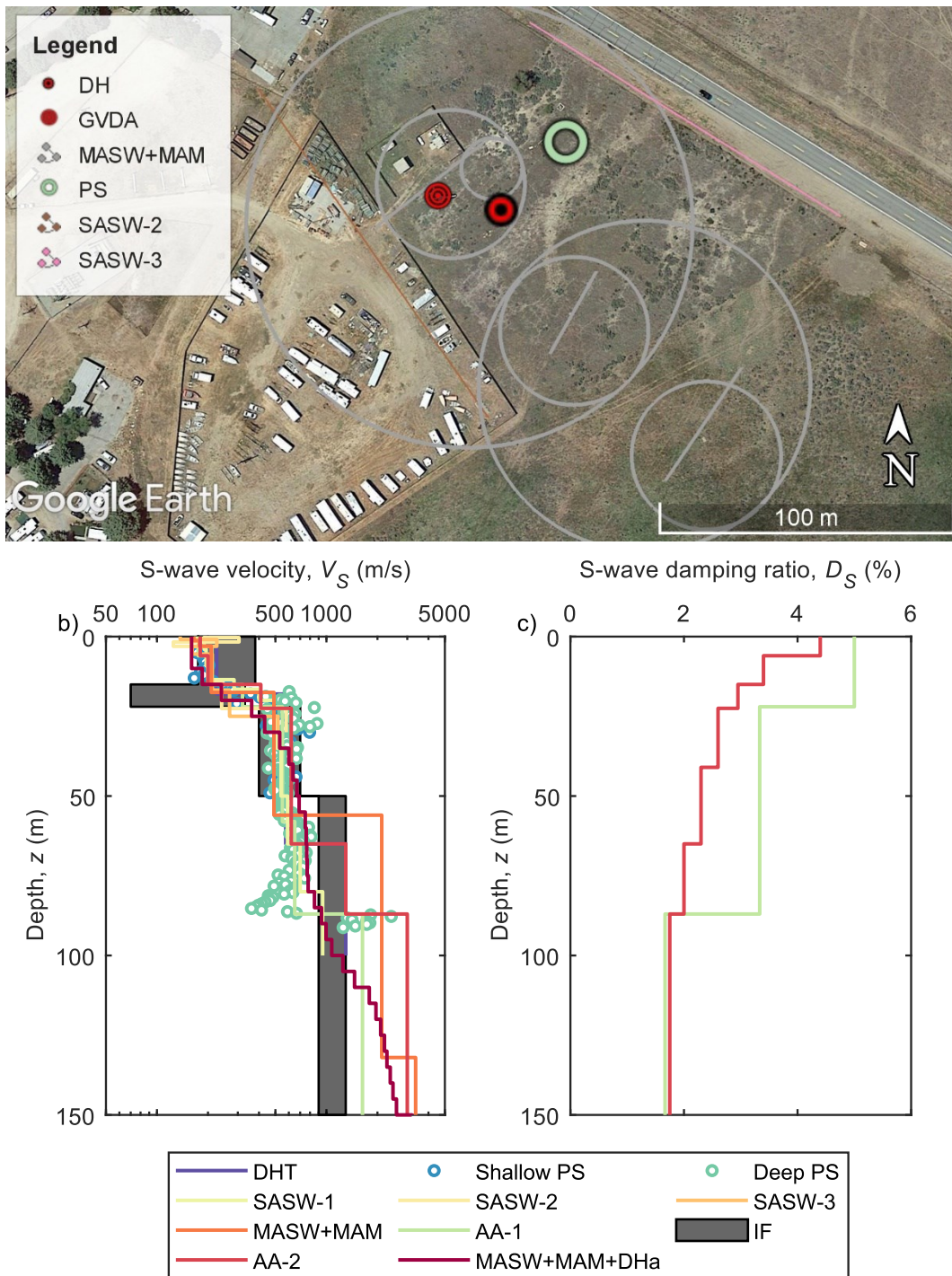


Figure 6-2. a) Plane view of the GVDA, showing the location of some invasive and non-invasive surveys carried out at the site. As for the active-source (SASW and MASW) and passive measurements (MAM), the lines and the circles denote the shape underlying the sensors' setup; b) Estimated S-wave velocity profiles from various studies carried out at the GVDA; c) Estimated S-wave damping ratio profiles from various studies carried out



at the GVDA. In the figure, DHT stands for results from the DHT by Gibbs (1989); Shallow PS and Deep PS report results from Steller (1996); SASW-1 labels results from the SASW survey by Brown et al. (2002); SASW-2 and SASW-3 label results from the SASW survey by Stokoe II et al. (2004); MASW+MAM labels results from the survey by Teague et al. (2018b); AA-1 denotes results from the fitting of DH-array data by Bonilla et al. (2002); IF labels results from the interferometry study by Chandra et al. (2015); AA-2 identifies results of the amplification analysis of DH-array data by Tao and Rathje (2019); and MASW+MAM+DH<sub>a</sub> denotes results from the combined inversion of SWM data and DH-array data by Seylabi et al. (2020). Only the first 150 m of depth are represented.

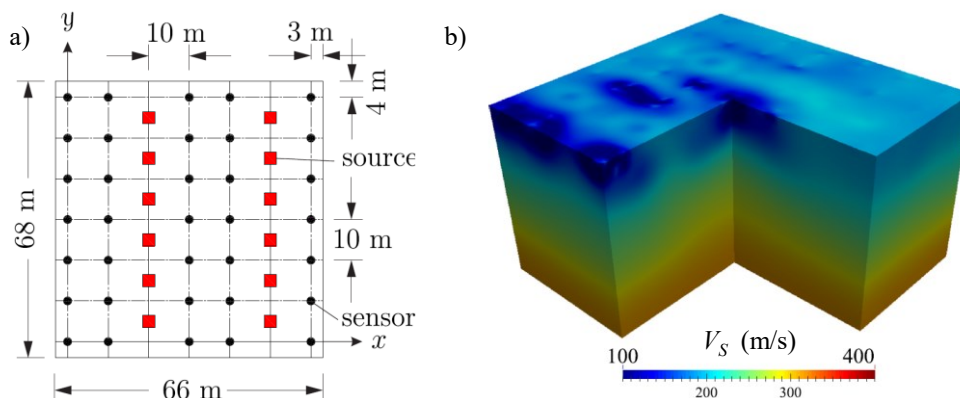


Figure 6-3. Three-dimensional velocity structure reconstruction by full waveform inversion: a) Acquisition setup; b) Estimated S-wave velocity model (after Fathi et al., 2016).

### 6.1.3 MASW survey

The investigation of the small-strain parameters of the soil deposit at the GVDA site was carried out by means of a MASW survey. The testing involved two two-dimensional arrays. One array consisted of a regular, square grid of 196 geophones, with a uniform inter-receiver spacing equal to 5 m and a total extent of 65 m for each side (Figure 6-4). The grid orientation was from North-West to South-East and the base lines are orthogonal with each other. This testing setup is hereafter labeled as GV-H5. The second array was an irregular grid of 196 sensors, with spacing equal to 5 m in the paracentral region and 10 m in the peripheral portion. Thus, the total extent was 100 m in the North-West to South-East direction and 90 m in the perpendicular one (Figure 6-5). This testing setup is henceforth identified as GV-HN. The investigated areas by the two arrays are adjacent to or they partially contain the GVDA and they include the central portion of the surface array of accelerometers.

The receivers were Magseis Fairfield Nodal ZLand 3C nodes. These instrumentations are all-in-one nodes, including both a sensor, a built-in

datalogger and a power supply. The nodes are cable-free, and the time synchronization is guaranteed by onboard GPS time. The sensor unit is a three-component geophone, with passband corner frequency equal to 5 Hz, viscous damping ratio of 70% and a sensitivity of 1.95 Volts/in/s, namely 76.7 Volts/m/s. This kind of equipment is suitable for both active and passive surveys. The data acquisition system continuously recorded the particle velocity with a sampling rate of 200 Hz, storing data in an internal unit. Receivers were buried in the ground, to limit the influence of undesirable noise on the measured wavefield and ensure adequate coupling with the ground, as suggested by the InterPACIFIC guidelines (Foti et al., 2018).

Waveforms were generated through a vibrating source, namely the NHERI@UTexas Thumper vibroseis truck (Stokoe II et al., 2020) and an impulsive source. In both cases, various shot points were employed, with variable offsets from the closest receiver. In this way, thanks to the multiple-source offset technique (Cox et al., 2014), the influence of near-field effects on the estimated R-wave parameters can be mitigated, and the corresponding uncertainties can be rigorously quantified.

The impulsive source was a 20-lb instrumented sledgehammer striking on a metal plate, at different locations both inside and outside the spatial array. An accelerometer installed inside the sledgehammer allowed to record the force transmitted onto the ground. Internal shot points were located at the midpoint between each couple of sensors inside alternate NE-to-SW grid lines, whereas external shot points were placed at 5 m and 15 m off both ends (Figure 6-4a). At each shot point, five repetitions were run.

The vibrating source generated a 12-s long sweep signal, namely a nonstationary signal whose frequency linearly increases with the time, shifting from 5 Hz to 30 Hz. The input force was recorded by an accelerometer installed on the base plate. When possible, two external shot points were employed for each side, with offsets from the closest sensor ranging between 2 m and 5 m, and 30 m and 35 m, respectively. Instead, internal shot points were applied at the midpoint of specific couples of sensors. However, some shot points were non-symmetrical or even missing, mostly due to logistic issues linked with the accessibility of the vibroseis truck (Figure 6-4b). At each shot point, three repetitions were performed, whereas the number was increased to ten at the farthest source-offsets.

The peculiar acquisition setup adopted in this survey primarily aims at developing a three-dimensional model of the soil deposit at the GVDA, by exploiting a full waveform inversion algorithm. However, measured data can be

still effectively interpreted according to canonical MASW processing schemes, by extracting information from each linear sub-array of sensors. Furthermore, the comparison of the experimental Rayleigh dispersion and attenuation curves at each sub-array might provide a valuable insight on spatial variations of the near-surface velocity and dissipation structure of the soil deposit. Finally, the closeness between both arrays and the GVDA allows to carry out a consistent comparison between the resulting soil model and the information provided by borehole data, thus assessing the reliability of the estimated  $V_S$  and  $D_S$  profiles.

## **6.2 Hornsby Bend**

### **6.2.1 Site description and previous geophysical studies**

The site of Hornsby Bend (HB, 30°13.918'N, 97°38.631'W – in the WGS84 Datum) is located on the outskirts of the city of Austin, Texas. The site is a flat area next to the Colorado River, owned by the City of Austin. The site stratigraphy is mostly characterized by layered alluvial soils. Specifically, a moderately stiff 15 m thick clayey layer overlies a loose-to-medium dense layer with fine sands. At greater depths, stiff clays are found (Figure 6-6c).

The site has been object of geophysical investigations by Van Pelt (2010), who carried out CHT and SASW measurements quite close to Hornsby Bend, in his study about the influence of soil dynamic parameters on foundations settlements. Kallivokas et al. (2013) attempted to develop a 2D velocity model of the site from measured active-source data on a spatial grid of sensors, by exploiting the full waveform inversion algorithm. The resulting velocity structure exhibits some lateral variations, although the deviation from the one-dimensional geometry is not significant (Figure 6-6b). Indeed, results were compatible with the  $V_S$  profile resulting obtained from a SASW survey carried out at the same location. Observed discrepancies were attributed to both lateral variability and limitations of the layered model used in the SASW-based estimate, that tends to return a coarse velocity model not representative of the actual, smooth variations. In general, near-surface layers exhibit moderately low  $V_S$  values, ranging between 200 m/s and 250 m/s, with moderately large variability. At depth, instead,  $V_S$  gradually increases up to 400 m/s, in correspondence of the shale layer (Figure 6-6d).

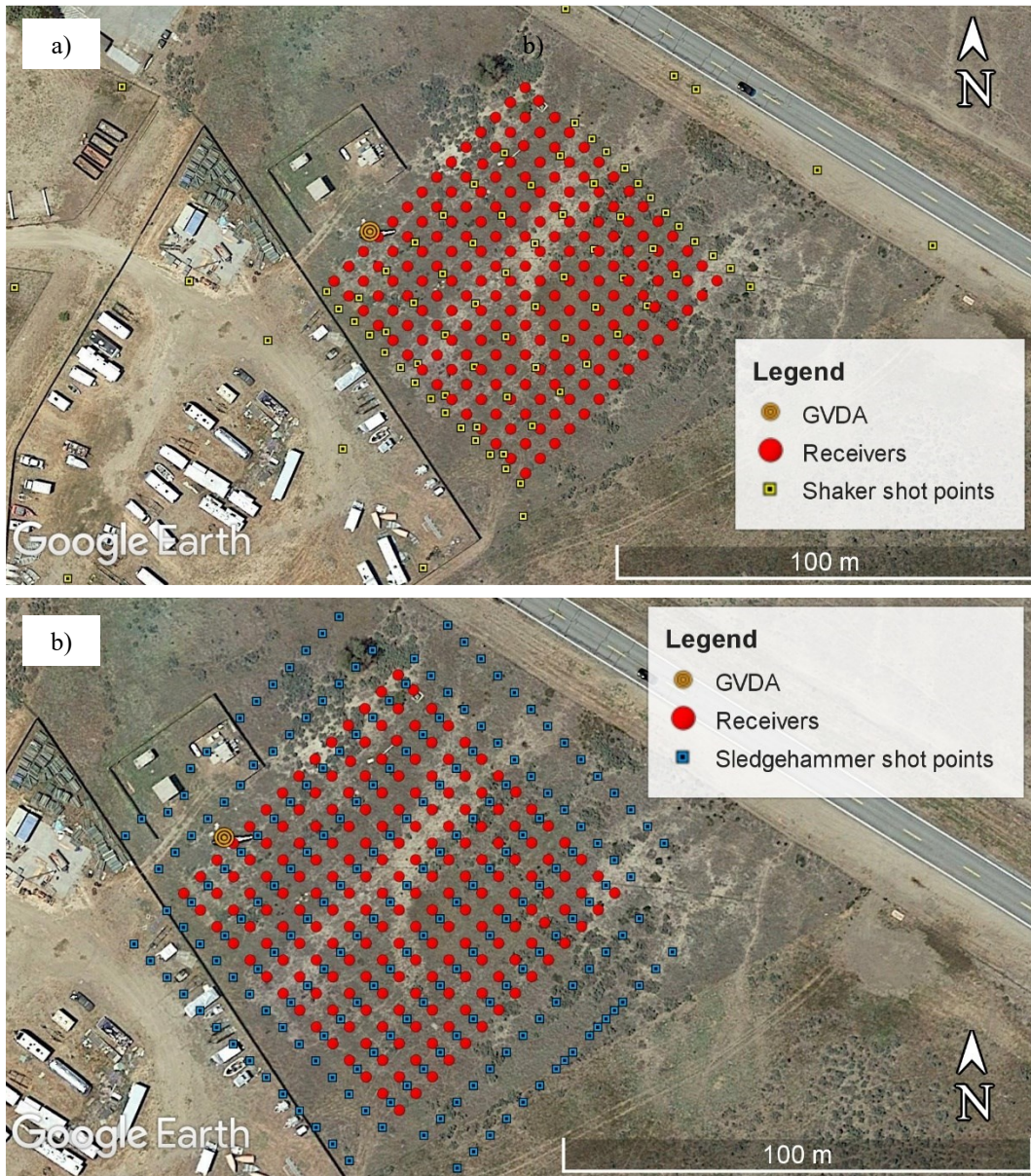


Figure 6-4. Acquisition setup of GV-H5 at the GVDA site: a) Location of sledgehammer shot points; b) Location of shaker shot points.

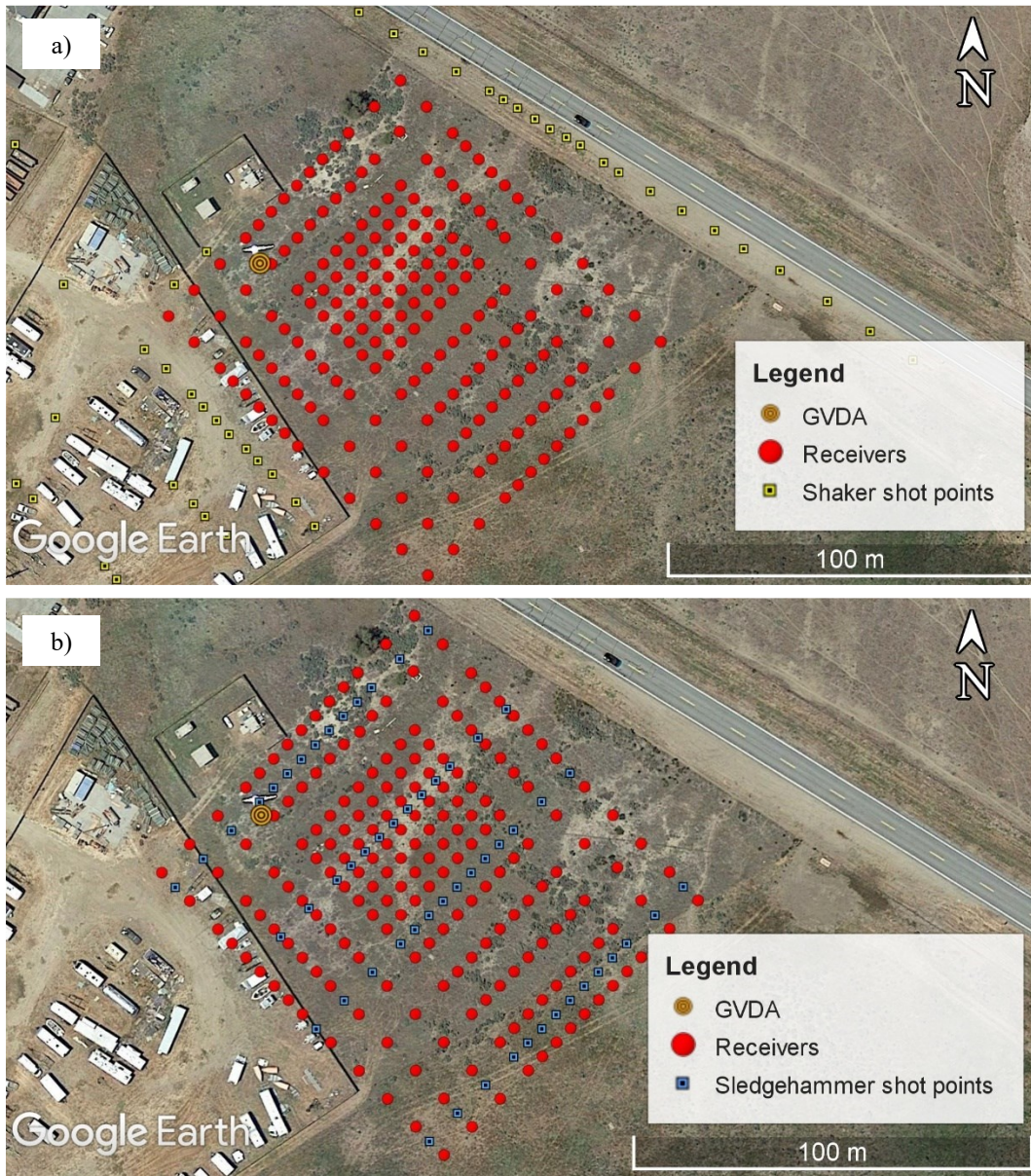


Figure 6-5. Acquisition setup of GV-HN at the GVDA site: a) Location of sledgehammer shot points; b) Location of shaker shot points.

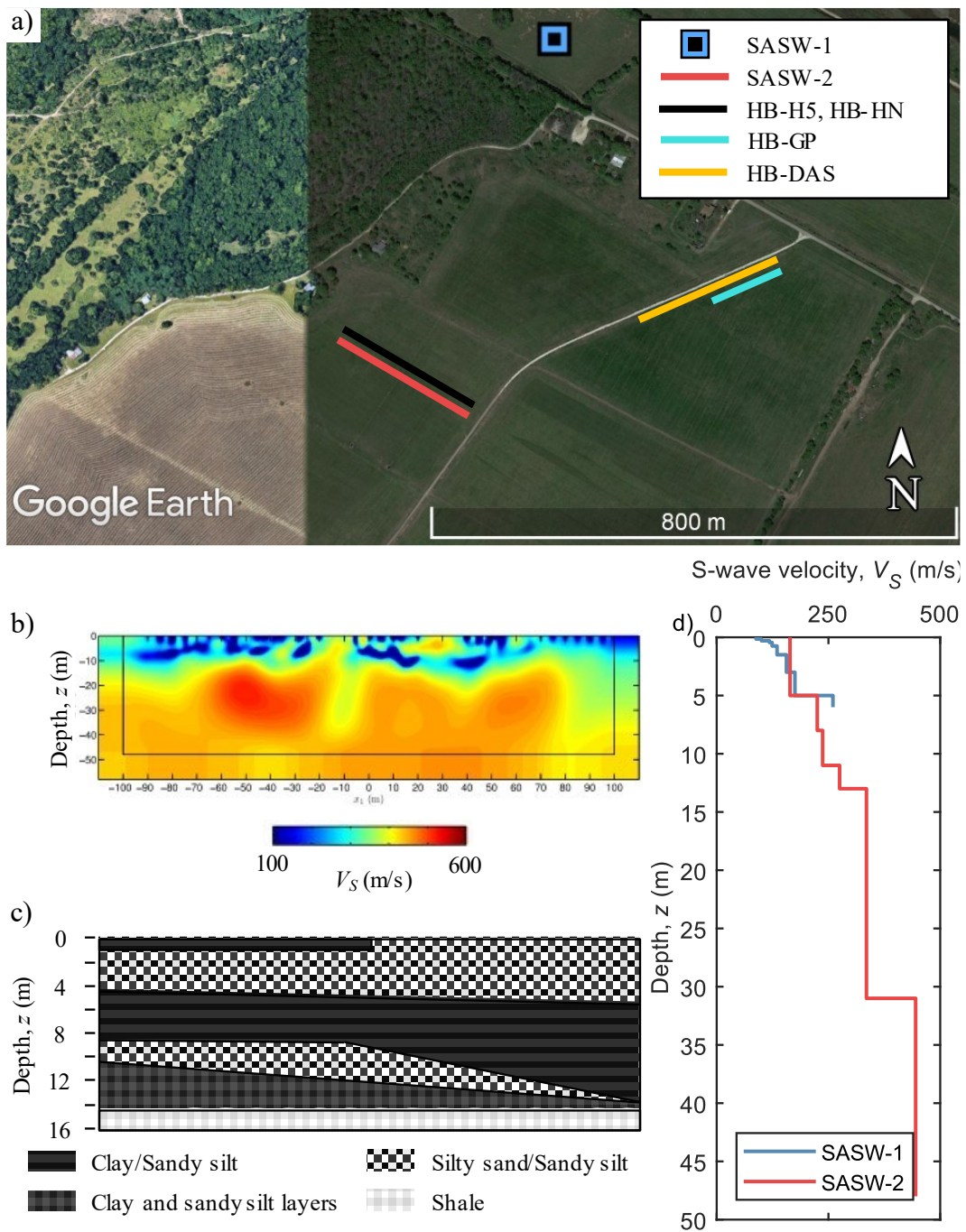


Figure 6-6. a) Hornsby Bend site. The map also reports the location of the SASW surveys by Van Pelt (2010) (SASW-1) and Kallivokas et al. (2013) (SASW-2), together with the location of the MASW surveys herein discussed, namely HB-H5, HB-HN, HB-GP, and HB-DAS; b) Two-dimensional velocity model along the SASW-2 line, developed by Kallivokas et al. (2013); c) Simplified geological cross section along the SASW-2 line; d) S-wave velocity profiles, estimated by Van Pelt (2010) (SASW-1) and Kallivokas et al. (2013) (SASW-2).

## 6.2.2 MASW survey

The geophysical investigation at the HB site was carried out by means of various MASW surveys, held at different stages. In all the cases, the investigated area is rather close to the location of the survey by Kallivokas et al. (2013). Differently from GVDA, all the surveys collected active-source data on linear arrays of sensors, albeit with different geometries, source types and receivers. Part of the in-situ tests used two arrays of geophones with variable geometry, and different sources generated the acquired waveforms. This survey aims at assessing the influence of two main acquisition parameters (i.e., the array geometry and the source characteristics) on the estimated R-wave parameters. Furthermore, an additional surface wave dataset collects waveform data by both an array of geophones and a fiber-optic device, thus allowing to address the influence of the receiver characteristics. This represents one of the first applications of fiber-optic data to retrieve the R-wave phase attenuation. As these surveys will focus on different factors affecting estimated R-wave parameters, they will be treated separately.

### 6.2.2.1 First round of testing

The first round of testing involved two one-dimensional arrays, both aligned along the North-West to South-East direction (Figure 6-7). The first layout was an array of 46, regular-spaced geophones. The inter-receiver spacing was equal to 5 m, hence the total extent of the array is 225 m. This testing setup is hereafter labeled as HB-H5 (Figure 6-7a). The second array was an irregular grid of 46 sensors, with spacing gradually increasing from 1 m to 8 m while moving towards North-West, with doubling steps. Thus, the array length was 192 m. This testing setup is henceforth identified as HB-HN (Figure 6-7b).

The receivers were GeoSpace GS-11D 4.5-Hz vertical geophones, that are sensors suitable for active surveys, with passband corner frequency equal to 4.5 Hz, viscous damping ratio of 70% and a sensitivity of 2.54 Volts/in/s, namely 97.4 Volts/m/s. Receivers were coupled with the ground by means of 7.6-cm metal spikes. Data were recorded by two interconnected 24-channel Geometric Geode seismographs, with a sampling time of 0.03125 ms. The remaining two channels were used to record source data. One recorded the drive signal from the shaker, when used, whereas the other recorded the actual input force, by means of an accelerometer installed on the base plate.

Part of the waveforms recorded in HB-H5 and HB-HN were generated through the NHERI@UTexas Thumper vibroseis truck (Stokoe II et al., 2020). The vibrating source applied a 20-s chirp, with a log-linear increase of the

characteristic frequency between 3 Hz and 100 Hz. In addition, the vibroseis generated a stepped sine signal, i.e. a sequence of monochromatic signals with different frequencies. Also in this case, the frequency shifted logarithmically between 3 Hz and 100 Hz in 51 steps, and 50 harmonic cycles were applied in each step. In this specific case, the data acquisition system returned frequency-domain data, where each frequency is associated with an average value of the spectral ground velocity at the corresponding stage. Waveforms were generated at five external shot points at the South-East side, with offsets from the closest sensor equal to 10 m, 20 m, 30 m, 40 m, and 50 m. Recorded data in HB-H5 include also waveforms generated on reversed shot points (Figure 6-7a). As for HB-HN, additional shot points were included inside the array, next to locations where the receiver spacing changes (Figure 6-7b). The internal shot points seek to isolate sub-sections of the array, thus improving the quality of high-frequency estimates of R-wave parameters.

Besides, waveforms in HB-HN were also generated by a 20-lb instrumented sledgehammer striking a metal plate lying on the ground. Waveforms were generated at three external shot points at the South-East side, with offsets from the closest sensor equal to 3 m, 7 m, and 10 m. Offsets were smaller than those of shaker shots to preserve the high-frequency components of the impulsive source. However, some internal shot points were included as well (Figure 6-7b).

The main purpose of this survey is the assessment of the influence of the acquisition geometry and of the source characteristics on the estimated R-wave parameters, in terms of investigated frequency range and related uncertainties. As for the geometry, due the moderately large receiver spacing, HB-H5 is suitable for investigating the soil deposit structure at large depths. Indeed, the maximum resolvable wavelength approximately equals the array length, i.e. 225 m, thus the survey can potentially reconstruct the velocity and damping structure down to  $75 \div 110$  m depth. Instead, the HB-HN acquisition setup seeks to fulfil a trade-off between two opposing needs, namely accurate resolution of shallow layers and extended investigation at great depths. On the one side, the portion with small inter-receiver distance allows to obtain a significantly small minimum resolvable thickness, which is about  $0.3 \div 0.5$  m – at least theoretically. On the other side, the maximum resolvable wavelength approximately equals 192 m, thus HB-HN can reconstruct the velocity and damping structure down to  $65 \div 95$  m depth. In this way, HB-HN array should contribute to investigate at greater depths, while preserving good resolution at shallow depths. As for source characteristics, the application of a stepped sine is more time-consuming, but it guarantees very high signal-to-noise ratio, hence it is expected that the quality of estimated R-wave



parameters will be excellent. However, sweep signals still provide high-quality data covering a broad range of frequencies in a single application (Foti et al., 2014).

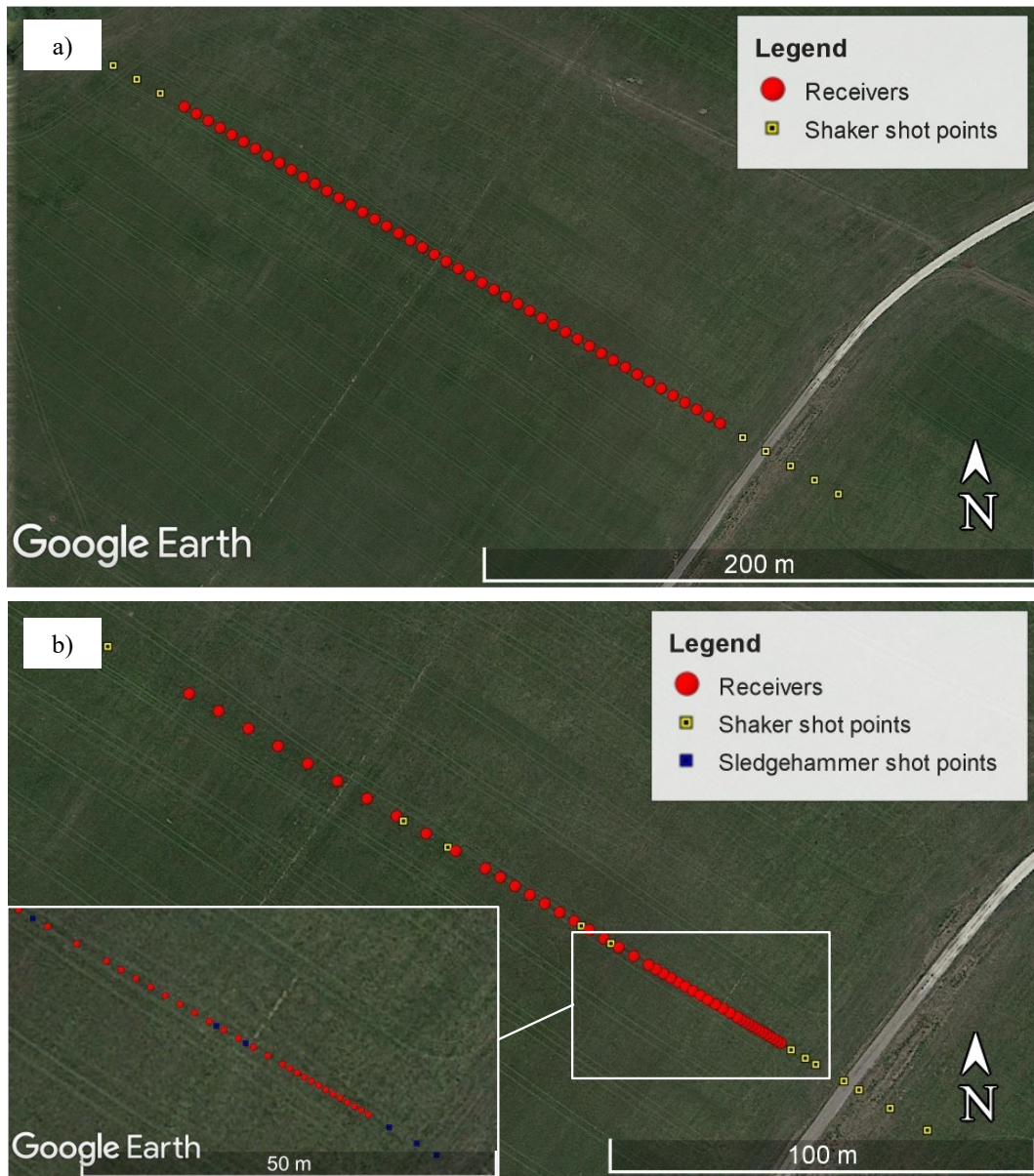


Figure 6-7. a) Acquisition setup of HB-H5 at the HB site; b) Acquisition setup of HB-HN at the HB site.

#### 6.2.2.2 Second round of testing

The second round of testing involved two one-dimensional arrays, investigating an area next to the one explored with HB-H5 and HB-HN. Specifically, both

arrays developed on the side of a small unpaved road, along the South-West to North-East direction (Figure 6-6a).

The first layout was an array of 48, regular-spaced vertical and horizontal geophones. The inter-receiver spacing was equal to 2 m, hence the total extent of the array equaled 94 m. This testing setup is hereafter labeled as HB-GP (Figure 6-8). The receivers were GeoSpace GS-11D 4.5-Hz vertical geophones, whereas four interconnected 24-channel Geometric Geode seismographs recorded waveform data, with a sampling rate of 1 kHz.

The second acquisition scheme was a distributed acoustic sensing (DAS), fiber-optic array. DAS technology measures the axial strain of the fiber-optic cable induced by external perturbations (e.g., mechanical waves), using the phase interferometry principle (Hartog, 2017; Bakulin et al., 2020). Specifically, an interrogator unit measures variations in phase of a laser pulse traveling inside the cable over a reference length, called gauge length, that are linked with variations in relative distance, whence the axial strain is derived. This survey utilized a 200-m long NanZee Sensing Technology (NZZS-DSS-C02) fiber-optic cable, which was installed adjacent to HB-GP. The cable was buried inside a trench, backfilled with compacted soil to ensure an appropriate coupling of the cable with the ground. In this way, the measured axial strain along the cable corresponds to the actual strain experienced by the ground. Axial strain data were recorded by the ODH4 OptaSense Interrogation Unit, according to a gauge length equal to 2.04 m and a channel separation of 1.02 m, i.e., measurements of the wavefield were provided approximately every 1 m along the cable. However, each measured value represents an average cable response over the gauge length (i.e., 2.04 m) surrounding each channel location, at 94 locations, over a total length of 94 m. The interrogator unit returned data sampled at 100 kHz rate, that were then down sampled at 1 kHz and high-pass filtered above 3 Hz to remove artifacts at low frequencies linked with the acquisition. This testing setup is hereafter identified as HB-DAS (Figure 6-8).

HB-GP and HB-DAS simultaneously recorded waveforms generated through different sources, namely an instrumented sledgehammer, the NHERI@UTexas Thumper vibroseis truck and the three-dimensional T-Rex vibroseis truck (Stokoe II et al., 2020), that were applied at different locations. External triggering was used to synchronize the source and both acquisition systems. However, this study focuses on waveforms generated by the Thumper truck, which generated a 12-s long chirp signal, with frequency shifting from 5 Hz to 200 Hz. Furthermore, this study will address only data associated with the source locations on the North-East side, with offsets equal to 5 m, 10 m, 20 m, and 40 m from both HB-GP and

HB-DAS. At each shot point, three repetitions were run. Only the vertical motion data are considered for the HB-GP array.

The choice of using different acquisition layouts aimed at investigating the influence of the array geometry and the equipment type onto the estimated dispersion and attenuation data. A 94-m section of the fiber-optic cable, which is adjacent to HB-GP, is selected in this study.

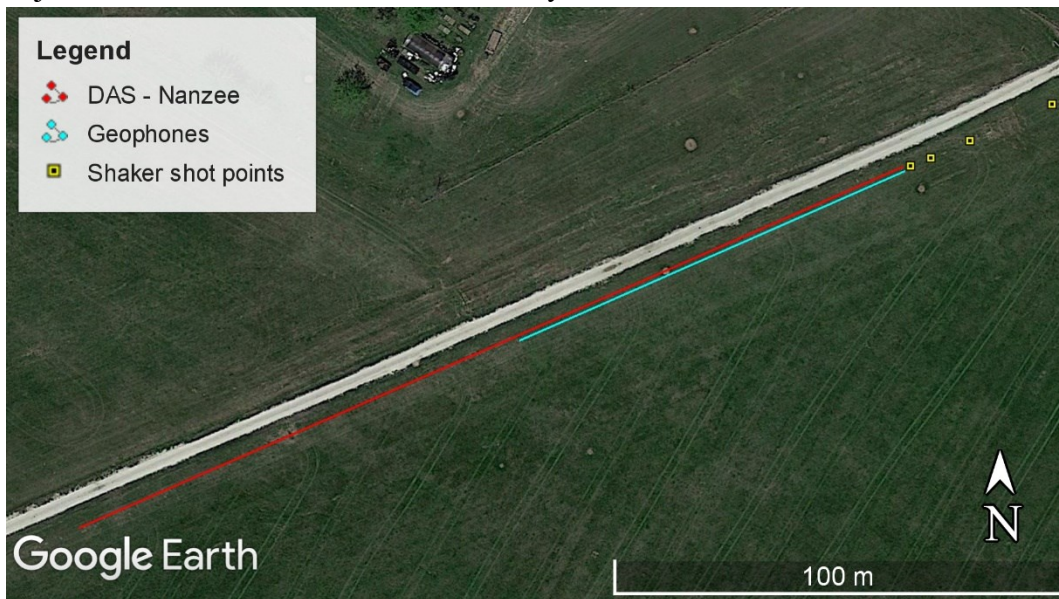


Figure 6-8. Acquisition setup of HB-DAS and HB-GP at the HB site.

# Chapter 7

## Uncertainties in dispersion and attenuation estimates

The interpretation of MASW surveys should account for the sources of uncertainties that might affect the estimated R-wave parameters. Specifically, all the uncertainty components must be correctly identified, properly modeled and finally quantified (IQM procedure; Passeri, 2019). As uncertainty components have various nature, an effective taxonomy distinguishes between epistemic uncertainties and aleatory variability. Epistemic uncertainty rises from the lack of knowledge about the phenomenon under investigation and it incorporates all the features that appear as unexplained by the model that is adopted for the interpretation. Their quantification is a complex task; however, they can be theoretically removed by adopting more refined and complete interpretation models. Instead, aleatory variability clusters all the mechanisms linked with the natural randomness affecting measured data of the phenomenon under investigation. Aleatory variability cannot be reduced to zero, although the repetition of measurements may provide a reliable estimate. Besides, the quantification of the related magnitude can be achieved through statistical tools.

In SWM surveys, the separation between epistemic uncertainties and aleatory variability is not trivial, as they often appear as lumped together. For instance, variations in the estimated R-wave parameters due to different source-receiver configurations are usually an effect of lateral heterogeneities of soil deposits, which is a combination of aleatory variability and epistemic uncertainty. On the one side, standard surface wave testing intrinsically assumes 1D modeling for soil stratigraphy, hence the scatter in estimated data might be interpreted as an epistemic uncertainty. However, in sites where lateral variations are negligible, this uncertainty can be modeled as an aleatory variability (Foti et al., 2018).

A critical epistemic uncertainty is related to the so-called near-field effects. They are the result of model incompatibility issues, as usual processing schemes rely on the hypothesis that the recorded wavefield consists solely of planar Rayleigh waves, whereas actual waveforms include both surface waves and body waves, and surface waves propagate according to cylindrical wavefronts. The

influence of near-field effects on the estimated R-wave phase velocity and phase attenuation has been addressed in Chapter 5. Furthermore, the recorded wavefield data may be corrupted by the presence of reflected or refracted body waves, back-scattered waves, other surface waves (e.g., Lamb waves) and the air blast. Typically, all the wave components other than the target one (i.e., Rayleigh waves) are labeled as coherent noise (Strobbia, 2003). An additional source of epistemic uncertainty is linked with the specific processing scheme adopted to interpret waveform data. Indeed, each approach relies on specific modeling assumptions of the wavefield, hence the degree of consistency with real data is variable. For instance, some algorithms include an explicit modeling of the cylindrical shape of the Rayleigh wavefront (Zywicki, 1999; Zywicki and Rix, 2005; Maranò et al., 2017), hence they mitigate the influence of near-field effects. Furthermore, each processing scheme relies on different computation algorithms, with variable degree of sensitivity to incoherent noise and capacity of identifying different wave components (i.e., Rayleigh propagation modes). The mode separation itself represents another relevant source of epistemic uncertainties, as the recorded Rayleigh wavefield is typically multimodal and the correct identification of each mode depends on the adopted processing technique, on site conditions and on the acquisition geometry. The mode misidentification might result in physically unrealistic soil profiles, far from the actual stratigraphy of the investigated soil deposit.

In SWM, aleatory variability is usually associated with lateral variations in the soil stratigraphy and incoherent noise. The influence of local heterogeneities and lateral variability in the soil deposit is a well-known source of uncertainty, as it introduces a perturbation into the Rayleigh wavefield. The resulting variability in the estimated R-wave parameters can be interpreted as aleatory variability, when deviations from the 1-D model are not relevant. The related influence depends also on the acquisition layout, because long receiver arrays sample a rather large portion of the soil deposit, and the probability of finding significant lateral variability is greater. As for incoherent noise, this represents the perturbations in the wavefield due to ambient vibrations, that are not generated by the active source. Due to the random nature of this component, the effect of incoherent noise on the estimated R-wave parameters represents an excellent example of aleatory variability. Its presence is usually tackled by a stacking procedure, that allows to increase the signal-to-noise ratio and to reduce the influence of noise on experimental data. However, incoherent noise has a significant impact on the estimated wave attenuation, as it has been demonstrated in Chapter 5.

The first part of this Chapter addresses some relevant sources of epistemic uncertainties affecting the estimated phase velocity and phase attenuation. On the one side, this study assesses the role of the processing technique on the quality of derived R-wave parameters, with reference to both synthetic cases and field surveys carried out at Hornsby Bend (HB) and Garner Valley (GV). Furthermore, the influence of source characteristics on the experimental data is investigated, by adopting the wavefield data recorded at the HB site as the experimental dataset. The overview of epistemic uncertainties ends with a comparison between the derived phase velocity and attenuation values obtained from geophone and fiber-optic data at the HB site, thus investigating the capability of this new system in retrieving attenuation data. This assessment also allows to understand the sensitivity of the estimated R-wave parameters to the specific acquisition device. The final part of this Chapter focuses on the aleatory variability, introducing a statistical model to jointly describe the variability of the experimental dispersion and attenuation data.

## **7.1 Inter-method differences**

This Section addresses the epistemic uncertainties linked with the specific methodology to process surface wave data, by inspecting the inter-method differences in the estimated phase velocity and phase attenuation data. The analysis is firstly carried out on synthetic wavefields (SW3 and SW4; see Section 5.1), to assess the performance of each processing technique in ideal, noiseless conditions. Furthermore, the solution of the Rayleigh eigenvalue problem provides theoretical estimates of the R-wave parameters, that represent a benchmark for checking the reliability of each technique. Then, the inter-method comparison is carried out on in situ recorded data, in which the influence of incoherent noise is fundamental. This study focuses on results of the surveys performed at GV and HB sites. Indeed, the recorded wavefield at the former site is dominated by a single Rayleigh propagation mode, hence it can be used to simultaneously compare techniques providing modal estimates of the R-wave parameters (e.g., the CFM) and methods providing an effective value (e.g., the CFDBFa). Instead, the multimodal nature of the wavefield recorded at HB allows to investigate the effectiveness of various processing techniques in capturing different propagation modes, with a focus on the modal phase attenuation. For the same reason, this site represents a potential application to assess the capability of the proposed modal filtering techniques in extracting R-wave modes from real data.

In general, the inter-method comparison focuses on different features describing the quality of the estimated R-wave parameters, namely the reliability, the accuracy and the capability of each scheme of returning acceptable data over a broad range of frequencies.

### 7.1.1 Synthetic data

In this study, the investigation of the epistemic uncertainties linked with the specific methodology to process surface wave data is carried out by inspecting the inter-method differences in the estimated wave parameters, for the synthetic wavefields SW3 and SW4.

This study investigates the inter-method differences in terms of both the investigated frequency range and the reliability. For each methodology, the reliability is quantified by measuring the relative error between the estimated dispersion and attenuation data –  $V_{R,e}(\omega)$  and  $\alpha_{R,e}(\omega)$ , respectively – and the theoretical  $V_R(\omega)$  and  $\alpha_R(\omega)$  values, for each synthetic soil profile (e.g., Badsar et al., 2010; Verachtert et al., 2017; Bergamo et al., 2019). However, the considered processing techniques rely on different modeling of waveforms composed by multiple propagation modes. Some methods include an explicit modeling of multiple propagation modes (namely, GHPB, CFM, WD, FDBFaMF, and CFDBFaMF), hence they ideally provide estimates of the modal dispersion and attenuation curves. In this case, the reliability of each approach is addressed by comparing estimated modal data with the corresponding ones obtained from the solution of the R-wave eigenvalue problem. Other methods, instead, return estimates of effective dispersion and attenuation curves (i.e., TFM, FDBFa, and CFDBFa). In this case, a comparison with the modal values would be misleading, as the intrinsic discrepancy between effective and modal data might be misinterpreted as a source of bias. Thus, the study of inter-method differences should rely on a comparison between estimated and theoretical values of the effective dispersion and attenuation data. However, this section focuses on the performance of modal-based estimation techniques, whereas the reliability of the TFM, FDBFa, and CFDBFa will be addressed on real-case data, as it will be shown in the next Section. Furthermore, this study does not report results from the GHPB because of the almost equivalent performance compared with the CFM (see Appendix B). For the same reason, the FDBFa and the FDBFaMF are not considered either.

For each synthetic wavefield and each processing technique, results were sampled with a sampling frequency of 1 Hz, across the frequency band ranging between 3

Hz and 100 Hz. The comparison takes place both by superimposing estimated data with theoretical curves, and by inspecting the relative error, expressed in terms of normalized phase velocity  $V_{R,e}/V_R$  (i.e., the ratio between the estimated and the theoretical modal value) and normalized phase attenuation  $\alpha_{R,e}/\alpha_R$ . This ratio equals the unity when the estimates are identical, whereas a value greater than 1 denotes an overestimation of the modal value. In addition, a quantitative measure of the relative differences is provided in terms of root mean square error  $\Delta V$  and  $\Delta\alpha$ , for the phase velocity and phase attenuation data respectively:

$$\Delta V = \sqrt{\frac{1}{N} \sum_{n=1}^N (\ln V_{R,e} - \ln V_R)^2} \quad \Delta\alpha = \sqrt{\frac{1}{N} \sum_{n=1}^N (\ln \alpha_{R,e} - \ln \alpha_R)^2} \quad (7.1)$$

where  $N$  is the number of samples. This quantity is computed over the frequency range wherein all the considered techniques return wave parameters.

Furthermore, a synthetic graph highlights the investigated frequency range, to allow an immediate comparison in terms of relative performance. Although synthetic data virtually enable the investigation of a broad frequency range, a proper investigation of the performance of each processing scheme should account for the restrictions due to the limited spatial sampling in the acquisition layout. Therefore, data above the maximum investigable wavelength  $\lambda_{max} = D$  (where  $D = 100$  m is the array length; however, this criterion is a conservative choice, see for instance Socco and Strobba, 2004) and below the minimum one  $\lambda_{min} = d$  (where  $d = 2$  m is the receiver spacing) – if any – are included in the comparison, but a different coloring is adopted to highlight their peculiar condition. In a similar way, data beyond the resolution limits of the simulated array are not included in the computation of  $\Delta V$  and  $\Delta\alpha$ .

### 7.1.1.1 Results for SW3

Figure 7-1 compares estimated and theoretical fundamental-mode (labeled as R0) R-wave parameters for SW3 data. Results on the first two higher modes (i.e., R1 and R2) are reported in synthetic way in Figure 7-2. The corresponding  $\Delta V$  and  $\Delta\alpha$  are reported in Table 7.1.

The resulting dispersion curves are rather close to each other and match the theoretical one, for almost each approach, as demonstrated by the similar  $\Delta V$  values (Figure 7-1a). This is valid especially at high frequencies, whereas some discrepancies are observed at low frequencies. Specifically, all the methods tend to underestimate  $V_R(\omega)$  at  $f < 15$  Hz, with a significant deviation at  $f < 10$  Hz (i.e.,  $\lambda > 25$  m; Figure 7-1c). The maximum error is about 10%, which is consistent with other studies (Figure 7-1; e.g., Bodet et al., 2009). The main source of such divergence is near-field effects, especially the model incompatibility effect due to



the contribution of body waves. However, there are some exceptions. On the one side, WD returns a dispersion estimate perfectly compatible with  $V_R(\omega)$  even at frequencies between 10 Hz and 15 Hz. Instead, the CFDBFaMF returns oscillating estimates of dispersion data at low  $f$  values, and the error magnitude is bounded between 5% and 10%. This oscillation might be an artifact introduced by the modal filtering procedure, which may have returned a mixture of the fundamental-mode R-wave and body waves. Indeed, this erratic behavior in  $V_{R,e}(\omega)$  is typical of a wavefield corrupted by strong body waves (e.g., Rahimi et al., 2021).

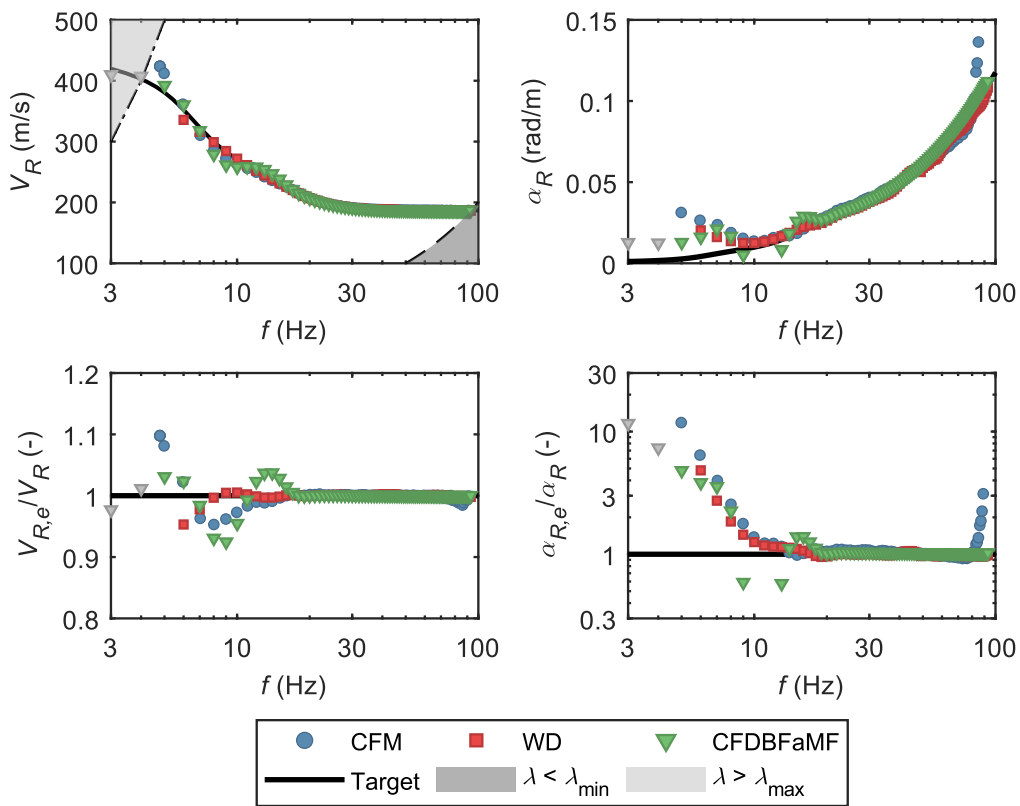


Figure 7-1. Assessment of the inter-method differences for the fundamental mode R-wave dispersion and attenuation curve, with reference to SW3: a) Theoretical vs. estimated dispersion curves; b) Theoretical vs. Estimated attenuation curves; c) Normalized phase velocity  $V_{R,e}/V_R$  (i.e., the ratio between the estimated and the theoretical phase velocity), as a function of the frequency; d) Normalized phase attenuation  $\alpha_{R,e}/\alpha_R$  (i.e., the ratio between the estimated and the theoretical phase attenuation), as a function of the frequency; and normalized phase attenuation  $\alpha_{R,e}/\alpha_R$ . The vertical axis is represented in logarithmic scale as  $\alpha_{R,e}/\alpha_R$  spans multiple orders of magnitude. Estimated data points beyond the array resolution limits – i.e., the grey areas in a) – are colored in grey.

As for attenuation data, all the approaches agree quite well at high frequencies and the estimation error is negligible in this range (Figure 7-1b-d). On the other side, they tend to overestimate  $\alpha_R(\omega)$  at low frequencies, with a much larger drift than what observed for dispersion data. As a result,  $\Delta\alpha$  is generally quite large. Specifically, the estimated value can be even several orders of magnitude larger than  $\alpha_R(\omega)$ . For all the considered methods, differences are moderately small at  $f > 15$  Hz (i.e.,  $\lambda < 13$  m) and they slowly increase up to  $f = 10$  Hz (i.e.,  $\lambda = 20$  m). This trend is not exactly matched by the CFDBFaMF, as the corresponding  $\alpha_{R,e}/\alpha_R$  undergoes oscillations that are compatible with those observed in the dispersion data. Furthermore, the CFM tends to overestimate high-frequency attenuation data. At lower  $f$  values, the estimated attenuation increases monotonically and  $\alpha_{R,e}/\alpha_R$  rises up to 3 for the CFDBFaMF and up to 10 for the CFM, whereas the overestimates  $\alpha_R$  by a factor of 5, at  $f = 6$  Hz. Beyond the resolution limits of the array, only CFDBFaMF data are available, and the divergence from  $V_R(\omega)$  is moderately low, whereas  $\alpha_{R,e}/\alpha_R$  slowly grows up to 10. Interestingly, the drift in dispersion and attenuation data occurs at wavelengths greater than 10 m, which is consistent with similar findings on near-field effects. For this reason, both the drift in dispersion and in attenuation data may be linked with near-field effects, that are not modeled in an explicit way, especially in terms of the body-wave contribution.

Table 7.1. Estimated root mean square error for the phase velocity  $\Delta V$  and for the phase attenuation  $\Delta\alpha$  for the circle fit method (CFM), the wavefield decomposition approach (WD), and the cylindrical frequency-domain beamforming-attenuation with modal filtering (CFDBFaMF). The total error  $\Delta V + \Delta\alpha$  is included in brackets. Residuals are computed with reference to the lowest-order three propagation modes (labeled as R0, R1 and R2, respectively) of the synthetic wavefield SW3.

Mode	$\Delta V; \Delta\alpha (\Delta V+\Delta\alpha)$		
	CFM	WD	CFDBFaMF
R0	0.023; 0.43 (0.46)	0.0060; 0.22 (0.22)	0.015; 0.36 (0.20)
R1	0.015; 0.16 (0.18)	0.010; 0.37 (0.38)	0.020; 0.35 (0.20)
R2	0.0059; 0.23 (0.24)	0.0083; 2.62 (2.64)	0.031; 0.12 (0.16)

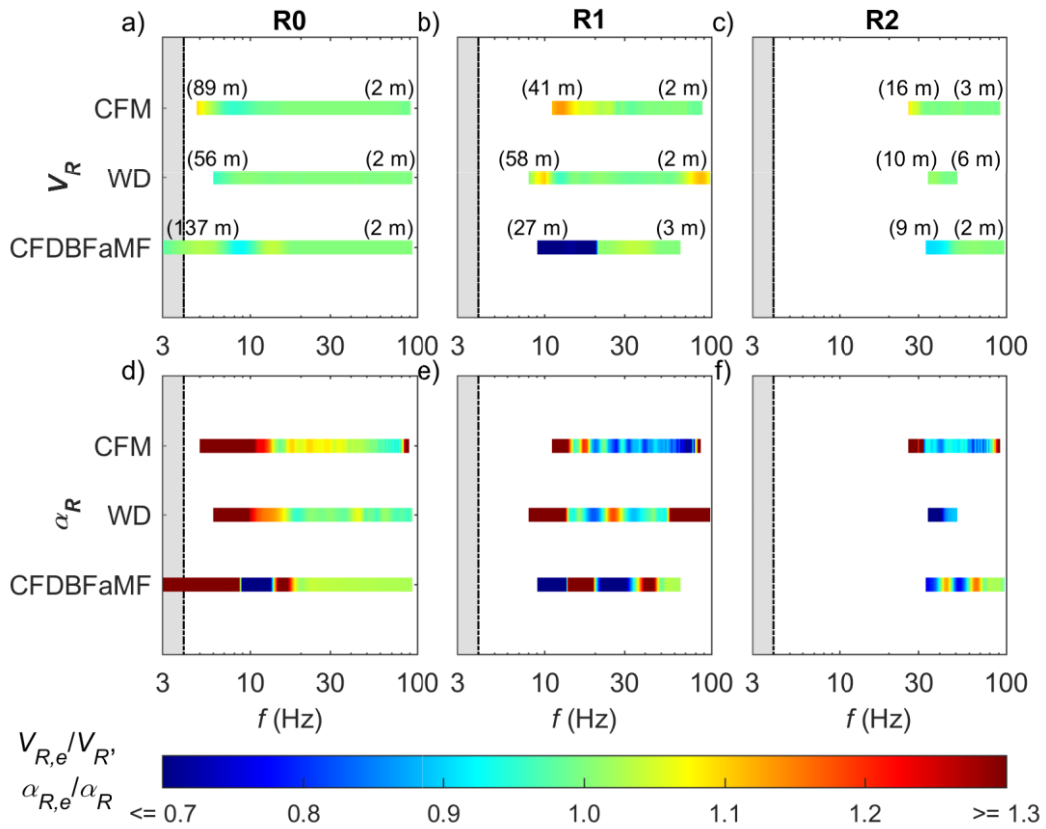


Figure 7-2. Assessment of the inter-method differences for the R-wave dispersion and attenuation curves, with reference to SW3. Each plot contains bars spanning along the frequency range at which each method returned estimates of R-wave dispersion data (top row) and attenuation data (bottom row). The color scale is a function of the magnitude of the normalized phase velocity  $V_{R,e}/V_R$  (i.e., the ratio between the estimated and the theoretical phase velocity), or the normalized phase attenuation  $\alpha_{R,e}/\alpha_R$  (i.e., the ratio between the estimated and the theoretical phase attenuation): a-d) Fundamental mode; b-e) First higher mode; c-f) Second higher mode. The numeric values in brackets denote the maximum and the minimum detected wavelength.

A synthetic description of results is reported in Figure 7-2, for R0 (Figure 7-2a-d), R1 (Figure 7-2b-e), and R2 (Figure 7-2c-f). For each investigated mode, the figure represents the frequency range at which each method returned dispersion and attenuation data, at the boundaries of which are included the wavelength limits. Besides, each bar includes a pseudo-color scheme that indicates the  $V_{R,e}/V_R$  and  $\alpha_{R,e}/\alpha_R$ . As for R0, all the considered techniques return estimates across a broad range of frequencies. Focusing on higher modes, the overall quality in the estimated data is lower than what observed for the fundamental mode. Indeed, the contribution of R1 and R2 in SW3 is less relevant than R0, and it becomes even negligible across a broad frequency range.

However, the investigated methods are still able to identify the corresponding modal parameters. All the methods successfully identify the R1 dispersion curve, at moderately high frequencies, although the CFM tends to overestimate  $V_R(\omega)$  at low frequencies because of the influence of other modes on the correct definition of the spectral peak. In the same range, the CFDBFaMF significantly underestimates  $V_R(\omega)$ , due to the inability of the modal filter in effectively separating the weak target mode from the dominant one (i.e., R0). If the degree of matching in terms of dispersion is acceptable at high frequencies, the fitting quality of  $\alpha_R(\omega)$  is generally poor and the estimated value is often erratic, for all the considered methods. The only exception is the CFDBFaMF, which achieves a good level of compatibility at  $f > 50$  Hz, and the WD at intermediate frequencies. Similar results apply for the R2. In this case, the WD identifies this propagation mode just over a narrow frequency range, whereas the CFDBFaMF is quite effective in characterizing the corresponding modal parameters. Specifically, the CFDBFaMF well captures  $V_R(\omega)$  above 50 Hz, whereas a good level of fitting with  $\alpha_R(\omega)$  is achieved above 70 Hz, which is the frequency range where  $V_R(\omega)$  is exactly matched.

#### *7.1.1.2 Results for SW4*

In the inversely dispersive medium, characterized by the wavefield SW4, all the methods tend to return reliable estimates of both  $V_R(\omega)$  and  $\alpha_R(\omega)$  for R0, R1, and R2, as shown in Figure 7-3, Figure 7-4, and Table 7.2. This result is not surprising, as SW4 is a remarkably multimode wavefield, where the contribution of each propagation mode is dominant at specific frequency ranges. Thus, being each frequency component of SW4 mainly dominated by a single propagation mode (either R0, R1, or R2), the investigated methodologies successfully retrieve the corresponding modal wave parameters.

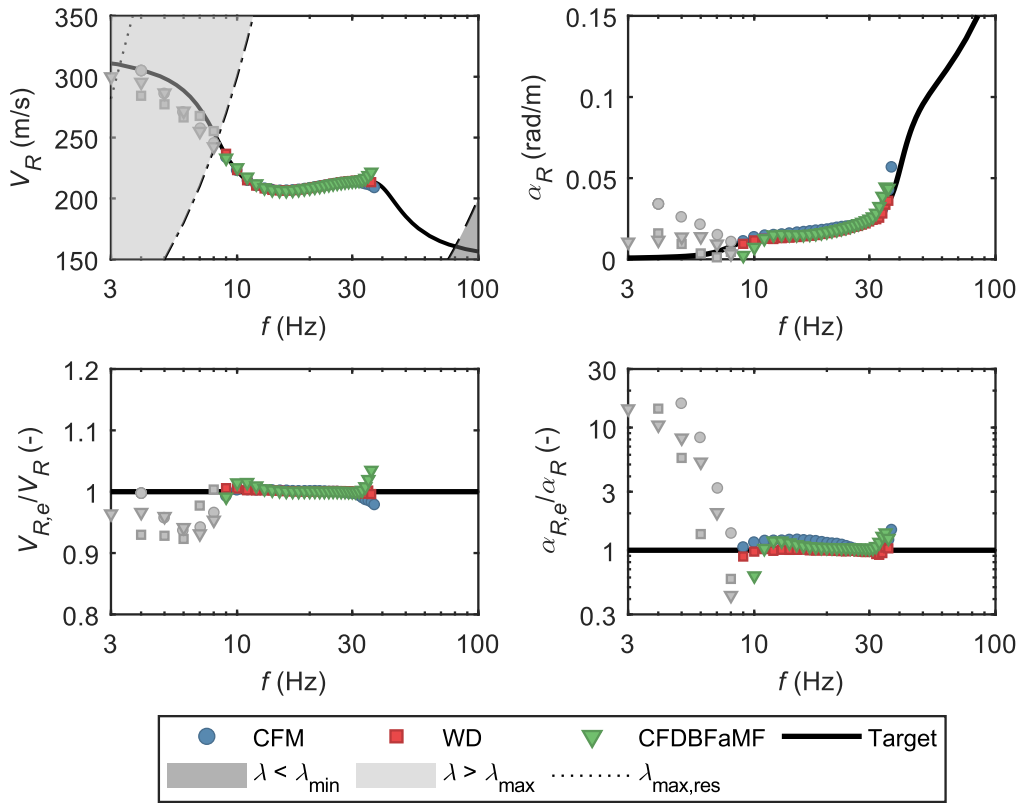


Figure 7-3. Assessment of the inter-method differences for the fundamental mode R-wave dispersion and attenuation curve, with reference to SW4: a) Theoretical vs. estimated dispersion curves; b) Theoretical vs. Estimated attenuation curves; c) Normalized phase velocity  $V_{R,e}/V_R$  (i.e., the ratio between the estimated and the theoretical phase velocity), as a function of the frequency; d) Normalized phase attenuation  $\alpha_{R,e}/\alpha_R$  (i.e., the ratio between the estimated and the theoretical phase attenuation), as a function of the frequency; and normalized phase attenuation  $\alpha_{R,e}/\alpha_R$ . The vertical axis is represented in logarithmic scale as  $\alpha_{R,e}/\alpha_R$  spans multiple orders of magnitude. Estimated data points beyond the array resolution limits – i.e., the grey areas in a) – are colored in grey.

With a focus on R0 (Figure 7-3a-b), all the estimators tend to match  $V_R(\omega)$  and  $\alpha_R(\omega)$  at moderately high frequencies, up to 30 Hz – above this value, the contribution of R0 in SW4 becomes negligible and it becomes no longer detectable. On the other side,  $V_R(\omega)$  is slightly underestimated at low frequencies (i.e., at  $f < 10$  Hz, corresponding to  $\lambda > 22$  m), with a difference bounded within 10% (Figure 7-3c), as demonstrated by the low  $\Delta V$  values. In the same frequency range, all the considered methods dramatically overestimate the low-frequency  $\alpha_R(\omega)$ , due to the unmodeled contribution of body waves (Figure 7-3d). However, if the comparison is restricted to  $\lambda_{max} = 30$  m, then the relative differences are negligible and the overall performance of all the processing schemes is good. This

$\lambda$  value represents the upper boundary of the range of wavelengths needed to fully resolve the layers' interfaces of the medium, as the deepest one is located at 10 m depth. Therefore, if SW4 represented the output of a survey deemed to characterize the corresponding soil profile, this would represent the range of interest. On the other side, some divergence is observed at high frequencies ( $f \sim 40$  Hz), because SW4 is here dominated by both R0 and R1.

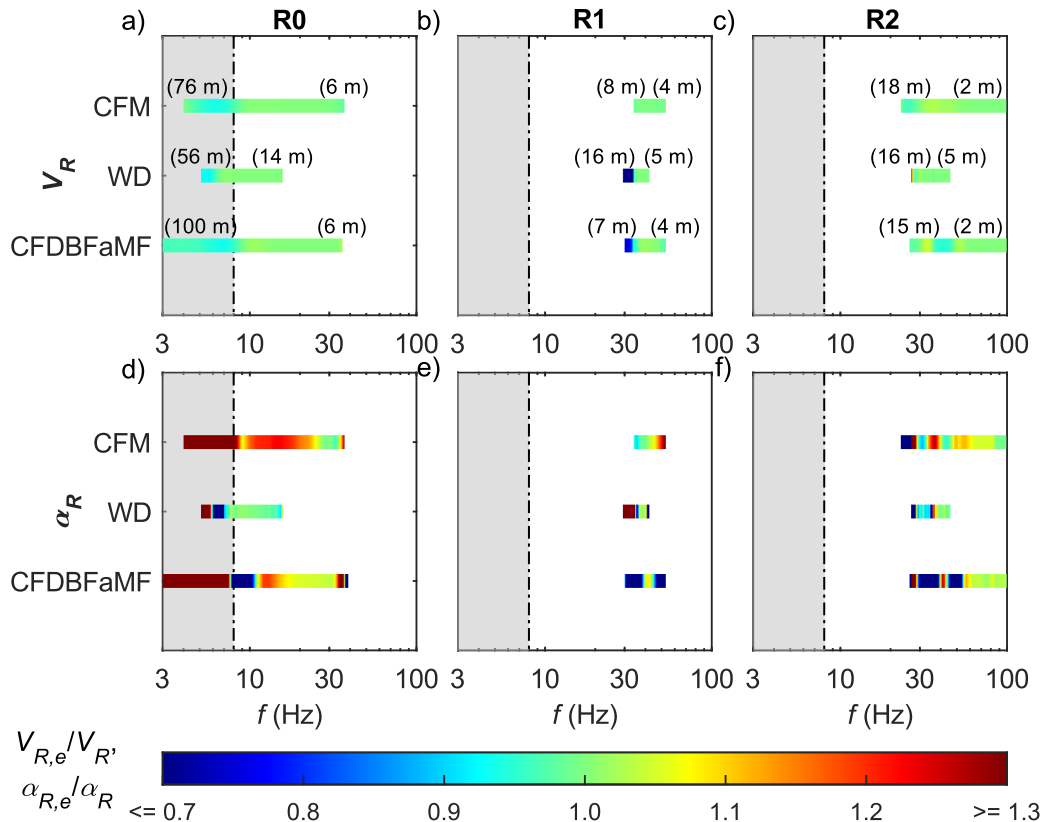


Figure 7-4. Assessment of the inter-method differences for the R-wave dispersion and attenuation curves, with reference to SW4. Each plot contains bars spanning along the frequency range at which each method returned estimates of R-wave dispersion data (top row) and attenuation data (bottom row). The color scale is a function of the magnitude of the normalized phase velocity  $V_{R,e}/V_R$  (i.e., the ratio between the estimated and the theoretical phase velocity), or the normalized phase attenuation  $\alpha_{R,e}/\alpha_R$  (i.e., the ratio between the estimated and the theoretical phase attenuation): a-d) Fundamental mode; b-e) First higher mode; c-f) Second higher mode. The numeric values in brackets denote the maximum and the minimum detected wavelength.

Figure 7-4 provides an overview on the quality of the estimated R-wave parameters for R1 and R2. As for R1,  $V_{R,e}(\omega)$  and  $\alpha_{R,e}(\omega)$  are generally obtained for a rather narrow range of frequencies, and the quality of the estimates is generally poor (Figure 7-4b-e). Indeed, R1 is dominant across a narrow frequency

range, where the contribution of R0 and R2 is also significant. The interference of other wave components does not affect the dispersion estimate. For instance, in transform-based methods, the location of the corresponding spectral peak in the  $f$ - $k$  representation of SW4 is generally not sensitive to the presence of other modes. However,  $\alpha_{R,e}(\omega)$  is highly biased because the interference on the amplitude due to other wave components cannot be successfully removed, in this case. In the CFM, the presence of multiple R-wave modes with similar wavenumbers results in a superposition of the related  $f$ - $k$  spectral peaks. In the CFDBFaMF, the filtering procedure does not effectively remove the contribution by R0 and R2, thus returning a corrected wave with amplitude variations not reflecting those linked with R1. Similar considerations are valid for R2 at low frequencies, due to the interference by R1 (Figure 7-4c-f). However, the CFDBFaMF and the CFM manage to identify reliable  $V_{R,e}(\omega)$  across a broad frequency, down to 30 Hz, where the contribution of R2 to SW4 is less significant. In that range, however, the resulting  $\alpha_{R,e}(\omega)$  is quite erratic, due to the strong interference by R1.

Table 7.2. Estimated root mean square error for the phase velocity  $\Delta V$  and for the phase attenuation  $\Delta\alpha$  for the circle fit method (CFM), the wavefield decomposition approach (WD), and the cylindrical frequency-domain beamforming-attenuation with modal filtering (CFDBFaMF). The total error  $\Delta V + \Delta\alpha$  is included in brackets. Residuals are computed with reference to the lowest-order three propagation modes (labeled as R0, R1 and R2, respectively) of the synthetic wavefield SW4.

Mode	$\Delta V; \Delta\alpha (\Delta V+\Delta\alpha)$		
	CFM	WD	CFDBFaMF
R0	0.018; 1.32 (1.34)	0.020; 0.41 (0.43)	0.020; 0.52 (0.53)
R1	0.007; 0.060 (0.07)	0.003; 0.09 (0.094)	0.06; 0.40 (0.45)
R2	0.007; 0.060 (0.07)	0.003; 0.11 (0.12)	0.010; 0.20 (0.20)

### 7.1.2 Field data: Garner Valley Downhole Array

The investigation of the influence of the processing technique into the estimated R-wave parameters from real data, i.e. in situ recorded wavefields, starts with an application at the GVDA site. Indeed, the recorded wavefield is expected to be mainly governed by the fundamental mode, whereas the contribution of higher propagation modes is negligible, as demonstrated in previous geophysical studies. Therefore, this site represents a benchmark for comparing different processing techniques when the influence of modal superposition is not relevant.

For simplicity, this study reports results obtained from on the South-East line of the GV-H5 testing setup, which is a linear array composed by 14 geophones,

with inter-receiver distance equal to 5 m (Figure 7-5). Furthermore, the assessment only focuses on waveforms generated by the chirp signal applied by the VibroSeis truck, at two shot points with reversal. The source-offsets of roadside shot points are 4.5 m and 35.5 m respectively, whereas the ones on the parking side are 2.5 m and 33.5 m far from the closest sensor.

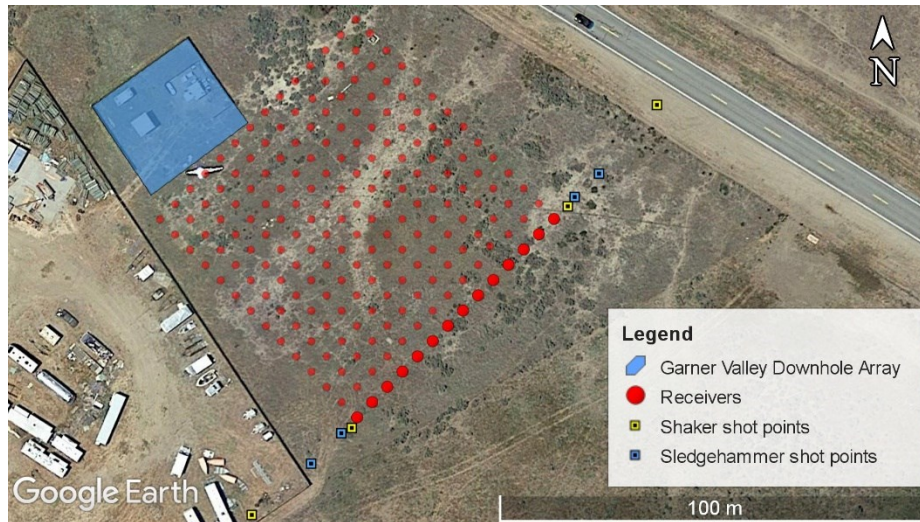


Figure 7-5. MASW array setup. The larger circles represent the receivers belonging to the GV-H5 array, analyzed in this study. The blue area identifies the Garner Valley Downhole Array, where the instrumented boreholes are located.

The wavefield recorded at GV-H5 is dominated by a single propagation mode, which is expected to be the R-wave fundamental mode, labeled as R0. This feature is apparent in Figure 7-6, which reports the  $f-k$  representation of the recorded wavefield at one of the selected sub-arrays, obtained by applying the spatial Fourier transform to recorded data. Spectral peaks are related to R-wave propagation modes that characterize the recorded wavefield. In this case, one dominant mode can be identified in the whole investigated frequency range.



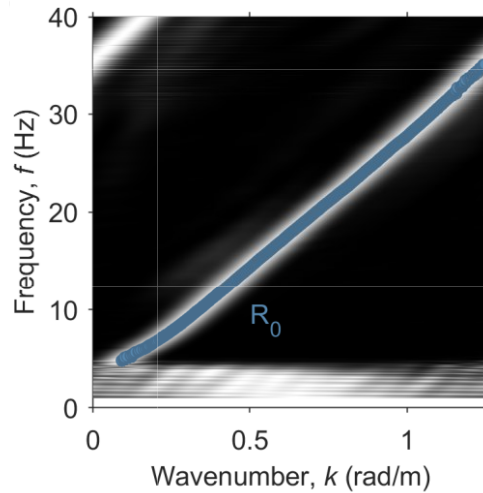


Figure 7-6. Frequency-wavenumber representation of the wavefield recorded at GV-H5.

Therefore, the inter-method comparison at GV-H5 focuses on the TFM, the WD, the CFM and the CFDBFa. Indeed, all these approaches can be tested simultaneously, as both modal techniques and those returning effective wave parameters should provide comparable results, in this case. Furthermore, as the array includes a moderately small number of sensors, this precludes a successful application of modal filtering techniques to well isolate the propagation features of the fundamental mode. Indeed, the modal filter effectively extracts information on the target mode when the number of sensors is greater than 20÷24, as demonstrated in Chapter 5. Therefore, the inter-method comparison for this site does not include results from the CFDBFaMF, as it returns identical results to CFDBFa. Finally, this study does not report results from the GHPB and the FDBFa, because of their equivalence with the CFM and the CFDBFa, respectively. The comparison includes data from multiple shots, for which statistics are computed by combining results from different source offsets and different sub-arrays, in consistency with the multi-offset approach (Wood and Cox, 2012), assuming a bivariate lognormal distribution of the experimental data. The reason behind the choice of using a lognormal distribution in this analysis and in the following will be discussed in Section 7.4.

Figure 7-7 compares the estimated dispersion and attenuation curves obtained for each method. On the one side, the investigation of inter-method differences compares the lognormal statistics (i.e., median and logarithmic standard deviation) of  $V_{R,e}(\omega)$  and  $\alpha_{R,e}(\omega)$ , computed from the elementary R-wave parameters corresponding to the 4 shot locations. Given the small size of the suite of elementary data, the inferred statistics are only indicative of the actual data

distribution. This comparison investigates both the reliability of each processing technique, by assessing the behavior and the presence of anomalous drifts in the median, and their accuracy, expressed by the variability in the estimated R-wave parameters. Besides, Figure 7-8 compares the frequency ranges wherein each method successfully identified the R-wave parameters, simultaneously reporting the number of elementary data points available at each frequency. This information helps in understanding the effectiveness of each processing technique in extracting R-wave parameters from each sub-array. Furthermore, it allows to assess the reliability of data statistics. In this case, all the considered techniques identify R-wave parameters in the frequency range between 5 Hz and 35 Hz (i.e.,  $\lambda = 5 \div 90$  m), and they return a similar number of elementary data points for each frequency. Besides, the number of attenuation data points is usually smaller than the corresponding dispersion data, because of the higher difficulties in retrieving reliable values.

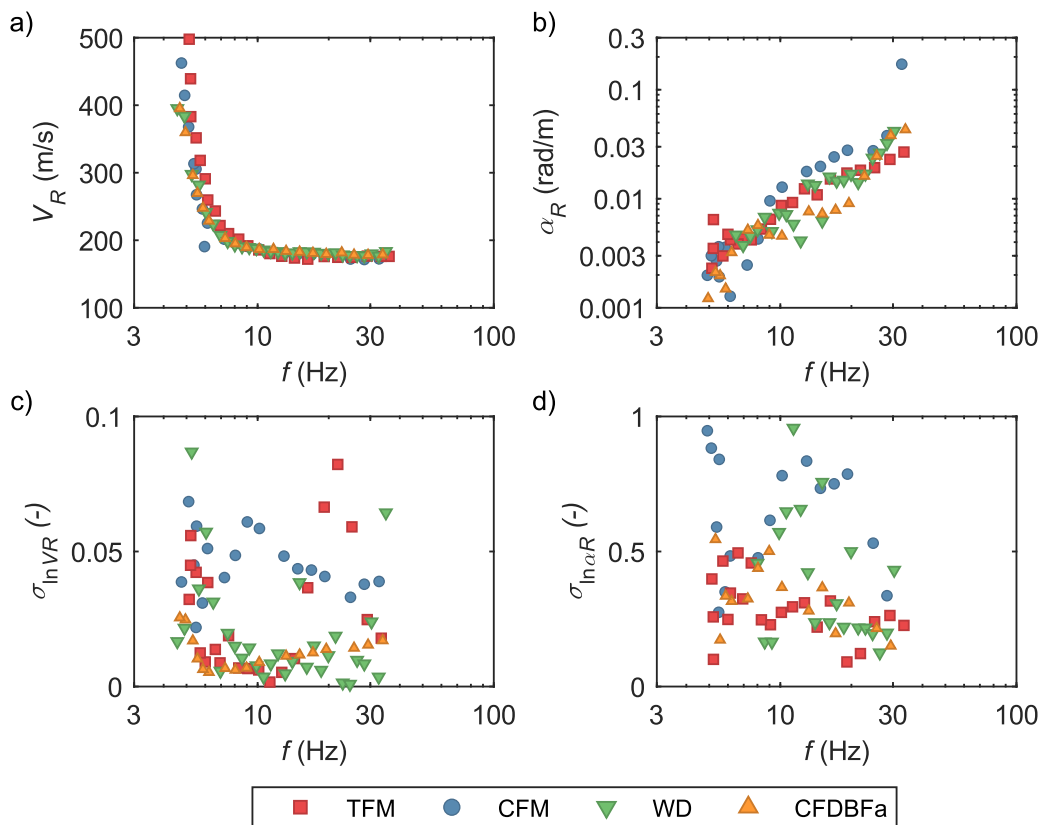


Figure 7-7. Assessment of the inter-method differences for the fundamental mode R-wave dispersion and attenuation curve, with reference to GV-H5: a) Median estimated dispersion curves; b) Median estimated attenuation curves; c) Logarithmic standard deviation of the estimated dispersion curves; d) Logarithmic standard deviation of the estimated attenuation curves.

In general, the dispersion curves are rather close to each other and affected by low variability. Specifically, the corresponding standard deviation  $\sigma_{\ln V_R}$  varies from 0.02 at high frequencies, up to 0.03–0.05 at longer wavelengths. The only exception is the CFM technique, with a data scatter uniformly equal to 0.05. As for the estimated  $\alpha_R(\omega)$ , all the approaches agree at short wavelengths. On the other side, the TFM matches the average values of all the other methods, even with less variability. However, it tends to overestimate  $\alpha_R(\omega)$  at greater wavelengths, probably because of near-field effects due to model incompatibility, that are not modeled in this case. Finally, the CFM and the CFDBFa methods provide similar results, though the former is affected by rather large variability both on  $V_R(\omega)$  and  $\alpha_R(\omega)$ . In general, estimated attenuation data at this site exhibit increasing variability as the wavelength is longer, with a variation from 0.3 and 0.4, whereas CFM data assume standard deviation  $\sigma_{\ln \alpha_R}$  oscillating around 0.75.

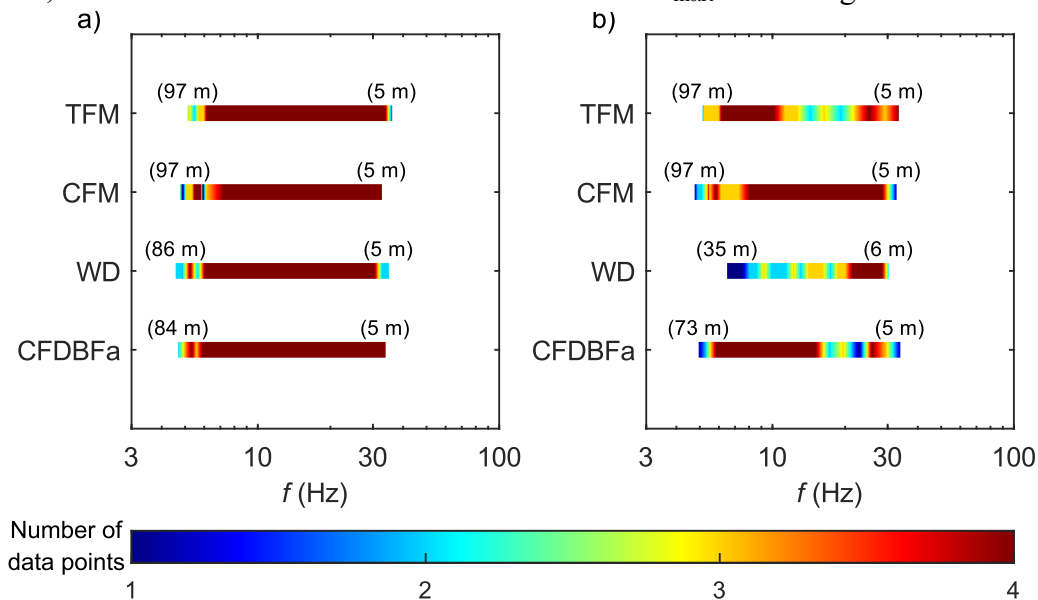


Figure 7-8. Assessment of the inter-method differences for the fundamental mode R-wave dispersion and attenuation curve, with reference to GV-H5. Each plot contains bars spanning along the frequency range at which each method returned estimates of R-wave dispersion data and attenuation data. The color scale is a function of the number of elementary data points returned at each frequency: a) Phase velocity; b-d) Phase attenuation. The numeric values in brackets denote the maximum and the minimum detected wavelength.

This result demonstrates, on the one hand, the reliability of the CFDBFa in retrieving dispersion and attenuation parameters, when the wavefield is mostly controlled by a single propagation mode. The reliability is demonstrated both in terms of strong compatibility in averaged terms as well as the similar degree of

variability. On the other hand, some remarks on other techniques should be pointed out. The WD approach returns robust and consistent estimates of R-wave parameters, with small variability for the attenuation and almost no variability for the dispersion, except at low frequencies. This positive result is also a consequence of the specific fitting procedure adopted to infer R-wave parameters, as the maximum likelihood approach ensures their retrieval across the whole investigated frequency range, although it may be affected by overfitting and it requires an a priori specification of the number of target waves. Furthermore, the CFM technique provides consistent dispersion and attenuation estimates, although with dramatically larger data variability. The strong scatter is an indicator of a possible instability of this approach, maybe linked with perturbations of the spectral shape of transformed data, as well as drawbacks linked with the need of adopting site-specific calibration parameters.

### **7.1.3 Field data: Hornsby Bend**

In this study, the investigation of the influence of the specific processing technique adopted to derive R-wave parameters referred to results of the HB-HN array (see Chapter 6). Indeed, the extent of this array is moderately short, thus limiting the influence of lateral variations in soil stratigraphy, that might introduce additional variability into the results, which is external to intrinsic epistemic uncertainties. However, the receiver spacing in HB-HN is not constant. Therefore, the CFDBFaMF technique cannot be applied as the modal filter requires uniformly sampled data to isolate the contribution of each R-wave propagation mode. Therefore, the analysis focuses on three sub-arrays extracted from HB-HN, with uniform spacing equal to 2 m, 4 m and 8 m, respectively (Figure 7-9). Ideally, also a 1 m-spacing array could have been included in the analysis. However, as it will be shown below, the recorded wavefield is multimodal and the interpretation of this array did not produce accurate results, due to the rather small number of sensors combined with the short length. Therefore, it was ignored. The isolation of subarrays also allows to exploit waveforms generated from internal shot locations. The resulting information will represent an additional reference to assess the relevance of lateral variations along the investigated array. Then, results are averaged and represented in terms of sample statistics, in consistency with the multi-offset approach (Wood and Cox, 2012).

For simplicity, the inter-method comparison only focuses on waveforms generated by the stepped sine signal applied by the VibroSeis truck. Indeed, the corresponding records are the most energetic ones, hence the influence of incoherent noise is minimized.

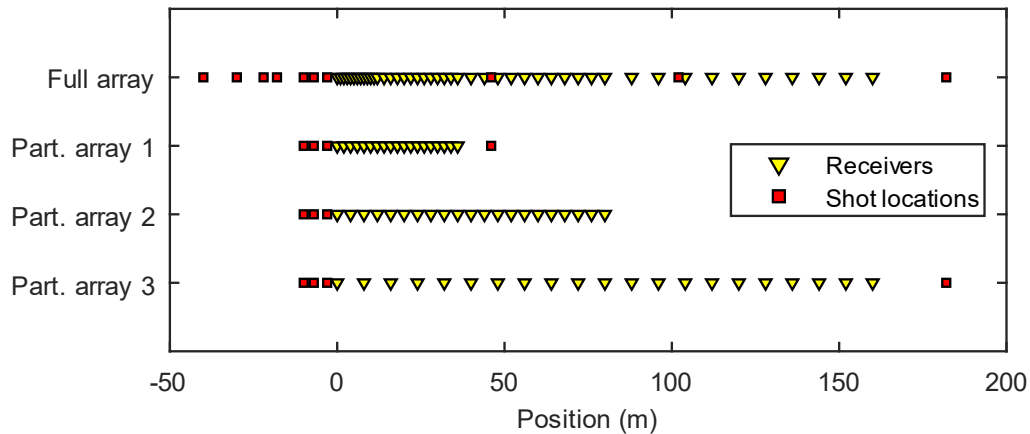


Figure 7-9. Selected sub-arrays in HB-HN. The figure includes the original array, as a reference.

The wavefield recorded at HB exhibits a remarkably multimodal propagation. This feature is apparent in Figure 7-10a, which reports the  $f$ - $k$  representation of the recorded wavefield at one of the selected sub-arrays, obtained by applying the spatial Fourier transform to recorded data. Spectral peaks are related to R-wave propagation modes that characterize the recorded wavefield. In this case, two dominant modes can be identified in the investigated frequency range. The highest wavenumber mode (which is expected to be the R-wave fundamental mode, labeled as R0) tends to disappear at  $f > 20$  Hz. The strong decay of R0 in the high-frequency range may be an indicator of large  $\alpha_R(\omega)$  characterizing such component, for which the corresponding high-frequency waves rapidly decay with the offset, becoming almost negligible at short distances. Instead, the second component of the wavefield (which may be representative of the first higher mode, labeled as R1) is relevant in the amplitude throughout the whole investigated frequency range. Figure 7-10b provides a clearer picture about the role of each propagation mode as a function of the frequency. In this case, the relevance of each component is quantified in terms of frequency-dependent relative energy, measured as the ratio between the squared amplitude of the corresponding spectral peak and the overall squared amplitude at each frequency band. Specifically, the wavefield is dominated by R0 at  $f$  less than 10 Hz, whereas high-frequency components are only dependent on R1. In the intermediate frequency range (i.e.,  $f = 10 \div 20$  Hz), both propagation modes contribute to the wavefield, although the influence of R0 rapidly decays as  $f$  increases. Therefore, the wavefield recorded at HB is quite complex, as the contribution of higher propagation modes is significant, across the whole frequency range. Furthermore, the modal superposition is relevant at low frequencies. Thanks to the multimodal

nature of the wavefield, the HB site is an appealing case study for the application of the CFDBFaMF technique and to assess the effectiveness of the modal filtering on real-site conditions.

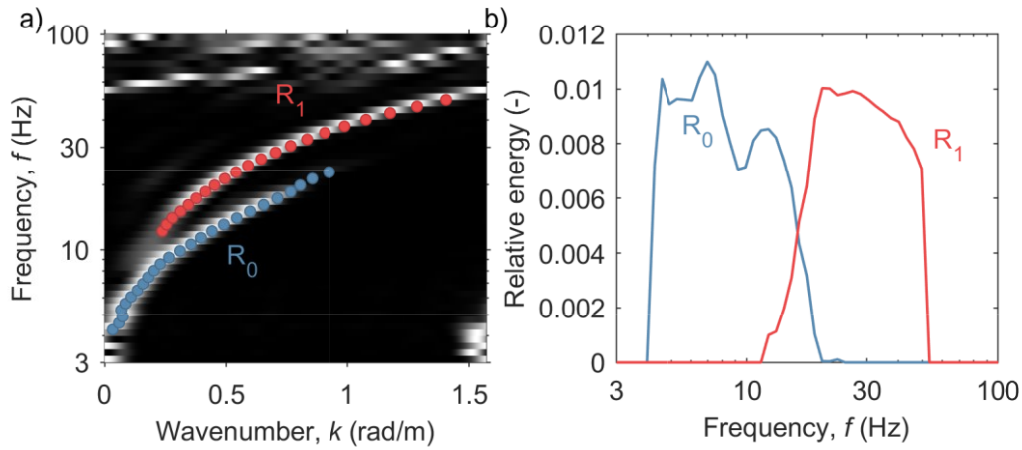


Figure 7-10. a) Frequency-wavenumber representation of the wavefield recorded at HB; b) Energy repartition between the fundamental and the first higher mode. Data refer to sub-array HB-HN-4m, with the source-to-receiver distance equal to 7 m.

As in SW3 and SW4, the inter-method comparison at HB focuses on the WD, the CFM and the CFDBFaMF, because they incorporate an explicit modeling of multiple propagation modes and return modal R-wave parameters. Furthermore, this study does not report results from the GHPB and the FDBFaMF, because of their equivalence with the CFM and the CFDBFaMF, respectively. In both cases, the comparison includes data from multiple shots, for which statistics are computed by combining results from different source offsets and different sub-arrays, in consistency with the multi-offset approach (Wood and Cox, 2012), assuming a bivariate lognormal distribution of the experimental data.

Figure 7-11 compares the estimated modal dispersion and attenuation data for  $R_0$ , according to the WD, the CFM and the CFDBFaMF techniques. On the one side, the investigation of inter-method differences compares the lognormal statistics (i.e., median and logarithmic standard deviation) of  $V_{R,e}(\omega)$  and  $a_{R,e}(\omega)$ . Given the relatively small size of the suite of elementary data, the inferred statistics are only indicative of the actual data distribution. This kind of comparison investigates both the reliability of each processing technique, by assessing the behavior and the presence of anomalous drifts in the median, and their accuracy, expressed by the variability in the estimated R-wave parameters. Besides, Figure 7-13a-c compares the frequency ranges wherein each method successfully identified the R-wave parameters, simultaneously reporting the number of elementary data points available at each frequency. This information

helps in understanding the effectiveness of each processing technique in extracting R-wave parameters from each sub-array. Furthermore, it allows to assess the reliability of data statistics.

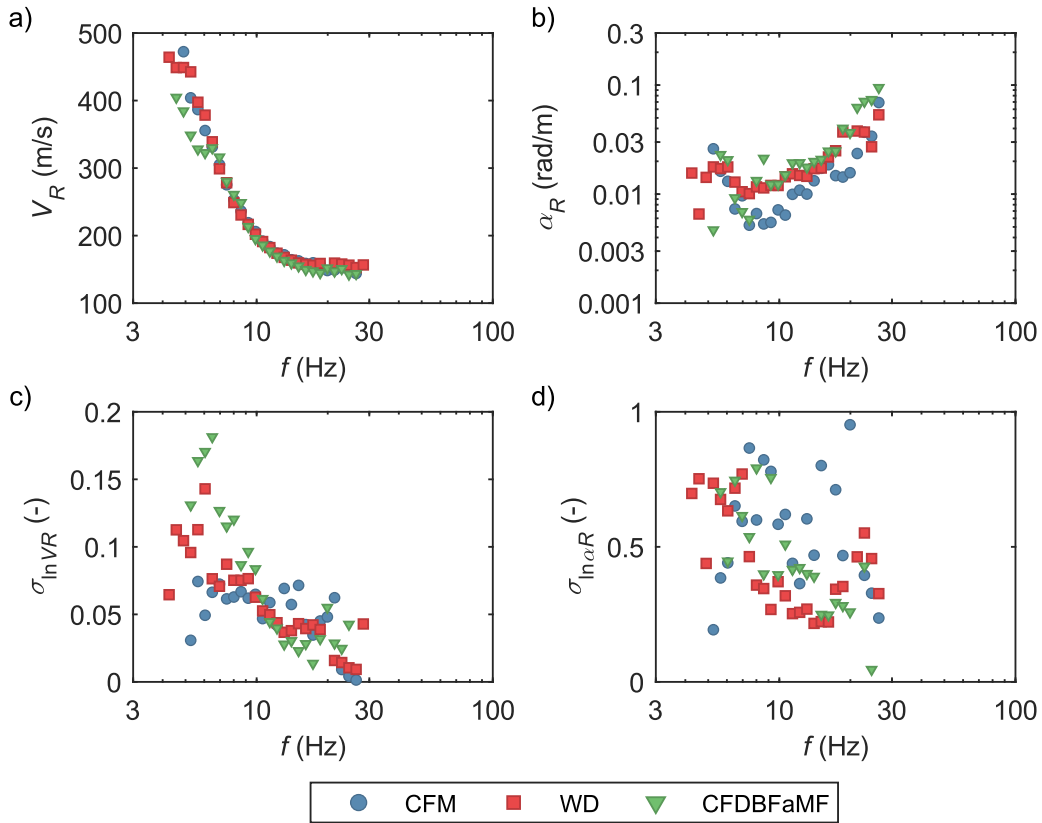


Figure 7-11. Assessment of the inter-method differences for the fundamental mode R-wave dispersion and attenuation curve, with reference to HB-HN: a) Median estimated dispersion curves; b) Median estimated attenuation curves; c) Logarithmic standard deviation of the estimated dispersion curves; d) Logarithmic standard deviation of the estimated attenuation curves.

In general, R0 data are estimated across a moderately narrow range of frequencies and  $\alpha_{R,e}(\omega)$  exhibit moderately large variability, regardless the considered method. Specifically, estimated R-wave parameters are defined at  $f$  from 5 Hz up to 30 Hz, as a consequence of the strong decay in the contribution of R0 to the wavefield at high frequencies. Furthermore, all the techniques return up to  $20 \div 25$  data points and resulting dispersion data are strongly similar to each other, whereas slightly larger differences characterize the attenuation data (Figure 7-11a-b). Indeed, the CFM tends to return slightly smaller  $\alpha_{R,e}(\omega)$ , whereas the WD and the CFDBFaMF are moderately compatible with each other, with moderately small relative differences. Inter-method differences tend to be

significant at  $f < 10$  Hz. On the one side, the attenuation estimates provided by the CFM start increasing as  $f$  gets smaller, with an apparent reversal in the trend. This sharp change in the behavior could be an effect of the influence of R1 in the wavefield, that induces a broadening in the  $f$ - $k$  spectral peak, resulting in an increase in the low-frequency  $\alpha_{R,e}(\omega)$ . On the other hand, the CFDBFaMF undergoes some oscillations at low  $f$ , linked with the influence of R1 and of body waves, as highlighted by some variations in the corresponding  $V_{R,e}(\omega)$ .

Data variability is both dependent on the frequency range and on the specific processing technique. Dispersion data are affected by moderately low variability, with  $\sigma_{\ln V_R}$  mostly ranging between 0.05 and 0.1. The variability associated with the CFM is almost frequency-independent, with a constant value around 0.07. Instead, the  $\sigma_{\ln V_R}$  related with the CFDBFaMF and WD ranges about 0.03 at high frequencies, whereas it grows up to 0.15 at low frequencies. This is an effect of the difficulties of correctly separating the target mode (i.e., R0) from the influence of R1 and body waves. Attenuation data, instead, are affected by large variability. The  $\sigma_{\ln \alpha_R}$  associated with intermediate-to-high frequencies is slightly smaller, and it ranges between 0.3 for the CFDBFaMF and WD and 0.5 for the CFM, whereas it dramatically rises up to 1 at  $f \sim 10$  Hz, with the CFM showing the highest values.

When focusing on R1, inter-method differences sensibly drop down, in terms of discrepancy between mean estimates (Figure 7-12a-b) and covered frequency range (Figure 7-13b). Specifically, all the considered techniques identify R-wave parameters in the frequency range between 9 Hz and 60 Hz (i.e.,  $\lambda = 5 \div 55$  m), and they return a similar number of elementary data points for each frequency. Besides, this number is generally greater than the one for R0. Mean values of  $V_{R,e}(\omega)$  and  $\alpha_{R,e}(\omega)$  stick well at low-to-intermediate frequencies, although the CFM slightly underestimates the phase attenuation at  $f > 30$  Hz. Furthermore, the variability in the estimated wave parameters is much smaller than the one affecting R0 data, for both dispersion and attenuation curves (Figure 7-12c-d). The  $\sigma_{\ln V_R}$  is about 0.02 at all the frequencies, except an increase up to 0.05 for the CFM at  $f < 30$  Hz. Instead, the  $\sigma_{\ln \alpha_R}$  decreases from 0.75 down to 0.1 for the WD, whereas it is frequency-independent for the CFDBFaMF and the CFM, with values equal to 0.4 and 0.65, respectively. Actually, a slight increase of  $\sigma_{\ln \alpha_R}$  occurs at high frequencies (i.e.,  $f > 50$  Hz), probably due to the smaller signal-to-noise ratio.



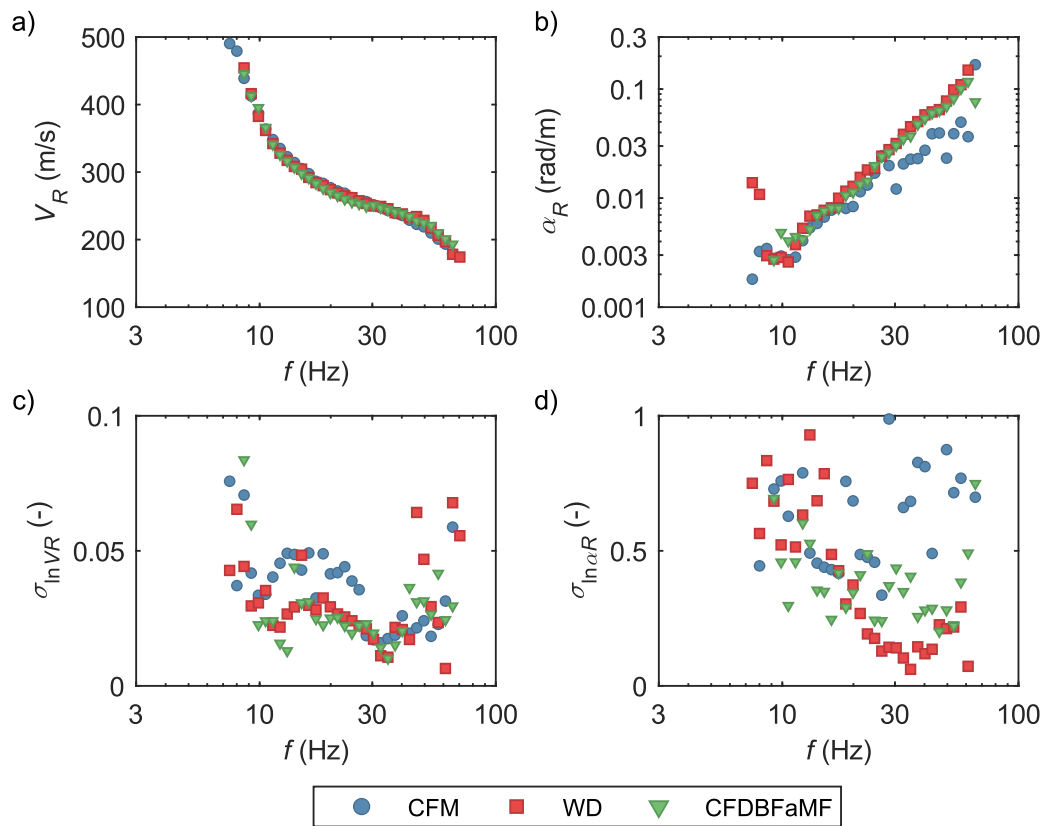


Figure 7-12. Assessment of the inter-method differences for the first higher mode R-wave dispersion and attenuation curve, with reference to HB-HN: a) Median estimated dispersion curves; b) Median estimated attenuation curves; c) Logarithmic standard deviation of the estimated dispersion curves; d) Logarithmic standard deviation of the estimated attenuation curves.

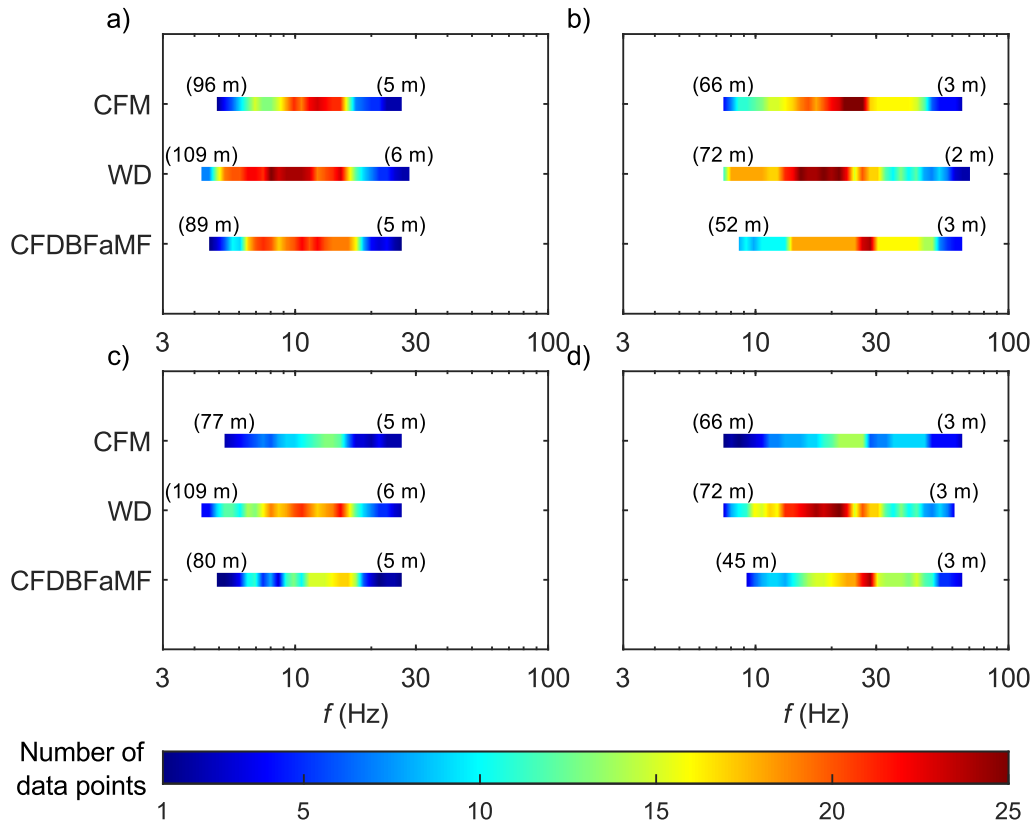


Figure 7-13. Assessment of the inter-method differences for the R-wave dispersion and attenuation curves, with reference to HB-HN. Each plot contains bars spanning along the frequency range at which each method returned estimates of R-wave dispersion data (top row) and attenuation data (bottom row). The color scale is a function of the number of elementary data points returned at each frequency: a-c) Fundamental mode; b-d) First higher mode. The numeric values in brackets denote the maximum and the minimum detected wavelength.

Interestingly, the quality of results as well as the relative performance of each processing technique strongly depend on the investigated mode. On the one side, R0 data are estimated across a moderately narrow range of frequencies and the related variability is rather large, regardless the considered method. Instead, R1 wave parameters can be tracked more easily along a broad frequency range, as highlighted by the low variability. This divergence reflects the energy repartition of the wavefield across the propagation modes (Figure 7-10b). Indeed, a broad frequency range of the wavefield is strongly controlled by R1 and the contribution of R0 is only relevant at low frequencies, although the influence of the higher mode is still significant. Therefore, estimating R0 attenuation data in this site is a challenging task, due to the strong influence of the other mode on the amplitude-offset changes. As a result, the corresponding  $\alpha_{R,e}(\omega)$  is highly variable and

sensitive to the specific processing technique, because of the different capability in extracting and isolating information about the target mode. The CFM directly extracts attenuation from the shape of the spectral transform of the wavefield, but the combined presence of two vibration modes that are moderately close with each other results in an apparent broadening of the spectral peak, that is not only related to the attenuation, thus resulting in an overestimation of  $\alpha_{R,e}(\omega)$ . The WD technique relies on a fitting procedure that explicitly models the contribution of different propagation modes; hence it is expected to provide reliable estimates of modal parameters. Finally, the CFDBFaMF tends to isolate quite well information related to R0. However, the modal filtering is not completely effective because of the strong contribution of the R1, that cannot be fully removed. This results in an erratic and highly variable  $\alpha_{R,e}(\omega)$  at low frequencies, where the modal separation is more challenging. Conversely, retrieving R1 wave parameters is less complex, and all the considered methods provide consistent and accurate estimates of the R1 wave parameters because it is the dominant component of the wavefield, hence its characterization is easy. Some divergence is only observed at lower frequencies, as an effect of the increased role of R0 into the overall energy of the wavefield, for which the proper extraction of  $\alpha_{R,e}(\omega)$  becomes more challenging. It is interesting to notice that the influence of multiple modes in the wavefield is different between attenuation and dispersion estimates. On the one side, reliable and well-defined dispersion values can be retrieved for both propagation modes, almost regardless the considered method. On the other hand, attenuation data are strongly sensitive, and the modal superposition dramatically affects the possibility of properly extracting correct modal attenuation values, especially when the target mode is not dominant or the energy is equipartitioned across different modes.

## 7.2 Influence of source characteristics

The source effect is critical in active-source characterization techniques. Indeed, the active source directly controls the frequency and amplitude characteristics of the recorded wavefield, especially the signal-to-noise ratio. It is highly desired that the source be capable of generating high-quality waveforms, with enough large amplitudes so that the influence of external, incoherent noise is negligible and the frequency and the amplitude components reflect the wave component that is under examination. In this way, additional sources of epistemic uncertainties, linked with the wrong modeling of the recorded wavefield according to an idealized scheme that is uncorrupted by noise, are significantly reduced. For this purpose, an ideal strategy may consist in generating waveforms by means of high-

energy, controlled sources, e.g., by shakers and vibrators. As these devices can apply high-magnitude ground forces, the quality of the resulting signal will be excellent, and the influence of external noise sources will be negligible. This aspect is crucial especially for amplitude data, which are even rather sensitive to ground noise than the phase, as demonstrated in Chapter 5. However, an alternative, smart technique relies on weak-energy sources, where the lack of energy is compensated by a stack averaging procedure, which increases the signal-to-noise ratio (Foti et al., 2014). Furthermore, a proper source characterization is crucial to avoid the inclusion of additional epistemic uncertainties. Indeed, some processing techniques (e.g., the TFM, the GHPB and the CFM) require a direct measure of the ground force, which needs specific instrumentation, and its quantification may be affected by imperfect coupling between the plate and the ground.

This Section investigates the influence of the specific source type on the reliability and the accuracy of the estimated R-wave parameters, by adopting the experimental data acquired at the HB-HN array as a reference. Indeed, the waveforms recorded in this array of sensors were generated by three different types of sources, with a different energy level and different frequency content. A more detailed description about the main features of the active sources is provided below. Due to the multimodal nature of the Rayleigh wavefield recorded at this site, wavefield data were interpreted according to the CFDBFaMF. Indeed, this technique returned reliable estimates of dispersion and attenuation data, compared with other approaches. As this technique requires uniformly sampled data to isolate the contribution of each R-wave propagation mode, the analysis focuses on three sub-arrays extracted from HB-HN, with uniform spacing equal to 2 m, 4 m and 8 m, respectively. The analysis of each sub-array focused on waveforms generated by different types of active source, with shared location. Specifically, wavefield data with active source located at 3 m, 7 m, and 10 m far from the closest sensor were considered, without reversal. In this way, the inter-source comparison is carried out by keeping the strongest equivalence in terms of boundary conditions.

### **7.2.1 Source characteristics**

Figure 7-14 represents some examples of wavefield generated by all the types of active source. Data refer to the sub-array with spacing equal to 4 m, and a source located 7 m far from the closest sensor (Figure 7-14a). Furthermore, Figure 7-15 provides a frequency-domain representation of the ground force, together with a

pseudo-color plot mapping the signal-to-noise ratio as a function of the frequency and the receiver location, for each source type. As the noise power derives from the pre-trigger and the post-trigger time windows only, this estimate may not be fully representative of the actual noise level. Indeed, the resulting signal-to-noise ratio is here represented for illustration purposes.

Part of the recorded wavefield was generated by an instrumented sledgehammer (Figure 7-14b-c). This source applies a pulse-like signal, and most of the energy is carried by moderate-to-high frequency harmonics, with  $f = 30 \div 80$  Hz (Figure 7-15a). The average energy transmitted onto the ground is moderately low, especially compared with mechanically-controlled sources. Furthermore, the applied energy level is quite variable, as it is sensitive to the operator and not perfectly reproducible. The low energy entails a strong relevance of incoherent noise in the wavefield, especially when dealing with sensor data recorded at moderately large distances from the source itself, as highlighted by the moderately low signal-to-noise ratio (Figure 7-15d).

The remaining waveforms were generated by means of a high-energy, vibroseis truck, that allows to apply high-energy signals, with an accurate control of the frequency content. The shaker was used to generate two different types of signals, namely a chirp and a stepped sine. The chirp appears as a non-stationary signal, with a linear increase of the frequency with time (Figure 7-14d). The corresponding frequency-domain representation results in a flat spectrum, with the largest amplitude at  $f = 5 \div 30$  Hz, namely the frequency range encompassed by the sweep (Figure 7-15b). Instead, the stepped sine is a multi-stage signal that applies a sequence of harmonic cycles, in which the ground response is measured by the acquisition device directly in the frequency-domain (Figure 7-14f; Figure 7-15c). This acquisition scheme shares some similarities with an ideal acquisition scheme, wherein a harmonic time history is applied onto the ground and the corresponding response is measured. In both cases, the energy of the input signal is large and lowly-variable, and the signal-to-noise ratio is moderately high (Figure 7-15e-f). Furthermore, the use of the stepped sine ensures a less pronounced decay of the signal-to-noise ratio with the offset and the frequency, compared with the chirp. Indeed, the stepped sine is capable to generate high-frequency signals preserving their characteristics even at moderately large distances from the source itself. This result does not strictly depend on the energy generated by the source, as it is the same for both signal types, but on the frequency content. Indeed, the sweep is a nonstationary signal, where the frequency content constantly changes with time, hence each frequency is not sustained and tends to damp more rapidly (Rahimi et al., 2022).

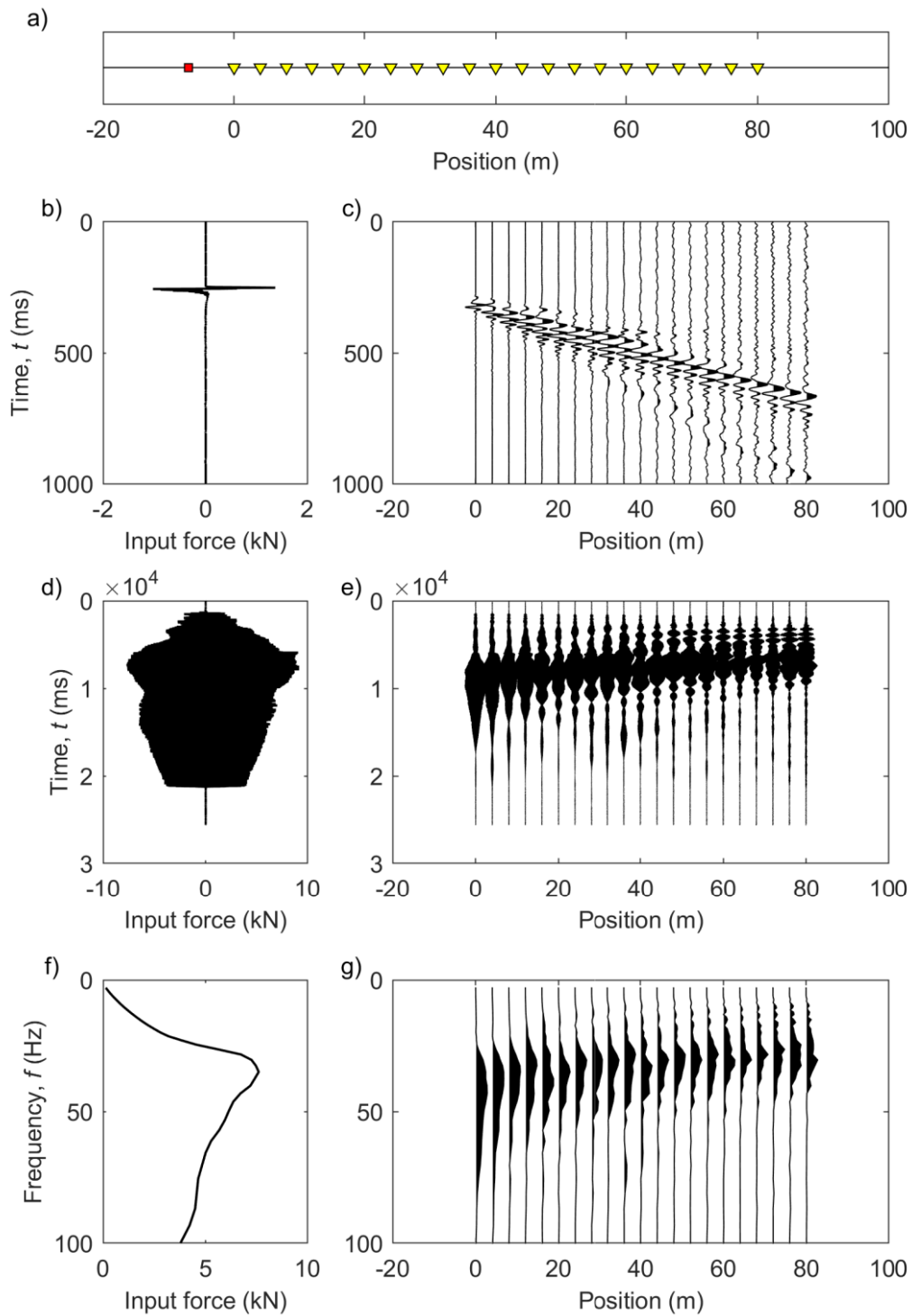


Figure 7-14. Recorded wavefield at HB-HN. The left column represents the input force, whereas the right column reports the recorded particle velocity data: b-c) Sledgehammer; d-e) Chirp; f-g) Stepped sine.

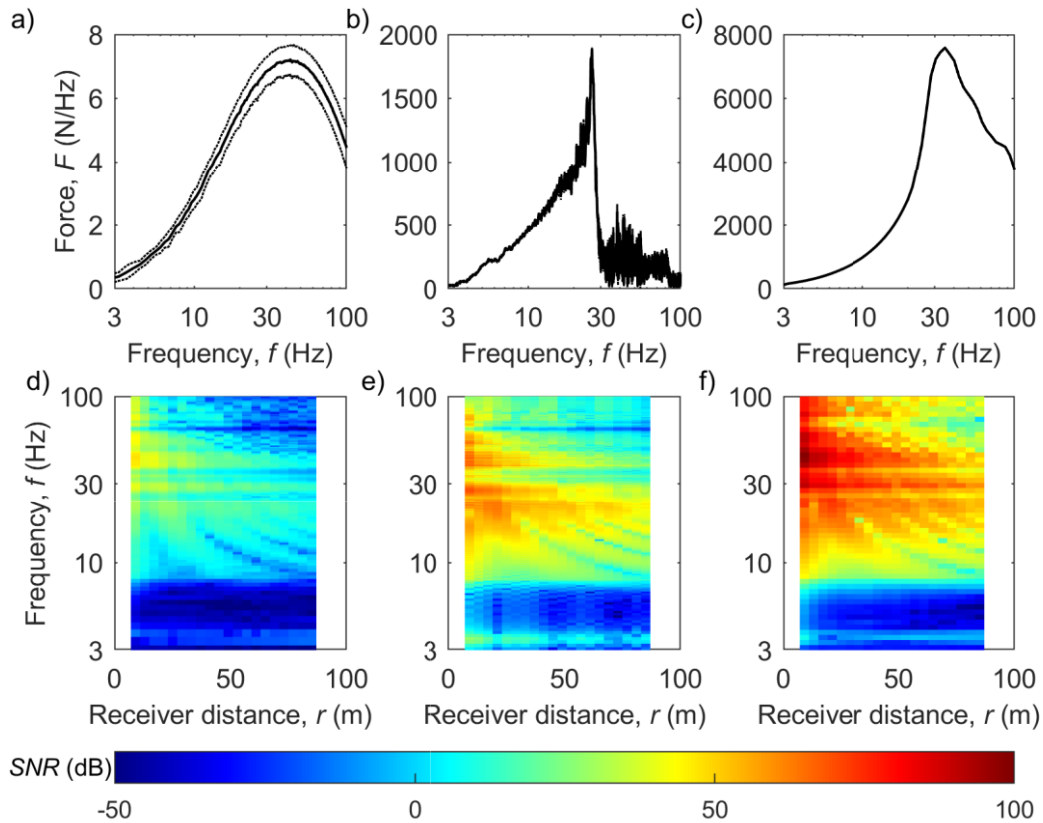


Figure 7-15. Frequency-domain data. The top row represents the input force, with the interval defined by one standard deviation, whereas the bottom row includes pseudo-color maps of the signal-to-noise ratio: a-d) Sledgehammer; b-e) Chirp; c-f) Stepped sine.

### 7.2.2 Source comparison

Figure 7-16 compares the statistics of the estimated dispersion and attenuation curves for R0. Data are clustered as a function of the specific source type under examination (i.e., sledgehammer, chirp and stepped sine) and, for each one, the corresponding statistics are obtained by combining results from different source offsets and different sub-arrays, in consistency with the multi-offset approach (Wood and Cox, 2012). Note that, given the small size of the suite of elementary data, the inferred statistics are only indicative of the actual data distribution. As in the inter-method comparison, the influence of the source type on the estimated R-wave parameters focuses on both the reliability and accuracy in the estimates – expressed by the median and the logarithmic standard deviation, respectively – as well as the covered frequency range and the number of elementary data points available at each frequency (Figure 7-18a-c). This information provides further

insight about the effectiveness of each source type in extracting R-wave parameters from each sub-array, as well as the reliability of data statistics.

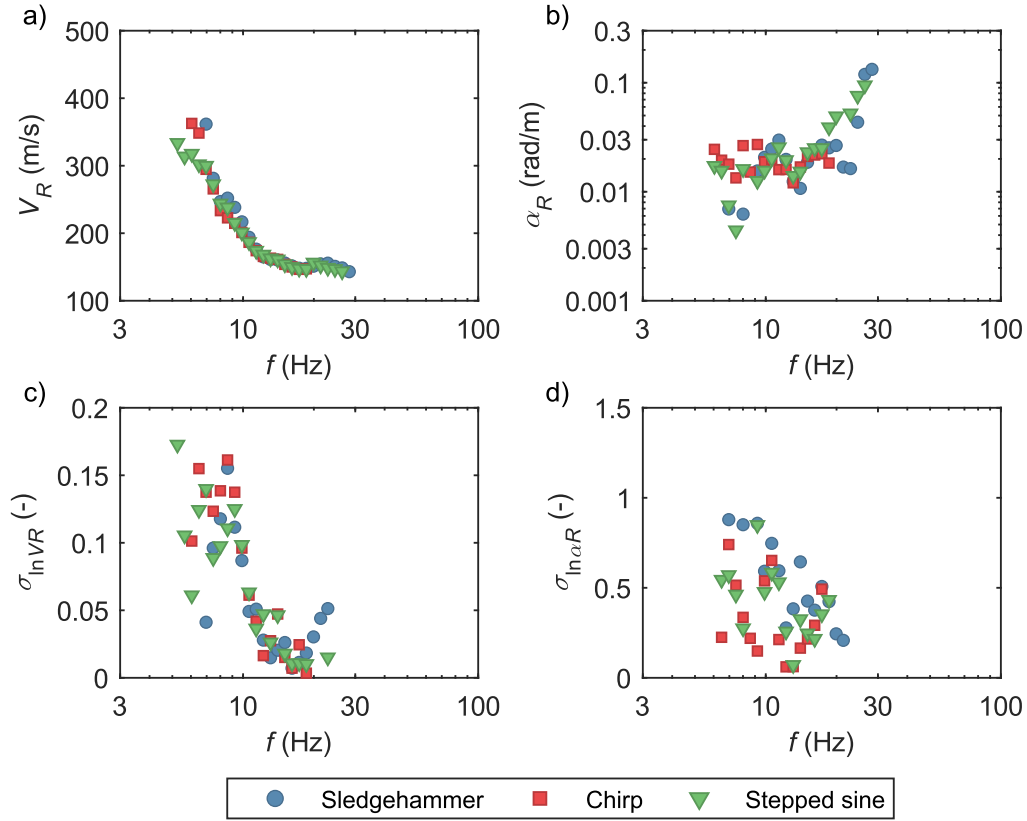


Figure 7-16. Influence of the source type on the fundamental mode R-wave dispersion and attenuation curve, with reference to HB-HN: a) Median estimated dispersion curves; b) Median estimated attenuation curves; c) Logarithmic standard deviation of the estimated dispersion curves; d) Logarithmic standard deviation of the estimated attenuation curves.

On the one side, the investigated frequency range does not strongly depend on the source type (Figure 7-18a-b). Indeed, the upper boundary of the available frequencies is about 30 Hz (i.e.,  $\lambda = 5$  m) for both the sledgehammer and the stepped sine, whereas the use of the chirp signal limits the characterization of the fundamental-mode R-wave at 20 Hz (i.e.,  $\lambda = 8$  m). At higher frequencies, no data are available because of the strong decay in the contribution of R0 to the wavefield at high frequencies. On the other side, shaker data extend at lower frequencies (down to 5 Hz), whereas sledgehammer-based data stop at  $f = 7$  Hz. However, the maximum identified  $\lambda$  varies between 50 m and 60 m, entailing an almost identical level of investigated depth for all the considered source types.



As for the quality of the estimated R-wave parameters, resulting dispersion data are strongly similar to each other, in terms of both the mean values and data variability. Specifically,  $\sigma_{\ln V}$  is close to 0.02 at  $f > 10$  Hz, whereas it increases up to  $0.1 \div 0.15$  at low frequencies. No significant influence of the source type is observed, although sledgehammer-based data exhibit slightly larger variability at high frequencies. Instead, larger differences characterize the estimated attenuation curves. Deviations are not significant when focusing on the median value, except some divergence at  $f < 10$  Hz. The related variability is large, with  $\sigma_{\ln \alpha}$  ranging between 0.3 at intermediate-to-high frequencies and  $0.5 \div 0.7$  at  $f < 10$  Hz. In general, sledgehammer-based data exhibit larger variability, especially at lower frequencies, because of the sensibly lower signal-to-noise ratio in this range. The negative influence of incoherent noise into the quality of the estimates also emerges in the small number of data points associated with this kind of source (around  $5 \div 6$ ), whereas other techniques provided up to 9 values.

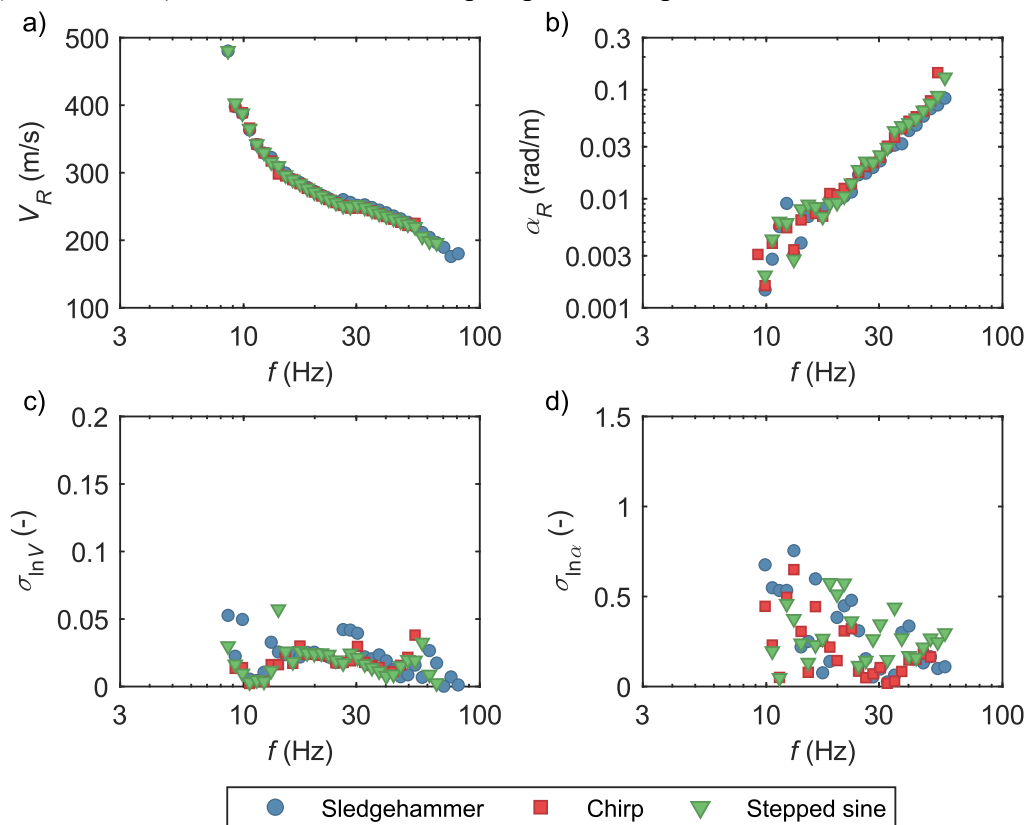


Figure 7-17. Influence of the source type on the first higher mode R-wave dispersion and attenuation curve, with reference to HB-HN: a) Median estimated dispersion curves; b) Median estimated attenuation curves; c) Logarithmic standard deviation of the estimated dispersion curves; d) Logarithmic standard deviation of the estimated attenuation curves.

When focusing on R1, the influence of the source used to generate experimental data on the estimated R-wave parameters is negligible, in a similar way to what occurred to the inter-method differences. Specifically, both the mean estimates (Figure 7-17) and the covered frequency range (Figure 7-18c-d) closely match with each other. Regardless the source type, R-wave parameters are identified at frequencies between 9 Hz and 70 Hz (i.e.,  $\lambda = 3 \div 60$  m). Besides, the number of elementary data points is similar.

As for data variability,  $\sigma_{\ln V_R}$  ranges on average around 0.02 at all the investigated frequencies. Instead,  $\sigma_{\ln \alpha_R}$  grows from 0.25 at high frequencies up to 0.5 at low frequencies. Interestingly, data scatter is poorly sensitive on the source type. A potential reason behind the high quality in results and the limited influence of source characteristics in R1 data may be its dominant role in the recorded wavefield, for which even low-energy sources are capable of properly exciting it with small noise levels.

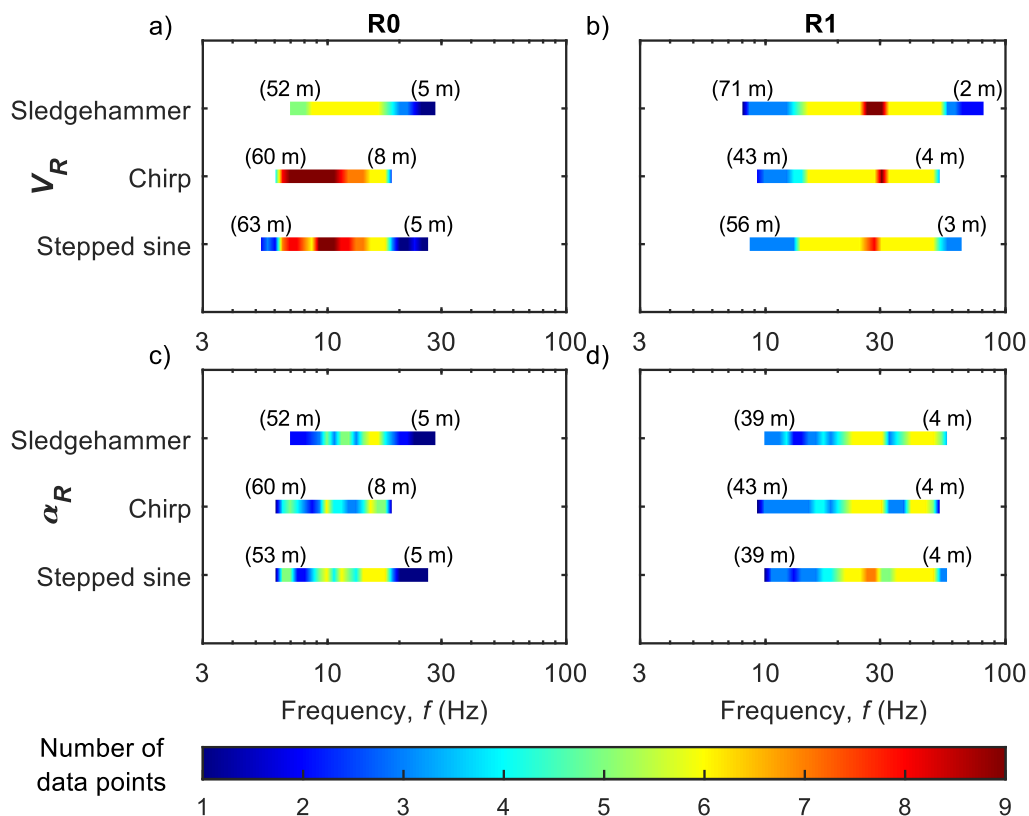


Figure 7-18. Assessment of the inter-source differences for the R-wave dispersion and attenuation curves, with reference to HB-HN. Each plot contains bars spanning along the frequency range at which each method returned estimates of R-wave dispersion data (top row) and attenuation data (bottom row). The color scale is a function of the number of elementary data points returned at each frequency: a-c) Fundamental mode; b-d) First

higher mode. The numeric values in brackets denote the maximum and the minimum detected wavelength.

In summary, the use of different source types returns, on average, equivalent dispersion and attenuation estimates. However, the use of high-energy controlled sources rather than a sledgehammer allows to investigate a slightly broader range of frequencies or wavelengths. Most of all, sledgehammer-based data tend to exhibit higher levels of variability. A potential reason behind such discrepancy can be linked with the energy level associated with each source mechanism combined with the incoherent ambient noise that characterizes the site, that results in different frequency characteristics of recorded data and in a different quality level. Indeed, the sledgehammer is not a high-energy source and the signal-to-noise ratio of recorded traces might be low. Thus, the traces amplitude might be corrupted by noise. However, the mean trend in the attenuation curve can still be captured. This result positively contributes to the capability of the sledgehammer for the attenuation estimate. This is helpful for ordinary applications, where high-energy sources are not typically available.

## **7.3 Influence of receiver characteristics: geophones vs. distributed acoustic sensing**

### **7.3.1 The DAS technique**

The distributed acoustic sensing (DAS) records perturbations induced on a fiber-optic cable by the propagation of mechanical waves in the ground.

Pioneering applications of the DAS technology were mainly for industrial purposes, as perimeter security (Choi et al., 2003) and railroad and pipelines monitoring (Strong et al., 2008; Costley et al., 2018). Then, several studies demonstrated the efficiency of this technology for seismological studies (e.g., for the structural and dynamic characterization of earthquake sources; Jousset et al., 2018), borehole monitoring (e.g., Mestayer et al., 2011; Daley et al., 2013; Parker et al., 2014), landslide monitoring (Lancelle, 2016), traffic monitoring (Lancelle, 2016), and invasive geophysical tests (e.g., Mateeva et al., 2014; Kuvshinov, 2016). Furthermore, this system has been widely used to measure ambient noise vibrations for near-surface characterization (e.g., Hornman et al., 2013; Freifeld et al., 2016; Yavuz et al., 2016; Ajo-Franklin et al., 2017). As for active-source SWM, only a few studies focused on the monitoring the quality of surface waves generated by active sources (Daley et al., 2013) and addressed the application of the DAS acquisition system to SASW surveys (Costley et al., 2018) and MASW

testing (Galan-Comas, 2015; Lancelle, 2016; Costley et al., 2018; Song et al., 2018).

In MASW testing, the main advantage of the DAS technology with respect to conventional acquisition devices is the enhanced spatial resolution using low-cost instrumentation. Indeed, the fiber-optic allows dense spatial sampling of the wavefield, potentially along a broad array extent. Thus, this device can return spatially un-aliased strain data over a broad frequency band useful for both seismological and geophysical studies. Conversely, achieving the same spatial resolution with ordinary receiver arrays would require a large number of sensors, entailing severe economic and logistic issues. Furthermore, high quality measurements can be even obtained from conventional fiber-optic cables, that are not specifically designed for seismic investigation and already deployed in the ground (e.g., the telecommunication infrastructure; Jousset et al., 2018). Therefore, the per-channel cost is moderately low. Finally, this technology is less sensitive to the ground coupling than geophones (Bakulin et al., 2020). Applications of this technology to MASW surveys demonstrated that the dispersion estimates well match those obtained from geophone measurements (Galan-Comas, 2015; Vantassel et al., 2022). Furthermore, the DAS acquisition tends to better identify higher propagation modes (Galan-Comas, 2015). However, fiber-optic systems are uniaxial devices, recording only perturbations acting in the longitudinal direction, and the correct location of measurement points may be uncertain in some cases (e.g., in the case of fiber overstuffing; Bakku, 2015). Also, the signal-to-noise ratio of measured data is lower compared to geophones. The lower quality in recorded traces limits the repeatability of the survey (Costley et al., 2018) and the reliability of the estimated wave parameters in the presence of weak signals (Mestayer et al., 2012). Finally, as it will be explained in the next section, the measurement technique involved in this technology partially limits the minimum investigable wavelengths at greater values than the one defined by the Nyquist-Shannon theorem (Lancelle, 2016; Bakulin et al., 2020). Therefore, the characterization of high-frequency R-wave data might be challenging.

### **7.3.2 Principles of processing DAS data**

DAS measurements do not return the same output as the geophones, and a proper interpretation should account for the differences in acquired data. On the one side, geophones record the particle motion at discrete points along the acquisition array, and the output is a time history of the particle velocity at the location where the instrument is installed. Instead, the DAS system records a spatially-averaged axial strain  $\epsilon_x(r, \omega)$  induced on the fiber optic by the passing wavefield. Indeed, the

passage of mechanical waves induces an axial strain in the fiber-optic cable, that is coincident with the horizontal, in-line strain  $\varepsilon_r(r, \omega)$  in the ground, when a proper coupling is ensured. An interrogator unit reads the consequent shift in phase-lag of a laser pulse traveling in the cable, induced by the variation in length of the cable itself. However, the device does not perform a point measurement, but it reads the variation in phase difference over a reference length  $2g$ , called gauge length, around the investigated location, from which the average strain  $e_r(r, \omega)$  is derived (Figure 7-19a; Grattan and Sun, 2000). The resulting average strain at each measurement point can be linked with the displacement, as it equals the difference of the radial displacement at two points separated by a distance equal to the gauge length (Mateeva et al., 2014; Bakku, 2015; Jousset et al., 2018; Vantassel et al., 2022):

$$e_r(r, \omega) = \frac{1}{2g} [u_r(r + g, \omega) - u_r(r - g, \omega)] \quad (7.2)$$

Note that the gauge length is not necessarily linked with the channel separation, i.e. the distance between two subsequent measurement points. Depending on their mutual relationship, the resulting strain measure may be obtained from independent windows or partially overlapping ones.

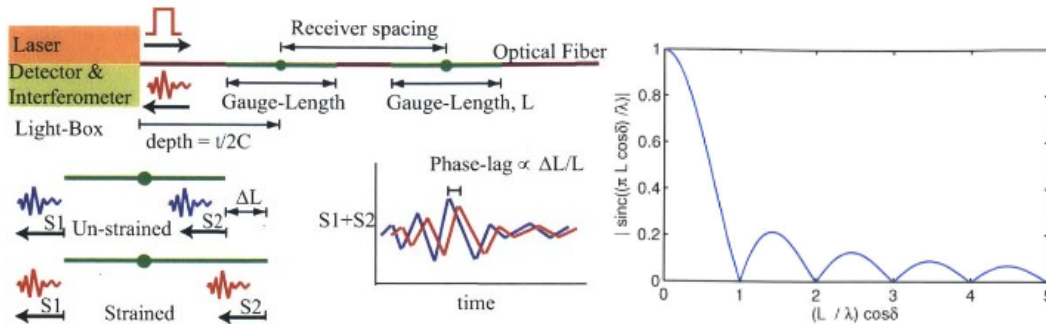


Figure 7-19. a) Schematic model of the DAS system; b) Amplitude response.

As the DAS device records a strain-related quantity and it provides a spatially averaged measure of the strain field, the interpretation of recorded data is slightly more complex with respect to conventional acquisition devices. On the one side, the gauge length affects the quality of spatial sampling, as it limits the range of investigable wavelengths. For instance, let us consider the simple case where the radial displacement field is spatially harmonic, with no amplitude decay. In this case, it is demonstrated that the recorded average strain  $e_r(r, \omega)$  is a scaled version of the “true” strain field  $\varepsilon_r(r, \omega)$ , and the scaling factor is a sinc function depending on both  $2g$  and the wavenumber  $k$  characterizing the wavefield:

$$e(x, \omega) = \varepsilon_x(x, \omega) \text{sinc}(kg) = \varepsilon_x(x, \omega) \text{sinc}\left(\frac{2\pi g}{\lambda}\right) \quad (7.3)$$

Therefore, the averaging procedure is equivalent to the application of a lowpass filter (i.e., a sinc filter) in the wavenumber domain, which tends to significantly attenuate high-wavenumber waves, i.e. short wavelengths. Besides, the sinc filter includes notches when  $2g/\lambda$  is an integer. Therefore, when the gauge length is an integer multiple of the passing wavelength, the recorded  $e_r(r, \omega)$  is null. Indeed, in this case the gauge undergoes both negative and positive strains in equal measure, that cancel out in the averaging procedure. Thus, the corresponding wave components cannot be detected by the DAS system, and they are lost. The loss of information mainly affects the high-frequency components of the R-wavefield, as they usually exhibit short  $\lambda$ . An increase in  $2g$  induces a greater loss of information of short-wavelength data, although the signal quality improves significantly, as the signal-to-noise ratio is greater (e.g., Bakulin 2020). For this reason, the design of the optimal gauge length is a critical task, that should account for the acquisition setup, for the quality of the source, the magnitude of incoherent noise, and the desired range of investigated wavelengths. A possible strategy to overcome the resolution issues induced by the spatial averaging consists in carrying out multiple measurements, where the gauge length is modified in each step (Bakku, 2015).

A proper interpretation of DAS-based surveys should account for the peculiar nature of the recorded data, as it returns a spatially-averaged radial strain. Indeed, usual processing techniques estimate R-wave parameters from displacement data, according to a planar or a cylindrical scheme.  $e_r(r, \omega)$  does not exhibit the same spatial variation as the radial displacement  $u_r(r, \omega)$ , and the different geometric spreading needs to be modeled to obtain reliable estimates of the R-wave parameters. To better understand the entity of this difference, let us consider a synthetic case, where the recorded wavefield consists of a Rayleigh wave recorded moderately far from the source, characterized by  $k_R = 0.1$  rad/m and  $\alpha_R = 0.0015$  rad/m. In this case,  $u_r(r, \omega)$  can be described through the asymptotic approximation of the solution for the Lamb's problem:

$$u_r(r, \omega) = \mathcal{A}_r \cdot \frac{1}{\sqrt{r}} e^{-i\mathcal{K}_R r} = \mathcal{A}_r \cdot \frac{1}{\sqrt{r}} e^{-\alpha_R r} e^{-ik_R r} \quad (7.4)$$

The expression is equivalent to that in Eq. 3.38, and the parameter  $\mathcal{A}_r$  includes all the information not linked with the spatial dependence (i.e., the source term, the initial phase, and the viscoelastic parameters). The radial strain  $\varepsilon_r(r, \omega)$  is obtained as the derivative with respect to the spatial coordinate:

$$\varepsilon_r(r, \omega) = \frac{\partial u_r(r, \omega)}{\partial r} = -\mathcal{A}_r \frac{1}{2r\sqrt{r}} \sqrt{4k_R^2 r^2 + 4\alpha_R^2 r^2 + 4\alpha_R r + 1} \cdot e^{-\alpha_R r} e^{-i\left(k_R r - \tan^{-1} \frac{2k_R r}{2\alpha_R r + 1}\right)} \quad (7.5)$$

Differently from the displacement field, the strain phase is no longer linear with  $r$ , hence the planar model is no longer valid. Besides, the spatial variation of the strain amplitude now involves a more complex geometrical spreading function, also depending on the (unknown) R-wave parameters.

Figure 7-20 compares the spatial variation of  $u_r(r, \omega)$  and  $\varepsilon_r(r, \omega)$ , in terms of the amplitude and the phase. Data for  $e_r(r, \omega)$  are included as well. Amplitude data are reported as corrected amplitude, defined as the logarithm of the amplitude scaled by the square root of the offset. Indeed, when the spatial change of amplitude is compatible with the one of a plane wave (as in the case of  $u_r(r, \omega)$ ), the corrected amplitude assumes a linear trend with the offset. The difference is negligible at large  $r$ , whereas the discrepancy becomes relevant at short offsets. The amplitude deviation is significant close to the source, where the relative difference rises up to 100%, but it rapidly decays as  $r$  increases. Instead, the relative difference in the phase is less than 5%. The discrepancy between  $e_r(r, \omega)$  and  $\varepsilon_r(r, \omega)$  is the result of the complex variation of the radial strain with the distance. At great distances, both the strain corrected amplitude and phase exhibit a quasi-linear variation with the distance from the source. In this case, the averaging procedure does not introduce significant changes with respect to the actual strain. Instead, close to the source, the relevant changes in both amplitude and phase induce large differences between  $e_r(r, \omega)$  and  $\varepsilon_r(r, \omega)$ .

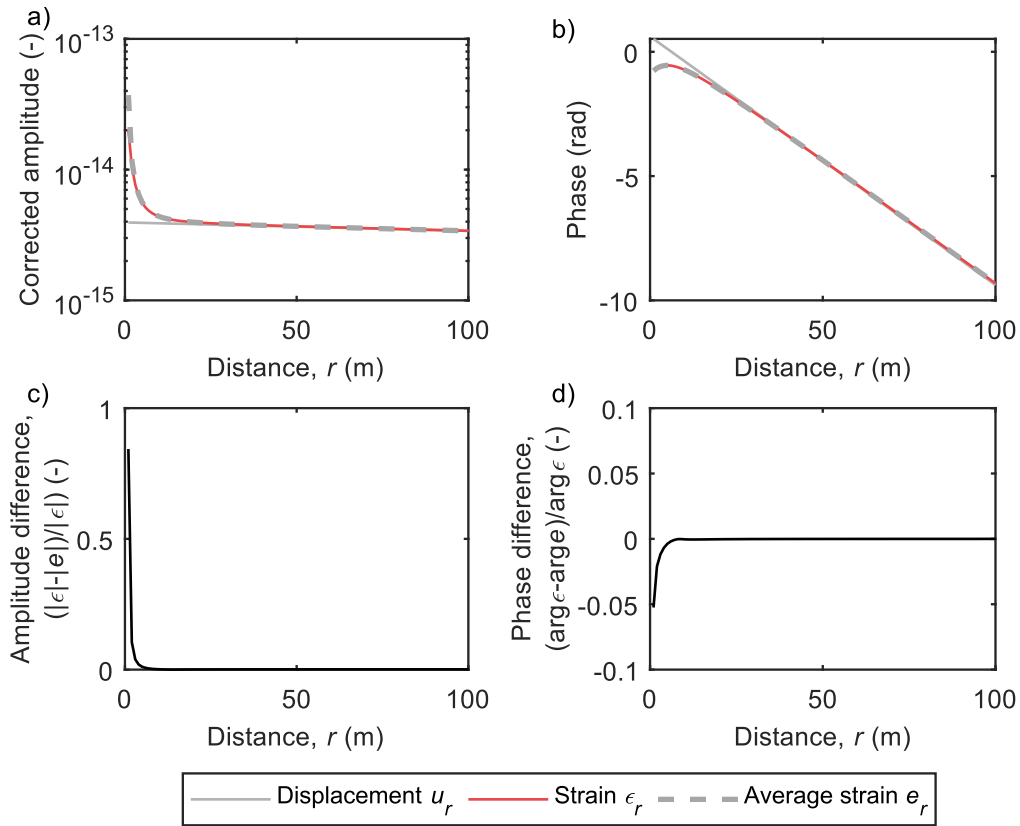


Figure 7-20. Radial displacement  $u_r(r, \omega)$  vs. radial strain  $\epsilon_r(r, \omega)$  vs. average radial strain  $e_r(r, \omega)$  induced by a cylindrical wave, characterized by  $k_R = 0.1$  rad/m and  $\alpha_R = 0.0015$  rad/m: a) Corrected amplitude; b) Phase; c) Relative difference in the corrected amplitude between the radial strain and the average radial strain; d) Relative difference in the phase between the radial strain and the average radial strain.

In view of the peculiar geometric attenuation exhibited by  $e_r(r, \omega)$ , an interesting aspect to be investigated consists in the influence of the specific model adopted to interpret the recorded wavefield in the DAS system. Indeed, a proper processing scheme for estimating R-wave parameters should account for the spatial variation of  $e_r(r, \omega)$ , with an adequate schematization of the geometric spreading. On the other hand, at the current state of knowledge, the existing processing techniques do not allow an explicit modeling of average strain data. For such reason, this study investigates three alternative strategies to infer R-wave parameters from the recorded average radial strain: displacement-based beamforming, strain-based beamforming, and average strain-based beamforming.

### *Displacement-based beamforming*



According to this scheme,  $e_r(r, \omega)$  may be interpreted as a measure of the radial displacement wavefield. Although this assumption violates the consistency with the recorded data, the spatial variation of the average strain is quite compatible with the one of  $u_r(r, \omega)$ , except at short distances. Therefore, the use of this model might result in biased estimates of the wave parameter, but the error may be small. Besides, this scheme allows the use of well-known and robust processing techniques. For this reason, this is the most commonly adopted processing scheme to interpret fiber-optic data.

In this case, the adopted estimator is the CFDBFa technique, wherein  $H_1^{(2)}(r)$  replaces  $H_0^{(2)}(r)$  in the trial steering vector to properly model the spatial variation of the radial displacement.

#### *Strain-based beamforming*

This alternative assumption interprets  $e_r(r, \omega)$  as equal to  $\varepsilon_r(r, \omega)$ . This scheme gains stronger physical consistency, as a strain-based parameter is modeled together with the related geometric spreading. However, the spatial averaging is still disregarded. In this study, the derivation of the R-wave parameters from the (assumed) radial strain data adopts a modified version of the CFDBFa, implementing a corrected steering vector to incorporate the geometrical features linked with the radial strain. Specifically, the wavenumber estimate exploits the following steering vector, dependent on the trial wavenumber  $k_t$ :

$$\mathbf{e}(k_t) = \left[ e^{-i \arg H_r(k_t r_1)}, \dots, e^{-i \arg H_r(k_t r_N)} \right]^T \quad (7.6)$$

where the function  $H_r$  is the spatial derivative of  $H_1^{(2)}(x)$ , which mimics the spatial variation of the phase of the radial strain field:

$$H_r(r) = \frac{dH_1^{(2)}(r)}{dr} = H_0^{(2)}(r) - \frac{1}{r} H_1^{(2)}(r) \quad (7.7)$$

As for the attenuation estimate, the steering vector  $\mathbf{a}(\hat{k}_t)$  is updated as follows:

$$\mathbf{a}(\hat{k}_t) = \left[ e^{-i \arg H_{r,0}(\hat{k}_t r_1)}, \dots, e^{-i \arg H_{r,0}(\hat{k}_t r_N)} \right]^T \quad (7.8)$$

where the function  $H_{r,0}$  is the power of  $H_r(r)$  to the imaginary unit.

#### *Average strain-based beamforming*

An accurate modeling of the recorded data explicitly models the spatial variation of  $e_r(r, \omega)$ . In this case, the CFDBFa can be updated by properly modifying the steering vector, as follows:

$$\mathbf{e}(k_t) = \left[ e^{-i \arg K_r(k_t r_1)}, \dots, e^{-i \arg K_r(k_t r_N)} \right]^T \quad (7.9)$$

where the function  $K_r$  is the spatial average of  $H_l^{(2)}(x)$ , which accounts for the spatial variation of a theoretical average radial strain field:

$$K_r(x) = \frac{1}{2g} \int_{x-g}^{x+g} H_r(r) dx = \frac{1}{2g} \left[ H_1^{(2)}(r+g) - H_1^{(2)}(r-g) \right] \quad (7.10)$$

As for the attenuation estimate, the steering vector  $\mathbf{a}(\hat{k}_t)$  is defined as follows:

$$\mathbf{a}(\hat{k}_t) = \left[ e^{-i \arg K_{r,0}(\hat{k}_t r_1)}, \dots, e^{-i \arg K_{r,0}(\hat{k}_t r_N)} \right]^T \quad (7.11)$$

where the function  $K_{r,0}$  is the power of  $K_r(r, \omega)$  to the imaginary unit.

The explicit modeling of the average radial strain allows to directly incorporate the influence of the averaging procedure, thus accounting for the specific acquisition layout, described in terms of the gauge length  $2g$ .

The definition of these three alternative strategies demonstrates the flexibility of the newly proposed method to handle with different wavefield conditions, as only a slight update of the trial steering vectors defined in Eq. 5.8 and 5.13 is required.

Table 7.3 summarizes the estimated wave parameters from the  $e_r(r, \omega)$  data represented in Figure 7-20 (corresponding to a wave with characterized by  $k_R = 0.1$  rad/m and  $\alpha_R = 0.0015$  rad/m), for the three alternative schemes. The displacement beamformer underestimates both  $k_R$  and  $\alpha_R$ , with a significant error in the latter. The bias is an effect of the difficulties of the displacement-based cylindrical beamforming in properly describing the spatial variations of both the amplitude and the phase of  $e_r(r, \omega)$ . On the converse, an explicit modeling of the average strain ensures a perfect matching of the theoretical wave parameters, as the geometry of the wavefield is properly accounted for. Interestingly, the use of a strain-based scheme returns reliable wavenumber data, whereas  $\alpha_R$  is slightly overpredicted, although the error is rather small. Indeed,  $e_r(r, \omega)$  and  $\varepsilon_r(r, \omega)$  usually exhibit similar spatial variation, with some divergence in the amplitude only close to the source. Thus, the derivation of dispersion data might refer to simplified models not fully compatible with the geometric features of the wavefield, as the phase information is poorly sensitive on this. Instead, an accurate modeling of the geometric features of the wavefield is crucial when attenuation estimates are of interest. By the virtue of its reliability, the interpretation of the HB-DAS data will adopt the CFDBFaMF procedure, modified to implement the average strain-based beamforming.

Table 7.3. Estimated wavenumber and phase attenuation from planar radial average strain data (representative of a Rayleigh wave with  $k_R = 0.1$  rad/m and  $\alpha_R = 0.0015$  rad/m), according to the displacement-based beamforming, strain-based beamforming, and average strain-based beamforming approaches. The values in brackets are the ratio between estimated and true values, that provide a measure of the entity of the error.

Beamforming method	Displacement-based	Strain-based	Average strain-based	True value
Estimated wavenumber $k_e$ (rad/m) [ $k_e / k_R$ ]	0.0920 [0.9200]	0.1000 [1.0000]	0.1000 [1.0000]	$k_R = 0.1$ rad/m
Estimated attenuation $\alpha_e$ (rad/m) [ $\alpha_e / \alpha_R$ ]	0.00030 [0.2000]	0.00153 [1.0200]	0.00150 [1.0000]	$\alpha_R = 0.0015$ rad/m

### 7.3.3 Data processing at Hornsby Bend

The interpretation of the data acquired at the HB-DAS array has a twofold aim. On the one side, the possibility of extracting both dispersion and attenuation data is addressed, with a focus on the issues linked with the processing scheme and the modeling of geometric spreading of the wavefield. Furthermore, the reliability of the estimated R-wave parameters is evaluated, by carrying out a comparison with results from the HB-GP array. For this reason, the analysis focuses on a 94 m-long portion of the fiber-optic cable coincident with the geophone array, so that they sample a comparable volume of the soil deposit. Besides, this study refers to waveforms generated at shot points located at 5 m, 10 m, 20 m, and 40 m far from the closest measurement point, whereas reversal shots are not included due to the smaller signal-to-noise ratio.

As an example, Figure 7-21a-b reports the time histories of recorded data in the HB-GP and the HB-DAS arrays, together with an estimate of the signal-to-noise ratio as a function of the frequency (Figure 7-21c-d). As the noise power derives from the pre-trigger and the post-trigger time windows only, this estimate may not be fully representative of the actual noise level. Indeed, the resulting signal-to-noise ratio is here represented for illustration purposes. Furthermore, Figure 7-21e-f reports the  $f$ - $k$  spectral images of the two waveforms, both obtained according to the cylindrical beamformer for comparison purposes. Data refer to the wavefield generated from the active source located at an offset equal to 10 m. The DAS acquisition scheme returns a dense and detailed picture of the wavefield, by the virtue of the small channel separation – data are measured approximately every 1 m along the cable. The increased number of measurement points enhances the resolution of the spectral image, allowing the clear identification of various vibration modes over a broad range of frequencies

(Figure 7-21f). However, the quality of the signal is generally poorer than the recorded velocity data in the geophone array, as highlighted by the slightly lower levels of the signal-to-noise ratio (Figure 7-21c-d), with sharper receiver-to-receiver variations at high frequencies. The reduced quality maps into blurred and more confused spectral peaks in the  $f$ - $k$  representation of the recorded average strain data.

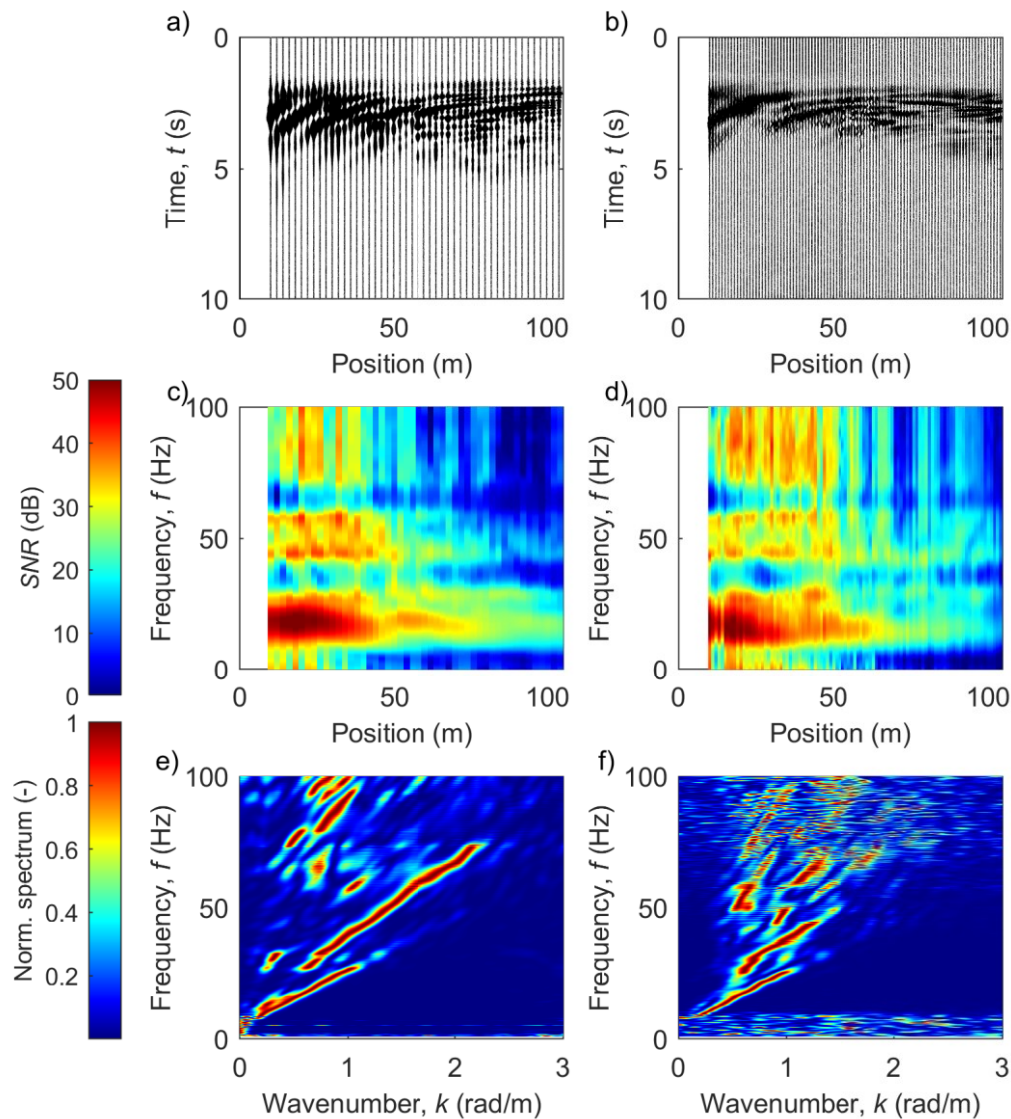


Figure 7-21. Recorded data at HB-GP (left column) and HB-DAS (right column). Data refer to the wavefield generated from the active source located at an offset equal to 10 m: a-b) Time histories of particle velocity and average radial strain, respectively; c-d) Estimated signal-to-noise ratio, as a function of the frequency and the receiver location; e-f)  $f$ - $k$  spectral images.

Figure 7-22 compares the estimated modal dispersion curves and attenuation data for the first two propagation modes, obtained from the interpretation of the HB-DAS and the HB-GP data. In this case, the data distribution is represented by the interval around the median value, the width of which equals one logarithmic standard deviation. Data statistics are obtained by combining results from different source offsets, in consistency with the multi-offset approach (Wood 2014).

In general, dispersion and attenuation data well match with each other, although the DAS data do not allow to obtain reliable values at low frequencies. This partially limits the capability of the DAS system in characterizing deeper layers. However, the corresponding degree of data variability is generally less or equal the one affecting geophone-based estimated parameters. This result is quite surprising, as the signal-to-noise ratio of DAS records is slightly lower, hence quite high variability in the derived attenuation was expected. A possible reason behind the low data scatter can be the remarkably larger number of measurement points that the DAS system includes, that provides a more exhaustive dataset of wavefield values to better constrain the velocity and the attenuation estimates. an effective constraint in the phase information.

In summary, the DAS technology can be successfully used to jointly estimate the phase dispersion and attenuation data, obtaining the same level of reliability of the canonical geophone array. Furthermore, the stronger influence of incoherent noise is balanced by the strong increase in the number of measurement points, thus resulting in a reduction in data variability, entailing an improvement in the accuracy of this system. As a potential solution to cope with this issue, it is recommended to carry out multiple measurements with variable gauge length, thus managing different levels of signal-to-noise ratio.

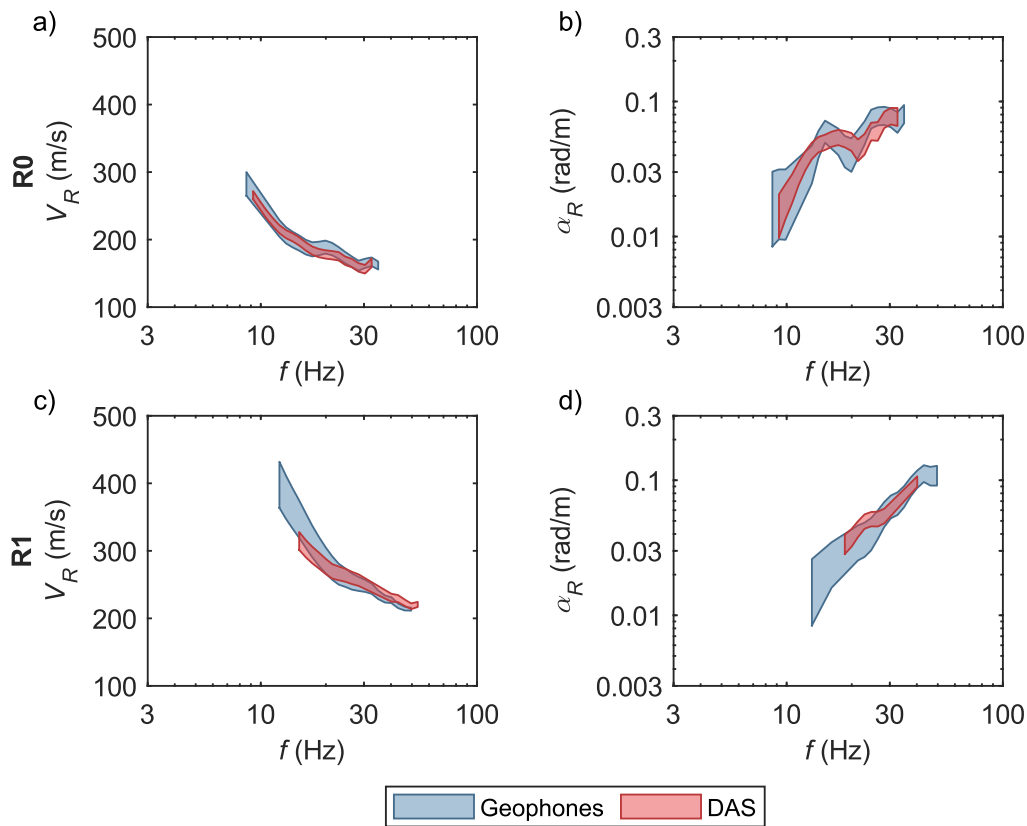


Figure 7-22. Comparison between the estimated dispersion and attenuation curves from the HB-DAS and the HB-GEO data: a-b) Resulting dispersion (a) and attenuation (b) curves for the fundamental mode; c-d) Resulting dispersion (c) and attenuation (d) curves for the first higher mode. Estimated data are represented in terms of intervals given by one logarithmic standard deviation around the median value.

## 7.4 Variability in dispersion and attenuation data

The characterization of the uncertainties affecting experimental dispersion and attenuation data in MASW surveys is not a trivial task, and a standard procedure for their quantification has not been developed yet. Indeed, the difficulty of separating epistemic uncertainties and aleatory variability does not allow a robust identification of the different components. Furthermore, uncertainties are strongly dependent on the acquisition layout as well as on site-specific conditions, both in terms of the stratigraphy (e.g., the entity of lateral variations) and the presence of incoherent noise. Finally, the estimated wave parameters are the result of complex processing algorithms, involving various computational steps, hence a direct mapping from uncertainties of measured displacement data into uncertainties of the estimated R-wave parameters might be complicate. On the one side,

regression-based techniques include statistical procedures that allow to directly obtain the wavenumber and the attenuation uncertainties from those affecting the measured displacement amplitude and phase (Strobbia and Foti, 2006). Instead, transform-based techniques often involve several complex and highly nonlinear computation steps, hence a straightforward propagation of measurement errors into parameters errors is not feasible. Therefore, the correct quantification of data uncertainties should refer to adequate statistical tools (e.g., FOSM), although there is no consensus about the best strategy to be adopted.

The most recommended approach consists in a direct statistical inference on the estimated R-wave parameters (Lai et al., 2005b). In this case, a robust quantification of uncertainties requires the performance of multiple measurements, by modifying the geometry of the array (whenever possible) and the offset of the active source, to capture the influence of spatial variations in soil mechanical properties. Besides, this procedure returns a suite of experimental dispersion and attenuation curves, that facilitates the identification of outliers or modeling issues (e.g., biases due to near-field effects). Furthermore, multiple source repetitions at each shot location should be carried out to tackle the influence of incoherent noise. Its influence on data uncertainty is not usually modeled in an explicit way and it is removed through a stacking procedure – typically, in the frequency domain.

The inference of statistical parameters for both the dispersion and the attenuation curves should account that these quantities are estimated simultaneously from the same set of experimental data. Therefore, a rigorous statistical model should identify a joint distribution that describes the probabilistic variations in a coupled way. However, statistical inference of multi-dimensional probabilistic distribution is a complex operation and only a few procedures are available. Indeed, the characterization and the description of a multi-dimensional random variable is much more complex than in the univariate case, as the suite of sufficient statistics does not only include descriptors about the location and the scatter for each variable, but also a quantity providing the mutual relationship between them (i.e., a correlation parameter). Furthermore, the proper choice of statistics requires a prior assumption about the related joint distribution, but robust statistical criteria for its identification are currently not available or they apply only for a rather narrow variety of distributions. A potential solution consists in a preliminary investigation of the statistical features of the single variables. Indeed, several tools are available for inspecting univariate distributions and the characteristics of the marginal distributions can provide useful indications for an effective selection of the multivariate distribution.

As for the phase velocity, a conventional assumption models experimental data as a normally distributed random variable. The validity of this hypothesis has been first demonstrated by Marosi and Hiltunen (2004), based on the visual inspection of the empirical frequency distribution. Lai et al. (2005b) and Olafsdottir et al. (2018) confirmed that this assumption is reasonable in the typically investigated frequency range, by using devoted statistical tests (e.g., chi-squared test and Shapiro-Wilk's test). However, other Authors claimed that the theoretical statistical distribution of the phase velocity is asymmetric especially at low frequencies (Strobbia, 2003). In this range, O'Neill (2004) observed that a good matching can be achieved by assuming a Lorentzian distribution for velocity data. Instead, only few studies attempted to infer statistical parameters on the estimated phase attenuation, often relying on the assumption of normally distributed data. However, no rigorous demonstration about the related statistical distribution has been provided yet.

This study investigates the possibility of modeling dispersion and attenuation data according to the normal and the lognormal distribution. The reference dataset is the collection of experimental data that derives from the combination of the HB-H5 and HB-HN arrays at the Hornsby Bend site in Texas, for different active sources (Figure 7-23; see Chapter 6). Experimental dispersion and attenuation curves are computed at 51 log-spaced frequency values, spanning between 3 Hz and 100 Hz. This specific sampling corresponds to the frequencies of the harmonics applied in the stepped sine signal. Besides, the logarithmic scale guarantees an adequate balance between low-frequency samples and high-frequency data, thus ensuring an adequate constraint both for near-surface and deep layers (Vantassel and Cox, 2021b). Furthermore, the moderately large number of sample points ensures a consistent reconstruction of the trend and of singular points of experimental data (e.g., Teague et al., 2018a; Vantassel and Cox, 2021b). As discussed in Section 7.1.3, the recorded wavefield at the HB site is the composition of two R-wave propagation modes, deemed to be representative of the fundamental and the first higher mode, hereafter labeled as R0 and R1, respectively.



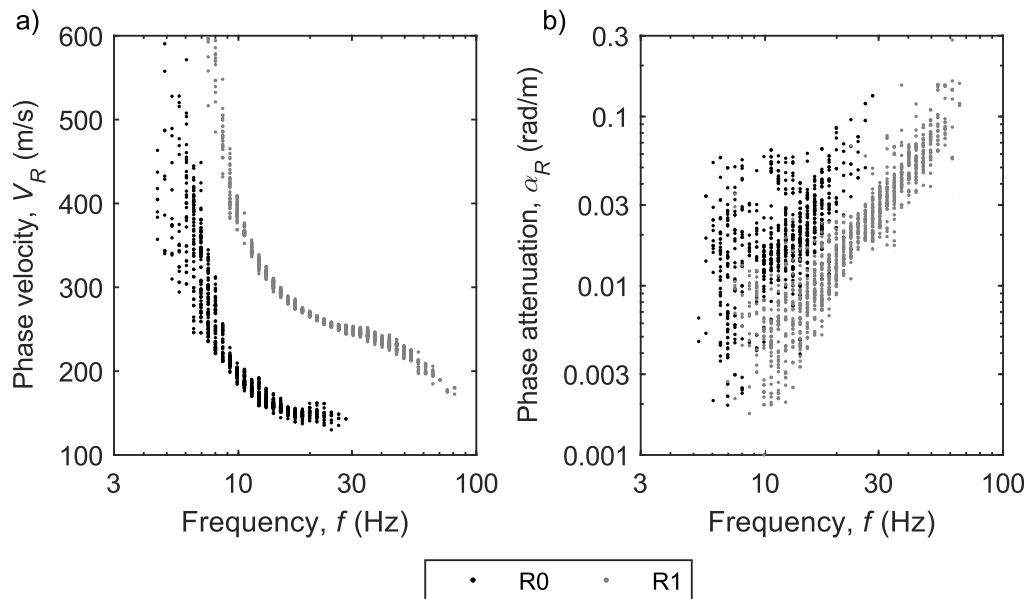


Figure 7-23. Elementary data points obtained from the combination of results of the HB-H5 and HB-HN arrays, for different locations and types of active source: a) Estimated dispersion curves; b) Estimated attenuation curves.

Usual modeling of variability of experimental data relies on the normal and the lognormal scheme. The main advantage of the normal and the lognormal distributions is the capability of describing data variability by means of a few parameters. When using a Gaussian model, sufficient statistics for describing data distribution are the mean ( $m_V$  and  $m_\alpha$ ) and the standard deviation ( $\sigma_{VR}$  and  $\sigma_{\alpha R}$ ) – alternatively, the latter may be replaced by the Coefficient of Variation (CoV), defined as the ratio between the mean and the standard deviation. Instead, lognormally distributed data can be effectively described in terms of the median ( $\mu_V$  and  $\mu_\alpha$ ) and the logarithmic standard deviation ( $\sigma_{\ln VR}$  and  $\sigma_{\ln \alpha R}$ ).

At least from the statistical point of view, both the normal and the lognormal model well describe the distribution of experimental data. On the one side, the normal model well suits the physical phenomenon involved in R-wave propagation, as measured data reflect the influence of a large volume of soil, within which the effects of individual elements add up to produce the macroscopic response. Therefore, the actual measure might be seen as an averaging process, which tends to produce a normal distribution by virtue of the central limit theorem (Baecher and Christian, 2005). However, the selection of an appropriate model should also account for additional constraints due to the physical nature of the problem. Indeed, both the phase velocity and the phase attenuation are positive-definite quantities, hence the lognormal distribution model is more suitable for

their description. For instance, Figure 7-24 provides a visual comparison of the distribution of the phase velocity and phase attenuation values of the elementary data points. Data refer to R1, with reference to  $f = 13$  Hz and  $f = 35$  Hz. As for dispersion data, the normal and the lognormal distribution produce identical curves, both compatible with the empirical data distribution (Figure 7-24a-c). A similar result is valid for high-frequency attenuation data, as the degree of similarity is still high (Figure 7-24d). Instead, using a normal or a lognormal model to describe low-frequency attenuation values produce significantly different theoretical distributions (Figure 7-24b). In this case, the lognormal distribution is the preferred choice because it allows to model highly-variable data (as the phase attenuation) without including negative values. Instead, the Gaussian scheme allows some probability even for negative attenuation data, hence this model is less consistent from the physical viewpoint. Furthermore, this result is consistent with the Monte Carlo simulations introduced in Chapter 5 to simulate the influence of incoherent noise.

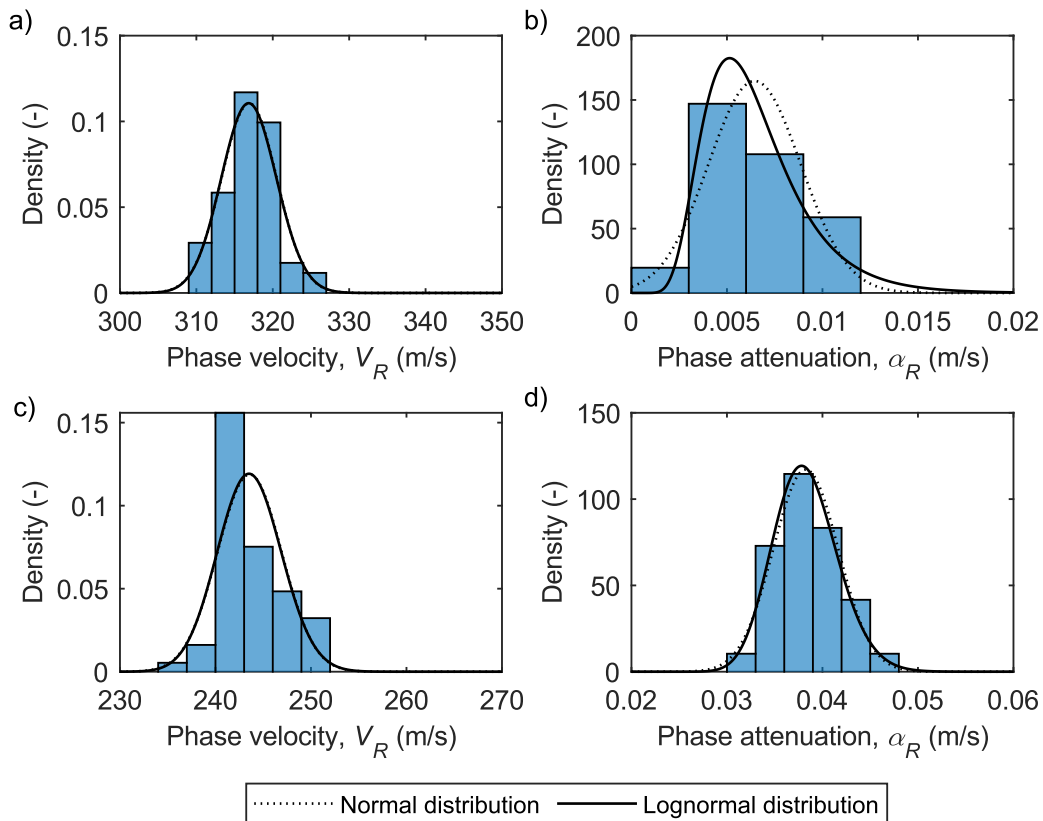


Figure 7-24. Comparison between the theoretical distribution, according to the normal and the lognormal model, and the empirical one, described in terms of a histogram, for

R1 data: a) Experimental phase velocity at  $f = 13$  Hz; b) Experimental phase attenuation at  $f = 13$  Hz; c) Experimental phase velocity at  $f = 13$  Hz; d) Experimental phase attenuation at  $f = 35$  Hz.

The effectiveness of the lognormal scheme in describing data variability is also demonstrated in Figure 7-25, which tests some the effectiveness of using such distribution for describing the R0 and the R1 dispersion and attenuation data, at two selected frequencies, namely  $f = 8.6$  Hz and  $f = 20$  Hz for R0, and  $f = 13$  Hz and  $f = 35$  Hz for R1. The selected frequencies contain different amounts of experimental data, with a different degree of variability. For each frequency, the degree of fitting is assessed by means of a quantile-quantile (Q-Q) plot, which compares empirical and predicted quantile data, according to the normal or the lognormal model. The fitting quality is good when the data points align along a straight line with inclination of  $45^\circ$ . The fitting quality is moderately poor for R0 data (Figure 7-25), especially when focusing on the phase attenuation. However, the drift in the trend may be a consequence of difficulties in characterizing the amplitude decay of this propagation mode, because of its weakness compared with R1. Instead, the degree of matching significantly improves when considering R1. This result is valid for both the normal and the lognormal model. Therefore, interpreting the variability of dispersion or attenuation data either with a normal distribution or a lognormal distribution may represent a reasonable choice.

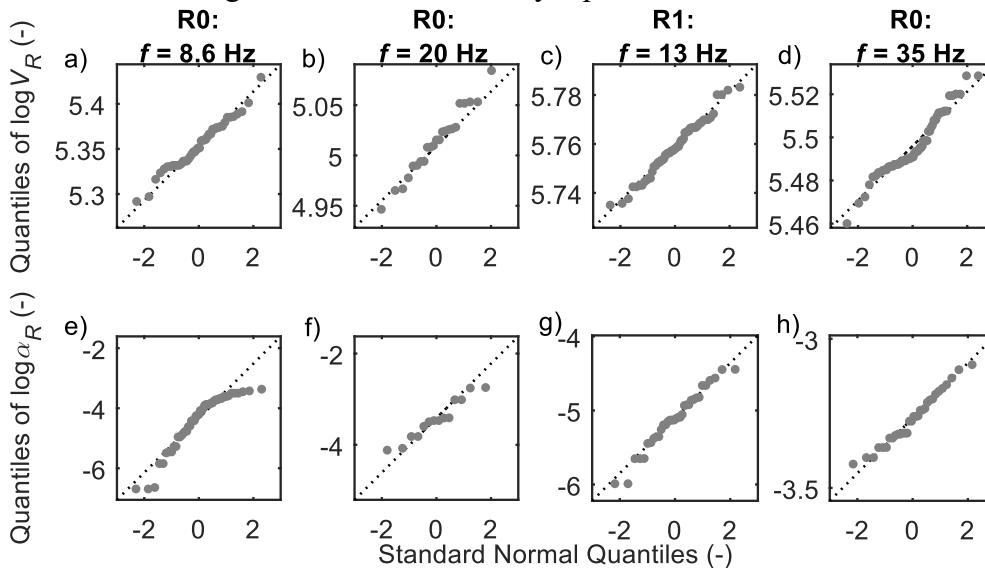


Figure 7-25. Lognormal quantile-quantile (Q-Q) plots for both the fundamental mode (R0) and the first higher mode (R1) data. The first row contains Q-Q plots for the phase velocity  $V_R$ , whereas the second row contains Q-Q plots for the phase attenuation  $\alpha_R$ ; each column correspond to a specific frequency for a given propagation mode: a-e) Lognormal

Q-Q plots of the experimental phase velocity (a) and phase attenuation (e) for R0 at  $f=8.6$  Hz; b-f) Lognormal Q-Q plots of the experimental phase velocity (c) and phase attenuation (f) for R0 at  $f=20$  Hz; c-g) Lognormal Q-Q plots of the experimental phase velocity (c) and phase attenuation (g) for R1 at  $f=13$  Hz; d-h) Lognormal Q-Q plots of the experimental phase velocity (d) and phase attenuation (h) for R1 at  $f=35$  Hz.

On the other hand, although both data may appear as lognormally distributed, this does not guarantee that they belong to a jointly lognormal bivariate distribution. Indeed, the nature of marginal distribution does not necessarily imply any specific constraint on the joint distribution. Therefore, additional statistical tests should be carried out to demonstrate whether the data vector can be described by a specific joint bivariate distribution. However, currently there is no robust statistical test to assess whether multidimensional data belong to a specific multivariate distribution. This study refers to the graphical tool represented by the  $\chi^2$ -plot, which represents a generalization of the Q-Q plot into the multivariate case. In this case, theoretical and observed quantiles are replaced by the chi-squared value and the squared Mahalanobis distance (SMD). The interpretation scheme is the same of the Q-Q plot, namely the assumed distribution model well describes experimental data when the data points align along a straight line with inclination of  $45^\circ$ . For instance, Figure 7-26 represents the  $\chi^2$ -plot for the coupled distribution of the elementary phase velocity and phase attenuation values, to assess the compatibility with the joint lognormal model. Figure 7-26a-b includes R0 data at  $f=8.6$  Hz and  $f=20$  Hz, respectively; Figure 7-26c-d refers to R1 data at  $f=13$  Hz and  $f=35$  Hz. In all the cases, data tend to be aligned along a straight line with unitary slope (with some drift for R0 data). Therefore, the assumed distribution is a reasonable choice to model data variability. Similar results apply for the bivariate normal distribution.

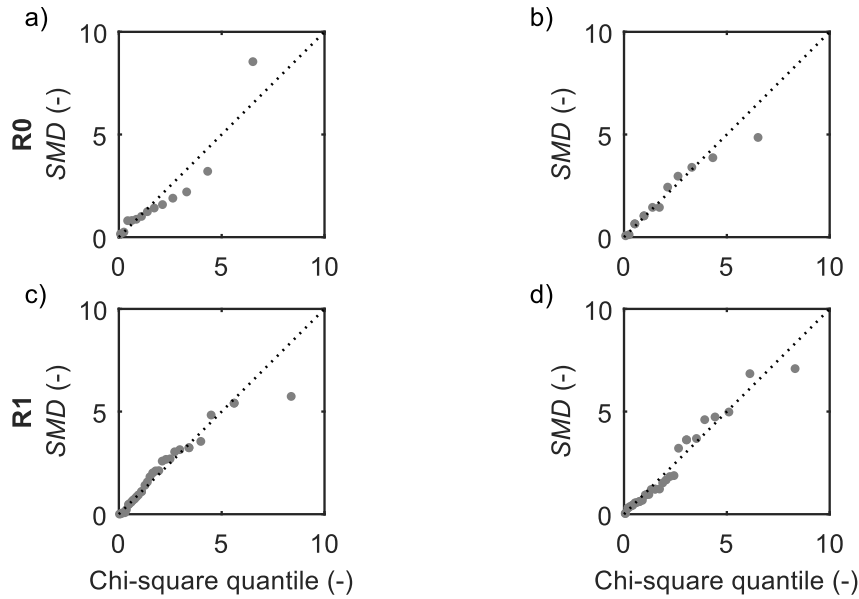


Figure 7-26. Bivariate lognormal  $\chi^2$ -plot for R0 and R1 data: a) Bivariate lognormal  $\chi^2$ -plot for the R0 experimental phase velocity and attenuation at  $f = 8.6$  Hz; b) Bivariate lognormal  $\chi^2$ -plot for the R0 experimental phase velocity and attenuation at  $f = 20$  Hz; c) Bivariate lognormal  $\chi^2$ -plot for the R1 experimental phase velocity and attenuation at  $f = 13$  Hz; d) Bivariate lognormal  $\chi^2$ -plot for the R1 experimental phase velocity and attenuation at  $f = 35$  Hz.

Thus, a reasonable scheme to describe the joint variability for both dispersion and attenuation data at each frequency can refer to the bivariate normal or the bivariate lognormal distribution, at almost all the investigated frequencies. When using a bivariate Gaussian model, sufficient statistics for describing data distribution are the mean vector ( $\mathbf{m}_{VR,aR}$ ), composed by the mean values of the marginals (i.e.,  $m_{VR}$  and  $m_{aR}$ ) and the covariance matrix ( $\mathbf{\Sigma}_{VR,aR}$ ), which depends on the standard deviation of the marginals (i.e.,  $\sigma_{VR}$  and  $\sigma_{aR}$ ) and the correlation coefficient  $\rho_{VR,aR}$ . A bivariate lognormal distribution refers to equivalent parameters, namely the median vector ( $\boldsymbol{\mu}_{VR,aR}$ ), composed by the mean values of the marginals (i.e.,  $\mu_{VR}$  and  $\mu_{aR}$ ) and the covariance matrix ( $\mathbf{\Sigma}_{\ln VR, \ln aR}$ ), which depends on the logarithmic standard deviation of the marginals (i.e.,  $\sigma_{\ln VR}$  and  $\sigma_{\ln aR}$ ) and the correlation coefficient  $\rho_{\ln VR, \ln aR}$ . These quantities can be derived from the elementary data points of the phase velocity and phase attenuation curves, frequency by frequency. Note that, however, the lognormal scheme is preferred.

Figure 7-27 summarizes the statistics obtained from the experimental dispersion and attenuation data, according to the bivariate lognormal scheme. The variability in the phase velocity is rather low, with  $\sigma_{\ln VR}$  close to 0.04 for R0 data

and 0.01 for R1 data. This value is compatible with the typical CoV of dispersion data, which ranges between 2% and 10% (Marosi and Hiltunen, 2004; O'Neill, 2004; Lai et al., 2005b; Foti et al., 2009; Comina et al., 2011; Cox et al., 2014; Garofalo et al., 2016a; Garofalo et al., 2016b; Olafsdottir et al., 2018; Teague et al., 2018a; Teague et al., 2018b). Indeed,  $\sigma_{\ln VR}$  and the CoV are similar when the corresponding values are quite small. Furthermore,  $\sigma_{\ln VR}$  decreases as the frequency gets higher, albeit with a further increase at very high frequencies, compatibly with Lai et al. (2005b) and Passeri et al. (2021). The large variability of low-frequency data is the combined result of the poor resolution of the SWM at long wavelengths and the difficulty of various sources of generating high-energy signals at low frequencies (Passeri, 2019). Instead, at high frequencies, the greater scatter is an effect of small-scale heterogeneities, attenuation and spatial aliasing (Passeri, 2019).

As for the attenuation variability,  $\sigma_{\ln \alpha R}$  is one order of magnitude greater than the corresponding  $\sigma_{\ln VR}$ , as it oscillates around  $0.2 \div 0.3$  and it increases up to 1 at low frequencies. Similar levels of variability were observed by Spang (1995), Rix et al. (2000), Verachtert (2018) and Bergamo et al. (2019). Furthermore, Figure 7-27e-f reports the estimated correlation coefficients, with a coloring scheme mapping the related  $p$ -value, that quantifies the reliability of the estimated correlation. The observed values of  $\rho_{\ln VR, \ln \alpha R}$  are generally small. Furthermore, the corresponding  $p$ -value is often above the significance threshold (fixed at 0.05), entailing that the correlation is not significantly different from zero, from the statistical viewpoint. Therefore, a weak level of correlation exists between the estimated phase velocity and phase attenuation values. Due to weak correlation level, this information will not be reported in the next sections, and the analysis mainly focused on the median and standard deviation estimates.

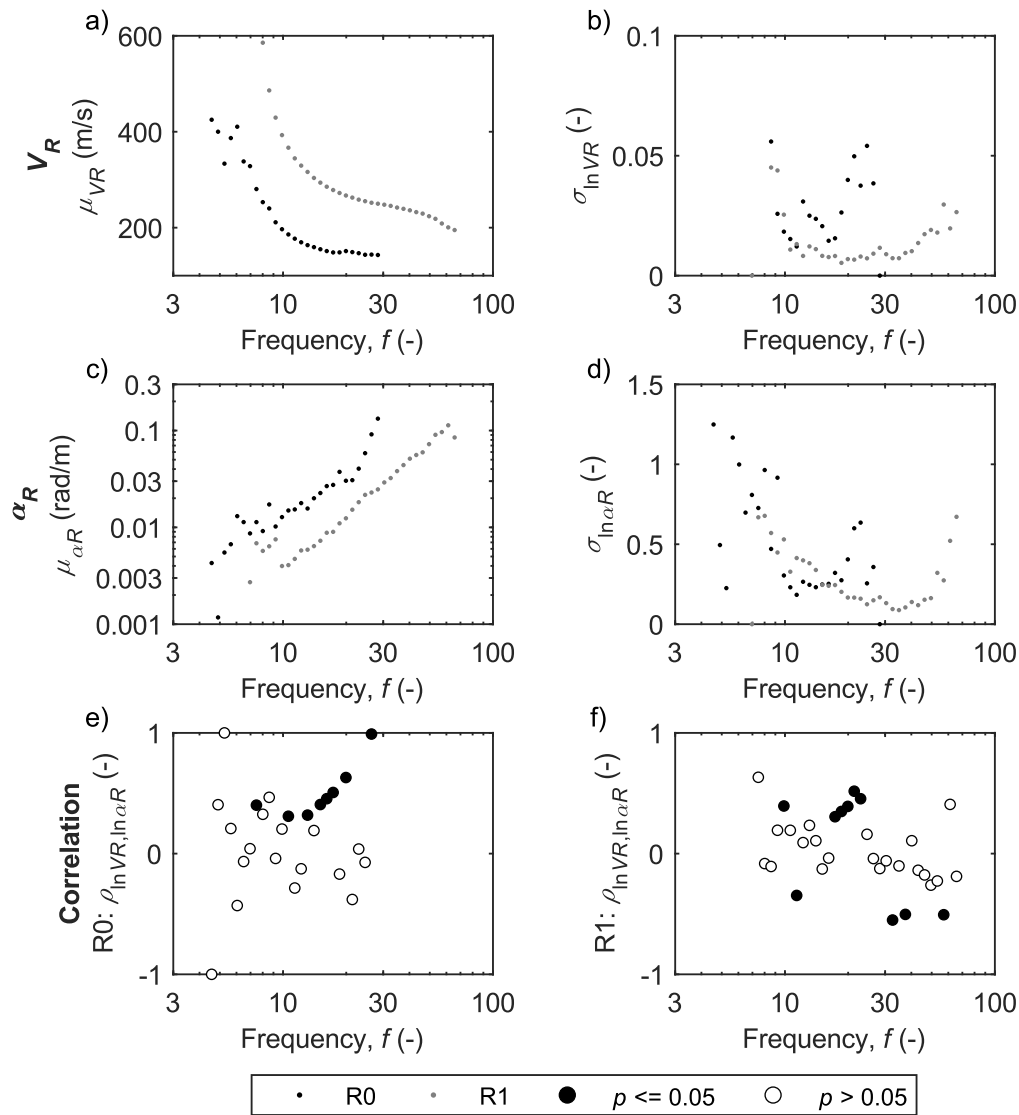


Figure 7-27. Inferred data statistics for the combined HB-HN and HB-H5 dataset, interpreted according to a bivariate lognormal distribution: a) Median phase velocity  $\mu_{VR}$ ; b) Median phase attenuation  $\mu_{\alpha R}$ ; c) Logarithmic standard deviation of the phase velocity  $\sigma_{\ln VR}$ ; d) Logarithmic standard deviation of the phase attenuation  $\sigma_{\ln \alpha R}$ ; e) Correlation coefficient  $\rho_{\ln VR, \ln \alpha R}$  for R0 data, as a function of the frequency; f) Correlation coefficient  $\rho_{\ln VR, \ln \alpha R}$  for R1 data, as a function of the frequency. Correlation data points are colored as a function of the  $p$ -value.

## 7.5 Summary

This Chapter addressed the main sources of uncertainties in the estimated dispersion and attenuation data, with a focus on the modeling of epistemic

uncertainties and a quantification of the aleatory variability. As for epistemic uncertainties, the influence of the specific processing method and the type of active source were investigated, as well as the role of the receiver type.

The inter-method comparison referred to both synthetic waveforms and measured data obtained from in situ surveys, addressing the performance of each processing technique in terms of the reliability and accuracy of the estimated wave parameters, as well as the capability of extracting such information over a broad frequency range. In general, both synthetic and real data demonstrated a similar performance of different processing techniques, both in terms of the quality of the estimate and of the investigated frequency range. Besides, the CFDBFa algorithm returns reliable estimates of R-wave parameters, when the wavefield is dominated by a single mode. In the case of a multimode wavefield, the modal filtering procedure successfully isolates the dominant mode, whereas the extraction of information related to low-energy modes is more challenging. Indeed, regardless the considered interpretation scheme, the quality of results strongly depends on the energy partition between different R-wave propagation modes. When the investigated mode dominates the wavefield, the corresponding wave parameters can be tracked over a broad frequency range, and the corresponding estimates are affected by low variability, even in the presence of other modes. Instead, the analysis of low-energy modes is more challenging. In this case, even though the phase velocity can still be well-identified, the resulting attenuation estimate is highly variable and sensitive to the specific processing technique, because of the different capability in extracting and isolating information about the target mode. A similar issue occurs when the wave energy is equally partitioned across different modes. Therefore, the analysis of wavefield data in the presence of inversely dispersive media or soil deposits with abrupt changes in the impedance requires special care, as the resulting wavefield is remarkably multimodal.

The analysis of the source influence investigated the quality of the estimated R-wave parameters as a function of the source type. For this purpose, the study focused on wavefield data generated by a sledgehammer source and by a mechanically-controlled vibrating source, which applied a chirp and a stepped sine signal. In general, the specific source type does not affect the average trend of the estimated dispersion and attenuation data. However, high-energy controlled sources allow to extract R-wave parameters across a broader range of frequencies. Most of all, the estimated data exhibit smaller variability. Indeed, seismic traces generated by the sledgehammer usually have smaller signal-to-noise ratio, which entails greater scatter in the estimated wave parameter, especially in terms of the



attenuation. However, the mean trend in the attenuation curve can still be captured. This result positively contributes to the capability of the sledgehammer for the attenuation estimate. This is helpful for ordinary applications, where high-energy sources are typically not available. Indeed, generating waveforms through a sledgehammer striking onto a metal plate represents the most accessible and affordable source.

Finally, the sensitivity of the estimated R-wave parameters to the specific acquisition device was assessed, by comparing estimated phase velocity and phase attenuation data obtained from geophone and fiber-optic DAS data at the HB site. In this way, the capability of this new system in retrieving attenuation data was also addressed. On the one side, the CFDBFa algorithm was adapted to account for the peculiar geometric attenuation that the recorded average strain by the fiber-optic assumes. Indeed, ignoring the geometric spreading would result in a slight overestimation of the phase attenuation, whereas the phase velocity appears not to be sensitive on this. This result also demonstrates the flexibility of the newly proposed method to handle with different wavefield conditions. On average, the resulting phase velocity and phase attenuation data are compatible with each other, although the DAS data exhibit lower variability. This improvement is perhaps the effect of the remarkably larger number of measurement points that the DAS system includes, that provides a more exhaustive dataset of waveform values to better constrain the velocity and the attenuation estimates, thus balancing the lower signal-to-noise ratio in the records. Therefore, the DAS technology can be successfully used to jointly estimate the phase dispersion and attenuation data, obtaining the same level of reliability of the canonical geophone array.

The modeling of aleatory variability requires the definition of a statistical model to describe the distribution nature of experimental data. Two factors led to this modeling. On the one side, various models have been proposed to quantify the dispersion variability, whereas no scheme was explicitly demonstrated for attenuation data. On the other side, as both the phase velocity and the phase attenuation derive from the same dataset, a robust modeling should rely on a multidimensional distribution. Based on real data recorded at the HB site, this Chapter demonstrated that both the bivariate normal and the bivariate lognormal distribution are a reasonable choice to describe experimental data. However, the latter is the preferred choice, especially when modeling low-frequency data. Indeed, it allows to model highly-variable data (as the phase attenuation) without including negative values, thus ensuring greater consistency from the physical viewpoint. Furthermore, the observed degree of correlation is negligible, hence the statistical characterization mostly focuses on the marginals.

# Chapter 8

## Joint inversion of dispersion and attenuation data

This Chapter introduces one of the key steps in SWM processing, namely the inversion procedure. The inversion is an operation that allows to map the experimental R-wave parameters into a suite of earth models, that synthesize the desired information in terms of mechanical parameters (i.e., S-wave velocity and damping ratio). This is a crucial and rather complex operation. Indeed, advanced and effective algorithms are required to produce reliable and accurate ground models. This Chapter proposes a new algorithm for the joint inversion of dispersion and attenuation data to retrieve both stiffness and dissipation parameters, that relies on an improved Monte Carlo scheme. In this approach, the optimization is achieved by exploiting the scaling properties of the Rayleigh eigenvalue problem. Therefore, the procedure derives from the algorithm introduced by Socco and Boiero (2008), which is generalized into the viscoelastic case

The Chapter starts with a general description of the inverse Rayleigh problem, to introduce basic notions and the relevant terminology. Then, the main steps of the inversion procedure are summarized, with a detailed description of the proposed algorithm. Additional information about the inversion stage can be retrieved in the devoted textbooks and guidelines (e.g., Foti et al., 2014; Foti et al., 2018). The Chapter includes the application of the algorithm to the HB-DAS dataset, already discussed in Chapter 7. Indeed, this set of experimental data represents a quite general and challenging condition, in which multiple R-wave propagation modes are jointly inverted.

### 8.1 The inversion problem

The inversion is a crucial step in SWM processing, as it maps observed experimental data into explicit information about mechanical parameters of the soil deposit (Mosegaard and Sambridge, 2002). The inversion stage can be defined as the “estimation of the parameters of a postulated earth model from a set

of observations” (Lines and Treitel, 1984). Indeed, the inversion relies on a physically-based model-data relationship, that can be described by the following general relationship:

$$\mathbf{d} = \mathbf{g}(\mathbf{m}) \quad (8.1)$$

where  $\mathbf{d}$  is the vector of measured data and  $\mathbf{m}$  is the vector of the desired model parameters, whereas  $\mathbf{g}$  is a functional relating these quantities. This expression provides an estimate of observed data when the model parameters are known, hence it is a forward problem, in mathematical terms (Tarantola, 2004). As experimental measures provide information on  $\mathbf{d}$ , the inference of  $\mathbf{m}$  requires a backward application of the relationship in Eq. (8.1). However, the inverse functional  $\mathbf{g}^{-1}$  might not exist, or the analytical formulation can be unknown. In this case, the model identification is tackled through the inversion theory, in which model parameters are calibrated so that the simulated system response (obtained by applying the forward problem in Eq. 8.1) suits the experimental data. The degree of fit to experimental data is quantitatively measured by a misfit function, whose minimization represents the goal of the inversion process.

In SWM processing deemed to jointly estimate stiffness and dissipation parameters of the soil deposit,  $\mathbf{d}$  is the collection of experimental modal phase velocity  $V_R(\omega)$  and phase attenuation  $\alpha_R(\omega)$  curves (when triaxial measurements are available, also R-wave ellipticity can be included, e.g. Bergamo et al., 2018), whereas  $\mathbf{m}$  is the collection of parameters describing the geometry and the mechanical behavior of the soil deposit. Under the assumption of viscoelastic layered medium (see Chapter 3),  $\mathbf{m}$  consists in the  $V_S$ ,  $V_P$ ,  $D_S$ ,  $D_P$ , and the  $\rho$  profiles with depth. The derivation of a subsurface model from experimental data relies on the dispersive behavior of Rayleigh waves in layered media, for which  $V_R(\omega)$  and  $\alpha_R(\omega)$  exhibit a dependence on frequency. The frequency-dependence of propagation parameters is a combined effect of geometric dispersion, which results from the variation of mechanical properties with depth, and intrinsic dispersion, due to the constitutive behavior of linear viscoelastic media (see Chapter 3). This relationship is synthesized by the Rayleigh wave eigenvalue problem, that maps the subsoil profile into the dispersive behavior of the R-waves (Eq. 3.16), hence it represents a forward relationship (i.e., the functional  $\mathbf{g}$ ). As the existence of the inverse functional  $\mathbf{g}^{-1}$  has not been demonstrated yet, the inversion theory should be applied. In this case, a single or a set of ground models is calibrated so that the response suits the experimental data.

From the mathematical viewpoint, the inversion problem in SWM is nonlinear, mixed-determined and ill-posed. The nonlinearity arises from the absence of a linear relationship between data and model parameters in the forward

problem. Instead, the mixed-determination is an effect of the inhomogeneous influence of the ground model parameters on  $V_R(\omega)$  and phase attenuation  $\alpha_R(\omega)$ . Indeed, high-frequency R-wave parameters mainly depend on the mechanical properties of shallow layers, whereas low-frequency data depend both on shallow and deep layers. Therefore, the characterization of the first few meters of the soil deposit can be easily achieved by focusing on the high-frequency portion of the experimental data. However, a correct identification is crucial, otherwise the whole ground model would be biased. Finally, the ill-posedness is an intrinsic feature of most inversion problems, and it is responsible of the solution non-uniqueness, namely different ground models may provide compatible degree of fit with the experimental data. Indeed, the inversion problem involves a weak relationship and it attempts to constrain several model parameters with few experimental data. Thus, solution non-uniqueness combined with the experimental uncertainties results in highly variable estimates of model parameters. On the other side, several strategies allow to significantly reduce the variability in the inferred ground model, e.g. by adopting a priori values for less influencing parameters (e.g., Foti and Strobbia, 2002) or introducing physically-based constraints in the model (e.g., smoothness criteria; Constable et al., 1987). Nevertheless, the interpretation of inversion results should account for solution non-uniqueness, by introducing an explicit modeling of variability. Therefore, uncertainty bounds on the best solution should be included or a set of equivalent solutions should be provided (Foti et al., 2018).

Furthermore, the retrieval of stiffness and dissipation parameters from SWM data might deal with experimental values in multifold ways. Some pioneering approaches adopted an uncoupled inversion approach, based on a separate inversion of  $V_R(\omega)$  and  $\alpha_R(\omega)$ . This strategy relies on a multistage procedure, in which the stiffness structure of the soil deposit is firstly obtained, by considering  $V_R(\omega)$  only. The resulting ground model can be used to approximate the geometric spreading of R-waves, thus improving the estimate of  $\alpha_R(\omega)$  (Rix et al., 2000; Xia et al., 2002; Xia et al., 2012). Furthermore, once fixed the stiffness model, the  $D_S$  profile can be obtained from the inversion of  $\alpha_R(\omega)$ . One advantage of this scheme is that the inversion of attenuation data can be solved with linear optimization algorithms in weakly dissipative media (e.g., Foti et al., 2014). However, the intrinsic coupling between the R-wave phase velocity and phase attenuation in linear, viscoelastic media is neglected. On the one side, this approximation is not expected to produce a significant bias in the resulting soil models when the inferred  $D_S$  is small enough, as the difference between elastic and viscoelastic phase velocities is negligible (Armstrong et al., 2020). On the other hand, a joint

inversion coupling both  $V_R(\omega)$  and  $\alpha_R(\omega)$  mitigates the ill-posedness of the inversion problem, because an explicit modeling of the coupling between stiffness and attenuation parameters introduces an internal constraint in the inversion, that derives from the Cauchy-Riemann equations (Lai and Rix, 1998b; Lai et al., 2002).

Finally, the misfit function involved in the inversion stage exhibits a complex and multi-dimensional shape, often with the presence of multiple minima. In this case, an a priori identification of the position of the global minimum is almost impossible. Besides, a brute-search approach based on a systematic investigation of the whole parameter space is unfeasible, as the computation cost due to the rather large number of forward simulations would be unacceptable. In general, the most popular methods aiming at identifying the global minimum of the misfit function can be clustered into two families: local search methods and global search methods. Local search methods are iterative, deterministic techniques that gradually adjust an initially assumed ground model to match the experimental data, by minimizing the misfit function. However, these schemes adopt local optimization algorithms, hence the choice of the initial model is crucial to ensure the identification of the global minimum (Spang, 1995; Lai and Rix, 1998b). Several Authors applied local search methods, with slight variations in the model updating procedure, smoothness and weighting criteria (e.g., Constable et al., 1987; Lai and Rix, 1998b; Xia et al., 1999; Badsar, 2012; Verachtert et al., 2017). Global search methods are stochastic techniques that randomly explore the whole parameter space to identify the global minimum of the misfit function. These approaches generate random samples of the parameter space, according to an assigned probability distribution. Each sample is representative of a randomized ground model, and the corresponding synthetic data are compared with the experimental ones. In some procedures, the sampling of the parameter space is optimized and iteratively refined over promising regions potentially including the global minimum of the misfit function, limiting the required number of samples and enhancing the quality of the final estimate (Sen and Stoffa, 1996; Al-Hunaidi, 1998; Martínez et al., 2000; Wathelet et al., 2004; Socco and Boiero, 2008; Verachtert, 2018; Passeri et al., 2019; Armstrong et al., 2020). In general, global search methods are preferred over local search methods, as they do not require the definition of a first tentative profile but only a statistical distribution of model parameters. Besides, they allow easier investigation of the uncertainties associated to solution non-uniqueness. On the other hand, they are usually more time consuming and computationally intensive (Foti et al., 2018). In some cases, a mixed inversion scheme is adopted, where a global search method identifies

promising regions of the parameter space and a least squares algorithm explores them to identify the best misfit solution (e.g., Picozzi and Albarello, 2007). Alternatively, the Monte Carlo procedure can be used to estimate uncertainties of the solution provided by a local estimator (Misbah and Strobbia, 2014).

Regardless the adopted inversion algorithm, the generic inversion procedure consists in a multistage operation, in which the most relevant steps are the following: the definition of the inversion target (i.e., the suite of experimental data); the definition of the investigated parameter space; the application of the inversion algorithm; the description of results. The differences between search methods rise from the specific operations and assumptions carried out in each step. In this study, a Monte Carlo-based global search approach to jointly invert phase velocity and phase attenuation data is introduced. Furthermore, the description of the main steps will refer to results of the HB-DAS survey. The reason behind this choice is to describe the proposed method in a quite general situation, where multiple R-wave propagation modes are involved.

## 8.2 Target function

The inversion target is the suite of observed data, wherein dispersion parameters are usually described as R-wave phase velocity  $V_R(\omega)$ , whereas attenuation data are provided as phase attenuation  $\alpha_R(\omega)$  (Badsar, 2012; Verachtert, 2018) or phase damping ratio  $D_R(\omega)$  (Misbah and Strobbia, 2014; Armstrong et al., 2020). Alternatively, the complex-valued phase velocity  $\mathcal{V}_R(\omega)$  can be used (Lai et al., 2002; Lai, 2005; Foti et al., 2014). Usual inversion procedures in SWM involve modal phase velocity and phase attenuation curves, typically focusing on R-wave fundamental mode data. However, some inversion schemes rely on a joint inversion of multiple mode data (e.g., Maraschini and Foti, 2010; Bergamo et al., 2011), resulting in a reduced variability in the estimated soil models and an increase of the investigated depth (e.g., Gabriels et al., 1987). Alternatively, effective mode data can be used to infer ground model parameters, although the latter requires a full simulation including the information of the array geometry and the source location (Tokimatsu, 1995). An appealing strategy is the full waveform inversion (Tran and Hiltunen, 2012; Pakravan et al., 2016), which directly employs measured particle motion as the target experimental data. Although this scheme is computationally intensive and not standardized yet, this approach inherently accounts for both the presence of multiple propagation modes and body waves, as it can potentially overcome limitations linked to the correct

modeling of geometric spreading and remove the influence of scattering (Sun, 2000).

Experimental data should be provided according to an adequate sampling in the frequency or the wavelength domain. On the one side, the number of sample points should ensure an exhaustive reconstruction of the trend and of singular points of experimental data. In general, a minimum of 20–40 sampling points is recommended (e.g., Teague et al., 2018a; Vantassel and Cox, 2021b). However, the number of data points should not be too large, as it would entail a dramatic rise in computation time for the forward simulation. Furthermore, data should be sampled according to a logarithmic representation in the frequency domain (Foti et al., 2018). This alternative representation is extremely useful at the inversion stage, as it guarantees an adequate equilibrium between low-frequency samples and high-frequency data, thus ensuring an adequate constraint both for near-surface and deep layers (Olafsdottir et al., 2018; Vantassel and Cox, 2021b). An alternative representation adopts the wavelength as the independent variable, typically according to a logarithmic scale to cope with the different resolution of the MASW technique at different wavelengths and still ensure adequate proportion between shallow and deep data (Olafsdottir et al., 2018). In general, the sampling grid, in terms of the sampling interval and the corresponding number, should also ensure that the resulting experimental curves exhibit gradual and smooth variations with the frequency.

The example herein presented adopts the  $V_R(\omega)$  and  $\alpha_R(\omega)$  data from HB-DAS, computed at log-spaced frequencies between 10 Hz and 50 Hz. The inversion target includes both fundamental-mode data (labeled as “R0”) as well as the first higher mode (“R1”), where experimental uncertainties are represented in terms of logarithmic error bars.

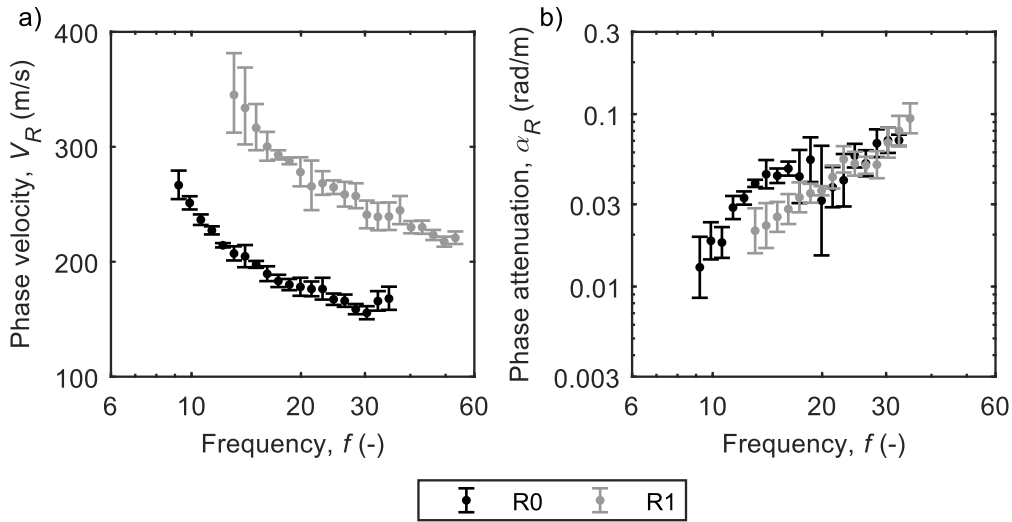


Figure 8-1. Experimental phase velocity (a) and phase attenuation (b) data obtained from the HB-DAS array, that represent the target for the inversion procedure. The experimental dataset includes information on the variability of the derived R-wave parameters, represented as error bars the width of which is related with the logarithmic standard deviation.

### 8.3 Model parameter space

The definition of the parameter space consists in the assignment of geometrical and mechanical parameters of the trial ground models. Usual SWM inversion procedures model the soil deposit as a vertical stack of homogeneous and isotropic linear viscous elastic layers, consistently with the hypothesis underlying most processing schemes used to extract experimental data from the measured waveforms. Therefore, the unknown parameters are the number of layers and, for each layer, the thickness  $H$  (excluding the half-space), the mass density  $\rho$ , the S-wave velocity  $V_S$ , the P-wave velocity  $V_P$  (alternatively, the Poisson ratio  $\nu$ ), the S-wave damping ratio  $D_S$ , and the P-wave damping ratio  $D_P$ . The parameterization procedure changes as a function of the adopted inversion algorithm. In local search approaches, the definition of the parameter space typically consists in assuming an initial ground model, which is the input in the local optimization scheme. Instead, Monte Carlo-based, global search procedures rely on a probabilistic description of the parameter space, wherein a probability distribution describes the model parameters. Many schemes assume a multivariate uniform distribution of the parameter vector (see next Section), hence the parameterization defines the investigated ranges of each parameter.



Sensitivity studies demonstrated that each unknown parameter has variable influence in the inversion process. Inversion results are mostly sensitive on  $H$ ,  $V_S$ , and  $D_S$ , whereas the role of  $\rho$ ,  $V_P$  (or  $v$ ), and  $D_P$  is generally less relevant (Nazarian and Stokoe II, 1984; Xia et al., 1999; Aki, 2002; Badsar, 2012; Verachtert, 2018). However, experimental data do not exhibit the same sensitivity to all the earth model parameters. On the one hand, modal dispersion data strongly depend on  $H$  and  $V_S$ , whereas the role of  $\rho$  and  $V_P$  (or  $v$ ) is generally less relevant (Nazarian and Stokoe II, 1984; Xia et al., 1999; Aki, 2002; Badsar, 2012; Verachtert, 2018). Furthermore,  $D_S$  and  $D_P$  do not significantly impact on their behavior, at least in weakly dissipative media (Nazarian and Stokoe II, 1984; Xia et al., 1999; Aki, 2002; Badsar, 2012; Verachtert, 2018). On the other hand, modal attenuation data are remarkably sensitive on  $H$ ,  $V_S$ , and  $D_S$ . The relevant role of  $V_S$  urges for robust inversion schemes to retrieve a reliable and accurate stiffness model, in order to achieve reliable  $D_S$  profiles. Instead,  $\rho$  and  $V_P$  (or  $v$ ) have a minor influence on attenuation curves. Finally, modal attenuation data are much less sensitive to  $D_P$  compared with  $D_S$  (Nazarian and Stokoe II, 1984; Xia et al., 1999; Aki, 2002; Badsar, 2012; Verachtert, 2018).

Therefore, an optimized model identification only investigates a model parameter subspace composed by the most influencing quantities, whereas the remaining are kept fixed to realistic values or related to other ones. Indeed, the reduced dimensionality of the search domain limits solution non-uniqueness. On the one side,  $\rho$  is usually assigned as a function of the site geology, whereas  $V_P$  can be expressed as a function of  $V_S$ , through  $v$ . The choice of  $\rho$  and  $v$  depends on the lithology and on the location of the water table (Foti and Strobbia, 2002; Foti et al., 2018). Instead,  $D_P$  is usually assumed as equal to  $D_S$  (e.g., Badsar, 2012; Armstrong et al., 2020).

A reasonable choice of the initial values of model parameters or the corresponding investigation range can mitigate solution non-uniqueness, improving the reliability and the accuracy in the resulting ground models. For this purpose, geological data or independent geophysical and geotechnical surveys often provide valuable information that help in optimizing the parameter choice (Foti et al., 2014). These data often allow an effective constraint in the model layering (i.e., the number of layers in the ground model and their thickness). In case of unavailable site-specific information, it is strongly recommended to include variations in the inversion parameterization to account for epistemic uncertainty, e.g. by means of the layering ratio approach (Cox and Teague, 2016) or by including a statistical model for the layering (Passeri et al., 2020). Besides, the interpretation of R0 experimental data allows to draw inference on the

investigated parameters. Indeed, the transformation of the experimental dispersion curve from the  $V_R - f$  domain into the  $(1.05 \div 1.1) \times V_R - \lambda/2.5$  domain returns an approximation of the time-weighted average  $V_S$  profile over the depth, the validity of which is as stronger as the R0 dominates the wavefield (Foti et al., 2018). The inspection of the transformed dispersion data provides some preliminary insights on the velocity structure of the medium. Furthermore, the experimental data point closest to the surface provides a twofold indication, as its depth is approximately equal to the minimum resolvable layer thickness (i.e.,  $\lambda_{\min}/3$ , where  $\lambda_{\min}$  is the minimum measured wavelength) and the corresponding velocity is a fairly close to the  $V_S$  of the surface layer – or the average value, if thin surface layers are involved. On the other side, the largest  $\lambda/2.5$  value is a conservative proxy of the maximum investigable depth, within which layer interfaces should be located (Herrmann and Al-Eqabi, 1991; Shtivelman, 1999). Similarly, the corresponding phase damping ratio usually matches the near-surface  $D_S$ . Therefore, these experimental data allow an effective constraint of mechanical parameters of the near-surface layer. Similar considerations apply for the dissipation structure, which can be guessed by transforming experimental attenuation data from the  $\alpha_R - f$  domain into the  $D_R - \lambda/2.5$  domain. Indeed, the near-surface  $D_R$  usually matches the corresponding  $D_S$ . However, the variation of  $D_R$  along the pseudo-depth usually does not allow an immediate inference of the dissipation structure of the medium, due to the great variability and the presence of oscillations linked with stiffness variations.

Figure 8-2 represents the investigated parameter space in the inversion of HB-DAS data, in terms of ranges of  $V_S$  and  $D_S$  as a function of the depth. Indeed, the adopted inversion algorithm relies on a uniform distribution of model parameters, hence the related range is an exhaustive descriptor. For simplicity, the model identification adopts a fixed layering scheme, based on a three-layer ground model. This choice relies on the stratigraphy inferred by cone penetration soundings carried out close to the DAS array (Fathi et al., 2016). The parameterization focuses on models with increasing layer thickness, to account for the loss of sensitivity of the R-wave parameters as the depth increases (Strobbia, 2003; Socco and Strobbia, 2004), with a minimum thickness equal to 2 m. This value is compatible with  $\lambda_{\min}$ . Besides, the investigated parameter space includes models with half-space interface at around 15 m, which is consistent with  $\lambda_{\max}$ . As for  $V_S$ , the parameter space mostly focuses on ground models with increasing  $V_S$  with the depth, as the monotonic increase of  $(1.05 \div 1.1) \times V_R$  over  $\lambda/2.5$  is typical of normally dispersive media. Note that the search domain for the half-space  $V_S$  includes values quite greater than the maximum available  $(1.05 \div 1.1) \times V_R$ . Indeed,

experimental data exhibit a continuous increase without any asymptote at depth, entailing that greater  $V_S$  values can be found beyond the last point. For simplicity, the search domain for  $D_S$  shares the same layering of  $V_S$ . In this case, the shallow  $D_S$  is inferred from experimental data, whereas not enough information is available to constrain  $D_S$  at depth. Therefore, the investigated ranges are rather broad to ensure an adequate exploration of the parameter space. On the other side, a gradual reduction of  $D_S$  with depth is accommodated, to comply with the gradual decrease of  $D_R$  when  $\lambda/2.5$  is great. For simplicity,  $\rho$  and  $\nu$  are fixed at realistic values, whereas  $D_P$  is assumed as equal to  $D_S$ . Parameter ranges are summarized in Table 8.1.

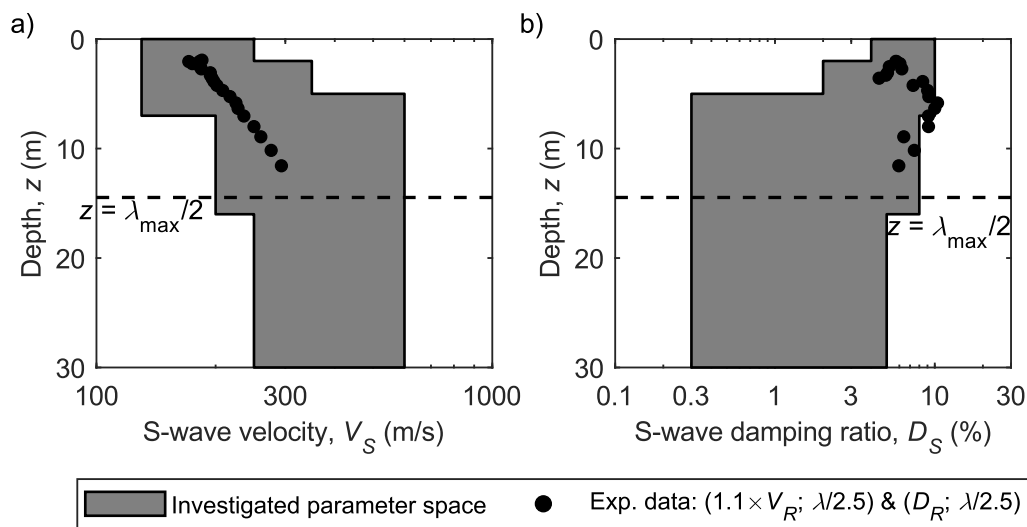


Figure 8-2. Range of  $V_S$  and  $D_S$  profiles corresponding to the investigated parameter domain, reported in Table 8.1. The search domain is overlapped by the “pseudo-depth” representation of the fundamental-mode experimental data, i.e.  $1.1 \times V_R$  vs.  $\lambda/2.5$  and  $D_R$  vs.  $\lambda/2.5$ .

Table 8.1. Boundaries of the investigated parameter domain.

Layer	Thickness $H$ (m)	Mass density $\rho$ (kg/m <sup>3</sup> )	S-wave velocity $V_S$ (m/s)	Poisson ratio $\nu$ (-)	S-wave damping ratio $D_S$ (%)	P-wave damping ratio $D_P$ (%)
1	2 ÷ 7	1600	130 ÷ 250	0.33	4 ÷ 10	Equal to $D_S$
2	2 ÷ 9	1600	200 ÷ 350	0.33	2 ÷ 8	Equal to $D_S$
Half-space	-	1800	250 ÷ 600	0.33	0.3 ÷ 5	Equal to $D_S$

## 8.4 A Monte Carlo algorithm for the joint inversion

### 8.4.1 Monte Carlo sampling

The Monte Carlo sampling procedure is a family of global search algorithms for the solution of the inversion problem, that falls within the framework of the Bayesian approaches.

The aim of the Bayesian approach is the derivation of a posterior probabilistic distribution  $\sigma(\mathbf{m})$  for a generic model  $\mathbf{m}$ , that statistically measures the ability of the model to be compatible with observed data and with a priori constraints. This scheme assumes an a priori statistical distribution  $\rho(\mathbf{m})$  on the model parameters to be estimated (e.g., a uniform distribution), that synthetizes any data-independent information (e.g., constraints derived from physical laws). Information from observed data is modeled through the likelihood function  $L(\mathbf{d} | \mathbf{m})$ , which quantifies the degree of fit between observed system response and the predicted one under the assumed validity of the generic model  $\mathbf{m}$ , as a function of the forward modeling  $\mathbf{g}$ . The posterior distribution  $\sigma(\mathbf{m})$  is proportional to the product of the prior model and the likelihood function, thus combining information provided by the measurement of the data vector and by the physical theory (Tarantola and Valette, 1982; Mosegaard and Tarantola, 1995; Mosegaard and Sambridge, 2002; Tarantola, 2004):

$$\sigma(\mathbf{m}) \propto \rho(\mathbf{m})L(\mathbf{d} | \mathbf{m}) \quad (8.2)$$

Eq. 8.2 can be interpreted as the mapping of the measured data into a distribution of the desired model parameters. Therefore, it is a statistical representation of the solution of an inverse problem. Furthermore, the interpretation of  $\sigma(\mathbf{m})$  allows to draw inference on the nature of the estimated model.

The main advantage of this formulation is that the derivation of information on the estimated model parameters refers to the characterization of  $\rho(\mathbf{m})$  and  $L(\mathbf{d} | \mathbf{m})$ , the characterization of which is usually an easier task than describing  $\sigma(\mathbf{m})$ . Typical modeling describes  $\rho(\mathbf{m})$  according to simple statistical schemes, for instance with a normal distribution or a uniform model. Instead,  $L(\mathbf{d} | \mathbf{m})$  usually depends on a misfit function  $S(\mathbf{m})$ , that measures the deviation between observed data and predicted data (Mosegaard and Tarantola, 1995), the latter being often obtained through the forward problem:

$$L(\mathbf{d} | \mathbf{m}) \propto e^{-S(\mathbf{m})} \quad (8.3)$$

The Monte Carlo procedure reconstructs  $\sigma(\mathbf{m})$  through a two-step procedure. Firstly, it simulates the prior distribution  $\rho(\mathbf{m})$ , drawing a suite of samples  $\mathbf{m}_i$ . As typical inverse problems adopt simple distribution models for  $\rho(\mathbf{m})$ , basic sampling methods allow an adequate simulation. Then, it computes the  $L(\mathbf{d} | \mathbf{m})$  value for each sample  $\mathbf{m}_i$ , derived from the corresponding misfit  $S(\mathbf{m}_i)$ . The combination of the prior information and the likelihood value for each sample  $\mathbf{m}_i$  returns samples of  $\sigma(\mathbf{m})$ , thus obtaining a suite of realizations for the posterior distribution.

In this study, the model  $\mathbf{m}$  is a ground model and it clusters the unknown geometric and mechanical parameters. The adopted simulation procedure assumes that  $\rho(\mathbf{m})$  is a multivariate, uniform distribution. Therefore, the generation of realizations  $\mathbf{m}_i$  from  $\rho(\mathbf{m})$  involves a sequential use of one-dimensional sampling methods (Mosegaard and Sambridge, 2002). In each step, each model parameter (i.e.,  $H$ ,  $\rho$ ,  $V_S$ ,  $v$ ,  $D_S$ , and  $D_P$ ) is randomly extracted from a uniform distribution, the range of which is defined based on experimental data. The advantage of using a multivariate, uniform model for  $\rho(\mathbf{m})$  is twofold. On the one side, the statistical characterization of the parameter space can be carried out for every single model parameter in a separate way, and each one requires only two statistics for an exhaustive description (e.g., the boundaries of the uniform distribution). Furthermore, for a uniform prior,  $\sigma(\mathbf{m})$  is determined primarily by  $L(\mathbf{d} | \mathbf{m})$  which, in turn, depends solely on the misfit function  $S(\mathbf{m})$  (Sen and Stoffa, 1996; Socco and Boiero, 2008). Therefore, a characterization of  $S(\mathbf{m})$  provides an adequate description of the posterior distribution, and inference on estimated ground models can be drawn from this quantity. For instance, the most suitable model (i.e., the one maximizing  $\sigma(\mathbf{m})$ ) coincides with the minimum of  $S(\mathbf{m})$ .

### 8.4.2 Misfit function

The ranking of each model with respect to observed data is quantified by the misfit function  $S(\mathbf{m})$ , which is a distance metric between the observed data and the predicted ones. In this case, experimental data are the  $V_R(\omega)$  and  $\alpha_R(\omega)$  data obtained at the HB-DAS survey, whereas the simulated values are the ones computed for each randomized earth model  $\mathbf{m}_i$ . The derivation of theoretical data requires the solution of the forward problem, corresponding to the Rayleigh-wave eigenvalue problem. This operation is carried out through the EDT toolbox (Schevenels et al., 2009), which implements the transfer matrix method (Thomson, 1950; Haskell, 1953).

A popular definition of the misfit function assumes that the prediction error is normally distributed (Oldenburg and Li, 2005). In this case, an effective metric to

quantify model accuracy with respect to experimental data is the Mahalanobis distance (Mosegaard and Tarantola, 1995), computed as the L2-norm of the prediction error vector, weighted by the experimental covariance matrix  $\Sigma^{-1}$  (Seber and Wild, 2003):

$$S(\mathbf{m}) = \sum_{i=1}^n [\mathbf{g}_i(\mathbf{m}) - \mathbf{d}_i]^T \Sigma_i^{-1} [\mathbf{g}_i(\mathbf{m}) - \mathbf{d}_i] \quad (8.4)$$

Eq. 8.10 is a specialized version of the  $S(\mathbf{m})$  formulation typically used in nonlinear model identification, for the joint inversion of multimode phase velocity and phase attenuation data. The label  $i$  denotes the  $i$ -th frequency sample ( $n$  is the number of data samples), at which the vector of observed data  $\mathbf{d}_i$  contains the median experimental  $V_R(\omega)$  and  $\alpha_R(\omega)$ , that are compared with the corresponding theoretical estimates contained in  $\mathbf{g}_i(\mathbf{m})$ . The covariance matrix  $\Sigma_i$  contains the variances and the correlation coefficients at the  $i$ -th frequency sample. Actually, as experimental data are modeled according to a lognormal distribution, these quantities should be represented in logarithmic scale.

This definition weights the fitting errors as a function of the uncertainties affecting  $V_R(\omega)$  and  $\alpha_R(\omega)$  as well as their linear correlation (in log scale, in this case). On the other side, the linear correlation between measured  $V_R(\omega)$  and  $\alpha_R(\omega)$  is statistically insignificant, for each frequency, as demonstrated in Chapter 7. Therefore, an alternative formulation for  $S(\mathbf{m})$  can be obtained by assuming uncorrelated experimental uncertainties:

$$S(\mathbf{m}) = \frac{1}{2Mn} \sum_{j=0}^{M-1} \sum_{i=1}^n \left[ \frac{(\ln V_{i,Rj,e} - \ln V_{i,Rj,t})^2}{\sigma_{\ln V,i,Rj}^2} + \frac{(\ln \alpha_{i,Rj,e} - \ln \alpha_{i,Rj,t})^2}{\sigma_{\ln \alpha,i,Rj}^2} \right] \quad (8.5)$$

The definition compares theoretical dispersion data  $V_{i,Rj,t}$  and attenuation data  $\alpha_{i,Rj,t}$  and observed values  $V_{i,Rj,e}$  and attenuation data  $\alpha_{i,Rj,e}$ , for each considered propagation mode  $Rj$  and each frequency sample  $i$ . Figure 8-3 provides a graphical representation of the involved quantities. The comparison is carried out in logarithmic scale, to be consistent with the assumption of lognormally distributed experimental data (see Chapter 7). This structure of the misfit function is a least-square objective function, that can be interpreted as a generalization of the version often adopted in the model identification from phase velocity data (e.g., Wathelet et al., 2004). This definition separates the contributions linked with  $V_R(\omega)$  and  $\alpha_R(\omega)$  fitting, and the normalization with respect to the corresponding variance (i.e.,  $\sigma_{\ln V,i,Rj}^2$  and  $\sigma_{\ln \alpha,i,Rj}^2$ ) guarantees proportional weighting to dispersion and attenuation data. Therefore, the model identification accounts for the different degree of accuracy in the observed data, also compensating for the

different order of magnitude that characterizes  $V_R(\omega)$  and  $\alpha_R(\omega)$  (and the related prediction errors), thus avoiding potential overfitting of part of the observed data. The multiplying factor  $1/2Mn$  is an additional quantity that simply scales the  $S(\mathbf{m})$  distribution without altering its shape, with the aim of providing a more intuitive interpretation of the numerical values of  $S(\mathbf{m})$  itself. Indeed,  $S(\mathbf{m})$  is unitary when the distance between predicted and experimental  $V_R(\omega)$  and  $\alpha_R(\omega)$  across the investigated frequency bandwidth and the considered propagation modes equals one standard deviation, on average.

Alternative misfit definitions are available, that rely on a complex-valued definition (Lai et al., 2002; Lai, 2005; Foti et al., 2014) or as the weighted sum of the separate misfits in terms of phase velocity and phase attenuation data, adopting a structure usually employed in joint inversion of multiple geophysical data (e.g., Verachtert, 2018).

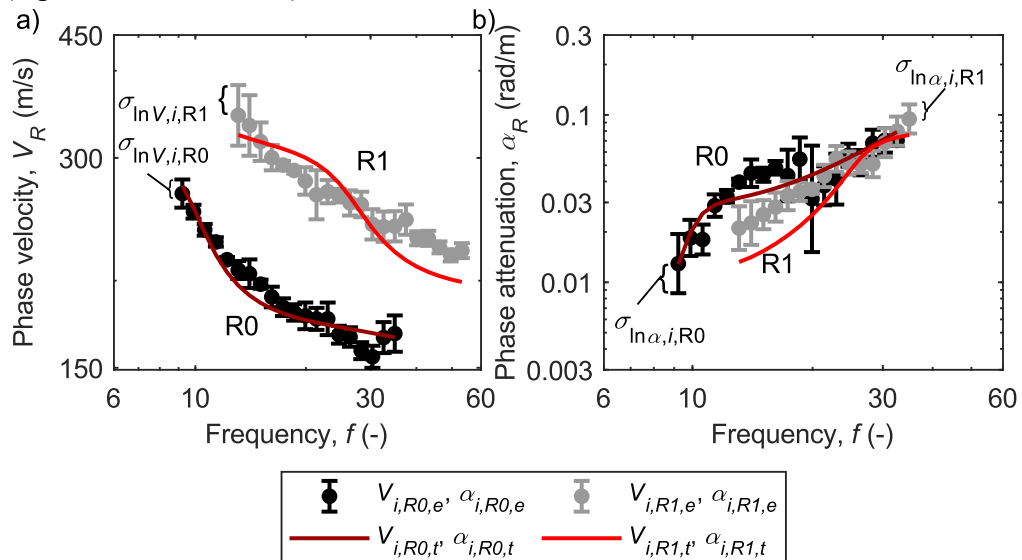


Figure 8-3. Quantities involved in the definition of the misfit function, namely theoretical estimates (subscript “t”) and observed data (subscript “e”).

### 8.4.3 Scaling properties of the forward problem

This Section provides a synthetic description of the scaling properties of the solution of the Rayleigh wave eigenvalue problem in viscoelastic conditions. Then, it specifies how this feature is implemented into the Monte Carlo procedure, improving the quality of the resulting earth models with limited computation effort.

#### 8.4.3.1 Description of the scaling properties

Strobbia (2003), Socco and Strobbia (2004), and Maraschini et al. (2011) demonstrated that the modal solution in elastic conditions scales with the wavelength. Specifically, a scaling of  $V_S$  results in an equivalent scaling of both  $V_R$  and  $\omega$  in the dispersion curve, whereas a scaling of  $H$  induces an inverse scaling of  $\omega$ . In this study, it is demonstrated that this property can be extended to the viscous-elastic model, thanks to the correspondence principle (Achenbach and Reddy, 1967). In such conditions, a scaling of  $V_S$  and  $H$  leads to a scaling of  $\alpha_R(\omega)$ . As for variations in  $D_S$ , their mapping on the modal solution is nontrivial but an approximate solution has been developed in this study. Although this approximation neglects the causality relationship between  $V_S$  and  $D_S$ , the resulting estimate is fairly accurate.

This section contains an intuitive explanation of the scaling properties of the R-wave modal parameters in viscous-elastic conditions, whereas a more detailed and mathematically rigorous demonstration is available in Appendix C.

Let us consider a layered, viscoelastic earth model, wherein each layer is characterized by thickness  $H_0$ , S-wave velocity  $V_{S,0}$  and S-wave damping ratio  $D_{S,0}$ . A harmonic Rayleigh wave with frequency  $f$  travels in this medium with a phase velocity  $V_{R,0}$  and a phase attenuation  $\alpha_{R,0}$  (alternatively, a phase damping ratio  $D_{R,0}$ ). On the other side, the propagation parameters of the R-wave mostly depend on the soil mechanical properties down to a depth equal to the corresponding wavelength  $\lambda_R$  (Foti, 2000). Thanks to this property, variations in thicknesses, velocities and damping ratios on the dispersion and attenuation curves can be mapped.

Firstly, the effect of scaling  $V_S$  is investigated. Let us consider a soil model identical to the original one, but with layer velocities  $V_{S,1}$  equal to  $c \times V_{S,0}$  (and  $V_{P,1} = c \times V_{P,0}$  for simplicity, namely  $\nu$  does not vary), where  $c$  is a real constant. In the original medium, a Rayleigh wave of wavelength  $\lambda$  travels with phase velocity  $V_{R,0}$  and phase damping  $D_{R,0}$ . In the scaled ground model, the same wavelength is sampling the same medium, but with scaled velocity. Hence, it propagates according to a velocity  $c \times V_{R,0}$ , whereas the attenuation is still equal to  $\alpha_R$ . In this situation, the corresponding frequency is:

$$f_1 = \frac{V_{R,1}}{\lambda} = \frac{c V_{R,0}}{\lambda} = c f_0 \quad (8.6)$$

Therefore, also the frequency is scaled. On the other side, the damping structure is unchanged, hence the phase damping ratio equals  $D_{R,0}$ . Thus, the corresponding attenuation is:



$$\alpha_{R,1} = \frac{2\pi f_1 D_{R,1}}{V_{R,1}} = \frac{2\pi c f_0 D_{R,0}}{c V_{R,0}} = \frac{2\pi f_0 D_{R,0}}{V_{R,0}} = \alpha_{R,0} \quad (8.7)$$

Hence,  $\alpha_R$  is unchanged. In summary, a scaling of all the S-wave velocities results in a scaling of both velocities and frequencies in the dispersion curve and of frequencies only in the attenuation curve (Figure 8-4).

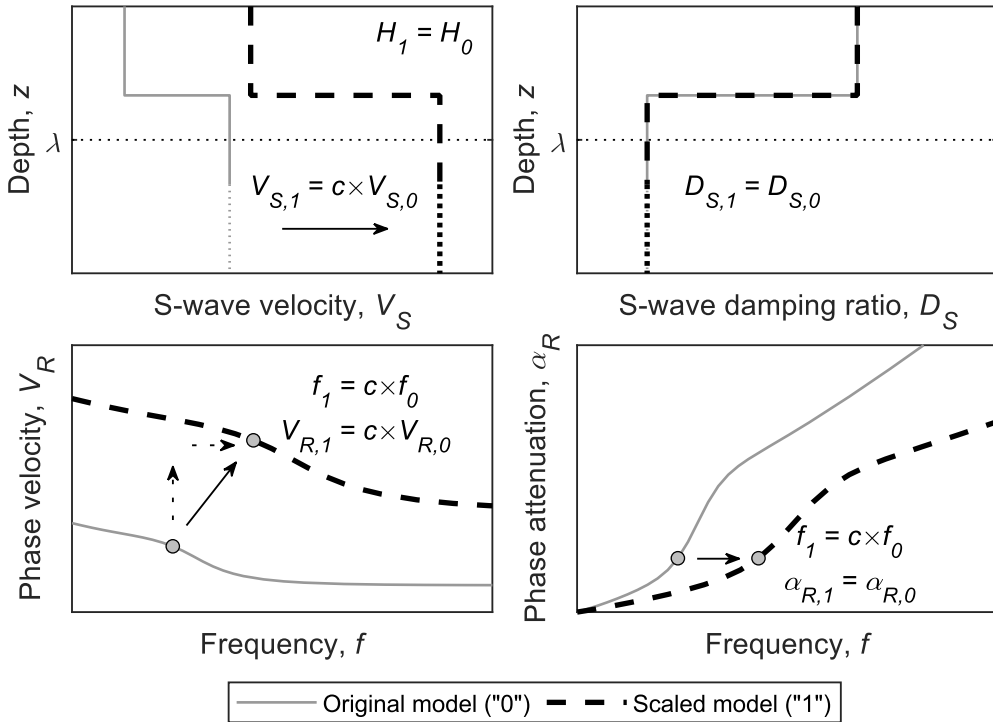


Figure 8-4. Effect of S-wave velocity scaling on the dispersion and attenuation curves.

Then, the effect of scaling  $H$  is investigated. In this case, the alternative soil model is characterized by layer thickness  $H_1$  equal to  $c \times H_0$ , where  $c$  is a real constant. In the original medium, a Rayleigh wave of wavelength  $\lambda$  propagates with phase velocity  $V_{R,0}$  and phase damping ratio  $D_{R,0}$ . In the scaled medium, a Rayleigh wave of wavelength  $\lambda_1 = c \times \lambda_0$  is sampling a medium with the same characteristics of the original one, hence it propagates according to a phase velocity  $V_{R,0}$  and phase damping ratio  $D_{R,0}$ . In this situation, the corresponding frequency is:

$$f_1 = \frac{V_{R,1}}{\lambda_1} = \frac{V_{R,0}}{c\lambda} = \frac{1}{c} f_0 \quad (8.8)$$

Therefore, the frequency is inversely scaled with respect to the change in thickness. The corresponding attenuation is:

$$\alpha_{R,1} = \frac{2\pi f_1 D_{R,1}}{V_{R,1}} = \frac{2\pi \frac{1}{c} f_0 D_{R,0}}{V_{R,0}} = \frac{1}{c} \frac{2\pi f_0 D_{R,0}}{V_{R,0}} = \frac{1}{c} \alpha_{R,0} \quad (8.9)$$

Hence,  $\alpha_R$  is scaled in a similar way as the frequency. In conclusion, a scaling of all the layers' thicknesses results in a scaling of frequencies only in the dispersion curve and of both phase attenuations and frequencies in the attenuation curves (Figure 8-5).

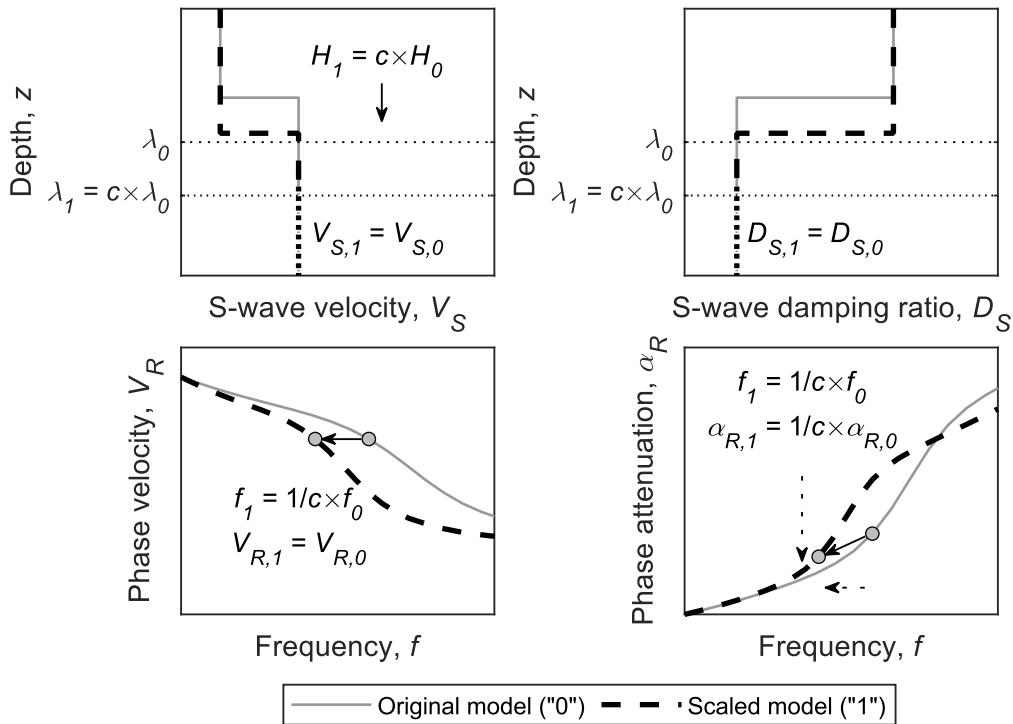


Figure 8-5. Effect of layer thickness scaling on the dispersion and attenuation curves.

When scaling S-wave damping ratios, the resulting soil model is characterized by damping ratio  $D_{S,1}$  equal to  $c \times D_{S,0}$  (and  $D_{P,1} = c \times D_{P,0}$  for simplicity), where  $c$  is a real constant. In the original medium, a Rayleigh wave of wavelength  $\lambda$  travels with phase velocity  $V_{R,0}$  and phase damping ratio  $D_{R,0}$ . In the scaled medium, the same wavelength is sampling a medium with scaled damping ratio, thus traveling according to the phase velocity  $V_{R,0}$  and phase damping ratio  $D_{R,1} = c \times D_{R,0}$ . In this situation, the corresponding frequency is unchanged, whereas the corresponding phase attenuation is scaled:

$$\alpha_{R,1} = \frac{2\pi f_1 D_{R,1}}{V_{R,1}} = \frac{2\pi f_0 c D_{R,0}}{V_{R,0}} = c \frac{2\pi f_0 D_{R,0}}{V_{R,0}} = c \alpha_{R,0} \quad (8.10)$$

Therefore, a scaling of all the damping ratios results in an unchanged dispersion curve and in a scaling of attenuations in the attenuation curves (Figure 8-6). However, this relationship is approximate because variations in the damping ratios induce more complex modifications in the modal solution than a simple scaling. Indeed, also variations in frequencies and phase velocities occur, but there is no closed-form solution for predicting them. Furthermore, the modification in the attenuation is slightly nonlinear and dependent on the frequency. However, such variations are rather small compared to the order of magnitude of phase velocities and frequencies of common application, when dealing with low dissipative media. Therefore, the error induced by the approximation may be considered negligible, as also numerically stated in Armstrong et al. (2020).

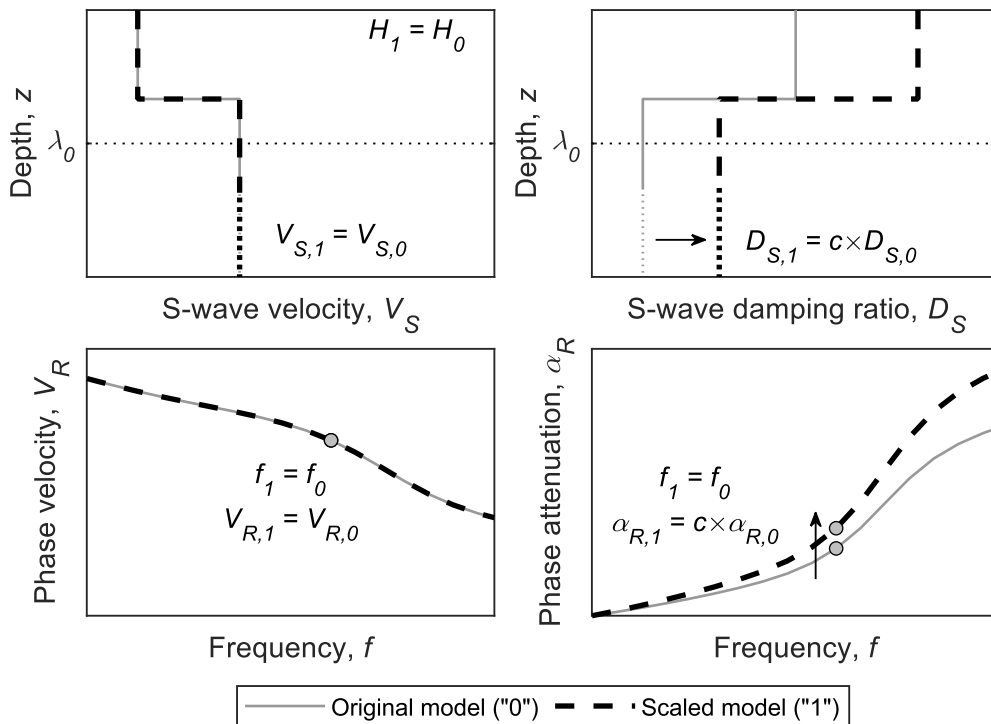


Figure 8-6. Effect of S-wave damping ratio scaling on the dispersion and attenuation curves.

#### 8.4.3.2 Implementation of the scaling properties in the inversion algorithm

One critical aspect of Monte Carlo-based global search methods is the need of effectively sampling the investigated parameter space. Indeed, as the search domain is broad and high-dimensional, a huge number of model realizations is required to minimize the risk of neglecting promising regions. However, increasing the number of generated models means a greater number of forward

simulations, entailing a significant rise in computation time. The computation burden is even more relevant when viscoelastic media are involved, due to the greater complexity of the forward algorithm. As an example, the performance of elastic and viscoelastic forward modeling codes are compared, with reference to the computation of modal  $V_R(\omega)$  and  $\alpha_R(\omega)$  for the synthetic wavefield SW3 (see Chapter 5), at 82 frequencies spanning between 0.5 Hz and 100 Hz. Elastic modeling was carried out by means of built-in MATLAB codes, whereas the EDT toolbox (Schevenels et al., 2009) was used for viscoelastic simulations. Numerical calculations were run on a workstation, with 24 Intel® Xeon® W-2265, 3.50 GHz CPUs. The computation time needed for computing fundamental-mode data is 0.15 s in elastic conditions, and it rises to 0.9 s when computing both  $V_R(\omega)$  and  $\alpha_R(\omega)$ . If the goal of the forward simulation is estimating the first two R-wave modes (e.g., for multi-mode inversion), elastic modeling takes 0.45 s, whereas the computation time is 2.3 s in viscoelastic conditions. Therefore, viscoelastic forward modeling is 5 ÷ 6 times more time consuming than the corresponding elastic computation. This dramatically affects the global search procedure as the number of trial earth models should be not large, to avoid excessively time-consuming inversion runs. For instance, running an inversion stage with  $10^4$  trial ground models needs about 12 ÷ 24 hours for being completed, depending on the size of the parameter space and on the number of propagation modes being simulated. On the other side, reducing the number of random samples hinders the capacity of the search algorithm to explore the parameter space, increasing the risk of discarding potentially good solutions.

The scaling properties of the solution of the Rayleigh wave eigenvalue problem can represent a valuable tool to optimize the generated Monte Carlo samples, with negligible increase in computation time. Indeed, these properties can be used to modify the random samples in order that the theoretical data match better observed values.

Specifically, the inversion algorithm implements a backwards version of the scaling properties. For each generated ground model, the predicted dispersion and attenuation data are scaled to improve the fitting with the experimental values, and the corresponding model parameters are modified through the inverse application of the scaling properties. This application in the inversion procedure was introduced by Socco and Boiero (2008), where the scaling of the theoretical data was based on the comparison of the barycenters between predicted and observed dispersion data. In this study, the scaling procedure jointly modifies the theoretical frequencies, phase velocities and phase attenuations according with three scaling coefficients, that are calibrated by means of an optimization

procedure which maximizes the degree of fit between theoretical and experimental data. The matching is quantified by means of a distance metric between the scaled version of theoretical data and experimental data, measured by misfit function introduced in Eq. 8-5. A local optimization solver identifies the best scaling coefficients, according to which the corresponding ground model is updated. Compared with measuring the distance on the gravity center only, this approach does not only guarantee a good matching between scaled and observed data at the gravity center, but it also introduces a constraint on the behavior of the remaining points. Therefore, the estimated scaling coefficients also accounts for the geometry of the dispersion and attenuation data, thus ensuring better matching between predicted and experimental data. Once obtained the scaling factors for the frequencies ( $c_f$ ), for the phase velocities ( $c_{VR}$ ) and for the phase attenuations ( $c_{\alpha R}$ ), the corresponding scaling factors for the layer thicknesses ( $c_H$ ), for the S-wave velocities ( $c_{VS}$ ) and for the S-wave damping ratios ( $c_{DS}$ ) are computed as follows:

$$c_H = \frac{c_{VR}}{c_F}, \quad c_{VS} = c_{VR}, \quad c_{DS} = \frac{c_{VR}}{c_F} c_{\alpha R} \quad (8.11)$$

The result of the scaling procedure is an alternative sampling of the parameter space, with the models concentrated in the high-probability region, which is closer to the true model (Socco and Boiero, 2008). This allows to optimize the sampled portion, converting the randomized parameter set into an alternative one, best suiting observed data. In this way, the number of required samples (hence, forward simulations) can be significantly reduced. Also, this correction does not require any further forward analyses to be run, thus saving computation time.

#### 8.4.4 Inversion results

The inversion was run using 10,000 trial earth models. Forward dispersion and attenuation modeling was carried out through the EDT toolbox (Schevenels et al., 2009), which implements the transfer matrix method (Thomson, 1950; Haskell, 1953).

An effective description of inversion results should refer to a representative suite of ground models, ensuring an adequate matching with experimental data (i.e., low misfit) and accounting for the uncertainties both in the inversion problem (due to solution non-uniqueness) and in the experimental data themselves (Mosegaard and Sambridge, 2002). For this purpose, various approaches have been proposed for the inversion of phase velocity data (e.g., Socco and Boiero, 2008; Griffiths et al., 2016b; Hallo et al., 2021). However, currently there are no methods for identifying a reference collection of samples from the joint inversion

of phase velocity and phase attenuation data. Furthermore, the generalization of existing criteria to select adequate damping models is not immediate because this should account for both the multivariate nature of the joint inversion and the different degree of variability affecting experimental data. In the context of Bayesian inversion, an effective strategy relies on specific statistics extracted from the posterior distribution (Hallo et al., 2021). Alternatively, a non-conventional, yet intriguing approach directly obtains the desired distribution by running multiple inversion simulations on a suite of experimental data, whose statistical features are compatible with measured ones (Vantassel et al., 2022). This study adopts a simple strategy reporting a collection of best fitting models as the representative suite. Despite its simplicity, this selection criterion provides an insight about the main features of inverted models and the related uncertainties.

Figure 8-7 shows results for the best fitting 30 models. Inverted S-wave velocity and damping ratio profiles are poorly scattered, and the velocity and dissipation structures are clearly identifiable in the near-surface layers. Specifically, the resulting  $V_S$  model exhibits a gradual increase in stiffness with depth. The depths of the identified layers interfaces are about 4 m and 12 m. This result is consistent with the main geological interfaces inferred at the site and with information from past geophysical surveys (see Chapter 6). Instead, the estimated  $D_S$  profiles are affected by greater variability, which increases with depth. However, variations in  $D_S$  with depth follow the same layer interfaces as  $V_S$ , and it ranges about 5% in the near-surface layer, whereas it increases to 7÷9% in the one below. As for the half-space, the variability in both  $V_S$  and  $D_S$  dramatically increases with respect to shallow layers. Indeed, the depth of the interface with the half-space is quite close to the maximum resolvable depth that can be achieved with the available experimental data, i.e.  $\lambda_{\max}/2$  (Foti et al., 2018). Therefore, the few amount of experimental data at long wavelengths does not allow an effective constraints of estimated profiles at greater depths. Thus, the  $V_S$  oscillates between 330 m/s and 400 m/s, whereas  $D_S$  spans over a much broader range, mostly between 0.5% and 5% (that is, the variation is about one order of magnitude). This is the combined effect of the high  $\sigma_{\ln\alpha}$  in low-frequency experimental data, the relevant influence of  $V_S$  on phase velocity and attenuation data, and the moderately low sensitivity of theoretical attenuation curves to  $D_S$  at great depths (e.g., Verachtert, 2018), that does not allow a constraint on  $D_S$  as effective as in the stiffness modeling.

However, it should be remarked that both the velocity and dissipation structures exhibit well defined trends, especially in the near-surface layers. Furthermore, the  $D_S$  increase at intermediate depths partially contradicts the

boundaries of the investigated search domain, which imposed a maximum  $D_S$  equal to 8% in this layer. This demonstrated the effectiveness of the improved Monte Carlo sampling procedure, which manages to well identify the ground models even when the adopted parameterization is non-optimal. These results highlight the effectiveness of the proposed inversion algorithm.

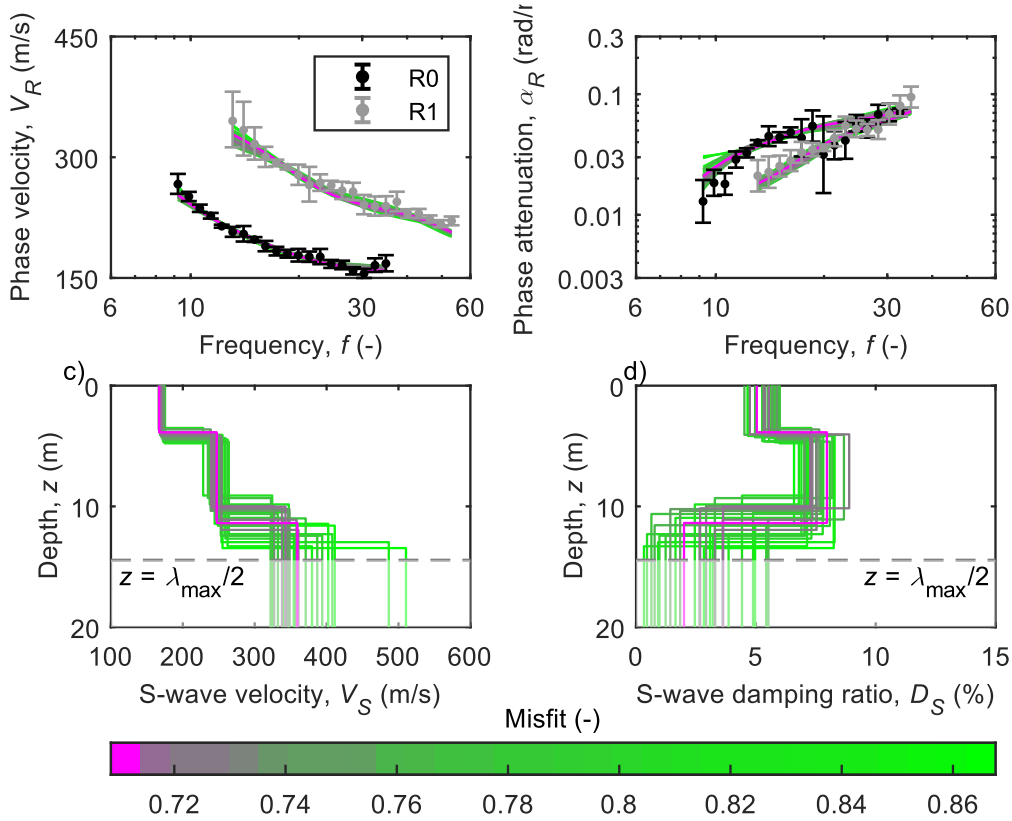


Figure 8-7. Best fitting ground models to HB-DAS experimental data: a-b) Theoretical vs. experimental data, for the phase velocity (a) and phase attenuation (b); c-d) Resulting S-wave velocity (c) and damping ratio (d) profiles. The boundary  $z = \lambda_{\max}/2$  is an approximated value of the maximum investigable depth, that can be achieved from the available experimental data – layer interfaces beneath it are usually less reliable.

## 8.5 Summary

This Chapter addressed the joint estimate of S-wave velocity and damping ratio profiles from the experimental R-wave parameters. This operation consists in an inversion procedure, which requires the use of effective algorithms to handle with the nonlinearity and the ill-posedness of the problem. For this purpose, a novel algorithm is introduced. The proposed scheme is a global search, Monte Carlo procedure that implements an optimized sampling procedure, based on the scaling

properties of the Rayleigh eigenvalue problem in viscoelastic conditions. The validity of these properties in the viscoelastic case has been demonstrated in this Chapter. On the one side, the Monte Carlo scheme allows to explore various candidate earth models, thus evidencing the local minima in the misfit function. On the other side, the implementation of scaling properties concentrates the random samples in high probability density zones, that are expected to be closer to the “true” ground model. Thanks to this strategy, the number of random samples required to effectively investigate the parameter space is smaller, and the computation time needed to run forward simulations is significantly reduced. Indeed, forward modeling in viscoelastic conditions is much more complex than in elastic conditions and running Monte Carlo simulations with  $10^5$ - $10^7$  trial earth models (i.e., the typical sample size used in the inversion of phase velocity data) would require a time which is incompatible with practical needs. Therefore, the inclusion of the scaling properties allows to optimize the available random samples, without additional computation effort.

The effectiveness of the proposed algorithm was tested on the inversion of the experimental data collected at the HB-DAS survey. This represents an interesting case study due to the complexity of the recorded wavefield, from which multi-mode R-wave parameters were extracted and inverted. Furthermore, this study represents the first joint inversion of dispersion and attenuation data extracted from a fiber-optic array, to our knowledge. The improved sampling scheme and the presence of multi-mode observed data resulted in well-constrained S-wave velocity and damping ratio profiles, especially in the near-surface layers. However, the estimated ground models are affected by greater variability at depth, especially in terms of the damping ratio. The great scatter is the combined effect of the high  $\sigma_{\ln\alpha}$  in low-frequency experimental data and the moderately low sensitivity of theoretical attenuation curves to  $D_S$  at great depths (e.g., Verachtert, 2018). Therefore, experimental data do not allow an effective constraint on  $D_S$  in the deeper portions of the earth models. On the other side, these considerations rely on a selected suite of best fitting ground models, that may not be fully representative of actual data uncertainties and inversion non-uniqueness. Although this selection criterion might seem arbitrary, currently there are no methods for selecting a statistical collection of samples from the joint inversion of phase velocity and phase attenuation data. For this reason, further studies on this topic will address this issue, by generalizing available criteria developed in the dispersion analysis or introducing new schemes, that account for the multivariate nature of the joint inversion.





# **Chapter 9**

## **Influence of the small-strain damping ratio on ground site analyses**

This Chapter addresses the interpretation of results of SWM testing, with a focus on ground response analyses. Indeed, site characterization for the prediction of the ground motion amplification represents one of the most usual applications of SWM. The aim of this Chapter is to understand the implications of uncertainties in both the S-wave velocity and damping ratio on the predicted ground response. For this purpose, results from the SWM survey carried out at the Garner Valley Downhole Array (GVDA) are considered. The choice of this site derives from multifold reasons. On the one side, the detailed site characterization allows to compare the estimated ground models with ones derived from past studies. Furthermore, the presence of a permanent DH-array provides valuable observations on the actual ground motion amplification, that are an effective benchmark for the validation of the predicted ground response.

After a brief introduction on the performance of SWM into modeling the seismic site response, this Chapter shortly describes the main stages adopted to derive the reference earth models at the GVDA. Then, the reliability of the derived S-wave velocity and damping ratio models is addressed, in terms of both the comparison with alternative results and the quality of the predicted ground motion amplification.

### **9.1 Application of surface wave methods for ground response analyses**

One of the main purposes of SWM is the derivation of ground models to be used for predicting the ground motion amplification, by means of Ground Response Analyses (GRAs). As recommended by Foti et al. (2018), a proper modeling of the site response requires a suite of profiles that are statistically representative of the experimental data distribution (Vantassel and Cox, 2021a) or equivalently

fitting the experimental R-wave parameters (e.g., Foti et al., 2009). This criterion accounts for both the solution non-uniqueness and the uncertainties in the experimental data.

Several studies investigated the potential of using SWM for GRAs, in terms of both the capacity of predicting the expected ground motion amplification and the accuracy in the estimate. However, these studies mainly focused on the influence of uncertainties in the S-wave velocity profile, whereas a constant, laboratory-based value was usually adopted for the material damping. As for the reliability, the estimated ground motion amplification usually matches observed data, with some discrepancies at high frequencies. The lack of fit is an effect of two main factors. On the one side, the limited investigated depth in SWM might not allow the identification of deep impedance contrasts, that would introduce a fictitious truncation in the resulting soil profiles. This is apparent as a discrepancy in the location of the peaks of the estimated linear viscoelastic transfer functions (Vantassel et al., 2018). On the other side, the unmodeled contribution of spatial variability combined with an implicit modeling of energy dissipation results in wrong estimates of the magnitude in the ground motion amplification (e.g., Tao and Rathje, 2019). Focusing on variability, Foti et al. (2009) and Foti et al. (2018) demonstrated that the mapping of uncertainties from inferred profiles into derived ground motion amplification is nonlinear, and the uncertainty in the derived amplification is much smaller than the one affecting the estimated profiles. Indeed, although equivalent  $V_S$  profiles are quite variable, ground motion amplification is mostly controlled by variations in the S-wave travel time (or the harmonic velocity), which is less uncertain than the interval velocity, even in challenging conditions (e.g., Socco et al., 2015). This justifies the high accuracy and reliability of SWM in estimating  $V_{S,30}$  (Comina et al., 2011; Passeri et al., 2021), wherein the solution non-uniqueness has limited influence.

## 9.2 Case Study: Garner Valley Downhole Array

### 9.2.1 Derivation of S-wave velocity and damping ratio profiles

Figure 9-1a-b represents the fundamental-mode  $V_R(\omega)$  and  $\alpha_R(\omega)$ , obtained from waveforms recorded at the GV-H5 array and generated by the VibroSeis truck. These data are computed at log-spaced frequencies between 5 Hz and 35 Hz (i.e.,  $\lambda = 5 \div 90$  m; see Chapter 7), by means of the CFDBFa method. The modeling of experimental uncertainties relies on a lognormal statistical distribution, where data variability is described by the log-standard deviation. The error bars denote the

interval defined by the mean and one log-standard deviation. This represents the target dataset used in the inversion procedure.

The model parameterization assumes that  $\rho$  is fixed at realistic values, and  $D_P$  is assumed as equal to  $D_S$ , whereas the identification of  $H$ ,  $V_S$ , and  $D_S$  is carried out by means of the optimized Monte Carlo algorithm proposed in Chapter 8. The definition of the investigated parameter space was mainly informed by experimental data, converted in the  $(1.05 \div 1.1) \times V_R - \lambda/2.5$  and the  $D_R - \lambda/2.5$  domains. The investigated parameter space includes models with half-space interface at around 40 m, which is consistent with  $\lambda_{\max}$ . Both the surface geology and invasive testing (e.g., Gibbs, 1989; Steller, 1996; Teague et al., 2018b) demonstrated the presence of a low-velocity alluvium layer overlying weathered rock, with remarkably greater stiffness. Therefore, the model identification adopts a fixed layering scheme, based on a four-layer ground model. The parameterization includes three shallow layers with moderately low  $V_S$ , which gradually increases with depth. These layers seek to capture  $V_S$  variations in the alluvium, as suggested by the gradual rise of  $(1.05 \div 1.1) \times V_R$  with  $\lambda/2.5$ . Note that the search domain also includes a near-surface thin layer, with thickness slightly below the minimum resolvable value according to experimental data (i.e.,  $\lambda_{\min}/3 = 1.8$  m). Indeed, the low-depth  $D_R$  exhibits a remarkable increase in value, without achieving a stable value. Therefore, it is assumed that the presence of a thin, highly dissipative layer might be responsible of such behavior. Instead, the half-space might be representative of weathered rock, for which the average  $V_S$  of the investigated range sensibly increases. Similar to HB-DAS results (see Chapter 8), not enough information is available to constrain  $D_S$  at depth. Therefore, the investigated ranges are rather broad to ensure an adequate exploration of the parameter space. On the other side, a gradual reduction of  $D_S$  with depth is accommodated, to comply with the gradual decrease of  $D_R$  when  $\lambda/2.5$  is large. Finally, the parameterization also allowed independent randomization for  $V_P$ , of which ranges were based on borehole data carried out at the GVDA (Steller, 1996). Also, to ensure realistic coupling with  $V_S$ ,  $\nu$  was constrained within realistic boundaries. Parameter ranges are summarized in Figure 9-2c-d and Table 9.1. In general, the search domain is broad enough to allow an effective exploration of the parameter domain and to accommodate for discrepancies from a priori information due to lateral variability at the GVDA site and variable test locations.

The inversion was run using 10,000 trial earth models. Forward dispersion and attenuation modeling was carried out through the EDT toolbox (Schevenels et

al., 2009), which implements the transfer matrix method (Thomson, 1950; Haskell, 1953).

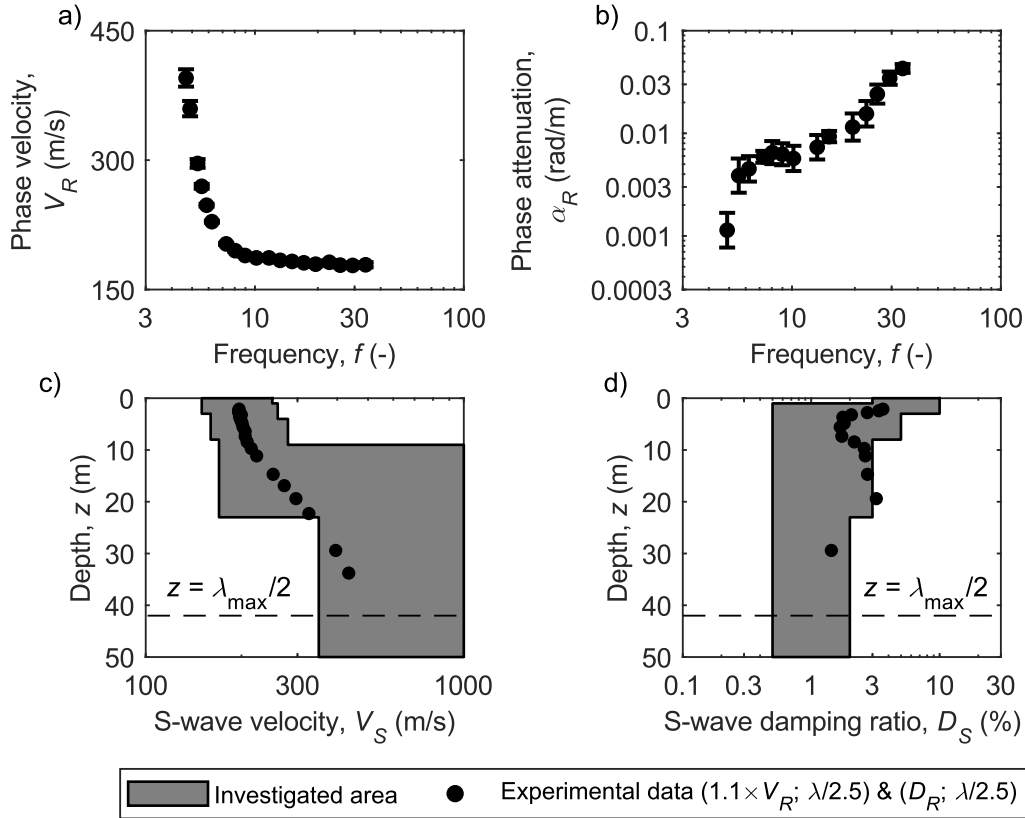


Figure 9-1. Range of  $V_S$  and  $D_S$  profiles corresponding to the investigated parameter domain, reported in Table 9.1. The search domain is overlapped by the “pseudo-depth” representation of experimental data, i.e.  $1.1 \times V_R$  vs.  $\lambda/2.5$  and  $D_R$  vs.  $\lambda/2.5$ .

Table 9.1. Boundaries of the investigated parameter domain.

Layer	Thickness $H$ (m)	Mass density $\rho$ (kg/m <sup>3</sup> )	S-wave velocity $V_S$ (m/s)	P-wave velocity $V_P$ (m/s)	Poisson ratio $\nu$ (-)	S-wave damping ratio $D_S$ (%)	P-wave damping ratio $D_P$ (%)
1	1 ÷ 3	1600	150 ÷ 250	300 ÷ 500	0.25 ÷ 0.40	1 ÷ 3	Equal to $D_S$
2	3 ÷ 5	1600	160 ÷ 260	320 ÷ 520	0.25 ÷ 0.40	0.05 ÷ 5	Equal to $D_S$
3	5 ÷ 15	1750	170 ÷ 280	1350 ÷ 1650	0.43 ÷ 0.49	0.03 ÷ 5	Equal to $D_S$
Half-space	-	2000	350 ÷ 1000	1800 ÷ 3000	0.43 ÷ 0.49	0.03 ÷ 2	Equal to $D_S$

Figure 9-2 shows results for the 30 best-fitting models. Inverted S-wave velocity profiles are poorly scattered, with a clearly identifiable velocity structure. Specifically, the resulting  $V_S$  model includes a low-velocity near-surface portion,

with  $V_S$  close to 200 m/s. Then, it suddenly increases at  $450 \div 500$  m/s at around 18 m of depth, which is compatible with the location of the interface between alluvium and weathered rock. Therefore, the derived velocity structure is consistent with both the site geology and information from past surveys. As for  $D_S$ , the estimated profiles are affected by large variability, which increases with depth. This is an effect of the high  $\sigma_{\ln\alpha}$  in experimental data, that does not allow a constraint on  $D_S$  as effective as in the stiffness modeling. However, inverted profiles exhibit a quite clear trend, characterized by  $D_S$  around 1%, which rises up to 5% in the near-surface layer. The moderately low variability in  $D_S$  in this layer highlights the effectiveness of using this peculiar parameterization in the inversion procedure. The large  $D_S$  in the shallow portion of the ground models might be an effect of heterogeneities on the top of the soil deposit, that have been also identified in Fathi et al. (2016). Lateral variations result in wave scattering phenomena, that induce an apparent increase of the material  $D_S$ .

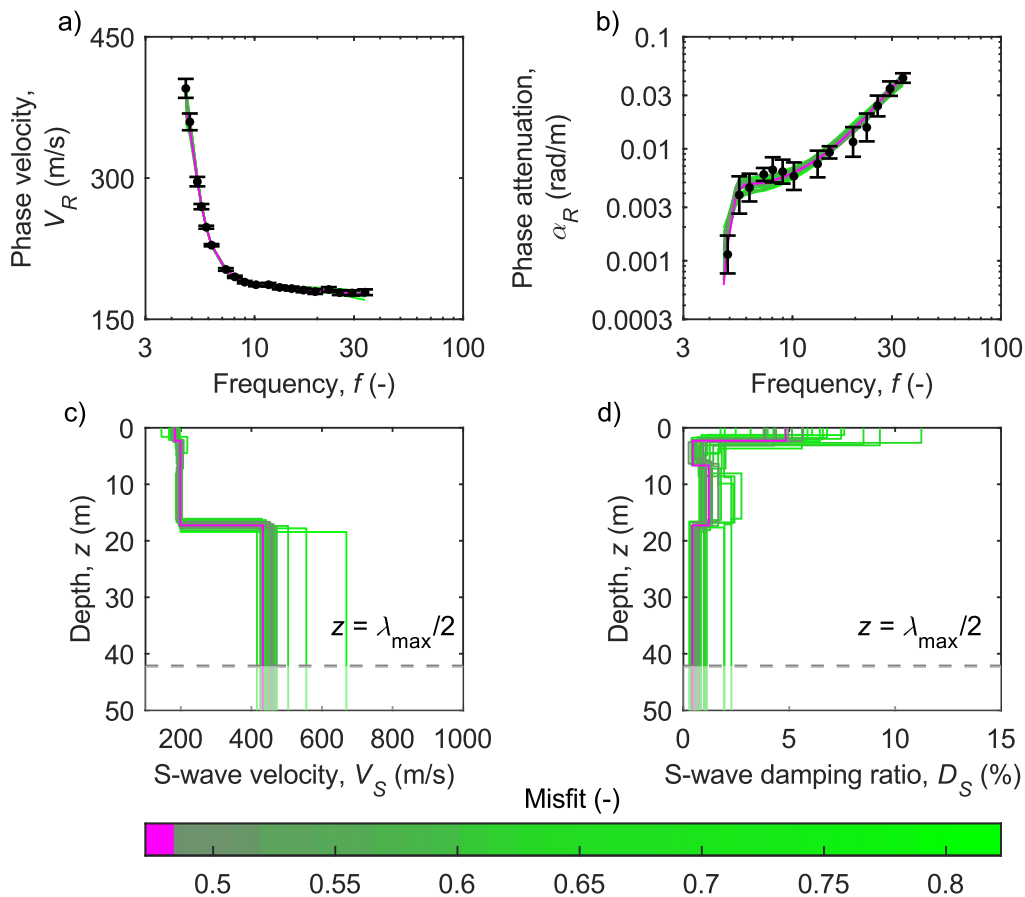


Figure 9-2. Best fitting ground models to GV-H5 experimental data: a-b) Theoretical vs. experimental data, for the phase velocity (a) and phase attenuation (b); c-d) Resulting S-wave velocity (c) and damping ratio (d) profiles. The boundary  $z = \lambda_{\max}/2$  is an

approximated value of the maximum investigable depth, that can be achieved from the available experimental data – layer interfaces beneath it are usually less reliable. Besides, derived profiles in c-d) are overlapped with velocity and damping ratio models obtained in past studies (see Figure 6.2).

## 9.2.2 Variability of the derived ground models

Figure 9-3 represents the standard deviation – in logarithmic scale – of the derived velocity and damping models (i.e.,  $\sigma_{\ln V}$  and  $\sigma_{\ln D}$ , respectively), computed as a function of depth from the 30 best-fitting models. The lognormal model is a common scheme to describe  $V_S$  statistics (e.g., Toro, 1995; Li and Assimaki, 2010; Passeri, 2019). This kind of distribution is often adopted also for modeling  $D_S$  (e.g., Schevenels, 2007). Note that this representation does not provide a rigorous picture of model uncertainties, as it describes the variability of the reference suite composed by the 30 best-fitting models, which is a subset of the collection of models that are compatible with experimental data. Furthermore, drawing inference from profiles of interval velocity and damping ratio might provide a biased description of variability, as the presence of layer interfaces introduces artificial variability which is not linked with the actual uncertainty in the layers' mechanical parameters. For this reason, an accurate statistical modeling of the stiffness structure should refer to profiles of travel-time or harmonic average of  $V_S$  (Passeri, 2019). However, an analogous parameter for damping data has not been identified yet. Therefore, this study refers to the  $\sigma_{\ln V}$  and  $\sigma_{\ln D}$  representation to provide an insight on uncertainties in the derived earth models.

As for  $V_S$ , the related standard deviation  $\sigma_{\ln V}$  is generally small, being less than 0.1 at almost all the investigated depths. Specifically, it ranges around 0.05 at shallow depths, as an effect of the low variability in the high-frequency phase velocity data. At about 20 m depth, it exhibits a sharp peak with  $\sigma_{\ln V} = 0.4$ . The increased  $\sigma_{\ln V}$  does not represent actual variability in  $V_S$ , as it is a consequence of uncertainties in the location of the layer interface in this depth range. Finally, it equals 0.1, showing a pattern typically observed at sites consisting of moderately soft soil overlying a significantly stiffer formation (Garofalo et al., 2016b).

As for  $D_S$ ,  $\sigma_{\ln D}$  mostly ranges around 0.5, which is almost one order of magnitude larger than  $\sigma_{\ln V}$ . This discrepancy is consistent with the different degree of variability affecting experimental phase velocity and attenuation data. However,  $\sigma_{\ln D}$  exhibits a peak in the shallow portion, in correspondence of the first identified layer interface (i.e.,  $z = 1 \div 3$  m). Indeed,  $\sigma_{\ln D}$  is computed from damping ratios of layers with rather different  $D_S$  values, as this quantity undergoes

an abrupt change at this location (Figure 9-2d). Therefore, this trend shares some similarities to the sharp changes in  $\sigma_{\ln V}$  at greater depths.

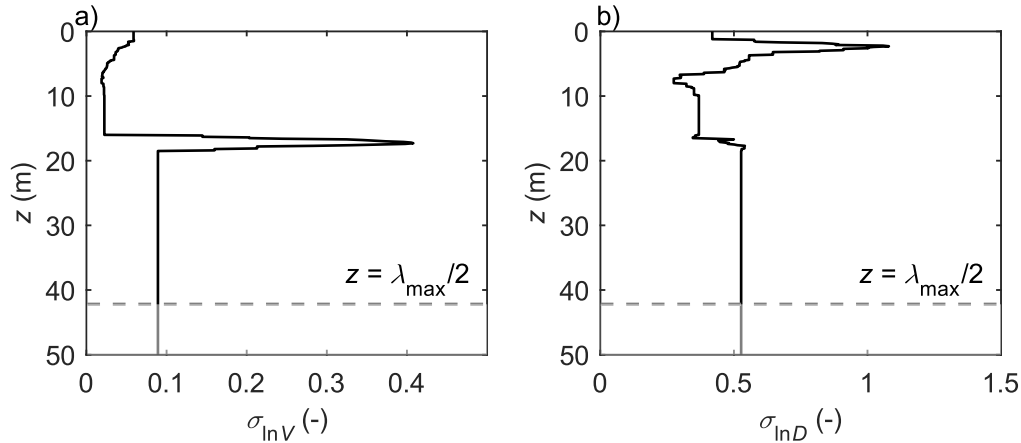


Figure 9-3. Variability of the best fitting ground models to GV-H5 experimental data: a) S-wave velocity profiles; b) Damping ratio profiles; c) Linear correlation coefficient between velocity and damping ratio profiles. The boundary  $z = \lambda_{\max}/2$  is an approximated value of the maximum investigable depth, that can be achieved from the available experimental data – layer interfaces beneath it are usually less reliable.

### 9.2.3 Comparison with alternative models

A first insight on the reliability of the estimated ground models can be obtained by comparing the resulting  $V_S$  and  $D_S$  profiles with those estimated in independent surveys or assumed in previous studies. However, a careful interpretation should account that alternative estimates do not usually represent a rigorous benchmark for assessing the reliability of the inferred model. Indeed, differences may arise due to specific processing schemes or spatial variability, linked with different testing locations and different investigation scale. Most of all, many available  $D_S$  profiles are exclusively or partially based on laboratory data, hence the comparison should be carried out with care. Indeed, the purpose of this section is just the assessment of the general compatibility between inversion results and existing information about the soil deposit at the GVDA.

Figure 9-4 overlaps the estimated earth models with results of previous studies, already discussed in Chapter 6 (Figure 6.2). Figure 9-4b includes a laboratory-based  $D_S$  estimate, which has been obtained through the Darendeli (2001) empirical model. Besides, it shows the  $D_S$  models proposed by Bonilla et al. (2002) and Tao and Rathje (2019), that were estimated according to the amplification approach and from the high-frequency spectral decay  $\kappa$  (see Chapter 4), respectively.



In general, the resulting  $V_S$  profiles well match other studies in the near-surface layers, with a good consistency both in terms of stiffness values and of the depth of the impedance variation. However, some divergence occurs for the  $V_S$  values below 20 m, that should be representative of the weathered rock unit. Indeed, this study returned  $V_S = 450 \div 500$  m/s, whereas past studies provided larger  $V_S$  values, spanning between 450 m/s and 600 m/s. This discrepancy may be justified as an effect of lateral variability at the GVDA site, which results in significant variations of  $V_S$  at intermediate depths, as also highlighted by the large variations in results from past studies (Teague et al., 2018b).

As for  $D_S$ , the estimated damping model is almost coincident with the laboratory-based profile. However, it should be remarked that the latter is not specific for this site, as it derives from an empirical model which provides an average damping ratio for typical fine-grained soil deposits. Therefore, no strong conclusions can be drawn from this comparison. On the other hand, the consistency between these two alternative schemes suggests that the MASW-based  $D_S$  estimate shares the same order of magnitude of the intrinsic damping ratio, hence the influence of scattering is not strongly significant – at least, in the depth range investigated in this survey. Actually, the laboratory-based  $D_S$  is significantly different in the shallow layer. This discrepancy may be an effect of local heterogeneities, that induce significant scattering of high-frequency Rayleigh waves. Indeed, as they propagate with moderately small wavelengths, they are rather sensitive to local fluctuations in the soil deposit characteristics. These considerations also explain why inverted  $D_S$  models are significantly lower than the values proposed by Bonilla et al. (2002), except in the shallow layer. Indeed, these results derive from the interpretation of down-hole array data recorded at the GVDA from both shallow and deep sensors, according to the amplification approach (see Chapter 4). Such values are moderately large, especially compared with laboratory-based estimates, because the estimation procedures inherently incorporate additional dissipation mechanisms than material damping, such as wave scattering and reflection/refraction phenomena at the layer interfaces. Indeed, it is expected that these phenomena are quite relevant at the GVDA site, as spatially variable mechanical properties and the consequent anisotropy in the velocity structure are significant especially at intermediate-to-large depths layers (Coutant, 1996; Bonilla et al., 2002). In a similar way, the  $\kappa$ -based  $D_S$  estimate proposed by Tao and Rathje (2019) is larger than the estimated earth model because it has been inferred from changes in  $\kappa$  over a depth of 150 m, that is range much broader than the one investigated in this survey. Therefore, this estimate relies on large scale variations, which includes additional scattering

phenomena and different impedance variations than those involved in the field test, thus resulting in increased attenuation.

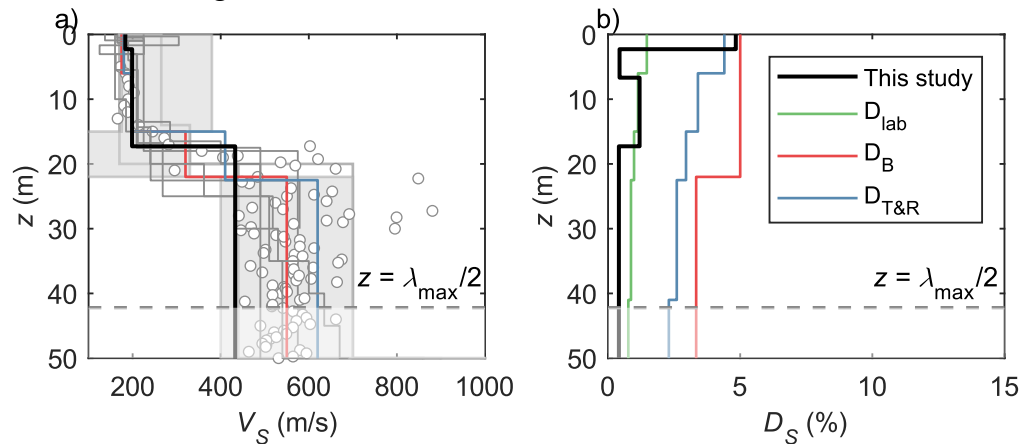


Figure 9-4. Comparison between the best fitting ground model to GV-H5 experimental data and velocity and damping ratio models obtained in past studies (see Figure 6.2 for further details): a) S-wave velocity profiles; b) S-wave damping ratio profiles. Results from past studies are represented in grey, with the exception of the models labeled as  $D_{lab}$ , computed according to Darendeli (2001);  $D_B$ , proposed by Bonilla et al. (2002); and  $D_{T\&R}$ , proposed by Tao and Rathje (2019).

## 9.2.4 Modeling of the ground response

Finally, implications of the inverted soil models into the site response were addressed, by comparing the estimated stratigraphic amplification with the one observed at GVDA. In this study, the amplification is described as acceleration transfer function (TF), i.e. the ratio of the Fourier amplitude spectra between acceleration time histories at different depths. Specifically, empirical TFs between the sensor GL-0 (i.e., the surface sensor) and GL-6, GL-15, and GL-22 (see Chapter 6, Figure 6.1b), located at 6 m, 15 m, and 22 m depth, were considered. Data from deeper sensors were not included, as they fall beyond the maximum investigable depth that have been achieved with surface-wave data in this study, hence the corresponding  $V_S$  and  $D_S$  would be unreliable. Empirical TFs (ETFs) were taken from Vantassel and Cox (2019). The corresponding theoretical TFs (TTFs) were computed through linear viscoelastic ground response analyses, assuming “within” conditions at each reference depth, for compatibility with empirical data (e.g., Teague et al., 2018b). Numerical simulations were carried out through the software DEEPSOIL v7.0 (Hashash et al., 2017).

Figure 9-5 compares the ETF with TTFs corresponding to the  $V_S$  and  $D_S$  profiles reported in Figure 9-2. Theoretical values are synthetically represented as

intervals defined by the median TTF and one log-standard deviation, computed frequency by frequency. Interestingly, the variability in the TTFs is almost negligible, notwithstanding the strong scatter in the estimated  $D_S$  profiles, especially in the weathered rock. This result is compatible with past findings on the influence of  $V_S$  uncertainties on GRAs, that demonstrated that variability in TFs is small even with highly scattered profiles (e.g., Foti et al., 2009). Therefore, it can be expected that a rigorous modeling of uncertainties in  $D_S$  should not refer to interval values, but to alternative quantities that exhibit a stronger link with the stratigraphic amplification, in a similar way to using S-wave travel times to model stiffness variations with depth (e.g., Socco et al., 2015; Passeri et al., 2020). For comparison purposes, TFs obtained from the  $V_S$  model proposed by Teague et al. (2018b) are included. In this case, as  $D_S$  was unknown, it was estimated according to the empirical model by Darendeli (2001). These TFs can be representative of the result of a typical survey, where the focus is the stiffness profile and  $D_S$  is obtained through laboratory testing – or laboratory-based relationships.

Data compare consistently when considering both the shallower sensor (Figure 9-5a) and the deep one (Figure 9-5c). In this case, the degree of matching is excellent in terms of locations of the fundamental peak and of higher-order peaks. As for the amplitude, the predicted model matches the troughs of the ETF, whereas it overestimates it in correspondence of the peaks, with a stronger difference in correspondence of the fundamental one. The overestimation at the peaks can be the result of limitations in 1D modeling of site conditions, as the presence of lateral variability and anisotropy effects at the GVDA may induce additional energy losses than just material dissipation. The divergence at higher order peaks derives from the sensitivity in the variable shallow layers (Foti et al., 2009; Comina et al., 2011; Griffiths et al., 2016a; Teague and Cox, 2016; Teague et al., 2018a; Passeri, 2019). On the contrary, the fitting quality for the fundamental mode is poor when the 15 m-depth sensor is adopted, whereas TFs are more similar to each other at high frequencies (Figure 9-5b). However, this situation was also observed in Vantassel and Cox (2019) and it was attributed to inaccuracies in the low-frequency data recorded in this sensor. Furthermore, the performance of predicted TFs from inverted  $V_S$  and  $D_S$  profiles and the one of those adopted in Teague et al. (2018b) are strongly similar with each other, with the latter predicting slightly smaller amplification close to the peaks of the ETF. These differences may rise from the different amount of profiles involved in the estimation of the theoretical TF and the different extent of the investigated portion of the site, as Teague et al. (2018b) clusters various arrays distributed throughout the site, thus involving different conditions. In this case, the averaging of different

profiles (due to spatial variability) tends to decrease the TF (Tao and Rathje, 2019). Under these considerations, the generally good fitting level and the compatibility with alternative observations confirm the reliability of the estimated  $V_S$  and  $D_S$  profiles.

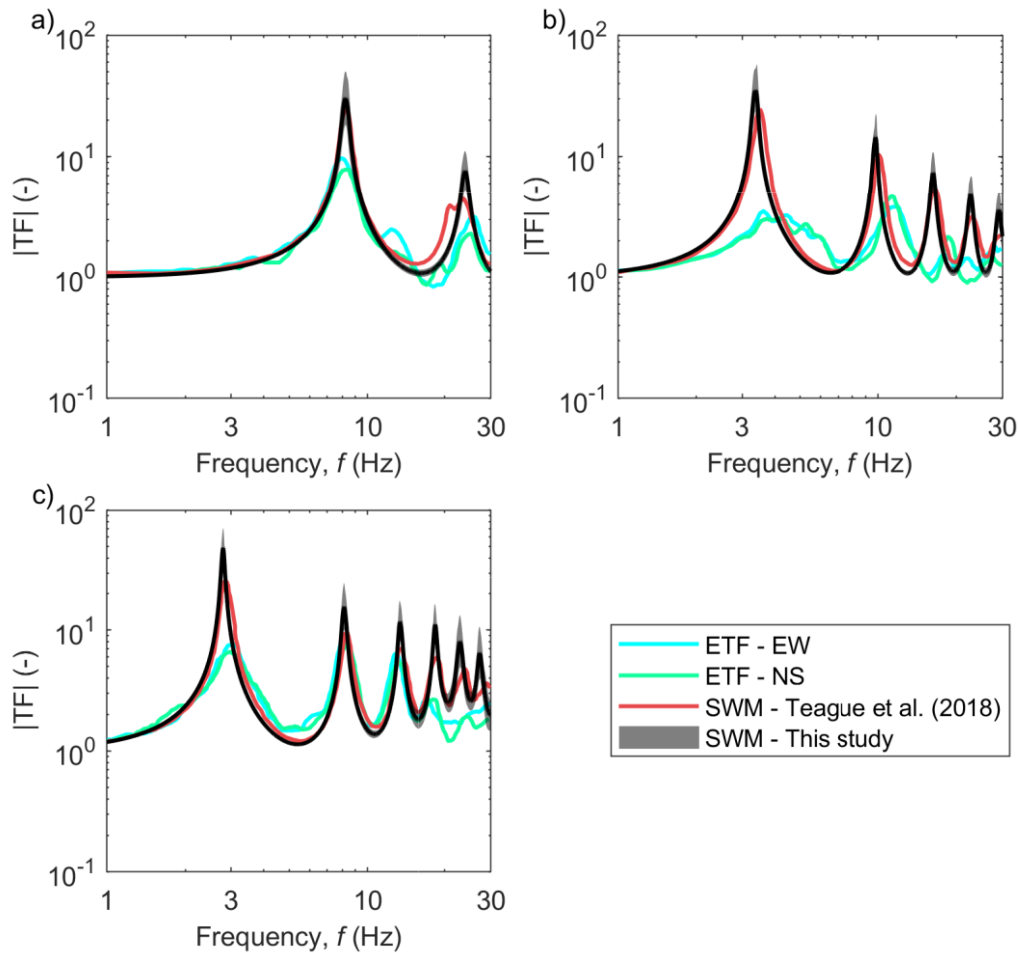


Figure 9-5. Comparison between experimental transfer function (ETF, extracted from Vantassel and Cox, 2019) and median theoretical transfer function for the best fitting 30 models in the inversion (SWM), for the reference depths of 6 m (a), 15 m (b), and 22 m (c). Experimental data are labelled as North-South (NS) and East-West (EW), corresponding to the components of seismometer records from which they were derived. Theoretical TFs obtained from results of the SWM survey by Teague et al. (2018b) are included.



# Chapter 10

## Conclusions and Recommendations

This dissertation addressed the joint characterization of the shear-wave velocity and damping ratio from the interpretation of Multichannel Analysis of Surface Waves (MASW) measurements. Specifically, it focused on the issues and the uncertainties related to the derivation of the Rayleigh wave parameters (i.e., R-wave phase velocity and phase attenuation) from measured wavefield data and the derivation of S-wave velocity and damping ratio profiles from the inversion of experimental data.

Part of the research aimed at developing a reliable dataset, including synthetic waveforms and data measured in situ. Part of the synthetic data are plane and cylindrical waves, corrupted by body waves and incoherent noise. In this way, the influence of model incompatibility effects (e.g., near field effects) on the estimated phase velocity and attenuation data could be addressed. The synthetic dataset also includes more complex waveforms, characterized by multi-mode Rayleigh waves combined with body waves. They simulate results of MASW surveys carried out on idealized earth models, that are representative of typical soil deposits in engineering practice. Furthermore, part of the database collects results of experimental surveys at the Garner Valley Down-Hole Array and the Hornsby Bend sites, in the United States. The result is a high-quality surface wave dataset that can represent an effective benchmark for investigating uncertainties affecting the estimate of the R-wave parameters, with a focus on the derivation of the phase attenuation. Furthermore, the instrumented borehole installed at the Garner Valley Down-Hole Array provides observations on the ground motion amplification, that can be used as a benchmark to assess the reliability of the derived soil models.

The main focus of this research was the derivation of the R-wave phase velocity and phase attenuation from experimental data. For this purpose, a novel family of techniques aimed at retrieving both the R-wave phase velocity and attenuation was introduced. This approach can handle multi-mode Rayleigh wavefields, and it allows an explicit modeling of the geometric shape of the wavefront. Furthermore, the research addressed epistemic uncertainties and aleatory variabilities affecting the estimated R-wave parameters. The investigation

of epistemic uncertainties focused on the quantification of the sensitivity of experimental data to model incompatibility effects (i.e., the influence of body waves) and to incoherent noise. Furthermore, it assesses the quality of experimental data as a function of different interpretation techniques and various source types, quantifying the performance in terms of the reliability and the accuracy of the estimated propagation parameters and the capability of covering an adequately large frequency range. Finally, the analysis of the influence of the acquisition device compares geophone versus fiber-optic data, to investigate the sensitivity of estimated parameters to the receiver type. This study also allows to understand the potential of the fiber-optic device in retrieving dissipation parameters. On the other side, the modeling of aleatory variability resulted in the introduction of a new statistical model, to describe the joint variations of phase velocity and phase attenuation data.

The final part of this dissertation dealt with the inversion procedure to map the experimental R-wave parameters into a suite of S-wave velocity and damping ratio profiles. A key result of this research is a novel algorithm for the joint inversion of dispersion and attenuation data to retrieve both stiffness and dissipation parameters, that relies on an improved Monte Carlo scheme. In this approach, the optimization is achieved by exploiting the scaling properties of the Rayleigh eigenvalue problem. The novel algorithm was applied to characterize the stiffness and dissipation structure for both the investigated sites. Furthermore, the reliability of results from the Garner Valley Downhole Array site was assessed, using in situ observations on the ground motion amplification as a benchmark.

The following section summarizes the main conclusions of the research. Still some aspects concerning the derivation of the Rayleigh wave parameters and the inversion procedure need to be investigated. Some recommendations are then given at the end of the section, including suggestions for future studies.

## **10.1 Conclusions**

The main result emerging from numerical simulations and experimental data is the different degree of reliability and accuracy affecting estimated R-wave phase velocity and phase attenuation. Indeed, the resulting attenuation is strongly sensitive to the modeling of the geometry of the Rayleigh wavefront, to the influence of body waves and to the presence of incoherent noise. As a result, derived attenuation data exhibit large variability, which is one order of magnitude greater than the corresponding phase velocity variability. The larger scatter and the different sensitivity of phase velocity and phase attenuation data to stiffness and damping parameters result into highly variable S-wave damping ratio profiles,

whereas stiffness models are usually well constrained even at depth. However, the damping model exhibits a well-identified trend and the impact on uncertainties in the ground motion amplification is moderately small, in all the investigated sites.

The following conclusions summarize the main findings on the modeling issues and uncertainties in the derivation of the S-wave velocity and damping ratio profiles from MASW surveys.

#### *A novel technique for estimating phase velocity and phase attenuation*

The Frequency-Domain BeamFormer – attenuation (FDBFa) is a novel technique aimed at estimating the R-wave phase velocity and attenuation from measured waveform data. This technique relies on a transformation of the recorded wavefield, for which the phase attenuation can be derived by carrying out a dispersion analysis on transformed pseudo-wavefield. Specifically, this scheme is based on a twofold application of the FDBF procedure: the application on measured data returns the phase velocity, whereas the application on transformed data provides the phase attenuation. As the algorithm inherits the flexible structure of the FDBF approach, one key advantage of the FDBFa is the possibility of an explicit modeling of the actual geometry of the investigated wavefront. This feature is crucial when interpreting Rayleigh wave data, as they propagate according to a cylindrical wavefront. Their modeling is implemented in a modified version of the FDBFa, namely the Cylindrical Frequency-Domain BeamFormer – attenuation (CFDBFa).

The FDBFa assumes that the recorded wavefield consists of a single mode, hence it theoretically returns an estimate of the effective phase velocity and phase attenuation, that might not be coincident with modal values. Therefore, a new modal filtering scheme is proposed, with the aim to isolate the contribution of each Rayleigh propagation mode and fulfil the main assumption of the FDBFa. The extraction of each wave component is carried out by applying a bandpass filter to the recorded wavefield, that preserves the mode of interest and removes additional waves. A calibration study addressed the influence of filter parameters on the estimated wave parameters. It is demonstrated that filters with order  $N = 1/2 \div 2/3$  times the number of receivers, passband extended up to  $k_{res}$  (i.e., the resolution wavenumber of the array) and stopband starting from  $2k_{res}$  may be considered as a valid reference for applying the FDBFa in various site conditions. However, the use of the modal filtering technique is recommended when data from at least 20–24 receivers are available, otherwise the filter might not effectively isolate the desired wave component. On the other side, common



acquisition setups in MASW surveys adopts 24, 48, or even more sensors, hence the modal filtering technique is suitable in many applications.

### *Influence of near- and far-field effects*

Results of the parametric study to address the role of near- and far-field effects demonstrated the limited influence on the estimated phase velocity on modeling issues. Instead, phase attenuation is more sensitive on these factors, hence a rigorous modeling of these phenomena is crucial to achieve reliable estimates.

The inclusion of body waves and incoherent noise in the recorded wavefield implies a drop in the quality of estimates. Specifically, these two elements are detrimental to both the reliability (i.e., the capacity of returning estimates close to the true value) and the accuracy (i.e., the capacity of returning lowly variable estimates). As for the phase velocity, the presence of body waves induces a slight underestimation when the average offset is small, compared with the investigated wavelength. Instead, the addition of incoherent noise mainly results in a slight loss in the accuracy. Focusing on the phase attenuation, the inclusion of body waves determines an overestimation of the true value, even at moderately long distances. Furthermore, the incoherent noise exerts a twofold negative effect on the quality of the estimated phase attenuation at great distances, with a loss of both reliability and accuracy. On the one side, the variability in the estimate is significantly large, and it is one order of magnitude greater than the one affecting dispersion data. On the other side, the average value gradually shifts towards lower attenuations, for increasing average offset. The drop in the quality is a consequence of the strong influence of incoherent noise on amplitude data.

Due to the combined effect of near-field and far-field phenomena, reliable and moderately accurate estimates of attenuation data can be retrieved only at a limited range of distances from the sources, where both these detrimental effects are minimized. In the specific case under investigation, the optimal offset range corresponds to  $NACD = 2 \div 4$ , where NACD is the distance between the active source and the array center, normalized by the investigated wavelength.

Finally, the planar and the cylindrical beamformer have a rather similar performance, although the CFDBFa tends to return slightly more reliable phase velocity estimates at short offsets. Indeed, by the virtue of the explicit modeling of the cylindrical shape of the Rayleigh wavefront, it mitigates the influence of near-field effects (Zywicki, 1999; Zywicki and Rix, 2005). On the other side, the relative performance towards far-field effects is similar. For this reason, the CFDBFa algorithm is the preferred choice in processing surface wave data.

### *Influence of the processing scheme*

A source of epistemic uncertainty is linked with the specific processing scheme adopted to interpret wavefield data. Indeed, each approach relies on specific modeling assumptions of the wavefield and different computation algorithms, with variable degree of sensitivity to incoherent noise and capacity of identifying different wave components (i.e., Rayleigh propagation modes). The inter-method comparison referred to both synthetic waveforms and measured data obtained from in situ surveys, addressing the performance of each processing technique in terms of the reliability and accuracy of the estimated wave parameters, as well as the capability of extracting such information over a broad frequency range.

In general, results demonstrated a similar performance of different processing techniques. The considered algorithms return reliable estimates of R-wave parameters, when the wavefield is dominated by a single mode. For a multimode wavefield, the characterization of the dominant mode is immediate, as the corresponding wave parameters can be tracked with low variability over a broad frequency range. Instead, the analysis related to low-energy modes is more challenging. In this case, the phase velocity can still be well-identified, whereas the resulting attenuation estimate is highly variable and sensitive to the specific processing technique, because of the different capability in extracting and isolating information about the target mode. Therefore, the analysis of wavefield data in the presence of inversely dispersive media or soil deposits with abrupt changes in the impedance requires special care, as the resulting wavefield is strongly multimodal.

In this study, the CFDBFa exhibits remarkably good performance. On the one side, the modal filtering procedure successfully isolates the investigate mode, even for low-energy ones in some cases. Furthermore, it manages to retrieve R-wave parameters almost continuously over a rather broad frequency range. Also, it appears that the filtering procedure allows to identify reliable velocity values even beyond the resolution limits of the acquisition array.

### *Influence of source characteristics*

The analysis of the source influence investigated the quality of the estimated R-wave parameters as a function of the type of active source. For this purpose, the study focused on wavefield data generated by a sledgehammer source and by a mechanically-controlled vibrating source, which applied a chirp and a stepped sine signal.

In general, using alternative source types does not affect the average trend of the estimated dispersion and attenuation data. However, high-energy controlled sources allow to extract R-wave parameters across a broader range of frequencies. Most of all, the estimated data exhibit smaller variability. Indeed, seismic traces generated by the sledgehammer usually have smaller signal-to-noise ratio. Therefore, the estimated phase attenuation is affected by larger variability, due to the greater relevance of incoherent noise. However, the mean trend in the attenuation curve can still be captured. This result positively contributes to the capability of the sledgehammer for the attenuation estimate. As it represents the most accessible and affordable source, this demonstrates the possibility of retrieving reliable attenuation data also in ordinary MASW surveys.

#### *Influence of receiver characteristics*

The sensitivity of the estimated R-wave parameters to the specific acquisition device was assessed, by comparing estimated phase velocity and phase attenuation data obtained from geophone and fiber-optic Distributed Acoustic Sensing (DAS) data at the Hornsby Bend site. In this way, the capability of this new system in retrieving attenuation data was also addressed.

In order to process DAS data, the CFDBFa algorithm was adapted to account for the peculiar geometric attenuation that the recorded average strain by the fiber-optic assumes. Indeed, ignoring the geometric attenuation affecting this kind of data would result in a slight overestimation of the phase attenuation, whereas the phase velocity appears not to be sensitive on this. This result also demonstrates the flexibility of the newly proposed method to handle with different wavefield conditions.

The comparison demonstrated that, on average, the resulting phase velocity and phase attenuation data are compatible with each other. However, DAS data exhibit lower variability. This improvement is perhaps the effect of the remarkably larger number of measurement points that the DAS system includes, that provides a more exhaustive dataset of wavefield values to better constrain the velocity and the attenuation estimates. This advantage balances the lower signal-to-noise ratio in the recorded data. Therefore, the DAS technology can be successfully used to jointly estimate the phase dispersion and attenuation data, obtaining the same level of reliability of geophone arrays and improved accuracy.

#### *A statistical model for aleatory variability in phase velocity and attenuation*

The modeling of aleatory variability requires the definition of a statistical model to describe the distribution nature of experimental data.

The development of the model accounted the shared dataset underlying the estimated phase velocity and the phase attenuation, for which a multidimensional distribution is needed. The statistical analysis on a vast dataset of experimental data collected at the Hornsby Bend site demonstrated that both the bivariate normal and the bivariate lognormal distribution can reasonably describe their variability. However, the latter is the preferred choice, especially when modeling low-frequency data. Indeed, it allows to model highly variable data (as the phase attenuation) without including negative values, thus ensuring greater consistency from the physical viewpoint. Furthermore, the observed degree of correlation is negligible, hence the statistical characterization can simply focus on lognormal marginals.

#### *Derivation of the S-wave velocity and damping ratio profiles*

A novel algorithm for the joint inversion of dispersion and attenuation data was proposed. The approach relies on a global search, Monte Carlo scheme, which implements a smart sampling procedure. This scheme exploits the scaling properties of the solution of the Rayleigh eigenvalue problem in linear viscoelastic media to modify the trial earth models. These properties are introduced in this study and their use helps improve the matching with experimental model. Thanks to this strategy, the number of random samples required to generate an adequate suite of trial models is smaller, and the computation time needed to run forward simulations is significantly reduced. This advantage becomes crucial when running viscoelastic inversions, as forward simulations need much longer computation time than in elastic conditions.

The performance of the proposed inversion procedure was excellent with experimental data, both in the case when they include fundamental-mode data only or in the joint inversion of multimode experimental datasets. The improved sampling scheme resulted in well-constrained S-wave velocity and damping ratio profiles, especially in the near-surface layers. However, the estimated ground models are affected by greater variability at depth, especially in terms of the S-wave damping ratio. The scatter is the combined effect of the high variability in low-frequency experimental data, the different sensitivity of phase velocity and attenuation data to stiffness and damping ratio, and the moderately low sensitivity of theoretical attenuation curves to the damping ratio at great depths.

Finally, the reliability of the derived ground models was addressed, by assessing the compatibility of the corresponding response with observed ground

motion data. The comparison was carried out for the Garner Valley Downhole Array site. On the one side, the uncertainties in the predicted ground motion amplification are small, even when the variability in the estimated damping ratio is large. This discrepancy may be linked with a pitfall in the description of the attenuation structure of the soil deposit. Indeed, some authors claimed that using S-wave travel time rather than interval velocities should be preferred to model stiffness variations with depth (e.g., Socco et al., 2015; Passeri et al., 2020). Similarly, it can be expected that a rigorous modeling of uncertainties in  $D_S$  should not refer to interval values, but to alternative quantities that exhibit a stronger link with the stratigraphic amplification. On the other side, the degree of matching between predicted and observed data is remarkably good, with an excellent fit of locations of resonance peaks, whereas the amplitude is overestimated. This discrepancy can be the result of limitations in 1D modeling of site conditions. However, the generally good fitting level and the compatibility with alternative observations confirm the reliability of the estimated  $V_S$  and  $D_S$  profiles. This result stresses the effectiveness of using damping ratio estimates from in situ surface wave data, as an alternative to other characterization techniques.

## 10.2 Recommendations for future research

One of the main contributions of this research was the implementation of a novel algorithm for retrieving Rayleigh wave phase velocity and phase attenuation from experimental surface wave data. This scheme is robust, flexible towards different geometric attenuation mechanisms, and it provides reliable and low-variable values of the R-wave parameters over a broad range of frequencies. Furthermore, the inclusion of a modal filtering schemes allows to successfully isolate the contribution of different propagation modes from the recorded wavefield, in various scenarios. Nevertheless, the modal filtering procedure incorporates two main limitations: 1) it can be successfully applied only in the presence of a moderately vast dataset of surface wave records, with at least 20 sensors; 2) the filtering procedure cannot be applied in the presence of unevenly spaced acquisition arrays. These limitations can be mitigated by implementing more advanced procedures, that deal with irregularly sampled data (e.g., Tarczynski et al., 1997; Bidégaray-Fesquet and Fesquet, 2009). This improvement shall be addressed in future studies, to generalize the modal filtering technique and, potentially, improve its performance.

Furthermore, another fundamental result is the different sensitivity of the estimated R-wave phase velocity and phase attenuation to near- and to far-field

effects, both in terms of reliability and accuracy. Indeed, it justifies the different trends in variability observed for these parameters in this dissertation as well as in past studies. However, this result derives from a parametric study on a rather simplified model, which may be representative of a single Rayleigh wave propagating in a homogeneous medium. Therefore, further simulations are necessary to address the role of incoherent noise and near-field effects in more realistic conditions. For this purpose, the analysis approach can be extended to synthetic waveforms that simulate MASW surveys in realistic earth models. In this way, multi-mode Rayleigh waves are included, and more complex variations of body and surface wave amplitude can be addressed. Furthermore, alternative noise levels (i.e., alternative source types) can be considered. Finally, findings shall be validated with in situ data from experimental surveys. The outcome of this study might result in the proposal of a novel processing scheme deemed to mitigate near- and far-field effects simultaneously, based on the interpretation of frequency-dependent, moving windows of the array. Specifically, this scheme might infer high-frequency R-wave parameters focusing on the near-offset portion of the array, thus involving records with high signal-to-noise ratio. Instead, low-frequency values should be obtained by discarding the sensors closest to the source, thus mitigating the influence of near-field effects. However, the definition of the optimal offset range as a function of the frequency and of site conditions has to be addressed in future studies.

The proposed inversion procedure successfully retrieved earth models well matching experimental data, although some improvement is possible. On the one side, the investigation of the parameter space can be enhanced by including a free-layering scheme method (e.g., Cox and Teague, 2016; Passeri, 2019). Furthermore, being a global search method, it requires the implementation of rigorous selection criteria to define a reliable suite of representative earth models. In this way, both the uncertainties in the experimental data and the non-uniqueness of the solution of the inversion problem are accounted for. For this reason, further studies will address this issue, by generalizing available criteria developed in the dispersion analysis (e.g., Socco and Boiero, 2008; Hallo et al., 2021; Vantassel and Cox, 2021a) or introducing new schemes, that account for the multivariate nature of the joint inversion of velocity and attenuation data (Anderson, 1962). Furthermore, the modeling can include an explicit frequency-dependence of the mechanical parameters, which might improve the estimate and the fit with observed data (e.g., Kausel and Assimaki, 2002; Armstrong et al., 2020). Finally, a more accurate and statistically robust description of uncertainties in the estimated stiffness and dissipation structure should be addressed. Indeed,

although effective statistical models are available to describe variability in the S-wave velocity (Passeri, 2019; Hallal et al., 2022), a scheme for the joint statistics of the stiffness and damping data would allow to properly understand actual uncertainties in the estimated earth models and to map variability in the experimental R-wave parameters into the variability of the inverted data.

A potential feature for future research is the compatibility between the MASW-based damping ratio and in situ measurements from alternative geophysical methods, such as invasive tests. Furthermore, the comparison with measured ground motion amplification data should be extended to different site conditions with respect to those investigated in this study. Besides, it should involve other parameters, such as the high-frequency spectral attenuation  $\kappa$  (e.g., Ktenidou et al., 2015). This comparison allows to get further insight on the reliability of the estimated mechanical parameters and to better understand other mechanisms that induce wave attenuation, especially those linked with wave scattering.

Finally, one aspect needing further investigation is the reconstruction of the attenuation structure of soil deposits at greater depths. Indeed, the high variability of experimental data and the limited investigated wavelength range do not allow an effective constraint on  $D_S$  in the deeper portions of the earth models. A potential strategy to tackle this issue relies on passive surveys, that provide useful information in the low-frequency range. Therefore, the possibility of extracting attenuation from ambient noise data can be addressed, to better constrain estimated damping ratios at greater depths.

# Appendix A

## Frequency-domain beamforming attenuation: some technical aspects

This Appendix deals with some technical details related to the Frequency-Domain BeamForming-Attenuation (FDBFa) scheme, introduced in Chapter 5. The first section focuses on a side effect of the wavefield transformation which is the basis of the FDBFa, that results in sidelobes in the estimated pseudo-spectrum. The remaining sections address some aspects linked with the modal filtering procedure. Firstly, some basic concepts of digital filtering are addressed, with a focus on complex filters. Then, the symmetry of complex filters is discussed, as it represents a key property for the proposed filtering technique. The last section contains results of the calibration procedure to identify the optimal parameters for the proposed modal filter, with reference to the synthetic wavefields SW3 and SW4 (see Section 5.1).

### A.1 Side lobes in FDBFa pseudospectrum

When dealing with a plane wave  $u(r)$ , the application of the transformation (5.9) returns a wave  $v(r)$ , the amplitude of which theoretically exhibits a sawtooth shape, whereas the corresponding phase linearly varies with the offset. This peculiar behavior produces sidelobes inside the pseudo-spectrum used to derive the wave attenuation, computed according to (5.11).

To demonstrate this, let us assume that both  $u(r)$  and  $v(r)$  are assumed to be infinitely extended, continuous signals, for simplicity. In this way, windowing and sampling effects are discarded. Therefore, the transformed wave  $v(r)$  can be expressed as the product of two signals, one carrying the amplitude information and one linked to the phase:

$$v(r) = x(r)y(r) \tag{A.1}$$

The signal  $x(r)$  is a periodic, sawtooth-shaped signal. The period length  $L$  is equal to  $2\pi/k$  and the truncated version of the signal on a single period of oscillation of the signal varies as  $x_L(r) = e^{kr}$ . Instead,  $y(r)$  is described by a



complex exponential function, as  $e^{-\alpha r}$ . This statement derives from the observations done on  $v(r)$  and represented in (5.10).

Under such assumptions, the resulting pseudospectrum  $P_{BFa}(\alpha_t)$  exhibits a main peak located at  $\alpha_t = \alpha$  located, combined with side lobes located at  $\alpha_t = \alpha + nk$ , being  $n$  an integer value. Indeed, the pseudospectrum  $P_{BFa}(\alpha_t)$  can be interpreted as an approximation of the squared amplitude of Fourier transform of  $v(r)$ , labeled as  $V(\alpha_t)$ :

$$P_{BFa}(\alpha_t) = |V(\alpha_t)|^2 = V^H(\alpha_t)V(\alpha_t) \quad (\text{A.2})$$

By exploiting the properties of the Fourier transform,  $V(\alpha_t)$  is the convolution of the spectra of the two factors  $x(r)$  and  $y(r)$ :

$$V(\alpha_t) = X(\alpha_t) \otimes Y(\alpha_t) \quad (\text{A.3})$$

The amplitude component  $X(\alpha_t)$  is the Fourier transform of periodic signal  $x(r)$ , and the only information from a single period is sufficient:

$$X(\alpha_t) = \frac{1}{2\pi} \sum_{n=-\infty}^{+\infty} \mu_n \delta\left(\alpha_t - \frac{2\pi n}{L}\right), \quad \mu_n = \frac{1}{L} \int_{-\frac{L}{2}}^{\frac{L}{2}} x_L(r) e^{-i\frac{2\pi}{L}nr} dr \quad (\text{A.4})$$

where  $\delta$  labels the Dirac's  $\delta$ -function. In this way, the spectral component  $X(\alpha_t)$  can be derived:

$$\begin{aligned} \mu_n &= \frac{1}{L} \int_{-\frac{L}{2}}^{\frac{L}{2}} x_L(r) e^{-i\frac{2\pi}{L}nr} dr = \frac{k}{2\pi} \int_0^{\frac{2\pi}{k}} e^{kr} e^{-iknr} dr = \frac{1}{2\pi(1-in)} (e^{2\pi} - 1) \\ \Rightarrow X(\alpha_t) &= \frac{1}{2\pi} \sum_{n=-\infty}^{+\infty} \mu_n \delta\left(\alpha_t - \frac{2\pi n}{L}\right) = \frac{1}{4\pi^2} \sum_{n=-\infty}^{+\infty} \frac{1}{1-in} (e^{2\pi} - 1) \delta(\alpha_t - nk) \end{aligned} \quad (\text{A.5})$$

As for  $Y(\alpha_t)$ , being  $y(r)$  a complex exponential, the Fourier transform is a Dirac's  $\delta$ -function:

$$Y(\alpha_t) = \delta(\alpha_t - \alpha) \quad (\text{A.6})$$

The spectrum  $V(\alpha_t)$  is the convolution of two signals involving Dirac's  $\delta$ -functions, thanks to which the resulting spectrum is still a Dirac's  $\delta$ -function:

$$\begin{aligned} V(\alpha_t) &= X(\alpha_t) \otimes Y(\alpha_t) = \int_{-\infty}^{+\infty} X(h)Y(\alpha_t - h)dh = \\ &= \int_{-\infty}^{+\infty} \left[ \frac{1}{4\pi^2} \sum_{n=-\infty}^{+\infty} \frac{1}{2\pi(1-in)} (e^{2\pi} - 1) \delta(h - nk) \right] \delta(\alpha_t - h - \alpha) dh = \\ &= \frac{1}{4\pi^2} \sum_{n=-\infty}^{+\infty} \frac{1}{2\pi(1-in)} (e^{2\pi} - 1) \delta(\alpha_t - nk - \alpha) \end{aligned} \quad (\text{A.7})$$

Thus, the DTFT is a sequence of Dirac's functions, each centered at  $\alpha+nk$ . The peak obtained at  $n = 0$  returns the desired attenuation value  $\alpha$ , and this corresponds to the main peak, as the multiplying factor is maximized at  $n = 0$ . Instead, side peaks are located at a relative distance from the main peak given by

integer multiples of  $k$ . Besides, for  $k \rightarrow 0$ , the period of  $x(r)$  dramatically lengthens, and discontinuities disappear. Under such conditions, the side peaks of  $V(\alpha_i)$  tend to collapse towards  $\alpha$ , hence only the main lobe appears. Such considerations are valid also for  $P_{CBFa}(\alpha_i)$ .

## A.2 Basic concepts of digital filtering

The aim of this section is to provide some key concepts of digital filtering, that will be helpful for a proper understanding of the proposed filtering technique developed in this study. The main references of this sections are the manual by Mitra (2006) and the study by Bruekers (2009).

Digital signal processing often requires some manipulation of discrete-time signals, to modify amplitude characteristics or the frequency content. This task is carried out by specific devices that are mathematically described as discrete-time systems, i.e. an operator  $T$  processing an input sequence  $x[n]$  to generate an output signal  $y[n]$ , where  $n$  denotes the discrete sample index (Figure A-1):

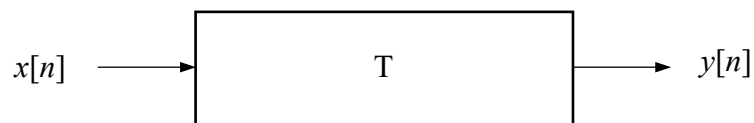
$$y[n] = T(x[n]) \quad (\text{A.8})$$


Figure A-1. Schematic representation of a discrete-time system (modified from Mitra, 2006).

The most popular category of discrete-time systems are digital filters. A digital filter is a linear, time-invariant system. The linearity attribute specifies that the system fulfils the superposition principle, whereas the time-invariance entails that the behavior of the system does not change with time. Furthermore, causal digital filters are usually considered, where the output at a time instant does not depend on future input states. In this case, the time response can be described by means of a finite difference equation, with constant coefficients  $a_m$  and  $b_m$ :

$$y[n] = -\sum_{m=1}^M a_m y[n-m] + \sum_{m=0}^N b_m x[n-m] \quad (\text{A.9})$$

However, an effective characterization of digital filters relies on a transformed representation, in terms of transfer function  $H(e^{i\omega})$ . The transfer function is the ratio between the Discrete-Time Fourier Transforms (DTFTs) of the output and the input sequences, which is a function of  $a_m$  and  $b_m$  for digital filters described as finite different equations:

$$H(e^{i\omega}) = \frac{Y(e^{i\omega})}{X(e^{i\omega})} = \frac{\sum_{m=1}^M b_m e^{-i\omega m}}{1 + \sum_{m=1}^M a_m e^{-i\omega m}} \quad (\text{A.10})$$

Thanks to the time-invariance property, an exhaustive time-domain characterization of digital filters can be achieved by means of its impulse response  $h[n]$ , namely the filter output when a Dirac's  $\delta$ -sequence is applied as the input. Indeed, the response to a generic sequence can be obtained through linear convolution between the input and  $h[n]$ . Furthermore,  $H(e^{i\omega})$  is exactly the DTFT of  $h[n]$ .

Several classification schemes for digital filters are available, based on the time-domain response or on the features in the transformed domain.

The time-domain classification clusters digital filter into two families, namely Finite Impulse Response (FIR) and Infinite Impulse Response (IIR) filters, based on the input-output relationship in the time domain. In FIR filters, the output only depends on the input signal and  $h[n]$  is a finite-length sequence. Therefore, the time- and the frequency-domain response can be obtained from Eq. A.9-10 by setting  $a_m = 0$ :

$$y[n] = \sum_{m=0}^N b_m x[n-m] \quad (\text{A.11})$$

$$H(e^{i\omega}) = \sum_{m=1}^M b_m e^{-i\omega m} \quad (\text{A.12})$$

Instead, IIR filters return an output signal depending both on the input sequence and on previous output states, and the corresponding  $h[n]$  is a sequence defined over an infinite support. In this case, the finite difference equation and the transfer function coincide with those provided in Eq. A.9-10.

Furthermore, digital filters can be clustered as real filters or complex filters, in which  $h[n]$  is real- and complex-valued, respectively. This classification reflects in a remarkable difference in the frequency response of the filter (i.e.,  $H(e^{i\omega})$ ). Real digital filters exhibit a symmetric response in the frequency domain, as  $H(e^{i\omega})$  is an even function. Instead, for complex filters,  $H(e^{i\omega})$  is asymmetric (Figure A-2).

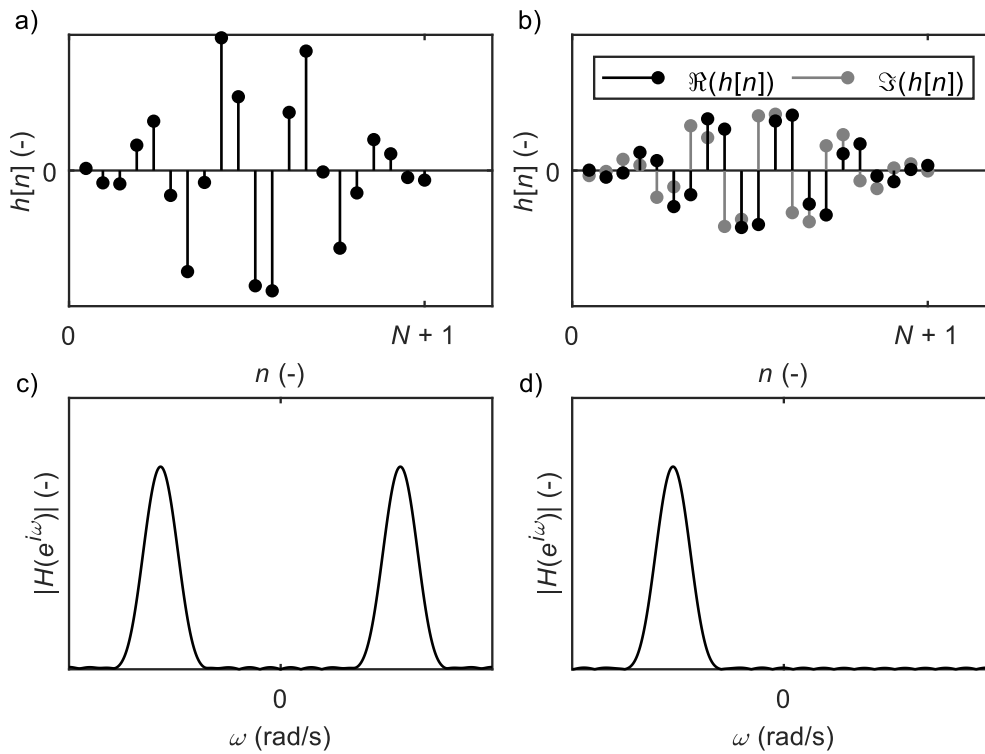


Figure A-2. Real vs. complex filter: a-b) Impulse response  $h[n]$  for a) a real filter and b) a complex filter; c-d) Transfer function  $H(e^{j\omega})$  for c) a real filter and d) a complex filter.

Alternative classification schemes of digital filters refer to the frequency response of the filter. On the one side, the magnitude  $|H(e^{j\omega})|$  vs. frequency curve controls variations in the frequency content between the input and the output sequence. Specifically, some regions in the frequency domain can be identified: the passband, which is the frequency range where  $|H(e^{j\omega})|$  is unitary; and the stopband, i.e., the frequency range where  $|H(e^{j\omega})|$  is zero. Digital filters are classified as a function of the location of the passband and the stopband. Lowpass filters exhibit a passband at low frequencies and a stopband elsewhere (Figure A-3a), whereas the converse applies for highpass filters (Figure A-3b). In bandpass filters, the passband is centered around a target frequency range, and a stopband is applied elsewhere (Figure A-3c). Instead, bandstop filters exhibit a specular frequency response with respect to bandpass ones (Figure A-3d).

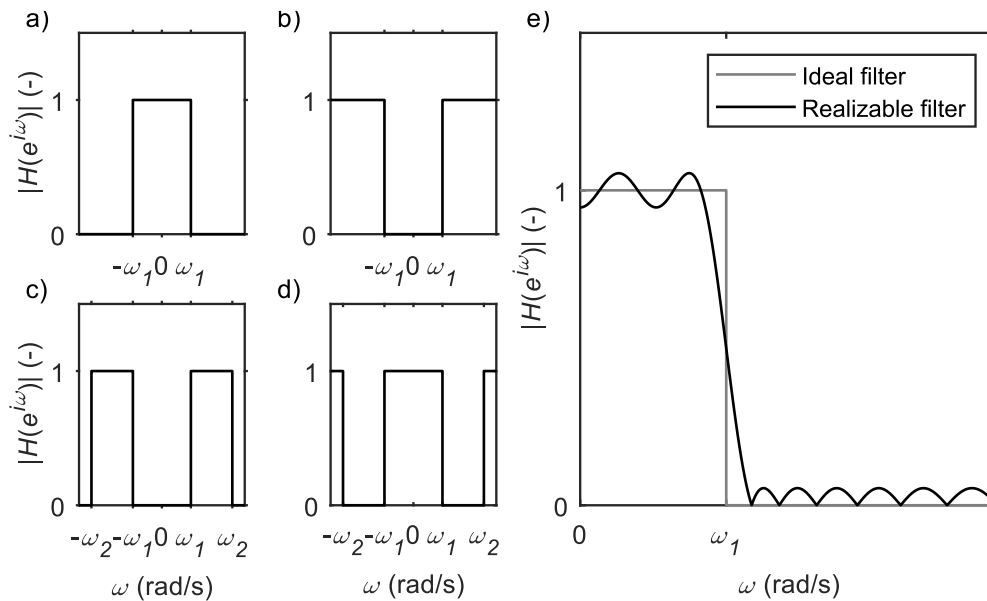


Figure A-3. a-d) Digital filter classification based on the magnitude vs. frequency response: a) Lowpass filter; b) Highpass filter; c) Bandpass filter; d) Bandstop filter; e) Ideal vs. physically realizable lowpass filter (only the positive frequency axis is represented).

However, each magnitude response reported in Figure A-3a-d is representative of an ideal filter, where  $|H(e^{j\omega})|$  is unitary in the passband and null in the stopband, with sharp transitions and zero phase everywhere. Such filters are not physically realizable because they can be achieved only by means of an infinite-length, acausal  $h[n]$ . Instead, a stable and realizable filter is characterized by a finite  $h[n]$ , hence the corresponding  $H(e^{j\omega})$  does not match the ideal transfer function. On the other side, it approximates the ideal trend, although it includes transition bands to allow smooth variations of the magnitude and undergoes small oscillations in the magnitude response in the passband and the stopband (Figure A-3e). In fact, one of the main goals in digital filter design is to minimize such oscillations and control the size of transition bands.

In addition, the characterization of the phase response of a digital filter is of paramount importance. Indeed, it is often desired that the application of the filter does not introduce any distortion to phase of the signal, at least in the passband. For this purpose, a useful family of digital filters consists in linear-phase filters, where the phase of  $H(e^{j\omega})$  is linear in the frequency range of interest (Figure A-4). A reliable indicator of phase linearity is provided by the group delay  $\tau_g(\omega)$ , which is defined as the differential of the phase response of the filter with respect to the frequency:

$$\tau_g(\omega) = -\frac{d \arg H(e^{j\omega})}{d\omega} \quad (\text{A.13})$$

The group delay expresses the time delay between the input and the output signal sequences. When  $\tau_g(\omega)$  is variable with the frequency (i.e., when the phase response is nonlinear), the filter introduces a distortion in the output signal. In linear-phase filters, the group delay is constant with the frequency, hence the output signal matches the desired component of the input sequence, unless some shift in the time domain.

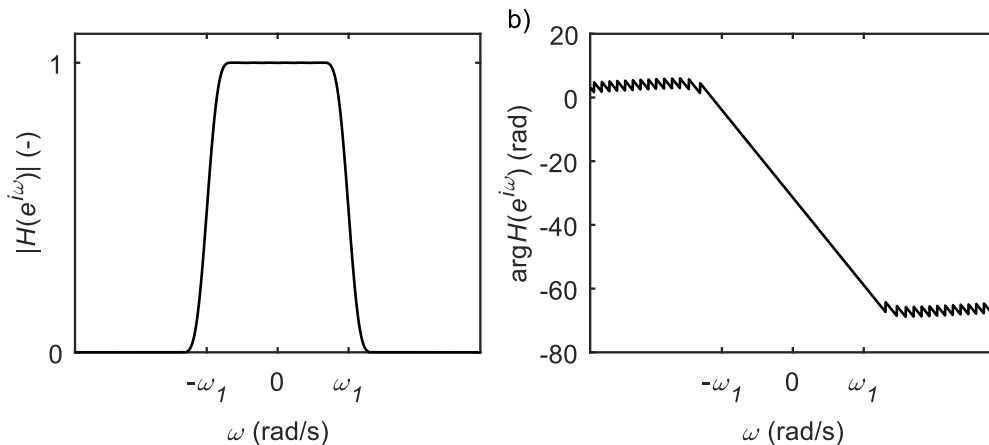


Figure A-4. Example of lowpass, linear-phase filter: a) Magnitude response; b) Phase response.

FIR filters exhibit interesting features, thanks to which they are an appealing tool in digital signal processing. On the one side, the estimation of the output response is straightforward. Instead, IIR filters often require recursive computational schemes. Furthermore, FIR filters usually are an effective choice, because of the stability of the filter structure. However, they are computationally more demanding because a high order filter is required to achieve the same performance of a IIR filter, in terms of magnitude response. Finally, when FIR filters exhibit a symmetric or antisymmetric impulse response, then they are linear-phase filters. Under this condition, indeed, it is demonstrated that the group delay is constant with the frequency and it equals  $N/2$ , being  $N$  the order of the FIR filter (i.e., the number of elements of  $h[n]$  minus 1). Therefore, the output signal will be a modified amplitude, delayed version of the input sequence. As it will be addressed in the next section, the design of symmetric FIR filters is straightforward, hence obtaining a linear phase response is quite an easy task. Instead, obtaining a linear-phase IIR filter is rather challenging, if not impossible.

For this reason, in those applications where the linearity in the phase response is crucial, the FIR filter is the preferred choice (Mitra, 2006).

In summary, the most suitable digital filter category to be used for the scope of this study is the linear-phase FIR filter. However, some care in the design and in its application is required. Indeed, although this kind of filters does not introduce any phase distortion on the desired component of the input signal, the resulting output is delayed and it includes a transient portion. To get an insight on these two aspects, let us consider a simplified example: a harmonic signal  $x_0[n]$  is corrupted by random Gaussian noise and it is desired to remove such component (Figure A-5). An effective strategy might rely on a bandpass FIR filter with order  $N$ , where the passband is centered around the frequency component of interest. However, the application of the digital filter to the input signal  $x[n]$  returns a sequence  $y[n]$ , the initial samples of which do not exhibit oscillations compatible with the expected result. This corresponds to the transient portion, which derives from the assumption of causality of  $x[n]$ , i.e. it is identically zero at negative times. Indeed, the output sequence is the result of a convolution between  $x[n]$  and  $h[n]$ , hence each sample of  $y[n]$  depends on a number of past input data. Thus, the initial data of the  $y[n]$  are affected by the assumed zero input sample values at  $n < 0$ . At large  $n$ , instead,  $y[n]$  depends solely on the actual input data and it is virtually identical to the expected result. The corresponding portion of the sequence is labeled as stationary response. Being an artifact due to the assumed causality of input signals, the transient response has to be removed from  $y[n]$ , otherwise the interpretation of the resulting sequence might be biased. In FIR filters, the length of the transient portion is equal to  $N$ , hence only the last  $n-N$  samples (where  $n$  is the number of samples of the input sequence) of  $y[n]$  should be considered.

However, even in the stationary portion, the output is a shifted version of the selected frequency component of the input. The entity of the shift is measured by  $\tau_g(\omega)$  which, in linear-phase FIR filters, equals  $N/2$ . Note that when  $N$  is odd, the output does not share identical features with the input sequence, but it is a translated version of the corresponding continuous version. This aspect may be critical as each output sample has to be associated with the correct sample location, accounting for this delay, in order to carry out a proper spectral analysis.

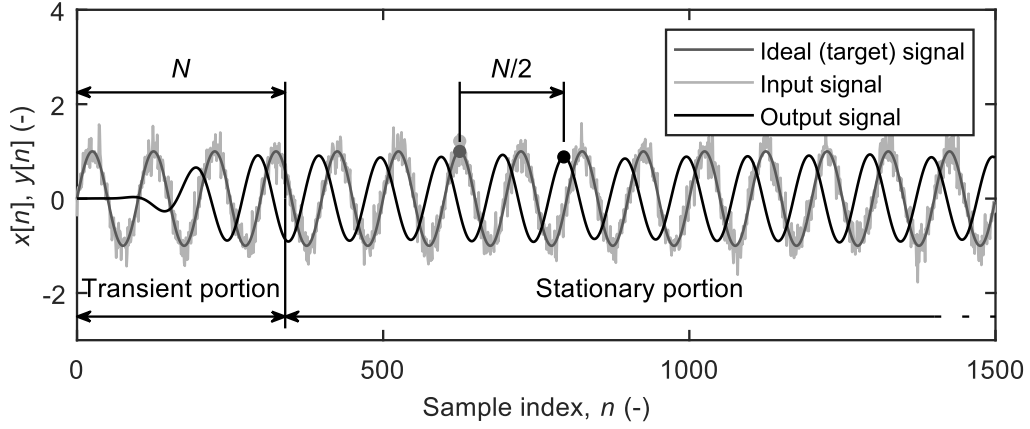


Figure A-5. Effect of a  $N$ -order FIR filter on a harmonic signal, highlighting the transient portion and the delay in the stationary response.

### A.3 Symmetry of complex filters

This section provides a quick overview about symmetry of complex filters, with a focus on the main results that are of interest for the specific digital filter that is adopted in this study. The main reference is the study by Bruekers (2009).

The description of the symmetry of complex-valued filters refers to two parameters, namely the shape of symmetry  $\sigma \in \mathbb{C}$  (with  $|\sigma| = 1$ ) and the center of symmetry  $\mu \in \mathbb{Z}/2$ . The parameter  $\sigma$  specifies whether a filter is symmetric or antisymmetric. As this couple of parameter allows a full characterization of symmetric complex filters, often the symmetry is denoted as  $(\sigma, \mu)$ -symmetry.

The definition of  $(\sigma, \mu)$ -symmetry for a complex filter  $h[n]$  applies both for the impulse response  $h[n]$  and the transfer function  $H(e^{i\omega})$ :

$$(\sigma, \mu)\text{-symmetry} \Leftrightarrow \begin{cases} h[n] = \sigma h^*[2\mu - n], \forall n \\ H(e^{i\omega}) = \sigma e^{-2i\mu\omega} H^C(e^{-i\omega}) \end{cases} \quad (\text{A.14})$$

where  $H^C(e^{i\omega})$  is the transfer function of  $h^*[n]$ .

The adopted filter is defined as follows (see Eq. 5.16):

$$h[n] = e^{-ik_{ig}n} g[n] \quad (\text{A.15})$$

being  $k_{ig}$  the target wavenumber and  $g[n]$  a real-valued, lowpass filter with order  $N$ . As  $g[n]$  is designed through the windowing approach,  $g[n]$  is a symmetric filter, specifically it exhibits  $(1, N/2)$ -symmetry. The transformation  $e^{-ik_{ig}n}$  still returns a symmetric filter. Indeed, if  $s[n]$  is  $(\sigma, \mu)$ -symmetric, then the filter  $t[n]$  defined as



$$t[n] = e^{i\theta n} s[n] \quad (\text{A.16})$$

is with  $(\sigma e^{2i\theta\mu}, \mu)$ -symmetric. Thus,  $h[n]$  is  $\left( e^{2ik_{ig}\frac{N}{2}}, \frac{N}{2} \right)$ -symmetric.

Finally, symmetric complex filters exhibit linear phase response. Indeed, the phase response of a  $(\sigma, \mu)$ -symmetric filter  $s[n]$  is the following:

$$\arg S(e^{i\omega}) = \frac{1}{2} \arg \sigma - \mu\omega \quad (\text{A.17})$$

For the specific case of  $h[n]$ , the phase varies as follows:

$$\arg H(e^{i\omega}) = \frac{1}{2} 2k_{ig} \frac{N}{2} - \frac{N}{2} \omega = \frac{N}{2} (k_{ig} - \omega) \quad (\text{A.18})$$

Therefore, the group delay is constant and it equals  $N/2$ .

## A.4 Calibration study of the FDBFaMF and the CFDBFaMF

This section reports results of the calibration study of the FDBFaMF and CFDBFaMF, for the parameter sets  $[k_p; k_s] = [1; 2], [2; 4],$  and  $[3; 10]$  and  $N = 10, 20, 30,$  and  $40$ . Data refer to synthetic waveforms SW3 and SW4 (see Section 5.1).

The following figures compare resulting dispersion and attenuation estimates obtained through the FDBFaMF and the CFDBFaMF algorithms for the first three modes for SW3 and SW4, labeled as R0, R1 and R2, respectively. Reported data are sampled with a sampling frequency of 1 Hz, across the frequency band ranging between 3 Hz and 100 Hz. Furthermore, the regions associated with wavelengths beyond the resolution limits of the simulated array are highlighted, as the corresponding results should be interpreted with care. Finally, Table A.1 to Table A.4 list the overall estimation error  $\Delta V + \Delta\alpha$ , as a function of filter parameters. Values  $\Delta V$  and  $\Delta\alpha$  are root mean square errors for the phase velocity and phase attenuation data respectively:

$$\Delta V = \sqrt{\frac{1}{N} \sum_{n=1}^N (\ln V_{R,e} - \ln V_R)^2} \quad \Delta\alpha = \sqrt{\frac{1}{N} \sum_{n=1}^N (\ln \alpha_{R,e} - \ln \alpha_R)^2} \quad (\text{10.19})$$

where  $N$  is the number of samples,  $V_{R,e}$  and  $\alpha_{R,e}$  are the estimated values, and  $V_R$  and  $\alpha_R$  are the theoretical ones. The error is computed as sum of the errors for the first three modes, considering data within the array resolution limits.

Table A.1. Estimation error  $\Delta V + \Delta \alpha$  in the phase velocity and phase attenuation data for the FDBFaMF algorithm on SW3, with a focus on the first three modes, as a function of filter calibration parameters.

$\downarrow [k_p; k_s]$ $N \rightarrow$	<b>10</b>	<b>20</b>	<b>30</b>	<b>40</b>
<b>[1; 2]</b>	1.48	1.43	2.18	2.02
<b>[2; 4]</b>	1.54	1.48	1.89	2.05
<b>[3; 10]</b>	1.59	1.29	1.99	3.13

Table A.2. Estimation error  $\Delta V + \Delta \alpha$  in the phase velocity and phase attenuation data for the CFDBFaMF algorithm on SW3, with a focus on the first three modes, as a function of filter calibration parameters.

$\downarrow [k_p; k_s]$ $N \rightarrow$	<b>10</b>	<b>20</b>	<b>30</b>	<b>40</b>
<b>[1; 2]</b>	1.13	1.14	2.73	2.13
<b>[2; 4]</b>	1.40	1.39	2.10	2.26
<b>[3; 10]</b>	1.58	1.49	2.37	3.51

Table A.3. Estimation error  $\Delta V + \Delta \alpha$  in the phase velocity and phase attenuation data for the FDBFaMF algorithm on SW4, with a focus on the first three modes, as a function of filter calibration parameters.

$\downarrow [k_p; k_s]$ $N \rightarrow$	<b>10</b>	<b>20</b>	<b>30</b>	<b>40</b>
<b>[1; 2]</b>	2.81	2.18	2.35	3.81
<b>[2; 4]</b>	2.81	2.21	2.55	2.03
<b>[3; 10]</b>	2.86	2.28	2.85	4.91

Table A.4. Estimation error  $\Delta V + \Delta \alpha$  in the phase velocity and phase attenuation data for the CFDBFaMF algorithm on SW4, with a focus on the first three modes, as a function of filter calibration parameters.

$\downarrow [k_p; k_s]$ $N \rightarrow$	<b>10</b>	<b>20</b>	<b>30</b>	<b>40</b>
<b>[1; 2]</b>	1.96	1.90	1.93	2.70
<b>[2; 4]</b>	1.96	3.01	3.17	2.53
<b>[3; 10]</b>	1.96	2.95	1.45	3.13

### A.4.1 Results for SW3 - FDBFaMF

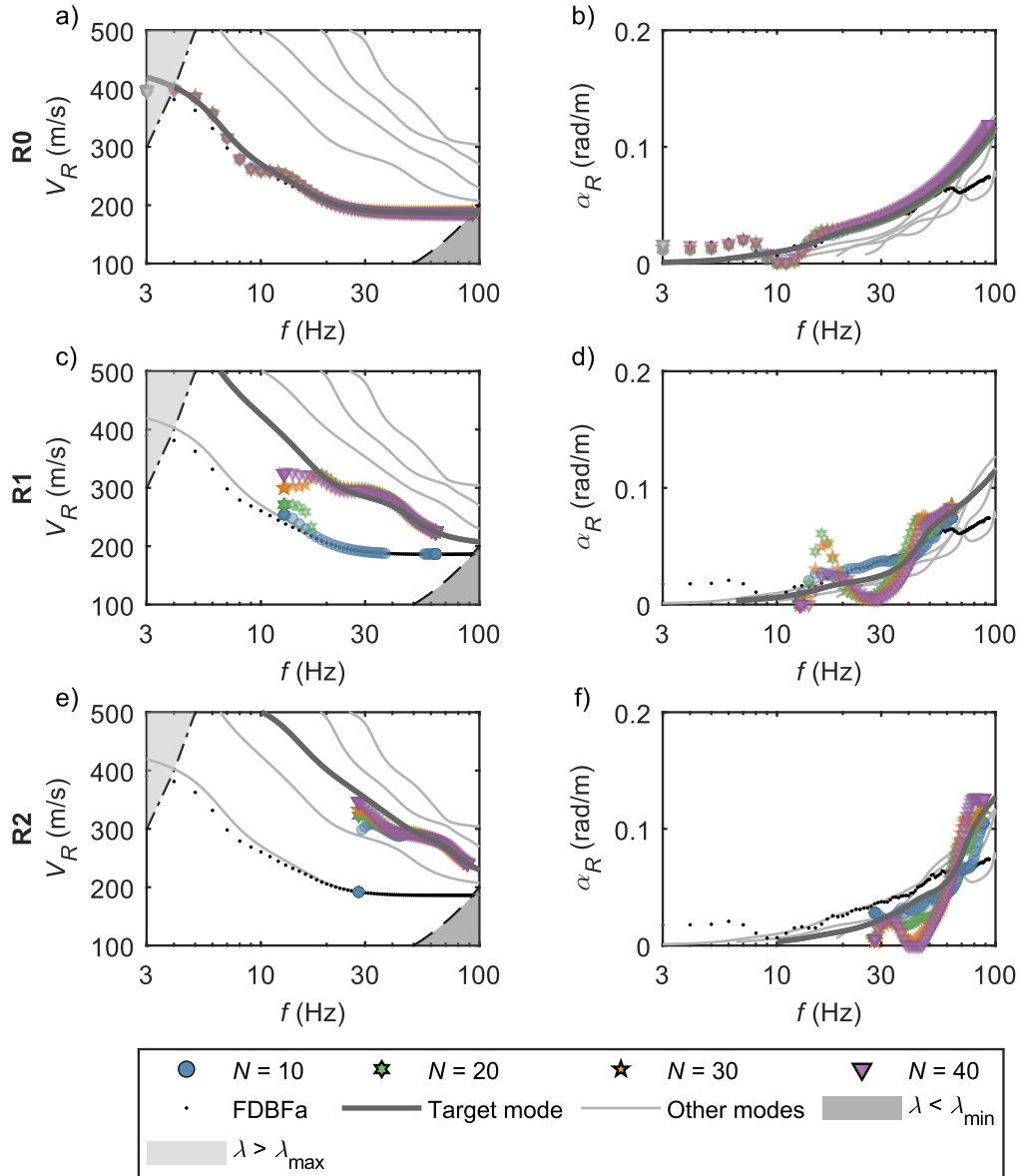


Figure A-6. Influence of filter calibration parameters in the application of the FDBFaMF algorithm on SW3, with a focus on the first three modes: a-b) Estimated dispersion curves (a) and attenuation curves (b) for the fundamental mode, labeled as R0; c-d) Estimated dispersion curves (c) and attenuation curves (d) for the first higher mode, labeled as R1; e-f) Estimated dispersion curves (e) and attenuation curves (f) for the second higher mode, labeled as R2. Results correspond to the set of parameters  $[k_p; k_s] = [1; 2]$ . Results of the FDBFa are also reported, for comparison purposes. Estimated data points beyond the array resolution limits – i.e., the grey areas in (a), (c), and (e) – are colored in grey.

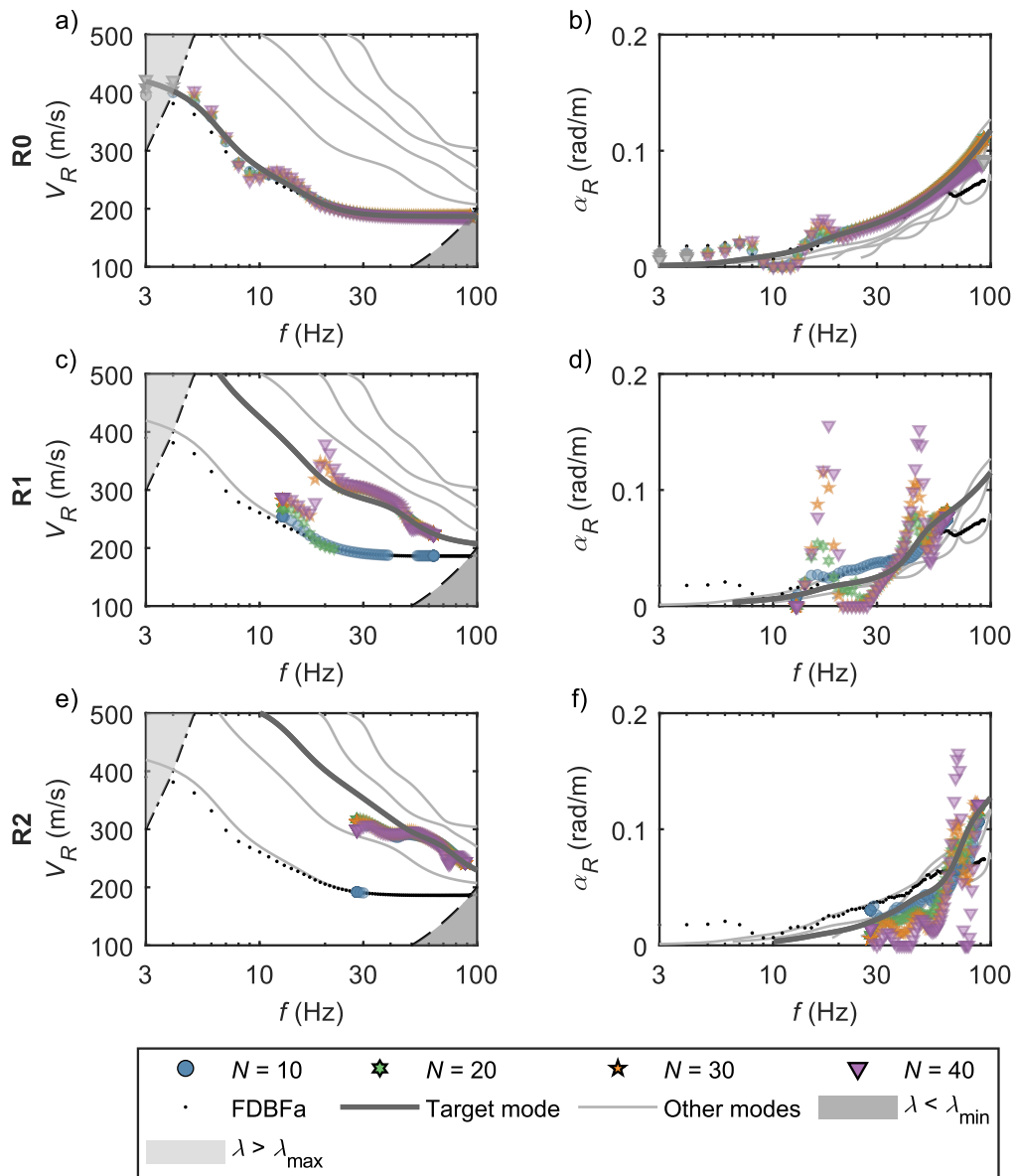


Figure A-7. Influence of filter calibration parameters in the application of the FDBFaMF algorithm on SW3, with a focus on the first three modes: a-b) Estimated dispersion curves (a) and attenuation curves (b) for the fundamental mode, labeled as R0; c-d) Estimated dispersion curves (c) and attenuation curves (d) for the first higher mode, labeled as R1; e-f) Estimated dispersion curves (e) and attenuation curves (f) for the second higher mode, labeled as R2. Results correspond to the set of parameters  $[k_p; k_s] = [2; 4]$ . Results of the FDBFa are also reported, for comparison purposes. Estimated data points beyond the array resolution limits – i.e., the grey areas in (a), (c), and (e) – are colored in grey.

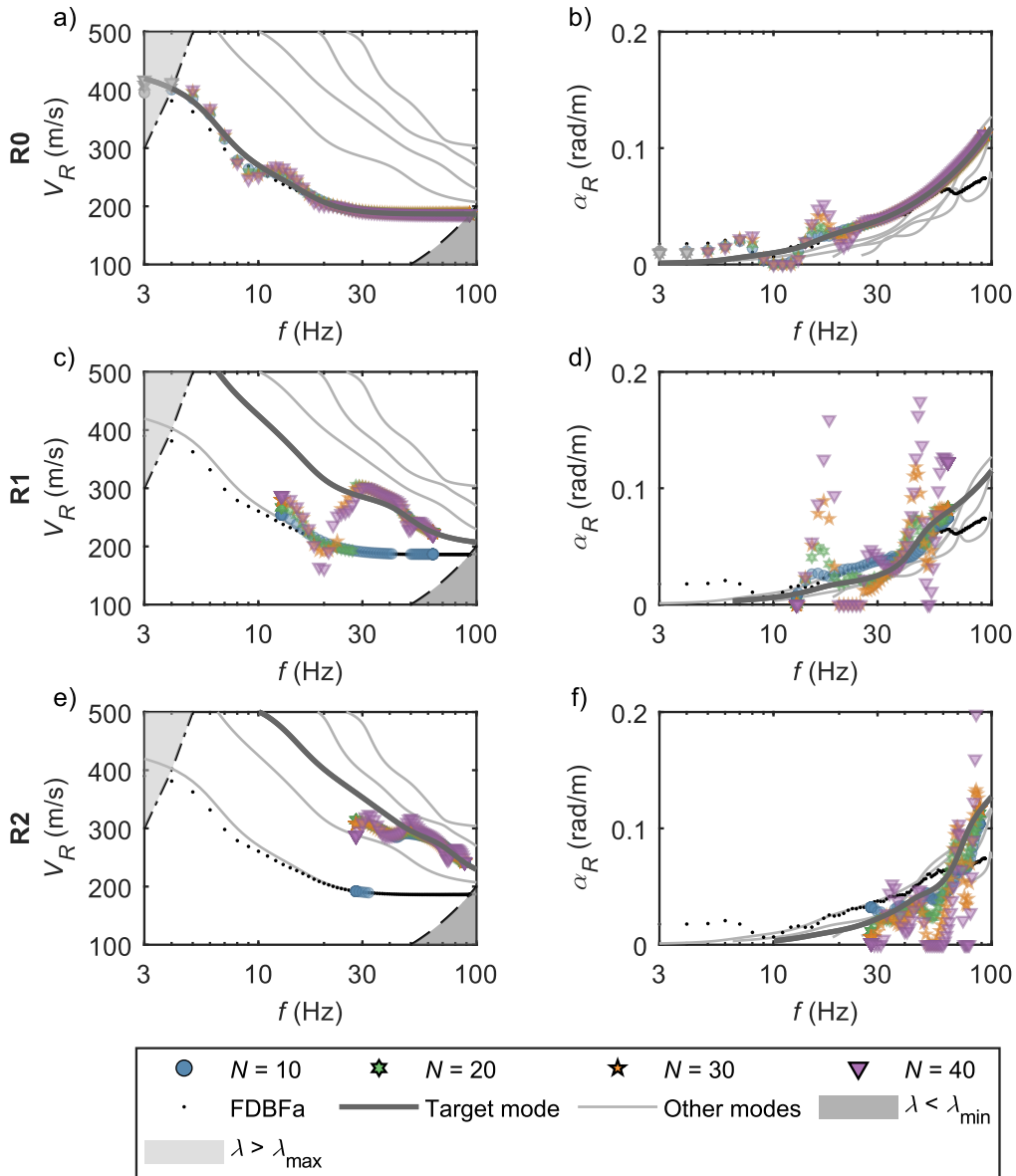


Figure A-8. Influence of filter calibration parameters in the application of the FDBFaMF algorithm on SW3, with a focus on the first three modes: a-b) Estimated dispersion curves (a) and attenuation curves (b) for the fundamental mode, labeled as R0; c-d) Estimated dispersion curves (c) and attenuation curves (d) for the first higher mode, labeled as R1; e-f) Estimated dispersion curves (e) and attenuation curves (f) for the second higher mode, labeled as R2. Results correspond to the set of parameters  $[k_p; k_s] = [3; 10]$ . Results of the FDBFa are also reported, for comparison purposes. Estimated data points beyond the array resolution limits – i.e., the grey areas in (a), (c), and (e) – are colored in grey.

### A.4.2 Results for SW3 - CFDBFaMF

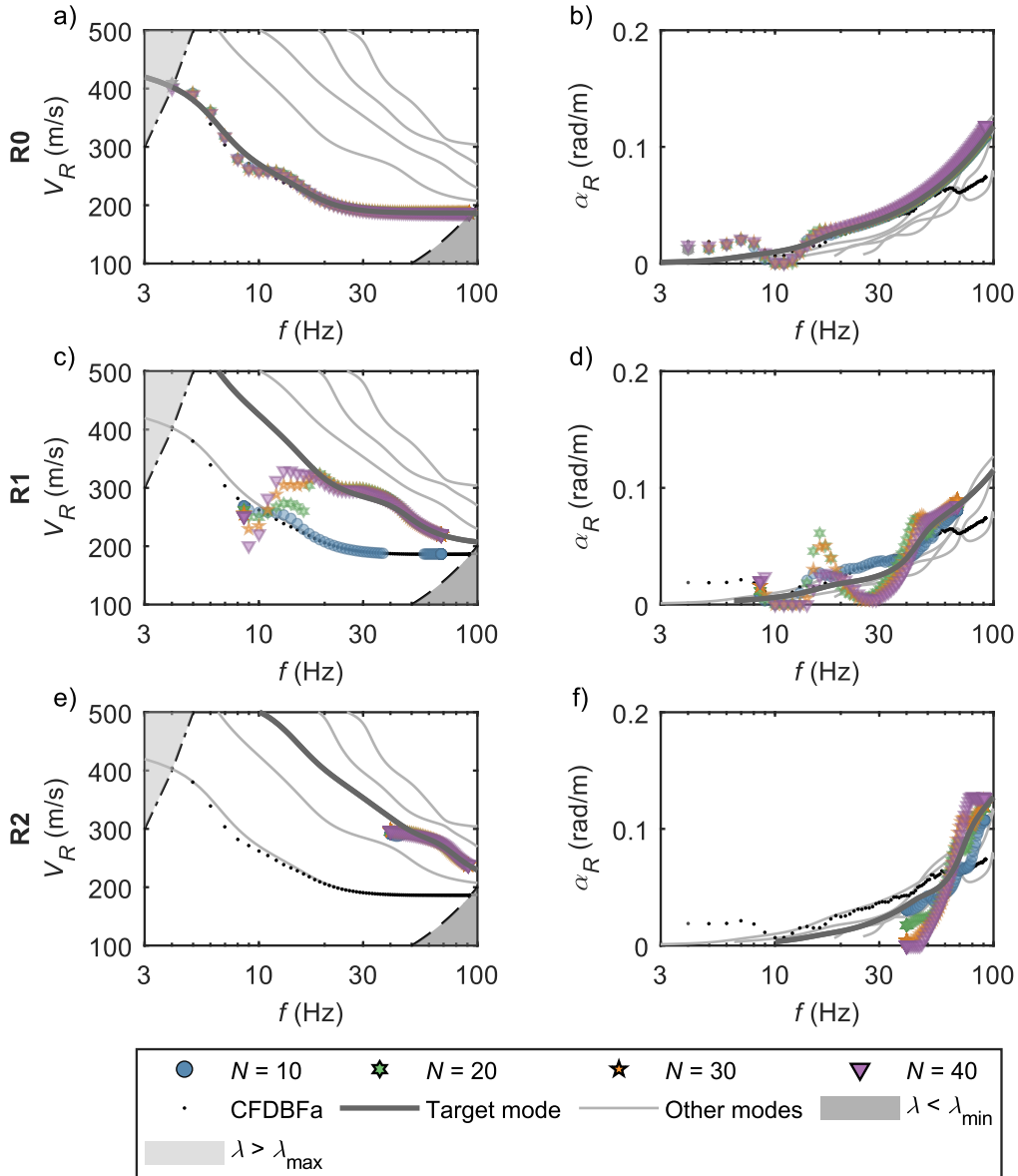


Figure A-9. Influence of filter calibration parameters in the application of the CFDBFaMF algorithm on SW3, with a focus on the first three modes: a-b) Estimated dispersion curves (a) and attenuation curves (b) for the fundamental mode, labeled as R0; c-d) Estimated dispersion curves (c) and attenuation curves (d) for the first higher mode, labeled as R1; e-f) Estimated dispersion curves (e) and attenuation curves (f) for the second higher mode, labeled as R2. Results correspond to the set of parameters  $[k_p; k_s] = [1; 2]$ . Results of the CFDBFa are also reported, for comparison purposes. Estimated data points beyond the array resolution limits – i.e., the grey areas in (a), (c), and (e) – are colored in grey.

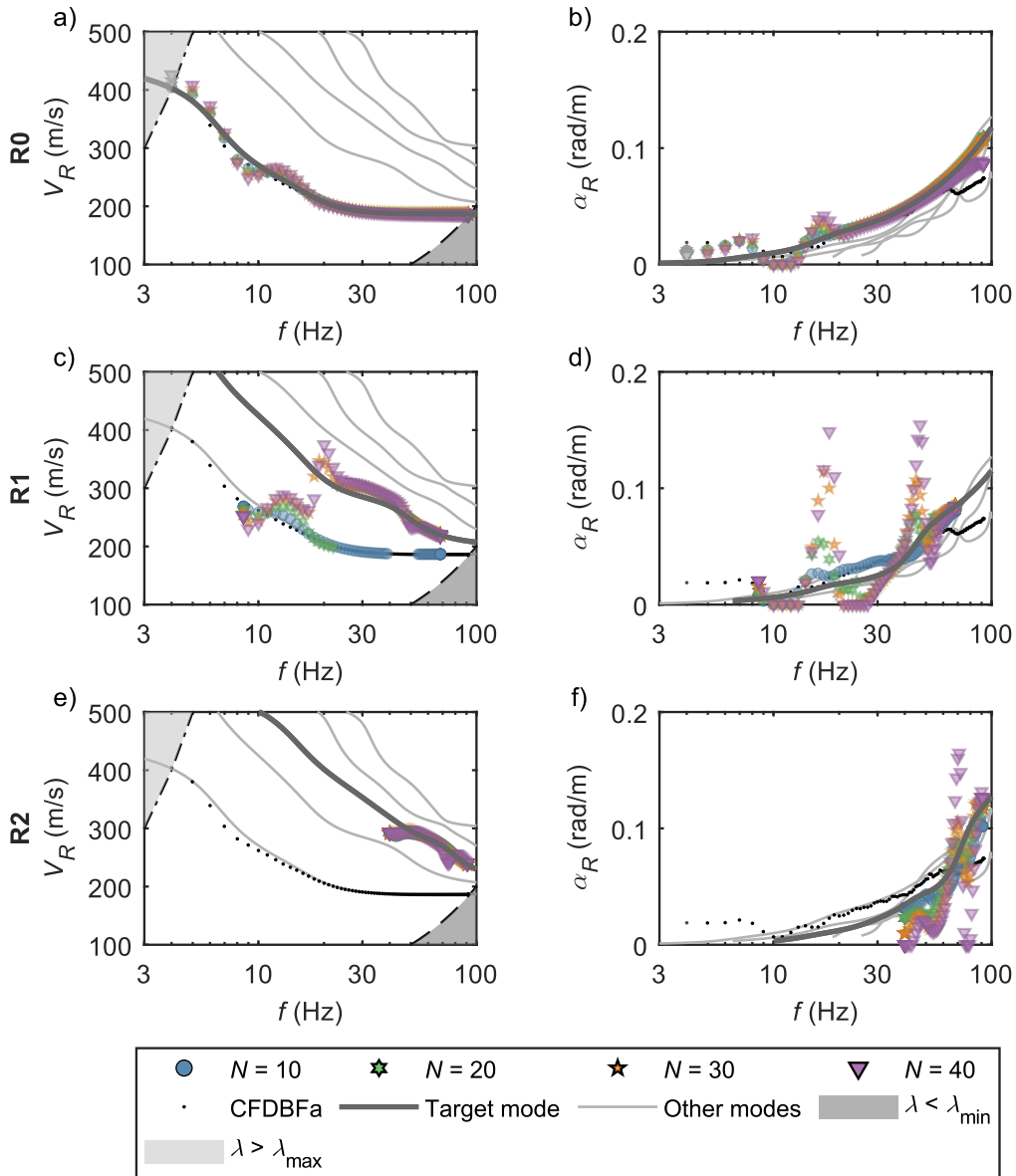


Figure A-10. Influence of filter calibration parameters in the application of the CFDBFaMF algorithm on SW3, with a focus on the first three modes: a-b) Estimated dispersion curves (a) and attenuation curves (b) for the fundamental mode, labeled as R0; c-d) Estimated dispersion curves (c) and attenuation curves (d) for the first higher mode, labeled as R1; e-f) Estimated dispersion curves (e) and attenuation curves (f) for the second higher mode, labeled as R2. Results correspond to the set of parameters  $[k_p; k_s] = [2; 4]$ . Results of the CFDBFa are also reported, for comparison purposes. Estimated data points beyond the array resolution limits – i.e., the grey areas in (a), (c), and (e) – are colored in grey.

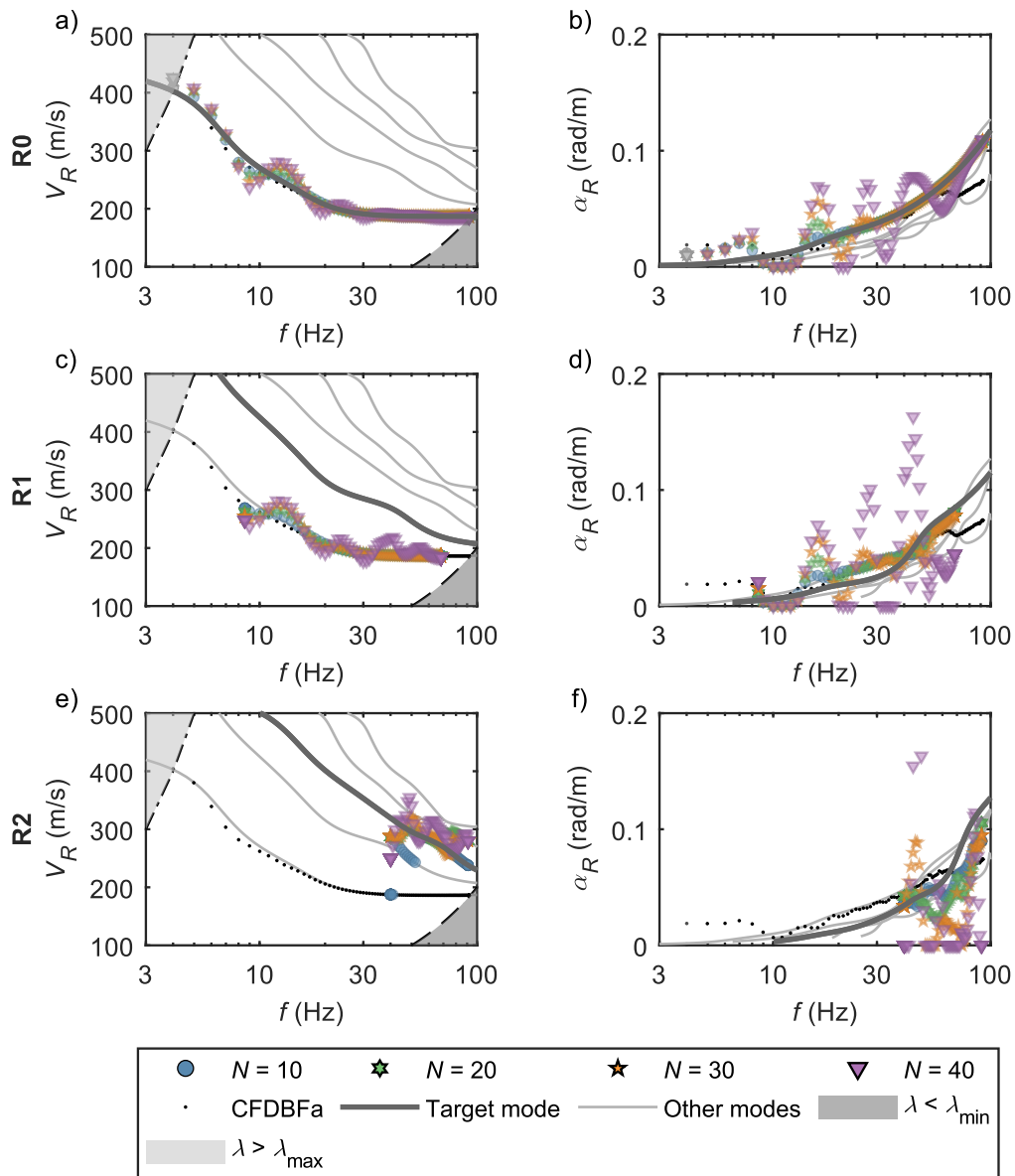


Figure A-11. Influence of filter calibration parameters in the application of the CFDBFaMF algorithm on SW3, with a focus on the first three modes: a-b) Estimated dispersion curves (a) and attenuation curves (b) for the fundamental mode, labeled as R0; c-d) Estimated dispersion curves (c) and attenuation curves (d) for the first higher mode, labeled as R1; e-f) Estimated dispersion curves (e) and attenuation curves (f) for the second higher mode, labeled as R2. Results correspond to the set of parameters  $[k_p; k_s] = [3; 10]$ . Results of the CFDBFa are also reported, for comparison purposes. Estimated data points beyond the array resolution limits – i.e., the grey areas in (a), (c), and (e) – are colored in grey.



### A.4.3 Results for SW4 - FDBFaMF

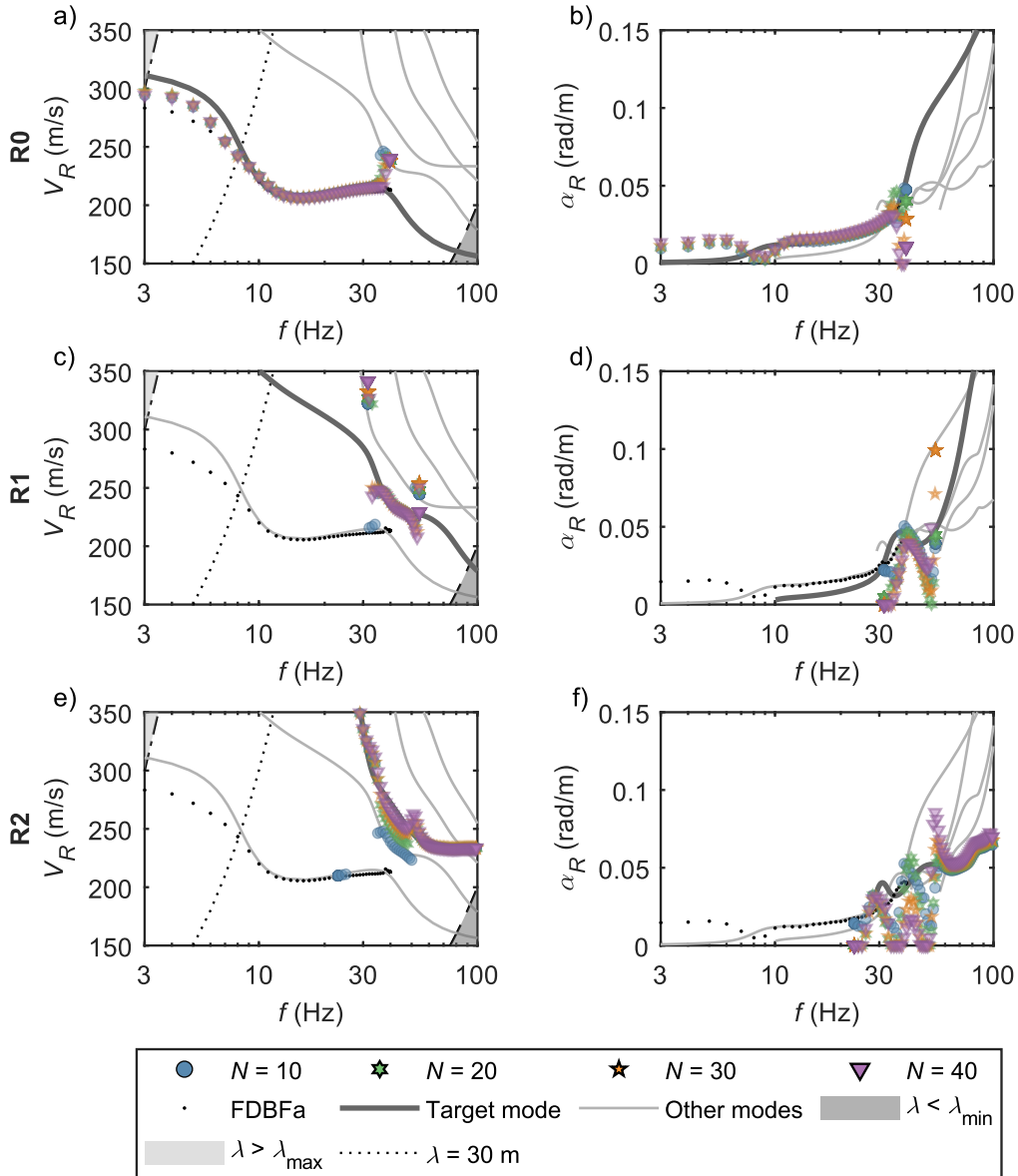


Figure A-12. Influence of filter calibration parameters in the application of the FDBFaMF algorithm on SW4, with a focus on the first three modes: a-b) Estimated dispersion curves (a) and attenuation curves (b) for the fundamental mode, labeled as R0; c-d) Estimated dispersion curves (c) and attenuation curves (d) for the first higher mode, labeled as R1; e-f) Estimated dispersion curves (e) and attenuation curves (f) for the second higher mode, labeled as R2. Results correspond to the set of parameters  $[k_p; k_s] = [1; 2]$ . Results of the FDBFa are also reported, for comparison purposes. Estimated data points beyond the array resolution limits – i.e., the grey areas in (a), (c), and (e) – are colored in grey.

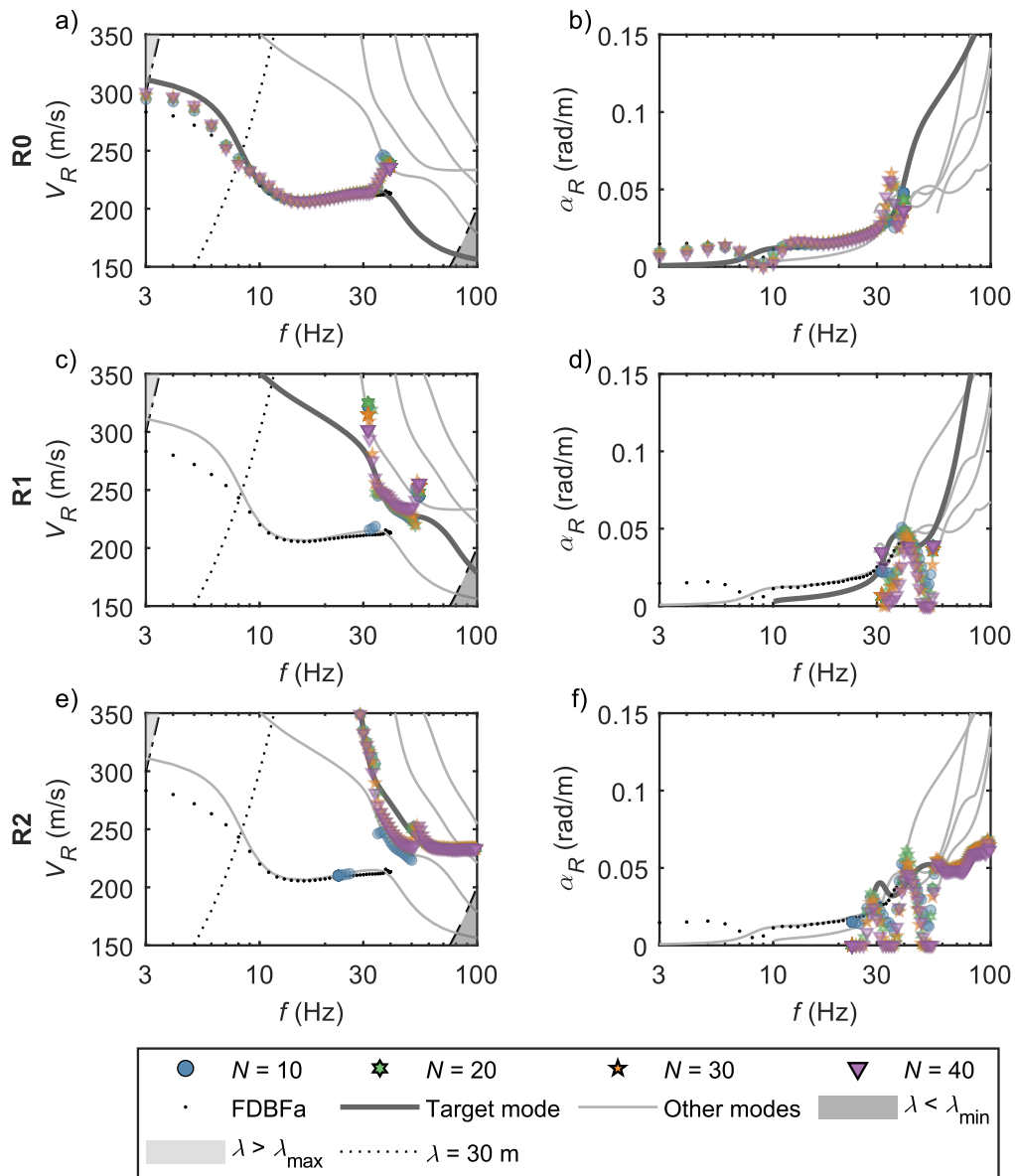


Figure A-13. Influence of filter calibration parameters in the application of the FDBFaMF algorithm on SW4, with a focus on the first three modes: a-b) Estimated dispersion curves (a) and attenuation curves (b) for the fundamental mode, labeled as R0; c-d) Estimated dispersion curves (c) and attenuation curves (d) for the first higher mode, labeled as R1; e-f) Estimated dispersion curves (e) and attenuation curves (f) for the second higher mode, labeled as R2. Results correspond to the set of parameters  $[k_p; k_s] = [2; 4]$ . Results of the FDBFa are also reported, for comparison purposes. Estimated data points beyond the array resolution limits – i.e., the grey areas in (a), (c), and (e) – are colored in grey.

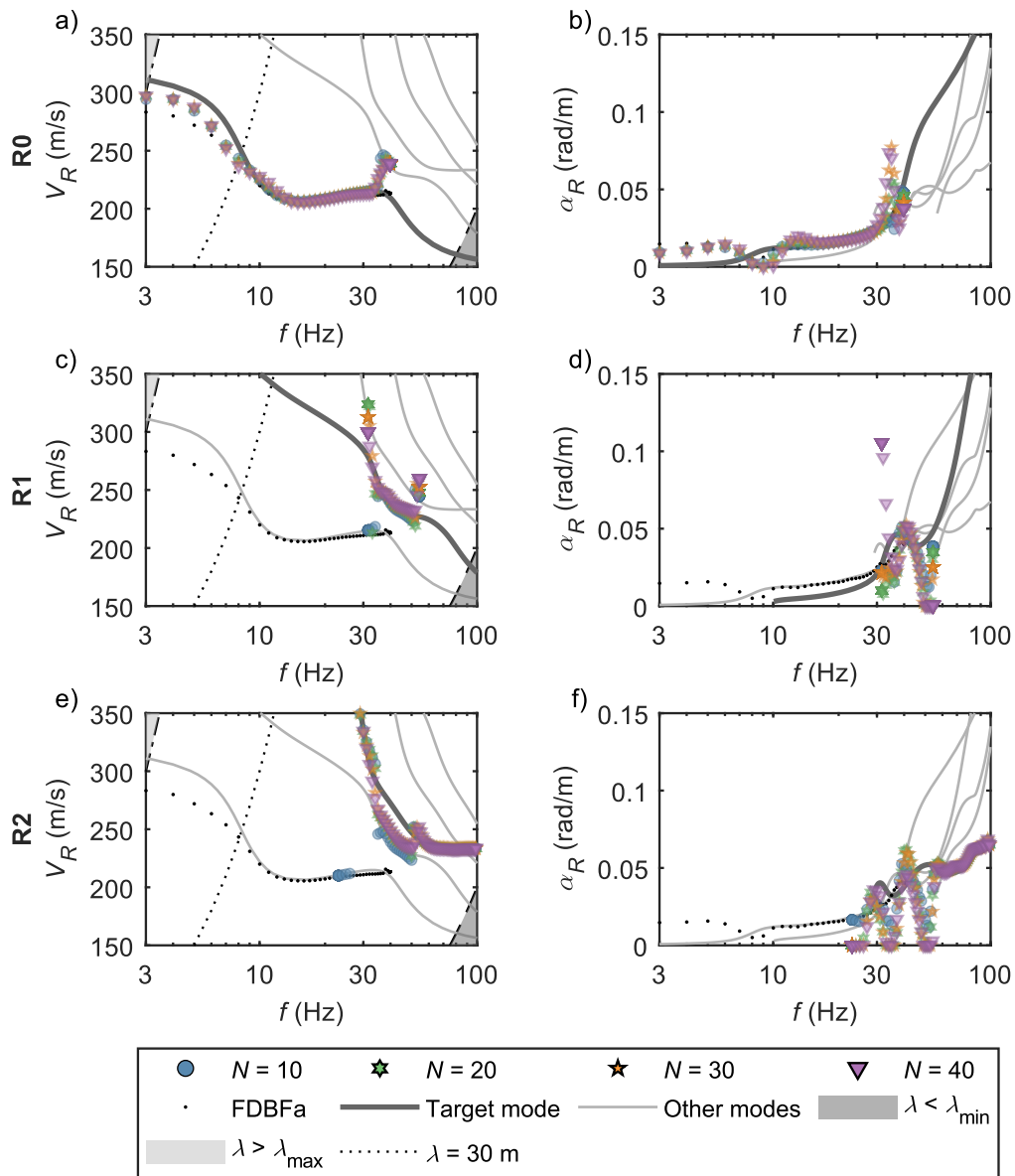


Figure A-14. Influence of filter calibration parameters in the application of the FDBFaMF algorithm on SW4, with a focus on the first three modes: a-b) Estimated dispersion curves (a) and attenuation curves (b) for the fundamental mode, labeled as R0; c-d) Estimated dispersion curves (c) and attenuation curves (d) for the first higher mode, labeled as R1; e-f) Estimated dispersion curves (e) and attenuation curves (f) for the second higher mode, labeled as R2. Results correspond to the set of parameters  $[k_p; k_s] = [3; 10]$ . Results of the FDBFa are also reported, for comparison purposes. Estimated data points beyond the array resolution limits – i.e., the grey areas in (a), (c), and (e) – are colored in grey.

#### A.4.4 Results for SW4 - CFDBFaMF

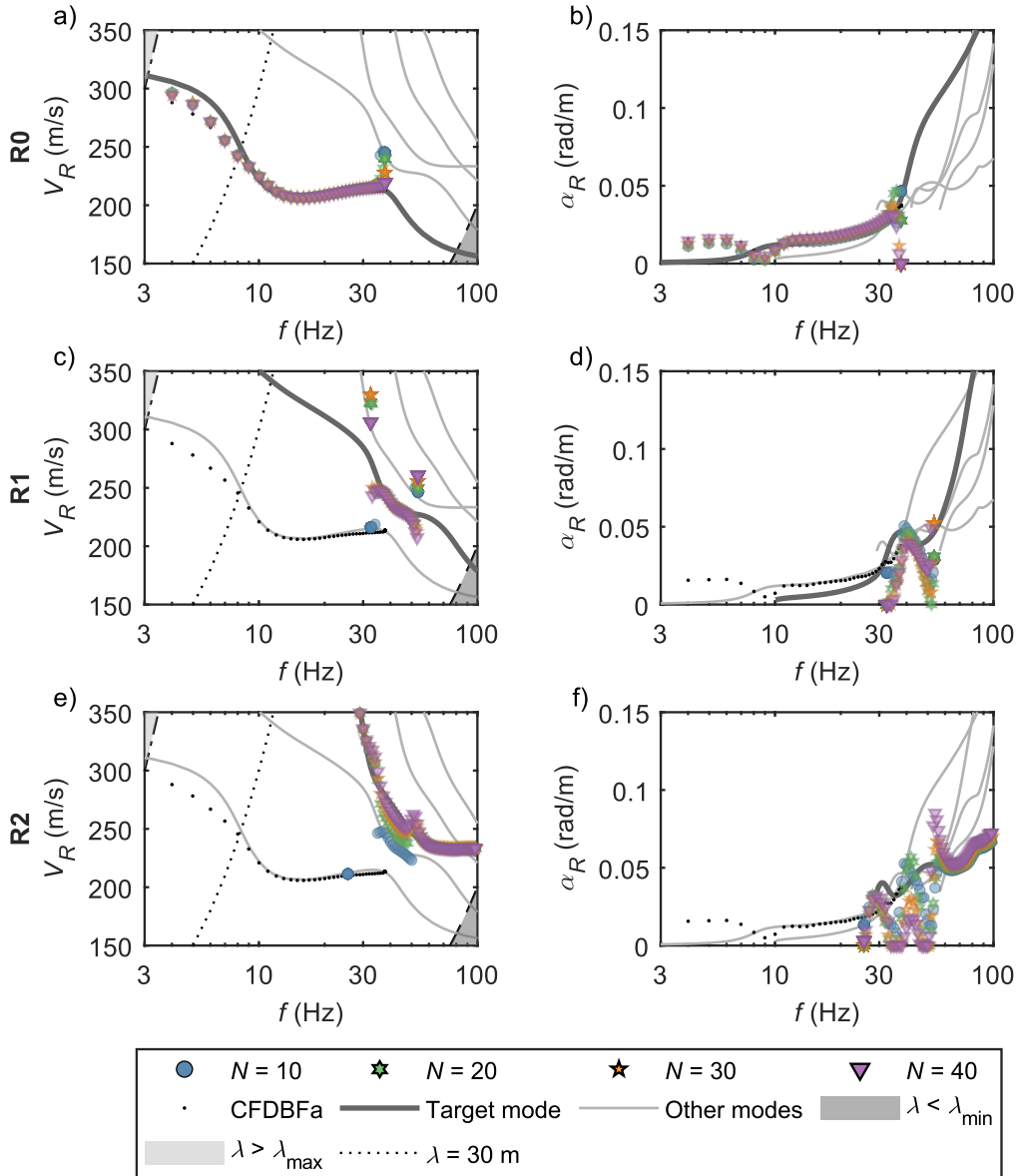


Figure A-15. Influence of filter calibration parameters in the application of the CFDBFaMF algorithm on SW4, with a focus on the first three modes: a-b) Estimated dispersion curves (a) and attenuation curves (b) for the fundamental mode, labeled as R0; c-d) Estimated dispersion curves (c) and attenuation curves (d) for the first higher mode, labeled as R1; e-f) Estimated dispersion curves (e) and attenuation curves (f) for the second higher mode, labeled as R2. Results correspond to the set of parameters  $[k_p; k_s] = [1; 2]$ . Results of the CFDBFa are also reported, for comparison purposes. Estimated data points beyond the array resolution limits – i.e., the grey areas in (a), (c), and (e) – are colored in grey.

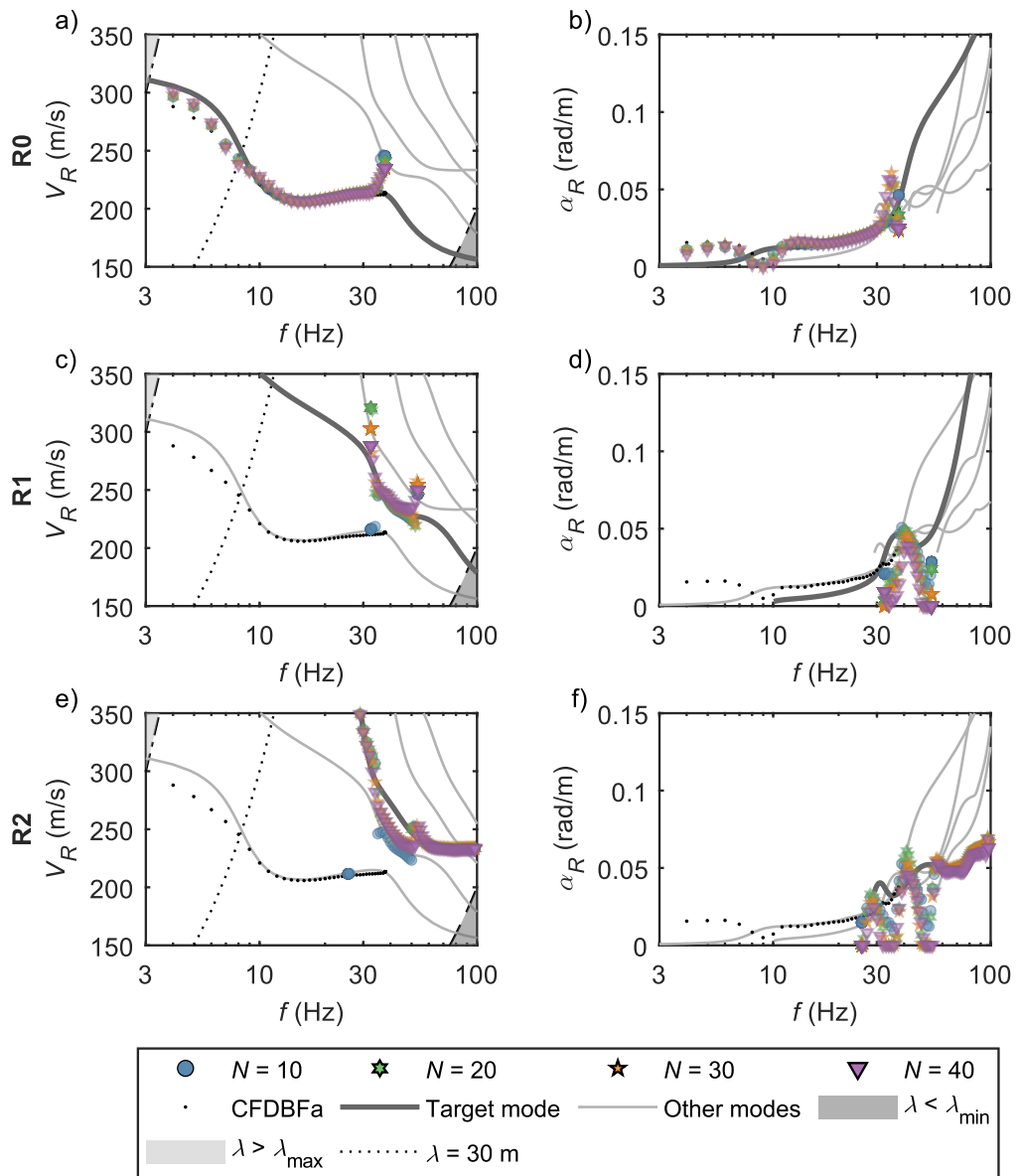


Figure A-16. Influence of filter calibration parameters in the application of the CFDBFaMF algorithm on SW4, with a focus on the first three modes: a-b) Estimated dispersion curves (a) and attenuation curves (b) for the fundamental mode, labeled as R0; c-d) Estimated dispersion curves (c) and attenuation curves (d) for the first higher mode, labeled as R1; e-f) Estimated dispersion curves (e) and attenuation curves (f) for the second higher mode, labeled as R2. Results correspond to the set of parameters  $[k_p; k_s] = [2; 4]$ . Results of the CFDBFa are also reported, for comparison purposes. Estimated data points beyond the array resolution limits – i.e., the grey areas in (a), (c), and (e) – are colored in grey.

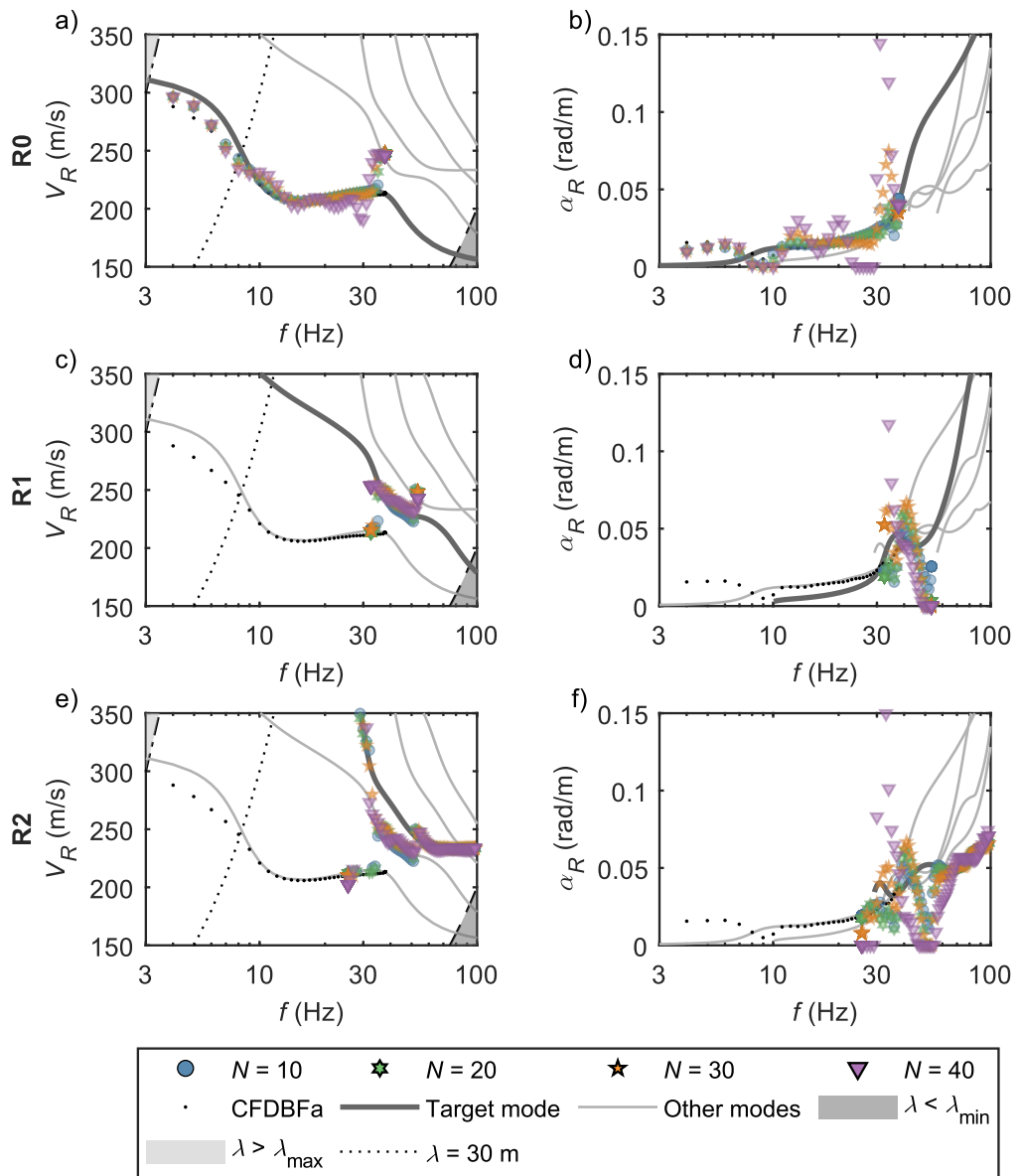


Figure A-17. Influence of filter calibration parameters in the application of the CFDBFaMF algorithm on SW4, with a focus on the first three modes: a-b) Estimated dispersion curves (a) and attenuation curves (b) for the fundamental mode, labeled as R0; c-d) Estimated dispersion curves (c) and attenuation curves (d) for the first higher mode, labeled as R1; e-f) Estimated dispersion curves (e) and attenuation curves (f) for the second higher mode, labeled as R2. Results correspond to the set of parameters  $[k_p; k_s] = [3; 10]$ . Results of the CFDBFa are also reported, for comparison purposes. Estimated data points beyond the array resolution limits – i.e., the grey areas in (a), (c), and (e) – are colored in grey.



# Appendix B

## Implementation details of other SWM processing methods

This Appendix describes some literature approaches for the estimation of R-wave phase velocity and phase attenuation. Although the main principles were already discussed in Section 4.3.1, this Appendix focuses on some technical aspects linked with their implementation. Firstly, the Transfer Function Method (TFM) is addressed, to specify the adopted regression algorithm. Then, the description of the Generalized Half-Power Bandwidth (GHPB) and of the Circle Fit Method (CFM) focuses on the relative differences and on some issues linked with some operative parameters. Finally, the WaveDec (WD) procedure is recalled, with a particularization to processing vertical displacement data only. The description uses the synthetic wavefields SW1, SW2, SW3, and SW4, introduced in Section 5.1.

### B.1 Transfer function method

The TFM estimates the phase velocity  $V_R(\omega)$  (alternatively, the wavenumber  $k_R(\omega)$ ) and the phase attenuation  $\alpha_R(\omega)$  of Rayleigh waves based on the nonlinear fitting of the R-wave experimental displacement transfer function  $T(r, \omega)$ , i.e. the ratio between the measured vertical displacement at each sensor and the force applied at the source in the frequency domain. The regression provides an estimate of the complex wavenumber  $\hat{k}_R(\omega)$ , from which  $V_R(\omega)$  and  $\alpha_R(\omega)$  are then derived. The fitting of  $T(r, \omega)$  can be performed in an uncoupled way, based on the separate fitting of its amplitude and phase (Lai et al., 2002). However, a coupled fitting of the transfer function in the complex domain is mathematically more robust (Foti, 2003; Figure B-1). The fitting procedure is solved via an optimization procedure, aimed at finding the global minimum of an objective function.

The nonlinearity of the regression model introduces various levels of complexity in the solution of the fitting procedure. On the one side, the fitting procedure requires an initial guess of the R-wave parameters. Furthermore, the



objective function tends to exhibit manifold local minima, as a function of the complexity of the recorded wavefield and of the noise level. In ideal conditions, such as a single planar wave (e.g., SW1; Figure 4-11a), the objective function only includes a global minimum, and any solver easily identifies it. However, usual acquisition setups return wavefield data that potentially include multiple wave components (even other than surface waves) and are affected by incoherent noise. Therefore, the shape of the objective function is more complex, and it exhibits manifold local minima combined with the global one, which theoretically represents the actual wave component of interest (Figure 4-11b). In this case, the estimator might get trapped, thus returning wrong estimates of the R-wave parameters. Therefore, a robust solver must be used to achieve reliable estimates of dispersion and attenuation data.

The present study solves the fitting procedure through a strategy compatible with the one implemented by Lai et al. (2002) and updated by Badsar (2012). This technique carries out a coupled fitting of the transfer function in the complex domain, wherein first-stage estimates of  $k_R(\omega)$  and  $\alpha_R(\omega)$  are obtained through two preliminary stages of uncoupled fitting. Specifically, a starting value of  $\alpha_R(\omega)$  is first estimated by means of a nonlinear fitting of the amplitude of  $T(r, \omega)$  with respect to the offset, which is modeled according to the amplitude component of Eq. 4.12. This stage can rely on a local optimization solver, as the simplex method (Nelder and Mead, 1965). Then, a reference value of  $k_R(\omega)$  is obtained by exploiting the phase information carried in  $T(r, \omega)$ . An intuitive way estimates  $k_R(\omega)$  through a linear fitting of the phase of  $T(r, \omega)$  itself, with the offset. However, this strategy is quite sensitive to the robustness of the phase unwrapping algorithm, which may lead to unreliable estimates, especially in the presence of noisy data (e.g., Strobbia and Foti, 2006). Alternatively,  $k_R(\omega)$  can be estimated by fitting  $T(r, \omega)$  according to the theoretical formulation given in Eq. 4.12. In this case, the attenuation component is kept fixed and equal to the  $\alpha_R(\omega)$  obtained in the previous stage. As the objective function exhibits multiple minima, a global optimization algorithm is required to achieve reliable estimates of the real wavenumber. This study adopts the sequential quadratic programming method (Nocedal and Wright, 2006), combined with a scatter-search mechanism (Ugray et al., 2007) to explore the whole parameter space in a fast and consistent way. Finally, the preliminary estimates of  $k_R(\omega)$  and  $\alpha_R(\omega)$  are plugged as initial values into a coupled nonlinear fitting procedure, wherein  $T(r, \omega)$  is modeled through the theoretical formulation given in Eq. 4.12 and both the amplitude and the phase term are not fixed, to obtain a final estimate of  $\hat{k}_R(\omega)$ . The solution is found by means of a local optimization solver, as the simplex method (Nelder and Mead,

1965), because the initial values are usually close enough to the target  $\hat{k}_R(\omega)$ . The multi-stage fitting improves the reliability, the stability and the robustness of the estimates with respect to a direct, nonlinear fitting.

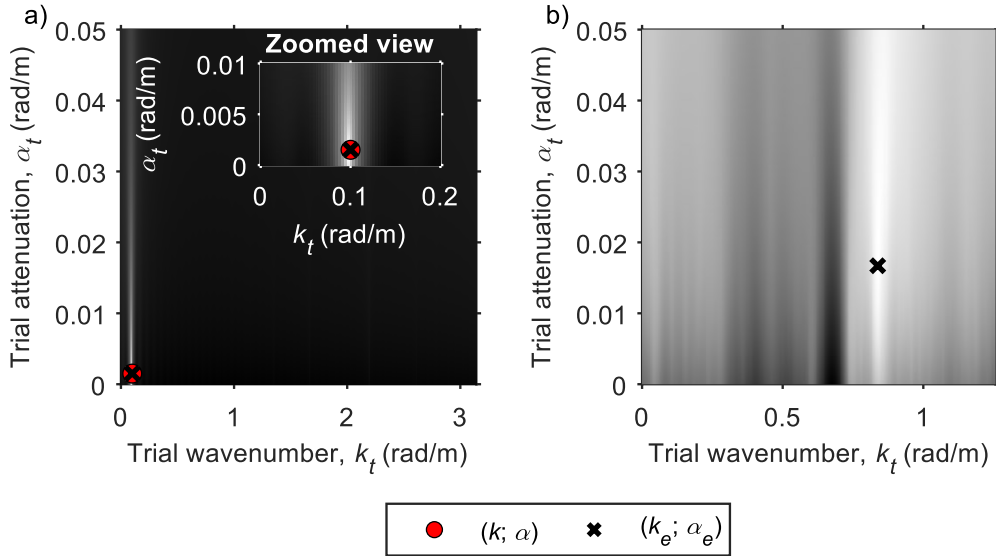


Figure B-1. Objective function of the nonlinear regression procedure adopted in the TFM, represent as pseudo-color plots mapping its magnitude as a function of trial values of the wavenumber and the attenuation: a) Waveform SW1, which represents the ideal case of a planar wave, where the estimated wave parameters  $(k_e; \alpha_e)$  are compared with the theoretical values  $(k; \alpha)$ ; b) Data from GV-H5 array (see Section 7.1), which represents a real case.

## B.2 Wavefield decomposition approach

The WD approach (e.g., Maranò et al., 2017; Bergamo et al., 2018; Bergamo et al., 2019) interprets measured three-component displacement data to jointly obtain a maximum likelihood estimate the Rayleigh wave parameters, i.e. the complex wavenumber  $\hat{k}_R(\omega)$  and the ellipticity angle  $\zeta(\omega)$ . This approach accommodates for the presence of multiple modes of propagation in the recorded wavefield, and it identifies the most reliable number of wave components based on the Bayesian Information Criterion (BIC; Schwartz, 1978). The output of the fitting procedure depends on the parameter  $\gamma$ , that allows to control the complexity of the model and the fitting quality – specifically, at smaller  $\gamma$ , the algorithm returns a larger number identified propagation modes and it tends to overfit experimental data. The value  $\gamma = 0$  is adopted. This choice forces the procedure to adopt the maximum likelihood criterion, thus ensuring the retrieval of wave components across the whole investigated frequency range. This assumption is necessary to

allow consistent comparison with alternative processing techniques. The WD algorithm is implemented in a Python-based software (available at the following URL: <https://stefanomarano.github.io/WaveDec/>).

However, usual MASW surveys utilize vertical geophones to acquire the wavefield, but the available options implemented in the WD software do not include the attenuation estimate from the vertical component of the Rayleigh waves. For this reason, an alternative version of the WD approach has been implemented. The modified version exploits the only information provided by vertical displacement data to constrain both  $V_R(\omega)$  and  $\alpha_R(\omega)$ . In this case, information about  $\zeta(\omega)$  is inevitably lost. Figure B-2 compares the estimated dispersion and attenuation data for SW3 and SW4, based on the vertical displacement only and on three-component data. The estimates of  $V_R(\omega)$  and  $\alpha_R(\omega)$  are identical with each other, entailing a good level of reliability and correctness of the modified scheme. However, when using single-component records, the resulting wave parameters are defined over a narrower frequency range, and less information about weak wave components (i.e., non-dominant R-wave modes) is retrieved. Indeed, less experimental data are available to constrain the wave propagation model. A potential solution to compensate for the lack of estimated wave parameters might consist in decreasing the  $\gamma$  parameter, which allows for a more flexible propagation model.

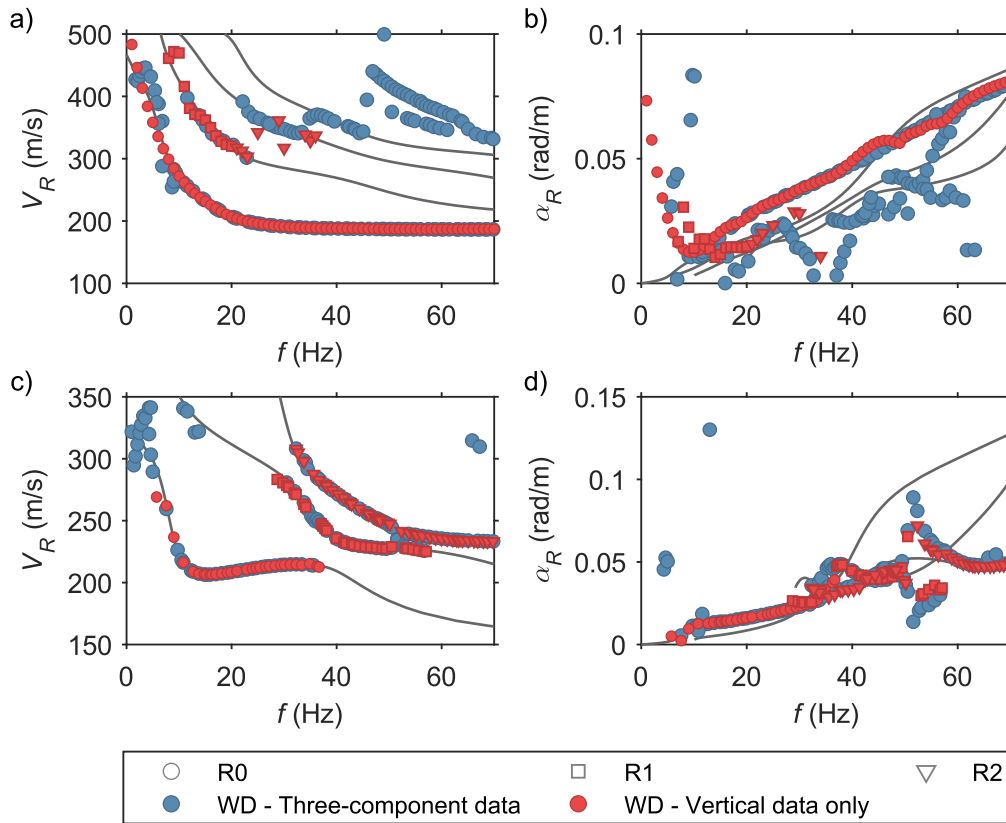


Figure B-2. Application of the WD approach in the presence of three-component data or vertical displacement data only, for SW3 and SW4: a-b) Estimated dispersion and attenuation curves for SW3; c-d) Estimated dispersion and attenuation curves for SW4.

### B.3 Generalized Half-Power Bandwidth and Circle Fit Methods

The GHPB (Badsar et al., 2010) provides an uncoupled estimate of  $V_R(\omega)$  and  $\alpha_R(\omega)$ , from the interpretation of the magnitude of the experimental  $T(r, \omega)$ , in the  $f$ - $k$  domain. Instead, the CFM infers the R-wave parameters based on the Nyquist plot of the  $f$ - $k$  spectrum of the displacement transfer function (Verachtert et al., 2017). In both cases, the transformation of  $T(r, \omega)$  into the  $f$ - $k$  domain is carried out through a Hankel transform, to account for the cylindrical shape of the wavefront (Forbriger, 2003). The transformation involves a numerical integration, which is achieved through a generalized version of the Filon's quadrature scheme (Filon, 1928; Frazer and Gettrust, 1984; Verachtert, 2018).

The GHPB first identifies the dispersion curves of each mode of propagation are first identified as spectral peaks of the  $f$ - $k$  spectrum. Then, for each

propagation mode, it derives  $\alpha_R$  at every frequency from the width of the corresponding peak. At each frequency, the bandwidth  $\Delta k_{R,j}(\omega)$  is the width of the  $f$ - $k$  spectral peak of the  $j$ -th mode, measured at an amplitude level equal to a fraction  $\gamma$  of the peak value (Figure 4-13a). Then,  $\alpha_R(\omega)$  is derived from such bandwidth, according to Eq. 4.18.

However, the estimate of the  $f$ - $k$  spectrum according to Eq. 4.17 is influenced by a truncation effect. Indeed, a rigorous estimate would require the integral to be extended up to  $r \rightarrow \infty$ , but the limited length of the acquisition array forces a truncation to a finite value of  $r$ . The result is a widening of the peaks in the  $f$ - $k$  spectrum, that induce an overestimation of  $\alpha_R(\omega)$ . For this reason, Badsar et al. (2010) apply an exponentially decaying window to recorded data prior to the calculation of the  $f$ - $k$  spectrum:

$$w(r, \omega) = e^{-\alpha_{art}(\omega)r} \quad (\text{B.1})$$

The aim of this window is to accelerate the spatial decay of the recorded signal, thus the truncation effect on the estimated attenuation becomes negligible (Fladung and Rost, 1997). The decay rate  $\alpha_{art}(\omega)$  is derived by forcing the amplitude of the windowed signal at the farthest receiver to be small enough compared with the one recorded at the closest sensor. Specifically,  $\alpha_{art}(\omega)$  is the smallest nonnegative value for which the following inequality is satisfied:

$$\frac{|w(r_N, \omega)T(r_N, \omega)|}{|w(r_1, \omega)T(r_1, \omega)|} \leq q \quad (\text{B.2})$$

The control parameter  $q$  should be chosen as a function of site characteristics and the survey setup, although it is typically equal to  $10^{-4}$ . On the other side, the application of such window introduces an artificial attenuation due to the stronger decay of the signal amplitude in space, resulting in an increase in  $\alpha_R(\omega)$  of a value equal to the decay rate  $\alpha_{art}(\omega)$ . Hence, the estimate obtained from the width of each peak should be reduced by this term to obtain a correct value of the R-wave attenuation. The whole procedure is synthetized in Algorithm 5.

Algorithm 5 Generalized Half-Power Bandwidth	
<b>Input:</b>	$\{u_z(r_n, t_s)\}_{n=1, s=1}^{N, N_T}$ : particle displacement recorded at $N$ sensors with offset $r_n$ , at $N_T$ time samples $t_s$
1:	Compute displacement transfer function $\{T(r_n, \omega_i)\}_{n=1, j=1}^{N, N_\omega}$ from Eq. 4.11, for $N_\omega$ frequencies $\omega_i$
2:	<b>for</b> $i = 1 : N_\omega$ <b>do</b>
3:	Calculate $\alpha_{art}(\omega_i)$ from Eq. B.2
4:	Apply the window $T(r, \omega_i) \leftarrow w(r, \omega_i)T(r, \omega_i)$
5:	Compute $f$ - $k$ spectrum $T(k_r, \omega_i)$ from Eq. 4.16

```

6:          Identify peaks  $\{k_{Re,j}(\omega_i); T(k_{Re,j}(\omega_i), \omega_i)\}_{j=1}^{M(\omega_i)}$  of the  $f$ - $k$  spectrum, for
            $M(\omega_i)$  modes
7:          for  $j = 1 : M(\omega_i)$  do
8:              Compute  $\alpha_{Re,j}(\omega_i)$  from Eq. 4.17
9:               $\alpha_{Re,j}(\omega_i) \leftarrow \alpha_{Re,j}(\omega_i) - \alpha_{art}(\omega_i)$ 
10:         end for
11:     end for

```

Instead, the CFM is intimately connected with the GHPB as it uses the corresponding  $V_R(\omega)$  and  $\alpha_R(\omega)$  estimates as starting point. The principle of the CFM relies on an alternative representation of the  $f$ - $k$  spectrum of the displacement transfer function, based on the Nyquist plot, which compares the real and the imaginary part of a complex number. From the analogy between the spectral shape of the R-wave spectrum at each frequency and the frequency response function of a Multiple-Degree-Of-Freedom (MDOF) system, it can be demonstrated that the Nyquist plot of the  $f$ - $k$  spectrum is a combination of circles, each one corresponding to a single Rayleigh mode (Ewins, 1984; Figure 4-14b). The CFM estimates  $V_R(\omega)$  and  $\alpha_R(\omega)$  based on the geometry of the circles. The whole procedure is synthesized in Algorithm 6.

```

Algorithm 6 Circle Fit Method
Input:  $\{u_z(r_n, t_s)\}_{n=1, s=1}^{N, N_T}$ : particle displacement recorded at  $N$  sensors with offset  $r_n$ , at  $N_T$  time
samples  $t_s$ 
1:     Compute displacement transfer function  $\{T(r_n, \omega_i)\}_{n=1, j=1}^{N, N_\omega}$  from Eq. 4.11, for  $N_\omega$ 
frequencies  $\omega_i$ 
2:     for  $i = 1 : N_\omega$  do
3:         Calculate  $\alpha_{art}(\omega_i)$  from Eq. B.2
4:         Apply the window  $T(r, \omega_i) \leftarrow w(r, \omega_i)T(r, \omega_i)$ 
5:         Compute  $f$ - $k$  spectrum  $T(k_r, \omega_i)$  from Eq. 4.16
6:         Identify peaks  $\{k_{Re,j}(\omega_i); T(k_{Re,j}(\omega_i), \omega_i)\}_{j=1}^{M(\omega_i)}$  of the  $f$ - $k$  spectrum, for
            $M(\omega_i)$  modes
7:         for  $j = 1 : M(\omega_i)$  do
8:             Compute  $k_{Re,j}(\omega_i)$  as the point with max. relative distance in the
           Nyquist plot of  $T(k_r, \omega_i)$ 
9:             Update  $k_{Re,j}(\omega_i)$  by maximizing the angular sweep
10:            Compute  $\alpha_{Re,j}(\omega_i)$  from Eq. 4.18
11:             $\alpha_{Re,j}(\omega_i) \leftarrow \alpha_{Re,j}(\omega_i) - \alpha_{art}(\omega_i)$ 
12:        end for
13:     end for

```

In the GHPB and the CFM method, the estimated  $V_R(\omega)$  and  $\alpha_R(\omega)$  depend on two parameters, i.e.,  $\gamma$  and  $q$ . The quantity  $q$  controls the exponential spatial

window which is applied to the experimental  $T(r, \omega)$ , to reduce the influence of spatial leakage on the  $f$ - $k$  spectrum. Instead,  $\gamma$  sets the reference power level corresponding to the bandwidth from which  $\alpha_R(\omega)$  is then derived. The CFM is also sensitive to  $q$ , whereas the dependence of the estimated R-wave parameters on  $\gamma$  is usually negligible. Indeed, this technique uses the GHPB estimate of  $\alpha_R(\omega)$  as a starting value, and it corrects it based on the shape of the  $f$ - $k$  spectrum. Badsar et al. (2010) and Verachtert et al. (2017) adopted  $\gamma = 0.99$  and  $q = 10^{-4}$ . However, both  $\gamma$  and  $q$  depend on the soil deposit characteristics and on the acquisition layout, hence a site-specific parametric study to assess their influence on the resulting R-wave parameters is required.

For instance, Figure B-3 reports results of the calibration analysis carried out on SW2, for both the GHPB and the CFM. The assessment considered 11 log-spaced  $q$  values, ranging between  $10^{-10}$  and 1, whereas the following  $\gamma$  values were adopted:  $\sqrt{2}/2$  (i.e., the basic half-power bandwidth), 0.9, 0.95, 0.99, 0.995, and 0.999. Interestingly, both techniques failed in returning an estimate of  $k_R(\omega)$  and  $\alpha_R(\omega)$  for a broad range of  $q$ , and results are available only for  $q > 10^{-2}$ . Furthermore, the observed influence of  $q$  on the obtained value  $k_{R,e}(\omega)$  in this small interval is almost negligible, and a small underestimation of  $k_R(\omega)$  is noticed – the relative difference is about 5%. Instead, the resulting attenuation  $\alpha_{R,e}(\omega)$  is remarkably sensitive to  $q$ , as the estimation error is minimum for  $q = 10^{-2}$  and it doubles itself elsewhere. As far as  $\gamma$  is concerned, the optimal choice corresponds to  $\sqrt{2}/2$  for the GHPB, whereas its influence on  $\alpha_{R,e}(\omega)$  is negligible when using the CFM.

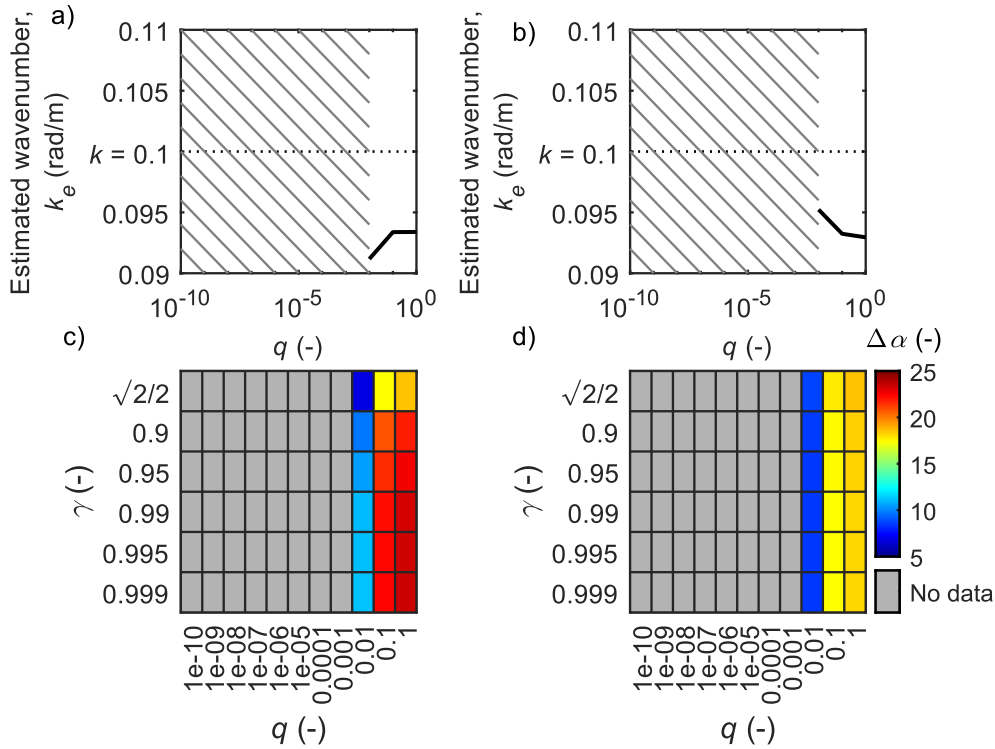


Figure B-3. Influence of the model parameters  $\gamma$  and  $q$  onto the estimated R-wave data, according to the GHPB and the CFM: a-b) Influence of  $q$  on the estimated wavenumber  $k_e$ , for the GHPB (a) and the CFM (b); c-d) Influence of  $q$  and  $\gamma$  on the estimated attenuation  $\alpha_e$ , for the GHPB (c) and the CFM (d). The estimation error in the attenuation is quantified by the relative error  $\Delta\alpha$ , i.e., the error normalized with respect to the theoretical value. Data refer to SW2.

These results may suggest a strong site- and acquisition setup-dependence of the optimal  $\gamma$  and  $q$ , due to the large discrepancy with the values proposed by Badsar et al. (2010) and Verachtert et al. (2017). However, the limited number of available data does not allow to draw general conclusions on the influence of these parameters on the estimated R-wave data, at least in this case. Furthermore, in no scenario the estimated attenuation well matches the theoretical value, as the estimation error is always greater than 5. On the other side, this result highlights a potential drawback of using the GHPB and the CFM to estimate R-wave parameters. Indeed, all the  $q$  values where no estimate of  $k_R(\omega)$  and  $\alpha_R(\omega)$  is returned correspond to conditions where no peak is identified in the  $f$ - $k$  spectrum. The absence of such peak arises from the combination of two factors. On the one side, the computation scheme used to transform  $T(r, \omega)$  into the  $f$ - $k$  domain suffers from numerical instability at very low  $k$  values, and the magnitude of transformed data can be rather large in this range. Furthermore, as  $q$  decreases, each spectral



peak becomes broader and with smaller amplitude, entailing an apparent loss in resolution in the spectral domain. Thus, at low  $q$  values, the spectral peak corresponding to the investigated wave component is quite small, and it may be masked by the anomalous increase in the magnitude at low  $k$ . This issue becomes critical when the investigated wave component is characterized by low  $k_R(\omega)$ , as in SW2, where  $k = 0.1$ . Therefore, both the GHPB and the CFM might not correctly identify the R-wave parameters in the low-frequency range, where the corresponding Rayleigh waves usually exhibit long wavelengths, i.e. small wavenumbers. This also probably represents the reason why both Badsar et al. (2010) and Verachtert et al. (2017) returned the R-wave parameters and information about calibration data only at frequencies greater than 15 Hz.

To highlight the influence of  $\gamma$  and  $q$  on the estimated wave parameters, Figure B-4 reports the results of the calibration study on an alternative cylindrical wavefield, with  $k = 1.5$  rad/m and  $\alpha = 0.025$  rad/m. The acquisition layout is the same of SW2. In this case, both the GHPB and the WD do not fail to estimate the R-wave parameters in all the investigated  $q$  range. Furthermore, the average estimation error for the wavenumber and the attenuation is much smaller. In general, the error in  $k_R$  is less than 5% and it reduces down as  $q$  increases, becoming negligible at  $q > 10^{-5} \div 10^{-2}$ . Furthermore, the sensitivity of the CFM on  $q$  is less relevant and the estimation error is smaller than in GHPB. As for the attenuation estimate, the best matching is achieved for  $q = 10^{-5}$ . The influence of  $\gamma$  on the GHPB results is still apparent, as the quality of the estimate is improved for  $\gamma = 0.99$ , whereas its role on the CFM is negligible. Furthermore, the closest match is achieved with the CFM.

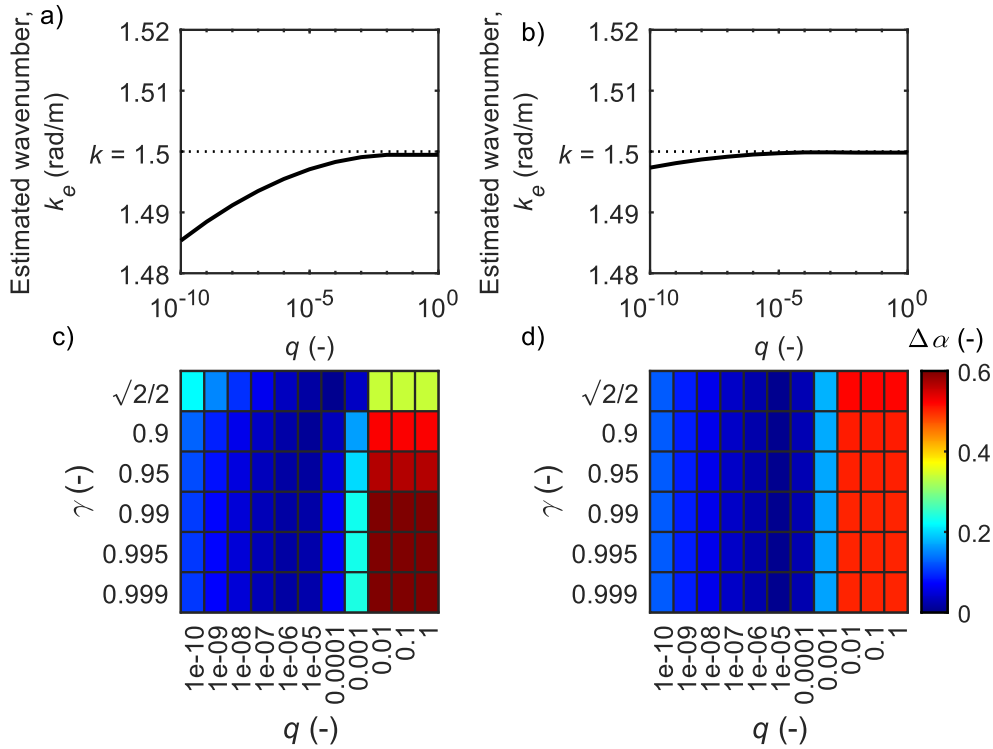


Figure B-4. Influence of the model parameters  $\gamma$  and  $q$  onto the estimated R-wave data, according to the GHPB and the CFM: a-b) Influence of  $q$  on the estimated wavenumber  $k_e$ , for the GHPB (a) and the CFM (b); c-d) Influence of  $q$  and  $\gamma$  on the estimated attenuation  $\alpha_e$ , for the GHPB (c) and the CFM (d). The estimation error in the attenuation is quantified by the relative error  $\Delta\alpha$ , i.e., the error normalized with respect to the theoretical value. Data refer to a modified version of SW2, with  $k = 1.5$  rad/m and  $\alpha = 0.025$  rad/m.

As the GHPB and the CFM exhibit strong similarities, the present study focuses on a single method, and any specific feature of the other is specified when needed. This study adopts the CFM as representative of this family of techniques. Indeed, Verachtert et al. (2017) demonstrated that the CFM provides more accurate estimates of  $V_R(\omega)$  than the peak picking of the  $f$ - $k$  spectrum and it is more reliable at deriving  $\alpha_R(\omega)$  than the GHPB, for both the fundamental mode and higher modes. The better performance is also highlighted in Figure B-4, for both the wavenumber and the attenuation. Besides, the estimated R-wave parameters are less sensitive to  $q$ , and they are independent from  $\gamma$ . Therefore, this technique is less affected by the epistemic uncertainty linked with the parameter choice.

Figure B-5 reports the results of the calibration study for the CFM, carried out on SW3 and SW4, that represent the outcome of a more realistic surface wave

test. As  $q$  increases, the matching between predicted and theoretical dispersion curves slightly improves, and a significant broadening in the investigated frequency range is noticed. The gradual extension at low frequencies results from the presence of narrower peaks in the  $f$ - $k$  spectrum, for which the influence of computation issues at low wavenumbers becomes less remarkable. As for attenuation data, the best matching is achieved for  $q = 10^{-4} \div 10^{-3}$ , although a significant overestimation occurs at low frequencies. Similar results are observed for higher modes, highlighting that the recommended values of the parameters are reliable also in these synthetic cases. Furthermore, no influence of  $\gamma$  on the estimated attenuation is observed.

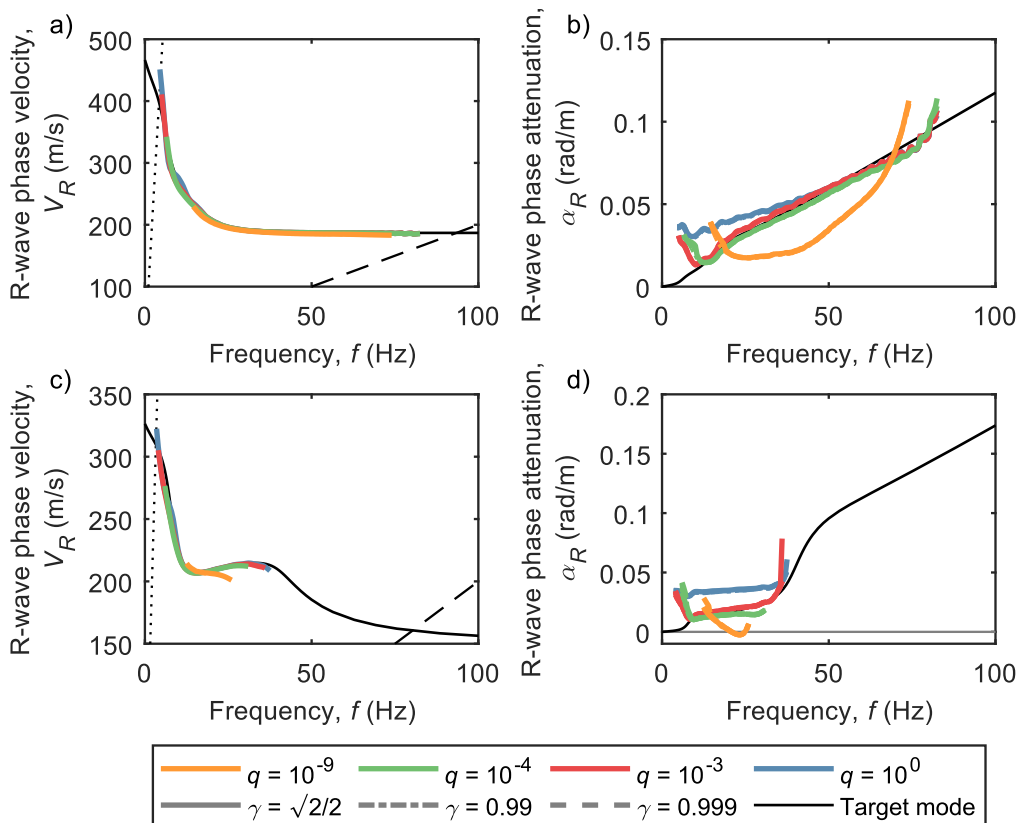


Figure B-5. Influence of the model parameters  $\gamma$  and  $q$  onto the estimated R-wave data, according to the CFM: a-b) Influence of  $q$  on the estimated wavenumber  $k_e$ , for SW3 (a) and SW4 (b); c-d) Influence of  $q$  and  $\gamma$  on the estimated attenuation  $\alpha_e$ , for SW3 (c) and SW4 (d). The comparison is carried out for the fundamental mode. The dashed lines denote the array resolution limits.

# Appendix C

## Scaling properties of the solution of the forward Rayleigh problem

The Rayleigh eigenvalue problem in linear, viscoelastic layered media can be solved according to the formalism of matrix notation. This study adopts the notation used in Strobbia (2003) and Socco and Boiero (2008). Although the original scheme is valid in elastic conditions, the generalization into a linear, viscoelastic medium is immediate by the virtue of the correspondence principle, according to which the analytical formulation is unchanged but with complex-valued parameters replacing the elastic ones.

The Rayleigh eigenvalue problem is associated with a characteristic equation, which assumes an implicit form:

$$\Phi_R[\mathcal{V}_S(z), \mathcal{V}_P(z), \rho(z), \mathcal{K}_R, \omega] = 0 \quad (\text{C.1})$$

The functional form  $\Phi_R[\cdot]$  is named “secular function” and it is a highly nonlinear, transcendental function of the arguments. In the equation, the unknown is the wavenumber  $\mathcal{K}_R$ , that includes the Rayleigh wave propagation characteristics at the considered frequency  $\omega$ . The parameters describing the layered medium are the complex-valued S-wave velocity  $\mathcal{V}_S$ , the complex-valued P-wave velocity  $\mathcal{V}_P$  and the mass density  $\rho$ . Each velocity term depends on the corresponding body-wave phase velocity ( $V_S$ ,  $V_P$ ) and phase damping ratio ( $D_S$ ,  $D_P$ ), as follows:

$$\mathcal{V}_\chi = \frac{V_\chi}{\sqrt{1+4D_\chi^2}} \left[ \frac{1 + \sqrt{1+4D_\chi^2}}{2} + iD_\chi \right] \approx V_\chi \cdot [1 + iD_\chi], \quad \chi = \text{P, S} \quad (\text{C.2})$$

Note that these quantities are dependent on the frequency, however this is not explicitly reported for simplicity.

In layered media, the secular function is linked with the 2<sup>nd</sup> order matrix quantity  $R_{II}$ :

$$\Phi_R[\mathcal{V}_S(z), \mathcal{V}_P(z), \rho(z), \mathcal{K}_R, \omega] = \det \mathbf{R}_{II} = 0 \quad (\text{C.3})$$

$\mathbf{R}_{ll}$  is a 2<sup>nd</sup> order matrix obtained from the partition of a matrix  $\mathbf{R}$ , that relates the displacement and the stress state at the free surface with the displacement potential at the interface with the half space:

$$\mathbf{R} = \begin{bmatrix} \mathbf{R}_{11} & \mathbf{R}_{12} \\ \mathbf{R}_{21} & \mathbf{R}_{22} \end{bmatrix} \quad (\text{C.4})$$

The matrix  $\mathbf{R}$  derives from the combination of matrices depending on the mechanical parameters and the thicknesses of each layer:

$$\mathbf{R} = \mathbf{A}_L^{-1} \mathbf{G}_{L-1} \cdots \mathbf{G}_2 \mathbf{G}_1, \quad \mathbf{G}_l = \mathbf{A}_l \mathbf{E}_l \mathbf{A}_l^{-1} \quad (\text{C.5})$$

The matrix  $\mathbf{A}_l$  collects the mechanical parameters of the  $l$ -th layer, as it contains  $\mathcal{V}_{S,l}$ ,  $\mathcal{V}_{P,l}$  and the mass density  $\rho_l$  as well as the unknown R-wave wavenumber  $\tilde{\kappa}_R$ :

$$\mathbf{A}_l = \begin{bmatrix} i\tilde{\kappa}_R & -n_l & i\tilde{\kappa}_R & n_l \\ m_l & i\tilde{\kappa}_R & -m_l & i\tilde{\kappa}_R \\ \mu_l a_l & i\tilde{\kappa}_R \mu_l n_l & \mu_l a_l & i\tilde{\kappa}_R \mu_l n_l \\ i\tilde{\kappa}_R \mu_l m_l & -\mu_l a_l & i\tilde{\kappa}_R \mu_l m_l & -\mu_l a_l \end{bmatrix} \quad (\text{C.6})$$

$$\mathbf{A}_l^{-1} = \frac{\mathcal{V}_{S,l}^2}{2\mu_l m_l n_l \omega^2} \begin{bmatrix} 2i\mu_l \tilde{\kappa}_R m_l n_l & \mu_l a_l n_l & m_l n_l & i\tilde{\kappa}_R n_l \\ -\mu_l a_l m_l & 2i\mu_l \tilde{\kappa}_R m_l n_l & i\tilde{\kappa}_R m_l & -m_l n_l \\ 2i\mu_l \tilde{\kappa}_R m_l n_l & -\mu_l a_l n_l & m_l n_l & -i\tilde{\kappa}_R n_l \\ \mu_l a_l m_l & 2i\mu_l \tilde{\kappa}_R m_l n_l & -i\tilde{\kappa}_R m_l & -m_l n_l \end{bmatrix}$$

where:

$$m_l^2 = \tilde{\kappa}_R^2 + \frac{\omega^2}{\mathcal{V}_{P,l}^2}, \quad n_l^2 = \tilde{\kappa}_R^2 + \frac{\omega^2}{\mathcal{V}_{S,l}^2}, \quad a_l = 2\tilde{\kappa}_R^2 + \frac{\omega^2}{\mathcal{V}_{S,l}^2} \quad (\text{C.7})$$

Instead, the matrix  $\mathbf{E}_l$  includes the influence of the layer thickness  $H_l$ :

$$\mathbf{E}_l = \begin{bmatrix} \exp(m_l H_l) & 0 & 0 & 0 \\ 0 & \exp(n_l H_l) & 0 & 0 \\ 0 & 0 & \exp(-m_l H_l) & 0 \\ 0 & 0 & 0 & \exp(-n_l H_l) \end{bmatrix} \quad (\text{C.8})$$

The demonstration of the scaling properties in the linear viscoelastic case relies on the formulation characterizing the  $\mathbf{R}_{ll}$  determinant, for which a simplified formula allows an immediate estimation. Indeed, as  $\mathbf{R}$  is a matrix product,  $R_{ll}$  can be computed as the product of related 2<sup>nd</sup> order sub-determinants:

$$\mathbf{R} = \mathbf{A}_L^{-1} \mathbf{G}_{L-1} \cdots \mathbf{G}_2 \mathbf{G}_1 \Rightarrow \det \mathbf{R}_{11} = \mathbf{R}_{12}^{12} = \left( \mathbf{A}_L^{-1} \right)_{ab}^{12} \cdot \left( \mathbf{G}_{L-1} \right)_{cd}^{ab} \cdots \left( \mathbf{G}_2 \right)_{uv}^{st} \left( \mathbf{G}_1 \right)_{12}^{uv} \quad (\text{C.9})$$

In the equation,  $\mathbf{M}_{cd}^{ab}$  is the 2<sup>nd</sup> order sub-determinant of the matrix  $\mathbf{M}$ , involving rows  $a$  and  $b$  and columns  $c$  and  $d$ . The formula is valid for any  $m < n$ , excluding couples as  $cd$  and  $dc$ . The sub-determinants are listed below:

$$\begin{aligned}
\mathbf{G}_l|_{12}^{12} = \mathbf{G}_l|_{34}^{34} &= -2\gamma_l(\gamma_l + 1) + (2\gamma_l^2 + 2\gamma_l + 1)c_{m,l}c_{n,l} - [(\gamma_l + 1)^2 + \gamma_l^2 p_l^2 q_l^2] s_{m,l} s_{n,l} \\
\mathbf{G}_l|_{13}^{12} = \mathbf{G}_l|_{34}^{24} &= (\rho_l \mathcal{V}_R^2 \tilde{\mathcal{K}}_R)^{-1} [-c_{m,l} s_{n,l} + p_l^2 s_{m,l} c_{n,l}] \\
\mathbf{G}_l|_{14}^{12} = \mathbf{G}_l|_{23}^{12} = \mathbf{G}_l|_{34}^{14} = \mathbf{G}_l|_{34}^{23} &= -i(\rho_l \mathcal{V}_R^2 \tilde{\mathcal{K}}_R)^{-1} \{ (2\gamma_l + 1)[1 - c_{m,l} c_{n,l}] + (\gamma_l + 1 + \gamma_l p_l^2 q_l^2) s_{m,l} s_{n,l} \} \\
\mathbf{G}_l|_{24}^{12} = \mathbf{G}_l|_{34}^{13} &= (\rho_l \mathcal{V}_R^2 \tilde{\mathcal{K}}_R)^{-1} [s_{m,l} c_{n,l} - q_l^2 c_{m,l} s_{n,l}] \\
\mathbf{G}_l|_{34}^{12} &= -(\rho_l \mathcal{V}_R^2 \tilde{\mathcal{K}}_R)^{-2} \{ 2[1 - c_{m,l} c_{n,l}] + (1 + p_l^2 q_l^2) s_{m,l} s_{n,l} \} \\
\mathbf{G}_l|_{12}^{13} = \mathbf{G}_l|_{24}^{34} &= -(\rho_l \mathcal{V}_R^2 \tilde{\mathcal{K}}_R) [\gamma_l^2 q_l^2 c_{m,l} s_{n,l} - (\gamma_l + 1)^2 s_{m,l} c_{n,l}] \\
\mathbf{G}_l|_{13}^{13} = \mathbf{G}_l|_{24}^{24} &= c_{m,l} c_{n,l} \\
\mathbf{G}_l|_{14}^{13} = \mathbf{G}_l|_{23}^{13} = \mathbf{G}_l|_{24}^{14} = \mathbf{G}_l|_{24}^{23} &= i[(\gamma_l + 1) s_{m,l} c_{n,l} - \gamma_l q_l^2 c_{m,l} s_{n,l}] \\
\mathbf{G}_l|_{24}^{13} &= -q_l^2 s_{m,l} s_{n,l} \\
\mathbf{G}_l|_{12}^{14} = \mathbf{G}_l|_{12}^{23} = \mathbf{G}_l|_{14}^{34} = \mathbf{G}_l|_{23}^{34} &= -i(\rho_l \mathcal{V}_R^2 \tilde{\mathcal{K}}_R) \{ \gamma_l(\gamma_l + 1)(2\gamma_l + 1)[1 - c_{m,l} c_{n,l}] + [(\gamma_l + 1)^3 + \gamma_l^3 p_l^2 q_l^2] s_{m,l} s_{n,l} \} \\
\mathbf{G}_l|_{13}^{14} = \mathbf{G}_l|_{13}^{23} = \mathbf{G}_l|_{14}^{24} = \mathbf{G}_l|_{23}^{24} &= -i[(\gamma_l + 1) c_{m,l} s_{n,l} - \gamma_l p_l^2 s_{m,l} c_{n,l}] \\
\mathbf{G}_l|_{14}^{14} = \mathbf{G}_l|_{23}^{23} &= 1 + 2\gamma_l(\gamma_l + 1)[1 - c_{m,l} c_{n,l}] + [(\gamma_l + 1)^2 + \gamma_l^2 p_l^2 q_l^2] s_{m,l} s_{n,l} \\
\mathbf{G}_l|_{23}^{14} = \mathbf{G}_l|_{14}^{23} &= \mathbf{G}_l|_{14}^{14} - 1 \\
\mathbf{G}_l|_{12}^{24} = \mathbf{G}_l|_{13}^{34} &= -(\rho_l \mathcal{V}_R^2 \tilde{\mathcal{K}}_R) [(\gamma_l + 1)^2 c_{m,l} s_{n,l} - \gamma_l^2 p_l^2 s_{m,l} c_{n,l}] \\
\mathbf{G}_l|_{13}^{24} &= -p_l^2 s_{m,l} s_{n,l} \tag{C.10} \\
\mathbf{G}_l|_{12}^{34} &= (\rho_l \mathcal{V}_R^2 \tilde{\mathcal{K}}_R)^2 \{ 2\gamma_l^2 (\gamma_l + 1)^2 [1 - c_{m,l} c_{n,l}] + [(\gamma_l + 1)^4 + \gamma_l^4 p_l^2 q_l^2] s_{m,l} s_{n,l} \}
\end{aligned}$$

On the other side, part of the subdeterminants of the half-space matrix  $\mathbf{A}_L$  are involved:

$$\begin{aligned}
\mathbf{A}_L^{-1}|_{12}^{12} &= (4\tilde{\mathcal{K}}_R)^{-2} [2\gamma_L + (\gamma_L + 1)^2 p_L^2 q_L^2] \\
\mathbf{A}_L^{-1}|_{13}^{12} &= (4\rho_L \mathcal{V}_R^2 \tilde{\mathcal{K}}_R^3 p_L)^{-1} \\
\mathbf{A}_L^{-1}|_{14}^{12} = \mathbf{A}_L^{-1}|_{23}^{12} &= i(4\rho_L \mathcal{V}_R^2 \tilde{\mathcal{K}}_R^3)^{-1} [(\gamma_L + 1) p_L^{-1} q_L^{-1} - \gamma_L] \\
\mathbf{A}_L^{-1}|_{34}^{12} &= (4\rho_L^2 \mathcal{V}_R^2 \tilde{\mathcal{K}}_R^2)^{-1} (p_L^{-1} q_L^{-1} - 1)
\end{aligned} \tag{C.11}$$

According to Eq. E.9, the secular function derives from the product of the factors listed in Eq. E.10 and Eq. E.11. As some parameters intervene only as a product and the solution is a zero of the secular function, the scaling properties should ensure that the quantities listed below remain simultaneously unchanged:

$\gamma_l, p_l = m_l / \bar{\kappa}_R, q_l = n_l / \bar{\kappa}_R, c_{m,l}$ , and  $c_{n,l}$  for  $l = 1, \dots, L$ . Note that the invariability of  $p_l$  and  $c_{m,l}$  guarantees the invariability for  $s_{m,l}$ ; similarly, unchanged  $q_l$  and  $c_{n,l}$  ensures constant  $s_{n,l}$ . The remaining quantities appear inside products, hence they do not directly affect the locations of the zeros.

At this point, let us consider a layered medium (labeled as medium “0”) with the following mechanical parameters:  $H_0 = H, V_{S,0} = V_S, V_{P,0} = V_P, D_{S,0} = D_S$ , and  $D_{P,0} = D_P$ . The density  $\rho$  is not considered in this study, because its role in the Rayleigh eigenvalue problem is less relevant (e.g., Foti et al., 2014). Also, the quantities  $H, V_S, V_P, D_S$ , and  $D_P$  have to be interpreted as depth-dependent discrete functions. For this medium, the eigenvalue problem returns the dispersion curve  $V_{R,0}(\omega) = V_R(\omega)$  and the attenuation curve  $\alpha_{R,0}(\omega) = \alpha_R(\omega)$ . Furthermore, the corresponding secular function involves parameters  $\gamma_0, \tilde{m}_0, \tilde{n}_0, c_{m,0}$ , and  $c_{n,0}$  – the layer index subscript “ $l$ ” is removed for simplicity.

## C.1 Layer velocities

Firstly, the effect of scaling body-wave phase velocities is investigated. In this case, for each layer,  $H, D_S, D_P$ , and  $\rho$  are unchanged, whereas  $V_S$  and  $V_P$  are simultaneously multiplied by a real-valued, positive constant  $c_{VB}$ . The simultaneous scaling guarantees no variations in the Poisson’s ratio. Therefore, the modified medium (labeled as medium “1”) is characterized by  $H_1 = H_0, V_{S,1} = c_{VB} \times V_{S,0}, V_{P,1} = c_{VB} \times V_{P,0}, D_{S,1} = D_{S,0}$ , and  $D_{P,1} = D_{P,0}$ .

This modification of the earth model is compatible with the causality constraint that a linear viscoelastic medium should fulfil. Indeed, this constraint relates stiffness and attenuation characteristics in a linear viscoelastic medium by means of the solution of the Kramers-Kronig relation (Christensen, 2012):

$$D_\chi(\omega) = \frac{\frac{2\omega V_\chi(\omega)}{\pi V_\chi(0)} \cdot \int_0^\infty \left( \frac{V_\chi(0)}{V_\chi(\tau)} \cdot \frac{d\tau}{\tau^2 - \omega^2} \right)}{\left[ \frac{2\omega V_\chi(\omega)}{\pi V_\chi(0)} \cdot \int_0^\infty \left( \frac{V_\chi(0)}{V_\chi(\tau)} \cdot \frac{d\tau}{\tau^2 - \omega^2} \right) \right]^2} - 1 \quad (\text{C.12})$$

where  $V_\chi(0) = \lim_{\omega \rightarrow 0} V_\chi(\omega)$ . This is not the general formulation, but it is a derived form valid when  $V_\chi$  is prescribed. However, assuming that  $V_{\chi,0}$  and  $D_{\chi,0}$  fulfil this relationship, also  $V_{\chi,1} = c_{VB} \times V_{\chi,0}$  and  $D_{\chi,1} = D_{\chi,0}$  are solution of the equation, as  $V_\chi$  appears only as the ratio with the zero-frequency value.

Furthermore, according to Eq. C-2, this operation is equivalent to scaling the magnitude of  $\mathcal{V}_\chi$  ( $\chi = P, S$ ) by the factor  $c$  or, alternatively,  $\mathcal{V}_\chi$  itself by the factor  $c_{VB}$ .

Under this assumption, it is demonstrated that the secular function does not change, when setting the dispersion curve as  $V_{R,1}(\omega) = c_{VB} \times V_{R,0}(c_{VB} \times \omega)$  and the attenuation curve  $\alpha_{R,1}(\omega) = \alpha_{R,0}(c_{VB} \times \omega)$ .

In this case, we have  $k_{R,1}(\omega) = k_{R,0}(c_{VB} \times \omega)$  and:

$$\begin{aligned}
m_1^2 &= \mathcal{K}_{R,1}^2 + \frac{c_{VB}^2 \omega^2}{\mathcal{V}_{P,1}^2} = \mathcal{K}_{R,0}^2 + \frac{c_{VB}^2 \omega^2}{c_{VB}^2 \mathcal{V}_{P,0}^2} = m_0^2 \\
n_1^2 &= \mathcal{K}_{R,1}^2 + \frac{c_{VB}^2 \omega^2}{\mathcal{V}_{S,1}^2} = \mathcal{K}_{R,0}^2 + \frac{c_{VB}^2 \omega^2}{c_{VB}^2 \mathcal{V}_{S,0}^2} = n_0^2 \\
p_1 &= \frac{\mathcal{M}_1}{\mathcal{K}_{R,1}} = \frac{\mathcal{M}_0}{\mathcal{K}_{R,0}} = p_0 \\
q_1 &= \frac{\mathcal{N}_1}{\mathcal{K}_{R,1}} = \frac{\mathcal{N}_0}{\mathcal{K}_{R,0}} = q_0 \\
c_{m,1} &= \cosh(\mathcal{K}_{R,1} p_1 H_1) = \cosh(\mathcal{K}_{R,0} p_0 H_0) = c_{m,0} \\
c_{n,1} &= \cosh(\mathcal{K}_{R,1} q_1 H_1) = \cosh(\mathcal{K}_{R,0} q_0 H_0) = c_{n,0} \\
\gamma_1 &= \frac{2\mathcal{K}_{R,1}^2 \mathcal{V}_{S,1}^2}{c_{VB}^2 \omega^2} = \frac{2\mathcal{K}_{R,1}^2 \cdot c_{VB}^2 \mathcal{V}_{S,0}^2}{c_{VB}^2 \omega^2} = \frac{2\mathcal{K}_{R,0}^2 \mathcal{V}_{S,0}^2}{\omega^2} = \gamma_0
\end{aligned} \tag{C.13}$$

Therefore, the scaling of body wave velocities induces the scaling of phase velocities combined with a simultaneous scaling of the frequency  $\omega$  by the same factor  $c$ .

## C.2 Layer thicknesses

Then, the effect of scaling layer thicknesses is investigated. In this case, for each layer,  $V_S$ ,  $V_P$ ,  $D_S$ ,  $D_P$ , and  $\rho$  are unchanged, whereas  $H$  is multiplied by a real-valued, positive constant  $c_H$ . Therefore, the modified medium (labeled as medium "1") is characterized by  $H_1 = c_H \times H_0$ ,  $V_{S,1} = V_{S,0}$ ,  $V_{P,1} = V_{P,0}$ ,  $D_{S,1} = D_{S,0}$ , and  $D_{P,1} = D_{P,0}$ .

Under this assumption, it is demonstrated that the secular function does not change, when setting the dispersion curve as  $V_{R,1}(\omega) = V_{R,0}(1 / c_H \times \omega)$  and the attenuation curve  $\alpha_{R,1}(\omega) = 1 / c_H \times \alpha_{R,0}(1 / c_H \times \omega)$ .

In this case, we have  $k_{R,1}(\omega) = 1 / c_H \times k_{R,0}(1 / c_H \times \omega)$  and:



$$\begin{aligned}
m_1^2 &= \tilde{\kappa}_{R,1}^2 + \frac{\omega^2}{c_H^2 \mathcal{V}_{P,1}^2} = \frac{1}{c_H^2} \tilde{\kappa}_{R,0}^2 + \frac{\omega^2}{c_H^2 \mathcal{V}_{P,0}^2} = \frac{1}{c_H^2} \left( \tilde{\kappa}_{R,0}^2 + \frac{\omega^2}{\mathcal{V}_{P,0}^2} \right) = \frac{1}{c_H^2} m_0^2 \\
n_1^2 &= \tilde{\kappa}_{R,1}^2 + \frac{\omega^2}{c_H^2 \mathcal{V}_{S,1}^2} = \frac{1}{c_H^2} \tilde{\kappa}_{R,0}^2 + \frac{\omega^2}{c_H^2 \mathcal{V}_{S,0}^2} = \frac{1}{c_H^2} \left( \tilde{\kappa}_{R,0}^2 + \frac{\omega^2}{\mathcal{V}_{S,0}^2} \right) = \frac{1}{c_H^2} n_0^2 \\
p_1 &= \frac{m_1}{\tilde{\kappa}_{R,1}} = \frac{\frac{1}{c_H} m_0}{\frac{1}{c_H} \tilde{\kappa}_{R,0}} = p_0 \\
q_1 &= \frac{n_1}{\tilde{\kappa}_{R,1}} = \frac{\frac{1}{c_H} n_0}{\frac{1}{c_H} \tilde{\kappa}_{R,0}} = q_0 \\
c_{m,1} &= \cosh(\tilde{\kappa}_{R,1} p_1 H_1) = \cosh\left(\frac{1}{c_H} \tilde{\kappa}_{R,0} p_0 \cdot c_H H_0\right) = \cosh(\tilde{\kappa}_{R,0} p_0 H_0) = c_{m,0} \\
c_{n,1} &= \cosh(\tilde{\kappa}_{R,1} q_1 H_1) = \cosh\left(\frac{1}{c_H} \tilde{\kappa}_{R,0} q_0 \cdot c_H H_0\right) = \cosh(\tilde{\kappa}_{R,0} q_0 H_0) = c_{n,0} \\
\gamma_1 &= \frac{2\tilde{\kappa}_{R,1}^2 \mathcal{V}_{S,1}^2}{\frac{1}{c_H^2} \omega^2} = \frac{2\frac{1}{c_H^2} \tilde{\kappa}_{R,0}^2 \mathcal{V}_{S,0}^2}{\frac{1}{c_H^2} \omega^2} = \frac{2\tilde{\kappa}_{R,0}^2 \mathcal{V}_{S,0}^2}{\omega^2} = \gamma_0
\end{aligned} \tag{C.14}$$

Thus, the scaling of layers' thicknesses induces the scaling of phase attenuations combined with a simultaneous scaling of the frequency  $\omega$  by the same factor  $c$ .

### C.3 Layer damping ratios

Finally, the effect of scaling body-wave damping ratios is investigated. In this case, for each layer,  $H$ ,  $V_S$ ,  $V_P$ , and  $\rho$  are unchanged, whereas  $D_S$  and  $D_P$  are simultaneously multiplied by a real-valued, positive constant  $c_{DB}$ . Therefore, the modified medium (labeled as medium "1") is characterized by  $H_1 = H_0$ ,  $V_{S,1} = V_{S,0}$ ,  $V_{P,1} = V_{P,0}$ ,  $D_{S,1} = c_{DB} \times D_{S,0}$ , and  $D_{P,1} = c_{DB} \times D_{P,0}$ .

At this point, an issue should be pointed out. This kind of modification of the earth model returns a set of viscoelastic parameters  $(V_{\chi,1}, D_{\chi,1})$  that is no longer a solution of the Kramers-Kronig relation equivalent to  $(V_{\chi,0}, D_{\chi,0})$ . In the general case,  $(V_{\chi,1}, D_{\chi,1})$  may even violate the causality constraint. Indeed, to accommodate the scaling in the damping ratios, the phase velocity should modify its value and its dependence on the frequency to still fulfil this constraint.

On the other side, some simplifying assumptions can be introduced. In practical applications,  $D_\chi(\omega)$  is typically assumed as constant, because experimental evidence shows that dissipative properties are not strongly sensitive to the loading frequency, at least over the seismic bandwidth (i.e., between 0.1 Hz and 10 Hz – see Section 2.2). Under this hypothesis, the Kramers-Kronig relations provide an explicit solution for  $V_\chi(\omega)$  (Aki, 2002), that allows to predict the corresponding dispersion model once the value at a reference frequency  $\omega_{ref}$  (typically equal to  $2\pi$ ) is known:

$$V_\chi(\omega) = \frac{V_\chi(\omega_{ref})}{\left[ 1 + \frac{2D_\chi}{\pi} \ln\left(\frac{\omega}{\omega_{ref}}\right) \right]} \quad (C.15)$$

Furthermore, in low-dissipative media (i.e.,  $D_\chi < 10\%$ ) under seismic loading, the frequency dependence of  $V_\chi(\omega)$  is weak, as variations range within 10% (see Chapter 3.1.2). For this reason,  $V_\chi$  is typically assumed as constant with the frequency and equal to the elastic value (e.g., Badsar, 2012). Although a linear viscoelastic model with frequency-independent stiffness and damping does not fulfil the causality constraint, this kind of model can incorporate the adopted transformation from the medium “0” to medium “1”, in which only  $D_\chi$  is scaled.

The scaling of  $D_\chi$  results in a variation of both the modulus and the phase of the complex-valued velocity  $\mathcal{V}_\chi$ . Specifically, a scaling factor can be defined for the magnitude:

$$\frac{|\mathcal{V}_{\chi,1}|}{|\mathcal{V}_{\chi,0}|} = \frac{\sqrt{1+4D_{\chi,0}^2} \cdot \left(1 + \sqrt{1+4D_{\chi,1}^2}\right)^2 + 4D_{\chi,1}^2}{\sqrt{1+4D_{\chi,1}^2} \cdot \left(1 + \sqrt{1+4D_{\chi,0}^2}\right)^2 + 4D_{\chi,0}^2} = \frac{\sqrt{1+4D_{\chi,0}^2} \cdot \left(1 + \sqrt{1+4c_{DB}D_{\chi,0}^2}\right)^2 + 4c_{DB}D_{\chi,0}^2}{\sqrt{1+4c_{DB}D_{\chi,0}^2} \cdot \left(1 + \sqrt{1+4D_{\chi,0}^2}\right)^2 + 4D_{\chi,0}^2} \quad (C.16)$$

The scaling of the magnitude in  $\mathcal{V}_\chi$  results in a scaling of both the R-wave phase velocity and the frequency, based on what stated in Section c.1. However, in low dissipative media, this scaling factor is close to the unit. Therefore, a good approximation can assume that the scaling of the damping ratio does not affect the phase velocity nor the frequency.

Instead, mapping the variations of the  $\mathcal{V}_\chi$  phase into  $\gamma_0$ ,  $p_0$ ,  $q_0$ ,  $c_{m,0}$ , and  $c_{n,0}$  is less trivial. However, a reasonable assumption might impose that the scaling of the damping ratio results in an identical scaling of the R-wave phase attenuation. The numerical example reported in Figure C-1 provides a quantification of the error introduced by this simplifying assumption. In this example, the only scaling of the damping ratio is modeled and, for the scaled model, theoretical dispersion and attenuation curves are compared with those obtained by scaling only the

original attenuation data. This example demonstrates the presence of an error between the simplified scaling procedure and the actual solution of the R-wave eigenvalue problem. However, the error is moderately small, hence the approximation introduced by this assumption is acceptable.

In summary, the scaling of all the damping ratios results in an unchanged dispersion curve and in the scaling of attenuations only in the attenuation curves.

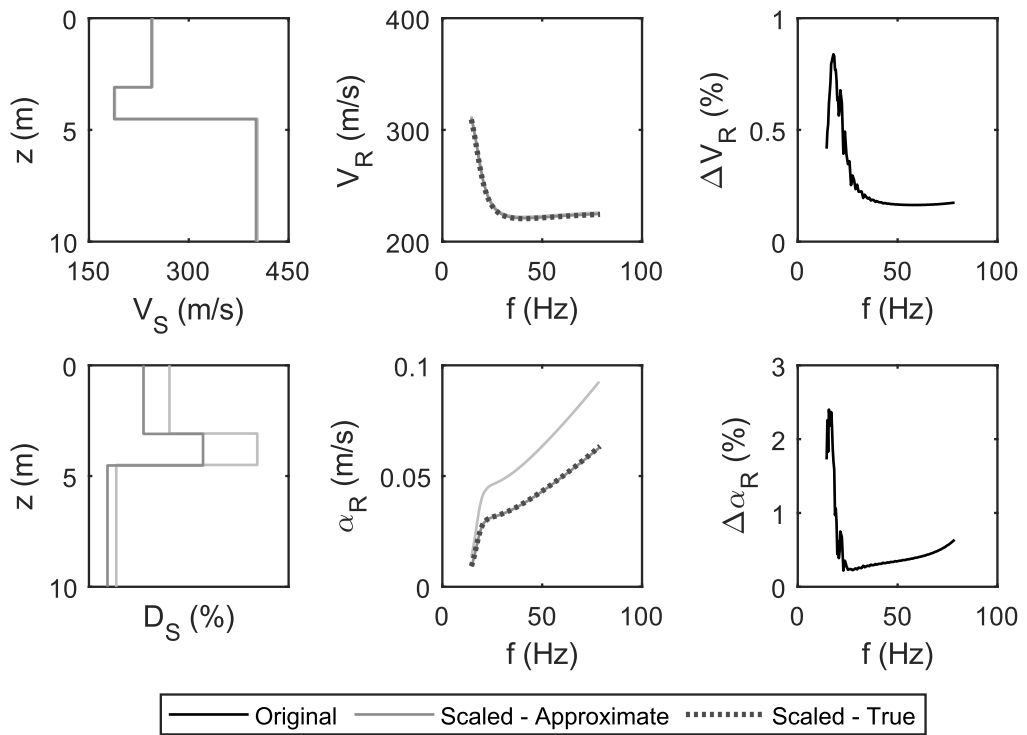


Figure C-1. Numerical example showing the approximation error introduced by the assumption that the scaling of the damping ratio maps into an equivalent scaling of the attenuation curves: a-d) Original and scaled S-wave velocity (a) and damping ratio profiles (d); b-e) Original and scaled dispersion curves (b) and attenuation curves (e); c-f) Relative difference between the approximate and the true dispersion (c) and attenuation (f) data, computed for the scaled model.

# References

- Achenbach, and Reddy. 1967. Note on wave propagation in linearly viscoelastic media, *Zeitschrift für angewandte Mathematik und Physik ZAMP*, 18: 141-144.
- Afshari, and Stewart. 2019. Insights from California Vertical Arrays on the Effectiveness of Ground Response Analysis with Alternative Damping Models, *Bulletin of the Seismological Society of America*, 109: 1250-1264.
- Aggour, Yang, and Al-Sanad. 1982. Application of the random decrement technique in the determination of damping of soils. In *European conference on earthquake engineering*. 7, 337-344.
- Aimar, Ciancimino, and Foti. 2020. An assessment of the NTC18 simplified procedure for stratigraphic seismic site amplification prediction, *Italian Geotechnical Journal - Rivista Italiana di Geotecnica*, 1.
- Ajo-Franklin, Dou, Daley, Freifeld, Robertson, Ulrich, Wood, Eckblaw, and Wagner. 2017. Time-lapse surface wave monitoring of permafrost thaw using distributed acoustic sensing and a permanent automated seismic source. In *SEG Technical Program Expanded Abstracts 2017*, edited by Society of Exploration Geophysicists, 5223-5227.
- Akeju, Senetakis, and Wang. 2017. Bayesian Parameter Identification and Model Selection for Normalized Modulus Reduction Curves of Soils, *Journal of Earthquake Engineering*: 1-29.
- Aki. 1957. Space and time spectra of stationary stochastic waves, with special reference to microtremors, *Bulletin of the Earthquake Research Institute*, 35: 415-456.
- Aki. 2002. *Quantitative seismology*.
- Al-Hunaidi. 1998. Evolution-based genetic algorithms for analysis of non-destructive surface wave tests on pavements, *NDT & E International*, 31: 273-280.
- Albarello, and Baliva. 2009. In-Situ estimates of material damping from environmental noise measurements. In *Increasing Seismic Safety by Combining Engineering Technologies and Seismological Data*, 73-84. Dordrecht: Springer.
- Ambrosini. 2006. Material damping vs. radiation damping in soil-structure interaction analysis, *Computers and Geotechnics*, 33: 86-92.
- Anderson. 1962. *An introduction to multivariate statistical analysis* (John Wiley & Sons: New York).
- Anderson. 2004. Quantitative measure of the goodness-of-fit of synthetic seismograms. In *13th World Conference on Earthquake Engineering*. International Association for Earthquake Engineering.

- Anderson, and Hough. 1984. A model for the shape of the Fourier amplitude spectrum of acceleration at high frequencies, *Bulletin of the Seismological Society of America*, 74: 1969-1993.
- Arai, and Tokimatsu. 2005. S-wave velocity profiling by joint inversion of microtremor dispersion curve and horizontal-to-vertical (H/V) spectrum, *Bulletin of the Seismological Society of America*, 95: 1766-1778.
- Archuleta, Seale, Sangas, Baker, and Swain. 1992. Garner Valley Downhole Array of Accelerometers: Instrumentation and Preliminary Data Analysis, *Bulletin of the Seismological Society of America*, 82: 1592-1621.
- Argyroudis, Kaynia, and Ptilakis. 2013. Development of fragility functions for geotechnical constructions: Application to cantilever retaining walls, *Soil Dynamics and Earthquake Engineering*, 50: 106-116.
- Arias. 1970. A measure of earthquake intensity. In *Seismic Design in Nuclear Power Plants*, 438-483. Massachusetts: MIT Press.
- Armstrong, Ravasio, Versteijlen, Verschuur, Metrikine, and Van Dalen. 2020. Seismic inversion of soil damping and stiffness using multichannel analysis of surface wave measurements in the marine environment, *Geophysical Journal International*, 221: 1439-1449.
- Askan, Sisman, and Pekcan. 2014. A regional near-surface high frequency spectral attenuation ( $\kappa$ ) model for northwestern Turkey, *Soil Dynamics and Earthquake Engineering*, 65: 113-125.
- Assimaki, Li, Steidl, and Tsuda. 2008. Site amplification and attenuation via downhole array seismogram inversion: A comparative study of the 2003 Miyagi-Oki aftershock sequence, *Bulletin of the Seismological Society of America*, 98: 301-330.
- Assimaki, Steidl, and Liu. 2006. Attenuation and velocity structure for site response analyses via downhole seismogram inversion, *Pure Applied Geophysics*, 163: 81-118.
- Asten, Dhu, and Lam. 2004. Optimized array design for microtremor array studies applied to site classification; comparison of results with SCPT logs. In *13th World Conference on Earthquake Engineering*. Vancouver, B.C., Canada.
- ASTM D3999/D3999M-11e1. 2011. Standard Test Methods for the Determination of the Modulus and Damping Properties of Soils Using the Cyclic Triaxial Apparatus. In West Conshohocken, Pennsylvania: American Society for Testing Material.
- ASTM D4015-15e1. 2015. Standard Test Methods for Modulus and Damping of Soils by Fixed-Base Resonant Column Devices.
- ASTM D4428/D4428M-14. 2014. Standard Test Methods for Cross-hole Seismic Testing.
- ASTM D5311/D5311M-13. 2013. Standard Test Method for Load Controlled Cyclic Triaxial Strength of Soil.
- ASTM D7400-17. 2017. Standard Test Methods for Downhole Seismic Testing.

- Badsar. 2012. In-Situ Determination of Material Damping in the Soil at Small Deformation Ratios (In situ bepaling van de materiaaldemping in de grond bij kleine vervormingen), KU Leuven.
- Badsar, Schevenels, Haegeman, and Degrande. 2010. Determination of the material damping ratio in the soil from SASW tests using the half-power bandwidth method, *Geophysical Journal International*, 182: 1493-1508.
- Baecher, and Christian. 2005. *Reliability and statistics in geotechnical engineering* (John Wiley & Sons).
- Bakku. 2015. Fracture characterization from seismic measurements in a borehole, Massachusetts Institute of Technology.
- Bakulin, Silvestrov, and Pevzner. 2020. Surface seismics with DAS: An emerging alternative to modern point-sensor acquisition, *The Leading Edge*, 39: 808-818.
- Balch, and Lee. 1984. *Vertical seismic profiling: technique, applications, and case histories* (Springer).
- Barker, and Stevens. 1983. Shallow shear wave velocity and Q structures at the El Centro strong motion accelerograph array, *Geophysical Research Letters*, 10: 853-856.
- Ben-Menahem, and Singh. 2012. *Seismic waves and sources* (Springer Science & Business Media).
- Beresnev, and Wen. 1996. Nonlinear soil response - A reality?, *Bulletin of the Seismological Society of America*, 86: 1964-1978.
- Bergamo, Comina, Foti, and Maraschini. 2011. Seismic characterization of shallow bedrock sites with multimodal Monte Carlo inversion of surface wave data, *Soil Dynamics and Earthquake Engineering*, 31: 530-534.
- Bergamo, Maranò, Imperatori, and Fäh. 2018. Wavedec code: an application to the joint estimation of shear modulus and dissipative properties of the near-surface from multi-component, active surface-wave surveys. In *36th General Assembly of the European Seismological Commission, ESC2018*. Valletta, Malta.
- Bergamo, Maranò, Imperatori, Hobiger, and Fäh. 2019. Wavefield decomposition technique applied to active surface wave surveys: towards joint estimation of shear modulus and dissipative properties of the near-surface. In *EPOS@SERA "Strong Motion Site Characterization" workshop*.
- Bettig, Bard, Scherbaum, J., Cotton, Cornou, and Hatzfeld. 2001. Analysis of dense array noise measurements using the modified spatial auto-correlation method (SPAC): application to the Grenoble area, *Bollettino di Geofisica Teorica ed Applicata*, 42: 281-304.
- Bidégaray-Fesquet, and Fesquet. 2009. A fully nonuniform approach to FIR filtering. In *SAMPTA'09 - International Conference on Sampling Theory and Applications*.
- Biot. 1956. Theory of elastic waves in a fluid-saturated porous solid. 1. Low frequency range, *Journal of the Acoustical Society of America*, 28: 168-178.

- Boaga, Renzi, Deiana, and Cassiani. 2015. Soil damping influence on seismic ground response: A parametric analysis for weak to moderate ground motion, *Soil Dynamics and Earthquake Engineering*, 79: 71-79.
- Bodet, Jacob, Tournat, Mourgues, and Gusev. 2009. Surface-wave dispersion inversion in an unconsolidated granular medium. In *71st EAGE Conference and Exhibition-Workshops and Fieldtrips*, edited by European Association of Geoscientists & Engineers.
- Bonilla, Steidl, Gariel, and Archuleta. 2002. Borehole response studies at the Garner Valley downhole array, southern California, *Bulletin of the Seismological Society of America*, 92: 3165-3179.
- Bonnefoy-Claudet, Köhler, Cornou, Wathelet, and Bard. 2008. Effects of Love waves on microtremor H/V ratio, *Bulletin of the Seismological Society of America*, 98: 288-300.
- Borcherdt. 1973. Rayleigh-type surface wave on a linear viscoelastic half-space, *The Journal of the Acoustical Society of America*, 54: 1651-1653.
- Boxberger, Pilz, and Parolai. 2017. Shear wave velocity versus quality factor: results from seismic noise recordings, *Geophysical Journal International*, 210: 660-670.
- British Standard Institution. 1992. BS 6472:1992: Evaluation of human exposure to vibration in buildings (1 Hz to 80 Hz).
- Brown, Boore, and Stokoe II. 2002. Comparison of Shear-Wave Slowness Profiles at 10 Strong-Motion Sites from Noninvasive SASW Measurements and Measurements Made in Boreholes, *Bulletin of the Seismological Society of America*, 92: 3116-3133.
- Bruekers. 2009. Symmetry and efficiency in complex FIR filters, Technische Universiteit Eindhoven.
- Burg. 1964. Three-dimensional filtering with an array of seismometers, *Geophysics*, 29: 693-713.
- Burland, and Symes. 1982. A simple axial displacement gauge for use in the triaxial apparatus, *Géotechnique*, 32: 62-65.
- Cabas, and Rodriguez-Marek. 2018. Toward Improving Damping Characterization for Site Response Analysis. in, *Geotechnical Earthquake Engineering and Soil Dynamics V: Seismic Hazard Analysis, Earthquake Ground Motions, and Regional-Scale Assessment* (American Society of Civil Engineers Reston, VA).
- Cabas, Rodriguez-Marek, and Bonilla. 2017. Estimation of site-specific Kappa ( $\kappa$ )-consistent damping values at KiK-Net sites to assess the discrepancy between laboratory-based damping models and observed attenuation (of seismic waves) in the field, *Bulletin of the Seismological Society of America*, 107: 2258-2271.
- Cadet, Bard, and Rodriguez-Marek. 2012. Site effect assessment using KiK-net data: Part 1. A simple correction procedure for surface/downhole spectral ratios, *Bulletin of Earthquake Engineering*, 10: 421-448.

- Campanella. 1994. Field methods for dynamic geotechnical testing: An overview of capabilities and needs. in, *Dynamic Geotechnical Testing II* (ASTM International).
- Campanella, and Stewart. 1991. Downhole seismic cone analysis using digital signal processing. In *Second International Conference on Recent Advances in Geotechnical Earthquake Engineering and Soil Dynamics*, 77-82. Saint Louis, Missouri, US.
- Campbell. 2009. Estimates of shear-wave  $Q$  and  $\kappa_0$  for unconsolidated and semiconsolidated sediments in Eastern North America, *Bulletin of the Seismological Society of America*, 99: 2365-2392.
- Capon. 1969. High-resolution frequency-wavenumber spectrum analysis, *Proceedings of the IEEE*, 57: 1408-1418.
- Carcione. 2007. *Wave fields in real media: wave propagation in anisotropic, anelastic, porous and electromagnetic media* (Elsevier: London).
- Cascante, Vanderkooy, and Chung. 2003. Difference between current and voltage measurements in resonant-column testing, *Canadian Geotechnical Journal*, 40: 806-820.
- Castellaro. 2016. Soil and structure damping from single station measurements, *Soil Dynamics and Earthquake Engineering*, 90: 480-493.
- Chandra, Guégen, Steidl, and Bonilla. 2015. In Situ Assessment of the  $G-\gamma$  Curve for Characterizing the Nonlinear Response of Soil: Application to the Garner Valley Downhole Array and the Wildlife Liquefaction Array, *Bulletin of the Seismological Society of America*, 105: 993-1010.
- Chapman, Talwani, and Cannon. 2003. Ground-Motion Attenuation in the Atlantic Coastal Plain near Charleston, South Carolina, *Bulletin of the Seismological Society of America*, 93: 998-1011.
- Cheng, Hallal, Vantassel, and Cox. 2021. Estimating Unbiased Statistics for Fundamental Site Frequency Using Spatially Distributed HVSR Measurements and Voronoi Tessellation, *Journal of Geotechnical and Geoenvironmental Engineering*, 147: 04021068.
- Cheng, and Leong. 2018. Determination of damping ratios for soils using bender element tests, *Soil Dynamics and Earthquake Engineering*, 111: 8-13.
- Choi. 2007. Dynamic properties of ash-flow tuffs, The University of Texas at Austin.
- Choi, Juarez, and Taylor. 2003. Distributed fiber-optic pressure/seismic sensor for low-cost monitoring of long perimeters. In *Unattended Ground Sensor Technologies and Applications V*, edited by Edward M. Carapezza, 134-141. SPIE.
- Chopra. 2017. *Dynamics of structures. Theory and applications to earthquake engineering* (Prentice Hall).
- Christensen. 2012. *Theory of viscoelasticity: an introduction* (Elsevier).
- Ciancimino, Jones, Sakellariadis, and Anastasopoulos. 2021. Experimental assessment of the performance of a bridge pier subjected to flood-induced foundation scour, *Géotechnique*: 1-18.



- Ciencimino, Lanzo, Alleanza, Amoroso, Bardotti, Biondi, Cascone, Castelli, Di Giulio, d' Onofrio, Foti, Lentini, Madiari, and Vessia. 2020. Dynamic characterization of fine-grained soils in Central Italy by laboratory testing, *Bulletin of Earthquake Engineering*, 29.
- Clouteau, Degrande, and Lombaert. 2001. Numerical modelling of traffic induced vibrations, *Meccanica*, 36: 401-420.
- Comina, Foti, Boiero, and Socco. 2011. Reliability of VS<sub>30</sub> Evaluation from Surface-Wave Tests, *Journal of Geotechnical and Geoenvironmental Engineering*, 137: 579-586.
- Constable, Parker, and Constable. 1987. Occam's inversion: A practical algorithm for generating smooth models from electromagnetic sounding data, *Geophysics*, 52: 289-300.
- Cormier. 1982. The effect of attenuation on seismic body waves, *Bulletin of the Seismological Society of America*, 72: S169-S200.
- Cornell. 1968. Engineering seismic risk analysis, *Bulletin of the Seismological Society of America*, 58: 1583-1606.
- Costley, Galan-Comas, Kirkendall, Simms, Hathaway, Parker, Ketcham, Smith, Folks, Milburn, and Wadman. 2018. Spectral Analysis of Surface Waves with Simultaneous Fiber Optic Distributed Acoustic Sensing and Vertical Geophones, *Journal of Environmental and Engineering Geophysics*, 23: 183-195.
- Coutant. 1996. Observation of Shallow Anisotropy on Local Earthquake Records at the Garner Valley, Southern California, Downhole Array, *Bulletin of the Seismological Society of America*, 86: 477-488.
- Cox, and Beekman. 2010. Intramethod variability in ReMi dispersion measurements and VS estimates at shallow bedrock sites, *Journal of Geotechnical and Geoenvironmental Engineering*, 137: 354-362.
- Cox, Stolte, Stokoe II, and Wotherspoon. 2018. A direct-push crosshole test method for the in-situ evaluation of high-resolution P-and S-wave velocity, *Geotechnical Testing Journal*, 42.
- Cox, and Teague. 2016. Layering ratios: a systematic approach to the inversion of surface wave data in the absence of a priori information, *Geophysical Journal International*, 207: 422-438.
- Cox, Wood, and Teague. 2014. Synthesis of the UTexas1 Surface Wave Dataset Blind-Analysis Study: Inter-Analyst Dispersion and Shear Wave Velocity Uncertainty. In *Geo-Congress 2014*, 850-859. Atlanta.
- Crow, Hunter, and Motazedian. 2011. Monofrequency in situ damping measurements in Ottawa area soft soils, *Soil Dynamics and Earthquake Engineering*, 31: 1669-1677.
- d'Onofrio, Silvestri, and Vinale. 1999. Strain rate dependent behaviour of a natural stiff clay, *Soils and Foundations*, 39: 69-82.
- Daley, Freifeld, Ajo-Franklin, Dou, Pevzner, Shulakova, Kashikar, Miller, Goetz, Hennings, and Lueth. 2013. Field testing of fiber-optic distributed

- acoustic sensing (DAS) for subsurface seismic monitoring, *The Leading Edge*, 32: 699-706.
- Darendeli. 2001. Development of a new family of normalized modulus reduction and material damping curves, Doctoral Dissertation, University of Texas at Austin.
- Deutsches Institut für Normung. 1999. DIN 4150 Teil 2: Erschütterungen im Bauwesen, Einwirkungen auf Menschen in Gebäuden.
- Di Benedetto. 1997. Small strain behavior of geomaterials: modelling of strain rate effects, *Soils and Foundations*, 37: 127-138.
- Dobry, and Vucetic. 1987. Dynamic properties and seismic response of soft clay deposits.
- Dobry, Whitman, and Roesset. 1971. *Soil properties and the one-dimensional theory of earthquake amplification* (MIT Department of Civil Engineering, Inter-American Program).
- Doroudian, and Vucetic. 1998. Small-strain testing in an NGI-type direct simple shear device. In *Proc. 11th Danube-European Conf. on Soil Mechanics and Geotech. Engrg., Porec, Croatia, AA Balkema*, 687-693.
- Dos Santos, Colaço, Costa, and Calçada. 2016. Experimental analysis of track-ground vibrations on a stretch of the Portuguese railway network, *Soil Dynamics and Earthquake Engineering*, 90: 358-380.
- Douglas, Gehl, Bonilla, and Gélis. 2010. A  $\kappa$  model for mainland France, *Pure and Applied geophysics*, 167: 1303-1315.
- Drnevich, Hardin, and Shippy. 1978. *Modulus and damping of soils by the resonant-column method* (ASTM International: West Conshohocken, PA, USA).
- Elgamal, Lai, Yang, He, and Prakash. 2001. Dynamic soil properties, seismic downhole arrays and applications in practice. In *4th International Conference on Recent Advances in Geotechnical Earthquake Engineering and Soil Dynamics*. San Diego, CA.
- Ewing. 1957. *Elastic waves in layered media* (McGraw-Hill: New York).
- Ewins. 1984. *Modal Testing: Theory and Practice* (Research Studies Press Ltd.).
- Fathi, Poursartip, Stokoe II, and Kallivokas. 2016. Three-dimensional P- and S-wave velocity profiling of geotechnical sites using full-waveform inversion driven by field data, *Soil Dynamics and Earthquake Engineering*, 87: 63-81.
- Fernández-Heredia, Huerta-López, Castro-Escamilla, and Romo-Jones. 2012. Soil damping and site dominant vibration period determination, by means of random decrement method and its relationship with the site-specific spectral decay parameter  $\kappa$ , *Soil Dynamics and Earthquake Engineering*, 43: 237-246.
- Field, and Jacob. 1993. Monte-Carlo simulation of the theoretical site response variability at Turkey Flat, California, given the uncertainty in the geotechnically derived input parameters, *Earthquake Spectra*, 9: 669-701.

- Filon. 1928. On a quadrature method for trigonometric integrals, *Proc. Roy. Soc. Edinburgh*, 49: 3847.
- Fladung, and Rost. 1997. Application and correction of the exponential window for frequency response function, *Mechanical Systems and Signal Processing*, 11: 23-36.
- Forbriger. 2003. Inversion of shallow-seismic wavefields: I. Wavefield transformation, *Geophysical Journal International*, 153: 719-734.
- Foti. 2000. Multistation methods for geotechnical characterization using surface waves, Politecnico di Torino.
- Foti. 2003. Small-strain stiffness and damping ratio of Pisa clay from surface wave tests, *Géotechnique*, 53: 455-461.
- Foti. 2004. Using transfer function for estimating dissipative properties of soils from surface-wave data, *Near Surface Geophysics*, 2: 231-240.
- Foti, Aimar, and Ciancimino. 2021. Uncertainties in small-strain damping ratio evaluation and their influence on seismic ground response analyses. in, *Latest Developments in Geotechnical Earthquake Engineering and Soil Dynamics* (Springer: Singapore).
- Foti, Aimar, Ciancimino, and Passeri. 2019a. Recent developments in seismic site response evaluation and microzonation. In *Geotechnical Engineering, foundation of the future, Proceedings of the XVII ECSMGE*, 223-248.
- Foti, Comina, Boiero, and Socco. 2009. Non-uniqueness in surface-wave inversion and consequences on seismic site response analyses, *Soil Dynamics and Earthquake Engineering*, 29: 982-993.
- Foti, Hollender, Garofalo, Albarello, Asten, Bard, Comina, Cornou, Cox, Di Giulio, Forbriger, Hayashi, Lunedei, Martin, Mercerat, Ohrnberger, Poggi, Renalier, Sicilia, and Socco. 2018. Guidelines for the good practice of surface wave analysis: a product of the InterPACIFIC project, *Bulletin of Earthquake Engineering*, 16: 2367-2420.
- Foti, Lai, Rix, and Strobbia. 2014. *Surface wave methods for near-surface site characterization* (CRC press).
- Foti, Passeri, and Rodriguez-Marek. 2019b. Uncertainties and variabilities in seismic ground response analyses. In *Earthquake Geotechnical Engineering for Protection and Development of Environment and Constructions: Proceedings of the 7th International Conference on Earthquake Geotechnical Engineering, (ICEGE 2019), June 17-20, 2019, Rome, Italy*, 153. CRC Press.
- Foti, Sambuelli, Socco, and Strobbia. 2002. Spatial sampling issues in  $f_k$  analysis of surface waves. In *15th EEGS Symposium on the Application of Geophysics to Engineering and Environmental Problems*. European Association of Geoscientists & Engineers.
- Foti, and Strobbia. 2002. Some notes on model parameters for surface wave data inversion. In *15th EEGS Symposium on the Application of Geophysics to Engineering and Environmental Problems*, edited by European Association of Geoscientists & Engineers.

- François, Pyl, Masoumi, and Degrande. 2007. The influence of dynamic soil–structure interaction on traffic induced vibrations in buildings, *Soil Dynamics and Earthquake Engineering*, 27: 655-674.
- Frazer, and Gettrust. 1984. On a generalization of Filon's method and the computation of the oscillatory integrals of seismology, *Geophysical Journal International*, 76: 461-481.
- Freifeld, Pevzner, Dou, Correa, Daley, Robertson, Tertyshnikov, Wood, Ajo-Franklin, Urosevic, Popik, and Gurevich. 2016. The CO2CRC Otway Project deployment of a distributed acoustic sensing network coupled with permanent rotary sources. In *78th EAGE Conference and Exhibition 2016*, edited by European Association of Geoscientists & Engineers, 1-5.
- Gabriels, Snieder, and Nolet. 1987. In situ measurements of shear-wave velocity in sediments with higher-mode Rayleigh waves, *Geophysical Prospecting*, 35: 187-196.
- Galan-Comas. 2015. Multichannel analysis of surface waves using distributed fiber optic sensors, Mississippi State University.
- Gao, Pan, Tian, and Xia. 2018. Estimating Q Factor from Multi-mode Shallow-Seismic Surface Waves, *Pure and Applied geophysics*, 175: 2609-2622.
- Gardner, Wyllie, and Droschak. 1964. Effects of pressure and fluid saturation on the attenuation of elastic waves in sands, *Journal of Petroleum Technology*, 16: 189-198.
- Garofalo, Foti, Hollender, Bard, Cornou, Cox, Dechamp, Ohrnberger, Perron, Sicilia, Teague, and Vergnault. 2016a. InterPACIFIC project: Comparison of invasive and non-invasive methods for seismic site characterization. Part II: Inter-comparison between surface-wave and borehole methods, *Soil Dynamics and Earthquake Engineering*, 82: 241-254.
- Garofalo, Foti, Hollender, Bard, Cornou, Cox, Ohrnberger, Sicilia, Asten, and Di Giulio. 2016b. InterPACIFIC project: Comparison of invasive and non-invasive methods for seismic site characterization. Part I: Intra-comparison of surface wave methods, *Soil Dynamics and Earthquake Engineering*, 82: 222-240.
- Gaudio, and Rampello. 2019. The influence of soil plasticity on the seismic performance of bridge piers on caisson foundations, *Soil Dynamics and Earthquake Engineering*, 118: 120-133.
- Gibbs. 1989. Near-surface P- and S-wave velocities from bore hie measurements near Lake Hemet, California. In.: USGS.
- Gladwin, and Stacey. 1974. Anelastic degradation of acoustic pulses in rock, *Physics of the Earth and Planetary Interiors*, 8: 332-336.
- Gold, and Jordan. 1969. A direct search procedure for designing finite-duration impulse response filters, *IEEE Transactions on Audio and Electroacoustics*, 17: 33-36.

- Gordon. 1991. Generic criteria for vibration-sensitive equipment. In *Proceedings of the SPIE Conference on Vibration Control and Metrology*, 71-85. San Jose.
- Goto, Tatsuoka, Shibuya, Kim, and Sato. 1991. A simple gauge for local small strain measurements in the laboratory, *Soils and Foundations*, 31: 169-180.
- Grattan, and Sun. 2000. Fiber optic sensor technology: an overview, *Sensors and Actuators A: Physical*, 82: 40-61.
- Griffiths, Cox, Rathje, and Teague. 2016a. Surface-wave dispersion approach for evaluating statistical models that account for shear-wave velocity uncertainty, *Journal of Geotechnical and Geoenvironmental Engineering*, 142: 04016061.
- Griffiths, Cox, Teague, and Rathje. 2016b. Mapping dispersion misfit and uncertainty in  $V_s$  profiles to variability in site response estimates, *Journal of Geotechnical and Geoenvironmental Engineering*, 142: 04016062.
- Gucunski. 1992. Numerical simulation of the SASW test, *Soil Dynamics and Earthquake Engineering*, 11: 213-227.
- Hall, and Bodare. 2000. Analyses of the cross-hole method for determining shear wave velocities and damping ratios, *Soil Dynamics and Earthquake Engineering*, 20: 167-175.
- Hallal, Cox, Foti, and Rodriguez-Marek. 2022. Improved implementation of travel time randomization for incorporating  $V_s$  uncertainty in seismic ground response, *Soil Dynamics and Earthquake Engineering*, 157: 107277.
- Hallo, Imperatori, Panzera, and Fäh. 2021. Joint multizonal transdimensional Bayesian inversion of surface wave dispersion and ellipticity curves for local near-surface imaging, *Geophysical Journal International*, 226: 627-659.
- Hara, and Kiyota. 1977. Dynamic shear tests of soils for seismic analysis. In *9th International Conference on Soil Mechanics and Foundation Engineering*, 247-250.
- Hardin, and Drnevich. 1972a. Shear modulus and damping in soils: design equations and curves, *Journal of Soil Mechanics & Foundations Div*, 98: 667-692.
- Hardin, and Drnevich. 1972b. Shear modulus and damping in soils: measurement and parameter effects, *Journal of the Soil Mechanics and Foundations Division*, 98: 603-624.
- Hartog. 2017. *An introduction to distributed optical fibre sensors* (CRC Press).
- Hashash, Musgrove, Harmon, Okan, Groholski, Phillips, and Park. 2017. DEEPSOIL 7.0, user manual. In.: University of Illinois at Urbana-Champaign.
- Haskell. 1953. The dispersion of surface waves on multilayered media, *Bulletin of the Seismological Society of America*, 43: 17-34.
- Herrmann, and Al-Eqabi. 1991. Surface wave inversion for shear wave velocity. in, *Shear waves in marine sediments* (Springer: Dordrecht).

- Hill. 1981. Geology of Garner Valley and vicinity. in A.R. Brown and Ruff. R.W. (eds.), *Geology of the San Jacinto Mountains, Annual Field Trip Guidebook No. 9* (South Coast Geological Society: Santa Ana, California).
- Hoar, and Stokoe. 1984. Field and laboratory measurements of material damping of soil in shear. In *8th World Conference on Earthquake Engineering*, 47-54. San Francisco.
- Hornman, Kuvshinov, Zwartjes, and Franzen. 2013. Field trial of a broadside-sensitive distributed acoustic sensing cable for surface seismic. In *75th EAGE Conference & Exhibition incorporating SPE EUROPEC 2013*, edited by European Association of Geoscientists & Engineers.
- Hough, and Anderson. 1988. High-frequency spectra observed at Anza, California: implications for Q structure, *Bulletin of the Seismological Society of America*, 78: 692-707.
- Huerta, Acosta, Roesset, and Stokoe II. 1994. In situ determination of soil damping from earthquake records. In *2nd International Conference on Earthquake Resistant Construction and Design*, 227-234. Berlin, Germany.
- Huerta, Roesset, and Stokoe II. 1998. Evaluation of the random decrement method for in-situ soil properties estimation. In *2nd International Symposium on the effects of Surface Geology on Seismic Motion*, 749-756. Yokohama, Japan.
- Hunt, and Hussein. 2007. Vibration from railways: can we achieve better than +/- 10dB prediction accuracy? In *14th International Congress on Sound & Vibration*. Cairns, Australia.
- Hussein, and Hunt. 2007. A numerical model for calculating vibration from a railway tunnel embedded in a full-space, *Journal of Sound and Vibration*, 305: 401-431.
- Hwang. 1997. Dynamic properties of natural soils, PhD Dissertation, University of Texas at Austin.
- Idriss. 2004. Evolution of the state of practice. In *Int. Workshop on the Uncertainties in Nonlinear Soil Properties and Their Impact on Modeling Dynamic Soil Response*. Richmond, CA: Pacific Earthquake Engineering Research Center.
- Idriss. 2011. Use of Vs30 to represent local site conditions. In *4th IASPEI/IAEE International Symposium. Effects of source geology on seismic motion*, 23-26.
- International. 2011. Standard Guide for Using the Seismic Refraction Method for Subsurface Investigation—ASTM D5777.
- International Organization for Standardization. 1999. ISO 2631-2:1999: Mechanical vibration and shock - Evaluation of human exposure to wholebody vibration - Part 2: Vibration in buildings (1 to 80 Hz).
- Iranpour, Muyzert, and Grion. 2002. Local velocity analysis by parametric wavenumber estimation in seismic-fk-music. In *64th EAGE conference & exhibition*. European Association of Geoscientists & Engineers.

- Ishibashi, and Zhang. 1993. Unified dynamic shear moduli and damping ratios of sand and clay, *Soils and Foundations*, 33: 182-191.
- Ishihara. 1996. *Soil behaviour in earthquake geotechnics* (Oxford, United Kingdom).
- Ivanov, Park, Miller, and Xia. 2005. Analyzing and filtering surface-wave energy by muting shot gathers, *Journal of Environmental & Engineering Geophysics*, 10: 307-322.
- Johnston, Toksoz, and Timur. 1979. Attenuation of seismic waves in dry and saturated rocks: II. Mechanisms, *Geophysics*, 44: 691-711.
- Jones. 1958. In-situ measurement of the dynamic properties of soil by vibration methods, *Géotechnique*, 8: 1-21.
- Jongmans. 1990. In-situ attenuation measurements in soils, *Engineering Geology*, 29: 99-118.
- Jousset, Reinsch, Ryberg, Blanck, Clarke, Aghayev, Hersir, Henninges, Weber, and Krawczyk. 2018. Dynamic strain determination using fibre-optic cables allows imaging of seismological and structural features, *Nature communications*, 9: 1-11.
- Kaklamanos, and Bradley. 2018. Challenges in Predicting Seismic Site Response with 1D Analyses: Conclusions from 114 KiK-net Vertical Seismometer Arrays, *Bulletin of the Seismological Society of America*, 108: 2816-2838.
- Kaklamanos, Bradley, Thompson, and Baise. 2013a. Critical parameters affecting bias and variability in site-response analyses using KiK-net downhole array data, *Bulletin of the Seismological Society of America*, 103: 1733-1749.
- Kaklamanos, Bradley, Thompson, and Baise. 2013b. Critical parameters affecting bias and variability in site-response analyses using KiK-net downhole array data, *Bulletin of the Seismological Society of America*, 103: 1733-1749.
- Kallivokas, Fathi, Kucukcoban, Stokoe II, Bielak, and Ghattas. 2013. Site characterization using full waveform inversion, *Soil Dynamics and Earthquake Engineering*, 47: 62-82.
- Karl. 2005. Dynamic soil properties out of SCPT and bender element tests with emphasis on material damping, Universiteit Gent.
- Karl, Haegeman, and Degrande. 2006. Determination of the material damping ratio and the shear wave velocity with the Seismic Cone Penetration Test, *Soil Dynamics and Earthquake Engineering*, 26: 1111-11126.
- Karl, Haegeman, Degrande, and Domms. 2008. Determination of the material damping ratio with the bender element test, *Journal of Geotechnical and Geoenvironmental Engineering*, 134: 1743-1756.
- Karray, and Lefebvre. 2009. Techniques for mode separation in Rayleigh wave testing, *Soil Dynamics and Earthquake Engineering*, 29: 607-619.
- Kausel, and Assimaki. 2002. Seismic simulation of inelastic soils via frequency-dependent moduli and damping, *Journal of Engineering Mechanics*, 128: 34-47.

- Kausel, and Roësset. 1981. Stiffness matrices for layered soils, *Bulletin of the Seismological Society of America*, 71: 1743-1761.
- Kelner, Bouchon, and Coutant. 1999. Characterization of Fractures in Shallow Granite from the Modeling of the Anisotropy and Attenuation of Seismic Waves, *Bulletin of the Seismological Society of America*, 89: 706-717.
- Kementzetzidis, Corciulo, Versteijlen, and Pisanò. 2019. Geotechnical aspects of offshore wind turbine dynamics from 3D non-linear soil-structure simulations, *Soil Dynamics and Earthquake Engineering*, 2019: 181-199.
- Kennett. 1974. Reflections, rays, and reverberations, *Bulletin of the Seismological Society of America*, 64: 1685-1696.
- Kim. 1991. Deformational characteristics of soils at small to intermediate strains from cyclic test, PhD dissertation, University of Texas at Austin.
- Kim, Hashash, Stewart, Rathje, Harmon, Musgrove, Campbell, and Silva. 2016. Relative differences between nonlinear and equivalent-linear 1-D site response analyses, *Earthquake Spectra*, 32: 1845-1865.
- Kim, and Stokoe. 1994. Torsional motion monitoring system for Small-Strain (10<sup>-5</sup> to 10<sup>-3</sup>%) soil testing, *Geotechnical Testing Journal*, 17: 17-26.
- Kjartansson. 1979. Constant Q-wave propagation and attenuation, *Journal of Geophysical Research: Solid Earth*, 84: 4737-4748.
- Kokusho. 2017. *Innovative earthquake soil dynamics* (CRC Press).
- Kokusho, Yoshida, and Esashi. 1982. Dynamic properties of soft clay for wide strain range, *Soils and Foundations*, 22: 1-18.
- Kouroussis, Verlinden, and Conti. 2011. Free field vibrations caused by high-speed lines: measurement and time domain simulation, *Soil Dynamics and Earthquake Engineering*, 31: 692-707.
- Kramer. 1996. *Geotechnical earthquake engineering* (New Jersey).
- Kristeková, Kristek, Moczo, and Day. 2006. Misfit criteria for quantitative comparison of seismograms, *Bulletin of the Seismological Society of America*, 96: 1836-1850.
- Ktenidou, Abrahamson, Drouet, and Cotton. 2015. Understanding the physics of kappa ( $\kappa$ ): Insights from a downhole array, *Geophysical Journal International*, 203: 678-691.
- Ktenidou, Cotton, Abrahamson, and Anderson. 2014. Taxonomy of  $\kappa$ : A review of definitions and estimation approaches targeted to applications, *Seismological Research Letters*, 85: 135-146.
- Ktenidou, Gélis, and Bonilla. 2013. A study on the variability of kappa ( $\kappa$ ) in a borehole: Implications of the computation process, *Bulletin of the Seismological Society of America*, 103: 1048-1068.
- Kuvshinov. 2016. Interaction of helically wound fibre-optic cables with plane seismic waves, *Geophysical Prospecting*, 64: 671-688.
- Kwok, Stewart, and Hashash. 2008. Nonlinear ground-response analysis of Turkey Flat shallow stiff-soil site to strong ground motion, *Bulletin of the Seismological Society of America*, 98: 331-343.



- Lacoss, Kelly, and Toksoz. 1969. Estimation of seismic noise structure using arrays, *Geophysics*, 34: 21-38.
- Ladd, and Dutko. 1985. Small Strain Measurements Using Triaxial Apparatus. In *Advances in the Art of Testing Soils Under Cyclic Conditions*, 148-165. ASCE.
- Lai. 2005. Surface waves in dissipative media: Forward and inverse modelling. in, *Surface waves in geomechanics: direct and inverse modelling for soils and rocks* (Springer: Vienna).
- Lai, Callerio, Faccioli, Morelli, and Romani. 2005a. Prediction of railway-induced ground vibrations in tunnels, *Journal of Vibration and Acoustics*, 127: 503-514.
- Lai, Foti, and Rix. 2005b. Propagation of data uncertainty in surface wave inversion, *Journal of Environmental & Engineering Geophysics*, 10: 219-228.
- Lai, and Özcebe. 2015. Non-conventional methods for measuring dynamic properties of geomaterials. In *6th International Conference on Earthquake Geotechnical Engineering. Christchurch, New Zealand*.
- Lai, and Özcebe. 2016. Non-conventional lab and field methods for measuring frequency-dependent low-strain parameters of soil dynamic behavior, *Soil Dynamics and Earthquake Engineering*, 91: 72-86.
- Lai, Pallara, Presti, and Turco. 2001. Low-strain stiffness and material damping ratio coupling in soils. in, *Advanced Laboratory Stress-Strain Testing of Geomaterials* (Routledge).
- Lai, and Rix. 1998a. Simultaneous inversion of Rayleigh phase velocity and attenuation for near-surface site characterization.
- Lai, and Rix. 1998b. Simultaneous inversion of Rayleigh phase velocity and attenuation for near-surface site characterization, Georgia Institute of Technology.
- Lai, and Rix. 2002. Solution of the Rayleigh eigenproblem in viscoelastic media, *Bulletin of the Seismological Society of America*, 92: 2297-2309.
- Lai, Rix, Foti, and Roma. 2002. Simultaneous measurement and inversion of surface wave dispersion and attenuation curves, *Soil Dynamics and Earthquake Engineering*, 22: 923-930.
- Laird. 1994. Linear and nonlinear dynamic properties of soils at high confining pressures, University of Texas at Austin.
- Lamb. 1904. On the propagation of tremors over the surface of an elastic solid, *Philosophical Transactions of the Royal Society of London*, A: 1-42.
- Lancelle. 2016. Distributed acoustic sensing for imaging near-surface geology and monitoring traffic at Garner Valley, California, The University of Wisconsin-Madison.
- Lanzo, and Silvestri. 1999. *Risposta sismica locale: teoria ed esperienze* (Hevelius).
- Lanzo, and Vucetic. 1999. Effect of soil plasticity on damping ratio at small cyclic strains, *Soils and Foundations*, 39: 131-141.

- Latham, Ewing, Dorman, Lammlein, Press, Toksoz, Sutton, Duennebier, and Nakamura. 1971. Moonquakes, *Science*, 174: 687-692.
- Latham, Ewing, Dorman, Press, Toksoz, Sutton, Meissner, Duennebier, Nakamura, Kovach, and Yates. 1970. Seismic data from man-made impacts on the Moon, *Science*, 170: 620-626.
- Lawrence, Denolle, Seats, and Prieto. 2013. A numeric evaluation of attenuation from ambient noise correlation functions, *Journal of Geophysical Research: Solid Earth*, 1181: 6134-6145.
- Legates, and McCabe Jr. 1999. Evaluating the use of “goodness-of-fit” measures in hydrologic and hydroclimatic model validation, *Water Resources Research*, 35: 233-241.
- Li, and Assimaki. 2010. Site-and motion-dependent parametric uncertainty of site-response analyses in earthquake simulations, *Bulletin of the Seismological Society of America*, 100: 954-968.
- Li, and Rosenblad. 2009. Experimental study of near-field effects in multichannel array-based surface wave velocity measurements, *Near Surface Geophysics*, 9: 357-366.
- Lines, and Treitel. 1984. A review of least-squares inversion and its application to geophysical problems, *Geophysical Prospecting*, 32: 159-186.
- Ling, and Okada. 1993. An extended use of the spatial autocorrelation method for the estimation of structure using microtremors. In *89th Society of Exploration Geophysicists of Japan Conference*. Nagoya, Japan: Society of Exploration Geophysicists of Japan.
- Liu, Boore, Joyner, Oppenheimer, Warrick, Zhang, Hamilton, and Brown. 2000. Comparison of Phase Velocities from Array Measurements of Rayleigh Waves Associated with Microtremor and Results Calculated from Borehole Shear-Wave Velocity Profiles, *Bulletin of the Seismological Society of America*, 90: 666-678.
- Liu, Warrick, Westerlund, and Kayen. 1994. In situ measurement of seismic shear-wave absorption in the San Francisco Holocene Bay Mud by the pulse-broadening method, *Bulletin of the Seismological Society of America*, 84: 62-75.
- Lo Presti, Jamiolkowski, Pallara, Cavallaro, and Pedroni. 1997. Shear modulus and damping of soils, *Géotechnique*, 47: 603-617.
- Loeliger, Dauwels, Hu, Korl, Ping, and Kschischang. 2007. The factor graph approach to model-based signal processing, *Proceedings of the IEEE*, 95: 1295-1322.
- Lombaert, and Degrande. 2003. The experimental validation of a numerical model for the prediction of the vibrations in the free field produced by road traffic, *Journal of Sound and Vibration*, 262: 309-331.
- Lombaert, Degrande, and Clouteau. 2000. Numerical modelling of free field traffic-induced vibrations, *Soil Dynamics and Earthquake Engineering*, 19: 473-488.

- Lombaert, Degrande, Kogut, and François. 2006. The experimental validation of a numerical model for the prediction of railway induced vibrations, *Journal of Sound and Vibration*, 297: 512-535.
- Louie. 2001. Faster, better: shear-wave velocity to 100 meters depth from refraction microtremor arrays, *Bulletin of the Seismological Society of America*, 91: 347-364.
- Luo, Xia, Miller, Xu, Liu, and Liu. 2008. Rayleigh-wave dispersive energy imaging using a high-resolution linear Radon transform, *Pure and Applied geophysics*, 165: 903-922.
- Macdonald. 1959. Rayleigh-wave dissipation functions in low-loss media, *Geophysical Journal International*, 2: 132-135.
- Magrini, and Boschi. 2021. Surface-wave attenuation from seismic ambient noise: numerical validation and application, *Journal of Geophysical Research: Solid Earth*, 126: e2020JB019865.
- Maranò, Hobiger, Bergamo, and Fäh. 2017. Analysis of Rayleigh waves with circular wavefront: a maximum likelihood approach, *Geophysical Journal International*, 210: 1570-1580.
- Maranò, Reller, Loeliger, and Fäh. 2012. Seismic waves estimation and wavefield decomposition: application to ambient vibrations, *Geophysical Journal International*, 191: 175-188.
- Maraschini, Boiero, Foti, and Socco. 2011. Scale properties of the seismic wavefield perspectives for full-waveform matching, *Geophysics*, 76: A37-A44.
- Maraschini, and Foti. 2010. A Monte Carlo multimodal inversion of surface waves, *Geophysical Journal International*, 182: 1557-1566.
- Marchetti, Monaco, Totani, and Marchetti. 2008. In situ tests by seismic dilatometer. In *Symposium Honoring Dr. John H. Schmertmann for His Contributions to Civil Engineering at Research to Practice in Geotechnical Engineering*. New Orleans, Louisiana, US.
- Marosi, and Hiltunen. 2004. Characterization of SASW phase angle and phase velocity measurement uncertainty, *Geotechnical Testing Journal*, 27: 205-213.
- Martakis, Taeseri, Chatzi, and Laue. 2017. A centrifuge-based experimental verification of Soil-Structure Interaction effects, *Soil Dynamics and Earthquake Engineering*, 103: 1-14.
- Martínez, Lana, Olarte, Badal, and Canas. 2000. Inversion of Rayleigh wave phase and group velocities by simulated annealing, *Physics of the Earth and Planetary Interiors*, 122: 3-17.
- Mateeva, Lopez, Potters, Mestayer, Cox, Kiyashchenko, Wills, Grandi, Hornman, Kuvshinov, Berlang, Zhahoui, and Detomo. 2014. Distributed acoustic sensing for reservoir monitoring with vertical seismic profiling, *Geophysical Prospecting*, 62: 679-692.

- Matešić, and Vucetic. 2003. Strain-rate effect on soil secant shear modulus at small cyclic strains, *Journal of Geotechnical and Geoenvironmental Engineering*, 129: 536-549.
- Mavko, Dvorkin, and Walls. 2005. A theoretical estimate of S-wave attenuation in sediment. In *SEG Technical Program Expanded Abstracts 2005*, 1469-1472. Society of Exploration Geophysicists.
- Mavko, and Nur. 1975. Melt squirt in the asthenosphere, *Journal of Geophysical Research*, 80: 1444-1448.
- McMechan, and Yedlin. 1981. Analysis of dispersive waves by wave field transformation, *Geophysics*, 46: 869-874.
- Meng, and Rix. 2003. Reduction of equipment-generated damping in resonant column measurements, *Géotechnique*, 53: 503-512.
- Menq. 2003. Dynamic properties of sandy and gravelly soils, The University of Texas at Austin.
- Mestayer, Cox, Wills, Kiyashchenko, Lopez, Costello, Bourne, Ugueto, Lupton, Solano, Hill, and Lewis. 2011. Field trials of distributed acoustic sensing for geophysical monitoring. In *Seg technical program expanded abstracts*, edited by Society of Exploration Geophysicists, 4253-4257.
- Mestayer, Karam, Cox, Wills, Mateeva, Lopez, Hill, and Lewis. 2012. Distributed acoustic sensing for geophysical monitoring. In *74th EAGE Conference and Exhibition incorporating EUROPEC 2012*, edited by European Association of Geoscientists & Engineers.
- Michaels. 1998. In situ determination of soil stiffness and damping, *Journal of Geotechnical and Geoenvironmental Engineering*, 124: 709-719.
- Miller, and Pursey. 1955. On the partition of energy between elastic waves in a semi-infinite solid, *Proceedings of the Royal Society of London. Series A. Mathematical and Physical Sciences*, 233: 55-69.
- Misbah, and Strobbia. 2014. Joint estimation of modal attenuation and velocity from multichannel surface wave data, *Geophysics*, 79: EN25-EN38.
- Mitra. 2006. *Digital Signal Processing - A Computer-Based Approach* (McGraw-Hill).
- Mok, Sanchez-Salinero, Stokoe, and Roesset. 1988. In situ damping measurements by crosshole seismic method. In *Earthquake Engineering and Soil Dynamics II - Recent Advances in Ground-Motion Evaluation*, 305-320. Park City, Utah, US.
- Morikawa, Sawada, and Akamatsu. 2004. A method to estimate phase velocities of Rayleigh waves using microseisms simultaneously observed at two sites, *Bulletin of the Seismological Society of America*, 94: 961-976.
- Mosegaard, and Sambridge. 2002. Monte Carlo analysis of inverse problems, *Inverse Problems*, 18: R29-R54.
- Mosegaard, and Tarantola. 1995. Monte Carlo sampling of solutions to inverse problems, *Journal of Geophysical Research: Solid Earth*, 100: 12431-12447.

- Mucciacciaro, and Sica. 2018. Nonlinear soil and pile behaviour on kinematic bending response of flexible piles, *Soil Dynamics and Earthquake Engineering*, 107: 195-213.
- Mucciarelli, and Gallipoli. 2006. Estimate of frequency and damping for large sets of buildings in dense urban areas. In *First European Conference on Earthquake Engineering and Seismology*, 3-8. Geneva, Switzerland.
- Mun, and Zeng. 2018. Estimation of Rayleigh wave modal attenuation from near-field seismic data using sparse signal reconstructions, *Soil Dynamics and Earthquake Engineering*, 107: 1-8.
- Mylonakis, and Gazetas. 2000. Seismic soil-structure interaction: beneficial or detrimental?, *Journal of Earthquake Engineering*, 4: 277-301.
- Nakahara. 2012. Formulation of the spatial autocorrelation (SPAC) method in dissipative media, *Geophysical Journal International*, 190: 1777-1783.
- Nakamura. 1989. A Method for Dynamic Characteristics Estimation of Subsurface using Microtremor on the Ground Surface, *Quarterly Report of Railway Technical Research Institute (RTRI)*, 30.
- Nazarian, and Stokoe II. 1984. Nondestructive testing of pavements using surface waves, *Transportation Research Record*, 993: 67-79.
- Nelder, and Mead. 1965. A simplex method for function minimization, *Computer Journal*, 7: 308-313.
- Nigbor, and Imai. 1994. The Suspension P-S velocity logging method. In *Geophysical characterization of sites*.
- Nocedal, and Wright. 2006. *Sequential quadratic programming*.
- Nogoshi, and Igarashi. 1970. On the propagation characteristics of microtremors, *Journal of the Seismological Society of Japan*, 23: 264-280.
- Nolet, and Panza. 1976. Array analysis of seismic surface waves: limits and possibilities, *Pure and Applied geophysics*, 114: 775-790.
- Nur. 1971. Effects of stress on velocity anisotropy in rocks with cracks, *Journal of Geophysical Research*, 76: 2022-2034.
- O'Connell, and Budiansky. 1977. Viscoelastic properties of fluid-saturated cracked solids, *Journal of Geophysical Research*, 82: 5719-5735.
- O'Doherty, and Anstey. 1971. Reflection on amplitudes, *Geophysical Prospecting*, 19: 430-458.
- O'Neill. 2004. Shear velocity model appraisal in shallow surface wave inversion. In *Symposium on the Application of Geophysics to Engineering and Environmental Problems*, edited by Society of Exploration Geophysicists.
- Okada, and Suto. 2003. *The microtremor survey method* (Society of Exploration Geophysicists).
- Olafsdottir, Bessason, and Erlingsson. 2018. Combination of dispersion curves from MASW measurements, *Soil Dynamics and Earthquake Engineering*, 113: 473-487.
- Oldenburg, and Li. 2005. Inversion for applied geophysics: A tutorial. in D.K. Butler (ed.), *Near-Surface Geophysics* (Society of Exploration Geophysicist: Tulsa, Oklahoma, U.S.A.).

- Olsen, Day, and Bradley. 2003. Estimation of Q for long-period ( $> 2$  sec) waves in the Los Angeles basin, *Bulletin of the Seismological Society of America*, 93: 627-638.
- Olsen, and Mayhew. 2010. Goodness-of-fit criteria for broadband synthetic seismograms, with application to the 2008 Mw 5.4 Chino Hills, California, earthquake, *Seismological Research Letters*, 81: 715-723.
- Paffenholz, and Burkhardt. 1989. Absorption and modulus measurements in the seismic frequency and strain range on partially saturated sedimentary rocks, *Journal of Geophysical Research*, 94: 9493-9507.
- Pakravan, Wang, and Newton. 2016. A Gauss–Newton full-waveform inversion for material profile reconstruction in viscoelastic semi-infinite solid media, *Inverse Problems in Science and Engineering*, 24: 393-421.
- Papadopoulos, François, Degrande, and Lombaert. 2018. The influence of uncertain local subsoil conditions on the response of buildings to ground vibration, *Journal of Sound and Vibration*, 418: 200-220.
- Papadopoulos, Kuo, Germonpré, Verachtert, Zhang, Maes, Lombaert, and Degrande. 2019. Numerical prediction and experimental validation of railway induced vibration in a multi-storey office building. In *Proceedings of the 13th International Workshop on Railway Noise, 16-20 September 2019*. Ghent: Springer.
- Park, and Carnevale. 2010. Optimum MASW survey—revisit after a decade of use. In *GeoFlorida 2010: Advances in Analysis, Modeling & Design*, 1303-1312.
- Park, and Hashash. 2005. Evaluation of seismic site factors in the Mississippi Embayment. II. Probabilistic seismic hazard analysis with nonlinear site effects, *Soil Dynamics and Earthquake Engineering*, 25: 145-156.
- Park, Miller, and Xia. 1999. Multichannel analysis of surface waves, *Geophysics*, 64: 800-808.
- Parker, Shatalin, and Farhadiroushan. 2014. Distributed Acoustic Sensing—a new tool for seismic applications, *First Break*, 32: 61-69.
- Parolai. 2014. Shear wave quality factor  $Q_s$  profiling using seismic noise data from microarrays, *Journal of Seismology*, 18: 695-704.
- Parolai, Bindi, Ansal, Kurtulus, Strollo, and Zschau. 2010. Determination of shallow S-wave attenuation by down-hole waveform deconvolution: a case study in Istanbul (Turkey), *Geophysical Journal International*, 181: 1147-1158.
- Parolai, Picozzi, Richwalski, and Milkereit. 2005. Joint inversion of phase velocity dispersion and H/V ratio curves from seismic noise recordings using a genetic algorithm, considering higher modes, *Geophysical Research Letters*, 32.
- Passeri. 2019. Development of advanced geostatistical models of shear wave velocity profiles to manage uncertainties and variabilities in Ground Response Analyses, Doctoral dissertation, Politecnico di Torino.

- Passeri, Comina, Foti, and Socco. 2021. The Polito Surface Wave flat-file Database (PSWD): statistical properties of test results and some inter-method comparisons, *Bulletin of Earthquake Engineering*, 19: 2343-2370.
- Passeri, Foti, and Rodriguez-Marek. 2019. Geostatistical models for the assessment of the influence of shear wave velocity uncertainty and variability on ground response analyses. In *7th International Conference of Earthquake Geotechnical Engineering*, edited by Silvestri & Moraci (Eds), 4387-4395. Roma, Italy: Associazione Geotecnica Italiana.
- Passeri, Foti, and Rodriguez-Marek. 2020. A new geostatistical model for shear wave velocity profiles, *Soil Dynamics and Earthquake Engineering*, 136.
- Pecker. 1995. Validation of small strain properties from recorded weak seismic motions, *Soil Dynamics and Earthquake Engineering*, 14: 399-408.
- Pecker, and Mohammadioun. 1991. Downhole Instrumentation for the Evaluation of Non-Linear Soil Response on Ground Surface Motion. In *11th International Conference on Structural Mechanics in Reactor Technology*.
- Peterson. 1993. Observations and modeling of seismic background noise. In Albuquerque, New Mexico: United States Geological Survey.
- Picozzi, and Albarello. 2007. Combining genetic and linearized algorithms for a two-step joint inversion of Rayleigh wave dispersion and H/V spectral ratio curves, *Geophysical Journal International*, 169: 189-200.
- Pilant, and Knopoff. 1964. Observations of multiple seismic events, *Bulletin of the Seismological Society of America*, 54: 19-39.
- Prieto, Lawrence, and Beroza. 2009. Anelastic earth structure from the coherency of the ambient seismic field, *Journal of Geophysical Research: Solid Earth*, 114.
- Pyl. 2004. Development and experimental validation of a numerical model for traffic induced vibrations in buildings, K.U. Leuven.
- Rahimi, Wood, and Himel. 2022. Practical guidelines for near-field mitigation on array-based active surface wave testing, *Geophysical Journal International*, 229: 1531-1549.
- Rahimi, Wood, and Teague. 2021. Performance of different transformation techniques for MASW data processing considering various site conditions, near-field effects, and modal separation, *Surveys in Geophysics*, 42: 1197-1225.
- Rathje, Kottke, and Trent. 2010. Influence of input motion and site property variabilities on seismic site response analysis, *Journal of Geotechnical and Geoenvironmental Engineering*, 136: 607-619.
- Rayleigh. 1885. On waves propagated along the plane surface of an elastic solid, *Proceedings of the London mathematical Society*, 1: 4-11.
- Redpath, Edwards, Hale, and Kintzer. 1982. Development of field techniques to measure damping values for near-surface rocks and soils. In NSF.
- Régnier, Bonilla, Bard, Bertrand, Hollender, Kawase, Sicilia, Arduino, Amorosi, Asimaki, Boldini, Chen, Chiaradonna, DeMartin, Elgamal, Falcone, Foerster, Foti, Garini, Gazetas, Gélis, Ghofrani, Giannakou, Gingery,

- Glinsky, Harmon, Hashash, Iai, Kramer, Kontoe, Kristek, Lanzo, Di Lernia, Lopez-Caballero, Marot, McAllister, Mercerat, Moczo, Montoya-Noguera, Musgrove, Nieto-Ferro, Pagliaroli, Passeri, Richteroval, Sajana, Santisi D'Avila, Shi, Silvestri, Taiebat, Tropeano, Vandeputte, and Verrucci. 2018. PRENOLIN: International Benchmark on 1D Nonlinear Site-Response Analysis—Validation Phase Exercise, *Bulletin of the Seismological Society of America*, 108: 876-900.
- Richart, Hall, and Woods. 1970. Vibrations of soils and foundations.
- Richter. 1958. *Elementary seismology* (W.H. Freeman).
- Rix, Hebel, and Orozco. 2002. Near-surface Vs profiling in the New Madrid seismic zone using surface-wave methods, *Seismological Research Letters*, 73: 380-392.
- Rix, Lai, and Foti. 2001a. Simultaneous measurement of surface wave dispersion and attenuation curves, *Geotechnical Testing Journal*, 24: 350-358.
- Rix, Lai, Orozco, Hebel, and Roma. 2001b. Recent advances in surface wave methods for geotechnical site characterization. In *International Conference on Soil Mechanics and Geotechnical Engineering*, 499-502. Balkema.
- Rix, Lai, and Wesley Spang Jr. 2000. In situ measurement of damping ratio using surface waves, *Journal of Geotechnical and Geoenvironmental Engineering*, 126: 472-480.
- Rix, and Meng. 2005. A non-resonance method for measuring dynamic soil properties, *Geotechnical Testing Journal*, 28: 1-8.
- Roblee, and Chiou. 2004. A proposed Geindex model for design selection of non-linear properties for site response analysis. In *International workshop on uncertainties in nonlinear soil properties and their impact on modeling dynamic soil response*. PEER Headquarters, UC Berkeley.
- Rodriguez-Marek, Bommer, Youngs, Crespo, Stafford, and Bahrapouri. 2021. Capturing epistemic uncertainty in site response, *Earthquake Spectra*, 37: 921-936.
- Sanchez-Saliner, Roesset, Shao, Stokoe II, and Rix. 1987. Analytical evaluation of variables affecting surface wave testing of pavements. In *Transportation Research Record*.
- Schevenels. 2007. The impact of uncertain dynamic soil characteristics on the prediction of ground vibrations, KU Leuven.
- Schevenels, Degrande, and François. 2009. EDT: an elastodynamics toolbox for MATLAB, *Computers & Geosciences*.
- Schwab, and Knopoff. 1971. Surface waves on multilayered anelastic media, *Bulletin of the Seismological Society of America*, 61: 893-912.
- Schwartz. 1978. Estimating the dimension of a model, *Annals of Statistics*, 6: 461-464.
- Seber, and Wild. 2003. *Nonlinear regression* (John Wiley & Sons: New Jersey).



- Seed, and Idriss. 1970. Soil moduli and damping factors for dynamic response analyses. In. Berkeley, California: Earthquake Engineering Research Center, University of California.
- Seed, Wong, Idriss, and Tokimatsu. 1986. Moduli and damping factors for dynamic analyses of cohesionless soils, *Journal of Geotechnical engineering*, 112: 1016-1032.
- Sen, and Stoffa. 1996. Bayesian inference, Gibbs' sampler and uncertainty estimation in geophysical inversion, *Geophysical Prospecting*, 44: 313-350.
- Senetakis, Anastasiadis, and Ptilakis. 2013. Normalized shear modulus reduction and damping ratio curves of quartz sand and rhyolitic crushed rock, *Soils and Foundations*, 53: 879-893.
- SESAME. 2004. Guidelines for the Implementation of the H/V Spectral Ratio Technique on Ambient Vibrations Measurements, Processing and Interpretation. In.: SESAME European research project.
- Seylabi, Stuart, and Asimaki. 2020. Site characterization at downhole arrays by joint inversion of dispersion data and acceleration time series, *Bulletin of the Seismological Society of America*, 110: 1323-1337.
- Shearer, and Orcutt. 1987. Surface and near-surface effects on seismic waves— theory and borehole seismometer results, *Bulletin of the Seismological Society of America*, 77: 1168-1196.
- Shi, and Asimaki. 2017. From stiffness to strength: Formulation and validation of a hybrid hyperbolic nonlinear soil model for site-response analyses, *Bulletin of the Seismological Society of America*, 107: 1336-1355.
- Shibuya, Mitachi, Fukuda, and Degoshi. 1995. Strain rate effects on shear modulus and damping of normally consolidated clay, *Geotechnical Testing Journal*, 18: 365-375.
- Shinkarenko, Lontsi, Kremer, Bergamo, Hobiger, Hallo, and Fäh. 2021. Investigating the subsurface in a shallow water environment using array and single-station ambient vibration techniques, *Geophysical Journal International*, 227: 1857-1878.
- Shtivelman. 1999. Using surface waves for estimating shear wave velocities in the shallow subsurface onshore and offshore Israel. In *5th EEGS-ES Meeting*. European Association of Geoscientists & Engineers.
- Socco, and Boiero. 2008. Improved Monte Carlo inversion of surface wave data, *Geophysical Prospecting*, 56: 357-371.
- Socco, Foti, and Boiero. 2010. Surface-wave analysis for building near-surface velocity models—Established approaches and new perspectives, *Geophysics*, 75: 75A83-75A102.
- Socco, Mabyalaht, and Comina. 2015. Robust static estimation from surface wave data. In *SEG Technical Program Expanded Abstracts 2015*, 5222-5227. Society of Exploration Geophysicists.
- Socco, and Strobbia. 2004. Surface-wave method for near-surface characterization: a tutorial, *Near Surface Geophysics*, 2: 165-185.

- Song, Zeng, Thurber, Wang, and Fratta. 2018. Imaging shallow structure with active-source surface wave signal recorded by distributed acoustic sensing arrays, *Earthquake Science*, 31.
- Spang. 1995. In situ measurements of damping ratio using surface waves, Georgia Institute of Technology.
- Steidl, Archuleta, Tumarkin, Bonilla, and Gariel. 1998. Observations and Modeling of Ground Motion and Pore Pressure at the Garner Valley, California, Test Site. In *2nd International Symposium on Effects of Surface Geology on Seismic Motion (ESG)*. Yokohama.
- Steidl, Tumarkin, and Archuleta. 1996. What is a reference site?, *Bulletin of the Seismological Society of America*, 86: 1733-1748.
- Stein, and Wysession. 2003. *An introduction to seismology, earthquakes and Earth structure*.
- Steller. 1996. New Borehole Geophysical Results at GVDA. In.
- Stewart, Afshari, and Hashash. 2014a. Guidelines for performing hazard-consistent one-dimensional ground response analysis for ground motion prediction. In *PEER Report 2014*.
- Stewart, Afshari, and Hashash. 2014b. Guidelines for performing hazard-consistent one-dimensional ground response analysis for ground motion prediction. In *PEER Report 2014*. Berkeley: University of California.
- Stewart, and Campanella. 1991. Insitu measurement of damping of soils. In *International Conferences on Recent Advances in Geotechnical Earthquake Engineering and Soil Dynamics*, 83-92.
- Stewart, and Kwok. 2008. Nonlinear seismic ground response analysis: Code usage protocols and verification against vertical array data. In *Geotechnical earthquake engineering and soil dynamics IV*, 1-24.
- Stokoe, Darendeli, Andrus, and Brown. 1999. Dynamic soil properties: laboratory, field and correlation studies. In *Second Int. Conf. on Earthquake Geotechnical Engineering*, edited by Seco e Pinto, 811-845. Lisbon: Balkema.
- Stokoe, Hwang, Lee, and Andrus. 1995. Effects of various parameters on the stiffness and damping of soils at small to medium strains. In *PRE-FAILURE DEFORMATION OF GEOMATERIALS. PROCEEDINGS OF THE INTERNATIONAL SYMPOSIUM, 12-14 SEPTEMBER 1994, SAPPORO, JAPAN. 2 VOLS.*
- Stokoe II, Cox, Clayton, and Menq. 2020. NHERI@UTexas Experimental Facility With Large-Scale Mobile Shakers for Field Studies, *Frontiers in Built Environment*, 6: 575973.
- Stokoe II, Kurtulus, and Menq. 2004. SASW Measurements at the NEES Garner Valley Test Site, California. In.: The University of Texas at Austin.
- Stokoe, and Santamarina. 2000. Seismic-wave-based testing in geotechnical engineering. In *ISRM International Symposium*. International Society for Rock Mechanics.
- Stoll. 1977. Acoustic waves in ocean sediments, *Geophysics*, 42: 715-725.

- Stoll, and Bryan. 1970. Wave attenuation in saturated sediments, *The Journal of the Acoustical Society of America*, 47: 1440-1447.
- Strobbia. 2003. Surface wave methods. Acquisition, processing and inversion., Politecnico di Torino.
- Strobbia, and Cassiani. 2011. Refraction microtremors: Data analysis and diagnostics of key hypotheses, *Geophysics*, 76: MA11-MA20.
- Strobbia, and Foti. 2006. Multi-offset phase analysis of surface wave data (MOPA), *Journal of Applied Geophysics*, 59: 300-313.
- Strong, Hartog, Hilton, Sanderson, Twohig, Khlybov, Lees, and Kader. 2008. A comprehensive distributed pipeline condition monitoring system and its field trial. In *7th International Pipeline Conference*. IPC2008.
- Sun. 2000. Determination of seismic attenuation from surface and downhole measurements, University of Oklahoma.
- Tao, and Rathje. 2019. Insights into Modeling Small-Strain Site Response Derived from Downhole Array Data, *Journal of Geotechnical and Geoenvironmental Engineering*, 145: 04019023.
- Tarantola. 2004. *Inverse Problem Theory and Methods for Model Estimation* (SIAM).
- Tarantola, and Valette. 1982. Generalized nonlinear inverse problems solved using the least squares criterion, *Reviews of Geophysics*, 20: 219-232.
- Tarczynski, Valimaki, and Cain. 1997. FIR filtering of nonuniformly sampled signals. In *1997 IEEE International Conference on Acoustics, Speech, and Signal Processing*, 2237-2240. IEEE.
- Teague, and Cox. 2016. Site response implications associated with using non-unique Vs profiles from surface wave inversion in comparison with other commonly used methods of accounting for Vs uncertainty, *Soil Dynamics and Earthquake Engineering*, 91: 87-103.
- Teague, Cox, Bradley, and Wotherspoon. 2018a. Development of deep shear wave velocity profiles with estimates of uncertainty in the complex interbedded geology of Christchurch, New Zealand, *Earthquake Spectra*, 34: 639-672.
- Teague, Cox, and Rathje. 2018b. Measured vs. predicted site response at the garner valley downhole array considering shear wave velocity uncertainty from borehole and surface wave methods, *Soil Dynamics and Earthquake Engineering*, 113: 339-355.
- Theodorsen, and Garrick. 1940. Mechanism of Flutter. A theoretical and experimental investigation of the flutter problem. In.: Nation Advisory Committee for Aeronautics.
- Thompson, Baise, Kayen, and Guzina. 2009. Impediments to predicting site response: Seismic property estimation and modeling simplifications, *Bulletin of the Seismological Society of America*, 99: 2927-2949.
- Thompson, Baise, Tanaka, and Kayen. 2012. A taxonomy of site response complexity, *Soil Dynamics and Earthquake Engineering*, 41: 32-43.

- Thomson. 1950. Transmission of elastic waves through a stratified solid medium, *1950*, 21: 89-93.
- Tokimatsu. 1995. Geotechnical site characterization using surface waves. In *1st International Conference on Earthquake Geotechnical Engineering*, 1333-1368. Tokyo, Japan: Balkema.
- Tokimatsu, Shinsawa, and Kuwayama. 1992. Use of short-period microtremors for Vs profiling, *Journal of Geotechnical engineering*, 118: 1544-1558.
- Toksöz, Johnston, and Timur. 1979. Attenuation of seismic waves in dry and saturated rocks: I. Laboratory measurements, *Geophysics*, 44: 681-690.
- Toro. 1995. Probabilistic models of site velocity profiles for generic and site-specific ground-motion amplification studies. In. Upton, New York: Brookhaven National Laboratory.
- Tran, and Hiltunen. 2012. One-dimensional inversion of full waveforms using a genetic algorithm, *Journal of Environmental and Engineering Geophysics*, 17: 197-213.
- Tsai, and Hashash. 2009. Learning of dynamic soil behavior from downhole arrays, *Journal of Geotechnical and Geoenvironmental Engineering*, 135: 745-757.
- Tsai, and Housner. 1970. Calculation of surface motions of a layered half-space, *Bulletin of the Seismological Society of America*, 60: 1625-1651.
- Ugray, Lasdon, Plummer, Glover, Kelly, and Martí. 2007. Scatter Search and Local NLP Solvers: A Multistart Framework for Global Optimization, *INFORMS Journal on Computing*, 19: 328-340.
- Valle-Molina. 2006. Measurements of Vp and Vs in dry, unsaturated and saturated sand specimens with piezoelectric transducers, The University of Texas at Austin.
- Van Pelt. 2010. Predicting settlements of shallow foundations on cohesionless, granular soil using dynamic soil measurements, The University of Texas at Austin.
- Vantassel, and Cox. 2019. Multi-reference-depth site response at the Garner Valley Downhole Array. In *7th International Conference on Earthquake Geotechnical Engineering*. Rome.
- Vantassel, and Cox. 2021a. A procedure for developing uncertainty-consistent Vs profiles from inversion of surface wave dispersion data, *Soil Dynamics and Earthquake Engineering*, 145: 106622.
- Vantassel, and Cox. 2021b. SWinvert: a workflow for performing rigorous 1-D surface wave inversions, *Geophysical Journal International*, 224: 1141-1156.
- Vantassel, Cox, Hubbard, and Yust. 2022. Extracting High-Resolution, Multi-Mode Surface Wave Dispersion Data from Distributed Acoustic Sensing Measurements using the Multichannel Analysis of Surface Waves, 2022.
- Vantassel, Cox, Wotherspoon, and Stolte. 2018. Mapping Depth to Bedrock, Shear Stiffness, and Fundamental Site Period at CentrePort, Wellington, Using Surface-Wave Methods: Implications for Local Seismic Site

- Amplification, *Bulletin of the Seismological Society of America*, 108: 1709-1721.
- Vardanega, and Bolton. 2013. Stiffness of clays and silts: Normalizing shear modulus and shear strain, *Journal of Geotechnical and Geoenvironmental Engineering*, 139: 1575-1589.
- Veletsos, and Meek. 1974. Dynamic behaviour of building-foundation systems, *Earthquake Engineering & Structural Dynamics*, 3: 121-138.
- Verachtert. 2018. Deterministic and probabilistic determination of dynamic soil characteristics, KU Leuven.
- Verachtert, Lombaert, and Degrande. 2017. Multimodal determination of Rayleigh dispersion and attenuation curves using the circle fit method, *Geophysical Journal International*, 212: 2143-2158.
- Viktorov. 1967. *Rayleigh and Lamb waves: physical theory and applications* (Plenum Press: New York).
- Vucetic. 1994. Cyclic threshold shear strains in soils, *Journal of Geotechnical engineering*, 120: 2208-2228.
- Vucetic, and Dobry. 1991. Effect of soil plasticity on cyclic response, *Journal of Geotechnical engineering*, 117: 89-107.
- Walsh. 1966. Seismic wave attenuation in rock due to friction, *Journal of Geophysical Research*, 71: 2591-2599.
- Wang, Cascante, and Santamarina. 2003. Resonant column testing: the inherent counter emf effect, *Geotechnical Testing Journal*, 26: 342-352.
- Wathelet, Guillier, Roux, Cornou, and Ohrnberger. 2018. Rayleigh wave three-component beamforming: signed ellipticity assessment from high-resolution frequency-wavenumber processing of ambient vibration arrays, *Geophysical Journal International*, 215: 507-523.
- Wathelet, Jongmans, and Ohrnberger. 2004. Surface-wave inversion using a direct search algorithm and its application to ambient vibration measurements, *Near Surface Geophysics*, 2: 211-221.
- Weemstra, Boschi, Gorertz, and Artman. 2012. Seismic attenuation from recordings of ambient noise, *Geophysics*, 78: 1-14.
- Weemstra, Westra, Snieder, and Boschi. 2014. On estimating attenuation from the amplitude of the spectrally whitened ambient seismic field, *Geophysical Journal International*, 197: 1770-1788.
- Winkler, and Nur. 1982. Seismic attenuation: effects of pore fluids and frictional sliding, *Geophysics*, 47: 1-15.
- Wood, and Cox. 2012. A comparison of MASW dispersion uncertainty and bias for impact and harmonic sources. In *GeoCongress 2012: State of the Art and Practice in Geotechnical Engineering*, 2756-2765.
- Woods. 1978. Measurement of dynamic soil properties. In *ASCE Geotechnical Engineering Division Specialty Conference*. Pasadena, California.
- Wu. 1985. Multiple scattering and energy transfer of seismic waves, separation of scattering effect from intrinsic attenuation, *Geophysical Journal of the Royal Astronomical Society*, 82: 57-80.

- Xia, Miller, and Park. 1999. Estimation of near-surface shear-wave velocity by inversion of Rayleigh waves, *Geophysics*, 64: 691-700.
- Xia, Miller, Park, and Tian. 2002. Determining Q of near-surface materials from Rayleigh waves, *Journal of Applied Geophysics*, 51: 121-129.
- Xia, Xu, and Miller. 2007. Generating an image of dispersive energy by frequency decomposition and slant stacking, *Pure and Applied geophysics*, 164: 941-956.
- Xia, Xu, Miller, and Ivanov. 2012. Estimation of near-surface quality factors by constrained inversion of Rayleigh-wave attenuation coefficients, *Journal of Applied Geophysics*, 82: 137-144.
- Xu, Rathje, Hashash, Stewart, Campbell, and Silva. 2019.  $\kappa_0$  for Soil Sites: Observations from Kik-net Sites and Their Use in Constraining Small-Strain Damping Profiles for Site Response Analysis, *Earthquake Spectra*: 0000-0000.
- Yang, Qi, Pavlin, Dureli, and Esteva. 1989. In-situ determination of soil damping in the lake deposit area of Mexico City, *Soil Dynamics and Earthquake Engineering*, 8: 43-52.
- Yavuz, Freifeld, Pevzner, Tertyshnikov, Dzunic, Ziramov, Shulakova, Robertson, Daley, Kepic, Urosevic, and Gurevich. 2016. Subsurface imaging using buried DAS and geophone arrays-preliminary results from CO2CRC Otway Projec. In *78th EAGE Conference and Exhibition 2016*, edited by European Association of Geoscientists & Engineers.
- Yee, Stewart, and Tokimatsu. 2013. Elastic and large-strain nonlinear seismic site response from analysis of vertical array recordings, *Journal of Geotechnical and Geoenvironmental Engineering*, 139: 1789-1801.
- Yoon. 2005. Array-based measurements of surface wave dispersion and attenuation using frequency-wavenumber analysis, Georgia Institute of Technology.
- Yoon, and Rix. 2009. Near-field effects on array-based surface wave methods with active sources, *Journal of Geotechnical and Geoenvironmental Engineering*, 135.
- Zalachoris, and Rathje. 2015. Evaluation of one-dimensional site response techniques using borehole arrays, *Journal of Geotechnical and Geoenvironmental Engineering*, 141: 04015053.
- Zhang, Andrus, and Juang. 2005. Normalized shear modulus and material damping ratio relationships, *Journal of Geotechnical and Geoenvironmental Engineering*, 131: 453-464.
- Zywicki. 1999. Advanced signal processing methods applied to engineering analysis of seismic surface waves, Georgia Institute of Technology.
- Zywicki. 2007. The impact of seismic wavefield and source properties on ReMi estimates. In *Innovative Applications of Geophysics in Civil Engineering*, 1-10.

Zywicki, and Rix. 2005. Mitigation of Near-Field Effects for Seismic Surface Wave Velocity Estimation with Cylindrical Beamformers, *Journal of Geotechnical and Geoenvironmental Engineering*, 131: 970-977.